Vector Meson Production and Nucleon Resonance Analysis in a Coupled-Channel Approach

Inaugural-Dissertation
zur
Erlangung des Doktorgrades
der Naturwissenschaftlichen Fakultät
der Justus-Liebig-Universität Gießen
Fachbereich 07 – Mathematik, Physik, Geographie

vorgelegt von
Gregor Penner
aus Gießen

Gießen, 2002

D 26
Dekan: Prof. Dr. Albrecht Beutelspacher
I. Berichterstatter: Prof. Dr. Ulrich Mosel
II. Berichterstatter: Prof. Dr. Volker Metag
Tag der mündlichen Prüfung:

Contents

Chapter 1

Introduction

> *"Nucleons are the stuff of which our world is made. As such they must be at the center of any discussion of why the world we actually experience has the character it does."*
> Nathan Isgur, *Why N^*'s are Important*, overview talk at N*2000 Conference, Thomas Jefferson Laboratory, Newport News, VA/USA, 16-19 Febr. 2000.
>
> *"One very powerful way of experimentally investigating the strongly interacting particles (hadrons) is to look at them, to probe them with a known particle; in particular the photon (no other is known as well). This permits a much finer control of variables, and probably decreases the theoretical complexity of the interactions."*
> Richard Feynman, *Photon-Hadron Interactions*, Addison-Wesley Pub., Reading/MA, 1998.

One of the major quests of contemporary theoretical physics is the search for a quantum field-theoretical description of all phenomena observed in nature. A major milestone towards this goal was the unification of the electromagnetic and weak force in the 1960s and 70s by the electroweak theory due to Salam and Weinberg, soon followed by Quantum Chromodynamics (QCD), the generally accepted field theory underlying the strong force which holds together the nucleons. To date, only the gravitational force has resisted a description within a unified quantum field-theoretical framework.

The success of the field-theoretical description of the subatomic world is based on the overwhelming predictive power of the electroweak theory, and in particular of Quantum Electrodynamics (QED). The smallness of the electromagnetic fine structure constant α_{em} allows for an expansion of the theory in powers of α_{em}, called "perturbation theory". Upon application of this powerful tool, the electromagnetic field theory has passed up to now all experimental tests with impressive accuracy.

At sufficiently high energies, QCD exhibits a perturbative nature similar to QED: The color coupling constant of QCD α_S becomes small, which is called "asymptotic freedom". Therefore, at these energies, quarks, which are subjected to the strong force, act as if they could be described by a free theory, giving rise to the applicability of constituent quark models. In contrast to the electromagnetic force, however, the color coupling becomes large at low energies, thereby "confining" the quarks permanently into the known hadrons and preventing QCD from being accessible by perturbation theory. A compelling description of QCD in this region could be achieved through Wilson's lattice gauge theory [193]. Wilson showed how to quantize a gauge field theory as QCD on a discrete four dimensional lattice in Euclidean space-time, while preserving exact gauge invariance and having a a computable strong-coupling limit. Thus the extraction of qualitative non-perturbative information concerning QCD became possible. In the absence of analytic solutions to QCD, lattice gauge theories today provide the most promising approach for theoretical predictions of properties of the hadronic ground states and also of their excited states. However, due to the enormous computational power necessary for the numerical treatment, lattice QCD has only started to be able to describe baryon resonance masses and decay widths (see, e.g., [196, 107, 154]). This gave rise to the development of a large number of quark models of hadrons (e.g. [17, 24, 151, 171]), aiming at the prediction of the properties of the hadrons by reducing the complexity of the strongly self-interacting multi-quark-gluon system to an effective two- or three-quark system.

On the experimental side, the low-energy behavior of QCD can not be adressed directly. The investigation of the inner structure of hadrons can only be achieved in a controlled way by exciting the nucleon with the help of a hadronic (meson) or an electromagnetic (photon or electron) probe. However, due to the extremely short lifetime of the excited hadron states, only the measurement of their decay products is possible. Consequently, the experiments for analyzing nucleon resonances have focussed on meson production off the nucleon. While for the meson-induced reactions, most of the experiments have been performed from the 1960s to the 1980s, the development of high-duty beams and detectors in the last decade has led to the collection of an increasing amount of photon-induced data. Ongoing experiments are being performed at facilities in Mainz/Germany (TAPS Collaboration), Bonn/Germany (SAPHIR, TAPS/Crystal Barrel Collaboration), Grenoble/France (GRAAL Collaboration), Newport News/USA (CLAS Collaboration at JLAB), Brookhaven/USA (LEGS Collaboration), and Hyogo/Japan (LEPS Collaboration at SPring-8). All these experiments concentrate on measuring meson photoproduction off the nucleon with the main purpose to provide information for the study of nucleon resonances up to center-of-mass energies of $\sqrt{s} \approx 2$ GeV.

Since (lattice) QCD calculations are still far from being amiable to solutions for low and intermediate energy scattering reactions, it is necessary to use effective methods for the description of the dynamical structure of these processes. Such effective methods account for the inner structure of the baryons by introducing explicit baryon resonance states, whose properties are extracted by comparison with the experimental observables. The goal is to be finally able to compare the extracted masses and partial decay widths to the predictions from lattice QCD and/or quark models.

Basically all information about nucleon resonances identified so far from experiment in this way stems from partial wave analyses of $\gamma N \to \pi N$ and $\pi N \to \pi N$ (to some degree also from $2\pi N$ production). This also explains why these resonance states are usually labeled by the πN relative orbital angular momentum L, the total isospin I, and the total angular momentum J. The present situation in comparison with the quark model predictions of Capstick et al. [24] is depicted in Figs. 1.1 and 1.2. For some of these

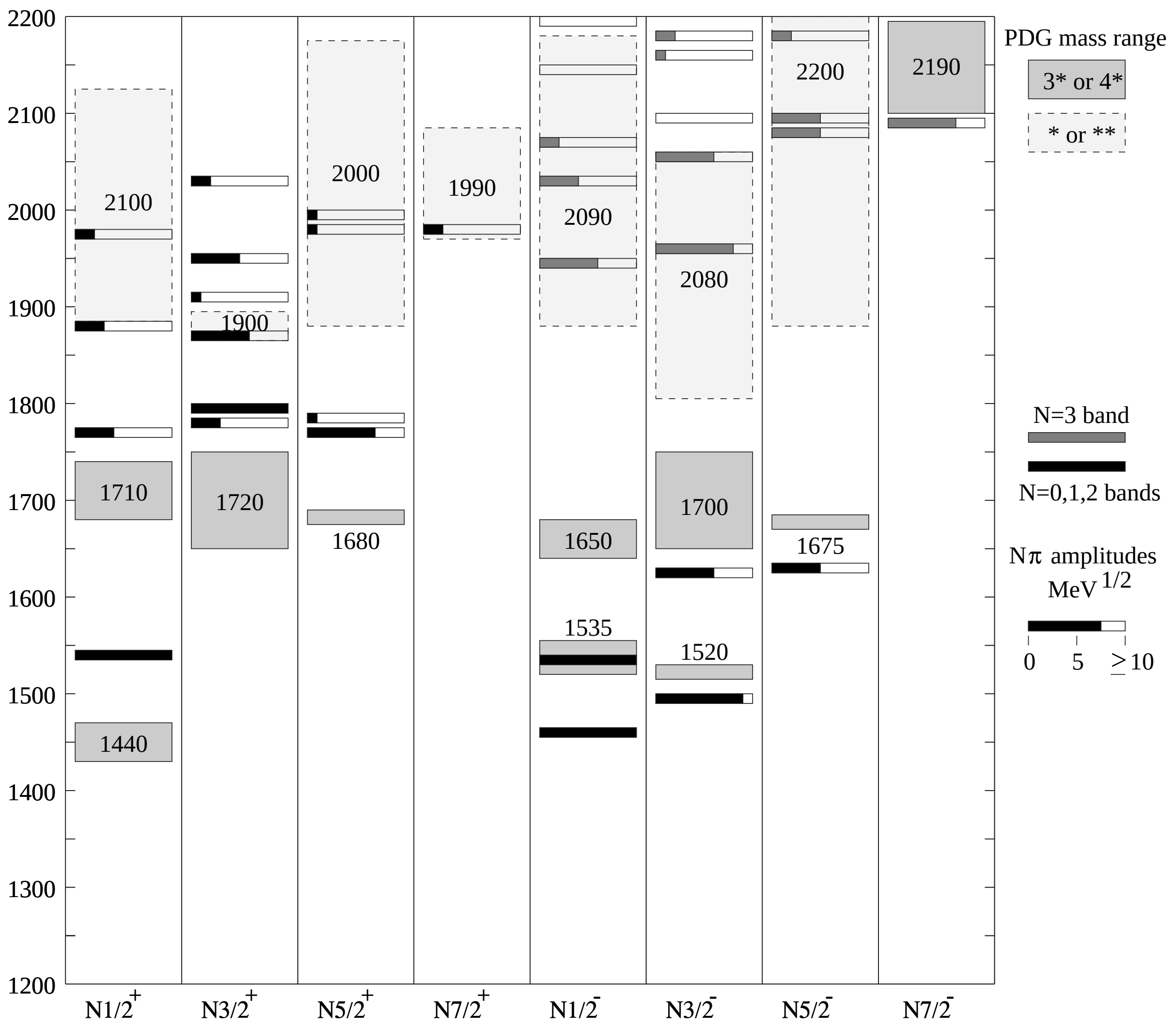

Figure 1.1: Calculated masses and πN decay amplitudes for nucleon ($I = \frac{1}{2}$) resonances below 2.2 GeV from the quark model of Capstick et al. [24], compared to the range of central values for resonances masses from the particle data group (PDG) [67], which are shown as boxes. The boxes are lightly shaded for one and two star states and heavily shaded for three and four star states (cf. Table 3.2 in Chapter 3). Predicted masses are shown as a thin bar, with the length of the shaded region indicating the size of the πN amplitude. Figure taken from Ref. [23].

resonances, as e.g. the $L_{(2I)(2J)} = P_{33}(1232)$ resonance (in brackets, the estimated mass is given) dominating low-energy πN scattering, the various analyses agree rather well in the extracted masses, total, πN and $2\pi N$ widths, while for others as the $S_{11}(1535)$ or the second and third resonance in a partial wave there are still large discrepancies. In the specific case of the $S_{11}(1535)$ the reason for the discrepancies is its closeness to the ηN threshold, which has a strong influence on the $\pi N \to \pi N$ reaction due to unitarity. This example already shows, that in many cases the simultaneous consideration of further final states, a so-called "coupled-channel analysis", for the resonance analysis is necessary. On the other

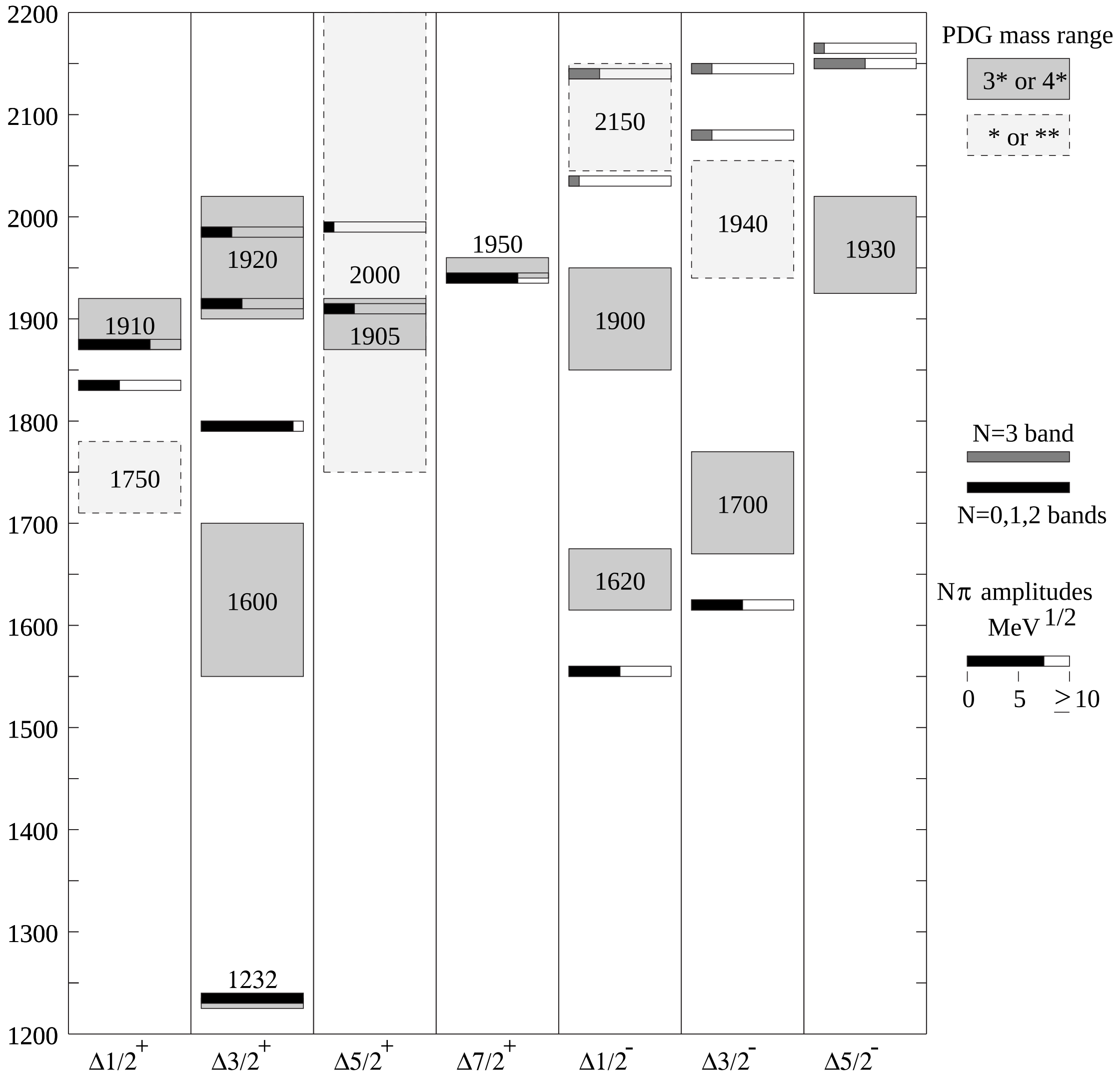

Figure 1.2: Calculated masses and πN decay amplitudes for Δ $(I = \frac{3}{2})$ resonances below 2.2 GeV from the quark model of Capstick et al. [24], compared to the range of central values for resonances masses from the particle data group [67]. Notation as in Fig. 1.1. Figure taken from Ref. [23].

side, quark models predict a much richer resonance spectrum than has been found in πN production so far, giving rise to speculations that many of these resonance states only become visible in other reaction channels. This has been the basis for a wealth of analyses concentrating on identifying these “missing” or “hidden” resonances in the production of other final states as ηN, $K\Lambda$, $K\Sigma$, or ωN. However, almost all of these analyses concentrate on one specific channel thereby neglecting the influence of the extracted resonance properties on other channels. Therefore, there is a strong need in the field of nucleon resonance analysis for a model that allows to consider and analyze all important reaction channels simultaneously. At the same time, this requires the determination of a priori unknown couplings and masses of a large number of resonances (cf. Table 3.2 in Chapter 3). The premise for the reliable extraction of these properties is therefore to develop a model, that not only analyses all production mechanisms simultaneously for as large an energy range as possible, but also consistently uses the *same Lagrangian* to describe the reaction mechanism of both the pion- *and* photon-induced reactions, thereby generating all non-resonant contributions dynamically from Born, u-, and t-channel contributions without new parameters. Since it is generally accepted that strong interactions are described by QCD, an effective theory describing meson-nucleon scattering reactions should ideally be derived from and therefore mirror as well as possible the properties of the fundamental theory QCD. Thus it should satisfy the same symmetries, while the degrees of freedom are mesons and baryons rather than quarks and gluons. For πN production, this mandates the conformity with chiral symmetry, which is known to be important for low-energy pion-nucleon physics.

The way towards a simultaneous analysis of all reaction channels respecting the above constraints has been paved by Feuster and Mosel [51, 52, 53], who have included in their resonance analysis up to center-of-mass energies of 1.9 GeV the production of γN, πN, $2\pi N$, ηN, and $K\Lambda$ off the nucleon using a unitary, effective Lagrangian framework. One of the major conclusions has been that indeed, the additional inclusion of high quality photoproduction data is inevitable for a reliable extraction of resonance masses and widths. However, due to the neglect of the contribution of the important vector meson final state ωN, the model had to put up with some discrepancies in the simultaneous description of the included channels at higher energies (see Chapter 3).

Consequently, this model is extended in the present work to also include the ωN final state, thereby allowing for a more reliable analysis of the properties of higher lying resonances. This final state has not yet been included consistently and to its full complexity in a coupled-channel analysis. The hitherto developed models have mostly considered the ωN state only separately, leaving the calculation rather unconstrained. This situation changes completely once the ωN production is considered in a choupled-channel approach, since due to unitarity any change in the ωN description immediately affects all other channels, in particular the πN production mechanism.

Vector meson production off the nucleon, however, is also of special interest by itself. Due to the electromagnetic decay of vector mesons into lepton pairs they represent an ideal probe to investigate the properties of hot and dense matter in heavy ion collisions. Since the leptons only interact by the electroweak force, their measurement allows a direct access to the influence of the surrounding medium on the vector mesons' properties and thereby the strongly interacting environment itself. In fact, the observed enhancement of the dilepton yield at small invariant dilepton masses in ultrarelativistic heavy ion collisions [25] is currently interpreted as a modification of the mass and width of the ρ vector meson in nuclear matter. For reliable and conclusive investigations of such QCD phenomena, the understanding of the underlying fundamental process of vector meson production in the vacuum is of vital importance. Experimentally, explorations in this direction will be realized by analyzing dilepton production with the spectrometer HADES at GSI in Darmstadt/Germany.

As pointed out above, a theoretical investigation of higher lying resonances and vector meson production requires the minimization of ambiguities by incorporating coupled-channel effects and simultaneously considering all possible reaction channels. In this thesis, the extended coupled-channel model, fulfilling all the aforementioned constraints, is presented and discussed in full detail. In the second Chapter of this work, the fundamental field-theoretical equation, the Bethe-Salpeter equation, which defines the unitary and analytic framework for the description of all underlying two-particle scattering processes, is discussed. The approximation to this equation, the so-called "K-matrix Born approximation", which is used in the present model, is introduced and its consequences are compared with other approximations. The following Chapter 3 concentrates on the final states, which have to be implemented in a unitary framework, and how this implementation is realized in the present and also in other works. For the inclusion of the photoproduction mechanism in the model, it is imperative to account for the hadronic substructure of background (Born) terms while properly maintaining gauge invariance in order to unambigously separate the resonance from background contributions. This is also discussed in Chapter 3.

The consideration of rescattering effects requires a partial-wave decomposition of all included reaction processes. A natural and straightforward generalization of the standard $\pi N \to \pi N$ partial-wave decomposition is presented in Chapter 4. This generalization allows for a uniform treatment and therefore the analysis and decomposition of any meson- and photon-baryon reaction on an equal footing. In Chapters 5 and 6, the formalism for the calculation of the spin-dependent amplitudes in all channels is presented. Moreover, a comparison is made between the partial waves resulting from our method and techniques used in other works. The data base, which is used for the extraction of the nucleon resonance properties is introduced in Chapter 7 and its treatment in view of balancing the various channels is discussed. Chapter 8 contains the results of the calculations performed for the extraction of a best description of the experimental data base. These results are discussed and also compared with extractions from other models.

Chapter 2

The Bethe-Salpeter Equation and the K-Matrix Approximation

The aim of this chapter is to set the framework for the determination of the scattering amplitude, which forms the basis for the extraction of any observable. General details of the underlying formal scattering theory are given in Appendix C and discussed extensively in the literature (e.g. [18, 56, 61, 82, 88, 144, 153]). In the processes considered in the present work, accounting for physical constraints such as relativistic invariance, unitarity, analyticity, and gauge invariance is essential. In the following, the Bethe-Salpeter (BS) equation for the scattering amplitude, which automatically leads to a two-particle scattering amplitude fulfilling the first three constraints, is derived and the useful K-matrix Born approximation is presented. The last constraint of analyticity and to which degree the BS equation is approximated in the present and other models are also discussed in the next Chapter 3.

2.1 Bethe-Salpeter Equation

When one deals with strong interactions one faces the problem of iterating the interaction potential. Due to the large couplings an expansion in orders of the potential becomes questionable. The BS equation [15] represents a possibility for summing the "ladder" contributions of the potential to the scattering amplitudes to all orders, cf. Fig. 2.1, while analyticity and two-particle unitarity are maintained. The only assumption entering the derivation of the scattering matrix is that all higher-order crossed diagrams are included in

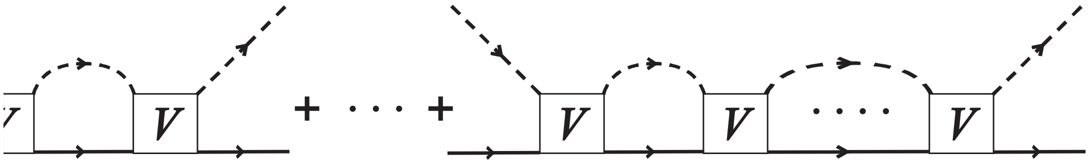

Figure 2.1: "Ladder" contributions to the amplitude $\mathcal{M}$.

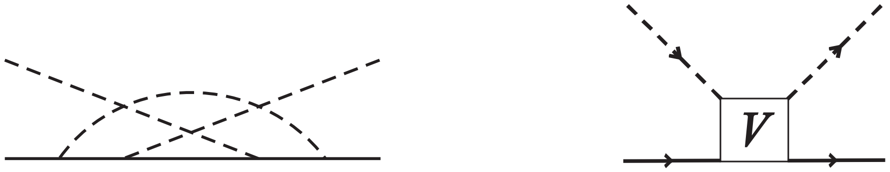

Figure 2.2: *Left:* Example of a higher-order crossed diagram neglected in the present model. *Right:* First order amplitude $\mathcal{M}^{(1)}$.

the potential V. In an effective Lagrangian model for the potential V as the one presented in Chapter 3, however, it is not possible to include all those diagrams. Therefore, only lowest order crossed diagrams (u-channel) are considered within the iteration, while the higher-order ones, as, e.g., the one shown in Fig. 2.2, are assumed to be negligible within the ladder summation.

In the following, we work in the center-of-mass (c.m.) kinematics and use two-particle asymptotic states $|\boldsymbol{p}\,\boldsymbol{k}\,,\lambda\rangle \equiv |i\rangle$ as given in Appendix A. Starting with the first order amplitude (cf. Fig. 2.2)

$$\mathcal{M}^{(1)} \equiv \langle f|M^{(1)}|i\rangle = \langle f|V|i\rangle \equiv \mathcal{V}^{fi} \tag{2.1}$$

containing all two-particle irreducible Feynman diagrams, one finds by applying standard Feynman rules [18, 82] for writing down the second order ladder (square) contribution of the potential V (see left graph in Fig. 2.1)

$$\langle f|M^{(2)}(p',p;\sqrt{s})|i\rangle = \int \frac{d^4q}{(2\pi)^4} \sum \langle f|V(p',q;\sqrt{s})\mathrm{i}G_{B_q}(q;\sqrt{s})\mathrm{i}G_{M_q}(q;\sqrt{s})V(q,p;\sqrt{s})|i\rangle \ , \tag{2.2}$$

where the sum runs over all allowed intermediate two-particle states. The lower index q is introduced to denote the properties of these states, since they can in general be different from the final states (e.g. $\pi N \to K\Lambda \to \pi N$). Furthermore, in Eq. (2.2) the intermediate baryon and meson propagators G_B and G_M have been introduced in the standard way, e.g. for a spin-$\frac{1}{2}$ baryon and a spin-0 meson:

$$\begin{aligned} G_{B_q}(q;\sqrt{s}) &= \frac{(\frac{1}{2}\sqrt{s}-q^0)\gamma_0 + \boldsymbol{q}\cdot\boldsymbol{\gamma} + m_{B_q}}{(\frac{1}{2}\sqrt{s}-q^0)^2 - \boldsymbol{q}^{\,2} - m_{B_q}^2 + \mathrm{i}\varepsilon} = \frac{2m_{B_q}\sum_{\lambda_{B_q}} u(p_q,\lambda_{B_q})\bar{u}(p_q,\lambda_{B_q})}{(\frac{1}{2}\sqrt{s}-q^0)^2 - \boldsymbol{q}^{\,2} - m_{B_q}^2 + \mathrm{i}\varepsilon} \\ G_{M_q}(q;\sqrt{s}) &= \frac{1}{(\frac{1}{2}\sqrt{s}+q^0)^2 - \boldsymbol{q}^{\,2} - m_{M_q}^2 + \mathrm{i}\varepsilon'} \ . \end{aligned} \tag{2.3}$$

The intermediate momenta are routed symmetrically with respect to the total four-momentum $P = (\sqrt{s},\boldsymbol{0}\,)$ in the c.m. system:

$$k_q = P/2 + q \qquad \text{and} \qquad p_q = P/2 - q \ . \tag{2.4}$$

Although we have introduced specific intermediate particle propagators (i.e. those of a spin-$\frac{1}{2}$ baryon and a spin-0 meson), the following derivations are valid for any meson-baryon intermediate state and only refer to the denominators in (2.3). For convenience,

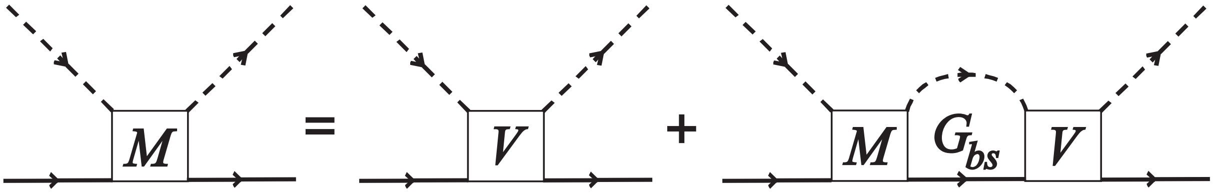

Figure 2.3: Bethe-Salpeter equation for the two-particle scattering amplitude $\mathcal{M}$.

in all the equations below the summation over the intermediate states in the rescattering part and the dependence of all quantities on the c.m. energy $\sqrt{s}$ are omitted and to be understood implicitly.

Looking at Eqs. (2.1) and (2.2), an implicit expression for summing up all orders in V is obvious:

$$\langle f|M(p',p)|i\rangle \;=\; \langle f|V(p',p)|i\rangle + \int \frac{d^4q}{(2\pi)^4}\langle f|M(p',q)\mathrm{i}G_B(q)\mathrm{i}G_M(q)V(q,p)|i\rangle .$$

Introducing the Bethe-Salpeter propagator

$$G_{BS}(q;\sqrt{s}) \;\equiv\; \mathrm{i}G_B(q;\sqrt{s})G_M(q;\sqrt{s}) \tag{2.5}$$

one arrives at the famous Bethe-Salpeter equation

$$\langle f|M(p',p)|i\rangle \;=\; \langle f|V(p',p)|i\rangle + \int \frac{d^4q}{(2\pi)^4}\langle f|M(p',q)G_{BS}(q)V(q,p)|i\rangle \;, \tag{2.6}$$

which is depicted in Fig. 2.3.

An equivalent formulation of the BS equation is achieved when the integration is split up into two steps. In the first step a $\tilde{K}$-matrix is introduced by the integration over the real (principal value) part of the BS propagator:

$$\langle f|\tilde{K}(p',p)|i\rangle \;=\; \langle f|V(p',p)|i\rangle + \int \frac{d^4q}{(2\pi)^4}\langle f|\tilde{K}(p',q)\mathrm{Re}\left(G_{BS}(q)\right)V(q,p)|i\rangle \;. \tag{2.7}$$

Now the matrix element $\mathcal{M} = \langle f|M(p',p)|i\rangle$ of the scattering matrix M is given by the integration over the imaginary part of the BS propagator:

$$\langle f|M(p',p)|i\rangle \;=\; \langle f|\tilde{K}(p',p)|i\rangle + \int \frac{d^4q}{(2\pi)^4}\langle f|M(p',q)\mathrm{i}\mathrm{Im}\left(G_{BS}(q)\right)\tilde{K}(q,p)|i\rangle \;, \tag{2.8}$$

which is easily proven by plugging in (2.7). The advantage of this formulation will become clear after a short look at the imaginary part of the BS propagator. As shown in Appendix D.2 it acts under the integral $\int \mathrm{d}^4q = \int \mathrm{d}q_0\mathrm{q}^2\mathrm{d}\mathrm{q}\mathrm{d}\Omega_q$ as

$$\begin{aligned} &\int \mathrm{d}^4q\,\mathrm{i}\mathrm{Im}\left(G_{BS}(q)\right) \\ =\;& \int \mathrm{d}^4q\left[-\mathrm{i}\pi^2\frac{m_{B_q}\sum_{\lambda_{B_q}}u(p_q,\lambda_{B_q})\bar{u}(p_q,\lambda_{B_q})}{\mathrm{q}\sqrt{s}}\delta(q^0+\sqrt{s}/2-E_{M_q})\delta(\mathrm{q}-\hat{\mathrm{q}})\right] \;. \end{aligned} \tag{2.9}$$

Here, $\hat{\mathrm{q}}$ is the c.m. three-momentum of the intermediate state when both particles are on their mass shell. Taking advantage of this property of the imaginary part we arrive at the two-dimensional BS equation:

$$\langle f|M(p',p)|i\rangle \;=\; \langle f|\tilde{K}(p',p)|i\rangle - \frac{\mathrm{i}\,\hat{\mathrm{q}}\, m_{B_q}}{(4\pi)^2\sqrt{s}} \int \mathrm{d}\Omega_q \sum_{\lambda_q} \langle f|M(p',q)|q\rangle\langle q|\tilde{K}(q,p)|i\rangle \tag{2.10}$$

with the intermediate two-particle momentum state $|q\rangle = |\boldsymbol{p}_q \boldsymbol{k}_q, \lambda_q\rangle$. Introducing the $\mathcal{T}$- and $\mathcal{K}$-amplitudes (cf. Appendix C)

$$\begin{aligned} \mathcal{T}^{fi}_{\lambda'\lambda} &\equiv -\frac{\sqrt{\mathrm{p}\mathrm{p}' m_{B'} m_B}}{(4\pi)^2\sqrt{s}} \langle f|M(p',p)|i\rangle \\ \mathcal{K}^{fi}_{\lambda'\lambda} &\equiv -\frac{\sqrt{\mathrm{p}\mathrm{p}' m_{B'} m_B}}{(4\pi)^2\sqrt{s}} \langle f|\tilde{K}(p',p)|i\rangle \;, \end{aligned}$$

Equation (2.10) simplifies to

$$\mathcal{T}^{fi}_{\lambda'\lambda} = \mathcal{K}^{fi}_{\lambda'\lambda} + \mathrm{i} \int \mathrm{d}\Omega_q \sum_{\lambda_q} \mathcal{T}^{fq}_{\lambda'\lambda_q} \mathcal{K}^{qi}_{\lambda_q\lambda} \;. \tag{2.11}$$

As shown in Chapter 4 this equation can be further simplified for parity conserving and rotationally invariant interactions by a decomposition into partial waves and one arrives at an algebraic equation relating the decomposed $\mathcal{T}^{fi}$and $\mathcal{K}^{fi}$:

$$\mathcal{T}^{IJ\pm}_{fi} = \left[\frac{\mathcal{K}^{IJ\pm}}{1 - \mathrm{i}\mathcal{K}^{IJ\pm}}\right]_{fi} \;. \tag{2.12}$$

Here, we have in addition introduced the decomposition into amplitudes of total isospin I ($I = \frac{1}{2}$ or $I = \frac{3}{2}$), see Appendix F.

Although the full isospin decomposition of the photon-induced amplitudess including Compton scattering can in principle be easily achieved (see Appendices F.1.2 and F.2.1), one runs into problems concerning gauge invariance of Compton scattering. This is due to the fact that the rescattering takes place via the $I = \frac{1}{2}$ and $I = \frac{3}{2}$ amplitudes thus weighing the Compton isospin amplitudes $T^{11,\frac{1}{2}}_{\gamma\gamma}$ with $I = \frac{1}{2}$ and $T^{11,\frac{3}{2}}_{\gamma\gamma}$ with $I = \frac{3}{2}$ (cf. Eq. (F.21)) differently, while gauge invariance for the nucleon contributions is only fulfilled for the proton and neutron amplitude (more precisely, for the combination $T^{11,\frac{1}{2}}_{\gamma\gamma} + 2T^{11,\frac{3}{2}}_{\gamma\gamma}$, see Appendix F.2.2). Consequently, the electromagnetic interaction is included only perturbatively in the present calculation. The perturbative inclusion is equivalent to neglecting all intermediate electromagnetic states a in the rescattering part of Equation (2.11). Due to the smallness of the fine structure constant α, this approximation is reasonable. The consequence is that the calculation of the hadronic reactions decouples from the electromagnetic ones and can be extracted independently. Hence, the full K-matrix equation (2.12) is only solved for the hadronic states. In the second step, the meson-photoproduction amplitudes can be extracted via

$$\mathcal{T}^{IJ\pm}_{f\gamma} = \mathcal{K}^{IJ\pm}_{f\gamma} + \mathrm{i} \sum_{a} \mathcal{T}^{IJ\pm}_{fa} \mathcal{K}^{IJ\pm}_{a\gamma} \;. \tag{2.13}$$

The sum over a runs only over hadronic states. Finally, the Compton amplitudes result from

$$\mathcal{T}^{IJ\pm}_{\gamma\gamma} = \mathcal{K}^{IJ\pm}_{\gamma\gamma} + \mathrm{i}\sum_a \mathcal{T}^{IJ\pm}_{\gamma a}\mathcal{K}^{IJ\pm}_{a\gamma} \tag{2.14}$$

with a running again only over hadronic states. Since the Compton isospin amplitudes of the potential only enter in the direct contribution $\mathcal{K}^{IJ\pm}_{\gamma\gamma}$ and only the proton and neutron Compton amplitudes of Eq. (F.22) are of interest, gauge invariance is fulfilled. This is also discussed in some more detail in Appendix F.2.2.

2.2 Unitarity and the K-Matrix Approximation

Apart from the appealing simplicity of Eq. (2.12), the introduction of the $\tilde{K}$-matrix in (2.7) leads to a further advantage concerning the proper treatment of unitarity in the scattering problem.

From the unitarity of the scattering matrix $SS^\dagger = S^\dagger S = 1$ follows the optical theorem under the assumption of two-particle unitarity (see Appendix C.2):

$$\begin{aligned}\langle f|M(p',p) \; &- \; M^\dagger(p,p')|i\rangle \\ &= \; -\mathrm{i}\int \mathrm{d}^4q\,\delta(\sqrt{s}/2 - E_{B_q} - q_0)\delta(\sqrt{s}/2 - E_{M_q} + q_0)\frac{2m_{B_q}}{(4\pi)^2 E_{B_q}E_{M_q}} \times \\ &\qquad\qquad \langle f|M(p',q)\sum_{\lambda_{B_q}} u(p_q,\lambda_{B_q})\bar{u}(p_q,\lambda_{B_q})M^\dagger(p,q)|i\rangle \; .\end{aligned}$$

On the other hand, one can derive from the BS equation the relation (see Appendix D.1):

$$\langle f|M(p',p) - M^\dagger(p,p')|i\rangle \;\; = \;\; \int \frac{d^4q}{(2\pi)^4}\langle f|M(p',q)2\mathrm{iIm}\left(G_{BS}(q)\right)M^\dagger(p,q)|i\rangle \; .$$

Comparing these two equations, one sees that to preserve unitarity any two-particle propagator can be used in the BS equation as long as its imaginary part acts under the integral $\int \mathrm{d}^4q = \int \mathrm{d}q_0\mathrm{q}^2\mathrm{dq}\mathrm{d}\Omega_q$ in the same way as the BS propagator (cf. Eq. (2.9)), i.e. as

$$\begin{aligned}&\int \mathrm{d}^4q\mathrm{iIm}\left(G_{BS}(q)\right) \\ &= \int \mathrm{d}^4q\left[-\mathrm{i}\pi^2\frac{m_{B_q}\sum_{\lambda_{B_q}} u(p_q,\lambda_{B_q})\bar{u}(p_q,\lambda_{B_q})}{E_{B_q}E_{M_q}}\delta(k^0_q - E_{M_q})\delta(p^0_q - E_{B_q})\right] \; ,\end{aligned}$$

where Eq. (2.4) has been used. Looking back at (2.7) shows, that one can carry out approximations in the $\tilde{K}$-matrix by modifying the real part of the two-particle propagator without violating unitarity. Thus, the simplest choice for the two-particle propagator, that still preserves unitarity, is the so called "K-matrix propagator":

$$\begin{aligned}G_K(q;\sqrt{s}) \;\; &\equiv \;\; \mathrm{iIm}(G_{BS}(q)) \\ &= \;\; -\mathrm{i}\pi^2\frac{m_{B_q}\sum_{\lambda_{B_q}} u(p_q,\lambda_{B_q})\bar{u}(p_q,\lambda_{B_q})}{E_{B_q}E_{M_q}}\delta(k^0_q - E_{M_q})\delta(p^0_q - E_{B_q}) \qquad (2.15) \\ &= \;\; -\mathrm{i}(2\pi)^2 m_{B_q}\sum_{\lambda_{B_q}} u(p_q,\lambda_{B_q})\bar{u}(p_q,\lambda_{B_q})\delta(k^2_q - m^2_{M_q})\delta(p^2_q - m^2_{B_q})\Theta(k^0_q)\Theta(p^0_q) \; ,\end{aligned}$$

where the first equality refers to the action under the integral $\int \mathrm{d}^4q$. The last equality shows that the K-matrix propagator simply sets the intermediate particles on their mass shell. This is equivalent to setting $\mathrm{Re}G_{BS} = 0$ thus completely ignoring the integral part in Eq. (2.7). Then the equation for the $\tilde{K}$-matrix reduces to

$$\tilde{K}(p', p) = V(p', p) \ , \tag{2.16}$$

which is the so-called *K-matrix Born approximation*. However, even though two-particle unitarity is fulfilled in this approximation, the complete relation between the real and imaginary part of the amplitude is lost and analyticity is violated, because the real part of the BS propagator is neglected. It has been shown by Pearce and Jennings [139], however, that the contributions of G_{BS} to the principal value part of the scattering equation are of minor importance, since they have to be reduced by a very soft cutoff dictated by experimental data. This leads to noticeable differences between a fully analytic and a K-matrix calculation only very close to thresholds (see also Section 8.4.1). It has also been argued by Goudsmit et al. [63], that for πN scattering the main effect of the real part of the intermediate loop integrals is a renormalization of the coupling constants and masses of the involved particles, which can therefore be taken to be physical values in the K-matrix Born approximation. See also Section 3.2.

A glance at Eq. (2.12) reveals, that the proper treatment of unitarity in the scattering problem can also be addressed in a more direct way. Since the scattering matrix S and the transition matrix T are related by (cf. Appendix C)

$$S_{fi} \equiv 1 + 2\mathrm{i}T_{fi} \ , \tag{2.17}$$

any T matrix, which is extracted via (2.12) from a *Hermitian* K-matrix, fulfills unitarity. Therefore, in the literature, many other approximations to the BS Equation (2.6) preserving unitarity can be found (see also Section 3.1). Many of these approximations reduce the four-dimensional BS Equation (2.6) to a three-dimensional Lippmann-Schwinger equation, thus accounting for analyticity to some extent. However, due to technical feasibility, most of them are restricted to elastic pion-nucleon scattering, while only a few ones also include inelastic channels. A general problem of the $3D$ reduction is the way how the reduction is performed. There is no unique method [68]; it can even be shown, that the $3D$ reduction can be achieved in an infinite number of ways, all of which satisfy Lorentz invariance and elastic two-body unitarity [195].

Chapter 3

The Model

Due to unitarity, a problem arises in the treatment of scattering reactions. If there is more than one important channel energetically allowed, the various channels can influence each other in different ways. Graphically, this means that flux can go away from one reaction channel into another one, leading to significant effects especially at thresholds. A well established observation is, e.g., the influence of the ηN threshold on πN scattering, cf. Fig. 3.1. Without the ηN threshold cusp, the sudden change in slope of the real part of the $IJ^P = \frac{1}{2}\frac{1}{2}^-$ (S_{11})[1] partial wave cannot be explained; i.e. a calculation without ηN results in a strongly altered behavior. For that reason, all the resonance models for πN scattering described below have also included the ηN final state at least in the $\frac{1}{2}\frac{1}{2}^-$ partial wave. Similar, but less dramatic effects can also be observed in other channel, see Chapter 8.

Looking at the experimentally observed $\pi^- p$ cross sections in Fig. 3.1 one deduces, that in the resonance region, i.e. up to energies of about $\sqrt{s} \approx 2$ GeV, the πN elastic scattering is the dominant channel. Only the $2\pi N$ flux approaches the πN contributions at the highest energies. This also explains why πN and $2\pi N$ constitute at least $80 - 90\%$ of the total widths of almost all resonances analysed up to now [67]. The only known exception is the $S_{11}(1535)$, which has an ηN decay width of about 50%. This makes the inclusion of ηN at least in the S_{11} partial wave mandatory (see above). For higher energies, the ωN cross section rises up to about the same magnitude as the ηN threshold cross section, underlining the necessity of the consideration of the ωN final state in a resonance analysis. Manley and Saleski [113], e.g., have suspected that the large inelasticity in the $\frac{1}{2}\frac{3}{2}^+$ (P_{13}) wave at higher energies could be explained by the ωN channel; see also Section 8.1.3. In addition, η and ω production on the nucleon represent a possibility to project out $I = \frac{1}{2}$ resonances in the reaction mechanism. Furthermore, Manley and Saleski have also found hints that the $K\Lambda$ channel has some impact on the $\frac{1}{2}\frac{1}{2}^+$ (P_{11}) partial wave, which has also been confirmed by Feuster and Mosel [51, 52]; see, however, our findings in Sections 8.1.3 and 8.1.5.

Therefore, also these two final states have to be considered. Finally, the inclusion of $K\Sigma$ gives additional information on resonance properties, since especially in the pure $I = \frac{3}{2}$

---

[1] In brackets, the conventional πN notation is given.

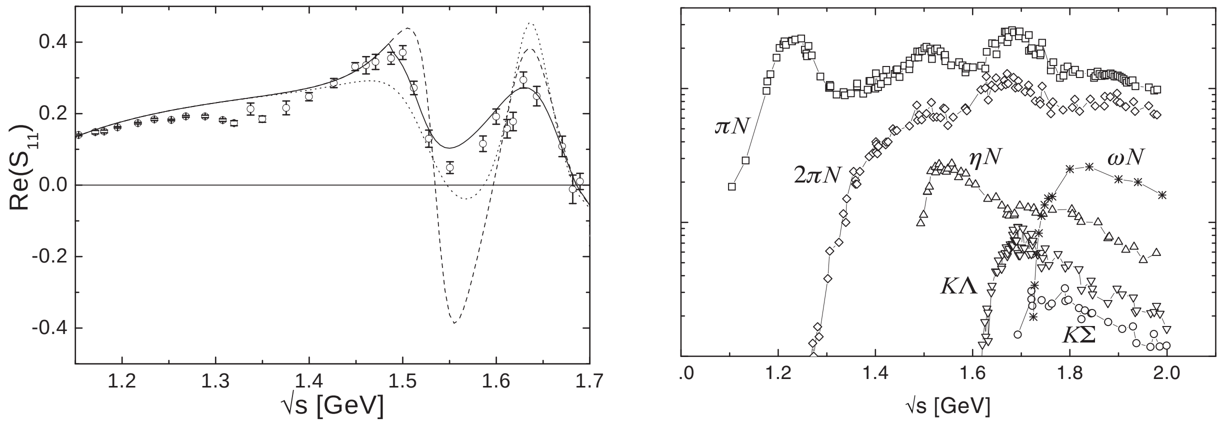

Figure 3.1: *Left:* $IJ^P = \frac{1}{2}\frac{1}{2}^-$ (S_{11}) πN partial wave. The solid line shows the full calculation C-p-$\pi\not\chi+$, the dashed line the calculation neglecting the ηN final state, and the dotted line the calculation where the ηN width of the $S_{11}(1535)$ was moved to $2\pi N$, i.e. restoring the total $S_{11}(1535)$ width. Data are from [277]. *Right:* Total cross sections for the reactions $\pi^- p \to X$ with X as given in the figure. All data are from Ref. [105]; the lines are to guide the eye.

reaction $\pi^+ p \to K^+\Sigma^+$ many data have been taken in the 60s and 70s. It is also known [148], that the inclusion of the $K\Sigma$ final state can have an important influence on the description of $K\Lambda$ observables.

This leads to the mandatory inclusion of the final states πN, $2\pi N$, ηN, $K\Lambda$, $K\Sigma$, and ωN in a unitary description for analyzing nucleon resonance properties. In addition, since there are much more precise data on photon- than on pion-induced reactions, the inclusion of γN should also be realized. For example, it has been shown in [53, 103] that the ηN photoproduction data cannot be explained by using the ηN widths extracted from pion-induced data alone. Those problems can only be resolved by a simultaneous, unitary analysis of all avaible photon- and pion-induced data on the nucleon.

At this point, a remark on the importance of a $3\pi N$ final state is in order. From the relative behavior of the πN and $2\pi N$ production cross sections in Fig. 3.1, one could conclude, that there might also be important contributions from $3\pi N$ production. Unfortunately, there are only few data on $\pi N \to 3\pi N$ available [105], indicating contributions of about the same magnitude as ωN and ηN. But considering that both the η and the ω decay dominantly into three pions, a large fraction of these indicated $3\pi N$ cross sections is already considered by including ηN and ωN and only small contributions are to be expected from other $3\pi N$ states as, e.g., $\rho\Delta$. As it will turn out in the present calculation, only in the $IJ^P = \frac{3}{2}\frac{3}{2}^+$ (P_{33}) and $\frac{1}{2}\frac{3}{2}^+$ (P_{13}) partial waves indications for the necessity of the inclusion of such a final state can be deduced, see discussions in Sections 7.1.2 and 8.1.3.

3.1 Other Models Analyzing Pion- and Photon-Induced Reactions on the Nucleon

Over the last 30 years, many different models for analyzing pion- and photon-induced reactions on the nucleon in the resonance region have been developed. In this section, we try to give an overview of their general properties, advantages, and drawbacks, in particular relative to the model implemented here.

In general, these models can be divided into three groups, where the first two mainly refer to pion- and the third one to photon-induced reactions:

3.1.1 Resonance Models:

The primary goal of these models is to provide a unitary framework for the extraction of resonance properties by a comparison to $\pi N \to \pi N$ and $\pi N \to 2\pi N$ data, basically neglecting all other channels; see below. Effects from analyticity are also included to some degree. By including the most important final states, phase space and threshold effects are accounted for properly. These are, however, no dynamical models, i.e. the background of the reactions is not extracted from an underlying theory and they do not account for the relativistic spin structure of the final state particles. The resonances are put in by hand, and an energy dependent background is simulated separately for each partial wave, i.e. by either a low order polynomial function or artificial resonances outside the considered energy region. It should be mentioned, however, that the resonance description in those partial waves which are dominated by a single resonance with only one decay channel, e.g. $\frac{3}{2}\frac{3}{2}^{+}$ (P_{33}) in $\pi N \to \pi N$, is comparable to the dynamical prescription of the present model, see also [51, 52] and beginning of Section 8.1.

In the literature, there are basically three different models:

Carnegie-Mellon Berkeley (CMB) Model

The CMB model has been developed by Cutkosky et al. [32] for a resonance analysis of mainly elastic πN scattering data. It is a separable coupled-channel model with generalized Breit-Wigner vertex functions. Unitarity is satisfied by solving an algebraic Dyson equation with bare resonance propagators. By applying a subtracted dispersion relation, analyticity is guaranteed. The correct threshold effects are modelled by including in addition to πN the final states $\pi\Delta$[2), ρN, ηN, σN, ωN, $\pi N^*(1440)$, and $\rho\Delta$; however, apart from $\pi N \to \pi N$, only the $\pi^- p \to \eta n$ total cross section has been compared to experimental data by assuming that ηN only arises from S_{11} contributions. The background is generated by including up to three unphysical resonances per partial wave which lie outside the considered energy region. In [183], Vrana et al. have revived this analysis. In addition to the single energy $\pi N \to \pi N$ amplitudes of Arndt et al. [4], the model has been compared to $\pi N \to 2\pi N$ amplitudes extracted by Manley et al. [278] and $\pi N \to \eta N$

[2)] Δ is the usual short-hand notation for the $P_{33}(1232)$ resonance.

partial waves. The latter ones have been extracted by Batinić et al. [10], where the CMB model has been used for analyzing simultaneously $\pi N \to \pi N$ for $I = \frac{1}{2}$ and $\pi^- p \to \eta N$ up to energies of 2.5 GeV including an effective $2\pi N$ flux channel. Note that [10] have not compared their $2\pi N$ channel to experimental data. There have also been attempts by Dytman et al. [44] to include photon-induced πN and ηN production in this model for a coupled-channel analysis up to 2.2 GeV; unfortunately the final results have not yet been published.

Kent-State University (KSU) Model

In the KSU model of Manley and Saleski [113] the resonance contributions are modelled by generalized Breit-Wigners and the background is unitarized separately by the K-matrix method. The functional form of the background is given by a polynomial (in $\sqrt{s}$), independently for each partial wave. Although the final states πN, $\pi\Delta$, ρN, ηN, σN, $K\Lambda$, ωN, $\pi N^*(1440)$, and $\rho\Delta$ have been included, these authors have only compared to $\pi N \to \pi N$ and their $\pi N \to 2\pi N$ data [278]. Thus they have allowed for each partial wave the inclusion of πN, all $2\pi N$ final states, and one of the mentioned other final states to account for the missing inelasticity. For example, in the S_{11} partial wave ηN and in P_{13} ωN have been added.

Although the above two resonance analyses [32, 113] include final states beyond πN, $2\pi N$, and ηN, those are only considered to account for the correct threshold behavior and to absorb additional flux contributions. Therefore, results for those channels are at best of qualitative nature. In that respect, e.g., the reliability of the extraction of a $10 - 15\%$ $K\Lambda$ branching ratio of the $P_{11}(1710)$ in [113] is questionable.

Virginia Polytechnic Institute and State University (VPI) Model

The VPI[3)] model of Arndt et al. [4] uses the K-matrix unitarization method (cf. Chapter 2) with free Breit-Wigner resonance propagators, whose widths are generated dynamically. An additional first order polyonomial parametrization of the background is included in each partial wave and analyticity is fulfilled by extracting the real part of the amplitudes via a dispersion relation. Besides πN, one dummy inelastic ($2\pi N$) channel is considered and only the $S_{11}(1535)$ is also allowed to couple to ηN. The same model has been used by Green and Wycech [65] for analyzing the coupled-channel system γN, πN, and ηN around the ηN threshold.

The drawback of all of the above models is that the background is not generated dynamically, but modelled separately for each partial wave by some (unphysical) function. This leads to a large number of free parameters, making the extraction of the sought-after resonance properties more difficult. For example, in the revived CMB model of Vrana et al. [183] up to 38 parameters in a single partial wave have been to be fitted; in the $\pi N \oplus 2\pi N \oplus \eta N$ coupled-channel analysis of Batinić et al. [10] 132 parameters have been used, out of which only 60 have been resonance parameters, see also Section 3.8 below.

[3)] The group has recently moved to George Washington University, Washington D.C..

3.1.2 Separable Potential Models

In contrast to the resonance models, in the separable potential models the aim is to model in some way the dynamics underlying the reaction process. The motivation is to be able to generate resonance structures dynamically, in particular by also accounting for the real part in the rescattering of the BS equation (2.7). The consequence, however, is, that the underlying interaction has to be simplified in such a way that a separate evaluation of the rescattering part in Eq. (2.7) is possible. Thus, the parameters of these separable potential models do not have a clear physical meaning, making the interpretation in terms of resonances and background questionable. Hence, although they often result in a good description of the experimental data, they provide no clear physical information about the interaction process.

Examples are the chiral SU(3) model of Kaiser et al. [148], which includes the final states γN, πN, ηN, $K\Lambda$, and $K\Sigma$ applying an approximated separable interaction Lagrangian. Although a fair description of experimental data seems possible, the model suffers from the neglect of $2\pi N$ inelasticities and higher partial waves ($\ell_\pi \geq 2$), i.e. they only consider S and P waves. In a similar model by Nieves and Arriola [128], which includes the final states πN, ηN, $K\Lambda$, and $K\Sigma$, it is possible to solve the BS equation for an approximated chiral SU(3) Lagrangian in the S_{11} wave resulting in a fair description of the S_{11} $\pi N \to \pi N$ partial wave and a good description of the $\pi N \to \eta N$ and $\pi N \to K\Lambda$ total cross sections. This model has been extended by Inoue, Oset, and Vacas [81] to also include $2\pi N$ final state effects.

The most recent model in this category is the one of Lutz et al. [109], where, as in our analysis, also vectormeson-nucleon final states have been included. There, the complexity of the vectormeson-nucleon states is strongly simplified by the use of only one specific combination of the VN helicity states (cf. Sections 5.2, 5.3, and 5.4.2). Due to the lack of $J^P = \frac{1}{2}^+$ and $J^P = \frac{3}{2}^+$ (P) waves in this model, these authors are only able to compare to production cross sections at energies very close to the corresponding threshold by assuming S-wave dominance. The photon coupling is implemented via strict vector meson dominance (VMD), i.e. the photon can only couple to any other particle via its "hadronic" components, the ρ and ω mesons. As a consequence of the energy limitation for the data range and the neglect of $\pi N \to \rho N$ data of [278], these assumptions are not strictly tested by comparing to experimental data and the results remain debatable.

3.1.3 Effective Lagrangian Models

The idea of the effective Lagrangian models is to account for the symmetries of the fundamental theory QCD but including only effective degrees of freedom instead of quarks. These effective degrees of freedom are modelled by baryons and mesons known to exist as (quasi-) bound quark states. The advantage of this method is that it gives more insight on the underlying production mechanism leading to less freedom and making the interpretation of the results easier. At the same time, due to the more complicated interaction structure, the meeting of the physical constraints unitarity and analyticity becomes technically more involved. Therefore, almost all of the effective Lagrangian models are not analytic, many of them not even unitary. To give an overview, some effective Lagrangian models are discussed in the following by first concentrating on models for pion-induced and then for photon-induced reactions.

Effective descriptions of πN low-energy properties using phenomenological interactions originate back to the 1950s and 60s (see, e.g., [27, 190, 191]). Peccei [140] has performed one of the first extended calculations of πN scattering lengths using a chiral effective Lagrangian including the $P_{33}(1232)$ resonance. Olsson and Osypowski [134] have used a model including an effective Lagrangian for the $\pi N \Delta$ interaction to extend the comparison to low-energy πN phase shifts. In addition to the contributions discussed below in Section 3.3.2 they have had to introduce a diffractive term, whose justification was questioned later on by Bofinger and Woolcock [19].

Accounting for unitarity within a relativistic chirally symmetric effective Lagrangian model by the K-matrix method has first been tested by Pearce and Jennings [139] in a fit of πN elastic phase shifts up to ≈ 1.38 GeV, see also Section 3.2 below. The extension of the effective Lagrangian K-matrix method to include further final state has first been realized by Sauermann [156, 157]. The model has been, however, restricted to a description of $\gamma N/\pi N \to \pi N/\eta N$ up to $\sqrt{s} = 1.75$ GeV using just the $\frac{1}{2}\frac{1}{2}^-$ (S_{11}) partial wave. The model has already included the idea of absorbing the complete $2\pi N$ flux by an artificial isoscalar 2π meson called ζ (see Section 3.2), but the $2\pi N$ channel has not been compared to experimental data. Scholten et al. [160] have introduced an extended effective Lagrangian K-matrix model, which is able to describe $\gamma N/\pi N \to \gamma N/\pi N$ up to ≈ 1.3 GeV neglecting $2\pi N$ contributions but including also higher partial waves. The model has later been extended to somewhat higher energies and Compton scattering [101], and recently modified to restore analyticity to a large extent within the K-matrix formalism [100]. Unfortunately, the restoration of analyticity leads to large complications in the feasibility of the model. Gridnev and Kozlenko [66] have also put forward an effective Lagrangian K-matrix model, analyzing $\pi N \to \pi N$ and $\pi N \to \eta N$ up to $\sqrt{s} \approx 1.67$ GeV. An additional dummy channel has also been included to account for all inelasticities apart from ηN.

There are a variety of unitary models for πN scattering using effective Lagrangians in three-dimensional reduction schemes (often denoted as Lippmann-Schwinger equations) of the full BS equation, thus accounting for analyticity to some extent. Most of them are restricted to elastic scattering (e.g., [139, 68, 63, 155, 79, 137]), while only a few ones also include inelastic channels [68, 102, 46]. An interesting $3D$ model is the solitary boson-exchange model of Jäde [84]. It is thought as an interpolation between QCD inspired and phenomenological hadron-hadron interaction models, thus explicitly evaluating and regularizing self-energy diagrams by meson-exchange contributions instead of using form factors. He finds a unified description of low-energy NN and πN scattering data.

A general problem of the $3D$ reduction is the way how the reduction is achieved. For example, in the model of Gross and Surya [68], which takes into account $\pi N \to \pi N$ and $\gamma N \to \pi N$, the four-dimensional BS integral equation is reduced to three dimensions by restricting the intermediate pion to its mass shell. However, they have demonstrated that this method is not unique; on the contrary, the $3D$ reduction can be achieved in an infinite number of ways, all of which satisfy Lorentz invariance and elastic two-body unitarity [195].

A full solution of the BS equation using an effective Lagrangian model for pion-induced reactions has up to now only been possible in the single channel analysis of πN elastic scattering for energies up to ≈ 1.35 GeV, put forward by Lahiff and Afnan [104]. They have used the same chiral πN background Lagrangian as in our model and in addition taken the $P_{33}(1232)$ resonance into account.

For completeness, we also mention a somewhat special case in this context, the model of Ellis and Tang [45]. Their effective chiral Lagrangian model for $\pi N \to \pi N$ fulfills unitarity by using heavy baryon chiral perturbation theory, within which unitarity is ensured order by order. Thus, they do not have to solve for the full scattering equation.

For the pseudoscalar meson photoproduction (πN, ηN, $K\Lambda$, $K\Sigma$), since the late 1950s a wealth of effective Lagrangian models have been developed (e.g. [28, 38, 141, 172, 184]). In such a model, the important constraint of gauge invariance can be addressed on the operator level (see also Sections 3.3.1 and 3.7 below), while unitarity and coupled-channel effects have only been considered in a few calculations, mostly on low-energy pion [34, 68, 129] or eta photoproduction [14, 157]. The problem in all other single-channel photoproduction models is an inherent inconsistency, see the end of this section.

To the same category of models, i.e. single-channel analysis (often called "T-matrix models"), also belong almost all effective Lagrangian models on pion- and photon-induced ωN production to date. They are discussed in the following.

Up to now, the pion-induced ω production channel has resisted a consistent effective Lagrangian description in line with experiment. Especially the inclusion of nucleon Born contributions overestimates the data at energies above 1.77 GeV [97] and only either the neglect of these diagrams [145] or very soft form factors [179] has led to a rough description of the experimental data[4]. None of these models has included rescattering effects or a detailed partial-wave analysis of interference effects, which will prove to lead to strong modifications of the observed cross section, see Section 8.1.7.

The same problem of the treatment of the nucleon Born contributions is apparent in the effective Lagrangian models on ω photoproduction. The first calculation has been performed by Friman and Soyeur [54], giving a rough description of the experimental data by only including π and σ t-channel exchange. In the model of Oh, Titov, and Lee [131] the nucleon contributions are damped by rather soft formfactors ($\Lambda_N = 0.5 - 0.7$ GeV using F_p, Eq. (3.29) below). A similar observation has been made in the model of Babacan et al. [8], where the Born contributions have not been damped by soft formfactors, but a very small ωNN coupling constant has been extracted ($g_{\omega NN} \leq 1$). Hence in both models, the Born contributions are effectively neglected. Since Babacan et al. have not included any baryon resonances, the effective reaction process is almost purely given by t-channel exchanges and thus close to the model of Friman and Soyeur. Oh et al., however, have included baryon resonances by using non-relativistic Breit-Wigners with vertex functions taken from the quark model of Capstick [24] and thus have not consistently generated a u-channel background. The imaginary part of the amplitude has

---

[4] Note that Ref. [179] has not used the correct experimental data, but has followed the claim of Ref. [73]; see Section 7.2.9.

only been taken into account via total widths in the denominator of the implemented Breit-Wigner resonance description. In a similar way resonances have also been included in the effective Lagrangian quark model of Zhao [198][5] on ω photoproduction. As in the pion-induced reaction, none of the models on ω photoproduction has included rescattering effects. Only in the most recent two works of Oh et al. [131], the authors have started to consider coupled-channel effects of intermediate πN and ρN states, neglecting the ρ spectral function in the latter case.

This restriction to a single-channel analysis is a fundamental weakness of all the T-matrix models. Although the above models on ωN and also others on $K\Lambda$ or $K\Sigma$ [1, 26, 108, 114, 115] photoproduction aim to provide a tool for the search and identification of so-called "missing" resonances, i.e. resonances which are predicted by quark models but have not yet been identified in the theoretical analysis of experimental data, an inherent problem of such an extraction is ignored: Due to the restriction on one single reaction channel, rescattering effects can only be incorporated in these models by putting in by hand a total width in the denominator of the included resonances. The parameters for these widths either have to be taken from other analyses, or enter as additional fit parameters. But if only one channel is analysed, the main part of the width of the "missing" resonance is shifted to some "rest" channels, which are not compared to any data. Hence, it is not clear from a single-channel analysis how these "rest" channels should be split up into different physical channels and how that would influence — e.g. due to cusp and/or rescattering effects — the analysis of the corresponding reactions. Thus, the "hunt for hidden resonances" by single channel analyses becomes questionable.

This problem can only be circumvented if all channels are compared simultaneously to experimental data thereby restricting the freedom severely. This is done in the model underlying the present calculation, whose ingredients are discussed in the following section.

3.2 The Giessen Model

The above discussion shows that within the aforementioned models there are no reliable and consistent extractions of resonance parameters beyond the final states πN, $2\pi N$, and ηN. Hence, there is a need for a unitary, consistent dynamical model covering the full resonance region up to $\sqrt{s} \sim 2$ GeV, including all important channels and higher partial waves, thus allowing to incorporate as much experimental information as possible for a reliable extraction of resonance parameters. At the same time, the consistency between experimental data from various reactions can be analyzed. A first step in this direction has been put forward by the model of Feuster and Mosel [51, 53], in the following called Giessen model. There, the model space is spanned by the final states γN, πN, $2\pi N$, ηN, and $K\Lambda$, allowing for a simultaneous description of all pion- and photon-induced reactions of these final states up to $\sqrt{s} = 1.9$ GeV. The idea is to include as many

---

[5] Note, that the models of Zhao [198] and Oh [131] also include the Pomeron exchange, which is a purely phenomenological exchange particle with the quantum numbers of the vacuum ($S^P = 0^+$). Its properties are extracted by effectively describing the corresponding reaction especially in the high energy region. This particle is not included in the present calculation, since here only well-known mesons are allowed as t-channel exchange particles.

channels as technically feasible. This is especially important for the treatment of the second most important flux channel, the $2\pi N$ channel. As a three-particle final state, it makes the treatment of unitarity more involved. Manley et al. [278] have split up the $2\pi N$ state in the quasi-two-body states $\pi\Delta$, ρN, σN, and $\pi N^*(1440)$ and have thereby achieved an excellent description of the $\pi N \to 2\pi N$ experimental data. However, already the inclusion of these 4 additional final states tremendously complicates the calculation, especially due to the widths of the final state isobars (Δ, ρ, σ, and $N^*(1440)$). Hence, so far, in the Giessen model the $2\pi N$ channel is only included effectively as a ζN channel, where the scalar-isovector meson ζ is an artificial 2π state with a mass of $m_\zeta = 2m_\pi$. Although this final state is not supposed to model the "real" $2\pi N$ complexity, its flux contributions are compared to the $\pi N \to 2\pi N$ partial wave cross sections that have been extracted by Manley et al. [278]. That allows to get a handle on the $2\pi N$ partial wave contributions and their consistencies with other reaction channels. Thereby, the parameters of those other channels can be reliably extracted, since no dummy channel is included in the calculation, but **all** final states are compared to experimental data. Even though a significant change of the latter parameters is not to be expected, an extension of the Giessen model by including the same quasi-two body $2\pi N$ states as in [278] would be desirable, thereby being able to also extract detailed information on the $2\pi N$ complexity.

Forming the basis of the present calculation, the model of [51, 53] is extended to further include the final states $K\Sigma$ and ωN. As pointed out in the introduction to this chapter, a minimum set of final states for a complete resonance analysis up to $\sqrt{s} = 2$ GeV has to include πN, $2\pi N$, ηN, and ωN. Especially for energies above 1.7 GeV the ωN final state is a mandatory flux channel in a unified, unitary description, and has, so far, only been considered in the model of Lutz et al. [109]; see Section 3.1.2. Thus the inclusion of the ωN final state in the present calculation differs from all other calculations on ω production on the nucleon in various respects. All pion- and photon-induced data for γN, πN, $2\pi N$, ηN, $K\Lambda$, $K\Sigma$, and ωN production are simultaneously described in such a large energy region, which means there are more restrictions from experiment. At the same time, the ωN reaction process is influenced by all other channels and vice versa. This leads to strong constraints of the choice of the ωN contributions (and also all others). Therefore, it is possible to extract them more reliably and a partial-wave analysis of interference effects becomes possible.

The interaction in the Giessen model is constructed in all channels by incorporating the effective degrees of freedom that are relevant in the considered energy region. Therefore, the potential V_{fi} is built up consistently by a sum of s-, u-, and t-channel Feynman diagrams by means of effective Lagrangians, see Fig. 3.2. The only assumption entering in the generation of the potential is, that the contributions of higher-order crossed diagrams as the one depicted in Fig. 2.2 are negligible or can be absorbed in the formfactors of non-crossed diagrams, see also Section 3.6 below. The advantage of generating the potential via Feynman diagrams is that the background (non-resonant) contributions are created dynamically and the total number of parameters is greatly reduced, as compared to Breit-Wigner driven models or those including only pointlike interactions, see Sections 3.1.1, 3.1.2 above, and 3.8 below. However, a coupled-channel model with a non-separable effective Lagrangian potential makes the solution of the Bethe-Salpeter scattering equation much more complicated. In view of the number of parameters that

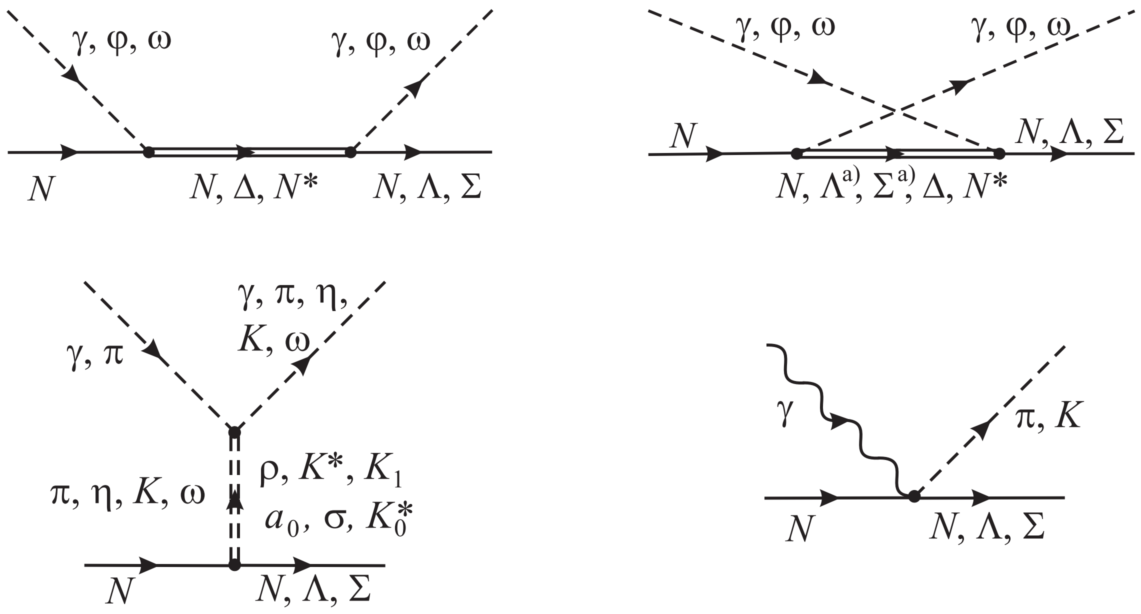

Figure 3.2: Feynman diagrams considered in this work. *First row:* s- and u-channel contributions with propagating final state baryons (N, Λ, Σ) or baryon resonances (Δ, N^*). *Second row:* t-channel contributions with propagating asymptotic and intermediate mesons, and the four-point interaction (Kroll-Rudermann) required by gauge invariance in the photoproduction of charged mesons. φ denotes the spin-0 final state mesons. $^{a)}$: u-channel contributions of Λ and Σ only exist for $\gamma N \to K\Lambda/\Sigma$.

have to be determined by comparison of the model calculation with experimental data, the K-matrix Born approximation is at present the only feasible method that still satisfies the important condition of unitarity; see also Section 2.2.

The validity of the effective Lagrangian K-matrix method as compared to calculations accounting also for analyticity has first been tested by Pearce and Jennings [139]. By fitting the πN elastic phase shifts up to ≈ 1.38 GeV with various approximations to the intermediate two-particle propagator G_{BS} (cf. (2.7)), these authors have found no significant differences in the parameters extracted in the various schemes. It has also been deduced that the contributions of G_{BS} to the principal value part of the scattering equation are of minor importance, since they have been reduced by a very soft cutoff dictated by experimental data. It has been concluded that — in order to fulfill the low-energy soft-pion theorems [2, 189] — an important feature of the reduced intermediate two-particle propagator is a delta function on the energy transfer. It has also been argued in [63], where the K-matrix effective Lagrangian model for low-energy πN elastic scattering of [62] has been extended, that for πN scattering the main effect of the real part of the intermediate loop integrals is a renormalization of the coupling constants and masses of the involved particles. Therefore, in the present K-matrix calculation these are taken to be physical values and are either taken from other reliable sources (if available) or to be determined by comparison with experimental data.

It should, however, be mentioned, that within the K-matrix method the nature of a resonance can not be explained. There are, e.g., hints, that the Roper $P_{11}(1440)$ resonance is a quasi-bound σN state [102]. In addition, in the chiral model of [148] the $S_{11}(1535)$ can be explained as a quasi-bound $K\Sigma$ state. Moreover, it has been shown in [39] by using a generalized separable Lee model, that explicit $S_{11}(1535)$ resonance contributions might not play a large role if the coupled-state system $\pi N \oplus \eta N$ is treated analytically, i.e. the real part of the Bethe-Salpeter propagator G_{BS} (2.5) is taken into account. Because of the omittance of the principal value part of the integral in (2.7) in the K-matrix approximation, the real part of G_{BS} is neglected and these resonances cannot be generated dynamically as quasi-bound meson-baryon states, but have to be put into the potential explicitly.

In the following sections, the full effective Lagrangian of the Giessen model will be discussed.

3.3 Asymptotic Particle (Born) Contributions

3.3.1 Electromagnetic Interactions

The introduction of electromagnetic interactions into an effective Lagrangian model is governed by the local gauge field theory QED; the question of gauge invariance can therefore be addressed on a fundamental level [118]:

From classical electrodynamics it is known that the electromagnetic vector potential is not uniquely determined. In particular, the electromagnetic field tensor $F_{\mu\nu} = \partial_\mu A_\nu - \partial_\nu A_\mu$ is invariant under a local gauge transformation

$$A_\mu(x) \rightarrow A_\mu(x) + \partial_\mu \alpha(x) \ , \tag{3.1}$$

where $\alpha(x)$ is an arbitrary Lorentz scalar depending on space and time.

To lowest order in the electromagnetic coupling constant e, the electromagnetic field A_μ is given by the plane wave mode expansion [82, 118]

$$A_\mu(x) = \sum_\lambda \int \frac{\mathrm{d}^3 k}{(2\pi)^3 2E_k} \left(\hat{a}(k_\mu, \lambda) \varepsilon^\lambda_\mu(k_\mu) e^{-\mathrm{i}kx} + \mathrm{h.c.} \right) \ , \tag{3.2}$$

where k^μ is the photon four-momentum, λ denotes the photon polarization, and $\varepsilon^\lambda_\mu(k_\mu)$ its polarization vector, see Appendix A.2.2. This means that the photon polarization vector ε_μ, which enters the evaluation of the Feynman diagrams, is changed as a function of the photon momentum by a gauge transformation (3.1) in the following way:

$$\varepsilon_\mu(k_\mu) \rightarrow \varepsilon_\mu(k_\mu) + \tilde{\alpha}(k_\mu) k_\mu \ . \tag{3.3}$$

Here, $\tilde{\alpha}(k_\mu)$ is the Lorentz scalar resulting from $\alpha(x)$ via Fourier transformation. Since all observables have to be independent under a gauge transformation (3.1), all matrix elements have to be invariant under the transformation (3.3).

The invariance of the theory under (3.1) can be achieved if the fields of the particles coupling to the photon field are simultaneously changed by a "local" phase transformation $e^{-\mathrm{i}\hat{e}\alpha(x)}$, where $\hat{e}$ is the charge operator. These combined transformations form the local gauge transformation of QED. Gauge invariance can be ensured if the couplings of all particles to the electromagnetic field are consistently introduced by the "minimal coupling scheme" in the full hadronic Lagrangian [82, 118]:

$$\partial_\mu \longrightarrow \partial_\mu + \mathrm{i}e\hat{e}A_\mu \tag{3.4}$$

or, equivalently modifying the four-momentum p_μ:

$$p_\mu \longrightarrow p_\mu - e\hat{e}A_\mu \ .$$

This scheme will be illustrated in the following for the Born term Lagrangian describing the photoproduction of ρ mesons on the nucleon.

The free Lagrangian for the nucleon leading to the Dirac equation (A.19) is given by

$$\mathcal{L} = \bar{u}\left(\mathrm{i}\partial_\mu\gamma^\mu - m_N\right)u \ ,$$

where u ($\bar{u}$) denotes the (adjungated) nucleon spinor. Applying minimal coupling (3.4), a vector coupling of the nucleon to the photon field is generated: $\mathrm{i}\partial_\mu\gamma^\mu \rightarrow \mathrm{i}\partial_\mu\gamma^\mu - e\hat{e}A_\mu\gamma^\mu$. Accounting for the fact that the magnetic moment of the nucleon does not correspond to the one of a pointlike spin-$\frac{1}{2}$ particle, the coupling to the anomalous magnetic moment κ_N has to be introduced and one arrives at the full electromagnetic Lagrangian of the nucleon:

$$\mathcal{L} \ = \ -e\bar{u}\left(\hat{e}\gamma_\mu - \frac{\kappa_N}{2m_N}\sigma_{\mu\nu}\partial^\nu_\gamma\right)uA^\mu \ . \tag{3.5}$$

The free Lagrangian of the ρ meson associated with the Proca equation (A.30) is

$$\mathcal{L} \ = \ -\tfrac{1}{4}\boldsymbol{\rho}_{\mu\nu}\boldsymbol{\rho}^{\mu\nu} + \tfrac{1}{2}m_\rho^2\boldsymbol{\rho}_\mu\boldsymbol{\rho}^\mu \tag{3.6}$$

with the antisymmetric $\boldsymbol{\rho}$ field tensor (cf. Appendix A.2.2) $\boldsymbol{\rho}^{\mu\nu} = \partial^\mu\boldsymbol{\rho}^\nu - \partial^\nu\boldsymbol{\rho}^\mu$. The interaction Lagrangian between the ρ meson and the nucleon is governed by the fact that the ρ has the same quantum numbers as the photon: $S^P = 1^-$. Thus the interaction is analogous to the electromagnetic coupling of the nucleon in Eq. (3.5) [34, 51, 55, 56]:

$$\mathcal{L}_{int} \ = \ -g_\rho\bar{u}\left(\gamma_\mu - \frac{\kappa_\rho}{2m_N}\sigma_{\mu\nu}\partial^\nu_\rho\right)u\boldsymbol{\tau}\,\boldsymbol{\rho}^\mu \ , \tag{3.7}$$

where the only difference is contained in the isospin part $\boldsymbol{\tau}\,\boldsymbol{\rho}$, see also Appendix F. Applying minimal coupling to the Lagrangians (3.6) and (3.7) generates the following electromagnetic interactions for outgoing ρ mesons and incoming photons:

$$\mathcal{L}_{min} = e_\rho\left[(k'+q)_\mu A^\mu g_{\nu\sigma} - \mathrm{i}F_{\nu\sigma}\right]\rho^\nu_q\rho^\sigma - \mathrm{i}\frac{e_\rho g_\rho\kappa_\rho}{2m_N}\bar{u}\sigma_{\mu\nu}uA^\nu\rho^\mu \ . \tag{3.8}$$

For the momentum notation, see Appendix A.1. The first part gives rise to a Bremsstrahlung contribution (as used in [197]) with an intermediate ρ meson (ρ_q) being put on its mass shell by capturing the incoming photon, while the part proportional to κ_ρ generates a four-point (Kroll-Rudermann) term.

Since in the evaluation of the Feynman diagrams the photon field A_μ is replaced by its polarization vector ε_μ (see above), the invariance of the theory under local gauge transformations can be tested by the replacement $\varepsilon_\mu \to k_\mu$ (cf. Eq. (3.3)) in the sum of all Born diagrams. This has to result in a vanishing expression. Applying standard Feynman rules [18] leads to the four contributions (nucleon s- and u-channel, ρ t-channel, and a four-point contribution, cf. Fig. 3.2):

$$\begin{aligned}
\tilde{\mathcal{M}}_s &= +e_N g_\rho f_I \bar{u}(p') \left(1 - \frac{\kappa_\rho}{2m_N} \not{k}'\right) \not{\rho} u(p) \\
\tilde{\mathcal{M}}_u &= -e_{N'} g_\rho f_I \bar{u}(p') \left(1 - \frac{\kappa_\rho}{2m_N} \not{k}'\right) \not{\rho} u(p) \\
\tilde{\mathcal{M}}_t &= -e_\rho g_\rho f_I \bar{u}(p') \left\{\not{\rho} - \frac{\kappa_\rho}{2m_N} \left[(\not{k}' - \not{k})\not{\rho} + k\cdot\rho\right]\right\} u(p) \\
\tilde{\mathcal{M}}_4 &= +e_\rho g_\rho f_I \frac{\kappa_\rho}{2m_N} \bar{u}(p') \left(\not{k}\not{\rho} - k\cdot\rho\right) u(p) \ ,
\end{aligned} \tag{3.9}$$

where the isospin factor f_I is $\pm\sqrt{2}$ for $\gamma n/p \to \rho^\mp p/n$ and ± 1 for $\gamma p/n \to \rho^0 p/n$ (see Appendix F.1.2). The sum of all four diagrams then is

$$\tilde{\mathcal{M}}_s + \tilde{\mathcal{M}}_u + \tilde{\mathcal{M}}_t + \tilde{\mathcal{M}}_4 = (e_N - e_{N'} - e_\rho) f_I g_\rho \bar{u}(p') \left(1 - \frac{\kappa_\rho}{2m_N} \not{k}'\right) \not{\rho} u(p) \ , \tag{3.10}$$

which vanishes as long as charge is conserved.

The case of ω photoproduction is identical to the case of ρ^0 photoproduction, i.e. follows from the above by the neglect of Bremsstrahlung and four-point contributions ($e_{\rho^0} = 0$). For the electromagnetic production of pseudoscalar mesons (πN, ηN, $K\Lambda$, and $K\Sigma$) the Dirac operator $\left(1 - \frac{\kappa_\rho}{2m_N} \not{k}'\right) \not{\rho}$ in (3.10) has to be replaced by $\gamma_5 \not{k}'$; see also [142], Section 3.3.2 below, and Appendix E.1.

This demonstrates that the Born diagrams are not individually gauge invariant. But as long as the photon is consistently coupled minimally to all asymptotic particles in the corresponding hadronic interactions and free Lagrangians, it turns out that the sum of all Born contributions is gauge invariant as long as charge is conserved. A problem arises, when one has to introduce form factors on the hadronic vertices, see Section 3.6 below.

3.3.2 Hadronic Interactions

Pion Nucleon Interaction and Chiral Symmetry

As pointed out in Chapter 1, an effective hadronic interaction Lagrangian should resemble the underlying fundamental theory QCD as closely as possible and thus satisfy the same symmetries concerning the conservation of quantum numbers as parity and total spin. While these symmetries are easily incorporated exactly in the effective Lagrangian, the interaction should also be in conformity with chiral symmetry, which is known to be important for low-energy πN physics. Chiral symmetry is a direct consequence of the negligible u- and d-quark masses leading to the decoupling of left- and righthanded states [118]. Consequently, one should replace the QCD Lagrangian by a hadronic Lagrangian, which at least fulfills the chiral symmetry low-energy constraints. In principle there are two ways of constructing chirally invariant Lagrangians. In the linear σ model [59, 161] the sigma meson and the pion couple to nucleons in the scalar-pseudoscalar combination $\sigma + \mathrm{i}\boldsymbol{\pi}\cdot\boldsymbol{\tau}\gamma_5$. In Weinberg's non-linear realization [191] the nonderivative couplings of the σ and π are eliminated by a chiral field-dependent rotation and replaced by a non-linear derivative coupling of the chiral rotation vector, which is identified with the new pion field. The arising pion-nucleon coupling $\gamma_5\gamma_\mu\partial^\mu\boldsymbol{\pi}\cdot\boldsymbol{\tau}$ is denoted as pseudovector coupling, while the σ meson does not appear anymore. In addition, the generated Weinberg-Tomazawa contact term [181, 189, 191], which automatically accounts for the values of the πN scattering lengths, can be identified with a ρ meson exchange provided the ρ couplings are fixed by the KSRF relation [91]: $\sqrt{g_\rho g_{\rho\pi\pi}} = m_\rho/(2f_\pi)$ with the pion-decay constant $f_\pi = 93$ MeV, which gives $g_\rho \approx 2.84$ using the value $g_{\rho\pi\pi} = 6.02$ (see Appendix E.1)[6]. It should be remarked that this equivalence only holds at threshold, while the energy dependence of the ρ exchange is different from the Weinberg-Tomazawa contact term. Since the aim of the present calculation is the analysis of a wide energy region, we allow for deviations from the KSRF relation by varying the ρ nucleon coupling g_ρ; see also Sections 8.1.2 and 8.2.1. The ρ nucleon tensor coupling κ_ρ (cf. Eq. (3.7)) — known to be important from many other analyses — is not subjected to chiral symmetry constraints since due to the derivative ρ coupling it does not contribute at the πN threshold in the chiral limit of a vanishing pion mass.

In the linear σ model, the σ exchange proves to be especially important for the reproduction of low-energy πN scattering [47, 99, 156]. However, in the non-linear σ model with pseudovector pion-nucleon coupling the low-energy theorems for πN scattering and pion photoproduction are automatically fulfilled [156, 157, 191]. Therefore, the non-linear chiral symmetry realization is used here. As pointed out above, from the point of view of chiral symmetry, the σ meson, which cannot really be identified with an existing particle anyway, is not needed any more. Nevertheless, a t-channel σ exchange can be used to model an effective interaction, representing higher-order processes such as the correlated 2π exchange in the scalar-isoscalar wave, which is not explicitly included in our potential. In principle, there are two possibilities for the pion-sigma coupling: the direct ($\sigma\boldsymbol{\pi}\boldsymbol{\pi}$) and the derivative coupling ($\sigma\partial_\mu\boldsymbol{\pi}\partial^\mu\boldsymbol{\pi}$). In order to keep the agreement with chiral symmetry and the soft-pion theorem [2, 189], the derivative coupling to the pion should be used. In this way, σ exchange does not contribute to low-energy πN scattering in the chiral limit of a vanishing pion mass.

Thus our full chirally-invariant background Lagrangian for πN elastic scattering is the same one as in [104, 137, 139]:

$$\begin{aligned}\mathcal{L}_\chi &= -\bar{u}\left[\frac{g_\pi}{2m_N}\gamma_5\gamma_\mu(\partial^\mu\boldsymbol{\pi})\boldsymbol{\tau} + g_\sigma\sigma + g_\rho\left(\gamma_\mu - \frac{\kappa_\rho}{2m_N}\sigma_{\mu\nu}\partial^\nu_\rho\right)\boldsymbol{\rho}^\mu\boldsymbol{\tau}\right]u \\ &\quad -\frac{g_{\sigma\pi\pi}}{2m_\pi}(\partial_\mu\boldsymbol{\pi})(\partial^\mu\boldsymbol{\pi}')\sigma - g_{\rho\pi\pi}\left(\boldsymbol{\pi}\times(\partial_\mu\boldsymbol{\pi}')\right)\boldsymbol{\rho}^\mu\,. \qquad (3.11)\end{aligned}$$

Note, that [104, 137, 139] normalized the ρNN coupling by a factor of $\frac{1}{2}$. Note also, that

---

[6] For a review on effective Lagrangians and chiral symmetry see also [57].

[137] allowed for an admixture of a direct $\sigma\boldsymbol{\pi}\boldsymbol{\pi}$ coupling, similarly to, e.g., [62, 63], to get a handle on chiral symmetry breaking effects; see chapter 8.1.2. For comparison, we also allowed for the use of this direct coupling.

Since the σ meson is supposed to model the scalar-isoscalar correlated two-pion exchange, its mass m_σ is a priori not fixed. In [104, 139] m_σ was thus used as a free parameter and fitted to $\pi N \to \pi N$ data. In our calculation, it turns out that the final quality of the fit is almost independent of the actual value. As long as it is in a reasonable range of $m_\sigma \approx 450 - 750$ MeV a change in m_σ can be compensated by a change in $g_{\sigma NN} g_{\sigma\pi\pi}$. For example, a mass change from $m_\sigma = 650$ MeV to 560 MeV leads to a coupling reduction of about 30% while all other πN parameters change at most by a few percent. The mass of the sigma meson has thus been chosen as 650 MeV, which was also used in [102]. There, the correlated two-pion exchange in the scalar-isoscalar wave was also parametrized by a σ meson exchange and m_σ was determined by comparison to the $\pi\pi$ dynamical model of [43]. The value for m_σ is in line with the values found by [139] and [104], and also in the range of $\pi\pi$ calculations and predictions [167, 182].

Remaining Nucleon Contributions

Since the mass of the strange quark is much higher than the u- and d-quark masses, one does not expect similarly strict chiral constraints as in the pion case for the other asymptotic pseudoscalar mesons $\varphi = \eta, K$ and thus preferences of either pseudoscalar (PS) or pseudovector (PV) $NN\varphi$ coupling. Several investigations on η production [14, 51, 53, 156, 157, 173] have found ηNN couplings $5-10$ times smaller compared to πNN, leading to a minor significance of the choice for the ηNN coupling. In particular, this has been demonstrated in [14], where several fits on η photoproduction data using PS and PV eta-nucleon coupling have been performed, showing that the resulting magnitude of the ηNN coupling and the quality of the fits hardly differ. In the case of $K\Lambda N$, however, from $SU(3)$ considerations, the coupling is expected to be larger. Thus one would expect observable differences between PS and PV coupling. This point has been examined in the Giessen model [53] and in a single-channel effective Lagrangian model [72]. Performing calculations with both coupling schemes, however, have revealed that neither the magnitude of $g_{K\Lambda N}$ nor the quality of the fit differ significantly in both cases as long as formfactors are used. Therefore, here the same PS-PV choice is made as in [53], i.e. using PV coupling for all Born couplings besides ηNN.

As already pointed out above, in the present model the $2\pi N$ channel is only accounted for effectively by the ζN channel. A consistent description of background contributions for the $2\pi N$ channels is hence difficult, since each background diagram would introduce meaningless coupling parameters. In the case of the resonant contributions, however, the situation is different because the decay into ζN can be interpreted as the total $(\sigma N + \pi\Delta + \rho N + \ldots)$ $2\pi N$ resonance widths. As it turns out, a qualitative description of the $\pi N \to 2\pi N$ partial-wave flux data from Manley et al. [278] is indeed possible by allowing for the $2\pi N$ production only via baryon resonances. Therefore, no t-channel and Born contributions to $2\pi N$ are included in the model, because they could not be interpreted in terms of a physical process as the above total $2\pi N$ resonance width. As soon as the $2\pi N$

state is described in a more detailed way, the above problem of interpreting the background contributions can be resolved and additional Born- and t-channel contributions have to be taken into account.

For the ωNN coupling, the same interaction Lagrangian is used as for the ρ meson and the photon:

$$\mathcal{L}_{NN\omega} \quad = \quad -g_\omega \bar{u} \left(\gamma_\mu - \frac{\kappa_\omega}{2m_N} \sigma_{\mu\nu} \partial_\omega^\nu \right) u \omega^\mu \ . \tag{3.12}$$

3.4 Baryon Resonances

In this section the resonance decay Lagrangians are presented from which all s- and u-channel resonance contributions can be consistently derived. Unfortunately, a problem still remains in the channels which contain a final state with associated strangeness ($K\Lambda$ and $K\Sigma$). The consideration of u-channel resonance and Born contributions in, e.g., $\pi N \to K\Lambda$ would require the inclusion of hyperon resonances and, for the Born diagrams, the inclusion of the cascade baryons Ξ. Since these are only non-resonant contributions, the determination of the needed coupling constants cannot be very conclusive within the present model. Therefore, the corresponding diagrams are neglected, although this might lead to missing background contributions in the aforementioned channels, see also Sections 8.1.5, 8.1.6, 8.4.4, and 8.4.5. This inconsistency, could, however, be removed by a simultaneous analysis of anti-kaon-induced reactions on the nucleon, where the corresponding couplings appear in resonant contributions. A first step in this direction has been undertaken by an analysis using the same K-matrix effective Lagrangian model for anti-kaon-induced reactions on the nucleon including the final states $\bar{K}N$, $\pi\Lambda$, and $\pi\Sigma$ [92]. A future merged analysis, including radiative capture processes (e.g. $\bar{K}N \to \gamma\Lambda$) to also have a handle on the electromagnetic properties of the hyperon resonances, would be desirable.

3.4.1 (Pseudo-)Scalar Meson Decay

Spin-$\frac{1}{2}$ Resonances

For spin-$\frac{1}{2}$ resonances, one has, in principle, the same freedom as for the nucleon to choose either PS or PV coupling at each decay vertex involving (pseudo-)scalar mesons. This question has been addressed in a coupled-channel effective Lagrangian K-matrix model for $\pi N \to \pi N$ and $\pi N \to \eta N$ [66] by introducing a mixing parameter between the two ways of coupling for the spin-$\frac{1}{2}$ resonances $P_{11}(1440)$, $S_{11}(1535)$, $S_{11}(1650)$, $P_{11}(1710)$, $S_{31}(1620)$, and $P_{31}(1910)$. The best fit has resulted in pseudovector πN and ηN couplings; however, the differences in χ^2 to a fit with pure PS couplings have been, especially for the ηN couplings, only marginal. This can easily be understood, because the PS and PV vertices are constructed in such a way (see Eqs. (3.13) and (3.14) below) that on-shell both couplings are equivalent. The different energy behavior becomes only evident far off-shell, where the resonance contribution is already largely damped due to the denominator of the resonance propagator. Only in the case of the nucleon-nucleon-pion vertex, due to the large $NN\pi$ coupling, a difference is obvious and results in a clear preference of PV coupling in line with chiral symmetry.

In principle, one could also allow for such a PS-PV mixture in the present model, but due to the obviously small differences between the two schemes and to avoid the introduction of additional parameters, we choose to follow the PS-PV convention used in [51, 52, 53]: For the positive-parity spin-$\frac{1}{2}$ resonances, PV coupling is used just as in the nucleon case:

$$\mathcal{L}^{PV}_{\frac{1}{2}B\varphi} = -\frac{g_{RB\varphi}}{m_R \pm m_B}\bar{u}_R \begin{pmatrix} \gamma_5 \\ \mathrm{i} \end{pmatrix} \gamma_\mu u_B \partial^\mu \varphi \; . \tag{3.13}$$

The upper (lower) sign and operator hold for pseudoscalar (scalar) mesons $\varphi = \pi, \eta, K$ (ζ). The spinor u denotes the corresponding final state baryon (N, Λ, Σ). Note, that due to the choice of normalization ($m_R \pm m_B$), PS and PV coupling are equivalent when both baryons are on-shell. For negative-parity spin-$\frac{1}{2}$ resonances (see also Appendix I), PS coupling is used since this coupling has also been applied in other models for the $S_{11}(1535)$ on ηN photoproduction [156, 157, 173]:

$$\mathcal{L}^{PS}_{\frac{1}{2}B\varphi} = -g_{RB\varphi}\bar{u}_R \begin{pmatrix} 1 \\ -\mathrm{i}\gamma_5 \end{pmatrix} u_B \varphi \; . \tag{3.14}$$

Here, the upper (lower) operator again holds for pseudoscalar (scalar) mesons φ. This choice of PS-PV coupling for the resonances is also supported by the fact, that in the $\pi N \to \pi N$ partial wave data, the resonant structures are more pronounced in the $J^P = \frac{1}{2}^-$ (S) than in in the $\frac{1}{2}^+$ (P) waves. Therefore, a decay vertex washing out the resonant behavior, i.e. with a contribution increasing with energy (cf. the PV-vertex Eqs. (3.13) and (E.26)), seems to be favorable in the $\frac{1}{2}^+$ case.

Spin-$\frac{3}{2}$ Resonances

Spin-$\frac{3}{2}$ resonances are described in the Rarita-Schwinger formalism given in Appendix A.2.3 by the coupling of a spin-1 polarization vector with a spin-$\frac{1}{2}$ spinor. The resulting spinor u^μ_R fulfills the Rarita-Schwinger equations [149]:

$$\begin{aligned} (\not{p} - m)u^\mu_R(p,s) &= 0 \\ p_\mu u^\mu_R(p,s) &= 0 \\ \gamma_\mu u^\mu_R(p,s) &= 0 \; , \end{aligned} \tag{3.15}$$

where the last two equations ensure that the number of independent fields is reduced from 16 to 8. The interaction with (pseudo-)scalar mesons for positive-parity resonances is conventionally chosen to be

$$\mathcal{L}_{\frac{3}{2}B\varphi} = \frac{g_{RB\varphi}}{m_\pi}\bar{u}^\mu_R \begin{pmatrix} 1 \\ -\mathrm{i}\gamma_5 \end{pmatrix} u_B \partial_\mu \varphi \tag{3.16}$$

and for negative-parity resonances (see also Appendix I)

$$\mathcal{L}_{\frac{3}{2}B\varphi} = -\frac{g_{RB\varphi}}{m_\pi}\bar{u}^\mu_R \begin{pmatrix} \mathrm{i}\gamma_5 \\ 1 \end{pmatrix} u_B \partial_\mu \varphi \; . \tag{3.17}$$

As in the spin-$\frac{1}{2}$ case, the upper (lower) operator holds for pseudoscalar (scalar) mesons φ. In the resulting contributions to the potential, however, the spin-$\frac{3}{2}$ resonances only contribute as intermediate particles described by the Rarita-Schwinger spin-$\frac{3}{2}$ propagator $G^{\mu\nu}_{\frac{3}{2}}$ (cf. Eq. (A.41)). It reads in terms of spin-projection operators $\mathcal{P}_J$ [90, 127, 136]:

$$-G^{\mu\nu}_{\frac{3}{2}}(q) = \frac{1}{\not{q}-m}\mathcal{P}^{\mu\nu}_{\frac{3}{2}}(q) - \frac{2}{3m^2}(\not{q}+m)\mathcal{P}^{\mu\nu}_{\frac{1}{2},22}(q) + \frac{1}{\sqrt{3}m}\left(\mathcal{P}^{\mu\nu}_{\frac{1}{2},12}(q)+\mathcal{P}^{\mu\nu}_{\frac{1}{2},21}(q)\right) , \tag{3.18}$$

where

$$\begin{aligned}
\mathcal{P}^{\mu\nu}_{\frac{3}{2}}(q) &= g^{\mu\nu} - \frac{1}{3}\gamma^{\mu}\gamma^{\nu} - \frac{1}{3q^2}(\not{q}\gamma^{\mu}q^{\nu} + q^{\mu}\gamma^{\nu}\not{q}) \\
\mathcal{P}^{\mu\nu}_{\frac{1}{2},22}(q) &= q^{\mu}q^{\nu}/q^2 \\
\mathcal{P}^{\mu\nu}_{\frac{1}{2},12}(q) &= (q^{\mu}q^{\nu} - \not{q}\gamma^{\mu}q^{\nu})/(\sqrt{3}q^2) \\
\mathcal{P}^{\mu\nu}_{\frac{1}{2},21}(q) &= (\not{q}q^{\mu}\gamma^{\nu} - q^{\mu}q^{\nu})/(\sqrt{3}q^2) \, .
\end{aligned}$$

Note the relation of the pure spin-$\frac{3}{2}$ projector $\mathcal{P}^{\mu\nu}_{\frac{3}{2}}$ with the spin-$\frac{3}{2}$ projection operator in Eq. (A.42) of Appendix A: $(\not{q}+m)\mathcal{P}^{\mu\nu}_{\frac{3}{2}}(q) = -\Lambda^{\mu\nu}_{\frac{3}{2}}(q)$. Thus, on-shell ($q^2 = m_R^2$) the Rarita-Schwinger propagator is proportional to $\mathcal{P}^{\mu\nu}_{\frac{3}{2}}$, while off-shell, there are also admixtures from the spin-$\frac{1}{2}$ sector denoted by $\mathcal{P}^{\mu\nu}_{\frac{1}{2},ij}$. This manifests itself also in the fact that off-shell, the last constraint in Eq. (3.15) $\gamma_{\mu}G^{\mu\nu}_{\frac{3}{2}} = G^{\mu\nu}_{\frac{3}{2}}\gamma_{\nu} = 0$ is not fulfilled anymore [90]. To examine the influence of the off-shell spin-$\frac{1}{2}$ contributions so-called off-shell projectors have been introduced [125] in the couplings (3.16) and (3.17):

$$\Theta_{\mu\nu}(a) = g_{\mu\nu} - a\gamma_{\mu}\gamma_{\nu} \, . \tag{3.19}$$

These projectors allow for a variation of the spin-$\frac{1}{2}$ components in terms of the parameter a, which is related to the commonly used off-shell parameter z [125, 126] by $a = (z+\frac{1}{2})$. There have been theoretical attempts to fix the value of a [126, 141] and to thereby remove the spin-$\frac{1}{2}$ contributions. However, in [12] it has been shown, that these contributions are always present for any choice of a. Moreover, it has been argued that in an effective theory, where the spin-$\frac{1}{2}$ spin-$\frac{3}{2}$ transition between composite particles is described phenomenologically, these parameters should not be fixed by a fundamental theory assuming pointlike particles, but rather be determined by comparison with experimental data. This is also confirmed by the fact that only a poor description of photoproduction multipoles is possible when the values for a given in [126] are used for the Δ resonance [12].

It has, furthermore, been shown [135], that for any choice of the off-shell parameters, the "conventional" $\pi N\Delta$ interaction given by (3.16) leads to inconsistencies: Either the constraints of the free theory are explicitly violated ($a \neq 1$) [125] or it gives rise to the Johnson-Sudarshan-Velo-Zwanziger problem [89] ($a = 1$). Pascalutsa and Timmermans [135, 136] have thus recently suggested an interaction that is invariant under gauge transformations of the Rarita-Schwinger field ($u^{\mu}_R \to u^{\mu}_R + \partial^{\mu}\epsilon$) and consequently consistent with the free spin-$\frac{3}{2}$ theory. The premise is that consistent interactions should not "activate" the spurious spin-$\frac{1}{2}$ degrees of freedom, and therefore the full interacting theory must obey similar symmetry requirements as the free theory. These interactions can be easily constructed by allowing only couplings to the manifestly gauge invariant Rarita-Schwinger field tensor

$$U_R^{\mu\nu} = \partial^\mu u_R^\nu - \partial^\nu u_R^\mu \tag{3.20}$$

and its dual $\tilde{U}_R^{\mu\nu} = \frac{1}{2}\varepsilon^{\mu\nu\alpha\beta}U_{R\alpha\beta}$. Note the relation to the introduction of gauge invariant electromagnetic resonance couplings in Section 3.4.2 below. Thereby, the corresponding vertex function will satisfy

$$q_\mu \Gamma^\mu(q) = 0 \; ,$$

where q denotes the four-momentum of the spin-$\frac{3}{2}$ particle. In the full Feynman amplitude $\sim \Gamma_\mu(q) G_{\frac{3}{2}}^{\mu\nu}(q) \Gamma_\nu(q)$ all the spin-$\frac{1}{2}$ contributions of the propagator (3.18) will drop out for any q. The resulting amplitude is therefore proportional to the spin-$\frac{3}{2}$ projector as already anticipated by the adhoc prescription used in [192]. Pascalutsa has proposed in [136, 135] the following $\pi N\Delta$ interaction:

$$\mathcal{L}_{\pi N\Delta} = f_{\pi N\Delta} \bar{\tilde{U}}_R^{\mu\nu} \gamma_\mu \gamma_5 u \partial_\nu \pi \; . \tag{3.21}$$

Using this interaction, the net result is a Feynman amplitude that resembles the conventional one, with the difference, that the full Rarita-Schwinger propagator $G_{\frac{3}{2}}^{\mu\nu}(q)$ is replaced by its spin-$\frac{3}{2}$ part $-(\not{q}-m)^{-1}\mathcal{P}_{\frac{3}{2}}^{\mu\nu}(q)$ and the amplitude is multiplied by an overall q^2. Demanding on-shell ($q^2 = m_\Delta^2$) equivalence with the conventional interaction, the coupling constant $f_{\pi N\Delta}$ can be identified to be

$$f_{\pi N\Delta} = \frac{g_{\pi N\Delta}}{m_\pi m_\Delta} \; .$$

This equivalence procedure can be generalized to any spin-$\frac{3}{2}$ vertex (in particular to the electromagnetic and vector meson decay vertices introduced below) by the replacement

$$\Gamma_\mu u_R^\mu \rightarrow \Gamma_\mu \gamma_5 \gamma_\nu \tilde{U}_R^{\nu\mu} \tag{3.22}$$

leading effectively to the substitution of the propagator $G_{\frac{3}{2}}^{\mu\nu}(q)$ by $-(\not{q}-m)^{-1}\mathcal{P}_{\frac{3}{2}}^{\mu\nu}(q)$ and an additional overall factor of q^2/m_R^2 in the Feynman amplitude.

Pascalutsa has also shown [138] that using the "inconsistent" conventional couplings leading to s- and u-channel contributions is equivalent at the S-matrix level to using the "consistent" (gauge-invariant) couplings plus additional contact interactions. The advantage, however, of using "consistent" couplings is that they allow for an easier analysis of separating background and resonance contributions. This has also been confirmed by Tang and Ellis [170] in the framework of an effective field theory. These authors have shown that the off-shell parameters are redundant since their effects can be absorbed by contact interactions. In addition, Pascalutsa and Tjon [137] have demonstrated that the gauge-invariant and the conventional $\pi N\Delta$ interaction result in the same πN threshold parameters once contact terms are included and some coupling constants are readjusted. Pascalutsa [138] has thus concluded that within an effective Lagrangian approach, any linear spin-$\frac{3}{2}$ coupling is acceptable, even an "inconsistent" one. The differences to the use of "consistent" couplings plus contact terms are completely accounted for by a change of coupling constants.

In our model, calculations with both spin-$\frac{3}{2}$ couplings are performed to extract information on the importance of off-shell contributions – or, correspondingly, contact interactions – from the comparison with experimental data. I.e., for the pion-induced reactions we present calculations where the additional spin-$\frac{1}{2}$ contributions are allowed in the spin-$\frac{3}{2}$ propagators and the off-shell parameters are used as free parameters, and calculations where these contributions are removed by the above prescription (3.22). The remaining background contributions are identical in both calculations, in particular the same t-channel exchange diagrams are taken into account and no additional contact diagrams are introduced when using the Pascalutsa couplings.

Note, that the isospin operators of the above interactions are discussed in Appendix F.2.

3.4.2 Electromagnetic Decays

The contributions of baryon resonances to photoproduction amplitudes cannot be extracted by minimal substitution (cf. Section 3.3.1 above) from the field theoretical hadronic Lagrangian, because the resonances only appear as intermediate states. Thus only the electromagnetic decay processes of the resonances contribute to the reaction mechanism and the electromagnetic transition vertices $R \to N\gamma$ have to be introduced by hand. This also means that each individual electromagnetic decay vertex has to fulfill gauge invariance by itself:

$$k_\mu \Gamma^\mu_{R\to N\gamma}(s,t) = 0 \; .$$

This can easily be accomplished by only allowing for couplings to the electromagnetic field tensor $F_{\mu\nu} = \partial_\mu A_\nu - \partial_\nu A_\mu$. Since the vertices are related to the Lagrangians via $\bar{u}_R \Gamma_\mu u A^\mu = \mathrm{i}\mathcal{L}_{int}$ the electromagnetic transition Lagrangians for spin-$\frac{1}{2}$ resonances can be chosen similarly to the magnetic coupling of the nucleon

$$\begin{aligned}\mathcal{L}_{\frac{1}{2}N\gamma} &= +e\frac{g_1}{2m_N}\bar{u}_R \begin{pmatrix} 1 \\ -\mathrm{i}\gamma_5 \end{pmatrix} \sigma_{\mu\nu}\partial^\nu_A u A^\mu \\ &= -e\frac{g_1}{4m_N}\bar{u}_R \begin{pmatrix} 1 \\ -\mathrm{i}\gamma_5 \end{pmatrix} \sigma_{\mu\nu} u F^{\mu\nu} \; . \end{aligned} \tag{3.23}$$

The upper (lower) factor 1 ($-\mathrm{i}\gamma_5$) corresponds to positive- (negative-) parity resonances. For the spin-$\frac{3}{2}$ resonances, there is an additonal possibility of combining the nucleon and the photon spin ($s_\gamma \oplus s_N = \frac{1}{2}$ or $\frac{3}{2}$), leading to two possible couplings in the Lagrangian for the $RN\gamma$ decay:

$$\begin{aligned}\mathcal{L}_{\frac{3}{2}N\gamma} &= -e\bar{u}^\mu_R \begin{pmatrix} \mathrm{i}\gamma_5 \\ 1 \end{pmatrix} \left(\frac{g_1}{2m_N}\gamma^\alpha + \mathrm{i}\frac{g_2}{4m_N^2}\partial^\alpha_N\right) \left(\partial^A_\alpha g_{\mu\nu} - \partial^A_\mu g_{\alpha\nu}\right) u A^\nu \\ &= +e\bar{u}^\mu_R \begin{pmatrix} \mathrm{i}\gamma_5 \\ 1 \end{pmatrix} \left(\frac{g_1}{2m_N}\gamma^\nu + \mathrm{i}\frac{g_2}{4m_N^2}\partial^\nu_N\right) u F_{\mu\nu} \; . \end{aligned} \tag{3.24}$$

Again, the upper (lower) factor corresponds to positive- (negative-) parity resonances. In principle, there could also be a coupling $\propto \partial^\gamma_\mu$ for all resonances; however, for real photons it does not contribute. Note, that for clarity, the spin-$\frac{3}{2}$ off-shell projectors $\Theta_{\mu\nu}(a)$ (cf. Eq. (3.19)), which are contracted with each coupling operator when the conventional spin-$\frac{3}{2}$ prescription is used (see Section 3.4.1 above), are not displayed.

3.4.3 Vector Meson Decays

The resonance ωN Lagrangians have been chosen as a compromise of an extension of the above $RN\gamma$ transitions [for vector meson dominance (VMD) reasons], and the compatibility with other RN vector meson couplings used in the literature [146, 151, 179]. For the spin-$\frac{1}{2}$ resonances we apply the same ωN Lagrangian as for the nucleon ($\omega N \to R$):

$$\mathcal{L}_{\frac{1}{2}N\omega} = -\bar{u}_R \begin{pmatrix} 1 \\ -\mathrm{i}\gamma_5 \end{pmatrix} \left(g_1 \gamma_\mu - \frac{g_2}{2m_N} \sigma_{\mu\nu} \partial^\nu_\omega \right) u \omega^\mu \ , \tag{3.25}$$

where the first coupling is the same one as in [151, 179] since the ω is polarized such that $k'_\mu \omega^\mu = 0$, see Appendix A. For the spin-$\frac{3}{2}$ resonances we use

$$\mathcal{L}_{\frac{3}{2}N\omega} = -\bar{u}^\mu_R \begin{pmatrix} \mathrm{i}\gamma_5 \\ 1 \end{pmatrix} \left(\frac{g_1}{2m_N}\gamma^\alpha + \mathrm{i}\frac{g_2}{4m_N^2}\partial^\alpha_N + \mathrm{i}\frac{g_3}{4m_N^2}\partial^\alpha_\omega \right) \left(\partial^\omega_\alpha g_{\mu\nu} - \partial^\omega_\mu g_{\alpha\nu} \right) u \omega^\nu \ . \tag{3.26}$$

In both equations the upper operator (1 or $\mathrm{i}\gamma_5$) corresponds to a positive- and the lower one to a negative-parity resonance. For positive-parity spin-$\frac{3}{2}$ resonances the first coupling is also the same as the one used in [151, 179]; for negative parity a combination of our first two couplings corresponds on-shell to those of [151, 179]. The above couplings have also been applied in [146] in calculations of the ρ spectral function. Note, that for clarity, the spin-$\frac{3}{2}$ off-shell projectors $\Theta_{\mu\nu}(a)$ (cf. Eq. (3.19)), which are contracted with each coupling operator when the conventional spin-$\frac{3}{2}$ prescription is used (see Section 3.4.1 above), are not displayed.

3.5 Intermediate Mesons

The t-channel meson exchanges are thought to generate background contributions to the reactions by introducing effective degrees of freedom (intermediate mesons) known to couple to the final state mesons [67]. In addition to the σ and ρ meson discussed in Section 3.3.2, the included intermediate mesons are $a_0(980)$, $K^*(892)$, $K_1(1270)$, and $K_0^*(1430)$. The properties of these mesons are summarized in Table 3.1 in Section 3.8 below, where also the channels to which these exchange mesons contribute are given. Note, that whenever one of the final state mesons is known to couple to two other final state mesons (e.g. $\omega \to \pi^0\gamma$), the corresponding t-channel contribution is also taken into account. For some quantum number combinations, there exist more than one intermediate meson. The higher-lying states are not included here since the t-channel contributions of two mesons having the same quantum numbers can hardly be disentangled. This applies especially to the $K_1(1270)$ meson, which is included for hyperon photoproduction in line with other models [1, 26, 108, 114, 115]. With a mass of 1.402 GeV there is a second K_1 meson close by, which is even predicted [7] and measured [3] to have a $3-4$ times larger radiative decay width $K_1 \to K\gamma$ than the $K_1(1270)$. Therefore, the $K_1(1270)$ included in the present calculation rather represents an effective $K_1(1270)$-$K_1(1400)$ exchange.

The interaction Lagrangians of the intermediate mesons with the final state baryons are chosen in the following way: The a_0 and K_0^* mesons are scalar mesons like the σ meson and thus couple in the same way to the baryons (a_0NN, $K_0^*\Lambda N$, $K_0^*\Sigma N$), see Section 3.3.2. The K^* is a vector meson as the ρ and ω thus coupling to $N\Lambda$ and $N\Sigma$ as given in Eqs. (3.11) and (3.12). The K_1 is an axialvector ($S^P = 1^+$) meson therefore requiring an additional parity operator ($\mathrm{i}\gamma_5$) as compared to the vector mesons ($S^P = 1^-$) K^*, ρ, and ω:

$$\mathcal{L}_{K_1\Lambda N} = -\mathrm{i}g_{K_1\Lambda N}\bar{u}_\Lambda \left(\gamma_\mu K_1^\mu + \frac{\kappa_{K_1\Lambda N}}{2m_N}\sigma_{\mu\nu}K_1^{\mu\nu}\right)\gamma_5 u_N$$

with $K_1^{\mu\nu} = \partial^\mu K_1^\nu - \partial^\nu K_1^\mu$ and in the same way for the $K_1\Sigma N$ vertex.

The isospin operators of the interactions are discussed in Appendix F.2.

3.5.1 Electromagnetic Decays

The two-photon decay vertex of the pseudoscalar mesons $\varphi = \pi, \eta$ is given with the help of the Levi-Civita tensor (cf. Appendix A.2):

$$\mathcal{L}_{\varphi\gamma\gamma} = -e^2 \frac{g_{\varphi\gamma}}{4m_\varphi}\varphi\varepsilon_{\mu\nu\alpha\beta}F^{\mu\nu}F'^{\alpha\beta} \; . \tag{3.27}$$

In analogy, also the radiative decay of the vector mesons $\rho \to \pi\gamma/\eta\gamma$, $\omega \to \pi\gamma/\eta\gamma$, and $K^* \to K\gamma$ is given:

$$\mathcal{L}_{V\varphi\gamma} = -e\frac{g_{V\varphi\gamma}}{4m_\varphi}\varphi\varepsilon_{\mu\nu\alpha\beta}F^{\mu\nu}V^{\alpha\beta} \; .$$

Due to its opposite parity, the radiative decay interaction of the axialvector K_1 meson has to be chosen differently:

$$\mathcal{L}_{K_1K\gamma} = e\frac{g_{K_1K\gamma}}{2m_K}KF_{\mu\nu}K_1^{\mu\nu} \; .$$

The radiative and hadronic decay constants of all intermediate mesons are extracted from the corresponding decay widths, see Appendix E.1.

3.5.2 Hadronic Decays

The hadronic decays of the intermediate mesons can mostly be extracted from the chiral Lagrangian in Eq. (3.11). The decay vertices of the the two pseudoscalar mesons ($a_0 \to$

$\eta\pi$, $K_0^* \to K\pi$) are analogous to the $\sigma\pi\pi$ vertex (either a direct or a derivative coupling, see Section 8.1.2), while the decay of the K^* vector meson to $K\pi$ is in analogy to the $\rho \to \pi\pi$ decay: $-g_{K^*K\pi}\pi(\partial^\mu K)K^{*\mu}$. A completely new interaction is introduced for the consideration of a ρ exchange in $\pi N \to \omega N$. The Lagrangian is chosen in the same way as the pion two-photon decay (3.27):

$$\mathcal{L}_{\omega\rho\pi} = -\frac{g_{\omega\rho\pi}}{4m_\pi}\boldsymbol{\pi}\,\varepsilon_{\mu\nu\alpha\beta}\boldsymbol{\rho}^{\mu\nu}\omega^{\alpha\beta}\ .$$

For the isospin part of all Lagrangians, see Appendix F.2.

Looking at the intermediate mesons listed in [67], one might wonder why the $b_1(1235)$ axialvector meson with a dominant decay to $\pi\omega$ is not included in the present model. The reason for that is two-fold: Firstly, there are only about 110 data points for the reaction $\pi N \to \omega N$, most of which are located in the range up to 50 MeV above threshold. In this energy region, t-channel contributions are still small, and since a ρ exchange is already included for this channel, it would not be possible to differentiate between the two t-channel meson contributions from the presently available data. Secondly, Oh and Lee (see first reference in [131]) have included the b_1 meson in their model on $\pi N \to \omega N$ and only found negligible contributions.

3.6 Formfactors

It is long known, that the direct application of the Lagrangians presented in the previous sections does not even allow for the description of a single channel problem as, e.g., $\pi N \to \pi N$ for energies below 1.4 GeV [16, 139]. This is not unexpected, since the particles in the effective Lagrangian model are not pointlike particles but have an internal structure. This, e.g., gives rise to the anomalous magnetic moments of baryons. Furthermore, the effects of higher order loop contributions at the vertices influencing the off-shell behavior of a vertex are neither taken into account. These two effects have to be considered since the internal structure of a particle participating in a reaction is probed as soon as it is going off-shell. A generalization of the vertex function is reqired, which is accomplished by the introduction of formfactors allowing for the extension of the effective theory to off-shell kinematics.

Scaling laws [21] suggest the asymptotic fall-off of scattering processes to some power (depending on the participating particles) of the four-momentum squared of the particle going off-shell. Therefore, in the literature the vertex formfactors are usually chosen such that they have their maximum at the on-shell point and are normalized to one at this point (giving a definite meaning to the coupling constant in the effective Lagrangian). The offshellness is often expressed by the three-momentum of one of the vertex particles. This parametrization, however, can cause problems as soon as one tries to extend the interactions to kinematical regions where one could run into a kinematical pole of the formfactor giving rise to divergences. Hence in a relativistic model for πN scattering [139], Pearce and Jennings have introduced a general pole-free (on the real axis) formfactor shape which just depends on the four-momentum squared q^2 of the off-shell particle:

$$F_{PJ}(q^2, m^2) = \left(\frac{n_\alpha\Lambda^4}{n_\alpha\Lambda^4 + (q^2 - m^2)^2}\right)^{n_\alpha}\ , \tag{3.28}$$

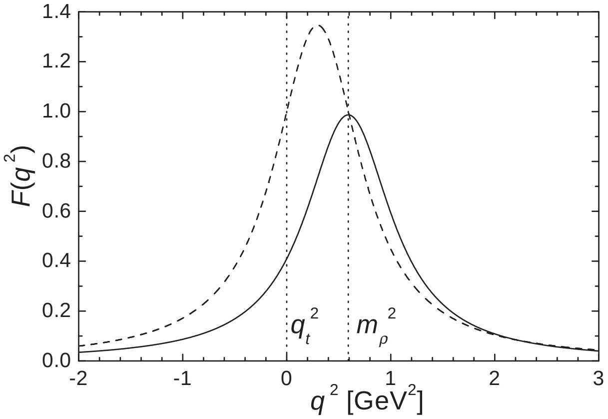

Figure 3.3: Comparison of the two formfactors $F_p(q^2)$ of Eq. (3.29) (solid line) and $F_t(q^2)$ of Eq. (3.30) (dashed line) for the ρNN vertex in πN elastic scattering with $\Lambda = 0.7$ GeV. The dotted lines give the threshold value q_t^2 for the t-channel and the on-shell value $(q^2 = m_\rho^2)$.

where m denotes the mass of the particle going off-shell. For large n_α, F_P approaches a Gaussian in $q^2 - m^2$ with width Λ^2. The so-called cutoff value Λ has to be extracted by comparison with experimental data. The specific forms applied here are

$$F_p(q^2, m^2) = \frac{\Lambda^4}{\Lambda^4 + (q^2 - m^2)^2} \tag{3.29}$$

$$F_t(q^2, m^2) = \frac{\Lambda^4 + \frac{1}{4}(q_t^2 - m^2)^2}{\Lambda^4 + \left(q^2 - \frac{1}{2}(q_t^2 + m^2)\right)^2} , \tag{3.30}$$

where q_t^2 denotes the value of q^2 at the kinematical threshold of the corresponding s-, u-, or t-channel. The first form F_p corresponds to Eq. (3.28) with $n_\alpha = 1$. The second form F_t is a slight modification of F_p and has also been used by [51, 52, 53]. It stresses the kinematical regime between the threshold and the on-shell point of the intermediate particle and ensures that t-channel contributions at threshold are directly given by their couplings. For example, using the non-linear σ model in πN scattering (i.e. pseudovector pion-nucleon coupling), only the isovector contact term (corresponding to the exchange of an infinitely heavy ρ meson) contributes to the scattering length a_π [156, 191]. Since the use of the coupling constants taken from chiral symmetry reproduces the experimental value for a_π very well, a formfactor being 1 at the πN threshold ($t = 0$) is desirable in this case. This is fulfilled by F_t . However, since we also allow for the variation of the ρ nucleon coupling constant in our calculation, the use of F_t for the t-channel contributions is not mandatory.

Summarizing the properties of the two formfactors F_p and F_t, both forms are only functions of the Lorentz invariant q^2, polefree on the real q^2 axis, and normalized to 1 for $q^2 = m^2$. The second form F_t is also 1 at threshold, but does not have its maximum at $q^2 = m^2$ like the first one. See Fig. 3.3 for a direct comparison of the two formfactors.

3.7 Formfactors, Photons, and Gauge Invariance

3.7.1 Born Contributions and Electromagnetic Formfactors

Using the conservation of the electromagnetic current $k_\mu j^\mu$, in addition to what is deduced in Section 3.3.1 one can derive a consistency requirement for the electromagnetic interactions, which yields a connection between the electromagnetic vertex Γ_μ and the full propagator G of a particle, the Ward-Takahashi identity (WTI) [82, 185]:

$$k_\mu \Gamma^\mu(p+k, p, k) = e\hat{e}\left[G^{-1}(p+k) - G^{-1}(p)\right] \tag{3.31}$$

with the charge operator $\hat{e}$. This identity is automatically fulfilled if the photon is introduced via minimal coupling $\partial_\mu \to \partial_\mu + \mathrm{i}e\hat{e}A_\mu$ in the hadronic Lagrangian (as described in Section 3.3.1 above), since the minimal coupling prescription guarantees gauge invariance and hence current conservation.

An interesting consequence of the WTI (3.31) is, that any modification performed on the charge coupling vertex also requires a modification in the propagator. In particular, the introduction of a formfactor $F(q^2)$, where q is the four-momentum of the intermediate propagating particle, at the charge vertex yields a self energy in the intermediate propagator. Moreover, it can be shown that gauge invariance requires for the nucleon electromagnetic half-offshell formfactor [40, 122, 123] $F_1(q^2) = 1$ (the same also holds true for the charge formfactor of other asymptotic particles [124]). Here, $F_1(q^2)$ is the formfactor describing the off-shell behavior of the charge coupling $(\hat{e}\gamma_\mu)$ in Eq. (3.5). Current conservation also requires that the unphysical, negative-energy part of the half-offshell formfactor $F_2(q^2)$ (modifying the coupling to the anomalous moment κ in (3.5)) is removed from the full amplitude and thus does not influence any observable [124, 122]. For a consistent description of the positive-energy part of the F_2 formfactor, one has to consider minimal coupling in loop-diagrams corresponding to higher order vertex corrections, since they generate additional transverse (with respect to the photon four-momentum) parts of the electromagnetic current [122]. However, this requires knowledge of the underlying strong interaction structure and may hence be model-dependent for real photons [122]. Recently [48], by using field transformations in Lagrangian field theories, it has also been argued, that it is impossible to measure any off-shell effects of F_1 and F_2 in nucleon-nucleon Bremsstrahlung and nucleon Compton scattering. Simply introducing a phenomenological term in the Lagrangian which produces an off-shell photon-nucleon-nucleon vertex can even lead to results which are inconsistent with data for related reactions [48].

To circumvent the above problems and ambiguities, we choose to use the free intermediate propagators for asymptotic particles and do not consider any formfactors at the photon vertices of the asymptotic particles.

3.7.2 Born Contributions and Hadronic Formfactors

As pointed out in Section 3.4.2, the photon couplings of all intermediate meson and baryon resonances are chosen in such a way that they are gauge invariant by themselves. Hence, they can be independently multiplied with a formfactor. This does not hold true for the intermediate propagation of a final state particle, since the photon also couples to its charge and thus the coupling is dictated by minimal coupling. As pointed out above, this leads to a gauge invariant sum of all Born diagrams. At the same time this gives rise to a problem upon introducing form factors at the hadronic vertices of the Born diagrams, since they should depend on the offshellness of the intermediate particle. This leads to putting q^2 dependent weights on the different diagrams. Since $q^2 = s$ for the direct graph, $q^2 = u$ for the exchange graph, and $q^2 = t$ for the Bremsstrahlung graph the sum becomes misbalanced and gauge invariance is violated. To circumvent this problem, already in the first effective Lagrangian models of pion photoproduction [38], gauge restoring terms have been added by hand.

The first microscopical treatment of this problem has been performed by Ohta [133]. He has expanded the electromagnetic formfactor of the pion-nucleon vertex in a Taylor series of the three four-momenta and has thereby shown that the minimal coupling scheme demands an additional amplitude contribution restoring gauge invariance when formfactors are used. In [194] it has been pointed out that Ohta's minimal-coupling scheme yields the same result as the simplest Born approach where point-like charge couplings without any formfactors are used. Thus Otha's additional amplitude just cancels all formfactor effects on the charge couplings, while the magnetic moment couplings can still be altered. In pseudoscalar meson photoproduction, Ohta's prescription hence translates in an unchanged A_2 part of the amplitude (see Section 5.4.1 and in particular Eq. (5.32)), while the other three amplitudes are still damped by the formfactors.

Leaving the A_2 contribution of the Born amplitude unchanged is, however, unsatisfactory for example from a dispersion theoretical point of view, because then, the Born amplitude is not square integrable. In addition, explicit microscopic one-loop meson calculations [20] show that the A_2 amplitude is indeed modified by off-shell effects. For these reasons, ad hoc prescriptions of using an overall formfactor for the Born diagrams have been introduced in pion photoproduction, see, e.g., [129].

Haberzettl [69] has been able to give a theoretical foundation to these phenomenological prescriptions. He has critized on Ohta's formalism that the Taylor expansion of the formfactor of the πNN vertex has been performed independently in the three four-momenta and consequently in the minimal-coupling scheme, although they are connected to each other via four-momentum conservation. Furthermore, in Ohta's prescription one is left with a formfactor contribution of $\hat{F}(s = m_N^2, u = m_N^2, t = m_\pi^2)$, which is unphysical. By using the two nucleon momenta as independent variables for minimal coupling, Haberzettl has shown that an additional counter term is generated effectively restoring gauge invariance by giving the same overall formfactor to all Born diagrams. This formfactor depends on the difference of the two nucleon momenta, i.e. on the pion momentum. Since the choice of the dependent four-momentum is arbitrary, he has deduced that any (reasonably behaved) formfactor that becomes unity for the limit $k = 0$ is sufficient to restore gauge invariance without any unwanted singularities. A general, "democratic" form of the formfactor for the Born diagrams in pion photoproduction has hence been deduced:

$$\hat{F}(s, u, t) = a_1 F_1(s) + a_2 F_2(u) + a_3 F_3(t) \ . \tag{3.32}$$

To ensure the above limit, the coefficients a_i have to add up to unity: $a_1 + a_2 + a_3 = 1$. In [52, 53] $a_1 = a_2 = a_3 = \frac{1}{3}$ has been chosen.

Davidson and Workman [35] have pointed out a flaw in the arguments of Haberzettl [69]. Since two of the three mandelstam variables are independent, merely requiring $a_1 + a_2 + a_3 = 1$ does not necessarily lead to the desired on-shell constraint ensuring the cancellation of poles:

$$\hat{F}(s = m_N^2, u, t) = \hat{F}(s, u = m_N^2, t) = \hat{F}(s, u, t = m_\pi^2) = 1 \ .$$

Moreover, crossing symmetry requires that the A_1 and A_2 amplitudes (see Eq. (5.32)) in pseudovector photoproduction only change sign under the replacement $s \leftrightarrow u$. This requires that $\hat{F}(s, u, t) = \hat{F}(u, s, t)$, which is violated in (3.32) if $a_1 \neq a_2$. Davidson and Workman have deduced a crossing symmetric form also satisfying the pole constraints:

$$\begin{aligned} \hat{F}(s, u, t) \quad = \quad & F_1(s) + F_1(u) + F_3(t) - \\ & F_1(s)F_1(u) - F_1(s)F_3(t) - F_1(u)F_3(t) + F_1(s)F_1(u)F_3(t) \ . \end{aligned} \tag{3.33}$$

Note, that this form is not unique. This can also be applied easily to η and ω photoproduction by setting $F_3(t) = 0$ and to $K\Lambda$ photoproduction by setting $F_2(u) = 0$ since the corresponding Born diagrams are absent.

Following the arguments of Ohta, Haberzettl, and Davidson and Workman, the gauge prescription of using an overall formfactor with the shape (3.33) is implemented in the present calculation.

3.7.3 Resonances and Intermediate Mesons

For the baryon intermediate resonances, each electromagnetic decay vertex is chosen in such a way, that it is gauge invariant by itself. Therefore, the introduction of formfactors does not cause any problem and one can allow for independent formfactors at the hadronic and electromagnetic decay vertices of the baryon resonances.

The same holds also true for the electromagnetic decay vertices of intermediate mesons, and one could also introduce independent formfactors at the baryon-baryon-meson and the meson-meson-photon vertex. Being two-quark states, the meson structure is revealed at smaller distances than in the baryon resonance case leading to the expectation that formfactors play a less important role in meson- than in baryon-exchange reactions. Therefore, in the t-channel diagrams, we only introduce a formfactor at the baryon-baryon-meson vertex and absorb all internal structure effects of the meson-meson-meson/meson-meson-photon vertex effectively in the baryon-baryon-meson vertex. This procedure also proves to be reasonable a posteriori since the use of only one t-channel cutoff formfactor turns out to lead to a good description of the experimental data. At the same time, the resulting cutoff value Λ_t turns out to be significantly smaller (≈ 0.7 GeV) than at all other vertices (≥ 1 GeV), indicating that the use of a formfactor at both t-channel vertices would be necessary to extract values for Λ_t in the range of the other cutoff values.

3.7.4 Formfactors and Free Parameters

In principle, at each interaction vertex one should allow for a different formfactor behavior because it is supposed to describe the internal structure of the participating particles. This would amount to allowing for a different cutoff value or even shape at each individual vertex, giving rise to a huge amount of free parameters. To reduce this number, we restrict ourselves to a minimum of distinction in the following way:

- The same formfactor shape (F_p of Eq. (3.29)) and cutoff value Λ_N is used at all nucleon-final-state vertices ($NN\pi$, $NN\eta$, $N\Lambda K$, $N\Sigma K$, and $NN\omega$) in the s- and u-channel.
- The same formfactor shape (F_p) is used at all baryon resonance vertices ($RN\gamma$, $RN\pi$, $RN\zeta$, $RN\eta$, $R\Lambda K$, $R\Sigma K$, and $RN\omega$), but it is distinguished between spin-$\frac{1}{2}$ and -$\frac{3}{2}$ resonances and between hadronic and electromagnetic final states. This leads to four different cutoff values $\Lambda^h_{\frac{1}{2}}$, $\Lambda^\gamma_{\frac{1}{2}}$, $\Lambda^h_{\frac{3}{2}}$, and $\Lambda^\gamma_{\frac{3}{2}}$.
- The same formfactor shape (F_p or F_t of Eqs. (3.29), (3.30)) and cutoff value Λ_t is used at all baryon-baryon-meson t-channel vertices.

The nucleon is treated differently as the resonances to account for the particular importance of the ground state contributions for all energies and channels. Since the vertex structure given by the Lagrangians is significantly different for spin-$\frac{1}{2}$ and spin-$\frac{3}{2}$ resonances (see Section 3.4 above), a distinction is also made between these two classes of diagrams[7)]. The t-channel gives rise to fundamentally different contributions and is therefore chosen independently from the s- and u-channel formfactors.

The choices of the formfactor shapes are guided by the results from Feuster and Mosel [51, 52, 53], who have found the best description of experimental pion- and photon-induced data when following the above. Since the differences between the choice of F_p or F_t for the formfactors in the t-channel contributions have been only marginal, we also allow for both possibilities in the present calculation. Whether the both choices still give comparable results even in the extended kinematic range considered here, is discussed in Chapter 8.

3.8 Model Parameters

The aim of this calculation is to perform a consistent extraction of nucleon resonance properties, while reducing the number of free parameters to a minimum. Therefore, the properties of all asymptotic particles and intermediate t-channel mesons entering the potential are not varied but taken from [67]; a summary is given in Table 3.1. The remaining free parameters of the model are

- the masses of the resonances, i.e. the values of m_R entering the propagator;

[7)] An alternative way for this classification could be the distinction between different orbital angular momentum transitions.

	mass [GeV]	S	P	I	t-channel contributions
N	0.939	$\frac{1}{2}$	$+$	$\frac{1}{2}$	
Λ	1.116	$\frac{1}{2}$	$+$	0	
Σ	1.193	$\frac{1}{2}$	$+$	1	
π	0.138	0	$-$	1	$(\gamma,\gamma),(\gamma,\pi),(\gamma,\omega)$
ζ	0.276	0	$+$	1	
K	0.496	0	$-$	$\frac{1}{2}$	$(\gamma,\Lambda),(\gamma,\Sigma)$
η	0.547	0	$-$	0	$(\gamma,\gamma),(\gamma,\omega)$
ω	0.783	1	$-$	0	$(\gamma,\pi),(\gamma,\eta)$
σ	0.650	0	$+$	0	(π,π)
ρ	0.769	1	$-$	1	$(\pi,\pi),(\pi,\omega),(\gamma,\pi),(\gamma,\eta)$
a_0	0.983	0	$+$	1	(π,η)
K^*	0.894	1	$-$	$\frac{1}{2}$	$(\pi,\Lambda),(\pi,\Sigma),(\gamma,\Lambda),(\gamma,\Sigma)$
K_1	1.273	1	$+$	$\frac{1}{2}$	$(\gamma,\Lambda),(\gamma,\Sigma)$
K_0^*	1.412	0	$+$	$\frac{1}{2}$	$(\pi,\Lambda),(\pi,\Sigma)$

Table 3.1: Properties of all asymptotic particles and intermediate t-channel mesons entering the potential. For the isospin, see also Appendix F. For those particles, that appear in several charge states, averaged masses are used. For the mesons also all reaction channels, where the corresponding meson appears in a t-channel exchange, are given.

- the couplings of the resonances to the final states, i.e. for each resonance one for each (pseudo-) scalar meson final state, one (two) for the γN final state, and two (three) for the ωN final state. The value in brackets holds for spin-$\frac{3}{2}$ resonances. When the conventional spin-$\frac{3}{2}$ resonance vertices (cf. Section 3.4.1) are used, an additional off-shell parameters a is required for each spin-$\frac{3}{2}$ resonance coupling.

- the couplings of the nucleon to the hadronic final states, i.e. one for each (pseudo-) scalar meson final state and two for ωN. Since the usual values for the $NN\omega$ couplings (cf. Ref. [53] and references therein) stem from different kinematical regimes than the one examined here, we also allow these two values to be varied during the fitting procedure; see also Section 8.2.1.

- the couplings of the nucleon to the intermediate mesons, i.e. one for each (pseudo-) scalar meson and two for the (axial-) vector mesons.

- the cutoff values of the formfactors, see Section 3.7.4 above.

Due to the large number of considered resonances[8)] (see Table 3.2) a large number of parameters results from the consideration of 6 hadronic final states. In principle, it would be desirable to use ranges for the parameters determined from quark models [24, 151] or QCD lattice calculations [107]. On the other side, there are still large uncertainties and discrepancies in the predicted resonance properties. Thus leaving them as free parameters

---

[8)] As it will turn out in the fitting procedure, however, 3 of the quoted resonances ($S_{11}(2090)$, $P_{11}(2090)$, and $P_{31}(1910)$) are not needed for the description of the experimental data, see Section 8.2.3.

$L_{2I,2S}$	status	mass	Γ_{tot}	$R_{\pi N}$	$R_{2\pi N}$	$R_{\eta N}$	$R_{K\Lambda}$	$R_{K\Sigma}$	$R_{\omega N}$	$R_{\gamma N}$
$S_{11}(1535)$	****	1535	150	45	6	43				0.2
$S_{11}(1650)$	****	1650	150	72	15	6	7			0.1
$S_{11}(2090)$	*	2090								
$P_{11}(1440)$	****	1440	350	65	35					0.04
$P_{11}(1710)$	***	1710	100	15	65		15			0.02
$P_{11}(2100)$	*	2100								
$P_{13}(1720)$	****	1720	150	15	> 70		8			0.1
$P_{13}(1900)$	**	1900	500	26	45					
$D_{13}(1520)$	****	1520	120	55	45					0.5
$D_{13}(1700)$	***	1700	100	10	90					0.04
$D_{13}(2080)$	**	2080								
$S_{31}(1620)$	****	1620	150	25	75	—	—		—	0.02
$S_{31}(1900)$	**	1900	200	20		—	—		—	
$P_{31}(1750)$	*	1750	300	8		—	—		—	
$P_{31}(1910)$	****	1910	250	23		—	—		—	0.1
$P_{33}(1232)$	****	1232	120	> 99	0	—	—		—	0.54
$P_{33}(1600)$	***	1600	350	18	82	—	—		—	0.01
$P_{33}(1920)$	***	1920	200	13		—	—		—	
$D_{33}(1700)$	****	1700	300	15	85	—	—		—	0.02

Table 3.2: Properties of all resonances considered in the calculation. The status gives the overall rating from the PDG [67] ranging from * ("Evidence of existence is poor.") to **** ("Existence is certain and properties are at least fairly well explored."). When available, the mass and decay widths (taken as the mean value of the given ranges) estimates from [67] are also quoted. L denotes the angular momentum in the resonance's πN decay. The mass and the total width Γ_{tot} are given in MeV, the partial decay width ratios R in percent of the total width. The long bars "—" indicate that the corresponding decay is forbidden due to isospin. As it will turn out, not all of these resonances are needed in the present calculation, see Chapter 8.

in the present calculation allows to compare the extracted resonance properties with the underlying theory, thereby restricting the models of hadron structure. The advantage for the extraction of these properties by an effective Lagrangian model becomes apparent when looking at Table 3.3. The comparison of our model parameters with the resonance model of Batinić et al. [10] (see Section 3.1.1) reveals, that in the resonance model of [10] the amount of background parameters exceeds the one of resonance parameters. This problem makes the reliable extraction of resonance parameters in resonance models more difficult. It is a result of the fact, that the background has to be parametrized separately for each partial wave. Hence the number of background parameters rises linearly with the number of included partial waves, while in an effective Lagrangian model the background is fixed by the consideration of inherent u-channel contributions, Born diagrams, and t-channel meson exchanges. While the first ones are completely fixed by the resonance properties and the Born diagrams only add one unknown coupling per considered final

	final states	J_{max}	I	S_R	max. $\sqrt{s}$	res.	para.	back.
P-p-π+	$\pi N, \zeta N, \eta N, K\Lambda, K\Sigma, \omega N$	$\frac{27}{2}$	$\frac{1}{2}, \frac{3}{2}$	$\frac{3}{2}$	2.0 GeV	15	120	20
Batinić	$\pi N, \zeta N, \eta N$	$\frac{7}{2}$	$\frac{1}{2}$	$\frac{7}{2}$	2.5 GeV	15	132	72

Table 3.3: Comparison of the model of Batinić et al. [10] with our calculation P-p-π+ (see Chapter 8). J_{max} is the maximal total spin considered, I the considered isospin amplitudes, S_R the maximum resonance spin, "para." the total number of parameters, and "back." the number of background parameters.

state, the meson exchanges give rise to only $1-2$ parameters per considered meson. Note, that some of the final state mesons (ω, π, η, see Table 3.1 above) of the present model also contribute as t-channel exchanges, thereby creating t-channel background without any free parameter. This shows in particular, that due to the dynamical background generation, the number of background parameters does not increase with the number of included partial waves and is drastically reduced compared to a resonance model.

Chapter 4

Helicity Amplitudes and Partial-Wave Decomposition of the BS Equation

It has been pointed out in Chapter 2 that the BS equation (2.11) can be further simplified by a partial-wave decomposition (PWD). The general idea is to directly implement the symmetry properties of the underlying potential in the scattering equation, i.e. the conservation of the quantum numbers total spin J, total parity P, and total isospin I, see Fig. 4.1. In this chapter, the consequences of the conservation of the total spin J and the parity P are discussed, while the isospin decomposition is deferred to Appendix F. Due to the complexity of our potential, the PWD in total spin and parity has to be performed by a generalization of the standard procedures (see, e.g., [52]), while the isospin decomposition is only slightly modified as compared to what is discussed in [52].

For many of the channels that enter the potential of the present model, PWD of the angle-dependent amplitudes into amplitudes with total spin J and parity P have been known for a long time; e.g. for $\pi N \rightarrow \pi N$ and $\gamma N \rightarrow \pi N$ since the late 1950s [27, 28]. In the previous chapter, it has been argued that also final states where both particles carry intrinsic spin as, e.g., ωN have to enter the unitary calculation consistently, i.e. also channels such as $\omega N \rightarrow \omega N$ have to be considered. Therefore, in the coupled-channel problem not all the final states consist of a $\frac{1}{2}^+$-baryon and a 0^--meson as in the $\pi N \rightarrow \pi N$ $(\eta N, K\Lambda, K\Sigma)$

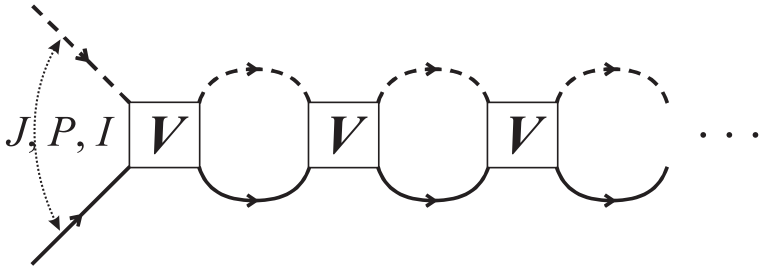

Figure 4.1: Illustration of the conservation of the quantum numbers J, P, and I during rescattering.

case. As a consequence, the orbital angular momentum ℓ is not necessarily a conserved quantity, and a standard PWD [27, 28] based on ℓ becomes inconvenient for many of the channels that have to be included. A more elegant and in particular uniform PWD for all channels would be desirable. Hence we use here a generalization of the standard PWD methods which represents a tool to analyze any meson- and photon-baryon reaction on an equal footing; even final states not yet considered in the model – as e.g. $\pi\Delta$ – can be incorporated easily. This generalization also has the advantage that – from a field-theoretical point of view – the resulting helicity partial waves are closely related to the Feynman spin matrix elements $\mathcal{M}^{fi}_{s's}$. The relation between this generalization and the above mentioned standard decompositions is discussed in Chapter 6.

4.1 Helicity Amplitudes

The aim in the construction of the helicity amplitudes is to take advantage of the symmetry properties of the interaction, i.e. that it is rotationally invariant, parity and four-momentum conserving. In describing a reaction $a+b \to c+d$ in the center-of-mass (c.m.) system, we use the total four-momenta $P = p_a + p_b = (\sqrt{s}, \mathbf{0})$, $P' = p_c + p_d$, the total spin J and its z-component $J_z = M$ together with the initial- and final-state helicities $\lambda = \lambda_a - \lambda_b$, $\lambda' = \lambda_c - \lambda_d$[1)] as the properties to characterize the initial and final state. The reaction matrix T then has the form:

$$\langle P'J'M', \lambda'|T|PJM, \lambda\rangle = \langle\lambda'|T^{JM}(\sqrt{s})|\lambda\rangle\delta^4(P-P')\delta_{JJ'}\delta_{MM'} \; . \tag{4.1}$$

To reexpress our Feynman amplitudes in such a way, we start with a basic two-particle momentum state in the c.m. system with three momenta $\boldsymbol{k} = -\boldsymbol{p}$ and particle helicities λ_k and λ_p: $|\boldsymbol{p}\,\boldsymbol{k}\,, \lambda_k\lambda_p\rangle$. In Eq. (A.5) of Appendix A.1 the relation between the three-momentum states $|\boldsymbol{p}\,\boldsymbol{k}\,, \lambda_k\lambda_p\rangle$ and the four-momentum states $|P; \vartheta\varphi, \lambda_k\lambda_p\rangle$ is established:

$$|\boldsymbol{p}\,\boldsymbol{k}\,, \lambda\rangle = \sqrt{\frac{\sqrt{s}}{\mathrm{k}E_B E_M}}|P; \vartheta\varphi, \lambda\rangle \; .$$

Hence, in the following it is sufficient to restrict the discussion on the angular part $|\vartheta\varphi, \lambda_k\lambda_p\rangle$ of the two-particle state. Consider the Wigner functions

$$\mathcal{D}^J_{M'M}(\alpha, \beta, \alpha) = e^{-\mathrm{i}\alpha M'} d^J_{MM'}(\beta) e^{-\mathrm{i}\alpha M} \; , \tag{4.2}$$

which are the matrix elements of a rotation transforming the $|J, M\rangle$ component of the unit vector $\boldsymbol{e}_z$ into the $|J, M'\rangle$ component of the vector $(\cos\alpha\sin\beta, \sin\alpha\sin\beta, \cos\beta)$. Now, the two-particle c.m. momentum states can be decomposed into states with definite total angular momentum J and z-component $J_z = M$ [83]:

$$|JM, \lambda\rangle = N_J \int \mathrm{d}\varphi \mathrm{d}(\cos\vartheta) {\mathcal{D}^J_{M\lambda}}^*(\varphi, \vartheta, -\varphi)|\vartheta\varphi, \lambda\rangle \tag{4.3}$$

[1)] The particle helicities λ_a etc. are the projections of the spin s_a on the direction of motion of the particle. Thus, since in the c.m. system the z-axis is chosen along the three-momentum of the incoming meson, one has $\lambda = s_z$ for final state mesons and $\lambda = -s_z$ for final state baryons, cf. Appendices A.1 and A.2.

The normalization constant N_J is chosen such that the helicity states are normalized in the following way ($\lambda = \lambda_k - \lambda_p$, $\lambda' = \lambda'_k - \lambda'_p$):

$$\begin{aligned}
\delta_{J'J}\delta_{M'M}\delta_{\lambda'_k\lambda_k}\delta_{\lambda'_p\lambda_p} &\overset{!}{=} \langle J'M', \lambda'_k\lambda'_p | JM\lambda_k, \lambda_p\rangle \\
&= N^*_{J'}N_J \int \mathrm{d}\Omega'\mathrm{d}\Omega \mathcal{D}^{J'}_{M'\lambda'}(\varphi', \vartheta', -\varphi'){\mathcal{D}^{J}_{M\lambda}}^*(\varphi, \vartheta, -\varphi) \times \\
&\qquad \langle \vartheta'\varphi', \lambda'_k\lambda'_p | \vartheta\varphi, \lambda_k\lambda_p\rangle \\
&= N^*_{J'}N_J\delta_{\lambda'_k\lambda_k}\delta_{\lambda'_p\lambda_p} \int \mathrm{d}\Omega e^{\mathrm{i}(M-M')\varphi} d^{J'}_{M'\lambda'}(\vartheta) d^J_{M\lambda}(\vartheta) \\
&= 2\pi N^*_{J'}N_J\delta_{\lambda'_k\lambda_k}\delta_{\lambda'_p\lambda_p}\delta_{M'M} \int \mathrm{d}(\cos\vartheta) d^{J'}_{M'\lambda'}(\vartheta) d^J_{M\lambda}(\vartheta) \\
&= \frac{4\pi}{2J+1}|N_J|^2\delta_{\lambda'_k\lambda_k}\delta_{\lambda'_p\lambda_p}\delta_{M'M}\delta_{J'J} \qquad (4.4)
\end{aligned}$$

and hence $N_J = \sqrt{(2J+1)/(4\pi)}$. The last equality follows from the normalization condition of the d-functions (B.8). Then the transformation is given by

$$\langle \vartheta\varphi, \lambda_k\lambda_p | JM, \lambda'_k\lambda'_p\rangle = N_J {\mathcal{D}^J_{M\lambda}}^*(\varphi, \vartheta, -\varphi)\delta_{\lambda'_k\lambda_k}\delta_{\lambda'_p\lambda_p} \; . \qquad (4.5)$$

For the incoming c.m. state ($\vartheta_0 = \varphi_0 = 0$) one gets[2)]

$$\langle JM, \lambda | \vartheta_0\varphi_0, \lambda\rangle = N_J\mathcal{D}^{J^*}_{M\lambda}(0,0,0) = N_J d^J_{M\lambda}(0) = N_J\delta_{M\lambda} \; , \qquad (4.6)$$

where property (B.6) of the d-functions was used. This result is not surprising since $\ell = 0$ and therefore $J_z \equiv M = \lambda$. Consequently, the index M of the reaction matrix T is dropped in the following, since it is fixed by the helicity λ of the initial state.

Using the rotational invariance of the interaction, we are now in a position to decompose the angle-dependent c.m. T-matrix (cf. Eq. (C.10)) into $\langle\lambda'|T^J(\sqrt{s})|\lambda\rangle$ matrix elements as in Eq. (4.1) by inserting complete sets of $|JM\rangle$ states:

$$\begin{aligned}
\mathcal{T}^{fi}_{\lambda'\lambda} &\equiv \langle \vartheta'\varphi', \lambda' | T | \vartheta_0\varphi_0, \lambda\rangle \\
&= \sum_{J',M'}\sum_{J,M} \langle \vartheta'\varphi', \lambda' | J'M', \lambda'\rangle\langle J'M', \lambda' | T(\sqrt{s}) | JM, \lambda\rangle\langle JM, \lambda | 00, \lambda\rangle \\
&= \sum_{J',M'}\sum_{J,M} N_{J'}N_J\mathcal{D}^{J'^*}_{M'\lambda'}(\varphi', \vartheta', -\varphi')\langle\lambda'|T^J(\sqrt{s})|\lambda\rangle\delta_{JJ'}\delta_{MM'}\delta_{M\lambda} \\
&= \sum_J \frac{2J+1}{4\pi}\langle\lambda'|T^J(\sqrt{s})|\lambda\rangle e^{\mathrm{i}(\lambda-\lambda')\varphi'} d^J_{\lambda\lambda'}(\vartheta) \; . \qquad (4.7)
\end{aligned}$$

Setting $\varphi' = 0$ (c.m. system, see Appendix A) and relabeling $\vartheta' \to \vartheta$, this equation can be inverted to extract amplitudes with total spin J

$$\mathcal{T}^J_{\lambda'\lambda}(\sqrt{s}) \;\; \equiv \;\; \langle\lambda'|T^J(\sqrt{s})|\lambda\rangle$$

---

2) From now on, the individual helicities are omitted where redundant and the states are only labeled by the total helicities λ and λ'.

$$\begin{aligned}
&\equiv \langle J,\lambda'|T(\sqrt{s})|J,\lambda\rangle \\
&= 2\pi\int_{-1}^{+1}\mathrm{d}(\cos\vartheta)d^J_{\lambda\lambda'}(\vartheta)\langle\vartheta,\varphi=0,\lambda'|T(\sqrt{s})|00,\lambda\rangle \\
&= 2\pi\int_{-1}^{+1}\mathrm{d}(\cos\vartheta)d^J_{\lambda\lambda'}(\vartheta)\mathcal{T}^{fi}_{\lambda'\lambda}\ ,
\end{aligned}\tag{4.8}$$

where the normalization of the d-functions (B.8) has been used again. Furthermore, the helicity states $|J,\lambda\rangle \equiv |J,\lambda_k\lambda_p\rangle$ fulfill the parity property [83]:

$$\hat{P}|J,\lambda\rangle = \hat{P}|J,\lambda_k\lambda_p\rangle = \eta_k\eta_p(-1)^{J-s_k-s_p}|J,-\lambda_k-\lambda_p\rangle = \eta_k\eta_p(-1)^{J-s_k-s_p}|J,-\lambda\rangle\ . \tag{4.9}$$

Here, η_k, η_p, and s_k, s_p are the intrinsic parities and spins, resp. of the two particles. The construction of normalized states with parity $(-1)^{J\pm\frac{1}{2}}$ is now straightforward:

$$\begin{aligned}
|J,\lambda;\pm\rangle &\equiv \frac{1}{\sqrt{2}}\left(|J,+\lambda\rangle \pm \eta|J,-\lambda\rangle\right) \\
\Rightarrow \hat{P}|J,\lambda;\pm\rangle &= (-1)^{J\pm\frac{1}{2}}|J,\lambda;\pm\rangle\ ,
\end{aligned}\tag{4.10}$$

where we have defined

$$\eta \equiv \eta_k\eta_p(-1)^{s_k+s_p+\frac{1}{2}}\ . \tag{4.11}$$

For parity conserving interactions $T=\hat{P}^{-1}T\hat{P}$ follows:

$$\langle J,-\lambda'_k-\lambda'_p|T(\sqrt{s})|J,-\lambda_k-\lambda_p\rangle = \eta(\eta')^{-1}\langle J,\lambda'_k\lambda'_p|T(\sqrt{s})|J,\lambda_k\lambda_p\rangle \tag{4.12}$$

and one can project out helicity partial-wave amplitudes with a definite parity of $(-1)^{J\pm\frac{1}{2}}$:

$$\begin{aligned}
\mathcal{T}^{J\pm}_{\lambda'\lambda} &\equiv \langle J,\lambda';\pm|T|J,\lambda;\pm\rangle \\
&= \mathcal{T}^{J}_{\lambda'\lambda} \pm \eta\mathcal{T}^{J}_{\lambda'-\lambda}\ .
\end{aligned}\tag{4.13}$$

These helicity partial-wave amplitudes $\mathcal{T}^{J\pm}_{\lambda'\lambda}$ have definite, identical J and definite, but opposite parity. It is quite obvious that this method is valid for any meson-baryon final state combination, even cases as e.g. $\omega N\to\pi\Delta$. As shown in Section 6.1, in the case of $\pi N\to\pi N$ ($\eta N, K\Lambda, K\Sigma$) the $\mathcal{T}^{J\pm}_{\lambda'\lambda}$ coincide with the conventional partial wave amplitudes: $\mathcal{T}^{J\pm}_{\frac{1}{2}\frac{1}{2}} \equiv \mathcal{T}_{\ell\pm}$.

The parity property (4.12) can also be used to extract the parity properties of the angle dependent c.m. helicity scattering amplitudes $\mathcal{T}^{fi}_{\lambda'\lambda}(\vartheta)$:

$$\begin{aligned}
\mathcal{T}^{fi}_{-\lambda',-\lambda}(\vartheta) &\equiv \langle\vartheta 0,-\lambda'|T|00,-\lambda\rangle \\
&= \eta(\eta')^{-1}(-1)^{\lambda-\lambda'}\langle\vartheta 0,\lambda'|T|00,\lambda\rangle \\
&= \eta(\eta')^{-1}(-1)^{\lambda-\lambda'}\mathcal{T}^{fi}_{\lambda'\lambda}(\vartheta)\ ,
\end{aligned}\tag{4.14}$$

where $\varphi=0$ and Eqs. (4.7), (B.5) have been applied.

For elastic scattering reactions ($\gamma N\to\gamma N$, $VN\to VN$, $\varphi N\to\varphi N$), it is also interesting to note, that similarly to Eq. (4.12), due to the time reversal property $T=\hat{T}^{-1}T\hat{T}$ of the interaction follows [83]

$$\langle J,\lambda'_k\lambda'_p|T(\sqrt{s})|J,\lambda_k\lambda_p\rangle = \langle J,\lambda_k\lambda_p|T(\sqrt{s})|J,\lambda'_k\lambda'_p\rangle \tag{4.15}$$

and for the angle-dependent c.m. helicity scattering amplitudes $\mathcal{T}^{fi}_{\lambda'\lambda}(\vartheta)$:

$$\begin{aligned}
\mathcal{T}^{fi}_{\lambda',\lambda}(\vartheta) &\equiv \langle\vartheta 0, \lambda'|T|00, \lambda\rangle \\
&= (-1)^{\lambda-\lambda'}\langle\vartheta 0, \lambda|T|00, \lambda'\rangle \\
&= (-1)^{\lambda-\lambda'}\mathcal{T}^{fi}_{\lambda\lambda'}(\vartheta) \ , \qquad (4.16)
\end{aligned}$$

where Eqs. (4.7), (B.4) have been used.

4.2 Partial-Wave Decomposition of the BS Equation

Since the Bethe-Salpeter (BS) equation, which is derived in Chapter 2, is in general a four-dimensional integral equation (2.6) its solution poses a tremendous problem. However, the problem can be simplified for rotationally invariant potentials by performing a partial-wave decomposition of the scattering equation. For the following discussion, we restrict ourselves to the angular part of the four-dimensional integral and evaluate it in the c.m. system, i.e. $\vartheta \equiv \vartheta_0 = 0$, $\varphi \equiv \varphi_0 = 0$. We start from the integral part of Eq. (2.11), insert complete sets of $|J, M\rangle$ states, and make use of the rotational invariance of the K- and T-matrices (in the following, the upper indices fi and the summation over different intermediate two-particle states $|a\rangle$ are omitted):

$$\begin{aligned}
&\int \mathrm{d}\Omega_q \sum_{\lambda_q} \mathcal{T}_{\lambda'\lambda_q}\mathcal{K}_{\lambda_q\lambda} \\
= \ &\int \mathrm{d}\Omega_q \sum_{\lambda_q}\sum_{J',M'}\sum_{J,M}\sum_{J'_q,M'_q}\sum_{J_q,M_q} \langle\Omega', \lambda'|J'M', \lambda'\rangle\langle J'M', \lambda'|T(\sqrt{s})|J'_qM'_q, \lambda_q\rangle \times \\
&\quad \langle J'_qM'_q, \lambda_q|\Omega_q, \lambda_q\rangle\langle\Omega_q, \lambda_q|J_qM_q, \lambda_q\rangle\langle J_qM_q, \lambda_q|K(\sqrt{s})|JM, \lambda\rangle\langle JM, \lambda|\Omega_0, \lambda\rangle \\
= \ &\int \mathrm{d}\Omega_q \sum_{\lambda_q}\sum_{J',M'}\sum_{J,M}\sum_{J'_q,M'_q}\sum_{J_q,M_q} N_{J'}\mathcal{D}^{J'^*}_{M'\lambda'}(\varphi', \vartheta', -\varphi')\mathcal{T}^{J'M'}_{\lambda'\lambda_q}\delta_{J'J'_q}\delta_{M'M'_q} \times \\
&\quad N_{J'_q}\mathcal{D}^{J'_q}_{M'_q\lambda_q}(\varphi_q, \vartheta_q, -\varphi_q)N_{J_q}\mathcal{D}^{J_q{}^*}_{M_q\lambda_q}(\varphi_q, \vartheta_q, -\varphi_q)\mathcal{K}^{JM}_{\lambda_q\lambda}\delta_{JJ_q}\delta_{MM_q}N_J\mathcal{D}^J_{M\lambda}(0,0,0) \\
= \ &\int \mathrm{d}\Omega_q \sum_{\lambda_q}\sum_{J',M'}\sum_{J,M} N^2_{J'}N^2_J d^{J'}_{M'\lambda'}(\vartheta')e^{\mathrm{i}(M'-\lambda')\varphi'}\mathcal{T}^{J'M'}_{\lambda'\lambda_q} \times \\
&\quad d^{J'}_{M'\lambda_q}(\vartheta_q)d^J_{M\lambda_q}(\vartheta_q)e^{\mathrm{i}(M-M')\varphi_q}\mathcal{K}^{JM}_{\lambda_q\lambda}\delta_{M\lambda} \\
= \ &2\pi\int \mathrm{d}(\cos\vartheta_q)\sum_{\lambda_q}\sum_{J',M'}\sum_{J} N^2_J N^2_{J'}d^{J'}_{M'\lambda'}(\vartheta')e^{\mathrm{i}(M'-\lambda')\varphi'}\mathcal{T}^{J'M'}_{\lambda'\lambda_q}d^{J'}_{M'\lambda_q}(\vartheta_q)d^J_{\lambda\lambda_q}(\vartheta_q)\delta_{M'\lambda}\mathcal{K}^{J\lambda}_{\lambda_q\lambda} \\
= \ &2\pi\sum_{\lambda_q}\sum_{J',J} N^2_J N^2_{J'}d^{J'}_{\lambda\lambda'}(\vartheta')e^{\mathrm{i}(\lambda-\lambda')\varphi'}\mathcal{T}^{J'\lambda}_{\lambda'\lambda_q}\frac{2}{2J+1}\delta_{JJ'}\mathcal{K}^{J\lambda}_{\lambda_q\lambda} \\
= \ &\sum_{\lambda_q}\sum_{J}\frac{2J+1}{4\pi}d^J_{\lambda\lambda'}(\vartheta')e^{\mathrm{i}(\lambda-\lambda')\varphi'}\mathcal{T}^J_{\lambda'\lambda_q}\mathcal{K}^J_{\lambda_q\lambda} \ ,
\end{aligned}$$

where the $\mathcal{T}^J_{\lambda'\lambda_q}$ and $\mathcal{K}^J_{\lambda_q\lambda}$ are defined in the same way as in (4.8). Now the BS equation reads:

$$\mathcal{T}_{\lambda'\lambda} = \mathcal{K}_{\lambda'\lambda} + \mathrm{i}\sum_{\lambda_q}\sum_J \frac{2J+1}{4\pi} d^J_{\lambda\lambda'}(\vartheta') e^{\mathrm{i}(\lambda-\lambda')\varphi'} \mathcal{T}^J_{\lambda'\lambda_q}\mathcal{K}^J_{\lambda_q\lambda} \, . \tag{4.17}$$

Integrating this equation over $2\pi\int \mathrm{d}(\cos\vartheta')$ and taking $\varphi' = 0$ we arrive at an algebraic BS equation for each partial wave:

$$\mathcal{T}^J_{\lambda'\lambda} = \mathcal{K}^J_{\lambda'\lambda} + \mathrm{i}\sum_{\lambda_q} \mathcal{T}^J_{\lambda'\lambda_q}\mathcal{K}^J_{\lambda_q\lambda} \, . \tag{4.18}$$

Finally, we also have to take into account that our interactions are parity conserving and the rescattering takes place only via states with the same parity. Thus we have to rewrite the BS equation correspondingly. Using the helicity partial-wave amplitudes with parity $(-1)^{J\pm\frac{1}{2}}$ as defined in (4.13) we find from (4.18):

$$\begin{aligned}
\mathcal{T}^{J\pm}_{+\lambda',\lambda} &= \mathcal{K}^{J\pm}_{+\lambda',\lambda} + \mathrm{i}\sum_{\lambda_q} \mathcal{T}^{J}_{+\lambda',\lambda_q}\mathcal{K}^{J\pm}_{\lambda_q,\lambda} \\
&= \mathcal{K}^{J\pm}_{+\lambda',\lambda} + \mathrm{i}\sum_{\lambda_q>0} \left(\mathcal{T}^{J}_{+\lambda',+\lambda_q}\mathcal{K}^{J\pm}_{+\lambda_q,\lambda} + \mathcal{T}^{J}_{+\lambda',-\lambda_q}\mathcal{K}^{J\pm}_{-\lambda_q,\lambda}\right) \\
&= \mathcal{K}^{J\pm}_{+\lambda',\lambda} + \mathrm{i}\sum_{\lambda_q>0} \left(\mathcal{T}^{J}_{+\lambda',+\lambda_q} \pm \eta_q \mathcal{T}^{J}_{+\lambda',-\lambda_q}\right)\mathcal{K}^{J\pm}_{+\lambda_q,\lambda} \\
&= \mathcal{K}^{J\pm}_{+\lambda',\lambda} + \mathrm{i}\sum_{\lambda_q>0} \mathcal{T}^{J\pm}_{+\lambda',\lambda_q}\mathcal{K}^{J\pm}_{+\lambda_q,\lambda} \, ,
\end{aligned} \tag{4.19}$$

where we have used (4.12) to derive

$$\begin{aligned}
\mathcal{K}^{J\pm}_{-\lambda_q,\lambda} &= \mathcal{K}^{J}_{-\lambda_q,+\lambda} \pm \eta \mathcal{K}^{J}_{-\lambda_q,-\lambda} \\
&= \eta_q\eta\left(\mathcal{K}^{J}_{+\lambda_q,-\lambda} \pm \eta\mathcal{K}^{J}_{+\lambda_q,+\lambda}\right) \\
&= \pm\eta_q\left(\pm\eta\mathcal{K}^{J}_{+\lambda_q,-\lambda} + \mathcal{K}^{J}_{+\lambda_q,+\lambda}\right) \\
&= \pm\eta_q\mathcal{K}^{J\pm}_{+\lambda_q,\lambda} \, .
\end{aligned}$$

The sum over $\lambda_q > 0$ in (4.19) has to be understood as the summation over various helicity states of the same final state, thus it only refers to final states with $s_1 + s_2 \geq \frac{3}{2}$. By introducing various final states for the different helicity states of one final state (in particular for ωN: $\omega N_{\frac{3}{2}}$, $\omega N_{\frac{1}{2}}$, ωN_0[3)]), (4.19) can be rewritten to calculate the scattering matrix via matrix inversion:

$$\mathcal{T}^{J\pm}_{fi} = \left[\frac{\mathcal{K}^{J\pm}}{1-\mathrm{i}\mathcal{K}^{J\pm}}\right]_{fi} \, , \tag{4.20}$$

where f (i) characterizes the final (initial) state $\varphi' B'$ (φB) via the total c.m. energy $\sqrt{s}$ and the helicity λ' (λ).

Note, that for the derivation of (4.19), (4.20) no assumption has been made about the intrinsic spins and parities of the particles!

[3)] Here, the same helicity notation for ωN is used as in Section 5.2.

Chapter 5

Calculation of Amplitudes

In the previous Chapter 4 the decomposition of spin dependent helicity amplitudes into amplitudes of good total spin and parity with the help of the Wigner functions has been established. In addition, for calculational purposes, it is desirable to find a minimal set of Lorentz (pseudo)scalars, (pseudo)vectors, or tensors, with the help of which one can express all occuring Feynman amplitudes. In this chapter these minimal sets are presented and the connection to the spin dependent amplitudes that are needed as the input for the partial-wave decomposition (PWD) is established.

Throughout this chapter, the notation is the same as given in Appendix A. I.e. incoming (outgoing) baryon momenta are labelled by p (p'), incoming (outgoing) meson momenta by k (k'), and we work in the c.m. system, where $\boldsymbol{k} = -\boldsymbol{p}$ and $\boldsymbol{k'} = -\boldsymbol{p'}$.

Starting point is always the potential $\mathcal{V}^{fi} \equiv \langle f|V|i\rangle$ calculated via the standard Feynman rules for the first order amplitude $\mathcal{M}^{(1)}$ (see also Appendix I):

$$\mathcal{V}^{fi}_{\lambda'\lambda} = \mathcal{M}^{(1)}{}^{fi}_{\lambda'\lambda} = \bar{u}(p', \lambda_{B'})\Gamma(s,u)u(p,\lambda_B) \; , \tag{5.1}$$

where $\mathcal{V}^{fi}$ is related to the $\mathcal{K}$-matrix amplitude $\mathcal{K}^{fi}_{\lambda'\lambda}$ via Eq. (C.11):

$$\mathcal{K}^{fi}_{\lambda'\lambda} = -\frac{\sqrt{\mathrm{p}\mathrm{p}' m_{B'} m_B}}{(4\pi)^2\sqrt{s}}\mathcal{V}^{fi}_{\lambda'\lambda} = -\frac{\sqrt{\mathrm{p}\mathrm{p}' m_{B'} m_B}}{(4\pi)^2\sqrt{s}}\mathcal{M}^{(1)}{}^{fi}_{\lambda'\lambda} \; . \tag{5.2}$$

The aim is to find the minimal set of operators in Dirac space for $\Gamma(s,u)$ on the right hand side of Eq. (5.1) and to reexpress the helicity dependent matrix elements for all helicity combinations in terms of this set.

Whenever there are spin 0 mesons involved in the final states the Dirac operators are further expanded in a two-component form by reexpressing the γ-matrices in terms of the Pauli σ-matrices, and the Dirac spinors $u(p,\lambda_B)$ in terms of the two-component Pauli spinors χ_{λ_B}:

$$\mathcal{V}^{fi}_{\lambda'\lambda} = \bar{u}(p', \lambda_{B'})\Gamma(s,u)u(p,\lambda_B) = \frac{4\pi\sqrt{s}}{\sqrt{m_B m_{B'}}}\chi^\dagger_{\lambda_{B'}}\mathcal{F}(s,u)\chi_{\lambda_B} \; . \tag{5.3}$$

5.1 Spin-0 Spin-$\frac{1}{2}$ Scattering

The case of spin-0 spin-$\frac{1}{2}$ scattering, as e.g. $\pi N \to \pi N$, is most frequently discussed in the literature ([47, 52, 61, 88]). However, as it will turn out in the following section, using the PWD presented in the previous chapter 4, the resulting formalism for the calculation of the helicity dependent amplitudes is at least as concise as for the conventional PWD.

5.1.1 Mesons with Identical Parity

Of the $2 \cdot 2 = 4$ helicity amplitudes only 2 are independent due to the parity conserving property of the interaction, cf. Eq. (4.14). This must also be reflected in the Dirac and Pauli operators in Eq. (5.3). Due to parity conservation the two independent Dirac operators are given by the unit four matrix and a four-momentum contracted with the γ matrix four-vector. The usual choice for the latter one is the average of the meson momenta: $\bar{k} = (k + k')/2$ [70] and hence one has

$$\Gamma(s, u) = A \mathbb{1}_4 + B \bar{\not{k}} \; . \tag{5.4}$$

All other Dirac operators appearing in the Feynman amplitudes can be cast into the form (5.4) by using four-momentum conservation and applying the Dirac equation (A.19). Using the explicit representation of the γ matrices and Dirac spinors (cf. Appendix A) it follows from Eq. (5.3) that $\mathcal{F}$ can be written as

$$\mathcal{F} = \tilde{A} \mathbb{1}_2 + \tilde{B} \boldsymbol{\sigma} \cdot \hat{\boldsymbol{k}}' \boldsymbol{\sigma} \cdot \hat{\boldsymbol{k}} \; . \tag{5.5}$$

Here, $\tilde{A}$ and $\tilde{B}$ are related to A and B in the following way:

$$\begin{aligned} \tilde{A} &= +\frac{\sqrt{R_+ R'_+}}{8\pi\sqrt{s}} \left(A + \tfrac{1}{2} B (S_- + S'_-) \right) \\ \tilde{B} &= -\frac{\sqrt{R_- R'_-}}{8\pi\sqrt{s}} \left(A - \tfrac{1}{2} B (S_+ + S'_+) \right) \; , \end{aligned} \tag{5.6}$$

where

$$\begin{aligned} R_\pm &= E_B \pm m_B \; , \quad R'_\pm = E_{B'} \pm m_{B'} \; , \\ S_\pm &= \sqrt{s} \pm m_B \; , \quad S'_\pm = \sqrt{s} \pm m_{B'} \; . \end{aligned} \tag{5.7}$$

Instead of the decomposition (5.5), in the literature (e.g. [61]) often

$$\mathcal{F} = f \mathbb{1}_2 + \mathrm{i} \boldsymbol{\sigma} \cdot (\hat{\boldsymbol{k}} \times \hat{\boldsymbol{k}}') g \tag{5.8}$$

is used. The functions f and g are related to $\tilde{A}$ and $\tilde{B}$ by

$$f = \tilde{A} + \cos\vartheta \tilde{B} \; , \qquad g = -\tilde{B} \; , \tag{5.9}$$

which can be proven by applying Eq. (A.17).

Using Eq. (A.25): $\boldsymbol{\sigma}\cdot\hat{\boldsymbol{k}}'\chi^f_{\pm\frac{1}{2}} = \pm\chi^f_{\pm\frac{1}{2}}$ and $\boldsymbol{\sigma}\cdot\hat{\boldsymbol{k}}\chi^i_{\pm\frac{1}{2}} = \pm\chi^i_{\pm\frac{1}{2}}$ and Eqs. (A.22), (A.23) one finds from Eq. (5.5) for the helicity-dependent amplitudes:

$$\begin{aligned}
\mathcal{V}_{+\frac{1}{2}+\frac{1}{2}} &= \mathcal{V}_{-\frac{1}{2}-\frac{1}{2}} = \frac{4\pi\sqrt{s}}{\sqrt{m_B m_{B'}}}\cos\frac{\vartheta}{2}\left(\tilde{A}+\tilde{B}\right) \\
\mathcal{V}_{+\frac{1}{2}-\frac{1}{2}} &= \mathcal{V}_{-\frac{1}{2}+\frac{1}{2}} = \frac{4\pi\sqrt{s}}{\sqrt{m_B m_{B'}}}\sin\frac{\vartheta}{2}\left(\tilde{A}-\tilde{B}\right) \ .
\end{aligned} \tag{5.10}$$

Here, the relation between the amplitudes with inverted helicities ($\lambda, \lambda' \to -\lambda, -\lambda'$) (4.14) has been applied.

5.1.2 Mesons with Opposite Parity

Due to the change of parity in one of the final states (e.g. the outgoing final state for $\pi N \to \zeta N$) the parity operator $\mathrm{i}\gamma_5$ is introduced. This is absorbed by replacing $\Gamma(s,u)$ of Eq. (5.4) by $\mathrm{i}\gamma_5\Gamma(u,s)$ and $\mathcal{F}$ of Eq. (5.5) by

$$\mathcal{F} = \mathrm{i}\boldsymbol{\sigma}\cdot\hat{\boldsymbol{k}}'\mathcal{F}_{\pi\pi} = \mathrm{i}\tilde{A}\boldsymbol{\sigma}\cdot\hat{\boldsymbol{k}}' + \mathrm{i}\tilde{B}\boldsymbol{\sigma}\cdot\hat{\boldsymbol{k}} \tag{5.11}$$

(s. Eqs. (A.17) and (A.26) in Appendix A). Then $\tilde{A}$ and $\tilde{B}$ are related to A and B in almost the same way as in Eq. (5.6); the only difference is the change of $E_{B'} + m_{B'}$ into $E_{B'} - m_{B'}$ (cf. Eq. (A.26)), i.e. $R'_\pm \to R'_\mp$ and $S'_\pm \to S'_\mp$:

$$\begin{aligned}
\tilde{A} &= +\frac{\sqrt{R_+ R'_-}}{8\pi\sqrt{s}}\left(A + \tfrac{1}{2}B(S_- + S'_+)\right) \\
\tilde{B} &= -\frac{\sqrt{R_- R'_+}}{8\pi\sqrt{s}}\left(A - \tfrac{1}{2}B(S_+ + S'_-)\right) \ .
\end{aligned} \tag{5.12}$$

Using now Eq. (A.25): $\boldsymbol{\sigma}\cdot\hat{\boldsymbol{k}}'\chi^f_{+\frac{1}{2}} = \chi^f_{+\frac{1}{2}}$, one deduces that the $\mathcal{V}_{+\frac{1}{2}+\frac{1}{2}}$ and $\mathcal{V}_{+\frac{1}{2}-\frac{1}{2}}$ of Eq. (5.10) still depend in the same way on $\tilde{A}$ and $\tilde{B}$ (up to a factor of i), while the other two amplitudes experience a sign switch (cf. Eq. (4.14)):

$$\begin{aligned}
\mathcal{V}_{+\frac{1}{2}+\frac{1}{2}} &= -\mathcal{V}_{-\frac{1}{2}-\frac{1}{2}} = \mathrm{i}\frac{4\pi\sqrt{s}}{\sqrt{m_B m_{B'}}}\cos\frac{\vartheta}{2}\left(\tilde{A}+\tilde{B}\right) \\
\mathcal{V}_{+\frac{1}{2}-\frac{1}{2}} &= -\mathcal{V}_{-\frac{1}{2}+\frac{1}{2}} = \mathrm{i}\frac{4\pi\sqrt{s}}{\sqrt{m_B m_{B'}}}\sin\frac{\vartheta}{2}\left(\tilde{A}-\tilde{B}\right) \ .
\end{aligned} \tag{5.13}$$

5.2 Pion-Induced Vector Meson Production

The relations established in this section refer to the production of vector mesons by scalar or pseudoscalar particles. They are closely related to the formalism for photoproduction of (pseudo)scalar mesons – with the only difference that real photons only have two (transversal) polarizations. The latter fact can be easily incorporated by taking into account gauge invariance and is demonstrated in Section 5.4 below.

5.2.1 Pseudoscalar ($J^P = 0^-$) Mesons

To be able to make use of results obtained for photo- and electroproduction of pseudoscalar mesons, which are abundantly examined in the literature, we actually do not develop the necessary formalism for $\pi N \to VN$, but rather for $VN \to \pi N$. Similarly to the $\pi N \to \pi N$ case we start from:

$$\bar{u}(p', \lambda_{B'})\Gamma(s,u)u(p,\lambda_B) \equiv \bar{u}(p', \lambda_{B'})\Gamma_\mu(s,u)\varepsilon^\mu_{\lambda_V}u(p,\lambda_B) = \frac{4\pi\sqrt{s}}{\sqrt{m_B m_{B'}}}\chi^\dagger_{\lambda_{B'}}\mathcal{F}(s,u)\chi_{\lambda_B} \, . \tag{5.14}$$

Note that this relation differs by a factor of i from the one used in e.g. [14, 53]. Applying parity considerations (Eq. (4.14)) we infer that both Γ_μ and $\mathcal{F}$ of Eq. (5.3) consist of $2 \cdot 3 \cdot 2 \cdot \frac{1}{2} = 6$ independent functions because of the spins of the asymptotic particles. For photo- and electroproduction of pseudoscalar mesons $\mathcal{F}$ has been derived [53, 14]:

$$\begin{aligned} \mathcal{F} &= \mathrm{i}\boldsymbol{\sigma}\cdot\boldsymbol{\varepsilon}\,\mathcal{F}_1 + \boldsymbol{\sigma}\cdot\hat{\boldsymbol{k}}'\,\boldsymbol{\sigma}\cdot(\hat{\boldsymbol{k}}\times\boldsymbol{\varepsilon})\mathcal{F}_2 + \mathrm{i}\boldsymbol{\sigma}\cdot\hat{\boldsymbol{k}}\,\boldsymbol{\varepsilon}\cdot\hat{\boldsymbol{k}}'\,\mathcal{F}_3 + \mathrm{i}\boldsymbol{\sigma}\cdot\hat{\boldsymbol{k}}'\,\boldsymbol{\varepsilon}\cdot\hat{\boldsymbol{k}}'\,\mathcal{F}_4 \\ &\quad -\mathrm{i}\varepsilon^0(\boldsymbol{\sigma}\cdot\hat{\boldsymbol{k}}'\,\mathcal{F}_5 + \boldsymbol{\sigma}\cdot\hat{\boldsymbol{k}}\,\mathcal{F}_6) \, , \end{aligned} \tag{5.15}$$

where $\varepsilon^\mu_{\lambda_V} = (\varepsilon^0, \boldsymbol{\varepsilon})$ is the polarization vector of the vector meson, cf. Appendix A.2.2. Obviously, $\mathcal{F}_5$ and $\mathcal{F}_6$ only contribute for longitudinal polarizations.

Looking at the general Dirac structure of $\mathcal{M}_{\lambda'\lambda}$ and using the Dirac equation (A.19), one finds that the Lorentz four-vector Γ_μ takes the form

$$\Gamma_\mu(s,u) = \mathrm{i}\gamma_5\left(\sum_i(A_i p_{i_\mu} + B_i p_{i_\mu}\not{k}) + C\gamma_\mu + D\not{k}\gamma_\mu\right) \tag{5.16}$$

with the vector meson four-momentum k_μ. The sum runs over the four asymptotic particles. Using four-momentum conservation and the four-transversality of the polarization vector of the incoming vector particle $k_\mu\varepsilon^\mu_\lambda = 0$, Γ_μ can be reduced for all Feynman diagrams to

$$\Gamma_\mu(s,u) = \mathrm{i}\gamma_5\left(A_p p_\mu + A_{p'}p'_\mu + (B_p p_\mu + B_{p'}p'_\mu)\not{k} + C\gamma_\mu + D\not{k}\gamma_\mu\right) \, , \tag{5.17}$$

where the A_p, $A_{p'}$, B_p, $B_{p'}$, C, and D are functions of the Mandelstam variables s and u. Some tidious, but straightforward algebra leads to the following relations:

$$\begin{aligned} \mathcal{F}_1 &= \frac{1}{8\pi\sqrt{s}}\sqrt{R'_+R_+}\,(C - S_-D) \\ \mathcal{F}_2 &= \frac{1}{8\pi\sqrt{s}}\sqrt{R'_-R_-}\,(C + S_+D) \\ \mathcal{F}_3 &= \frac{\mathrm{k}'}{8\pi\sqrt{s}}\sqrt{R'_+R_-}\,(-A_{p'} + S_+B_{p'}) \\ \mathcal{F}_4 &= \frac{\mathrm{k}'}{8\pi\sqrt{s}}\sqrt{R'_-R_+}\,(A_{p'} + S_-B_{p'}) \\ \mathcal{F}_5 &= -\frac{1}{\mathrm{k}'}\widetilde{\mathcal{F}}_4 - \frac{1}{8\pi m_M\sqrt{s}}\sqrt{R'_-R_-}\left(S_+C + m_M^2D\right) \\ \mathcal{F}_6 &= -\frac{1}{\mathrm{k}'}\widetilde{\mathcal{F}}_3 - \frac{1}{8\pi m_M\sqrt{s}}\sqrt{R'_+R_+}\left(S_-C - m_M^2D\right) \end{aligned} \tag{5.18}$$

with

$$\begin{aligned}
\widetilde{\mathcal{F}}_i &= \varepsilon\cdot p'\,\mathcal{F}_i + \varepsilon\cdot p\,\mathcal{F}_i(A_{p'}\to A_p, B_{p'}\to B_p)\\
\varepsilon\cdot p \equiv \varepsilon_0^{\mu} p_\mu &= \frac{\mathrm{k}\sqrt{s}}{m_M}, \qquad \varepsilon\cdot p' \equiv \varepsilon_0^{\mu} p'_\mu = \frac{1}{m_M}\left(E_{B'}\,\mathrm{k} + \mathrm{k}' E_M \cos\vartheta\right)
\end{aligned}$$

and $R_\pm$, $R'_\pm$, and $S_\pm$ as defined in Eq. (5.7). In the c.m. system the $\mathcal{F}_i$ are related to the helicity dependent amplitudes via[1]

$$\begin{aligned}
\mathcal{V}_{+\frac{1}{2}+\frac{3}{2}} &= +\mathcal{V}_{-\frac{1}{2}-\frac{3}{2}} = \mathrm{i}\frac{4\pi\sqrt{s}}{\sqrt{m_B m_{B'}}}\frac{1}{\sqrt{2}}\sin\vartheta\cos\frac{\vartheta}{2}(-\mathcal{F}_3-\mathcal{F}_4)\\
\mathcal{V}_{+\frac{1}{2}-\frac{3}{2}} &= -\mathcal{V}_{-\frac{1}{2}+\frac{3}{2}} = \mathrm{i}\frac{4\pi\sqrt{s}}{\sqrt{m_B m_{B'}}}\frac{1}{\sqrt{2}}\sin\vartheta\sin\frac{\vartheta}{2}(-\mathcal{F}_3+\mathcal{F}_4)\\
\mathcal{V}_{+\frac{1}{2}+\frac{1}{2}} &= -\mathcal{V}_{-\frac{1}{2}-\frac{1}{2}} = \mathrm{i}\frac{4\pi\sqrt{s}}{\sqrt{m_B m_{B'}}}\sqrt{2}\cos\frac{\vartheta}{2}\left[-\mathcal{F}_1+\mathcal{F}_2+\sin^2\frac{\vartheta}{2}(\mathcal{F}_3-\mathcal{F}_4)\right]\\
\mathcal{V}_{+\frac{1}{2}-\frac{1}{2}} &= +\mathcal{V}_{-\frac{1}{2}+\frac{1}{2}} = \mathrm{i}\frac{4\pi\sqrt{s}}{\sqrt{m_B m_{B'}}}\sqrt{2}\sin\frac{\vartheta}{2}\left[\mathcal{F}_1+\mathcal{F}_2+\cos^2\frac{\vartheta}{2}(\mathcal{F}_3+\mathcal{F}_4)\right]\\
\mathcal{V}_{+\frac{1}{2}+0} &= -\mathcal{V}_{-\frac{1}{2}-0} = \mathrm{i}\frac{4\pi\sqrt{s}}{\sqrt{m_B m_{B'}}}\varepsilon^0\cos\frac{\vartheta}{2}(-\mathcal{F}_5-\mathcal{F}_6)\\
\mathcal{V}_{+\frac{1}{2}-0} &= -\mathcal{V}_{-\frac{1}{2}+0} = \mathrm{i}\frac{4\pi\sqrt{s}}{\sqrt{m_B m_{B'}}}\varepsilon^0\cos\frac{\vartheta}{2}(-\mathcal{F}_5+\mathcal{F}_6)\,. \qquad (5.19)
\end{aligned}$$

Here, we have introduced the following notation for the VN helicity state: ± 0: $\lambda = \lambda_V - \lambda_B = 0 \pm \frac{1}{2}$, $\pm\frac{1}{2}$: $\lambda = \pm 1 \mp \frac{1}{2}$, and $\pm\frac{3}{2}$: $\lambda = \pm 1 \pm \frac{1}{2}$. The relation between the amplitudes with inverted helicities can be inferred from Eq. (4.14).

5.2.2 Scalar ($J^P = 0^+$) Mesons

The case of scalar meson production is hardly discussed in the literature (s. [64]). However, similarly as in the spin-0 spin-$\frac{1}{2}$ scattering case it is easily derived from the pseudoscalar meson production:

Due to the change of parity in one of the final states the parity operator $\mathrm{i}\gamma_5$ in Eq. (5.17) is dropped. This is absorbed by replacing $\mathcal{F}$ of Eq. (5.15) by $-\mathrm{i}\boldsymbol{\sigma}\cdot\hat{\boldsymbol{k}}'\mathcal{F}$ (s. Eq. (A.26) in Appendix A). Then, the relations between the $\mathcal{F}_i$ and the Lorentz operators are almost identical to Eq. (5.18); the only difference being the change of $E_{B'} + m_{B'}$ into $E_{B'} - m_{B'}$, i.e. $R'_\pm \to R'_\mp$ (cf. Eq. (A.26)). Using now Eq. (A.25): $\boldsymbol{\sigma}\cdot\hat{\boldsymbol{k}}'\chi^f_{+\frac{1}{2}} = \chi^f_{+\frac{1}{2}}$, one deduces that the $\mathcal{V}_{\lambda'\lambda}$ on the very left of Eq. (5.19) still depend in the same way on the $\mathcal{F}_i$ (up to a factor of $-\mathrm{i}$) and we have:

$$\begin{aligned}
\mathcal{V}_{+\frac{1}{2}+\frac{3}{2}} &= -\mathcal{V}_{-\frac{1}{2}-\frac{3}{2}} = \frac{4\pi\sqrt{s}}{\sqrt{m_B m_{B'}}}\frac{1}{\sqrt{2}}\sin\vartheta\cos\frac{\vartheta}{2}(-\mathcal{F}_3-\mathcal{F}_4)\\
\mathcal{V}_{+\frac{1}{2}-\frac{3}{2}} &= +\mathcal{V}_{-\frac{1}{2}+\frac{3}{2}} = \frac{4\pi\sqrt{s}}{\sqrt{m_B m_{B'}}}\frac{1}{\sqrt{2}}\sin\vartheta\sin\frac{\vartheta}{2}(-\mathcal{F}_3+\mathcal{F}_4)
\end{aligned}$$

---

[1] Note that there is a misprint in Eq. (B12) in [53]: The H_4 term should start with $-\sqrt{2}\sin\frac{\vartheta}{2}$.

$$
\begin{aligned}
\mathcal{V}_{+\frac{1}{2}+\frac{1}{2}} &= +\mathcal{V}_{-\frac{1}{2}-\frac{1}{2}} = \frac{4\pi\sqrt{s}}{\sqrt{m_B m_{B'}}}\sqrt{2}\cos\frac{\vartheta}{2}\left[-\mathcal{F}_1+\mathcal{F}_2+\sin^2\frac{\vartheta}{2}(\mathcal{F}_3-\mathcal{F}_4)\right] \\
\mathcal{V}_{+\frac{1}{2}-\frac{1}{2}} &= -\mathcal{V}_{-\frac{1}{2}+\frac{1}{2}} = \frac{4\pi\sqrt{s}}{\sqrt{m_B m_{B'}}}\sqrt{2}\sin\frac{\vartheta}{2}\left[\mathcal{F}_1+\mathcal{F}_2+\cos^2\frac{\vartheta}{2}(\mathcal{F}_3+\mathcal{F}_4)\right] \\
\mathcal{V}_{+\frac{1}{2}+0} &= +\mathcal{V}_{-\frac{1}{2}-0} = \frac{4\pi\sqrt{s}}{\sqrt{m_B m_{B'}}}\varepsilon^0\cos\frac{\vartheta}{2}(-\mathcal{F}_5-\mathcal{F}_6) \\
\mathcal{V}_{+\frac{1}{2}-0} &= +\mathcal{V}_{-\frac{1}{2}+0} = \frac{4\pi\sqrt{s}}{\sqrt{m_B m_{B'}}}\varepsilon^0\cos\frac{\vartheta}{2}(-\mathcal{F}_5+\mathcal{F}_6)\ , \qquad (5.20)
\end{aligned}
$$

where, again, the relative sign for the amplitudes with inverted helicities has been extracted from Eq. (4.14).

5.3 Vector Meson Nucleon Scattering

Since to our knowledge there is no decomposition to be compared to, the intermediate step of introducing the $\mathcal{F}_i$ amplitudes is omitted. Replacing $\Gamma(s,u)$ of Eq. (5.1) by $\Gamma_{\mu\nu}(s,u)\varepsilon^{\mu}_{\lambda_V}\varepsilon^{\dagger\ \nu}_{\lambda_{V'}}$, one finds for $VB \to V'B'$ after having used the Dirac equation, four-momentum conservation, four-transversality of the polarization vectors of the incoming and outgoing vector particles and the relations given in Appendix A:

$$
\Gamma_{\mu\nu}(s,u) = A_{\mu\nu} + B_{\mu\nu}\not{k} + C_\nu\gamma_\mu + D_\nu\not{k}\gamma_\mu + E_\mu\gamma_\nu + F_\mu\not{k}\gamma_\nu + G\gamma_\mu\gamma_\nu + H\not{k}\gamma_\mu\gamma_\nu \qquad (5.21)
$$

with

$$
\begin{aligned}
A_{\mu\nu} &= A_{pp}p_\mu p_\nu + A_{pp'}p_\mu p'_\nu + A_{p'p}p'_\mu p_\nu + A_{p'p'}p'_\mu p'_\nu + A_g g_{\mu\nu}, \quad \text{similarly for } B_{\mu\nu} \\
C_\nu &= C_p p_\nu + C_{p'}p'_\nu, \quad \text{similarly for } D_\nu \\
E_\mu &= E_p p_\mu + E_{p'}p'_\mu, \quad \text{similarly for } F_\mu\ . \qquad (5.22)
\end{aligned}
$$

This is not a minimal set of Lorentz tensors, since by applying parity considerations the minimal set should consist of $3\cdot 2\cdot 3\cdot 2\cdot\frac{1}{2} = 18$ elements, whereas the above set contains 20 elements. This is due to the mixing of Lorentz and Dirac space. An alternative approach would be to span the Lorentz space first via a basis $n_\mu \equiv \{p_\mu, p'_\mu, k_\mu, \varepsilon_{\mu\alpha\beta\delta}p^\alpha p'^\beta k^\delta\}$, and then combining this basis with the non-reducible contractions of the γ matrices with the basis' elements: $\Gamma_{\mu\nu} = n_\mu n_\nu \otimes \{\not{k}, 1/\gamma_5\not{k}, \gamma_5\}$, where the γ_5 is needed when exactly one Levi-Civita tensor is involved. By comparing these two sets one can deduce how to rewrite the set (5.22) in terms of a minimal set of 18 Lorentz tensors. However, since it is more straightforward to decompose the Feynman amplitudes in terms of the set given via (5.22) the corresponding formulae are presented for this set. In the notation

$$
\mathcal{V}_{\lambda'\lambda} \equiv \frac{1}{\sqrt{4m_B m_{B'}}R_+R'_+}\mathcal{A}_{\lambda'\lambda} \qquad (5.23)
$$

one finds

$$
\mathcal{A}_{+\frac{3}{2}+\frac{3}{2}} = -\cos^3\frac{\vartheta}{2}\left\{Q_-\left[2\,\mathrm{k}\,\mathrm{k}'\sin^2\frac{\vartheta}{2}(A_{p'p}-2F_{p'}) + A_g + 2G\right] +\right.
$$

$$\begin{aligned}
& Q^s_+ \left[2\mathrm{k}\mathrm{k}'\sin^2\frac{\vartheta}{2}B_{p'p} + B_g + 2H\right] \qquad\qquad \Bigg\} \\
\mathcal{A}_{+\frac{3}{2}-\frac{3}{2}} &= \sin^3\frac{\vartheta}{2}\Bigg\{Q_+\left[2\mathrm{k}\mathrm{k}'\cos^2\frac{\vartheta}{2}(A_{p'p}-2F_{p'}) - A_g - 2G\right] + \\
& Q^s_-\left[2\mathrm{k}\mathrm{k}'\cos^2\frac{\vartheta}{2}B_{p'p} - B_g - 2H\right] \qquad\qquad \Bigg\} \\
\mathcal{A}_{+\frac{1}{2}+\frac{3}{2}} &= \cos^2\frac{\vartheta}{2}\sin\frac{\vartheta}{2}\Bigg\{Q_+\left[2\mathrm{k}\mathrm{k}'\sin^2\frac{\vartheta}{2}(A_{p'p}-2F_{p'}) + A_g + 2G\right] + \\
& Q^s_-\left[2\mathrm{k}\mathrm{k}'\sin^2\frac{\vartheta}{2}B_{p'p} + B_g + 2H\right] + 2\mathrm{k}'\left[P_-E_{p'} + P^s_+F_{p'}\right]\Bigg\} \\
\mathcal{A}_{+\frac{1}{2}-\frac{3}{2}} &= -\sin^2\frac{\vartheta}{2}\cos\frac{\vartheta}{2}\Bigg\{Q_-\left[2\mathrm{k}\mathrm{k}'\cos^2\frac{\vartheta}{2}(A_{p'p}-2F_{p'}) - A_g - 2G\right] + \\
& Q^s_+\left[2\mathrm{k}\mathrm{k}'\cos^2\frac{\vartheta}{2}B_{p'p} - B_g - 2H\right] + 2\mathrm{k}'\left[P_+E_{p'} + P^s_-F_{p'}\right]\Bigg\} \\
\mathcal{A}_{+\frac{3}{2}+\frac{1}{2}} &= -\cos^2\frac{\vartheta}{2}\sin\frac{\vartheta}{2}\Bigg\{Q_+\left[2\mathrm{k}\mathrm{k}'\sin^2\frac{\vartheta}{2}(A_{p'p}-2F_{p'}) + A_g + 2G\right] + \\
& Q^s_-\left[2\mathrm{k}\mathrm{k}'\sin^2\frac{\vartheta}{2}B_{p'p} + B_g + 2H\right] - \\
& 2\mathrm{k}\left[P_-(C_p+2H) + P^s_+D_p\right] \qquad\qquad \Bigg\} \\
\mathcal{A}_{+\frac{3}{2}-\frac{1}{2}} &= \sin^2\frac{\vartheta}{2}\cos\frac{\vartheta}{2}\Bigg\{Q_-\left[2\mathrm{k}\mathrm{k}'\cos^2\frac{\vartheta}{2}(A_{p'p}-2F_{p'}) - A_g - 2G\right] + \\
& Q^s_+\left[2\mathrm{k}\mathrm{k}'\cos^2\frac{\vartheta}{2}B_{p'p} - B_g - 2H\right] + \\
& 2\mathrm{k}\left[P_+(C_p+2H) + P^s_-D_p\right] \qquad\qquad \Bigg\} \\
\mathcal{A}_{+\frac{1}{2}+\frac{1}{2}} &= -\cos\frac{\vartheta}{2}\Bigg\{Q_-\left[\left(2\mathrm{k}\mathrm{k}'\sin^2\frac{\vartheta}{2}(A_{p'p}-2F_{p'}) + A_g\right)\cos^2\frac{\vartheta}{2} - 2\sin^2\frac{\vartheta}{2}G\right] + \\
& Q^s_+\left[\left(2\mathrm{k}\mathrm{k}'\sin^2\frac{\vartheta}{2}B_{p'p} + B_g\right)\cos^2\frac{\vartheta}{2} - 2\sin^2\frac{\vartheta}{2}H\right] + \\
& 2\sin^2\frac{\vartheta}{2}\left[P_+\left\{\mathrm{k}(C_p+2H) + \mathrm{k}'E_{p'}\right\} + P^s_-(\mathrm{k}D_p + \mathrm{k}'F_{p'})\right] \qquad \Bigg\} \\
\mathcal{A}_{+\frac{1}{2}-\frac{1}{2}} &= -\sin\frac{\vartheta}{2}\Bigg\{Q_+\left[\left(2\mathrm{k}\mathrm{k}'\cos^2\frac{\vartheta}{2}(A_{p'p}-2F_{p'}) - A_g\right)\sin^2\frac{\vartheta}{2} + 2\cos^2\frac{\vartheta}{2}G\right] + \\
& Q^s_-\left[\left(2\mathrm{k}\mathrm{k}'\cos^2\frac{\vartheta}{2}B_{p'p} - B_g\right)\sin^2\frac{\vartheta}{2} + 2\cos^2\frac{\vartheta}{2}H\right] - \\
& 2\cos^2\frac{\vartheta}{2}\left[P_-\left\{\mathrm{k}(C_p+2H) - \mathrm{k}'E_{p'}\right\} + P^s_+(\mathrm{k}D_p - \mathrm{k}'F_{p'})\right] \qquad \Bigg\} \\
\mathcal{A}_{+\frac{3}{2}+0} &= \sqrt{2}\cos^2\frac{\vartheta}{2}\sin\frac{\vartheta}{2}\Bigg\{Q_-\bigg[\mathrm{k}\left\{\,\varepsilon\!\cdot\! p\,(A_{pp}-2F_p) + \,\varepsilon\!\cdot\! p'\,(A_{p'p}-2F_{p'})\right\} -
\end{aligned}$$

$$
\begin{aligned}
& \qquad \frac{E_M}{m_M}(A_g + 2G)\Bigg] + \\
& Q^s_+ \Bigg[\mathrm{k}\,(\,\varepsilon\!\cdot\! p\, B_{pp} + \,\varepsilon\!\cdot\! p'\, B_{p'p}) - \frac{E_M}{m_M} B_g\Bigg] + \\
& \frac{\mathrm{k}P^s_+}{m_M} C_p + m_M(\,\mathrm{k}P_- D_p - 2Q_+ H) \qquad\qquad \Bigg\}
\end{aligned}
$$

$$
\begin{aligned}
\mathcal{A}_{+\frac{3}{2}-0} \;=\; & \sqrt{2}\sin^2\frac{\vartheta}{2}\cos\frac{\vartheta}{2}\Bigg\{Q_+\Bigg[\mathrm{k}\,\{\,\varepsilon\!\cdot\! p\,(A_{pp} - 2F_p) + \,\varepsilon\!\cdot\! p'\,(A_{p'p} - 2F_{p'})\} - \\
& \qquad \frac{E_M}{m_M}(A_g + 2G)\Bigg] + \\
& Q^s_- \Bigg[\mathrm{k}\,(\,\varepsilon\!\cdot\! p\, B_{pp} + \,\varepsilon\!\cdot\! p'\, B_{p'p}) - \frac{E_M}{m_M} B_g\Bigg] + \\
& \frac{\mathrm{k}P^s_-}{m_M} C_p + m_M(\,\mathrm{k}P_+ D_p - 2Q_- H) \qquad\qquad \Bigg\}
\end{aligned}
$$

$$
\begin{aligned}
\mathcal{A}_{+\frac{1}{2}-0} \;=\; & +\mathcal{A}_{+\frac{3}{2}+0} + \sqrt{2}\sin\frac{\vartheta}{2}\Bigg\{P_+\,(\,\varepsilon\!\cdot\! p\, E_p + \,\varepsilon\!\cdot\! p'\, E_{p'}) + \\
& \qquad P^s_-\,(\,\varepsilon\!\cdot\! p\;\mathrm{k}F_p + \,\varepsilon\!\cdot\! p'\, F_{p'}) + \frac{Q^s_-}{m_M} G + m_M Q_+ H\Bigg\}
\end{aligned}
$$

$$
\begin{aligned}
\mathcal{A}_{+\frac{1}{2}+0} \;=\; & -\mathcal{A}_{-\frac{3}{2}+0} - \sqrt{2}\cos\frac{\vartheta}{2}\Bigg\{P_-\,(\,\varepsilon\!\cdot\! p\, E_p + \,\varepsilon\!\cdot\! p'\, E_{p'}) + \\
& \qquad P^s_+\,(\,\varepsilon\!\cdot\! p\, F_p + \,\varepsilon\!\cdot\! p'\, F_{p'}) + \frac{Q^s_+}{m_M} G + m_M Q_- H\Bigg\}
\end{aligned}
$$

$$
\begin{aligned}
\mathcal{A}_{+0+\frac{3}{2}} \;=\; & -\sqrt{2}\cos^2\frac{\vartheta}{2}\sin\frac{\vartheta}{2}\Bigg\{Q_-\Bigg[\mathrm{k}'(\,\varepsilon'\!\cdot\! p'\, A_{p'p'} + \,\varepsilon'\!\cdot\! p\, A_{p'p} + 2\,\varepsilon'\!\cdot\! k\, F_{p'}) - \\
& \qquad \frac{E_{M'}}{m_{M'}}(A_g + 2G)\Bigg] + \\
& Q^s_+ \Bigg[\mathrm{k}'(\,\varepsilon'\!\cdot\! p'\, B_{p'p'} + \,\varepsilon'\!\cdot\! p\, B_{p'p}) - \frac{E_{M'}}{m_{M'}}(B_g + 2H)\Bigg] + \\
& \frac{\mathrm{k}'}{m_{M'}}(P'^s_+ E_{p'} + P^{ss}_- F_{p'}) \qquad\qquad \Bigg\}
\end{aligned}
$$

$$
\begin{aligned}
\mathcal{A}_{+0-\frac{3}{2}} \;=\; & \sqrt{2}\sin^2\frac{\vartheta}{2}\cos\frac{\vartheta}{2}\Bigg\{Q_+\Bigg[\mathrm{k}'(\,\varepsilon'\!\cdot\! p'\, A_{p'p'} + \,\varepsilon'\!\cdot\! p\, A_{p'p} + 2\,\varepsilon'\!\cdot\! k\, F_{p'}) - \\
& \qquad \frac{E_{M'}}{m_{M'}}(A_g + 2G)\Bigg] + \\
& Q^s_- \Bigg[\mathrm{k}'(\,\varepsilon'\!\cdot\! p'\, B_{p'p'} + \,\varepsilon'\!\cdot\! p\, B_{p'p}) - \frac{E_{M'}}{m_{M'}}(B_g + 2H)\Bigg] + \\
& \frac{\mathrm{k}'}{m_{M'}}(P'^s_- E_{p'} - P^{ss}_+ F_{p'}) \qquad\qquad \Bigg\}
\end{aligned}
$$

$$
\mathcal{A}_{+0-\frac{1}{2}} \;=\; -\mathcal{A}_{+0+\frac{3}{2}} + \sqrt{2}\sin\frac{\vartheta}{2}\Bigg\{P_+\,(\,\varepsilon'\!\cdot\! p\, C_p + \,\varepsilon'\!\cdot\! p'\, C_{p'} - 2\,\varepsilon'\!\cdot\! k\, H) +
$$

$$
\begin{aligned}
& && P^s_-\,(\,\varepsilon'\!\cdot p\,D_p +\,\varepsilon'\!\cdot p'\,D_{p'}) + \frac{1}{m_{M'}}\left(Q'^s_-G + Q^{ss}_+H\right)\Bigg\} \\
\mathcal{A}_{+0+\frac{1}{2}} &=&& -\mathcal{A}_{+0-\frac{3}{2}} + \sqrt{2}\cos\frac{\vartheta}{2}\Bigg\{P_-\,(\,\varepsilon'\!\cdot p\,C_p +\,\varepsilon'\!\cdot p'\,C_{p'} - 2\,\varepsilon'\!\cdot k\,H) + \\
& && P^s_+\,(\,\varepsilon'\!\cdot p\,D_p +\,\varepsilon'\!\cdot p'\,D_{p'}) - \frac{1}{m_{M'}}\left(Q'^s_+G + Q^{ss}_-H\right)\Bigg\} \\
\mathcal{A}_{+0+0} &=&& \cos\frac{\vartheta}{2}\Bigg\{Q_-\,[\,\varepsilon\!\cdot p\,(\,\varepsilon'\!\cdot p\,A_{pp} +\,\varepsilon'\!\cdot p'\,A_{pp'} + 2\,\varepsilon'\!\cdot k\,F_p) + \\
& && \qquad \varepsilon\!\cdot p'\,(\,\varepsilon'\!\cdot p'\,A_{p'p'} +\,\varepsilon'\!\cdot p\,A_{p'p} + 2\,\varepsilon'\!\cdot k\,F_{p'}) +\,\varepsilon\!\cdot\varepsilon'\,(A_g + 2G)] + \\
& && Q^s_+\,[\,\varepsilon\!\cdot p\,(\,\varepsilon'\!\cdot p\,B_{pp} +\,\varepsilon'\!\cdot p'\,B_{pp'}) + \\
& && \qquad \varepsilon\!\cdot p'\,(\,\varepsilon'\!\cdot p'\,B_{p'p'} +\,\varepsilon'\!\cdot p\,B_{p'p}) +\,\varepsilon\!\cdot\varepsilon'\,(B_g + 2H)] + \\
& && \frac{P^s_+}{m_M}(\,\varepsilon'\!\cdot p'\,C_{p'} +\,\varepsilon'\!\cdot p\,C_p - 2\,\varepsilon'\!\cdot k\,H) + m_M P_-(\,\varepsilon'\!\cdot p'\,D_{p'} +\,\varepsilon'\!\cdot p\,D_p) + \\
& && \frac{P'^s_+}{m_{M'}}(\,\varepsilon\!\cdot p\,E_p +\,\varepsilon\!\cdot p'\,E_{p'}) + \frac{P^{ss}_-}{m_{M'}}(\,\varepsilon\!\cdot p\,F_p +\,\varepsilon\!\cdot p'\,F_{p'}) + \\
& && \frac{1}{m_{M'}m_M}(Q^{ss}_-G + m_M^2 Q'^s_+H) \qquad\qquad\qquad\qquad\qquad\qquad\qquad \Bigg\} \\
\mathcal{A}_{+0-0} &=&& \sin\frac{\vartheta}{2}\Bigg\{Q_+\,[\,\varepsilon\!\cdot p\,(\,\varepsilon'\!\cdot p\,A_{pp} +\,\varepsilon'\!\cdot p'\,A_{pp'} + 2\,\varepsilon'\!\cdot k\,F_p) + \\
& && \qquad \varepsilon\!\cdot p'\,(\,\varepsilon'\!\cdot p'\,A_{p'p'} +\,\varepsilon'\!\cdot p\,A_{p'p} + 2\,\varepsilon'\!\cdot k\,F_{p'}) +\,\varepsilon\!\cdot\varepsilon'\,(A_g + 2G)] + \\
& && Q^s_-\,[\,\varepsilon\!\cdot p\,(\,\varepsilon'\!\cdot p\,B_{pp} +\,\varepsilon'\!\cdot p'\,B_{pp'}) + \\
& && \qquad \varepsilon\!\cdot p'\,(\,\varepsilon'\!\cdot p'\,B_{p'p'} +\,\varepsilon'\!\cdot p\,B_{p'p}) +\,\varepsilon\!\cdot\varepsilon'\,(B_g + 2H)] + \\
& && \frac{P^s_-}{m_M}(\,\varepsilon'\!\cdot p'\,C_{p'} +\,\varepsilon'\!\cdot p\,C_p - 2\,\varepsilon'\!\cdot k\,H) + m_M P_+(\,\varepsilon'\!\cdot p'\,D_{p'} +\,\varepsilon'\!\cdot p\,D_p) + \\
& && \frac{P'^s_-}{m_{M'}}(\,\varepsilon\!\cdot p\,E_p +\,\varepsilon\!\cdot p'\,E_{p'}) - \frac{P^{ss}_+}{m_{M'}}(\,\varepsilon\!\cdot p\,F_p +\,\varepsilon\!\cdot p'\,F_{p'}) - \\
& && \frac{1}{m_{M'}m_M}(Q^{ss}_+G + m_M^2 Q'^s_-H) \qquad\qquad\qquad\qquad\qquad\qquad\qquad \Bigg\}
\end{aligned}
\tag{5.24}
$$

with

$$
\begin{aligned}
Q_\pm &= R'_+R_+ \pm \mathrm{k}\mathrm{k}' \\
Q^s_\pm &= R'_+R_+S_- \pm \mathrm{k}\mathrm{k}'S_+ \\
Q'^s_\pm &= R'_+R_+S'_- \pm \mathrm{k}\mathrm{k}'S'_+ \\
Q^{ss}_\pm &= R'_+R_+S_-S'_- \pm \mathrm{k}\mathrm{k}'S_+S'_+ \\
P_\pm &= \mathrm{k}R'_+ \pm \mathrm{k}'R_+ \\
P^s_\pm &= \mathrm{k}R'_+S_+ \pm \mathrm{k}'R_+S_- \\
P'^s_\pm &= \mathrm{k}R'_+S'_+ \pm \mathrm{k}'R_+S'_- \\
P^{ss}_\pm &= \mathrm{k}R'_+S_+S'_- \pm \mathrm{k}'R_+S_-S'_+
\end{aligned}
$$

and for λ_V, $\lambda_{V'} = 0$ (s. also Section 5.2):

$$\begin{aligned}
\varepsilon'\cdot p &= \frac{1}{m_{M'}}\left(E_B\,\mathrm{k}' + E_{M'}\,\mathrm{k}\cos\vartheta\right) \\
\varepsilon'\cdot k &= \frac{1}{m_{M'}}\left(E_M\,\mathrm{k}' - E_{M'}\,\mathrm{k}\cos\vartheta\right) \\
\varepsilon'\cdot p' &= \frac{\sqrt{s}\,\mathrm{k}'}{m_{M'}} \\
\varepsilon\cdot\varepsilon' &= \frac{1}{m_M m_{M'}}\left(\mathrm{k}\,\mathrm{k}' - E_M E_{M'}\cos\vartheta\right)\ .
\end{aligned} \tag{5.25}$$

The other helicity amplitudes follow via (cf. Eq. (4.14))

$$\mathcal{A}_{\lambda'\lambda} = (-1)^{\lambda'-\lambda}\mathcal{A}_{-\lambda'-\lambda}\ . \tag{5.26}$$

We have checked these formulae numerically against the calculation method developed by [158], where the combinations $\bar{u}\Gamma_{\mu\nu}u\varepsilon^{\mu}\varepsilon'^{\dagger\nu}$ have been calculated by a decomposition of $\Gamma_{\mu\nu}$ into the 16 4×4 Clifford algebra elements.

5.4 Reactions Including Photons: Gauge Invariance

For the decomposition presented above, the photon can just be treated as a vector meson. The only necessary modification arises from the property of the photon being the gauge boson of QED, see Section 3.3.1. As a massless particle, only two polarization states are allowed, i.e. the longitudinally polarized state ($\lambda_\gamma = 0$) and the corresponding amplitudes do not contribute. The consequence is a reduction of the set of possible helicity amplitudes, e.g. for $\gamma N \to \varphi N$ as compared to $VN \to \varphi N$ from 6 to 4, for $\gamma N \to VN$ as compared to $VN \to VN$ from 18 to 12 and for Compton scattering ($\gamma N \to \gamma N$) as compared to $VN \to VN$ from 18 to 6[2]. This should also be reflected in a reduction of the minimal set of Lorentz operators necessary to completely describe all Feynman amplitudes. It can be achieved by taking into account the interdependencies of the Lorentz operators following from gauge invariance: $k_\mu\Gamma^\mu = 0$ for $\gamma N \to \varphi N$, $k_\mu\Gamma^{\mu\nu} = 0$ for $\gamma N \to VN$ and $k_\mu\Gamma^{\mu\nu} = k'_\nu\Gamma^{\mu\nu} = 0$ for Compton scattering.

Looking at the Lorentz operators in detail, one finds the following expressions:

5.4.1 Photoproduction of (Pseudo-) Scalar Mesons

As discussed in Section 5.2.2 the production of pseudoscalar and scalar mesons are closely related. In the following we present the influence of gauge invariance on the decomposition of the amplitude for pseudoscalar meson photoproduction, since this case is also discussed in the literature [14, 38]. However, all the results derived in this section apply in the same

---

[2] In Compton scattering, the additional reduction from 8 to 6 is due to time reversal invariance, i.e. $\mathcal{T}^{\gamma\gamma}_{\pm\frac{3}{2},\frac{1}{2}} = \mathcal{T}^{\gamma\gamma}_{\frac{1}{2},\pm\frac{3}{2}}$; cf. Eq. (4.16).

way to scalar meson photo- and electroproduction; the only change is to replace $\mathrm{i}\gamma_5$ by $\mathbb{1}_4$.

For real photons two conditions have to be found to reduce the set of 6 Lorentz pseudovectors

$$\Gamma_\mu(s,u) = \mathrm{i}\gamma_5\left(A_p p_\mu + A_{p'} p'_\mu + (B_p p_\mu + B_{p'} p'_\mu)\not{k} + C\gamma_\mu + D\not{k}\gamma_\mu\right)$$

to 4. Requiring gauge invariance $\Gamma_\mu k^\mu = 0$ results in ($k^2 = \not{k}^2 = 0$)

$$\begin{aligned} A_p p\cdot k + A_{p'} p'\cdot k &= 0 \\ B_p p\cdot k + B_{p'} p'\cdot k + C &= 0\,, \end{aligned} \tag{5.27}$$

leading to the gauge invariant decomposition

$$\Gamma_\mu(s,u) = \mathrm{i}\gamma_5\Big((p_\mu p'\cdot k - p'_\mu p\cdot k)\tilde{A}_p + (p_\mu\not{k} - p\cdot k\gamma_\mu)\tilde{B}_p + (p'_\mu\not{k} - p'\cdot k\gamma_\mu)\tilde{B}_{p'} + D\not{k}\gamma_\mu\Big)\ .$$

Hence the amplitude $\mathcal{V}_{fi}$ can be represented by the standard set of four gauge invariant amplitudes as in [53]:

$$\begin{aligned} \mathcal{V}_{fi} &= \bar{u}(p',s')\sum_{j=1}^{4} A_j M_j u(p,s) \quad \text{with} \\ M_1 &= -\mathrm{i}\gamma_5\not{\varepsilon}\not{k} \\ M_2 &= 2\mathrm{i}\gamma_5(\,\varepsilon\!\cdot\! p\, k\cdot p' - \,\varepsilon\!\cdot\! p'\, k\cdot p) \\ M_3 &= \mathrm{i}\gamma_5(\not{\varepsilon} k\cdot p - \not{k}\,\varepsilon\!\cdot\! p\,) \\ M_4 &= \mathrm{i}\gamma_5(\not{\varepsilon} k\cdot p' - \not{k}\,\varepsilon\!\cdot\! p'\,)\,, \end{aligned} \tag{5.28}$$

where

$$\begin{aligned} A_1 &= D \\ A_2 &= -\frac{A_{p'}}{2p\cdot k} = \frac{A_p}{2p'\cdot k} \\ A_3 &= -B_p \\ A_4 &= -B_{p'}\ . \end{aligned} \tag{5.29}$$

Using Eq. (5.29) the $\mathcal{F}_1$ to $\mathcal{F}_4$ of Eq. (5.18) reduce to the well-known photoproduction case (cf. Eq. (B9) in [53]3)).

If one considers virtual photons, care has to be applied in the transition from Eq. (5.16) to Eq. (5.17). Since now $k^2 = \not{k}^2 \neq 0$, one has to keep two more terms in Eq. (5.17) proportional to k_μ for ensuring gauge invariance ($k_\mu\Gamma^\mu = 0$):

$$\Gamma_\mu(s,u) = \mathrm{i}\gamma_5\left(A_p p_\mu + A_{p'} p'_\mu + A_k k_\mu + (B_p p_\mu + B_{p'} p'_\mu + B_k k_\mu)\not{k} + C\gamma_\mu + D\not{k}\gamma_\mu\right)\ . \tag{5.30}$$

---

3) Note that there are four misprints in Eq. (B9) in [53]: The A_4 term in $\mathcal{F}_1$ and $\mathcal{F}_2$ should have a minus sign, A_3 in $\mathcal{F}_3$ and $\mathcal{F}_4$ should be an A_2.

The new terms do not contribute to the actual amplitude ($k_\mu \varepsilon^\mu = 0$) but are important for imposing gauge invariance:

$$\begin{aligned} A_p p\cdot k + A_{p'} p'\cdot k + (A_k + D)k^2 &= 0 \\ B_p p\cdot k + B_{p'} p'\cdot k + B_k k^2 + C &= 0\,. \end{aligned} \tag{5.31}$$

The idea is to extend the set for real photons to the case of virtual photons. Since $A_{p'} p'\cdot k = -A_p p\cdot k$ it follows that $A_k = -D$, and $M_1 \to -\mathrm{i}\gamma_5(\gamma_\mu \not{k} - k_\mu)\varepsilon^\mu$. M_2, M_3, and M_4 are identical to the real photon case. The second condition in Eq. (5.31) leads to a new gauge invariant pseudovector: $M_5 = \mathrm{i}\gamma_5(\not{k} k_\mu - k^2\gamma_\mu)\varepsilon^\mu$.

Due to the fact that A_k has been identified with $-D$, there is still a need for one more independent Lorentz pseudovector. It has to be constructed in such a way, that it does not influence gauge invariance in the real photon case. Thus it has to be proportional to k^2 and/or only enter in A_k, D, or B_k. The usual choice (cf. [14, 38]) is proportional to $(p-p')_\mu$ (which, of course, could also be expressed by the other three four-momenta): $A_6 k^2 (p-p')_\mu \varepsilon^\mu$. To make sure gauge invariance is still fulfilled, one also has to add a term $-A_6(p-p')\cdot k k_\mu \varepsilon^\mu$.

Thus the resulting amplitudes can be rewritten

$$\mathcal{V}_{fi} = \bar{u}(p',s') \sum_{j=1}^{6} A_j M_j u(p,s)\,, \tag{5.32}$$

where the 6 Lorentz pseudovectors are given by

$$\begin{aligned}
M_1 &= -\mathrm{i}\gamma_5(\gamma_\mu \not{k} - k_\mu)\varepsilon^\mu &&= -\gamma_5 \tfrac{1}{2}\gamma_\mu\gamma_\nu F^{\mu\nu} \\
M_2 &= 2\mathrm{i}\gamma_5(\,\varepsilon\cdot p\, k\cdot p' - \,\varepsilon\cdot p'\, k\cdot p) &&= -\gamma_5(p'+p)_\mu(p-p')_\nu F^{\mu\nu} \\
M_3 &= \mathrm{i}\gamma_5(\not{\varepsilon} k\cdot p - \not{k}\,\varepsilon\cdot p\,) &&= -\gamma_5 p_\mu \gamma_\nu F^{\mu\nu} \\
M_4 &= \mathrm{i}\gamma_5(\not{\varepsilon} k\cdot p' - \not{k}\,\varepsilon\cdot p'\,) &&= -\gamma_5 p'_\mu \gamma_\nu F^{\mu\nu} \\
M_5 &= \mathrm{i}\gamma_5(\not{k} k_\mu - k^2\gamma_\mu) &&= -\gamma_5 k'_\mu \gamma_\nu F^{\mu\nu} \\
M_6 &= \mathrm{i}\gamma_5(k'_\nu k_\mu - k_\nu k'_\mu)k^\mu \varepsilon^\mu &&= -\gamma_5(p-p')_\mu k_\nu F^{\mu\nu}
\end{aligned}$$

with the antisymmetric photon field tensor $F^{\mu\nu} = \partial^\mu \varepsilon^\nu - \partial^\nu \varepsilon^\mu = \mathrm{i}(\varepsilon^\mu k^\nu - \varepsilon^\nu k^\mu)$. The A_i are related to the functions in Eq. (5.30) by

$$\begin{aligned}
A_1 &= D \\
A_2 &= \frac{A_p + A_{p'}}{2k\cdot p' - 2k\cdot p - k^2} \\
A_3 &= -B_p \\
A_4 &= -B_{p'} \\
A_5 &= \frac{1}{k^2(2k\cdot p' - 2k\cdot p - k^2)}\left((2k\cdot p + \frac{1}{2}k^2)A_p + (2k\cdot p' - \frac{1}{2}k^2)A_{p'}\right) \\
A_6 &= \frac{1}{k^2}\left((k\cdot p + \frac{1}{2}k^2)B_p + (k\cdot p' - \frac{1}{2}k^2)B_{p'} + C\right)\,,
\end{aligned}$$

where we have neglected the terms A_k and B_k since they do not contribute to the actual amplitude and are restricted by Eq. (5.31). In the literature of pion electroproduction [14, 38], usually an extension of the Chew-Goldberger-Low-Nambu (CGLN) photoproduction amplitudes [28] is used:

$$
\begin{aligned}
\widetilde{M}_1 &= -\gamma_5 \tfrac{1}{2}\gamma_\nu \gamma_\mu F^{\mu\nu} \\
\widetilde{M}_2 &= -\gamma_5 (p' + p)_\mu (k' - \tfrac{1}{2}k)_\nu F^{\mu\nu} \\
\widetilde{M}_3 &= -\gamma_5 (p + \tfrac{1}{2}k)_\mu \gamma_\nu F^{\mu\nu} \\
\widetilde{M}_4 &= -\gamma_5 (p' - \tfrac{1}{2}k)_\mu \gamma_\nu F^{\mu\nu} \\
\widetilde{M}_5 &= -\gamma_5 (p - p')_\mu k_\nu F^{\mu\nu} \\
\widetilde{M}_6 &= -\gamma_5 k'_\mu \gamma_\nu F^{\mu\nu} \ .
\end{aligned}
$$

The functions $\widetilde{M}_i$ are related to the M_i by

$$
\begin{aligned}
\widetilde{M}_1 &= M_1, \ \widetilde{M}_2 = -M_2, \ \widetilde{M}_3 = M_4 - M_3, \ \widetilde{M}_4 = -M_4 - M_3 - 2m_B M_1, \\
\widetilde{M}_5 &= M_6, \ \widetilde{M}_6 = M_5, \ \ .
\end{aligned}
$$

The set presented here is more convenient as compared to the CGLN invariants for the use in cases where the incoming and outgoing baryons differ in mass.

5.4.2 Photoproduction of Vector Mesons

In the case of vector meson photoproduction $\gamma N \to VN$, applying gauge invariance to the Clifford algebra operator of Eq. (5.21) requires $\Gamma_{\mu\nu} k^\mu = 0$. Using the independence of $\mathbb{1}_4$ and $\not{k}$ and of the four-momenta p_μ and p'_μ leads to the following 6 conditions:

$$
\begin{aligned}
A_{pp} p\cdot k + A_{p'p} p'\cdot k - A_g &= 0 \\
A_{pp'} p\cdot k + A_{p'p'} p'\cdot k + A_g &= 0 \\
B_{pp} p\cdot k + B_{p'p} p'\cdot k - B_g + C_p &= 0 \\
B_{pp'} p\cdot k + B_{p'p'} p'\cdot k + B_g + C_{p'} &= 0 \\
E_p p\cdot k + E_{p'} p'\cdot k &= 0 \\
F_p p\cdot k + F_{p'} p'\cdot k + G &= 0 \ .
\end{aligned}
\tag{5.33}
$$

Hence the reduction from 18 down to 12 independent amplitudes is in line with the 6 conditions arising from gauge invariance.

5.4.3 Compton Scattering

In addition to the restrictions (5.33) found in the previous Section (5.4.2), gauge invariance for Compton scattering also applies to the outgoing photon: $\Gamma_{\mu\nu} k'^\nu = 0$ and the following 6 additional conditions hold true:

$$
\begin{aligned}
A_{pp} p\cdot k' + A_{pp'} p'\cdot k' + A_g - 2p'\cdot k F_p &= 0 \\
A_{p'p} p\cdot k' + A_{p'p'} p'\cdot k' - A_g - 2p'\cdot k F_{p'} - 2G &= 0
\end{aligned}
$$

$$
\begin{aligned}
B_{pp} p\cdot k' + B_{pp'} p'\cdot k' + B_g + E_p + 2m_N F_p &= 0 \\
B_{p'p} p\cdot k' + B_{p'p'} p'\cdot k' - B_g + E_{p'} + 2m_N F_{p'} - 2H &= 0 \\
C_p p\cdot k' + C_{p'} p'\cdot k' + 2m_N G + 2H p'\cdot k &= 0 \\
D_p p\cdot k' + D_{p'} p'\cdot k' - G &= 0\,. \qquad (5.34)
\end{aligned}
$$

This leads to a further reduction of the number of independent functions by 6, just as is required by the reduction from 12 independent amplitudes for $\gamma N \to VN$ down to 6 for $\gamma N \to \gamma N$. A similar strategy for the reduction of the independent operators for Compton scattering was presented by Bardeen and Tung [9]. Using gauge invariance and finally comparing their results with the minimal set of operators presented in section 5.3 $n_\mu \equiv \{p_\mu, p'_\mu, k_\mu, \varepsilon_{\mu\alpha\beta\delta} p^\alpha p'^\beta k^\delta\}$, combined with $\Gamma_{\mu\nu} = n_\mu n_\nu \otimes \{\not k, 1/\gamma_5 \not k, \gamma_5\}$ these authors were able to present a set of 6 operators.

An alternative approach directly based on the minimal set of Section 5.3 was given by Prange [147]. Using charge-conjugation invariance and crossing symmetry, he reduced the 18 invariants to the necessary 6. These invariants were further modified by Hearn and Leader [76] by normalization conditions. In [31, 76] the relation to a minimal operator set in Pauli space $\mathcal{F}$ was also derived.

Since neither of these sets are used for the present calculation, we refer to the references for the results.

Chapter 6

Partial Waves and Multipoles

In Chapter 4 we have presented an elegant and uniform way to decompose the angle-dependent amplitudes entering the potential into helicity partial-wave amplitudes of good total angular momentum J and parity $P = (-1)^{J\pm\frac{1}{2}}$ (4.13):

$$\mathcal{T}^{J\pm}_{\lambda'\lambda} \;=\; \mathcal{T}^{J}_{\lambda'\lambda} \pm \eta \mathcal{T}^{J}_{\lambda'-\lambda} \qquad\qquad \text{with} \quad \mathcal{T}^{J}_{\lambda'\lambda} = 2\pi \int_{-1}^{+1} \mathrm{d}x d^{J}_{\lambda\lambda'}(\vartheta) \mathcal{T}^{fi}_{\lambda'\lambda} \,. \tag{6.1}$$

The characteristic parity factor is given by (4.11): $\eta = \eta_k \eta_p (-1)^{s_k + s_p + \frac{1}{2}}$. Here, η_k (η_p) and s_k (s_p) are the intrinsic parity and spin, resp. of the incoming meson (baryon).

In this chapter we establish the explicit expression of $\mathcal{T}^{J\pm}_{\lambda'\lambda}$ for the various reaction channels$^{1)}$ and the relation of these amplitudes to the commonly used partial-wave decompositions based on the meson orbital-angular momentum ℓ_φ.

6.1 πN Scattering

The πN scattering case is a good introductary example because its partial-wave decomposition is abundantly treated in the literature. Since the pion is a spinless particle the total helicity of the πN final state is always $\pm\frac{1}{2}$ and there are only two different partial waves for a given total angular momentum J. Starting with Eq. (6.1) and using Eqs. (5.2), (5.10), and $\eta = \eta_\pi \eta_N (-1)^{s_\pi + s_N + \frac{1}{2}} = +1$ one finds ($x = \cos\vartheta$):

$$\begin{aligned}
\mathcal{T}^{J\pm}_{\frac{1}{2}\frac{1}{2}}(\pi N \leftarrow \pi N) \;&=\; \mathcal{T}^{J}_{+\frac{1}{2}+\frac{1}{2}} \pm \mathcal{T}^{J}_{+\frac{1}{2}-\frac{1}{2}} \\
&=\; -2\pi \frac{\sqrt{\mathrm{p}\,\mathrm{p}' m_{B'} m_B}}{(4\pi)^2 \sqrt{s}} \int_{-1}^{+1} \mathrm{d}x \left(d^{J}_{+\frac{1}{2}+\frac{1}{2}}(\vartheta) \mathcal{V}^{J}_{+\frac{1}{2}+\frac{1}{2}} \pm d^{J}_{-\frac{1}{2}+\frac{1}{2}}(\vartheta) \mathcal{V}^{J}_{+\frac{1}{2}-\frac{1}{2}} \right) \\
&=\; -\frac{\sqrt{\mathrm{p}\,\mathrm{p}'}}{2} \int_{-1}^{+1} \mathrm{d}x \left[d^{J}_{+\frac{1}{2}+\frac{1}{2}}(\vartheta) \cos\frac{\vartheta}{2} \left(\tilde{A} + \tilde{B} \right) \pm d^{J}_{-\frac{1}{2}+\frac{1}{2}}(\vartheta) \sin\frac{\vartheta}{2} \left(\tilde{A} - \tilde{B} \right) \right]
\end{aligned}$$

$^{1)}$For the readers convenience we write the commonly given $\mathcal{T}$ instead of $\mathcal{K}$, where the latter one actually underlies the partial-wave decomposition in the present calculation; cf. Chapters 4, 5, and Appendix C.

$$= -\frac{\sqrt{\mathrm{p}\mathrm{p}'}}{2(\ell_\pi+1)}\int_{-1}^{+1}\mathrm{d}x\left[\cos^2\frac{\vartheta}{2}\left(\tilde{A}+\tilde{B}\right)\left(P'_{\ell_\pi+1}(x)-P'_{\ell_\pi}(x)\right)\pm \right.$$
$$\left. \sin^2\frac{\vartheta}{2}\left(\tilde{A}-\tilde{B}\right)\left(P'_{\ell_\pi+1}(x)+P'_{\ell_\pi}(x)\right) \right] ,$$

where we have used Eq. (B.7) with $\ell_\pi = J-\frac{1}{2}$ to introduce the derivatives of the Legendre polynomials $P'_{\ell_\pi}(x)$ (see Appendix B). The functions $\tilde{A}$ and $\tilde{B}$ are given in Eq. (5.6). Splitting up this equation we can use (B.2) to find

$$\begin{aligned}\mathcal{T}^{J+}_{\frac{1}{2}\frac{1}{2}} &= -\frac{\sqrt{\mathrm{p}\mathrm{p}'}}{2(\ell_\pi+1)}\int_{-1}^{+1}\mathrm{d}x\left[\tilde{A}\left(P'_{\ell_\pi+1}(x)-P'_{\ell_\pi}(x)\cos\vartheta\right)+\tilde{B}\left(P'_{\ell_\pi+1}(x)\cos\vartheta-P'_{\ell_\pi}(x)\right)\right]\\ &= -\frac{\sqrt{\mathrm{p}\mathrm{p}'}}{2}\int_{-1}^{+1}\mathrm{d}x\left(\tilde{A}P_{\ell_\pi}(x)+P_{\ell_\pi+1}(x)\right)\end{aligned}$$

and

$$\begin{aligned}\mathcal{T}^{J-}_{\frac{1}{2}\frac{1}{2}} &= -\frac{\sqrt{\mathrm{p}\mathrm{p}'}}{2(\ell_\pi+1)}\int_{-1}^{+1}\mathrm{d}x\left[\tilde{A}\left(P'_{\ell_\pi+1}(x)\cos\vartheta-P'_{\ell_\pi}(x)\right)+\tilde{B}\left(P'_{\ell_\pi+1}(x)-P'_{\ell_\pi}(x)\cos\vartheta\right)\right]\\ &= -\frac{\sqrt{\mathrm{p}\mathrm{p}'}}{2}\int_{-1}^{+1}\mathrm{d}x\left(\tilde{A}P_{\ell_\pi+1}(x)+P_{\ell_\pi}(x)\right) .\end{aligned}$$

If we now redefine the orbital-angular momentum by $\ell_\pi = J\mp\frac{1}{2}$ these two equations can be merged:

$$T^{\pi\pi}_{\ell_\pi\pm} = -\frac{\sqrt{\mathrm{p}\mathrm{p}'}}{2}\int_{-1}^{+1}\mathrm{d}x(\tilde{A}P_{\ell_\pi}(x)+\tilde{B}P_{\ell_\pi\pm 1}(x)) .$$

This is identical[2] to the commonly used decomposition of πN scattering which can be found in many textbooks (e.g. [47, 56, 61, 88]) and is also derived in [51, 52]. The partial waves $T^{\pi\pi}_{\ell_\pi\pm}$ have total angular momentum $J=\ell_\pi\pm\frac{1}{2}$ and parity $P=-(-1)^{\ell_\pi}=(-1)^{J\pm\frac{1}{2}}$.

For the case of pion-induced production of a scalar (0^+) meson, the partial waves of total angular momentum J and parity $P=(-1)^{J\pm\frac{1}{2}}$ are given in the same way

$$\mathcal{T}^{J\pm}_{\frac{1}{2}\frac{1}{2}}(\zeta N\leftarrow\pi N) \;=\; \mathcal{T}^{J}_{+\frac{1}{2}+\frac{1}{2}}\pm\mathcal{T}^{J}_{+\frac{1}{2}-\frac{1}{2}}$$

and are therefore also identical to the ones in [51, 52].

6.2 Photoproduction

A vector particle (e.g. the photon) also carries an intrinsic spin of 1; therefore, the total spin J and parity P are not sufficient to completely describe a VN helicity state. The

---

[2] Usually, these partial waves are defined with a positive overall sign. This corresponds to a definition of $\mathcal{T}^{fi}_{\lambda'\lambda}$ different from (C.10) (and correspondingly also a change in (C.11)) requiring a different sign in the rescattering part of the BS equation (2.11) and (2.12).

additional characteristic is introduced as the total helicity λ and there are 6 independent two-particle helicity states of total spin J (see Eq. (4.10)):

$$|J,\lambda;\pm\rangle \quad = \quad \frac{1}{\sqrt{2}}\left(|J,+\lambda\rangle \pm \eta|J,-\lambda\rangle\right) \qquad \text{with} \quad \eta = \eta_V\eta_N(-1)^{s_V+s_N+\frac{1}{2}} = -1\ .$$

The parity of these states is $P = (-1)^{J\pm\frac{1}{2}}$. The three different helicities $\lambda = \lambda_V - \lambda_N$ have been introduced in Section 5.2.1 and are given by $\lambda = 0, \frac{1}{2}, \frac{3}{2}$.

Instead of 2 helicity partial-wave amplitudes as in the $\pi N \to \pi N$ case there are now 6 different ones belonging to the total spin J:

$$\begin{aligned}
\mathcal{T}^{J\pm}_{\frac{1}{2}\frac{3}{2}}(\pi N \leftarrow VN) &= \mathcal{T}^{J}_{+\frac{1}{2}+\frac{3}{2}} \mp \mathcal{T}^{J}_{+\frac{1}{2}-\frac{3}{2}}\\
\mathcal{T}^{J\pm}_{\frac{1}{2}\frac{1}{2}}(\pi N \leftarrow VN) &= \mathcal{T}^{J}_{+\frac{1}{2}+\frac{1}{2}} \mp \mathcal{T}^{J}_{+\frac{1}{2}-\frac{1}{2}}\\
\mathcal{T}^{J\pm}_{\frac{1}{2}0}(\pi N \leftarrow VN) &= \mathcal{T}^{J}_{+\frac{1}{2}+0} \mp \mathcal{T}^{J}_{+\frac{1}{2}-0}\ .
\end{aligned}$$

The parity is always $P = (-1)^{J\pm\frac{1}{2}}$. Note that the amplitudes $\mathcal{T}^{J\pm}_{\frac{1}{2}0}$ are only non-vanishing for vector mesons or virtual ($k^2 \neq 0$) photons.

In terms of a partial-wave decomposition, these helicity partial-wave amplitudes are sufficient for the description of $VN \leftrightarrow \varphi N$ amplitudes. However, in the literature, the additional spin degree of freedom is generally described as in classical and nuclear physics by magnetic (M[3)]), electric (E), and scalar (S) (longitudinal) photon states, where the latter one applies only to virtual photons. The first two are transversally polarized with respect to the three-momentum $\boldsymbol{k}$ of the photon and are therefore given by combinations of the polarization vectors of Eq. (A.33) with $\lambda_\gamma = s_{z\gamma} = \pm 1$ ($\boldsymbol{\varepsilon}_{\pm 1}$), while the last one is longitudinally polarized and hence proportional to $\boldsymbol{\varepsilon}_0$. This so-called multipole decomposition is also the one that is commonly used for the experimental partial-wave decomposition of $\gamma N \to \pi N$, hence we deduce in the following (see Eq. (6.6)) the (general) relation between our two-particle helicity states and the classical photon-nucleon states $|J; M/E/S\rangle$. With this relation, establishing the connection between the photoproduction multipoles of any final state and the two-particle helicity amplitudes is straightforward, and can also be easily achieved for more complicated reactions such as $\gamma N \to \pi\Delta$. This is demonstrated below in Sections 6.2.1 and 6.2.2 for pion photoproduction and Compton scattering, resp. on the nucleon.

The classification into magnetic and electric states is performed by assigning definite parities to these photon states:

$$\hat{P}|\gamma; j_\gamma, M\rangle = -(-1)^{j_\gamma}|\gamma; j_\gamma, M\rangle \quad \text{and} \quad \hat{P}|\gamma; j_\gamma, E\rangle = (-1)^{j_\gamma}|\gamma; j_\gamma, E\rangle\ . \tag{6.2}$$

Here, j_γ denotes the total spin of the photon state and is given by $j_\gamma = \ell_\gamma \oplus 1$, where ℓ_γ is the photon angular momentum in the photon-nucleon system. Therefore, one has $j_\gamma = \ell_\gamma$ for the magnetic and $j_\gamma = \ell_\gamma \pm 1$ for the electric states. The third (scalar) class of states $|\gamma; j_\gamma, S\rangle$ characterized by longitudinal polarizations ($s_{\gamma_z} = 0$) also has $j_\gamma = \ell_\gamma \pm 1$. This can be easily seen by looking, e.g., at a hypothetical scalar state with $j_\gamma = \ell_\gamma$ in

---

[3)] Not to be confused with the z-component of the total spin!

the c.m. system, where $j_{\gamma_z} = \ell_{\gamma_z} = 0$. This results in a vanishing Clebsch-Gordan $(j_\gamma = \ell_\gamma, 0|\ell_\gamma, 0; 1, 0) = 0$.

In terms of angular-momentum (spherical-harmonic) states the correctly normalized transversal states are then given by [61]:

$$\begin{aligned} |\gamma; j_\gamma, M\rangle &= |\gamma; j_\gamma, \ell_\gamma = j_\gamma\rangle \\ |\gamma; j_\gamma, E\rangle &= \frac{1}{\sqrt{2j_\gamma+1}}\left(\sqrt{j_\gamma}|\gamma; j_\gamma, \ell_\gamma = j_\gamma+1\rangle + \sqrt{j_\gamma+1}|\gamma; j_\gamma, \ell_\gamma = j_\gamma - 1\rangle\right) . \end{aligned}$$

Using the overlap between the angular momentum and the one-particle helicity states for the photon three-momentum along the z-axis [83, 111]

$$\langle\gamma; j_\gamma, j_{\gamma_z}; \lambda_\gamma|\gamma; j_\gamma, j_{\gamma_z}; \ell_\gamma\rangle = \sqrt{\frac{2\ell_\gamma+1}{2j_\gamma+1}}(j_\gamma, \lambda_\gamma|\ell_\gamma, 0; 1, \lambda_\gamma) , \tag{6.3}$$

which follows from the same reasons that lead to the normalization in Eq. (4.4), one finds by working out the Clebsch-Gordan coefficients $(j_\gamma, \lambda_\gamma|\ell_\gamma, 0; 1, \lambda_\gamma)$ the relation between the helicity and the magnetic, electric, and scalar photon states:

$$\begin{aligned} |\gamma; j_\gamma, M\rangle &= \frac{1}{\sqrt{2}}\left(|\gamma; j_\gamma, \lambda_\gamma = -1\rangle - |\gamma; j_\gamma, \lambda_\gamma = +1\rangle\right) \\ |\gamma; j_\gamma, E\rangle &= \frac{1}{\sqrt{2}}\left(|\gamma; j_\gamma, \lambda_\gamma = -1\rangle + |\gamma; j_\gamma, \lambda_\gamma = +1\rangle\right) \\ |\gamma; j_\gamma, S\rangle &= |\gamma; j_\gamma, \lambda_\gamma = 0\rangle . \end{aligned} \tag{6.4}$$

These pure photon states can be generalized to photon-nucleon states characterized by the photon properties and the total spin $J = j_\gamma \oplus \frac{1}{2}$ with z-component $J_z = \lambda_\gamma - \lambda_N$: $|J, J_z; j_\gamma, \lambda_\gamma\rangle \equiv |j_\gamma, \lambda_\gamma\rangle|J, J_z\rangle$. Since (cf. Eq. (6.3))

$$\langle J, J_z; j_\gamma, \lambda_\gamma|J, \lambda_\gamma - \lambda_N; \lambda_\gamma, \lambda_N\rangle = \sqrt{\frac{2j_\gamma+1}{2J+1}}(j_\gamma, \lambda_\gamma; \tfrac{1}{2}, -\lambda_N|J, \lambda_\gamma - \lambda_N)\delta_{J_z,\lambda_\gamma-\lambda_N} \tag{6.5}$$

these states are related to the two-particle helicity states $|J, \lambda = \lambda_\gamma - \lambda_N\rangle$ with total spin J and total helicity λ in the following way [111]:

$$\begin{aligned} |J, J_z; j_\gamma, +1\rangle &= \frac{1}{\sqrt{2(j_\gamma+1)}}\left(\sqrt{j_\gamma}|J, \lambda = +1-\tfrac{1}{2}\rangle + \sqrt{j_\gamma+2}|J, \lambda = +1+\tfrac{1}{2}\rangle\right) \\ |J, J_z; j_\gamma, -1\rangle &= \frac{1}{\sqrt{2(j_\gamma+1)}}\left(\sqrt{j_\gamma+2}|J, \lambda = -1-\tfrac{1}{2}\rangle + \sqrt{j_\gamma}|J, \lambda = -1+\tfrac{1}{2}\rangle\right) \\ |J, J_z; j_\gamma, 0\rangle &= \frac{1}{\sqrt{2}}\left(|J, \lambda = 0-\tfrac{1}{2}\rangle + |J, \lambda = 0+\tfrac{1}{2}\rangle\right) \end{aligned}$$

for $J = j_\gamma + \frac{1}{2}$ and

$$\begin{aligned} |J, J_z; j_\gamma, +1\rangle &= \frac{1}{\sqrt{2j_\gamma}}\left(\sqrt{j_\gamma+1}|J, \lambda = +1-\tfrac{1}{2}\rangle - \sqrt{j_\gamma-1}|J, \lambda = +1+\tfrac{1}{2}\rangle\right) \\ |J, J_z; j_\gamma, -1\rangle &= \frac{1}{\sqrt{2j_\gamma}}\left(\sqrt{j_\gamma-1}|J, \lambda = -1-\tfrac{1}{2}\rangle - \sqrt{j_\gamma+1}|J, \lambda = -1+\tfrac{1}{2}\rangle\right) \\ |J, J_z; j_\gamma, 0\rangle &= \frac{1}{\sqrt{2}}\left(|J, \lambda = 0-\tfrac{1}{2}\rangle - |J, \lambda = 0+\tfrac{1}{2}\rangle\right) \end{aligned}$$

Amplitude	J	P	ℓ_π
$\mathcal{T}^{M}_{j_\gamma+}$	$j_\gamma+\frac{1}{2}$	$-(-1)^{j_\gamma}$	j_γ
$\mathcal{T}^{M}_{j_\gamma-}$	$j_\gamma-\frac{1}{2}$	$-(-1)^{j_\gamma}$	j_γ
$\mathcal{T}^{E}_{j_\gamma+}$	$j_\gamma+\frac{1}{2}$	$(-1)^{j_\gamma}$	$j_\gamma+1$
$\mathcal{T}^{E}_{j_\gamma-}$	$j_\gamma-\frac{1}{2}$	$(-1)^{j_\gamma}$	$j_\gamma-1$
$\mathcal{T}^{S}_{j_\gamma+}$	$j_\gamma+\frac{1}{2}$	$(-1)^{j_\gamma}$	$j_\gamma+1$
$\mathcal{T}^{S}_{j_\gamma-}$	$j_\gamma-\frac{1}{2}$	$(-1)^{j_\gamma}$	$j_\gamma-1$

Table 6.1: Relation between the pion angular momentum ℓ_π and the total photon spin j_γ for the electromagnetic multipole amplitudes in pion electroproduction. The total spin J and parity P of the amplitudes are also indicated.

for $J=j_\gamma-\frac{1}{2}$. Using now Eq. (6.4), the relation between our two-particle helicity states $|J,\lambda;\pm\rangle$ and the magnetic, electric, and scalar photon-nucleon states finally results in:

$$\begin{aligned}
|J=j_\gamma+\tfrac{1}{2},M/E\rangle &= \mp\frac{1}{\sqrt{2(j_\gamma+1)}}\left(\sqrt{j_\gamma}|J,\tfrac{1}{2};\pm\rangle+\sqrt{j_\gamma+2}|J,\tfrac{3}{2};\pm\rangle\right)\\
|J=j_\gamma-\tfrac{1}{2},M/E\rangle &= \mp\frac{1}{\sqrt{2j_\gamma}}\left(\sqrt{j_\gamma+1}|J,\tfrac{1}{2};\mp\rangle-\sqrt{j_\gamma-1}|J,\tfrac{3}{2};\mp\rangle\right)\\
|J=j_\gamma\pm\tfrac{1}{2},S\rangle &= \pm|J,0;\mp\rangle\ .
\end{aligned}\tag{6.6}$$

This relation was also given in [58]. Since the two-particle helicity states $|J,\lambda;\pm\rangle$ are of parity $P=(-1)^{J\pm\frac{1}{2}}$, this also holds true for the corresponding photon-nucleon multipole states.

6.2.1 Photoproduction of Pions

Sandwiching the interaction matrix T between the multipole states (6.6) and the πN parity helicity states of (4.10): $\langle J,\lambda;\pm|_{\pi N}=(\langle J,+\lambda|\pm\langle J,-\lambda|)/\sqrt{2}$, one can project out the desired multipole amplitudes for the transition to a pion nucleon helicity state and the electromagnetic multipole amplitudes can be rewritten in terms of the $\gamma N\to\pi N$ helicity amplitudes:

$$\begin{aligned}
\mathcal{T}^{M/E}_{j_\gamma+} &= {}_{\pi N}\langle J,\lambda;\pm|\,T\,|j_\gamma+,M/E\rangle=\mp\frac{1}{\sqrt{2(j_\gamma+1)}}\left(\sqrt{j_\gamma}\,\mathcal{T}^{J\pm}_{\frac{1}{2}\frac{1}{2}}+\sqrt{j_\gamma+2}\,\mathcal{T}^{J\pm}_{\frac{1}{2}\frac{3}{2}}\right)\\
\mathcal{T}^{M/E}_{j_\gamma-} &= {}_{\pi N}\langle J,\lambda;\mp|\,T\,|j_\gamma-,M/E\rangle=\mp\frac{1}{\sqrt{2j_\gamma}}\left(\sqrt{j_\gamma+1}\,\mathcal{T}^{J\mp}_{\frac{1}{2}\frac{1}{2}}-\sqrt{j_\gamma-1}\,\mathcal{T}^{J\mp}_{\frac{1}{2}\frac{3}{2}}\right)\\
\mathcal{T}^{S}_{j_\gamma\pm} &= {}_{\pi N}\langle J,\lambda;\mp|\,T\,|j_\gamma\pm,S\rangle\qquad=\pm\mathcal{T}^{J\mp}_{\frac{1}{2}0}\ .
\end{aligned}\tag{6.7}$$

Here, Eq. (4.12) has been used and we have introduced the notation $j_\gamma\pm$: $J=j_\gamma\pm\frac{1}{2}$. The relation between the pion angular momentum ℓ_π and the total photon spin j_γ is given in Table 6.1. Comparing these multipole amplitudes with the Chew-Goldberger-Low-Nambu (CGLN) multipoles generally used in the literature (cf. Eqs. (B.6), (B.9) in [14], see also [28, 184]), one has to recall that those stem from an operatorial representation of the multipole wave functions, where the magnetic multipole is given by [61, 156] $\mathrm{i}\boldsymbol{\varepsilon}\cdot\boldsymbol{\ell}_\gamma/\sqrt{j_\gamma(j_\gamma+1)}$ and the electric by $\mathrm{i}\boldsymbol{\varepsilon}\cdot(\boldsymbol{k}\times\boldsymbol{\ell}_\gamma)/\sqrt{j_\gamma(j_\gamma+1)}$. The normalization factor is usually omitted and hence absorbed in the definition of the multipoles. Therefore, they are related to the above multipole amplitudes by[4)]

$$\begin{aligned}
M_{j_\gamma+} &\equiv \frac{+\mathcal{T}^M_{j_\gamma+}}{\sqrt{\mathrm{kk}'j_\gamma(j_\gamma+1)}}\,, &\qquad M_{j_\gamma-} &\equiv \frac{-\mathcal{T}^M_{j_\gamma-}}{\sqrt{\mathrm{kk}'j_\gamma(j_\gamma+1)}}\\
E_{j_\gamma+} &\equiv \frac{-\mathcal{T}^E_{j_\gamma+}}{\sqrt{\mathrm{kk}'j_\gamma(j_\gamma+1)}}\,, &\qquad E_{j_\gamma-} &\equiv \frac{-\mathcal{T}^E_{j_\gamma-}}{\sqrt{\mathrm{kk}'j_\gamma(j_\gamma+1)}}\\
S_{j_\gamma+} &\equiv \frac{-\mathcal{T}^S_{j_\gamma+}}{\sqrt{\mathrm{kk}'}(j_\gamma+1)}\,, &\qquad S_{j_\gamma-} &\equiv \frac{+\mathcal{T}^S_{j_\gamma-}}{\sqrt{\mathrm{kk}'}j_\gamma}\,,
\end{aligned}\tag{6.8}$$

where the overall signs and the factors for the scalar multipoles correspond to the usual convention. Note, that the multipole amplitudes in Eq. (6.7) are correctly normalized and hence would have to be used in the rescattering equation of a coupled-channel formalism.

Combining Eqs. (6.7) and (6.8) and using the relations between ℓ_π and j_γ (see Table 6.1) the multipoles explicitly result for $J=\ell_\pi+\frac{1}{2}$ in[5)]:

$$\begin{aligned}
M_{\ell_\pi+} &= -\tfrac{1}{\sqrt{2\mathrm{kk}'}(\ell_\pi+1)}\left(\mathcal{T}^{J+}_{\frac12\frac12}+\sqrt{\tfrac{\ell_\pi+2}{\ell_\pi}}\,\mathcal{T}^{J+}_{\frac12\frac32}\right)\\
M_{(\ell_\pi+1)-} &= +\tfrac{1}{\sqrt{2\mathrm{kk}'}(\ell_\pi+1)}\left(\mathcal{T}^{J-}_{\frac12\frac12}-\sqrt{\tfrac{\ell_\pi}{\ell_\pi+2}}\,\mathcal{T}^{J-}_{\frac12\frac32}\right)\\
E_{(\ell_\pi+1)-} &= -\tfrac{1}{\sqrt{2\mathrm{kk}'}(\ell_\pi+1)}\left(\mathcal{T}^{J-}_{\frac12\frac12}+\sqrt{\tfrac{\ell_\pi+2}{\ell_\pi}}\,\mathcal{T}^{J-}_{\frac12\frac32}\right)\\
E_{\ell_\pi+} &= -\tfrac{1}{\sqrt{2\mathrm{kk}'}(\ell_\pi+1)}\left(\mathcal{T}^{J+}_{\frac12\frac12}-\sqrt{\tfrac{\ell_\pi}{\ell_\pi+2}}\,\mathcal{T}^{J+}_{\frac12\frac32}\right)\\
S_{(\ell_\pi+1)-} &= -\tfrac{1}{\sqrt{\mathrm{kk}'}(\ell_\pi+1)}\;\mathcal{T}^{J-}_{\frac12 0}\\
S_{\ell_\pi+} &= -\tfrac{1}{\sqrt{\mathrm{kk}'}(\ell_\pi+1)}\;\mathcal{T}^{J+}_{\frac12 0}\,.
\end{aligned}\tag{6.9}$$

These are also used in the experimental pion-photoproduction multipole decomposition SP01 of Arndt et al. [221], since these authors applied the definitions from Walker [184]. In Section 8.4 our calculations are compared to this experimental extraction.

6.2.2 Compton Scattering

Proceeding in the same way as in pion photoproduction, the interaction matrix T is sandwiched between incoming and outgoing multipole states (6.6) to project out the desired multipole amplitudes, e.g.:

$$\mathcal{T}^{MM}_{j_\gamma+} = \langle j_\gamma+,M|\,T\,|j_\gamma+,M\rangle\,,$$

[4)] Note that $M_{j_\gamma+}$ and $E_{j_\gamma+}$ have the wrong sign in the relations given in [52].

[5)] Note that there are four sign typos in the relations given in [52].

and so on. In the case of a multipole change from electric to magnetic or vice versa, the total photon spin j_γ has to change by one unit. For example, if j_γ corresponds to the total spin of the incoming photon, then we have, for the transition of an electric multipole state with $J = j_\gamma + \frac{1}{2}$ to a magnetic state, a total spin of the outgoing photon of $j_\gamma + 1$. Therefore, it is convenient to rewrite the total spin J of the γN system in such a way that we always have $J = j_\gamma + \frac{1}{2}$, i.e. $j_\gamma - \to (j_\gamma + 1)-$. Then, for the $E \to M$ case one has a $|j_\gamma + \frac{1}{2}, E\rangle \to \langle (j_\gamma + 1) - \frac{1}{2}, M|$ transition. Using the lower index of $\mathcal{T}$ to characterize the incoming photon state, the Compton multipole amplitudes can be rewritten in terms of the $\gamma N \to \gamma N$ helicity amplitudes in the following way:

$$\begin{aligned}
\mathcal{T}^{\overset{MM}{EE}}_{j_\gamma +} &= \frac{1}{2(j_\gamma+1)} \left[j_\gamma\, \mathcal{T}^{J\pm}_{\frac{1}{2}\frac{1}{2}} + \sqrt{j_\gamma(j_\gamma+2)} \left(\mathcal{T}^{J\pm}_{\frac{3}{2}\frac{1}{2}} + \mathcal{T}^{J\pm}_{\frac{1}{2}\frac{3}{2}} \right) + (j_\gamma+2)\, \mathcal{T}^{J\pm}_{\frac{3}{2}\frac{3}{2}} \right] \\
\mathcal{T}^{\overset{MM}{EE}}_{(j_\gamma+1)-} &= \frac{1}{2(j_\gamma+1)} \left[(j_\gamma+2)\, \mathcal{T}^{J\mp}_{\frac{1}{2}\frac{1}{2}} - \sqrt{j_\gamma(j_\gamma+2)} \left(\mathcal{T}^{J\mp}_{\frac{3}{2}\frac{1}{2}} + \mathcal{T}^{J\mp}_{\frac{1}{2}\frac{3}{2}} \right) + j_\gamma\, \mathcal{T}^{J\mp}_{\frac{3}{2}\frac{3}{2}} \right] \\
\mathcal{T}^{\overset{ME}{EM}}_{j_\gamma +} &= \frac{-1}{2(j_\gamma+1)} \left[\sqrt{j_\gamma(j_\gamma+2)} \left(\mathcal{T}^{J\mp}_{\frac{1}{2}\frac{1}{2}} - \mathcal{T}^{J\mp}_{\frac{3}{2}\frac{3}{2}} \right) - j_\gamma\, \mathcal{T}^{J\mp}_{\frac{3}{2}\frac{1}{2}} + (j_\gamma+2)\, \mathcal{T}^{J\mp}_{\frac{1}{2}\frac{3}{2}} \right] \qquad (6.10) \\
\mathcal{T}^{\overset{ME}{EM}}_{(j_\gamma+1)-} &= \frac{-1}{2(j_\gamma+1)} \left[\sqrt{j_\gamma(j_\gamma+2)} \left(\mathcal{T}^{J\pm}_{\frac{1}{2}\frac{1}{2}} - \mathcal{T}^{J\pm}_{\frac{3}{2}\frac{3}{2}} \right) + (j_\gamma+2)\, \mathcal{T}^{J\pm}_{\frac{3}{2}\frac{1}{2}} - j_\gamma\, \mathcal{T}^{J\pm}_{\frac{1}{2}\frac{3}{2}} \right] ,
\end{aligned}$$

where the notation for the upper indices is MM: $|\gamma, M\rangle \to \langle \gamma, M|$, ME: $|\gamma, E\rangle \to \langle \gamma, M|$, and so on. Using time reversal invariance6) manifested in Eq. (4.15), which reduces the number of independent amplitudes from 8 to 6 (see Section 5.4), and the normalization factor (not the phases) $1/\sqrt{j_\gamma(j_\gamma+1)}$ of Eq. (6.8) one finds:

$$\begin{aligned}
f^{\overset{MM}{EE}}_{j_\gamma +} &= \frac{1}{2\mathrm{k}(j_\gamma+1)^2} \left[\mathcal{T}^{J\pm}_{\frac{1}{2}\frac{1}{2}} + 2\sqrt{\tfrac{j_\gamma+2}{j_\gamma}}\, \mathcal{T}^{J\pm}_{\frac{1}{2}\frac{3}{2}} + \tfrac{j_\gamma+2}{j_\gamma}\, \mathcal{T}^{J\pm}_{\frac{3}{2}\frac{3}{2}} \right] \\
f^{\overset{MM}{EE}}_{(j_\gamma+1)-} &= \frac{1}{2\mathrm{k}(j_\gamma+1)^2} \left[\mathcal{T}^{J\mp}_{\frac{1}{2}\frac{1}{2}} - 2\sqrt{\tfrac{j_\gamma}{j_\gamma+2}}\, \mathcal{T}^{J\mp}_{\frac{1}{2}\frac{3}{2}} + \tfrac{j_\gamma}{j_\gamma+2}\, \mathcal{T}^{J\mp}_{\frac{3}{2}\frac{3}{2}} \right] \\
f^{\overset{ME}{EM}}_{j_\gamma +} &= \frac{-1}{2\mathrm{k}(j_\gamma+1)^2} \left[\mathcal{T}^{J\mp}_{\frac{1}{2}\frac{1}{2}} + 2\tfrac{1}{\sqrt{j_\gamma(j_\gamma+2)}}\, \mathcal{T}^{J\mp}_{\frac{1}{2}\frac{3}{2}} - \mathcal{T}^{J\mp}_{\frac{3}{2}\frac{3}{2}} \right] \qquad (6.11) \\
f^{\overset{ME}{EM}}_{(j_\gamma+1)-} &= f^{\overset{EM}{ME}}_{j_\gamma +} \; . \qquad (6.12)
\end{aligned}$$

These Compton multipoles are identical to the ones given by Pfeil, Rollnik, and Stankowski [143].

---

6) This is only possible if we do not deal with isospin-decomposed photons (cf. Appendix F.1.2); otherwise one has to distinguish between isoscalar and isovector photons.

Chapter 7

Experimental Data and Fitting Strategy

For the determination of all parameters entering the model, the calculation has to be compared to as many experimental data points as possible. This comparison is performed via a χ^2 minimization procedure. The χ^2 (per datum) is defined by

$$\chi^2 = \frac{1}{N} \sum_{n=1}^{N} \left(\frac{x_c^n - x_e^n}{\Delta x_e^n} \right)^2 , \tag{7.1}$$

where N is the total number of data points, x_c^n (x_e^n) the calculated (experimental) value and Δx_e^n the experimental error bar. Unfortunately, for the various pion- and photon-induced reactions, the experimental data situation varies both in quality and quantity and the data points can not just be taken from the references for the inclusion in the fitting procedure. In the pion production reactions ($\gamma/\pi N \to \pi N$), abundant data covering a complete set of observables (see Appendix G) have been taken in the last decades, while for ωN production only very few data are available. Furthermore, not all data are of the same quality and in most data references, not even systematic errors are included in the given error bars, both leading to additional complications in the comparison. The consequence is, e.g., the necessity of introducing minimum (relative and/or absolute) errors for all data points in the fitting procedure, since otherwise the fit could attribute too high credit to a specific data set or get stuck at trying to describe only a few points with very small error bars.

Which data references are implemented in the fitting procedure and how the above is taken into account for a global comparison between the calculation of all channels and all available data points is discussed in this chapter.

7.1 Partial-Wave Analyses

7.1.1 Pion Production

The availability of partial waves or multipole[1)] amplitudes greatly simplifies the analysis of experimental data within a coupled-channel formalism. Not only is the experimental input more closely related to the resonance properties (and thereby to the parameters of the calculation), but also the number of fitted partial-wave/multipole datapoints is significantly smaller (than the count of data on the experimental observables) up to orders of magnitude and can account for issues associated with statistical and systematic errors, data rejection, and so on.

In the photon- and pion-induced pion production, enough experimental data have been taken, so that it is possible to reliably invert the relations between observables and partial waves listed in Appendix G. The necessary requirement is not only the availability of a complete set of observables, but also a sufficient coverage of these observables in the whole energy and angle region. Only in this case it is possible to define reasonably small energy bins, for each of which also higher partial waves with their real and imaginary parts can be extracted and dispersion relations can be checked. This procedure generates a so-called single-energy solution, which means that for each energy bin the partial waves are extracted independently. This has been done by the VPI group (cf. Section 3.1.1), who extracted single-energy solutions for $\pi N \to \pi N$ [277] and for $\gamma N \to \pi N$ [221]. There are also other partial-wave analyses available, however, they either consider only small energy regions or only extract energy-dependent solutions. The latter means that some energy-dependent function for the amplitudes is chosen, and the parameters of the functions are determined by comparison with experiment. The disadvantage of this method is that in the choice of the functions already some (model) assumptions enter and using the resulting solutions for comparison with our calculation could at worst amount to adjust one model to another model.

Rather than relying on a partial-wave analysis of some other group, the ideal procedure would be, however, to directly compare the present model to all available experimental data and thereby extract the partial waves directly from the model. As a consequence of the huge data base in the pion production reactions and the lack of higher spin ($\geq \frac{5}{2}$) resonances in our model (see also the beginning of Section 7.2 and in particular Fig. 7.1 below), this is not feasible at the present stage. Therefore, we use the partial-wave analyses of $\pi N \to \pi N$ [277] and $\gamma N \to \pi N$ [221] of the VPI group and compare the partial waves and multipoles up to total spin $J = \frac{3}{2}$. Thereby, we take advantage of the fact that in these partial-wave analyses the effects of the higher spin resonances do not influence the extraction of the parameters of the resonances considered in the calculation. In the following, our error treatment of these two partial-wave analyses is discussed.

[1)] The multipoles describe the photoproduction partial waves, where in addition to total spin and parity also the two helicity combinations of the nucleon and the photon are taken into accout; see also Section 6.2.1.

γ**N** $\rightarrow$ π**N**

Unfortunately, the single-energy solution for $\gamma N \rightarrow \pi N$ does not cover the complete energy region for all multipoles. Therefore, for those energies where the single-energy solution is not available, the gaps have been filled with the energy-dependent solution of the VPI group [221]. To account for possible model dependencies of the latter one, the data points of the two analyses are also treated differently:

- An absolute minimum error of 0.1 mfm (millifermi) for the single-energy solution and of 0.2 mfm for the energy-dependent solution is assumed.
- At the same time, a relative minimum error 5% is assumed for both solutions.

This treatment is applied if either the absolute or the relative minimum error exceeds the error given in [221][2)].

For the same reason of model dependence, we have refrained from using also the so-called speed extracted by the VPI group. The speed is given by the derivative of the amplitude with respect to energy and can hence only be calculated from an energy-dependent solution. To be as independent of other models as possible, the speed does consequently not enter as input for the fitting procedure.

To emphasize certain (resonant) structures in the multipole data (cf. Figs. 8.20, 8.21, and 8.22 in Section 8.4), however, we have refrained from the above treatment for some multipoles and directly used the experimental errors of the single-energy solution as given in [221]. In detail:

- in the real part of the E^p_{0+} multipole around the $S_{11}(1535)$ and $S_{11}(1650)$ (between 1.56 and 1.65 GeV),
- in the imaginary part of the E^p_{0+} multipole around the $S_{11}(1650)$ (between 1.62 and 1.69 GeV),
- in the imaginary part of the E^p_{2-} multipole around the $D_{13}(1520)$ (between 1.47 and 1.55 GeV),
- in the imaginary part of the M^p_{2-} multipole around the $D_{13}(1520)$ (between 1.47 and 1.55 GeV),
- in the imaginary part of the E^n_{2-} multipole around the $D_{13}(1520)$ (between 1.45 and 1.51 GeV),
- in the real and imaginary part of the $E^{\frac{3}{2}}_{1+}$ multipole around the $P_{33}(1232)$ (between 1.18 and 1.27 GeV),
- in the real and imaginary part of the $M^{\frac{3}{2}}_{1+}$ multipole around the $P_{33}(1232)$ (between 1.18 and 1.27 GeV),

---

[2)] Note, that in general, there are no experimental errors given for energy-dependent partial wave analyses.

- in the imaginary part of the $M_{1-}^{\frac{3}{2}}$ multipole between 1.15 and 1.21 GeV.

Here, the upper index of the multipole denotes the isospin of the amplitude (cf. Appendix F.1.2) and the lower one how the total spin is related to the pion angular momentum: $J = \ell_\pi \pm \frac{1}{2}$ (cf. Section 6.2.1).

Moreover, a glance at Figs. 8.20, 8.21, and 8.22 in Section 8.4.2 reveals, that the various multipoles behave at quite different scales. Especially the imaginary parts of certain multipoles are often well known to have extremely small values. A general error treatment as introduced above would effectively mean to ignore this knowledge. Thus, for the imaginary parts of the following multipoles we have refrained from the introduction of a general minimal error and have used the experimental errors of the single-energy solution as given in [221]:

- in the E_{2-}^p multipole above 1.7 GeV,
- in the M_{1+}^p multipole above 1.5 GeV,
- in the M_{1-}^p multipole above 1.8 GeV,
- in the M_{2-}^p multipole above 1.65 GeV,
- in the E_{1+}^n multipole above 1.59 GeV (here, we have also reduced the minimal error for the energy-dependent solution to 0.05 mfm),
- in the M_{1+}^n multipole above 1.48 GeV,
- in the M_{2-}^n multipole above 1.68 GeV,
- in the $E_{1+}^{\frac{3}{2}}$ multipole above 1.6 GeV.

The total number of data points included for this reaction amounts to 2772 (≡multipoles·isospin·(real+imaginary)·energy bins= $6 \cdot 3 \cdot 2 \cdot 77$).

$\pi\mathbf{N} \to \pi\mathbf{N}$

The VPI single-energy analysis for $\pi N \to \pi N$ covers almost the complete considered energy region from $\sqrt{s} = m_N + m_\pi$ up to 2 GeV, only in the low-energy tails of the D_{I3} waves, and the P_{13} and P_{31} waves it has not been possible to extract single-energy points. However, this is due to the fact that these partial waves are practically zero in these ranges, which can be deduced from the energy-dependent solution and also results from our calculation. Consequently, we have filled the corresponding bins with zeros.

The only remaining essential modification of the $\pi N \to \pi N$ partial-wave data is the introduction of minimum error values: As in most other pion-induced reactions, a minimum relative error of 3% is assumed for all partial waves and energies. The minimum absolute error is set to 0.015. The total number of data points included for this reaction amounts to 816 (≡total spin·total parity·isospin·(real+imaginary)·energy bins= $2 \cdot 2 \cdot 2 \cdot 2 \cdot 51$).

7.1.2 Two-Pion Production

Manley et al. [278] have performed a partial-wave analysis of pion-induced two-pion production on the nucleon taking into account the two-pion isobar states $\pi\Delta$, ρN, σN, and $\pi N^*(1440)$. Since in our model only one effective two-pion state (ζN) is included, it is not possible to compare the calculation to the partial waves extracted in [278] for the individual $2\pi N$ final states. To get a handle on the strength of the $2\pi N$ flux in the various partial waves, we use as experimental input the $\pi N \to 2\pi N$ partial-wave cross sections defined by

$$\sigma^{IJP} = \frac{4\pi}{\mathrm{k}^2} \sum_{\lambda,\lambda'} (J + \tfrac{1}{2}) \left| \mathcal{T}^{IJP}_{\lambda'\lambda} \right|^2 ,$$

which were also extracted in [278]. These cross sections correspond to the sum of all individual $2\pi N$ fluxes for one partial wave, thus representing the total $2\pi N$ inelasticity. As a consequence of modelling the $2\pi N$ state by a two-body state within our model, one cannot expect that all details of these data can be described within the model. In particular, the threshold and phase-space behavior is different from the individual three-body final states. As it will turn out (cf. Section 8.1.3), however, a qualitative description up to $J = \frac{3}{2}$ is possible, even with the assumption that the ζ meson only couples to resonances (cf. Section 3.2). Only in the low-energy region of the $J^P = \frac{3}{2}^-$ and the high-energy region of the $J^P = \frac{3}{2}^+$ waves, the final calculations show noticeable discrepancies with the Manley data (cf. Section 8.1.3). However, in the latter case the discrepancies might not be due to the $2\pi N$ simplification within the present model. The same discrepancy in the $IJ^P = \frac{1}{2}\frac{3}{2}^+$ $\pi N \to 2\pi N$ flux was also observed in the resonance parametrization of Manley and Saleski [113], see Section 3.1.1. The underlying problem can be analyzed in more detail by looking at the $\pi N \to \pi N$ inelastic partial-wave cross section:

$$\sigma^{in}_{IJ\pm} = \frac{4\pi}{\mathrm{k}^2} \left(J + \frac{1}{2} \right) \left(\mathrm{Im}\mathcal{T}^{IJ\pm}_{\frac{1}{2}\frac{1}{2}} - \left| \mathcal{T}^{IJ\pm}_{\frac{1}{2}\frac{1}{2}} \right|^2 \right) . \tag{7.2}$$

Comparing the inelastic with the $2\pi N$ partial-wave cross sections allows to figure out, in which partial waves inelastic contributions apart from $2\pi N$ are important and where there are inconsistencies between the πN and $2\pi N$ partial-wave analyses.

The $IJ^P = \frac{1}{2}\frac{3}{2}^+$ inelasticity grows up to 4 mb from 1.52 GeV up to the ωN threshold (cf. Figs. 8.5 and 8.6 in Section 8.1.3), while the $2\pi N$ partial-wave cross section extracted in [278] is still zero. At the same time the total cross sections from all other open inelastic channels (ηN, $K\Lambda$, and $K\Sigma$) add up to significantly less than 4 mb in this energy region. This indicates that either the extracted $2\pi N$ partial-wave cross section is not correct in the $\frac{1}{2}\frac{3}{2}^+$ partial wave or another inelastic channel (i.e., a $3\pi N$ channel as $\rho\Delta$) contributes significantly to this partial wave. Note that this effect is only observed in this partial wave and that above the ωN threshold the inelasticity and the $2\pi N$ data can again be described simultaneously in the $\frac{1}{2}\frac{3}{2}^+$ partial wave, see Section 8.1.3.

In the $\frac{3}{2}\frac{3}{2}^+$ partial wave, the $2\pi N$ data and πN inelasticity show the need for an additional inelastic channel with a flux contribution of about 1 mb in the energy region between 1.7 and 1.9 GeV. Since this lack of inelasticity cannot be explained by $K\Sigma$, the only remaining channel contributing to $I = \frac{3}{2}$ (cf. Fig. 8.5 in Section 8.1.3), this is also an indication that there could be a need for an additional $3\pi N$ state not included in the model. However, since apart from this small energy window in the $J^P = \frac{3}{2}^+$ partial waves a satisfying simultaneous description of all observables and partial waves can be achieved, the set of final states included in the present model can be well justified.

At the same time, such discrepancies have to be taken into account carefully when preparing the data base for the comparison between experiment and calculation. For example, in the nucleon resonance analysis of [33] and [183] the errors of the $\pi N \to 2\pi N$ data extracted by Manley et al. have been weighed with additional factors of 3 and 2, respectively. Here, we deviate from this procedure and perform more detailed modifications on the $\pi N \to 2\pi N$ partial-wave cross section data of Manley et al. [278] (see also Figs. 8.5 and 8.6 in Section 8.1.3):

- Due to the aforementioned inconsistencies in the $\frac{1}{2}\frac{3}{2}^+$ wave, we effectively neglect the $2\pi N$ data points in the energy region between 1.52 and 1.725 GeV by enlarging the error bars such that they increase smoothly from 0.06 mb for 1.52 GeV to 1.03 mb for 1.725 GeV.
- An error of 1 mb is added to the $\frac{1}{2}\frac{3}{2}^-$ partial-wave errors up to 1.46 GeV. See also the discussion of this partial wave in Sections 8.1.2 and 8.2.3. At the energies 1.7 and 1.79 GeV the errors have been doubled due to the contradiction with the πN inelasticity.
- For the same reason of contridicting the πN inelasticities an error of 1 mb is added to the $\frac{3}{2}\frac{3}{2}^-$ partial-wave errors up to 1.5 GeV and an error of 0.6 mb to the $\frac{3}{2}\frac{1}{2}^-$ partial-wave errors above 1.87 GeV.
- A minimum absolute error of 0.015 mb and a relative minimum error of 3% are assumed in all partial waves.

The total number of data points included for this reaction amounts to 168.

The same agreement as in the pion-induced $2\pi N$ production cannot be expected in the $2\pi N$ photoproduction reaction. It has been shown [78, 120, 121] that the $\gamma N \to 2\pi N$ reactions require strong background contributions from, e.g, ρ contact interactions as given in Eq. (3.8), which can only be included in the present model by the introduction of separate $2\pi N$ final states. Furthermore, there is no partial-wave decomposition of this reaction as the one by Manley et al. for $\pi N \to 2\pi N$ [278]. As pointed out above, in Manley's partial-wave analysis the total $2\pi N$ partial-wave flux is extracted, which is the only way for comparing our ζN production with experiment. For example, with the isovector ζ meson it is impossible to generate a $\gamma p \to 2\pi^0 p$ cross section, which can, e.g., result from the decay of a $\pi\Delta$ intermediate state. Therefore, the $\gamma N \to 2\pi N$ reaction is calculated in the model and included in the rescattering summation (cf. Appendix F.2.2), but not compared to experimental data (see, however, Section 8.4.7). The inclusion of the $2\pi N$ photoproduction data in the fitting procedure will only become reasonable upon the introduction of physical $2\pi N$ final states as ρN, $\pi\Delta$, etc., see Chapter 3. Only then it would also be possible to find agreement between the model calculation and measurements on photo-absorption on the nucleon, see Section 8.4.7.

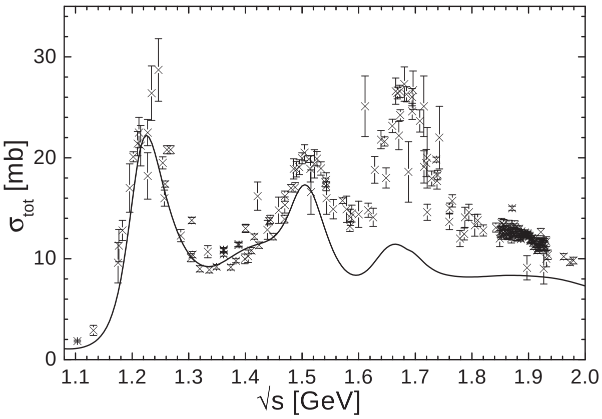

Figure 7.1: Comparison of the total $\pi^- p \to \pi^- p$ cross section of calculation C-p-π+ (see Chapter 8) with experimental data [105].

7.2 Direct Comparison with Observables

As discussed in the previous Section 7.1, due to the neglect of higher spin ($\geq \frac{5}{2}$) resonances in the potential of the model, a problem arises in the comparison with experimental observables. It is well known [67], that there are at least three spin-$\frac{5}{2}$ resonances with masses below 2 GeV ($D_{15}(1675)$, $F_{15}(1680)$, and $F_{35}(1905)$), that couple strongly to πN and γN. As can be seen from Fig. 7.1, our calculated total cross section for $\pi^- p \to \pi^- p$ starts deviating from the experimental data above the $D_{13}(1520)$ resonance, where the spin-$\frac{5}{2}$ resonances start to become important. Note, that the hump around 1.66 GeV is caused by the $S_{11}(1650)$ resonance. Furthermore, the neglect of these higher-spin contributions can lead to angle-dependent structures which cannot be explained within the present model. The consequence is that the fitting procedure tries to compensate the lack of these contributions by other effects, thereby shifting weight in the wrong direction.

On the other side, only in the pion-production reactions the data base is large enough for the extraction of single-energy partial-wave solutions. For some other channels, as e.g. $\pi N \to K\Lambda$ (cf. [165] and references therein) or $\pi N \to K\Sigma$ [22, 37], there were also attempts to perform energy-dependent partial-wave analyses[3)]. But since these analyses are inconsistent with each other and in order to avoid the influence of the model dependencies of the extracted partial waves on our results (see discussion in Section 7.1 above), we use cross sections and polarization observables as experimental input for the ηN, $K\Lambda$, $K\Sigma$, and ωN reactions. In this way, one can also extract information, in which reaction and energy regime it is not possible to explain the experimental observables within our model and higher-spin resonances might be important.

To account at least correctly for the angular structure of all contributions entering our potential, in particular the t- and u-channel diagram contributions, the partial-wave de-

---

[3)] For $\pi N \to K\Sigma$, there is also a single-energy partial-wave analysis [106]. However, the energy bins are rather large, no errors are given, and the two presented solutions are contradictory; hence this analysis cannot be used in the present calculation.

composition is performed up to a total spin of $J_{max} = \frac{27}{2}$[4]. The necessity of including that many partial waves only becomes evident in reactions with large spin-0 exchange contributions as $\gamma N \to \omega N$, see Section 8.4.6.

In the following sections, the implemented data base for the ηN, $K\Lambda$, $K\Sigma$, ωN reactions, and Compton scattering is presented in detail. For almost all reactions, the total cross sections that were taken before 1988 are also summarized in [105].

7.2.1 $\gamma N \to \gamma N$

The differential cross sections of various measurements [204, 205, 207, 208, 209, 210, 211, 212, 213, 214, 216, 218, 219, 220] are included, where the most recent ones [207, 208, 211] have not been considered in [52, 53]. Furthermore, the beam-polarization data of [203, 206, 207] are implemented. The recoil-proton polarization data of [215, 217] are not used for fitting because of their large error bars.

Looking at the photon helicity couplings given in [67], it is certain, that for higher energies contributions from the spin-$\frac{5}{2}$ resonances $D_{15}(1675)$ and $F_{15}(1680)$ will be important. Therefore, Compton scattering is only compared to experimental data up to a maximum energy of 1.6 GeV. Only in that energy region one can be sure, that effects of these resonances are negligible and all important contributions are contained in the potential.

To account for the fact that even the most recent measurements [207] and [208] tend to be inconsistent with each other, all data on Compton scattering are treated such that a minimum absolute error of 2 nb and a relative minimum error of 10% is assumed.

The total number of data points included for this reaction amounts to 538.

7.2.2 $\gamma N \to \eta N$

In the threshold region up to 1.54 GeV the precise Mainz differential cross section data of Krusche et al. [237] are used, for the higher energies the data of Refs. [222, 224, 225, 227, 228, 240] are implemented. The differential and total cross sections of [229, 231, 232, 235, 236, 238, 239, 241] are not used since there are more precise measurements for the same kinematics available. All the published cross section data above concentrate almost exclusively on the energy region below 1.7 GeV. Only recently, the CLAS Collaboration [230] has also accessed the energy region above 1.7 GeV. Therefore, the preliminary CLAS data are important to get a handle on the high-energy region of η photoproduction and are consequently included.

For the various polarization observables, we use the following data:

- recoil polarization: [233, 236],
- beam polarization: [222, 223, 241],

---

[4] Note that [51, 52, 53] performed the partial-wave decomposition only up to $J_{max} = \frac{11}{2}$.

- target polarization: [226].

Furthermore, the differential neutron-proton ratio $\mathrm{d}\sigma_n/\mathrm{d}\sigma_p$ of [234] measured on deuterium also enters the fitting procedure.

All data on η photoproduction are treated such that a minimum absolute error of 0.02 μb and a relative minimum error of 5% is assumed. To account for the high quality threshold data of Krusche et al. [237], the error bars of these data points remain unchanged.

The total number of data points included for this reaction amounts to 533.

7.2.3 $\gamma N \to K\Lambda$

In the calculation the differential and total cross sections of [242, 243, 245, 247, 249, 250, 251, 253, 255, 257] and the Λ-polarization measurements of [250, 252, 253, 254, 256, 257] are included. The older SAPHIR data of Bockhorst et al. [244] are not included, since they have been reanalyzed in [257].

A thorough examination of the early $\gamma p \to K^+\Lambda$ photoproduction data taken from the late 1950s until the early 1970s [242, 243, 245, 247, 248, 249, 250, 251, 253, 255] was pursued by Adelseck and Saghai [1]. They found internal and external inconsistencies among these data and here we follow their suggestion to account for systematic errors and increase the errors of some measurements. Furthermore, they deduced internal inconsistencies – and also discrepancies with the other measurements – of the Orsay differential cross section data [246] and consequently excluded this data set. This is also done here.

In addition to the suggestions by [1], all data points on $K\Lambda$ photoproduction are treated such that a minimum absolute error of 0.02 μb and a relative minimum error of 5% is assumed.

The total number of data points included for this reaction amounts to 226.

7.2.4 $\gamma N \to K\Sigma$

For this reaction, experimental data are available on three different charge reactions:

- $\gamma p \to K^+\Sigma^0$:
  In this reaction, the most data points are included: The differential and total cross sections of [258, 260, 261, 263, 262, 265, 266, 267] and the Σ^0-polarization measurement of [267] are included.

- $\gamma p \to K^0\Sigma^+$:
  In this reaction, basically only the recent SAPHIR measurement [264] has extracted data and hence their differential and total cross sections and Σ^+-polarization data are included. In addition, one total cross section data point of [261] is taken into account.

- $\gamma n \to K^+\Sigma^-$:
  The first reference of [258] has been a measurement on deuterium and two data points on $K^+\Sigma^-$ production have been extracted. Unfortunately, the error bars are rather large and therefore these points are not included in the calculation, but displayed for comparison in Section 8.4.5.

Since Adelseck and Saghai [1] rejected the Orsay data [246] in $K\Lambda$ photoproduction due to inconsistencies (see above), the $K\Sigma$ measurement of the same group is neither included in the fitting procedure. Similarly, the older SAPHIR data of Bockhorst et al. [259] are not taken into account, since they have been reanalyzed in [267].

For all data points on $K\Sigma$ photoproduction a minimum absolute error of 0.02 μb and a minimum relative error of 5% is assumed as in the $K\Lambda$ case. The number of data points included for $\gamma p \to K^+\Sigma^0$ amounts to 157 and for $\gamma p \to K^0\Sigma^+$ to 28, leading to a total of 185 $\gamma N \to K\Sigma$ data points.

7.2.5 $\gamma N \to \omega N$

For this reaction, only the cross section measurements of the ABBHHM Collaboration [271] and of Crouch et al. [270] are published up to now. There have been several Ph.D. theses of the SAPHIR Collaboration [272, 274, 276], but no publication yet besides a NStar contribution [273]. Also, the data taken at JLAB by the CLAS Collaboration have not yet been published but only presented at conferences [275]. Using only the published data, even in combination with the pion-induced data, it is difficult to extract the ωN couplings reliably. Thus, in addition to the ABBHHM data also the preliminary data of the SAPHIR Collaboration [269] are included in the fitting procedure, supplemented by those differential cross section data of [273], where no other data are available, i.e. at 1.898 GeV. There are conference contributions for beam-polarization measurements of ωN photoproduction of the GRAAL Collaboration [268], but since these data are still very preliminary, they are not included in the fitting procedure.

For the error treatment, we adopted the procedure of ηN photoproduction, i.e. a minimum absolute error of 0.02 μb and a relative minimum error of 5% is assumed. The total number of data points included for this reaction amounts to 182.

7.2.6 $\pi N \to \eta N$

For the adjustment procedure, besides the total and differential cross section data [280, 281, 283, 284, 285, 287] also used in [51, 52], the data of [282, 286] have been added. In view of their resonance model analysis of $\pi N \to \pi N$ and $\pi N \to \eta N$ (see Section 3.1.1), Batinić et al. [10, 29] have evaluated the data of [280, 281, 283, 284, 285, 287] concerning consistency among each other and possible systematic error sources. We follow the suggestion of Batinić et al. and perform the following modifications on the data set:

- A systematic error of 10% (at least 0.01 mb) is added to all data because the given errors are usually only of statistical nature.

- Compared to the other references, the data of Brown et al. [280] are systematically too low, which is due to an error in the beam momentum calibration. Batinić et al. have deduced, that no smooth parametrization of resonance contributions is able to describe these data. This makes the data at lower energies (1.511, 1.542, and 1.571 GeV) unusable. At higher energies, it is safe to just shift the beam momentum downwards by 4%.

- The data taken at the energy of 1.507 GeV by Richards et al. [287] tend to be too low compared to the "world trend". Therefore, an additional systematic error of 0.04 mb is added to the data from this reference. For similar reasons, a systematic error of 0.02 mb is added to the data from Debenham et al. [283].

- In total, a minimum absolute error of 0.015 mb and minimum relative error of 6% is assumed for all data points.

The few available experimental data on the target polarization by Baker et al. [279] are not implemented since in this experiment the same apparatus as in Brown et al. [280] has been used and the cross sections of the latter experiment entered the analysis for normalization. For comparison, these data are shown in Section 8.1.4.

The total number of data points included for this reaction amounts to 321.

7.2.7 $\pi N \to K\Lambda$

In addition to the data on differential and total cross sections [288, 295], which have been used in Refs. [51, 52], four more references are included [290, 292, 293, 296]. Furthermore, although the differential cross sections of Knasel et al. [294] have large error bars, these points are used where no other data are available, i.e. at the energies 1.687, 1.701, and 1.743 GeV. To reduce the statistical uncertainty of the Knasel data points the angle intervals have been rebinned by combining always two neighboring intervals.

The Λ-polarization measurements of Refs. [279, 291, 295] are also included, however, due to the large errors these values do not have a large effect on the extracted parameters. Even worse is the situation for the spin-rotation (see Appendix G) measurement of Bell et al. [289], which is consequently not used.

For the general treatment of the errors of the $\pi N \to K\Lambda$ data base, we follow Refs. [51, 52]: A minimum absolute error of 0.015 mb and a relative minimum error of 3% are assumed for all data points.

The total number of data points included for this reaction amounts to 392.

7.2.8 $\pi N \to K\Sigma$

For this reaction, experimental data are available on three different charge reactions:

- $\pi^+ p \to K^+\Sigma^+$:
  The differential and total cross sections of [298, 301, 302, 309] and the Σ^+-polarization measurements of [299, 301, 307, 309] are taken into account.

- $\pi^- p \to K^0\Sigma^0$:
  The differential and total cross sections of [297, 300, 303, 308] and the Σ^0-polarization measurement of [308] are included in the fitting procedure. The differential cross section data of [310] are not used because of their large error bars.

- $\pi^- p \to K^+\Sigma^-$:
  For this reaction, only differential and total cross sections [292, 304, 305, 293] are available and thus considered in the fit.

The treatment of the errors of the $\pi N \to K\Sigma$ data base is performed in analogy to $\pi N \to K\Lambda$, i.e. a minimum absolute error of 0.015 mb and a relative minimum error of 3% are assumed for all data points.

The number of data points included for $\pi^+ p \to K^+\Sigma^+$ amounts to 270, for $\pi^- p \to K^0\Sigma^0$ to 223, and for $\pi^- p \to K^+\Sigma^-$ to 90, leading to a total of 583 $\pi N \to K\Sigma$ data points.

7.2.9 $\pi N \to \omega N$

In the 70's a series of experiments [311, 314, 313] has been performed to measure the $\pi^- p \to \omega n$ cross section just above threshold. As pointed out in Chapter 3, prior to the present calculation these data have resisted a consistent theoretical description, mainly caused by too large Born contributions [97]. As a consequence these diagrams have been either neglected (see [145] and the second reference in [109]) or suppressed by very soft formfactors [179]. These findings have motivated a discussion in the literature about the experimentalists' way to extract the two-body cross section [73] and readjustments of the published $\pi^- p \to \omega n$ cross section data have been performed [75, 163, 179].

The cause of the discussion is the experimentalists' unusual method to cover the full range of the ω spectral function. An integration over at least one kinematical variable is necessary to make sure that all pion triples with invariant masses around m_ω are taken into account, so that the ω spectral function with a width of 8 Mev is well covered. Instead of fixing the incoming pion momentum and integrating out the invariant mass of the pion triples directly, the authors of [311, 313, 314] fixed the outgoing neutron laboratory momentum and angle and have performed an integration over the incoming pion momentum.

Led by the observation that the cross sections of [311, 313, 314] result in a hard-to-understand energy dependence of the transition matrix element the authors of [73] have claimed that due to the experimental method just described the count rates have covered only a fraction of the ω spectral function. As a consequence, the authors of [73, 163, 179] have advocated that the two-body total cross sections given in [313, 105] should be modified. Imposing this modification on the threshold cross section, in [73] a practically constant transition matrix element up to 1.74 GeV corresponding to an S_{11} $(IJ^P = \frac{1}{2}\frac{1}{2}^-)$

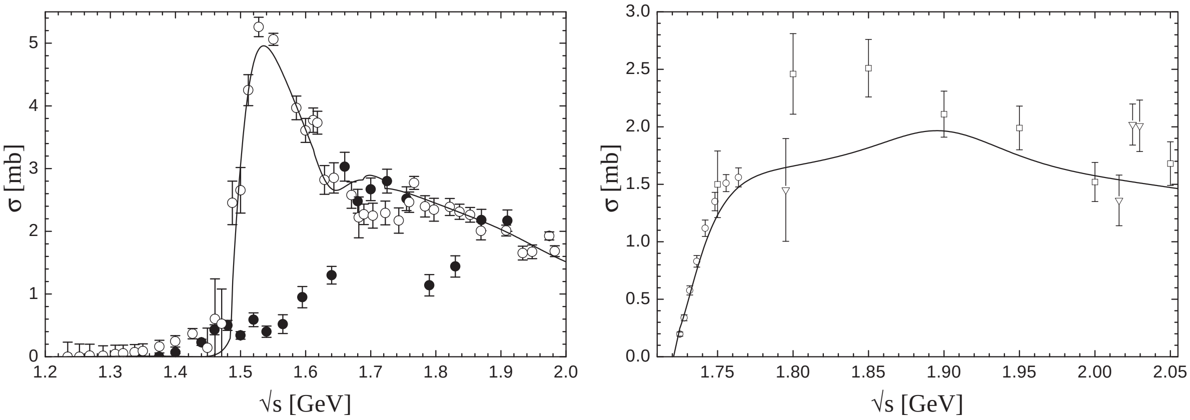

Figure 7.2: *Left:* S_{11} inelastic partial wave cross section of $\pi N \to \pi N$ as deduced from SM00 [277] ○ and $\pi N \to 2\pi N$ partial wave cross section as deduced by [278] ●. *Right:* $\pi N \to \omega N$ total cross section. Data are from ○: [313], ▽: [105], □: [312]. In both panels, the solid curve gives the result of C-p-γ+, see Chapter 8.

or D_{13} $(IJ^P = \frac{1}{2}\frac{3}{2}^-)$ [74] (since the pion momentum is almost constant in this region) wave production mechanism has been deduced.

This modification, however, immediately raises another problem. Taking into account this "spectral function correction" increases the ωN cross section for $1.72 \leq \sqrt{s} \leq 1.74$ up to $\sigma \geq 3$ mb, which is in contradiction to the inelasticity deduced from $\pi N \to \pi N$ partial wave analyses (e.g. SM00 [277]). As can be seen in Fig. 7.2 the $\pi N \to \pi N$ inelasticity in the S_{11} partial wave is already saturated by $\pi N \to 2\pi N$ in this energy region, i.e. an additional ωN contribution of $\sigma^{S_{11}} \geq 3$ mb would lead to a gross overestimate of the inelasticity:

$$\begin{aligned} \sigma^{S_{11}}_{in} &\geq \sigma^{S_{11}}_{2\pi N} + \sigma^{S_{11}}_{\omega N} \\ &\geq 2.5\ \text{mb} + 3\ \text{mb} \gg 2.4\ \text{mb} \approx \sigma^{S_{11}}_{in}(\text{SM00})\ . \end{aligned} \tag{7.3}$$

The same argument holds for the D_{13} wave (see Figs. 8.5 and 8.6 in Section 8.1.3).

Because of this inconsistency of the modified cross sections with existing inelasticities and because of the importance of the $\pi N \to \omega N$ cross section for both unitary models analyzing reactions on the nucleon in the c.m. energy range $1.7 \leq \sqrt{s} \leq 2.0$ GeV as the present one and in-medium models of vector mesons (see [98, 145] and also the last reference in [109]) we reanalyze the extraction method used in Refs. [311, 313, 314] by presenting in the following a complete derivation (given in parts in [311]) of the relation between the experimental count rates and the extracted two-body cross section for $\pi N \to \omega N$.

Count Rates and Two-Body Cross Sections

The experimental count rates are given by (B3) (we label all equations to be found in [311] with the letter B and those in [73] by the letter H):

$$\bar{N} = N_H \int\limits_{\Delta\Omega_L} \int\limits_{\Delta \mathrm{p}'_L} \frac{\mathrm{d}^3\sigma}{\mathrm{d}\Omega_L \mathrm{dp}'_L} \mathrm{d}\Omega_L \mathrm{dp}'_L \;, \tag{7.4}$$

where the cross section σ describes the process $\pi^- p \to n\pi^+\pi^-\pi^0$. All variables are taken in the c.m. system, unless they are denoted by the label L (laboratory frame). p (k) and p' (q) denote the incoming proton and outgoing neutron (incoming π and outgoing ω) four momenta. Absolute values of three momenta are denoted by upright letters, s and t are the usual Mandelstam variables. Ω_L is the neutron laboratory solid angle and N_H the number of target particles per unit area. The integral ranges in (7.4) refer to the binning of the count rates, i.e. they are the integrals to be performed for averaging over the experimental resolution intervals $\Omega_L \pm \Delta\Omega_L$ and $\mathrm{p}'_L \pm \Delta \mathrm{p}'_L$ and are not related to an integration over the ω spectral function. This will become clearer below (cf. Eq. (7.21)). The kinematics of the reaction are extracted from the center values of these intervals. Using

$$\begin{aligned} t = (p_L - p'_L)^2 &= m_p^2 + m_n^2 - 2m_p E_{nL} \\ &= m_p^2 + m_n^2 - 2m_p\sqrt{m_n^2 + {\mathrm{p}'_L}^2} \end{aligned} \tag{7.5}$$

and

$$\begin{aligned} (q_L - p_L)^2 &= (k_L - p'_L)^2 \;, \quad E_{\omega L} = E_{\pi L} + m_p - E_{nL} \\ \Longrightarrow \; q^2 &= m_\pi^2 + m_n^2 + m_p^2 + 2(m_p E_{\pi L} - m_p E_{nL} - E_{\pi L}E_{nL} + \mathrm{k}_L \mathrm{p}'_L x_L) \end{aligned} \tag{7.6}$$

($x_L = \cos\vartheta_L$) one finds

$$\bar{N} = \frac{N_H}{2\pi} \int\limits_{\Delta\Omega_L} \int\limits_{\Delta \mathrm{p}'_L} \frac{\mathrm{d}^2\sigma}{\mathrm{d}t\mathrm{d}\sqrt{q^2}} J_P \mathrm{d}\Omega_L \mathrm{dp}'_L \;, \tag{7.7}$$

assuming the cross section is independent of the neutron azimutal angle φ. The Jacobian J_P is given by

$$J_P = \left| \begin{array}{cc} \mathrm{d}\sqrt{q^2}/\mathrm{dp}'_L & \mathrm{d}\sqrt{q^2}/\mathrm{d}x_L \\ \mathrm{d}t/\mathrm{dp}'_L & \mathrm{d}t/\mathrm{d}x_L \end{array} \right| = \frac{2m_p \mathrm{k}_L {\mathrm{p}'_L}^2}{\sqrt{q^2}E_{nL}} \;, \tag{7.8}$$

because $\mathrm{d}t/\mathrm{d}x_L = 0$. Since in the actual experiment the time of flight τ_L of the neutron over a distance d,

$$\tau_L = \frac{1}{\beta_L}\frac{d}{c} \tag{7.9}$$

with the velocity $\beta_L = \mathrm{p}'_L/E_{nL}$, is measured – not its three-momentum –, the count rate is reexpressed in terms of the time of flight:

$$\bar{N} = \frac{N_H}{2\pi} \int\limits_{\Delta\Omega_L} \int\limits_{\Delta\tau_L} \frac{\mathrm{d}^2\sigma}{\mathrm{d}t\mathrm{d}\sqrt{q^2}} J_\tau \mathrm{d}\Omega_L \mathrm{d}\tau_L \;, \tag{7.10}$$

with

$$J_\tau = J_P \frac{\mathrm{dp}'_L}{\mathrm{d}\tau_L} \ . \tag{7.11}$$

The factor linking the Jacobians is

$$\frac{\mathrm{dp}'_L}{\mathrm{d}\tau_L} = \frac{\mathrm{dp}'_L}{\mathrm{d}\beta_L}\frac{\mathrm{d}\beta_L}{\mathrm{d}\tau_L} = \frac{{\mathrm{p}'_L}^2 E_{nL}}{m_n^2}\frac{c}{d} \quad \text{because of} \quad \frac{\mathrm{d}\beta_L}{\mathrm{dp}'_L} = \frac{m_n^2}{E_{nL}^3} \ . \tag{7.12}$$

We now relate this count rate to the two-body cross section [82]

$$\frac{\mathrm{d}\sigma^{2b}}{\mathrm{d}t} = \frac{1}{64\pi s \mathrm{k}^2}\frac{1}{2}\sum_{\lambda_p,\lambda_n,\lambda_\omega} |\mathcal{M}(s,t)|^2 \tag{7.13}$$

of $\pi^- p \longrightarrow \omega n$, assuming a stable ω. In order to do so, we deviate from the derivation in [311] and start with the general cross section formula for $\pi N \longrightarrow 3+4+5+\ldots+l$ in the c.m. system [82]:

$$d\sigma \;=\; \frac{1}{4\mathrm{k}\sqrt{s}}\frac{1}{2}\sum |\tilde{\mathcal{M}}|^2 (2\pi)^4 \prod_{j=3}^{l} \frac{\mathrm{d}^3 k'_j}{(2\pi)^3 2E'_j}\delta^4(p+k-\textstyle\sum_{j=3}^{l} k'_j) \ , \tag{7.14}$$

where the sum stands for summing over initial and final spins. Here (for simplicity, we assume that the ω only decays into 3 pions: $\pi^- p \longrightarrow n\omega \longrightarrow n\pi^+\pi^-\pi^0$), the matrix element reads:

$$\tilde{\mathcal{M}} = \mathcal{M}^{\mu}_{\pi^- p\to\omega n} D^{\omega}_{\mu\nu}(q^2)\mathcal{H}^{\nu}_{\omega\to 3\pi} \tag{7.15}$$

with $D^{\omega}_{\mu\nu}(q^2) = \sum_{\lambda_\omega} \varepsilon^\dagger_\mu(\lambda_\omega)\varepsilon_\nu(\lambda_\omega)\Delta_\omega(q^2)$ and $\Delta_\omega(q^2) = (q^2 - m_\omega^2 + i\sqrt{q^2}\Gamma_{\omega\to 3\pi})^{-1}$. Thus, in $|\tilde{\mathcal{M}}|^2$ a sum over λ_ω and λ'_ω appears. However, since the ω decay amplitude $\varepsilon_{\lambda_\omega}\cdot\mathcal{H}_{\omega\to 3\pi}$ can be decomposed into spherical harmonics $Y_{1\lambda_\omega}$ and the outgoing pion angles are integrated out, there are only contributions for $\lambda_\omega = \lambda'_\omega$. To introduce the ω spectral function $\rho_\omega(q^2)$ in (7.14), we note that we can evaluate the decay $\varepsilon_{\lambda_\omega}\cdot\mathcal{H}_{\omega\to 3\pi}$ in the ω rest frame, which is hence independent of the polarization λ_ω. Then the width of the ω is given by

$$\Gamma_{\omega\to 3\pi}(q^2) \;=\; \frac{1}{2\sqrt{q^2}}\int \prod_{j=4}^{6} \frac{\mathrm{d}^3 k'_j}{(2\pi)^3 2E'_j} \left|\varepsilon^{\mu}_{\lambda_\omega}\cdot\mathcal{H}_\mu\right|^2 (2\pi)^4 \delta^4(q - \textstyle\sum_{j=4}^{6} k'_j), \tag{7.16}$$

valid for any λ_ω, and related to the ω spectral function in the following way:

$$\begin{aligned}
\rho_\omega(q^2) &= -\frac{1}{\pi}\mathrm{Im}\Delta_\omega(q^2) \\
&= \frac{1}{\pi}\left|\Delta_\omega(q^2)\right|^2 \sqrt{q^2}\,\Gamma_\omega(q^2) \\
&= \frac{1}{\pi}\left|\Delta_\omega(q^2)\right|^2 \frac{1}{2}\int \prod_{j=4}^{6} \frac{\mathrm{d}^3 k'_j}{(2\pi)^3 2E'_j} |\varepsilon^{\mu}_{\lambda_\omega}\cdot\mathcal{H}_\mu|^2 (2\pi)^4 \delta^4(q - \textstyle\sum_{j=3}^{6} k'_j) \ .
\end{aligned}$$

Now, we can rewrite the cross section of Eq. (7.14) by introducing $1 = \int \mathrm{d}^4 q \delta^4(q - \sum_{j=3}^{6} k'_j)$ and using the spectral function:

$$
\begin{aligned}
\mathrm{d}^2\sigma &= \frac{1}{4\mathrm{k}\sqrt{s}} \frac{1}{2} \sum_{\lambda_p,\lambda_n,\lambda_\omega} \int \left|\mathcal{M}\cdot\varepsilon_{\lambda_\omega}\right|^2 (2\pi)^4 \delta^4(p+k-p'-q) \frac{\mathrm{d}^3 p'}{(2\pi)^3 2E_n} \frac{2\pi}{(2\pi)^4} \rho_\omega(q^2) \mathrm{d}^4 q \\
&= \frac{1}{4\mathrm{k}\sqrt{s}} \frac{1}{(2\pi)^2} \frac{1}{2} \sum_{\lambda_p,\lambda_n,\lambda_\omega} \int \left|\mathcal{M}\cdot\varepsilon_{\lambda_\omega}\right|^2 \frac{\mathrm{d}^3 p'}{2E_n} \rho_\omega(q^2) \bigg|_{q=p+k-p'} \\
&= \frac{1}{8\mathrm{k}\sqrt{s}} \frac{1}{2\pi} \frac{1}{2} \sum_{\lambda_p,\lambda_n,\lambda_\omega} \left|\mathcal{M}\cdot\varepsilon_{\lambda_\omega}\right|^2 \frac{\mathrm{p}'^2 \mathrm{d}\mathrm{p}'}{E_n} \mathrm{d}x \rho_\omega(q^2) \bigg|_{q=p+k-p'} \qquad (7.17) \\
&= \frac{\mathrm{p}'}{32\pi\sqrt{s}\mathrm{k}^2} \frac{1}{2} \sum_{\lambda_p,\lambda_n,\lambda_\omega} \left|\mathcal{M}\cdot\varepsilon_{\lambda_\omega}\right|^2 \frac{\mathrm{d}\mathrm{p}'\mathrm{d}t}{E_n} \rho_\omega(q^2) \bigg|_{q=p+k-p'} \\
&\overset{(7.13)}{=} 2\sqrt{q^2} \frac{\mathrm{d}\sigma^{2b}}{\mathrm{d}t} \rho_\omega(q^2) \mathrm{d}t \mathrm{d}\sqrt{q^2} \bigg|_{q=p+k-p'} ,
\end{aligned}
$$

where we have used

$$
\begin{aligned}
t = (p-p')^2 &= m_p^2 + m_n^2 - 2(E_p E_n - \mathrm{k}\mathrm{p}' x) \qquad (7.18) \\
\Longrightarrow \left|\frac{\mathrm{d}t}{\mathrm{d}x}\right| &= 2\mathrm{k}\mathrm{p}' ,
\end{aligned}
$$

and

$$
\begin{aligned}
E_n &= \frac{s + m_n^2 - q^2}{2\sqrt{s}} \qquad (7.19) \\
\Longrightarrow \frac{\mathrm{d}\mathrm{p}'}{\mathrm{d}\sqrt{q^2}} &= \frac{\mathrm{d}\mathrm{p}'}{\mathrm{d}E_n} \frac{\mathrm{d}E_n}{\mathrm{d}\sqrt{q^2}} = \frac{\sqrt{q^2} E_n}{\mathrm{p}'\sqrt{s}} .
\end{aligned}
$$

Thus we have

$$
\frac{\mathrm{d}^2\sigma}{\mathrm{d}t\mathrm{d}\sqrt{q^2}} = 2\sqrt{q^2} \frac{\mathrm{d}\sigma^{2b}}{\mathrm{d}t} \rho_\omega(q^2) \bigg|_{q=p+k-p'}
$$

and finally for the experimental count rate

$$
\bar{N} = \frac{N_H}{2\pi} \int_{\Delta\Omega_L} \int_{\Delta\tau_L} 2\sqrt{q^2} \frac{\mathrm{d}\sigma^{2b}}{\mathrm{d}t} \rho_\omega(q^2) \bigg|_{q=p+k-p'} J_\tau \mathrm{d}\Omega_L \mathrm{d}\tau_L . \qquad (7.20)
$$

To eliminate the ω spectral function, the experimentalists [311, 314, 313] have performed an integration over the incoming pion three-momentum k_L by summing over all beam settings, which can be transformed into an integration over the ω four-momentum squared:

$$
N = \int \mathrm{d}\mathrm{k}_L \bar{N}
$$

$$
\begin{aligned}
&= \frac{N_H}{2\pi}\int \mathrm{dk}_L \int\limits_{\Delta\Omega_L}\int\limits_{\Delta\tau_L} 2\sqrt{q^2}\frac{\mathrm{d}\sigma^{2b}}{\mathrm{d}t}\rho_\omega(q^2) J_\tau \mathrm{d}\Omega_L \mathrm{d}\tau_L \\
&= \frac{N_H}{2\pi}\int\limits_{\Delta\Omega_L}\int\limits_{\Delta\tau_L} \frac{\mathrm{d}\sigma^{2b}}{\mathrm{d}t} J_k J_\tau \mathrm{d}\Omega_L \mathrm{d}\tau_L \ , \qquad (7.21)
\end{aligned}
$$

where we have used the normalization of the spectral function $\int \rho_\omega(q^2)\mathrm{d}q^2 = 1$ and the assumption that the matrix element in Eq. (7.13) only varies slightly around the peak of the ω spectral function5) for fixed t corresponding to fixed p'_L via Eq. (7.5)6). In the first line, due to four-momentum conservation, the ω momentum is restricted to $q = p + k - p'$. The Jacobian J_k is given by

$$
J_k \equiv \frac{\mathrm{dk}_L}{\mathrm{d}\sqrt{q^2}} \overset{(7.6)}{=} \frac{\sqrt{q^2}}{\frac{\mathrm{k}_L}{E_{\pi L}}(m_p - E_{nL}) + \mathrm{p}'_L x_L} \ . \qquad (7.22)
$$

In the derivation of Eq. (7.21) two more assumptions enter that are checked in the following:

- Sufficient coverage of the ω spectral function for all kinematics extracted, even at low p' values:
  The incoming pion lab-momentum range has been $\mathrm{k}_L \in [1.04, 1.265]$ GeV, which translates into a c.m. energy range of $\sqrt{s} \in [1.6938, 1.8133]$ GeV. Using $\mathrm{p}' \in [0.03, 0.21]$ GeV, this leads to the following ranges for the upper and lower limits in the q^2 integration: $q_+^2 \in [0.822^2, 0.869^2]$ GeV^2 and $q_-^2 \in [0.7^2, 0.753^2]$ GeV^2. Even in the worst case the integration extends over at least 7 half widths $\Gamma_\omega/2$ on either side of m_ω^2 and thus covers more than 92% of the spectral function.

- Constancy of the product of the Jacobians $J_k J_\tau$:
  By using Eqs. (7.5), (7.6), (7.18), and (7.19) one can easily show that the product

  $$
  J_k J_\tau = \frac{2 m_p \mathrm{k}_L {\mathrm{p}'_L}^4}{m_n^2 \left[\frac{\mathrm{k}_L}{E_{\pi L}}(m_p - E_{nL}) + \mathrm{p}'_L x_L\right]}\frac{c}{d}
  $$

  varies for fixed t by less than 2.5 percent in the interval $\sqrt{q^2} \in [m_\omega - 2\Gamma_\omega,\ m_\omega + 2\Gamma_\omega]$ for all kinematics considered in the experiment.

Since the countrate of Eq. (7.21) is identical to the one given between Eqs. (B9) and (B10) in [311], the method used in Refs. [311, 313, 314] and correspondingly their two-body cross sections are correct.

It is important to note that in the data analysis both p'_L **and** x_L are needed to fix the kinematics of the measured events. During the count rate corrections (flux normalization in dependence on k_L, background subtraction via missing mass spectra), for each k_L beam

---

5) The approximate constancy of the matrix element is the basic assumption for extracting the two-body cross section from **any** experiment dealing with decaying final state particles.

6) Remember that the integral range $\Delta\tau_L$ in Eq. (7.21) corresponds to the experimental resolution.

setting the measured p'_L and x_L translate into $\sqrt{q^2}$ (see (7.6)) and can also be Lorentz transformed into their c.m. values $\mathrm{p}' = \mathrm{p}'(E_{\pi L}, \mathrm{p}'_L, x_L)$ and $x = x(E_{\pi L}, \mathrm{p}'_L, x_L)$. The events can now be regrouped in p', $\sqrt{q^2}$, and x intervals. Then, after having performed the integration over all $\sqrt{q^2}$ as in (7.21), the translation of a given p' into $\sqrt{s}$ can only be done by assuming that the main contribution to the corrected count rates comes from around the peak of the omega spectral function $q^2 \sim m_\omega^2$.

The main assertion of Ref. [73], manifested in Eq. (H4), is that instead of (7.21) only a fraction of the cross section for the production of an unstable particle had been measured in [311, 313, 314]. This fraction is determined by translating the experimental p' binning intervals given in [313] into interval bounds for the integration over the ω spectral function. Equation (H4), which is used for the cross section corrections in [75, 163, 179], is identical to the third line of Eq. (7.17) under the assumption that p' is bound to the p' binning intervals. However, as pointed out above, in an experimental event $E_{\pi L}$, p'_L, and x_L are fixed and hence Eq. (7.20) has to be applied to the experimental count rate for a fixed pion momentum.

The experimental integration over the incoming pion momentum is introduced in Ref. [73] only in the subsequent discussion between Eqs. (H9) and (H10). In the paragraph following Eq. (H16) the authors of Ref. [73] argue that the range of this integral is narrowed due to the p' binning (as in (H4)). The ω mass is thus allowed to vary only in the interval given by the p' interval ranges for a fixed pion momentum. But as shown above, fixing p' only fixes the incoming pion momentum if one assumes a specific ω mass. Hence the pion momentum integration performed in the data analysis indeed translates into an ω mass integration only bounded by the pion momentum range and thus leads to Eq. (7.21). This relation between the neutron momentum p', the pion momentum k, and the ω mass were thus treated improperly in Ref. [73].

The second correction factor extracted in Ref. [73] due to the neutron momentum binning of $\Delta\mathrm{p}' = 10$ MeV is nothing but the result of averaging the third line of Eq. (7.17) over the neutron c.m. momentum: $(\Delta\mathrm{p}')^{-1} \int_{\mathrm{p}'-\Delta\mathrm{p}'}^{\mathrm{p}'+\Delta\mathrm{p}'} \tilde{\mathrm{p}}^2 d\tilde{\mathrm{p}} = \mathrm{p}'^2 + (\Delta\mathrm{p}')^2/12$ (cf. (H10)). This differs at most ("worst" case: $\mathrm{p}' = 30$ MeV) by 1 percent from p'^2 and is therefore negligible.

Furthermore, it is obvious from Fig. 7.3 that the differential ωN data from all three references [311, 313, 314][7] are completely in line with each other and also with Ref. [312][8]. The same holds true for the total cross sections of Ref. [313] in comparison with other experiments[9], see Fig. 7.2. There is, therefore, no reason to hypothesize – as in [75] – that the formalism developed in [311] could have been used incorrectly in [314] and [313].

In this context we stress one more point. Very close to threshold, the two-body cross section $\pi^- p \to \omega n$ extracted from experimental count rates could be influenced by the strong πN interaction for slow pions stemming from $\omega \to 3\pi$. However, this point has

---

[7] The total cross sections given in Refs. [311, 314] are actually angle-differential cross sections (mostly at forward and backward neutron c.m. angles) multiplied with 4π.

[8] The differential cross sections are extracted from the corrected cosine event distributions given in Ref. [312] with the help of their total cross sections.

[9] Note, that all other experiments measured $\pi^+ n \to \omega p$.

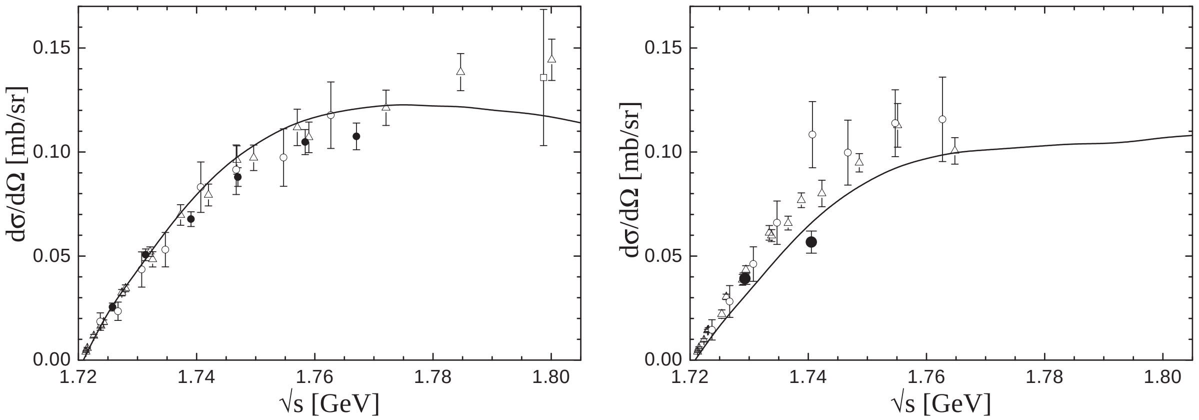

Figure 7.3: Differential cross section for *left:* backward and *right:* forward ω c.m. angles. The data points are from •: [311], △: [314], ○: [313], and □: [312]. The curve gives the result of the calculation C-p-γ+, see Chapter 8.

been checked in Ref. [314] by also looking at $\omega \to \pi^0\gamma$; they did not find any deviations between the two ways of extraction.

Summarizing, we have shown that the extraction method presented in [311] and also used in [314, 313] is indeed correct. There is no reason to doubt the correctness of the data presented in these references; they are in line with each other and also with other experimental data. The reanalysis of the ωN-production data in Ref. [73], on which the theoretical descriptions of Refs. [163, 179] are based, as well as the speculations in Ref. [75] thus lack any basis.

Consequently, we use the angle-differential cross sections of [311, 313, 314] and also of [312] (see footnote 8)) and the total cross sections of [105, 312, 313] as input for the fitting procedure. The total number of data points included for this reaction amounts to 113. As in the other pion-induced reactions, for all these data, a minimum absolute error of 0.015 mb and a relative minimum error of 3% have been assumed.

7.3 Data-Base Balance and Fitting Strategy

As pointed out in the introduction and in previous sections of this chapter, the experimental data situation is very different for the various reactions and also for the various energy regions, which makes a simultaneous fitting procedure involved. Just taking all available data points would lead to stressing those energies where the most data are available far more than the others, misbalancing the analysis of the complete energy region. Therefore, a strategy has to be implemented to balance the different energy regions and reactions. Consequently, the numbers for the implemented data points of the various reaction channels are not identical to the sum of data points as given in the references. Here, we bin the complete considered energy region ($m_N \leq \sqrt{s} \leq 2$ GeV) into 96 energy bins and allow for each angle-differential observable up to $10-15$ data points per energy bin. This still allows to stress – but not overstress – those energy bins where more data are

Total^a	$\gamma N \to \gamma N$	$\gamma N \to \pi N$	$\gamma N \to \eta N$	$\gamma N \to K\Lambda$	$\gamma N \to K\Sigma$	$\gamma N \to \omega N$
6829	538	2772	533	226	185	182
Total π	$\pi N \to \pi N$	$\pi N \to 2\pi N$	$\pi N \to \eta N$	$\pi N \to K\Lambda$	$\pi N \to K\Sigma$	$\pi N \to \omega N$
2393	816	168	321	392	583	113

Table 7.1: Number of data points used during the fitting procedure. ^{a}: This number includes all pion- and photon- induced data points.

available. The resulting situation of the data points included in the individual reactions is summarized again in Table 7.1.

However, even when using this binning and also taking into account that the covered energy regions can be quite different (e.g. $\gamma N \to \pi N$: $(m_N + m_\pi) \to 2.0$ GeV as compared to $\gamma N \to \omega N$: $1.72 \to 2.0$ GeV), the data base is still not well balanced. This leads to the necessity of additionally introducing different weights for some channels.

Since a special interest of the present calculation is on the ω production mechanism, the $\pi N \to \omega N$ data base has to be modified. In this channel there are only few data points (113) available and the data above 1.77 GeV have large error bars. Thus, the errors of the total cross sections of this reaction are reduced in the following way (cf. Fig. 7.2 above):

- For the three Karami total cross section data points [313] above 1.745 GeV the error is reduced to 0.03 mb.
- For the Danburg data [312] at 1.95 and 2.0 GeV, the total cross section error is reduced to 0.045 mb.

Fortunately, with the preliminary SAPHIR data [269], being of high quality and uniformly distributed over the energy range, a similar procedure is not necessary for ωN photoproduction.

In $K\Sigma$ photoproduction, one faces another weighing problem: For the reaction $\gamma p \to K^+\Sigma^0$ there are 157 data points included, while for $\gamma p \to K^0\Sigma^+$ only 28 with large error bars are considered. A direct fitting of these two reactions without modifying the statistical weights would effectively amount to neglecting the $K^0\Sigma^+$ reaction, in particular because the pion-induced $K\Sigma$ data are considered simultaneously. Therefore, we assign additional weight to the $K^0\Sigma^+$ reaction by reducing the errors of the total cross sections in the following way (cf. Fig. 8.29 in Section 8.4.5):

- For the energies below 1.76 GeV, the total cross section errors of the data from [261] and [264] is reduced to 0.05 μb.
- For the energies above 1.76 GeV, the total cross section errors of the SAPHIR data [264] is reduced to 0.07 μb.

Furthermore, additional remarks on the pion production reactions in a global fit, i.e. including all pion- and photon-induced data, are in order. Firstly, one has to take into account that the implemented data points of the partial-wave analyses represent a much larger amount of originally measured data points. This is especially important for $\pi N \to \pi N$, since we only include 8 partial waves ($J \leq \frac{3}{2}$) and thus 16 data points per energy bin (see Section 22). At the same time, there are 18 multipoles for $\gamma N \to \pi N$ and thus 36 data points per energy bin (see Section 21), with also smaller error bars and available for more energy bins. Including the data points for these two reactions ($\gamma N \to \pi N$: 2772, $\pi N \to \pi N$: 816) without any modification in a global fit would lead to a large overweighing of the photoproduction reaction. Therefore, we choose to reduce the $\gamma N \to \pi N$ statistical weight by a factor of 2 and enlarge the $\pi N \to \pi N$ weight by a factor of 3. Since the pion photoproduction data still dominates the total χ^2 value, the final quality of the description of this channel hardly changes ($\leq 5\%$) due to the weight reduction, while the elastic scattering is significantly better described. On the other side, the quality of the description of all other reactions remains practically unchanged. Since in the other reactions the situation between pion- and photon-induced data is rather well balanced, no additional weighing is needed (besides what is described above for $\pi N \to \omega N$ and $\gamma p \to K^0 \Sigma^+$).

A consequence of the implemented additional weights is that the final χ^2 value does not necessarily reflect the "real" χ^2 minimum, but only the one with the above reduced and enlarged statistical weights. For means of comparison, however, in the χ^2 results given in Chapter 8, the additional weights described in this Section 7.3 are taken out again and the only modifications entering the final χ^2 calculation are the error procedures described in the Sections 21 to 7.2.9 above.

7.4 Fitting Strategy

This section is supposed to provide a short overview of the strategy that has been applied to find the results presented in Chapter 8. Working out a strategy is not only important in view of the data-base situation but also in view of the number of parameters included, since the less parameters are allowed to vary simultaneously the easier a χ^2 minimum is found.

For all parameter sets extracted, the starting point is always a fitting of the pion-induced data alone ("hadronic fits"). The idea is to account for all unitary effects correctly and only after a reasonable splitting of the partial-wave flux contributions of the different channels is found, it is reasonable to further include the photoproduction data ("global fits").

In the hadronic fits, we start from the results of the preferred global fit SM95-pt-3 of [52, 53], which forms a reliable basis for the energy range up to 1.9 GeV. Since the most dominant flux contributions stem from πN and $2\pi N$, in a first step, only the πN, $2\pi N$ parameters, and masses of the resonances are allowed to vary until convergence is reached. Then the free parameter space is extended to include the next important contributions ηN and ωN. For the subsequent inclusion of the associated strangeness channels $K\Lambda$ and $K\Sigma$, one can take advantage of splitting all reaction channels into the two isospin channels[10]: First, all $K\Sigma$, πN, and $2\pi N$ parameters contributing to isospin $\frac{3}{2}$, i.e. the Δ resonance parameters and the $K^*\Sigma N$ and $K_0^*\Sigma N$ couplings are determined by fitting the $\pi N \to \pi N/2\pi N$ $I = \frac{3}{2}$ partial waves and the copious data on $\pi^+ p \to K^+\Sigma^+$, a pure $I = \frac{3}{2}$ reaction. When all these $I = \frac{3}{2}$ parameters are fixed, one switches over to the $I = \frac{1}{2}$ section keeping the $I = \frac{3}{2}$ parameters unchanged. There, first only the $K\Lambda$ and $K\Sigma$ $I = \frac{1}{2}$ parameters are varied, and afterwards all $I = \frac{1}{2}$ final state parameters are varied, i.e. the nucleon couplings to ηN, ωN, $K\Lambda$, and $K\Sigma$ and all isospin-$\frac{1}{2}$ resonance parameters. Finally, the hadronic fits are terminated by including all hadronic parameters, i.e. both, the parameters of the $I = \frac{1}{2}$ and $I = \frac{3}{2}$ channels.

The strategy for the global fits, i.e. when the photoproduction data are included, is similar to the hadronic fitting strategy with the exception, that the splitting into $I = \frac{1}{2}$ and $I = \frac{3}{2}$ is not possible anymore. This is due to the fact that experimentally, Compton scattering cannot be isospin decomposed and $\gamma p \to \gamma p$ contains $I = \frac{1}{2}$ and $I = \frac{3}{2}$ contributions (see Appendix F.1.2). Moreover, in $K\Sigma$ photoproduction not enough data have been taken yet to be able to perform an isospin decomposition as in pion photoproduction and both measured reactions $\gamma p \to K^+\Sigma^0$, $\gamma p \to K^0\Sigma^+$ are composed of isospin-$\frac{1}{2}$ and isospin-$\frac{3}{2}$ amplitudes. Therefore, the global fitting strategy is as follows. Starting from a final hadronic set, first only the photon couplings are varied. Thereby it turns out, that due to the comparison to 6 photoproduction channels simultaneously and the much more precise data implemented, it is not possible any more as in [52, 53], where only 4 photoproduction channels ($\gamma N \to \gamma N/\pi N/\eta N/K\Lambda$) have been compared to data, to already find a satisfactory description of the global data base when keeping the hadronic parameters fixed. Note, that, in the $\gamma N \to \eta N$ reaction, the data base used in [52, 53] has essentially ended at 1.7 GeV and Compton scattering has only been fitted up to 1.6 GeV. This means that only in the energy window from 1.49 to 1.7 GeV three photoproduction channels have been fitted simultaneously; above and below effectively only two photoproduction channels have had to be considered at the same time. In the present calculation, especially the fitting of the ω photoproduction channel turns out to be difficult by using the ω couplings determined by a comparison to only 113 $\pi N \to \omega N$ data points. A similar observation is made in η photoproduction due to the poor quality of the $\pi N \to \eta N$ data, see Section 7.2.6. In the channels with associated strangeness production, a problem arises due to the Born couplings. Since they only play a minor role in the hadronic reactions, but become much more important in photoproduction due to the gauging procedure prohibiting the introduction of a formfactor at the electromagnetic vertex (cf. Section 3.7.2), the comparably large $NK\Lambda$ and $NK\Sigma$ couplings extracted in the pion-induced reactions lead to a large overestimation of the photoproduction cross sections, especially in the threshold region. Consequently, the best fit with keeping the hadronic couplings fixed has only resulted in an overall χ^2 of about 15, with even much higher values (~ 50) in the ω photoproduction channel. Therefore, results of those fits are not presented here as has been done in [52, 53]. This also shows, that for a reliable extraction of resonance parameters, the pion-induced data base alone is not sufficient and the consideration of the photon-induced data is mandatory. After convergence has been achieved by varying only the photon couplings, the set of free parameters is extended to

---

[10] This is only possible because the u-channel contributions of the resonances to the other isospin channels do not vary largely during the fitting procedure.

also include the hadronic couplings to the four most important hadronic flux states: πN, $2\pi N$, ηN, and ωN. This, of course, also requires the inclusion of the pion-induced data in the comparison. Then, keeping all the γN, πN, $2\pi N$, ηN, and ωN parameters fixed, the $K\Lambda$ and $K\Sigma$ parameters are varied while comparing to the complete data base. Finally, all parameters[11)] are allowed to vary in the global fit.

The parameter ranges are initialized by the ranges given by the PDG [67] when available; the range for the spin-$\frac{3}{2}$ off-shell parameters a is chosen as $-2 \leq a \leq 2$. Only when a parameter approaches the boundary of the interval, the interval is moved. The fits are performed using the IMSL library routines ZXSSQ and ZXMWD [80], where the first one is based on a Levenberg-Marquardt and the second on a quasi-Newton algorithm (see, e.g., [130]). In general, during the fitting process we switch between the two IMSL routines to prevent the fitting from getting stuck at a local minimum due to the implemented routine. Furthermore, additional starting points are continously Monte-Carlo generated to avoid staying in a local minimum. The minimum found by the above strategy is accepted as the global minimum after convergence with a free parameter set is reached. Final cross-checks are performed by
1) reducing the free-parameter set by taking out those parameters, which change only slightly as e.g. the $P_{33}(1232)$ mass,
2) applying in addition a simulated-annealing minimization algorithm, which, however, has not given any improvement.
In view of the number of free parameters, however, it cannot be excluded that there exists a better global minimum; but in view of the smallness of the final χ^2 in comparison with other calculations and the good convergence reached in the fitting procedure, we do not expect that there is a much better ($> 5\%$) description possible within the presented K-matrix model.

[11)] At this stage, those parameters that turn out to hardly vary at all in the fits (e.g. the $P_{33}(1232)$ mass) are kept fixed to minimize the number of parameters that are varied simultaneously.

Chapter 8

Results

After having discussed all the ingredients of the model, the results of the fitting procedure are presented in this chapter. Section 8.1 concentrates on the pion-induced reactions, where the results from the fits to the pion-induced data (hadronic fits) are also compared to those from the fits to pion- and photon-induced data (global fits). The extracted hadronic background and resonance parameters are presented in Sections 8.2.1 and 8.2.3, followed by Section 8.4, where the results for the photon-induced reaction channels are discussed. The extracted electromagnetic properties of the resonances are discussed in Section 8.4.8.

We have started the fitting procedure with an extension of the preferred global fit parameter set SM-95-pt3 of Feuster and Mosel [52, 53]. The first step has been the inclusion of the $K\Sigma$ and ωN data in a fit to the pion-induced reaction data. In addition to the t-channel exchange processes included in [51, 52, 53], we have taken into account the exchange of the two scalar mesons $K_0^*(1430)$ and σ to improve the description of the associated strangeness production and pion-nucleon elastic scattering, respectively, as compared to [51, 52, 53]. Furthermore, this allows for more background contributions in the extended energy range up to $\sqrt{s} = 2$ GeV. The σ exchange is supposed to model the correlated isoscalar-scalar two-pion exchange in $\pi N \to \pi N$. Since the direct coupling of the scalar a_0 meson to $\pi\eta$ ($\mathcal{L} = -g_{a_0} m_{a_0} \pi\eta a_0$) was chosen in [51, 52, 53], this coupling has also been used for the K_0^* and the σ meson in our first calculation, thereby also accessing chiral symmetry breaking effects as in [62, 63], see Section 3.3.2. At the same time, in this first calculation we have tried to minimize the number of parameters and only varied a subset of all possible ωN coupling constants, i.e. in the fitting process we have allowed for two different couplings (g_1 and g_2) to ωN for those resonances, that lie at or above the ωN threshold ($P_{11}(1710)$, $P_{13}(1720)$, $P_{13}(1900)$, $D_{13}(1950)$[1]) and one coupling (g_1) for the sub-threshold resonance highest in mass: $S_{11}(1650)$.

Since it has turned out in this calculation, that especially in the ωN channel (and to some minor degree also in $K\Lambda$ and ηN production) large background contributions, manifested by large spin-$\frac{3}{2}$ off-shell parameters (cf. Eq. (3.19)), are needed, the subsequent calculations have been performed by also allowing for more contributions from sub-threshold

---

[1] The $D_{13}(1950)$ is denoted by $D_{13}(2080)$ by the PDG [67].

resonances — as, e.g., $S_{11}(1535) \to K\Lambda$ — and coupling possibilities[2]. Note, that in the coupled-channel model of Lutz et al. [109], the authors have also found large sub-threshold contributions to $\gamma N/\pi N \to \omega N$, in particular a contribution assigned to the $D_{13}(1520)$. Recently, Titov and Lee [180], Zhao [199], and also Oh et al. [132] have extracted important $D_{13}(1520)$ and $S_{11}(1535)$ contributions in $\gamma N \to \omega N$. Similarly, Post and Mosel [145] have extracted in their VMD analysis strong couplings from the subthreshold $S_{11}(1650)$ and $D_{13}(1520)$ resonances. Moreover, allowing for all coupling possibilities is the only way to fully compare to predictions from quark models as e.g. [151], and to model all different helicity combinations of the ωN production mechanism (see Eqs. (E.29) and (E.39)). It is important to note, that due to the coupled-channel calculation, the couplings to one specific final state are not only determined by the comparison to the experimental data of this channel, but via rescattering also strongly constrained by all other channels. Finally, upon the inclusion of the photoproduction data in the global fitting analysis, the extracted parameters can be further pinned down.

Not unexpected, the inclusion of the chiral symmetry breaking $\sigma\pi\pi$ coupling does not improve the description of πN elastic scattering significantly. Therefore, and to be in conformity with chiral symmetry, all subsequent fits have been performed with the chirally symmetric derivative $\sigma\pi\pi$ coupling (cf. Eq. (3.11)). The effects of the chiral symmetry breaking coupling in comparison with the chiral symmetric one are discussed in Section 8.1.1.

Feuster and Mosel [51, 52, 53] have found similarly good descriptions of experimental pion- and photon-induced data on the final states γN, πN, $2\pi N$, ηN, and $K\Lambda$ up to 1.9 GeV, when either using the formfactor F_p (Eq. (3.29)) or F_t (Eq. (3.30)) for the t-channel meson exchanges. Since it is not a priori clear, whether these findings will hold true for the extended energy region and model space, calculations have been performed using both formfactors. In addition, we have checked the dependence of the results on the choice of the spin-$\frac{3}{2}$ resonance vertices (see Section 3.4.1) and the a priori unknown $g_{\omega\rho\pi}$ coupling sign.

Choosing the following notation for the labeling of the fits

- "C" or "P" denotes whether the conventional or Pascalutsa couplings are used for the spin-$\frac{3}{2}$ resonance vertices.
- The following letter "p" or "t" denotes whether the formfactor F_p or F_t (cf. Eqs. (3.29) and (3.30) and Section 3.7.4) is used in the t-channel contributions.
- The following symbol denotes whether the fit is a purely hadronic ("π") or global ("γ") fit.
- The concluding symbol denotes the sign of the $g_{\omega\rho\pi}$ coupling.
- For the chiral symmetry breaking calculation, a χ is inserted.

---

[2] Since the ωN couplings of the $S_{11}(1650)$ have always turned out to be very small in the hadronic fits, finally only one coupling has been used in these fits.

the 7 hadronic fits and 4 global fits, which have been performed, can be summarized as follows:

- Using the conventional spin-$\frac{3}{2}$ vertices, 4 fits have been carried out allowing for both formfactor shapes (F_p (3.29) or F_t (3.30)) in the t-channel and also both signs of the couplings of $g_{\rho\omega\pi}$:
  C-p-π+, C-p-π−, C-t-π+, C-t-π−.
  For the results of the last two fits, see in particular Section 8.2.1.

- One calculation has been performed with the chiral symmetry breaking direct $\boldsymbol{\sigma\pi\pi}$ coupling (see Section 3.3.2):
  C-p-$\pi\not\chi$+.3)

- Since in the conventional coupling fits, it has turned out that the F_p t-channel formfactor results in a better χ^2 result, only two fits using the Pascalutsa spin-$\frac{3}{2}$ vertices have been carried out:
  P-p-π+, P-p-π−.

- For the global fits, we have extended the best hadronic fits (C-p-$\pi\pm$, C-t-$\pi\pm$) to also include the photon-induced data:
  C-p-γ+, C-p-γ−, C-t-γ+, C-t-γ−.
  For the results of the last two fits, see in particular Section 8.2.1.

8.1 Results on Pion-Induced Reactions

The extension of the Giessen model to also include a vector meson final state requires some checks whether the new final state is incorporated correctly. As pointed out in Chapter 4, in the presented partial-wave formalism this inclusion is straightforward by simply splitting up the ωN final state into its three helicity states $\omega N_{\frac{3}{2}}$, $\omega N_{\frac{1}{2}}$, ωN_0, where the same helicity notation for ωN is used as given in Section 5.2. Thus, effectively one has introduced three new final states. The correct inclusion of these three final states has been checked by simulating a single-channel problem, where just one resonance, which couples to only one ωN helicity state, has been initialized with the help of Eqs. (E.29) and (E.39), while all other final states are switched off. It has been shown in [51, 52], that the resulting partial-wave K-matrix

$$\mathcal{K}^{IJ\pm}_{\omega_\lambda\omega_\lambda} \sim \frac{-\sqrt{s}\Gamma_{\omega_\lambda}(s)}{s - m_R^2} \tag{8.1}$$

leads via (4.20) to a $\mathcal{T}$-matrix that resembles a conventional relativistic Breit-Wigner. This artificial situation is then similar to the low-energy P_{33} $\pi N \to \pi N$ partial wave, which can be well approximated by a single resonance ($P_{33}(1232)$) only decaying and consequently contributing to πN. Thus, we have successfully checked that the partial-wave amplitude $\mathcal{T}^{IJ\pm}_{\omega_\lambda\omega_\lambda}$ resulting from the single-helicity ωN situation has the correct width

---

3) Some of the results of this calculation are published under G. Penner and U. Mosel, *Phys. Rev.* **C65**, 055202 (2002).

Fit	Total π	$\chi^2_{\pi\pi}$	$\chi^2_{\pi 2\pi}$	$\chi^2_{\pi\eta}$	$\chi^2_{\pi\Lambda}$	$\chi^2_{\pi\Sigma}$	$\chi^2_{\pi\omega}$
C-p-π+	2.66	3.00	6.93	1.85	2.19	1.97	1.24
C-p-π−	2.69	2.76	6.86	1.84	2.40	2.36	1.12
P-p-π+	3.53	3.72	9.62	2.47	2.69	2.92	2.17
P-p-π−	3.60	3.96	8.49	2.50	3.31	2.79	2.03
C-p-$\pi\not\chi$+	3.09	3.75	6.79	2.07	2.16	2.47	2.13
C-t-π+	3.09	3.32	7.46	2.06	2.48	2.42	3.48
C-t-π−	3.03	3.24	6.74	1.91	2.84	2.48	2.81
C-p-γ+	3.78	4.23	7.58	3.08	3.62	2.97	1.55
C-p-γ−	4.17	4.09	8.52	3.04	3.87	3.94	3.73
SM95-pt-3	6.09	5.26	18.35	2.96	4.33	—	—
Fit	**Total^a**	$\chi^2_{\gamma\gamma}$	$\chi^2_{\gamma\pi}$	$\chi^2_{\gamma\eta}$	$\chi^2_{\gamma\Lambda}$	$\chi^2_{\gamma\Sigma}$	$\chi^2_{\gamma\omega}$
C-p-γ+	6.57	5.30	10.50	2.45	3.95	2.74	6.25
C-p-γ−	6.66	5.15	10.54	2.37	2.85	2.27	6.40
SM95-pt-3	24.40	16.45	42.07	8.01	4.64	—	—

Table 8.1: Resulting χ^2 of the various fits. For comparison, we have also applied the preferred parameter set SM95-pt-3 of [52, 53] to our extended and modified data base for energies up to 1.9 GeV. For the χ^2 results of the fits C-t-$\gamma\pm$, see text. ^{a}: This value includes all pion- and photon-induced data points.

and energy behavior and that all poles due to the resonance denominator in (8.1) cancel in the matrix inversion (4.20).

The resulting χ^2 values for all calculations performed are presented in Table 8.1. Note, that in contrast to [51, 52, 53], we have included in the present calculation all experimental data up to the upper end of the energy range, in particular also for all partial-wave and multipole data up to $J = \frac{3}{2}$. At first sight it seems that the global χ^2 is only fair; however one has to note that the main part of this value stems from the pion-photoproduction multipoles [221], which have very small error bars but also scatter a lot (cf. Figs. 8.20, 8.21, and 8.22 in Section 8.4.2 below). Note, that in this channel there are 40% of all data points. Taking this channel out, the total χ^2 per data point is reduced from 6.56 to 3.87 for the preferred global fit. Thus, a very good simultaneous description of all reactions is possible, especially if only the pion-induced reactions are considered. This shows that the measured data for all reactions are compatible with each other, concerning the partial-wave decomposition and unitarity effects. As a guideline for the quality of the present calculation, we have also included a comparison with the preferred parameter set SM95-pt-3 of [53] applied to our extended and modified data base. It is interesting to note that although this comparison has only taken into account data up to 1.9 GeV for the final states γN, πN, $2\pi N$, ηN, and $K\Lambda$, the present best global calculation C-p-γ+ results in a better description in almost all channels; only for $\pi N \to \eta N$ the χ^2 of [53] is slightly better. This is a consequence of the fact, that for example for the understanding of $K\Lambda$ production, the coupled-channel effects due to the final states $K\Sigma$ and ωN have to be included. This is discussed in Sections 8.1.5 and 8.4.4 below.

The results for the hadronic fits in Table 8.1 also reveal, that while ωN production seems to be rather independent of the sign of $g_{\omega\rho\pi}$, the effect of sign-switching becomes most obvious in the $K\Lambda$ and $K\Sigma$ results, showing that both reactions are very sensitiv to rescattering effects due to the ωN channel. Only the global fitting procedure gives a significant preference of the positive sign for $g_{\omega\rho\pi}$, especially in the pion-induced ωN production. It is also interesting, that while in [51] similar results have been found using either one of the formfactors F_t and F_p for the t-channel meson exchanges, the extended data base and model space shows a clear preference of using the formfactor F_p for all vertices, i.e. also for the t-channel meson exchange. Especially in the global fitting procedure, not even a fair description of the experimental data has been possible using F_t. This is discussed in detail in Section 8.2.1.

Therefore, we do not display the results of the fits C-t-$\pi\pm$/C-t-$\gamma\pm$ in the following; furthermore, for reasons of clarity, we restrict ourselves in this section to displaying the pion-induced results for the best global fit C-p-$\gamma+$, the best hadronic fit C-p-$\pi+$, and the calculation using the Pascalutsa spin-$\frac{3}{2}$ vertices P-p-$\pi+$. Only in those cases, where important differences are found, also the other calculations are discussed.

In the subsequent sections, we start with a discussion of the influence of the treatment of the σ meson and the spin-$\frac{3}{2}$ vertices on πN elastic scattering. Then the different pion-induced channels are discussed separately and the section ends with the presentation of the background and resonance properties.

8.1.1 σ meson, Chiral Symmetry, and Spin-$\frac{3}{2}$ Vertices

As compared to the calculation of [51, 52, 53] we have added a σ meson t-channel exchange. In Section 3.3.2 it has been pointed out, that the inclusion of a σ meson is not necessary from the viewpoint of chiral symmetry, when pseudovector πNN coupling is used. However, the σ meson can still be used to simulate the correlated two-pion scalar-isoscalar exchange, but conformity with chiral symmetry then requires a derivative $\sigma\pi\pi$ coupling. The preference of a chirally symmetric coupling has become obvious, when we have switched from the chiral symmetry breaking coupling (calculation C-p-$\pi\not\chi+$) to the chirally symmetric derivative coupling (calculation C-p-$\pi+$): Even without any refitting the χ^2 in the πN partial waves improves by about 10 percent. This improvement comes especially from the threshold region in the S_{11} (and also P_{13}) partial wave, see Fig. 8.1, and even extends up to the energy region of the second resonance ($\sqrt{s} \approx 1.65$ GeV).

The importance of the inclusion of a chirally symmetric σ meson becomes especially obvious in the calculations, where the Pascalutsa spin-$\frac{3}{2}$ vertices (cf. Section 3.4.1) are used. It turns out in the present model that the use of the chirally symmetric coupling is mandatory: With the non-derivative coupling, not even a fit to low-energy (up to 1.4 GeV) πN-scattering has been possible. In [51, 52, 53], where the σ meson was not included, it was shown, that in particular the πN S_{31} partial wave can hardly be described when the spin-$\frac{1}{2}$ off-shell contributions of the $P_{33}(1232)$ were neglected. In the present calculations, however, we find that the inclusion of a chirally symmetric σ meson exchange with a derivative $\sigma\pi\pi$ coupling allows the description of low-energy πN elastic scattering even without this off-shell contributions, i.e. using the Pascalutsa prescription for the spin-$\frac{3}{2}$ vertices. From Fig. 8.2 it is obvious, that a good description of the S_{31} partial

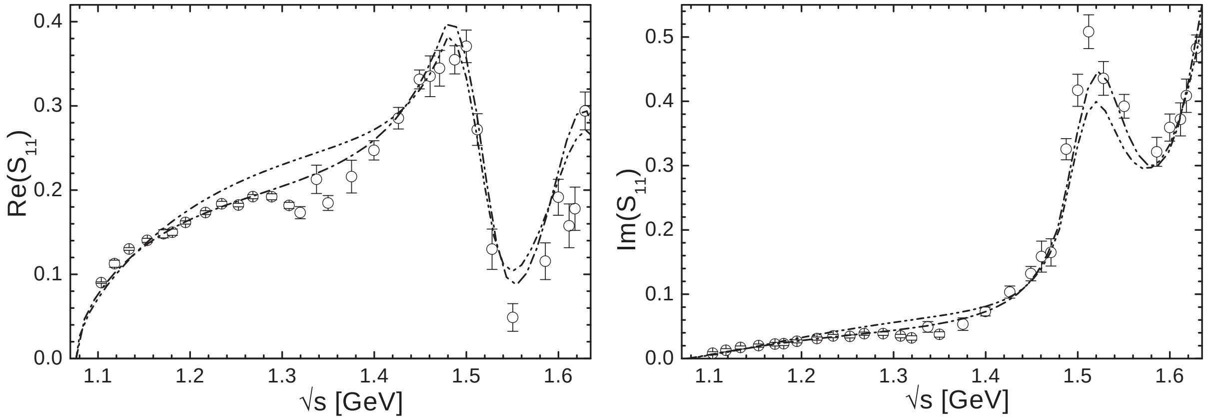

Figure 8.1: Effect of the chirally symmetric (calculation C-p-π+: dash-dotted) as compared to the chiral symmetry breaking $\sigma\pi\pi$ (calculation C-p-$\pi\chi$+: dash-double-dotted) coupling in the S_{11} πN elastic partial wave. *Left:* real part, *right:* imaginary part. Data are from [277].

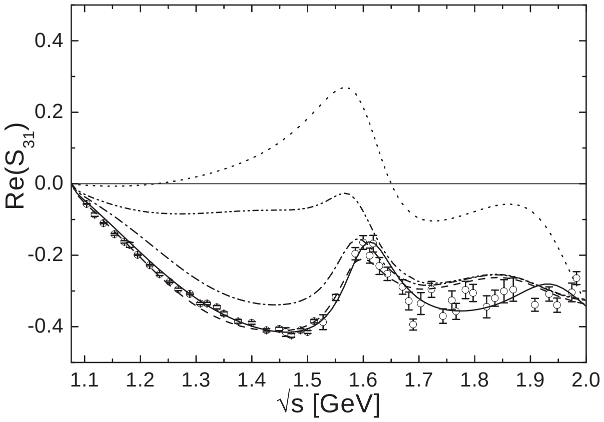

Figure 8.2: Effect of the σ meson exchange on the real part of the S_{31} partial wave in πN scattering. P-p-π+ (solid line), P-p-π+ without σ (dotted), C-p-π+ (dashed), C-p-π+ without σ (dash-dot), C-p-π+ without $P_{33}(1232)$ (dash-double-dotted). Data are from [277].

wave is indeed possible when the Pascalutsa couplings are used. At the same time it turns out, that the σ meson as a background contribution is enhanced as compared to when the conventional spin-$\frac{3}{2}$ couplings are used. This is not only manifested in the increase of the σ couplings (see Table 8.3 below), but also the t-channel cutoff parameter Λ_t (see Table 8.4 below) increases by a factor of 2, meaning that the missing spin-$\frac{1}{2}$ off-shell background contributions of the spin-$\frac{3}{2}$ resonances are compensated by larger t-channel diagram contributions in the lower partial waves of all reaction channels. The resemblance of the calculations P-p-π+ without the σ meson and C-p-π+ without the $P_{33}(1232)$ resonance also asserts the finding of Pascalutsa [138] and Pascalutsa and Tjon [137] that the two prescriptions for the spin-$\frac{3}{2}$ vertices become equivalent when additional background contributions are included, i.e. when the spin-$\frac{1}{2}$ off-shell contributions are reshuffled into other contributions. Similar observations concerning the importance of the inclusion of a σ meson have also been made in the full BSE $\pi N \to \pi N$ model of Lahiff and Afnan [104]. These authors have also allowed for the inclusion and neglect of the $P_{33}(1232)$ spin-$\frac{1}{2}$ off-shell contributions by using conventional and Pascalutsa $\pi N \Delta$ couplings. A ten times smaller $g_{\sigma NN} g_{\sigma\pi\pi}$ value in the conventional as compared to the Pascalutsa case was found. At the same time, the cutoff value of the σ formfactor in the conventional case has been much softer thus reducing the σ contribution even further.

8.1.2 $\pi N \to \pi N$

The resulting descriptions of the πN elastic scattering partial waves are shown in Figs. 8.3 and 8.4. In most partial waves, the hadronic calculations using the Pascalutsa (P-p-π+) and conventional (C-p-π+) spin-$\frac{3}{2}$ vertices are very similar and equally well reproduce the $\pi N \to \pi N$ single-energy data points of [277]. The largest differences are found in the

- P_{11} wave around the $P_{11}(1710)$ resonance. Since there is no prominent structure in the πN elastic scattering data, the width of this resonance is difficult to fix resulting in the different structures in Fig. 8.3. This also explains why the $P_{11}(1710)$ mass as given by the references in the PDG review [67] ranges from about 1.69 to 1.77 GeV.
- S_{11} wave around the $S_{11}(1650)$ resonance. Due to the missing off-shell contributions a more pronounced resonance behavior is needed in the Pascalutsa calculation to be able to describe the high-energy tails of the real and imaginary part.
- S_{31} wave above 1.7 GeV. In this partial wave, it has turned out that adding a second resonance (besides the $S_{31}(1620)$) around 1.98 GeV improves the χ^2 considerably in the Pascalutsa calculation. However, the same does not hold true for the other calculations, which consequently show less structure in the high energy tail. See also Section 8.2.3 below.
- D_{13} wave above 1.8 GeV. In this partial wave, it has also turned out that adding a third resonance between 1.7 and 1.8 GeV, improves the χ^2 considerably in the Pascalutsa calculation. Since the resulting resonance is rather narrow ($\Gamma_{tot} \approx 55$ MeV), the difference to the other calculations remains small and is only visible in the imaginary part between 1.7 and 1.8 GeV. See also Section 8.2.3 below.

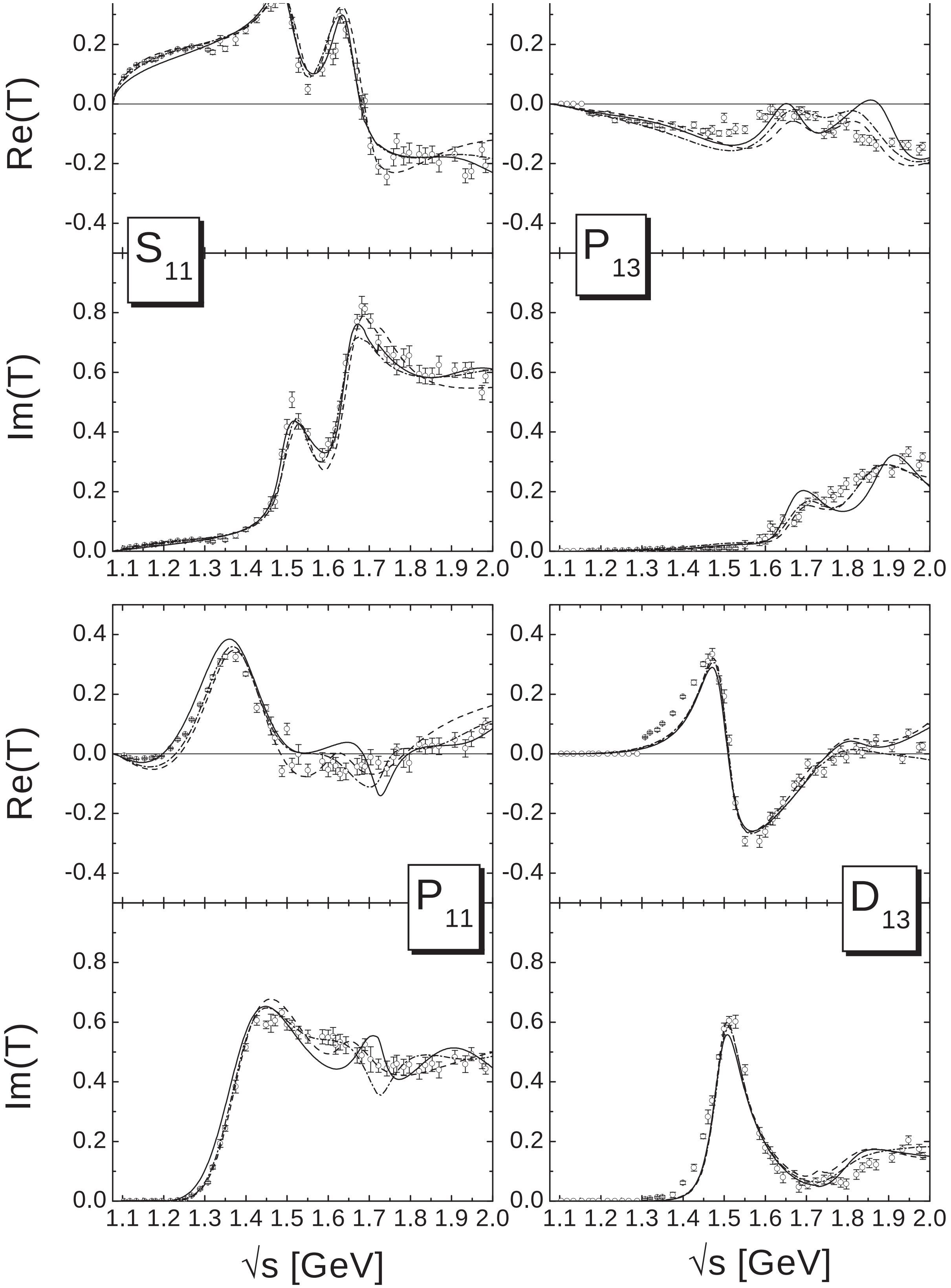

Figure 8.3: $\pi N \to \pi N$ partial waves for $I = \frac{1}{2}$. Calculation C-p-γ+: solid line, C-p-π+: dotted line, P-p-π+: dashed line. Data are from [277].

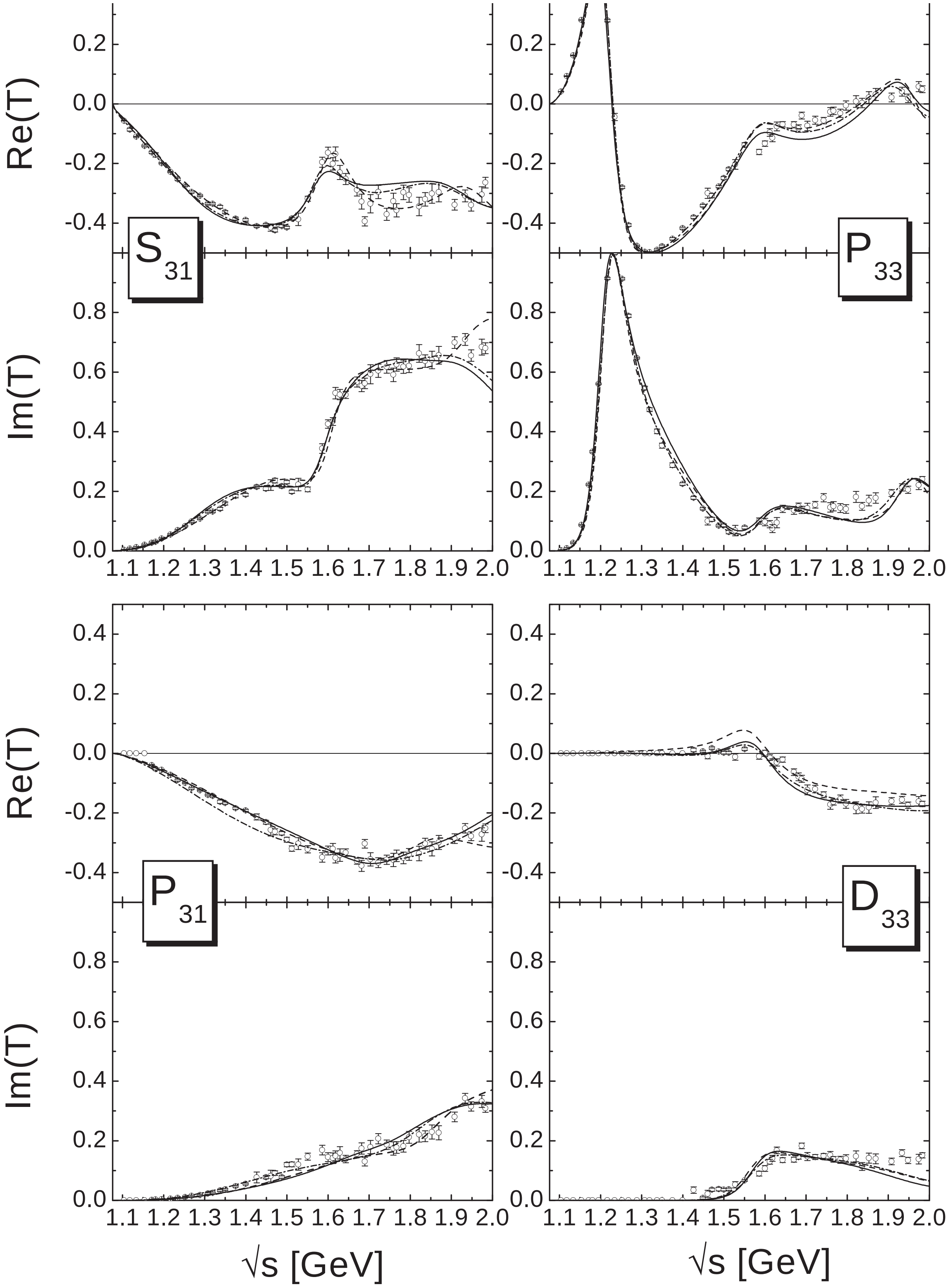

Figure 8.4: $\pi N \to \pi N$ partial waves for $I = \frac{3}{2}$. Notation and data as in Fig. 8.3.

The calculation with the chiral symmetry breaking σ contribution is not shown in Figs. 8.3 and 8.4 since it is very similar to the calculation C-p-$\pi+$; the main differences are contained in the low-energy tails of the spin-$\frac{1}{2}$ partial waves and especially in the S_{11} wave, see Fig. 8.2 above.

For the extension of the model up to 2 GeV it turns out to be essential to add a resonance in the P_{13}, P_{31}, and P_{33} partial waves as compared to [51, 53]. This is in line with Manley and Saleski [113], who found additional states around 1.88, 1.75, and 2.01 GeV, respectively. Without these resonances, those three partial waves cannot completely be described above 1.8 GeV in our model, see also [51, 53]. However, in the P_{I3} waves, the new resonances are at the boundary of the energy range of the present model. This means that their properties cannot be extracted with certainty, but in both partial waves there is a clear indication for an additional contribution. See also Section 8.2.3 below.

The most striking differences between the global and the purely hadronic fits can be seen in the low-energy tails of the S_{11} and P_{11} waves, which in the latter case is accompanied by an increase of the mass and widths of the $P_{11}(1440)$. While in the hadronic calculations the threshold behavior of all $J = \frac{1}{2}$ partial waves is nicely reproduced, which also leads to ρNN couplings in line with the KSRF relation (see Section 8.2.1 below), in the global calculation this description is inferior. The reason for this behavior can be found in the necessity of the reduction of the nucleon formfactor cutoff Λ_N in the global fits due the $E_{0+}^{p/n}$ multipoles, see Section 8.4.2. Thereby the low-energy interference pattern in πN scattering between the ρ meson and the nucleon is misbalanced and deteriorates in comparison with the hadronic fits. Moreover, the resonant structure due to the $P_{13}(1900)$ in the P_{13} wave turns out to be more pronounced in the global fits as compared to the hadronic calculations. This is a consequence of the necessity of an enhanced P_{13} contribution in the ωN production mechanism, see Sections 8.1.7 and 8.4.6. In the isospin-$\frac{3}{2}$ partial waves, there is hardly any difference between the hadronic and the global fit results. The reason is, that the $I = \frac{3}{2}$ resonances only contribute to pion and $K\Sigma$ photoproduction, and are hence not submitted to that many additional constraints of the photoproduction data as the isospin-$\frac{1}{2}$ resonances.

For a detailed discussion of the individual resonance contributions to the partial waves and the discrepancies in the D_{13} partial wave below 1.45 GeV, see Section 8.2.3 below.

8.1.3 $\pi N \to 2\pi N$

Although the $2\pi N$ production is simplified in the present model through the isovector-scalar ζ meson, the $2\pi N$ flux is well reproduced in most partial waves, see Fig. 8.5. This indicates, that the pion-induced $2\pi N$ production is indeed dominated by baryon resonances, which represent the only production mechanism for the ζ meson in our model. Since the $2\pi N$ final state clearly dominates all partial-wave inelasticities besides S_{11}, P_{11}, and P_{13} (see below), cf. Fig. 8.5, the qualitative description of this channel is mandatory in a unitary model. The various calculations for the $2\pi N$ partial-wave cross sections are very similar in all partial waves, with the exception of the S_{11} wave. There, the Pascalutsa calculation results in a largely decreased S_{11} $2\pi N$ production above 1.7 GeV, below the 2π production data. Although the S_{11} ωN partial-wave cross section is

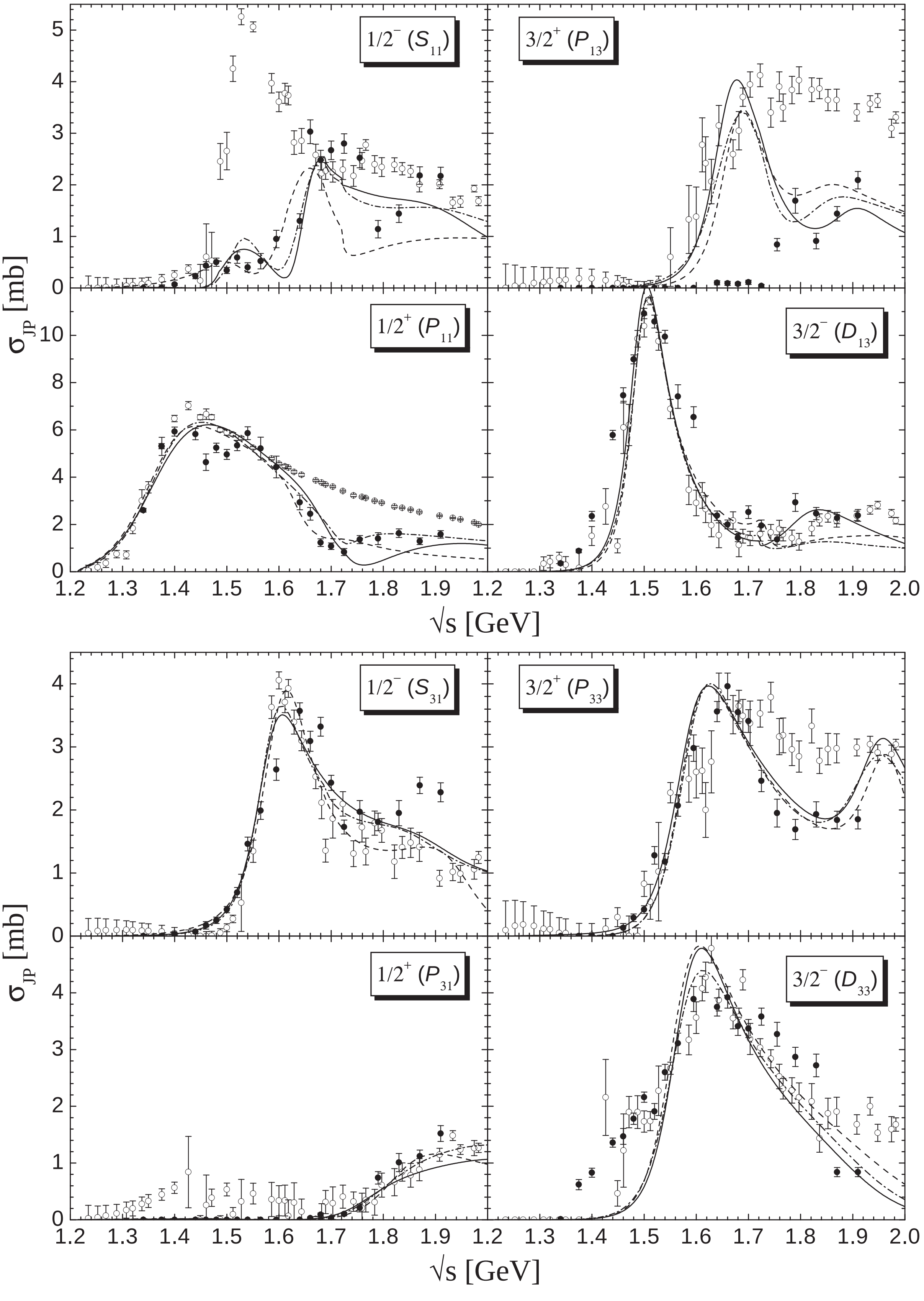

Figure 8.5: $\pi N \to 2\pi N$ partial-wave (J^P) cross sections for $I = \frac{1}{2}$ (*upper panel*) and $I = \frac{3}{2}$ (*lower panel*). The solid dots (●) are taken from [278], the open dots (○) are the inelastic $\pi N \to \pi N$ partial-wave cross sections extracted from the VPI analysis [277]. Notation as in Fig. 8.3.

increased simultaneously by about 0.5 mb as compared to the conventional calculations, the resulting total inelasticity is still reduced, see Fig. 8.6. All calculations show a kink structure in the S_{11} and the D_{13} $2\pi N$ flux at the $K\Sigma$ and the ωN thresholds, respectively, indicating that $2\pi N$ flux is moved to the corresponding channels.

The largest changes in the $2\pi N$ production upon inclusion of the photoproduction data can be observed in the P_{11} and D_{13} waves above the ωN threshold. The inclusion of the very precise preliminary ωN photoproduction data of the SAPHIR Collaboration [269] requires, that inelastic contributions are moved from $2\pi N$ to ωN in the P_{11} wave and vice versa in the D_{13} case. This can also be seen in the dramatic change of the total $\pi N \to \omega N$ cross section behavior when the photoproduction data are included, see Fig. 8.16 below. Otherwise, similarly to the $\pi N \to \pi N$ case, also the $2\pi N$ production is only slightly changed by the inclusion of the photoproduction data. A small, but interesting change can, however, be observed in the high energy tail of the P_{31} and P_{33} waves, which can be traced back to the shift of inelasticity caused by $K\Sigma$ from P_{33} in the hadronic calculations to P_{31} in the global calculations; see also Section 8.1.6.

The only obvious discrepancy between the calculated $2\pi N$ partial-wave cross sections and the Manley et al. [278] data is given in the P_{13} partial wave. In the energy region between 1.55 and 1.72 GeV the inelasticity increases up to 4 mb in line with the calculated $2\pi N$ cross section, while the measured $2\pi N$ cross section is still zero. At the same time the total cross sections from all other open inelastic channels (ηN, $K\Lambda$, and $K\Sigma$) add up to significantly less than 4 mb. This indicates that either the extracted $2\pi N$ partial-wave cross section is not correct in the P_{13} partial wave or another inelastic channel (i.e. an additional $3\pi N$ channel) gives noticeable contributions to this partial wave. The same problem with the P_{13} inelasticity has also been observed in a resonance parametrization of $\pi N \to \pi N$ and $\pi N \to 2\pi N$ by Manley and Saleski [113]. Since this is the only partial wave where such a large discrepancy is observed, no additional final state is introduced in the present model, but instead, we have largely increased the error bars of the $2\pi N$ data points in this energy region. However, it would be desirable to account for $3\pi N$ contributions in future investigations by the inclusion of, e.g., a $\rho\Delta$ final state. This might also clarify, whether there is a missing ($3\pi N$) contribution in the P_{33} wave above 1.7 GeV, see Fig. 8.5 and Section 8.2.3 below. So far, no analysis has given such a contribution.

In addition, there is the same problem as in πN scattering with the description of the rise of the $2\pi N$ production in the D_{I3} waves, i.e. in the D_{13} wave below 1.45 GeV and in the D_{33} wave below 1.55 GeV, see Fig. 8.5. This effect is probably due to the effective description of the $2\pi N$ state in the present model; see the detailed discussion in Section 8.2.3 below.

It is interesting to note that the inelasticities of $\pi N \to \pi N$ scattering only enter the fitting procedure indirectly, since the real and imaginary part of the partial waves are the input for the calculations. Therefore, the very good description of the partial-wave inelastic πN cross sections in all calculations, see the upper panel in Fig. 8.6, is an outcome of summing up the partial-wave cross sections of all other πN-induced channels. Note, that the inelasticities for the $I = \frac{3}{2}$ partial waves are not shown for the different calculations, since due to the smallness of the $K\Sigma$ contributions, the results are almost identical to

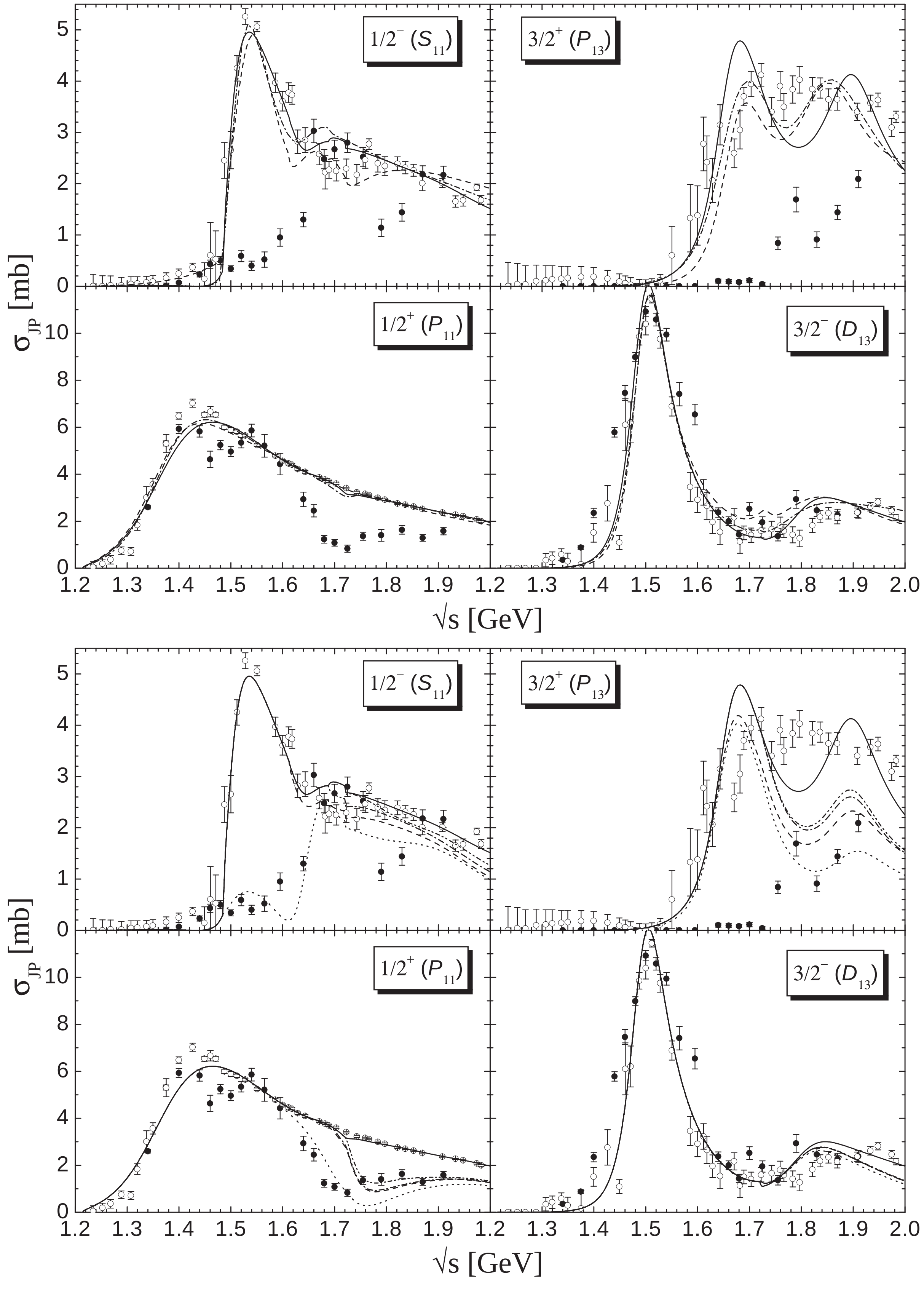

Figure 8.6: Inelastic partial-wave cross sections of $\pi N \to \pi N$ for $I = \frac{1}{2}$. Data as in Fig. 8.5. *Upper panel:* Notation as in Fig. 8.3. *Lower panel:* Decomposition of the inelasticities for calculation C-p-γ+. Partial-wave cross section of $2\pi N$: dotted, $+\eta N$: dashed, $+K\Lambda$: dash-dotted, $+K\Sigma$: dash-double-dotted, total ($+\omega N$): solid line.

the $2\pi N$ partial-wave cross sections. From Figs. 8.5 and 8.6 we can thus deduce, that not only the PWD of all inelastic channels is on safe grounds, but also that all important channels for the considered energy region are included. At the same time, this shows that the experimental data on the various reactions are indeed compatible with each other, in particular no significant discrepancy between the measured πN inelasticity and the sum of all partial-wave cross sections is observed. The only exceptions are the aforementioned indications for missing $(3\pi N)$ contributions in the P_{I3} waves.

Note also, that the inclusion of the photoproduction data only slightly changes the total inelasticities of the individual partial waves. The only noticeable differences between the hadronic and global calculation is a decrease of the S_{11} inelasticity between 1.6 and 1.7 GeV, and an increase in the P_{13} inelasticity around the $P_{13}(1720)$.

In the lower panel of Fig. 8.6, the decomposition of the πN inelasticity of the best global fit C-p-γ+ is shown. It can be deduced that the πN inelasticities are made up in all partial waves mainly by the $2\pi N$ channel. This also allows to deduce, that the Manley $2\pi N$ data [278] are in line with the πN inelasticitis of the VPI analysis [277]. The only contradictions can be observed in the D_{13} wave at 1.6, 1.7, and 1.8 GeV, in the S_{31} wave above 1.85 GeV and the D_{33} wave between 1.7 and 1.85 GeV.

Besides the $2\pi N$ channel, there are in all partial waves important contributions to the inelasticities from other channels. Thus, the necessity of the inclusion of a large set of final states in a coupled-channel calculation can be seen in various partial waves:

- In the S_{11} wave there is the well known ηN contribution around the $S_{11}(1535)$. Note, that the ηN inelasticity also exhibits a second hump, which is due to the interference between the $S_{11}(1535)$ and the $S_{11}(1650)$ resonances, although the latter only has a very small ηN width. See also Section 8.1.4.
- In the P_{11} wave there is also an important contribution by the large ηN and ωN widths of the $P_{11}(1710)$ resonance. This contrasts previous analyses [53, 113], where this contribution has been assigned to the $K\Lambda$ channel.
- The P_{13} wave contains important contributions from ηN and ωN as well, where the first one stems from the $P_{13}(1900)$ resonance, while the latter one consists of important contributions from both P_{13} resonances.
- The D_{13} wave is also fed by a smoothly increasing ωN contribution.

The other final states, i.e. the associated strangeness channels $K\Lambda$ and $K\Sigma$, are only of minor importance for the πN inelasticities. While both give visible contributions in the S_{11} wave, $K\Lambda$ also shows up in the P_{13} and $K\Sigma$ in the P_{11} wave.

8.1.4 $\pi N \to \eta N$

In the first coupled-channel effective Lagrangian model on ηN production by Sauermann et al. [157], this channel has been described by a pure S_{11} mechanism for energies up to

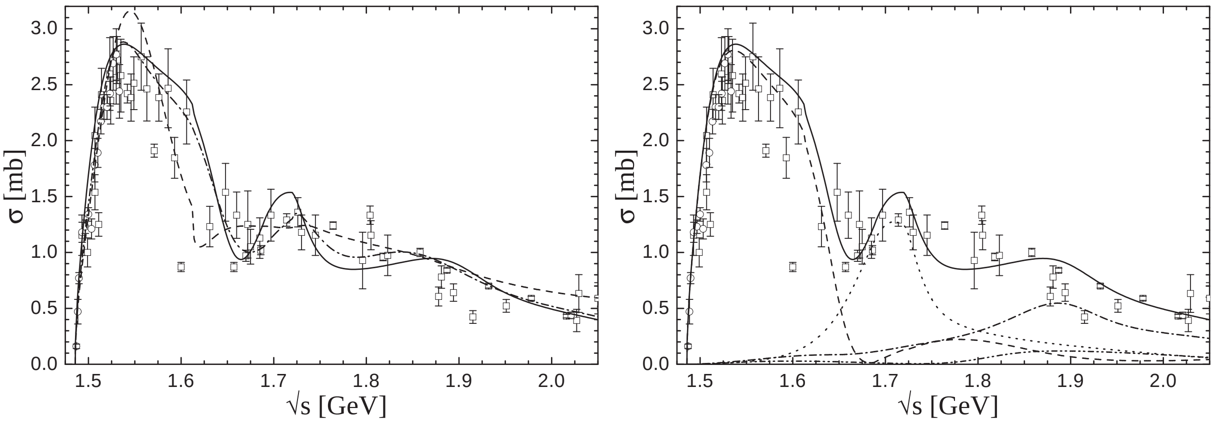

Figure 8.7: $\pi^- p \to \eta n$ total cross section. The new threshold data from [286] are denoted by ∘, all other data (see Section 7.2.6) by □. *Left:* Results from the different calculations. Notation as in Fig. 8.3. *Right:* Partial-wave decomposition of the total cross section for the calculation C-p-γ+. $J^P = \frac{1}{2}^-(S_{11})$: dashed line; $\frac{1}{2}^+(P_{11})$: dotted line; $\frac{3}{2}^+(P_{13})$: dash-dotted line; $\frac{3}{2}^-(D_{13})$: dash-double-dotted line (in brackets the πN notation is given). The sum of all partial waves is given by the solid line.

$\sqrt{s} = 1.75$ GeV. As Fig. 8.7 shows, the $\pi N \to \eta N$ reaction is indeed dominantly composed of the S_{11} contribution due to the $S_{11}(1535)$, however, only for energies up to ≈ 1.65 GeV. Due to its large ηN width the $P_{11}(1710)$ dominates in the following energy window up to 1.8 GeV, while for the highest energies, the $P_{13}(1900)$ resonance is strongest. The double hump structure in the S_{11} contribution is due to the destructive interference between the $S_{11}(1535)$ and $S_{11}(1650)$ resonances, even though the latter one has a much smaller ηN decay ratio. This interference pattern exhibits maximal destructive interference at the $S_{11}(1650)$ resonance position, while above 1.7 GeV the S_{11} contribution is resurrected.

The importance of the $P_{11}(1710)$ contribution has also been found in the resonance parametrization of $\pi N \to \pi N$ for $I = \frac{1}{2}$ and $\pi N \to \eta N$ by Batinić et al. [10], who extracted a total width for this resonance of about 120 MeV and an ηN decay ratio of almost 90%. However, in contrast to the results of these authors, we also find in the present calculation important contributions of the $P_{13}(1900)$ at higher energies. These contributions are in line with the observed differential cross section at higher energies, see Fig. 8.8. However, some deviations in the differential cross section behavior between calculation and experimental data are observed and the angular structure cannot be fully described. But one has to note, that at higher energies, there are almost only experimental data available from Brown et al. [280], which enter with enlarged error bars due to problems with the momentum calibration in the experiment, see [10, 51] and Section 7.2.6. Hence these discrepancies hardly influence the fitting procedure and the resulting χ^2 is still rather good. Since at energies above 1.8 GeV, there are almost only data available from Brown et al. [280], a reliable decomposition in this region can only be achieved after the inclusion of the ηN-photoproduction data.

In this reaction channel, large differences between the Pascalutsa and conventional calculations are observed. This is related to the visible differences in the S_{11} $\pi N \to \pi N$

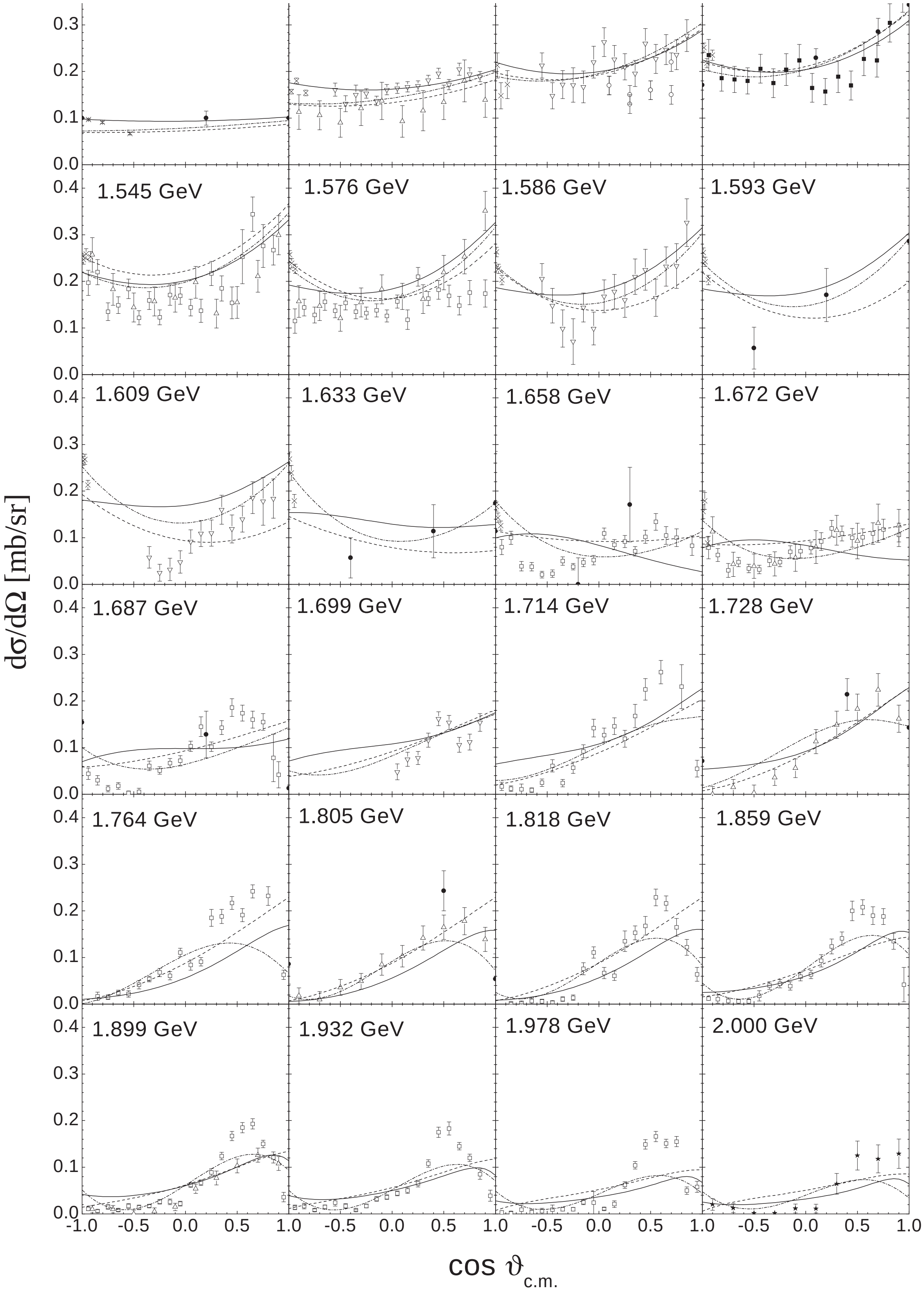

Figure 8.8: $\pi^- p \to \eta n$ angle-differential cross section. Data are from [280] (□), [287] (△), [284] (▽), [286] (○), [281] (●), [285] (■), [282] (⋆), [283] (×). Notation as in Fig. 8.3.

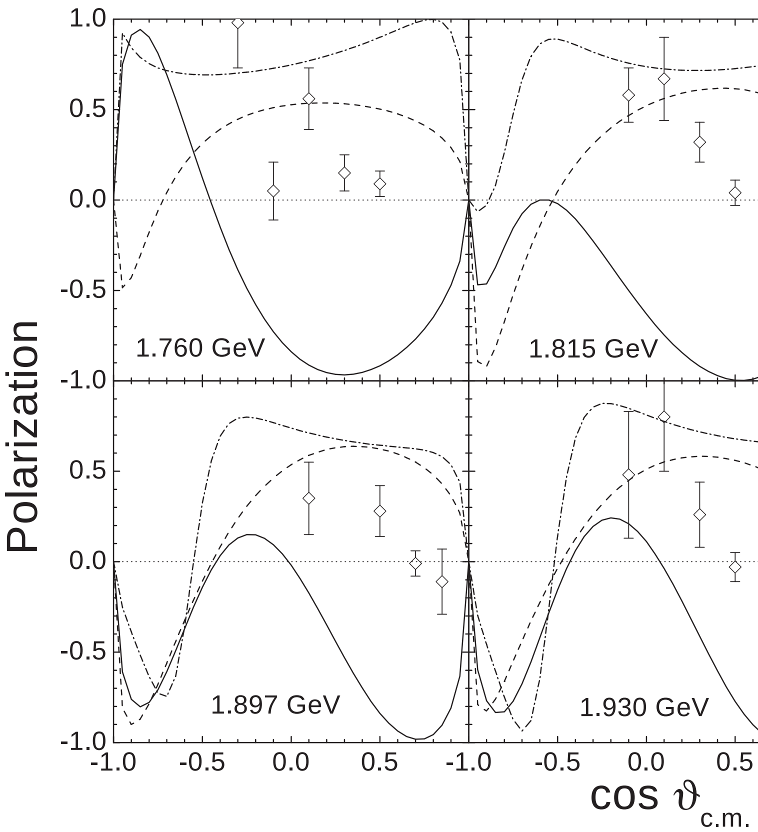

Figure 8.9: $\pi^- p \to \eta n$ polarization measurement. Note that the displayed data from [279] are not used in the fitting procedure. Notation as in Fig. 8.3.

partial wave, since this partial wave constitutes the largest contribution in the ηN production mechanism. An obvious difference is that the Pascalutsa calculation results in less angular structure of the angle-differential cross section at higher energies, however influencing the resulting χ^2 only to a minor degree, see above. On the other side, the inclusion of the photoproduction data hardly changes the total cross section behavior. Only the $P_{11}(1710)$ contribution is slightly emphasized, which also leads to the observed differences in the differential cross section. Moreover, the ωN threshold effect in the P_{11} wave can be clearly observed in calculation C-p-γ+ and C-p-π+.

For comparison, we have also included the resulting angle-differential polarization in Fig. 8.9. Note that the displayed data from Baker et al. [279] have not been included in the fitting procedure, since they are based on the apparatus and angle-differential cross sections of Brown et al. [280]. The resulting behavior is rather similar for the hadronic calculations, while the global calculation shows the opposite behavior at forward angles due to the sign switch of the t-channel a_0 contribution, see Table 8.3 below.

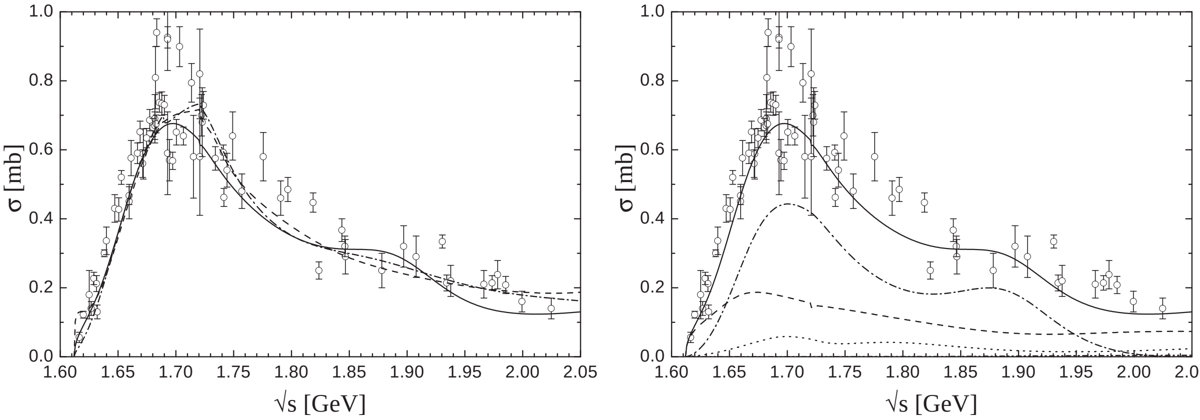

Figure 8.10: $\pi^- p \to K^0\Lambda$ total cross section. For the data references, see Section 7.2.7. *Left:* Results of the different calculations. Line code as in Fig. 8.3. *Right:* Partial-wave decomposition of the total cross section. Notation as in Fig. 8.7.

8.1.5 $\pi N \to K\Lambda$

$K\Lambda$ production turns out to be a channel which is very sensitive to rescattering effects. The inclusion of the $K\Sigma$ and ωN final states strongly alters the total cross section in this reaction, especially in the hadronic calculations, see Fig. 8.10. In both of the displayed hadronic calculations, the $K\Sigma$ channel leads to a kink in the S_{11} partial wave, which has already been observed in the coupled-channel chiral SU(3) model of [148] including only S and P waves, while the ωN channel strongly influences the P waves. The inclusion of these coupled-channel effects and of the $P_{13}(1900)$ resonance are major improvements as compared to [51, 53]. There, these mechannisms were not included and thus, the $K\Lambda$ channel was not subjected to any threshold effect and the peaking behavior around 1.7 GeV had to be fully described by the $P_{11}(1710)$ resonance. In the extended model space, this resonance-like behavior is mainly caused by the $P_{13}(1720)$ resonance, but also influenced by the opening of these two channels.

The S wave behavior in the Pascalutsa calculation P-p-π+ differs from that in the conventional calculation C-p-π+ (see Section 8.1.2 and Fig. 8.3). The largest differences between these calculations can be observed in the S_{11} wave contribution, which is more pronounced in the Pascalutsa calculation giving rise to a slightly different behavior at the lowest energies and at the $K\Sigma$ threshold. The coupled-channel effects become less obvious once the photoproduction data are included. In the global calculation C-p-γ+ the S_{11} and P_{13} waves are only slightly influenced by the ωN threshold, while the $K\Sigma$ threshold effect has completely vanished. Note, that the P_{13} wave dominates over almost the complete considered energy region. The second most important part comes from the S_{11} staying almost constant in the upper energy range, while close to threshold, a slight peak caused by the $S_{11}(1650)$ is visible.

Although the new $P_{13}(1900)$ only has a small $K\Lambda$ width, it improves the description of the reaction significantly due to rescattering, similarly to the $S_{11}(1650)$ resonance in $\pi N \to \eta N$. Thus the $P_{13}(1900)$ gives rise to a good description of the angle differential

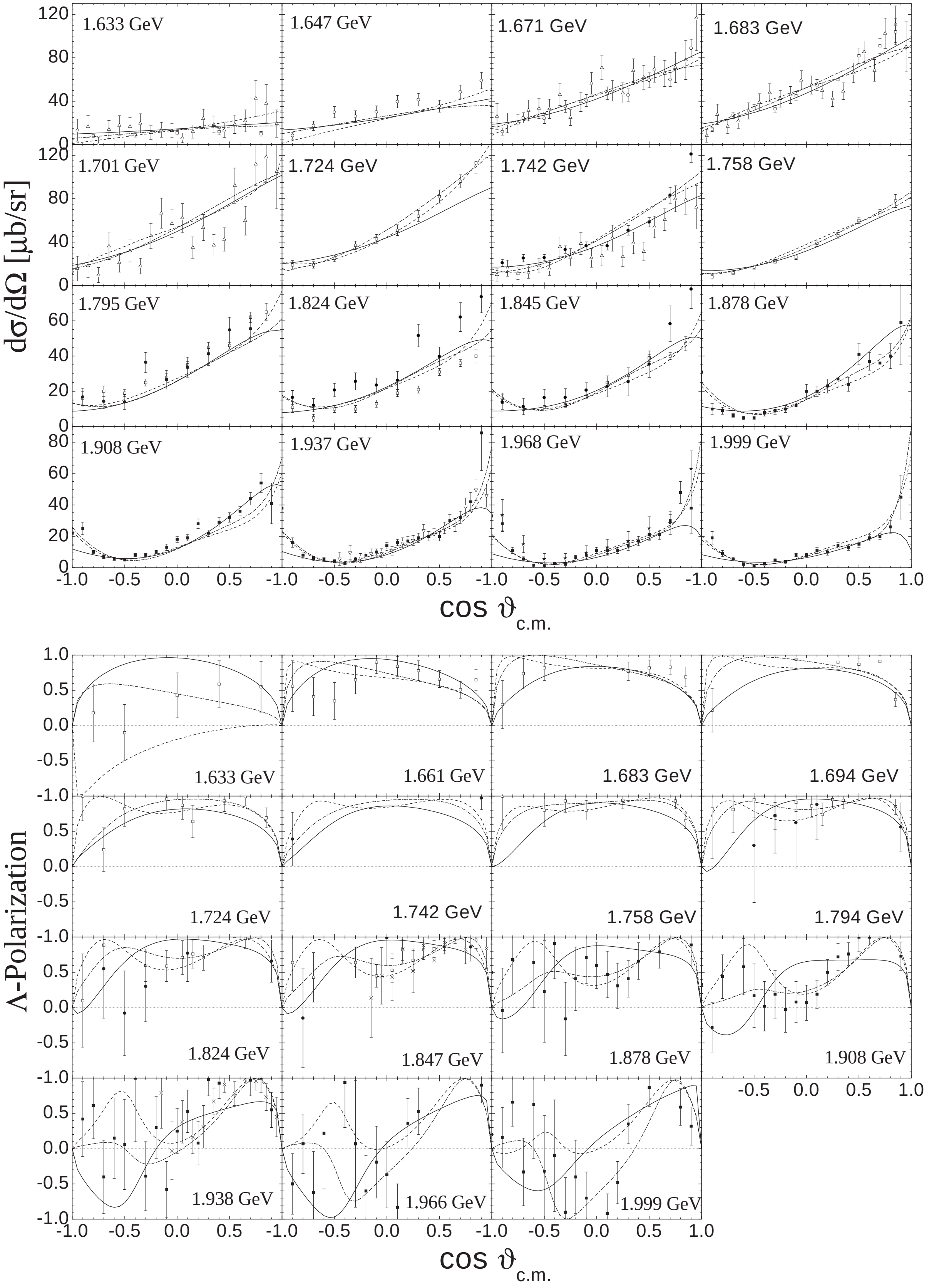

Figure 8.11: $\pi^- p \rightarrow K^0\Lambda$ angle-differential cross sections (*upper panel*) and polarization measurements (*lower panel*). Data are from [288] (□), [294] (△), [290] (○), [291] (●), [295] (■), [293] ($\star$), [289] (×). Notation as in Fig. 8.3.

Fit	Total $\chi^2_{\pi\Sigma}$	$\chi^2(\pi^- p \to K^0\Sigma^0)$	$\chi^2(\pi^- p \to K^+\Sigma^-)$	$\chi^2(\pi^+ p \to K^+\Sigma^+)$
C-p-$\pi+$	1.97	2.14	1.85	1.97
C-p-$\pi-$	2.37	3.08	1.86	1.96
P-p-$\pi+$	2.93	3.34	1.67	3.01
P-p-$\pi-$	2.80	3.04	1.90	2.91
C-p-$\pi\not\chi+$	2.48	2.63	2.29	2.42
C-t-$\pi+$	2.42	3.18	1.61	2.05
C-t-$\pi-$	2.48	3.67	1.92	1.66
C-p-$\gamma+$	2.97	2.76	2.06	3.45
C-p-$\gamma-$	3.94	4.06	4.90	3.53

Table 8.2: Resulting χ^2 of the various fits for the three different charge reactions of $\pi N \to K\Sigma$.

observables, while in [51] only contributions from the $S_{11}(1650)$ and $P_{11}(1710)$ resonances were found. The improvement becomes most visible in the high energy region, where the full angular structure of the cross section and polarization of the $K\Lambda$ channel can be described, see Fig. 8.11. Especially for a description of the upward bending behavior of the differential cross section at backward angles at the highest energies, the inclusion of the $P_{13}(1900)$ turns out to be important. Note, that due to the change of the K_0^* coupling (cf. Table 8.3), the extreme forward peaking behavior of the hadronic calculations is not visible any more in the global calculation.

The polarization data hardly influence the determination of the parameters due to the large error bars, see Fig. 8.11. However, all calculations give a good description of the angular and energy dependent structure, in particular the pure positive polarization for lower energies and the change to negative values for the backward angles at higher energies.

8.1.6 $\pi N \to K\Sigma$

Due to the isospin structure of the $K\Sigma$ final state, the $\pi N \to K\Sigma$ channel is similar to πN elastic scattering. The reaction process is determined by two isospin amplitudes ($I = \frac{1}{2}$ and $I = \frac{3}{2}$), while data have been taken for the three charge reactions $\pi^+ p \to K^+\Sigma^+$, $\pi^- p \to K^0\Sigma^0$, and $\pi^- p \to K^+\Sigma^-$. Since the first reaction is purely $I = \frac{3}{2}$, it allows a stringent test of the $I = \frac{3}{2}$ (resonance) contributions in the present model, while the other two are a mixture of $I = \frac{1}{2}$ and $I = \frac{3}{2}$ contributions (see Eqs. (F.10)). Within our model it is possible to describe all three charge reactions with approximately the same quality, see Table 8.2, corroborating the isospin decomposition of the $K\Sigma$ channel in the present calculation. From the total cross section behavior, shown in Fig. 8.12, one deduces, that the threshold behavior of the reactions with $I = \frac{1}{2}$ contributions is influenced by a strong S_{11} wave, arising from the $S_{11}(1650)$ just below the $K\Sigma$ threshold, and P_{I1}-wave dominance for increasing energies, which stem from the $P_{31}(1750)$ and in particular the $P_{11}(1710)$. However, the $P_{13}(1900)$ is also visible in the $K^+\Sigma^-$ channel. In the pure $I = \frac{3}{2}$ reaction the S wave importance is largely reduced, and the P waves dominating over

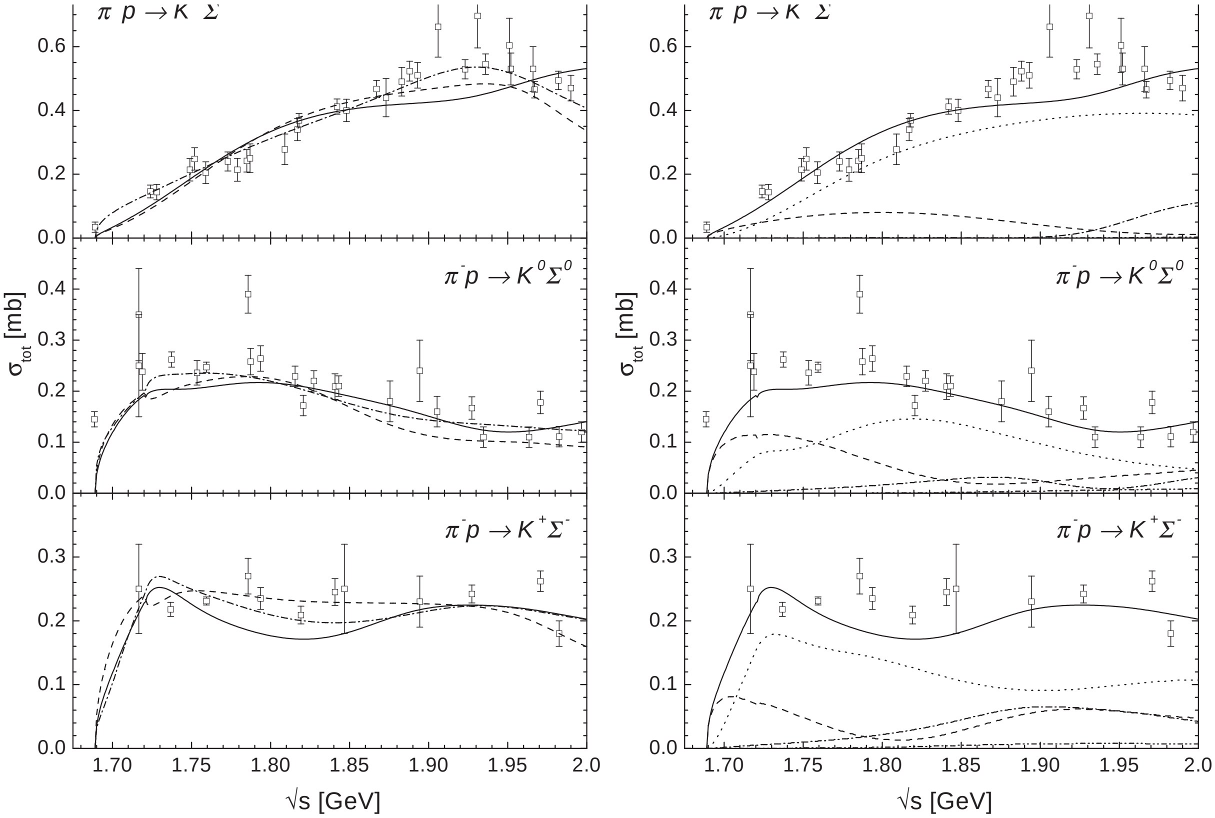

Figure 8.12: $\pi N \to K\Sigma$ total cross sections for the different charge reactions. Notation as in Fig. 8.3. For the data references, see Section 7.2.8. *Left:* Results of the different calculations. Notation as in Fig. 8.3. *Right:* Partial-wave decomposition of the total cross section for the calculation C-p-γ+. $J^P = \frac{1}{2}^-(S_{I1})$: dashed line; $\frac{1}{2}^+(P_{I1})$: dotted line; $\frac{3}{2}^+(P_{I3})$: dash-dotted line; $\frac{3}{2}^-(D_{I3})$: dash-double-dotted line. The sum of all partial waves is given by the solid line.

the complete energy range. Note, that the $J^P = \frac{3}{2}^-$ waves do not give any noticeable contribution to the cross sections, see also below. In the hadronic reactions it turns out, that the main contribution to the $I = \frac{3}{2}$ channel comes from the $P_{33}(1920)$, however, the inclusion of the photoproduction data moves this strength over to the $P_{31}(1750)$; see also Section 8.1.3 above. A similar observation is made in the $I = \frac{1}{2}$ sector, where strength is also moved over from the P_{13} to the P_{11} waves and the latter one is realized in a large $P_{11}(1710)$ $K\Sigma$ width.

These contributions result in a very good description of the differential cross sections and polarization measurements for all three reactions, see Figs. 8.13, 8.14, and 8.15. As pointed out above, the three reaction channels, which are built up by only two isospin amplitudes, allow for strong constraints on the partial wave decomposition of the $K\Sigma$ production. Within our model the full angular structure of all three charge reactions can be well described, while in the SU(3) model of [148] problems have been observed with the description of the backward peaking behavior of the angle differential $\pi^- p \to K^+\Sigma^-$ cross section at higher energies. This large difference to the other two charge reactions, who both show a forward peaking behavior in this energy range, can, however, be easily explained with the help of the t-channel meson contributions of K^* and K_0^*. Since both are $I = \frac{1}{2}$ particles, they can only contribute to $\pi^- p \to K^0\Sigma^0$ and $\pi^+ p \to K^+\Sigma^+$, but not to $K^+\Sigma^-$ production, which consequently tends to small values at forward angles. The lack of t-channel contributions also explains the good result of the calculation C-t-π+ for $\pi^- p \to K^+\Sigma^-$, where the formfactor F_t has been used, although this formfactor leads in general to worse results (see Tables 8.1 and 8.2). On the other hand, the very good result of C-t-π− for $\pi^+ p \to K^+\Sigma^+$ has to be compensated by a much worse $\pi^- p \to K^0\Sigma^0$ result.

This is also related to the observed difference between the Pascalutsa and the conventional calculations in the differential cross section of $K\Sigma$ production at higher energies. The large forward peaking behavior for higher energies in the $K^+\Sigma^+$ and $K^0\Sigma^0$ production cannot be described in the Pascalutsa calculation. Due to the lack of the spin-$\frac{3}{2}$ offshell contributions, in this calculation a larger cutoff value Λ_t is extracted, thus giving rise to more background contributions over the complete angle and energy range. At the same time, a description of the forward peaking behavior at high energies requires large couplings to the t-channel mesons, but in the Pascalutsa calculations this would spoil the agreement at backward angles and lower energies. Consequently, the most striking differences between the Pascalutsa and conventional calculations are found in the high-energy region. For more details on the t-channel formfactors and couplings, see the discussion in Sections 8.2.1 and 8.2.1.

While the polarization measurements for $\pi^- p \to K^0\Sigma^0$ hardly influence the parameter extraction due to the large error bars, the measurements for $\pi^+ p \to K^+\Sigma^+$ largely constrain the $I = \frac{3}{2}$ contributions, see Figs. 8.13 and 8.14. The change of negative to positive polarization values at forward angles with increasing energy, peaking around $\cos\vartheta \approx 0.4$ is nicely described as a result of the $P_{33}(1920)$ contribution, confirming the strong necessity of $K\Sigma$ flux in the P_{33} partial wave at higher energies. Note further, that although the contribution of the $D_{33}(1700)$ to the total cross section is negligible (cf. Fig. 8.12), it leads to the negative bump at $\cos\vartheta \approx 0.7$ in the Σ^+ polarization close to threshold, thus affirming the necessity of sub-threshold contributions. Polarization measurements of comparable quality for the reactions with isospin-$\frac{1}{2}$ contributions would be very interesting for testing

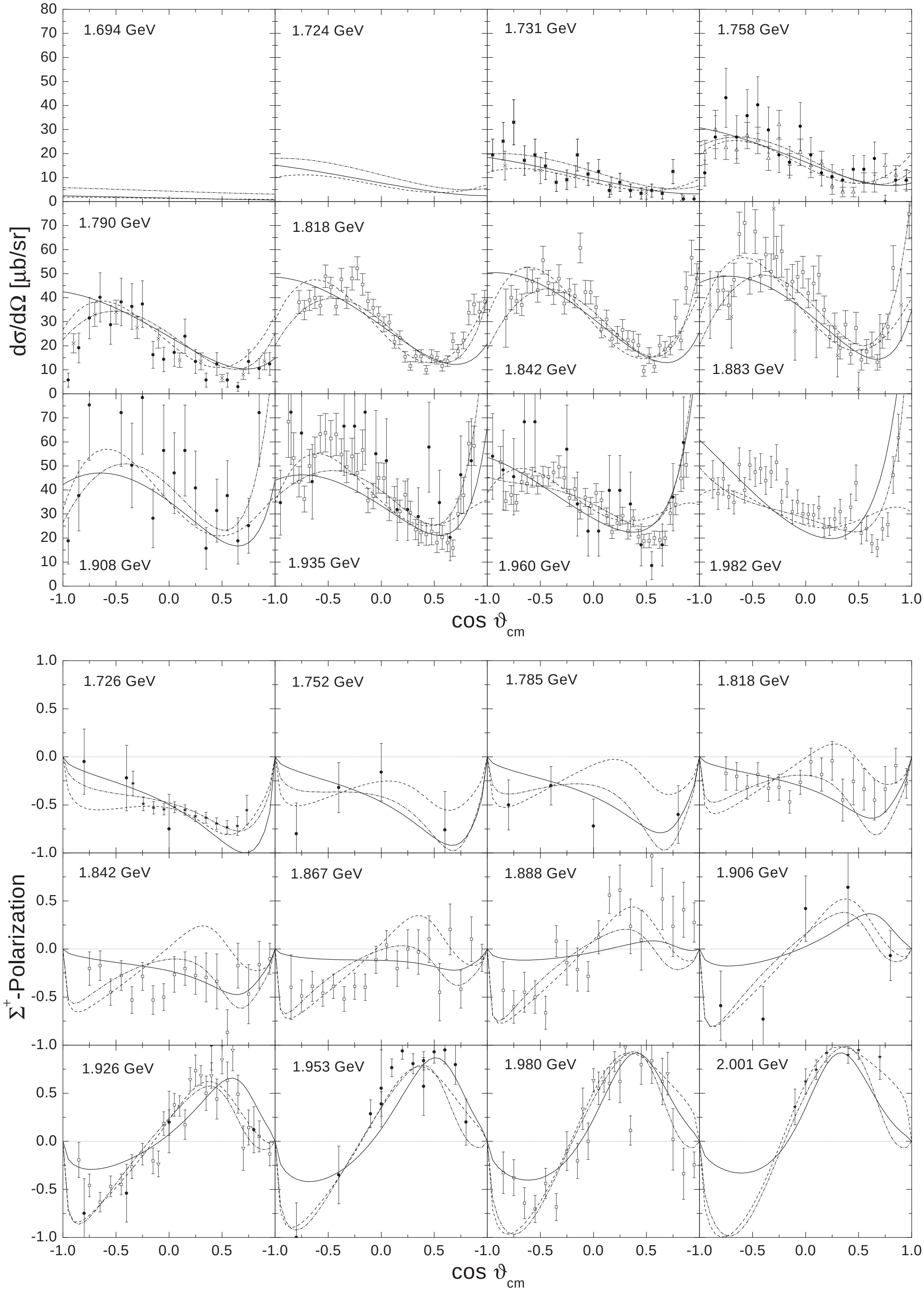

Figure 8.13: $\pi^+ p \to K^+\Sigma^+$ differential cross sections (*upper panel*) and Σ^+-polarization measurements (*lower panel*). Notation as in Fig. 8.3. Data are from [301] (□), [302] (△), [309] (●), [299] (⋆), [298] (×), [307] (▽).

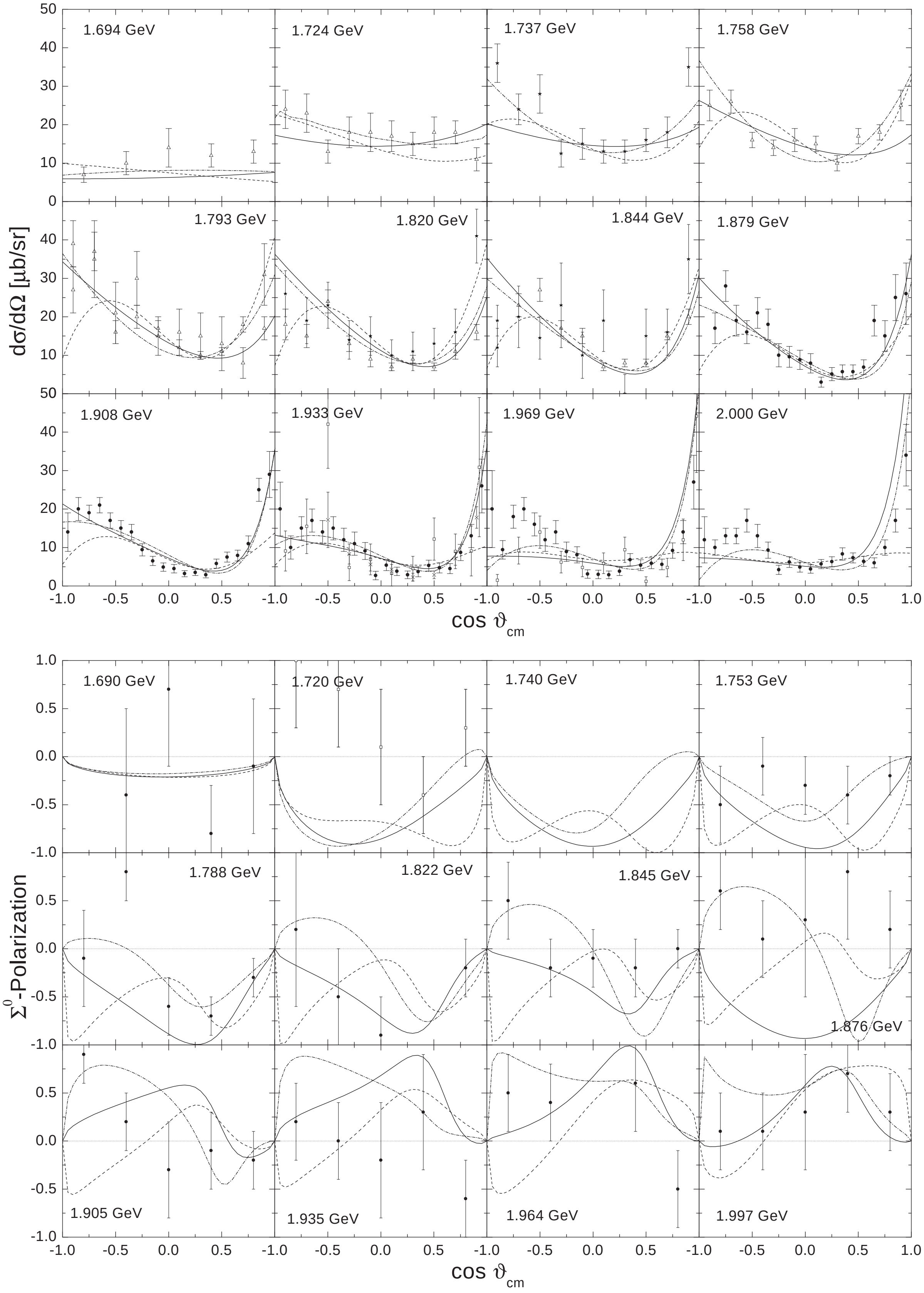

Figure 8.14: $\pi^- p \to K^0\Sigma^0$ differential cross sections (*upper panel*) and Σ^0-polarization measurements (*lower panel*). Notation as in Fig. 8.3. Data are from [303] (□), [297] (△), [308] (●), [300] (⋆), [310] (×).

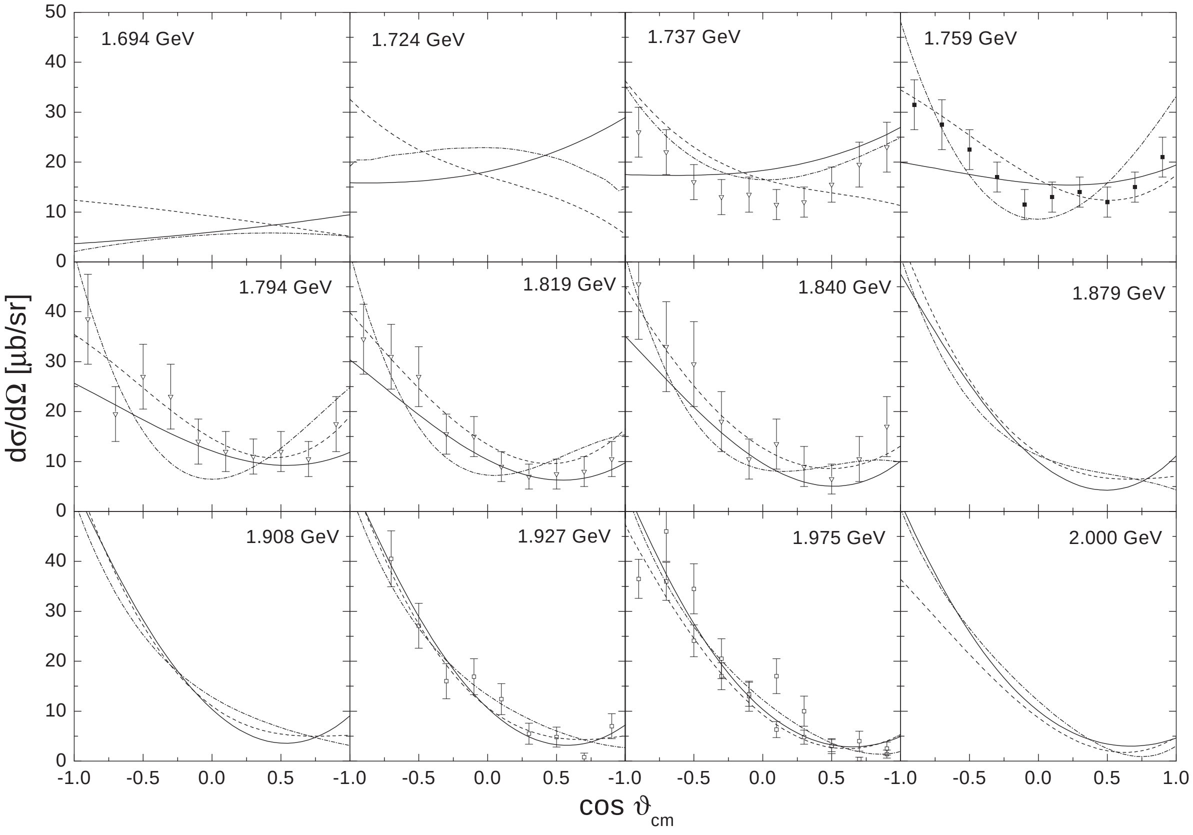

Figure 8.15: $\pi^- p \rightarrow K^+\Sigma^-$ angle-differential cross section. Notation as in Fig. 8.3. Data are from [303] (□), [305] (▽), [304] (■), [306] (○).

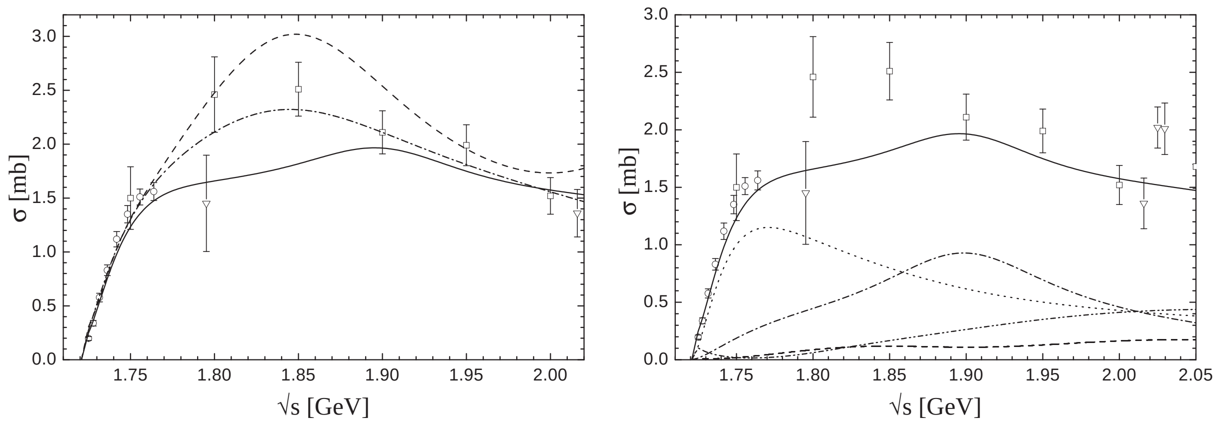

Figure 8.16: $\pi^-p \to \omega n$ total cross section. Data are from ○: [313], ▽: [105], □: [312]. *Left:* Results of different calculations. Line code as in Fig. 8.3. *Right:* Partial-wave decomposition of the total cross section. $J^P = \frac{1}{2}^-$: dashed line, $\frac{1}{2}^+$: dotted, $\frac{3}{2}^+$: dash-dotted, $\frac{3}{2}^-$: dash-double-dotted.

the importance of the various resonance contributions, since due to the large error bars, the different calculations for the polarization measurement in $\pi^-p \to K^0\Sigma^0$ result in a quite different behavior. The only common characteristic of the different calculations in the $K^0\Sigma^0$ polarization is caused by the $D_{33}(1700)$ and $P_{33}(1920)$ resonances, enforcing the change from negative polarization values at low energies to positive values at high energies in the forward region.

8.1.7 $\pi N \to \omega N$

As can be seen from Fig. 8.16 the ωN channel, which strongly influences all other reactions, cannot be completely fixed by using the pion-induced data alone. While in the hadronic calculations C-p-π+ and P-p-π+, the total cross section is dominated by a $J^P = \frac{3}{2}^-$ wave, resonating below 1.85 GeV and accompanied by a strong $\frac{3}{2}^+$ wave, this picture is changed once the much more precise ωN photoproduction data from the SAPHIR Collaboration [269] are included. In the global calculation, the $\frac{1}{2}^+$ and $\frac{3}{2}^+$ waves dominate up to energies of 2 GeV. The $P_{11}(1710)$ leads to the peaking in the $\frac{1}{2}^+$ wave around 1.76 GeV, while the $P_{13}(1900)$ gives rise to the peaking behavior of the $\frac{3}{2}^+$ contribution around 1.9 GeV, see Fig. 8.16. This decomposition leads to a slower increase of the total cross section at energies above 1.745 GeV; a property, which is also indicated by the precise Karami total cross section data [313]. This is especially interesting in comparison with the coupled-channel model of Lutz et al. [109], where $\pi N \to \omega N$ is described by a pure $\frac{3}{2}^-$ production mechanism. This is due to the fact that in the model of [109] no P wave contributions are included. These authors' findings seem to lead to an overestimation of the πN inelasticity in the $\frac{3}{2}^-$ (D_{13}) channel, which just starts overshooting the experimental data at the ωN threshold. Unfortunately, they do not compare their calculation to the angle-differential Karami cross section [313], which would allow for a further evaluation of the quality of their calculation. There has also been a single-channel analysis on

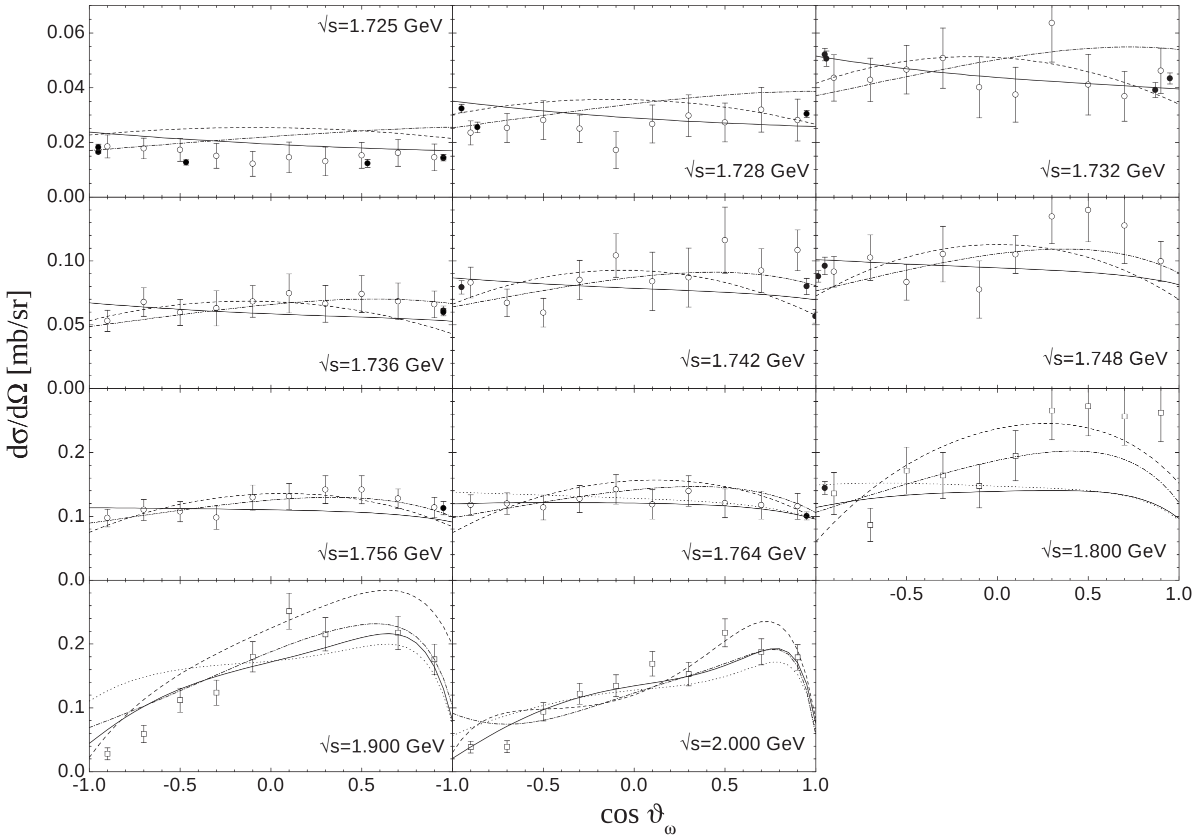

Figure 8.17: $\pi^- p \to \omega n$ angle-differential cross section. Line code as in Fig. 8.3. In addition, calculation C-p-γ+ with the ωNN couplings used in [53] are displayed for energies above 1.76 GeV (dotted line), see Section 8.2.1. Data are from ○ [313], ● [311, 314], □ [312].

$\pi N \to \omega N$ by Titov et al. [179][4]. These authors have extracted dominant contributions from the subthreshold $S_{11}(1535)$, $S_{11}(1650)$, and $P_{11}(1440)$ resonances, which only give minor contributions in the present calculation. These authors also neglected the $P_{11}(1710)$ and resonances beyond the $P_{13}(1720)$, both of which turn out to be most important in the present calculation.

This once again shows the necessity of the inclusion of photoproduction data for a reliable analysis of resonance properties, especially in channels (as the ωN production), where only few precise pion-induced data are available.

The differential cross section shows an almost flat behavior close to threshold, see Fig. 8.17, even for the global calculation dominated by P waves. To get a handle on the angle-differential structure of the cross section for higher energies ($\sqrt{s} \geq 1.8$ GeV) we have used the corrected cosine event distributions given in Ref. [312] to also extract differential cross sections with the help of the given total cross sections. While the differential cross section at forward angles is almost constant above 1.8 GeV, the backward cross section decreases.

---

[4] Note that Ref. [179] has not used the correct experimental data, but followed the claim of Ref. [73]; see Section 7.2.9.

These data points strongly constrain the nucleon u-channel contribution thereby restricting the ωNN coupling constants, and the downbending behavior is best described by the global fit. At these energies also the forward peaking behavior becomes visible which is due to the t-channel ρ meson exchange. This contribution is also the reason why the forward peaking behavior is more pronounced in the Pascalutsa calculation. Although the extracted ρNN coupling is smaller than in the other calculations, the cutoff value Λ_t (cf. Tables 8.3 and 8.4 below) is much larger than in the other calculations resulting in an effectively larger contribution, see also the discussion in Sections 8.2.1 and 8.2.1 below.

It should also be noted, that the ωN parameters are not constrained by the ωN data points alone but also greatly influenced by the πN inelasticities and cusp effects appearing in ηN, $K\Lambda$, and $K\Sigma$ production due to the ωN threshold opening. Therefore, the extracted partial-wave decomposition of $\pi N \to \omega N$ is on safe grounds, since all other channels and in particular the $\pi N \to \pi N$ partial waves and inelasticities and the pion-induced $2\pi N$ production are well described in the energy region above the ωN threshold. However, more precise cross section measurements at energies above 1.76 GeV and polarization measurements of the $\pi N \to \omega N$ production would be the perfect tool to corroborate the present findings.

8.2 Extracted Hadronic Parameters

8.2.1 Background Contributions and t-Channel Formfactors

The values of all Born and t-channel coupling constants, which have been varied during the calculation, are listed in Table 8.3. Note, that no other background parameters are used in the calculations, emphasizing the reduced freedom of the background in our model as compared to analyses driven by resonance models (see, e.g., [183]).

Born Couplings

Our values of $g_{\pi NN}$ are consistently lower than the values extracted by other groups, for example the value of $g_{\pi NN} = 13.13$ from the VPI group [277]. However, one has to keep in mind that the present calculation considers a large energy region using only one πNN coupling constant, thereby putting large constraints through all production channels on this coupling and the threshold region only plays a minor role. For example in the global fits, the πNN coupling is especially influenced by the t-channel pion exchange mechanism of ωN photoproduction, which is due to the restriction of using only one cutoff value $\Lambda_t = 0.7$ GeV for all t-channel diagrams (see Table 8.4 below).

For the other couplings of the nucleon to the pseudoscalar final state mesons, the situation in the pion-induced reactions is different. As found in previous analyses [157, 51, 53] the ηNN coupling turns out to be very small and the precise value thus hardly influences the χ^2 of ηN production. Also in $\pi N \to K\Lambda/K\Sigma$, the Born couplings are only of minor importance due to the large offshellness of the nucleon and the associated large reduction

g	value	g	value	g	value	g	value
$g_{NN\pi}$	12.85	$g_{NN\sigma}\cdot g_{\sigma\pi\pi}$	22.92	$g_{NN\rho}$	4.53	$\kappa_{NN\rho}$	1.47
	12.75		25.14		4.40		1.41
	12.77		26.88		5.59		1.51
	12.80		39.16		2.71		1.16
	13.01		13.66		2.21		1.30
$g_{NN\eta}$	0.10	g_{NNa_0}	−70.60	$g_{NN\omega}$	3.94	$\kappa_{NN\omega}$	−0.94
	0.12		−45.82		3.87		0.17
	0.06		39.56		4.06		0.48
	0.07		−2.98		3.90		0.59
	0.29		8.60		3.94		-0.90
$g_{N\Lambda K}$	−12.20	$g_{N\Lambda K_0^*}$	52.54	$g_{N\Lambda K^*}$	−27.61	$\kappa_{N\Lambda K^*}$	−0.50
	−12.88		2.32		−28.29		−0.55
	−18.48		−25.56		−27.85		−0.36
	−14.35		2.36		3.10		0.01
	−11.53		−11.58		−5.86		−0.39
$g_{N\Sigma K}$	2.48	$g_{N\Sigma K_0^*}$	−52.30	$g_{N\Sigma K^*}$	4.33	$\kappa_{N\Sigma K^*}$	−0.86
	1.56		−54.44		3.88		−0.98
	15.39		65.28		2.29		0.40
	12.44		−2.14		−4.22		−0.33
	2.50		11.06		0.71		−0.11
$g_{N\Lambda K_1}$	−19.20	$\kappa_{N\Lambda K_1}$	−1.83	$g_{N\Sigma K_1}$	22.80	$\kappa_{N\Sigma K_1}$	2.40
	−24.35		−1.99		23.29		2.06

Table 8.3: Nucleon and t-channel couplings. First line: C-p-$\gamma+$, 2nd line: C-p-$\gamma-$, 3rd line: C-p-$\pi+$, 4th line: P-p-$\pi+$, 5th line: C-t-$\pi+$. The values for the K_1 meson are given for the global calculations C-p-$\gamma+$ and C-p-$\gamma-$.

of its contributions by the hadronic formfactor. For example, a doubling of the $KN\Lambda/\Sigma$ coupling constants keeping all other contributions fixed leads to a worsening in χ^2 for $\pi^- p \to K^0\Sigma^0/K^+\Sigma^-$ of only about 10%, and for $\pi^- p \to K^0\Lambda$ of about 15%. This also explains, why the $NK\Sigma$ coupling extracted from the pion-induced data alone, always ends up to be large compared to SU(3) expectations. However, the situation changes drastically when the photoproduction data is included. As a result of gauge invariance, the importance of the Born diagrams is enhanced in the photoproduction reactions and allows to determine the Born couplings more reliably. The resulting relations between the Born couplings for the pseudoscalar mesons of our best global fit are actually close to SU(3) relations with $\alpha_{FD} = F/(F+D) \in [0.25; 0.41]$ (see, e.g., [42]), which is around the value of $\alpha_{FD} \approx 0.35$ predicted by the Cabibbo-theory of weak interactions and the Goldberg-Treiman relation [42].

The ωNN coupling constants, however, have more influence on the angular dependent behavior of the pion-induced reaction process than the $NK\Lambda$ and $NK\Sigma$ couplings and can therefore be better fixed already in the hadronic fits, see Table 8.3. This is a result of the nucleon u-channel contribution, which strongly influences the behavior of the angle-differential cross section in the backward direction at higher energies, and explains, why the resulting values for this coupling are very similar in all calculations. This is displayed in Fig. 8.17 in Section 8.1.7. There, we have included the results of a calculation with the parameters of C-p-γ+, where the ωNN couplings are replaced with the values used in [53]: $g_{\omega NN} = 7.98$, $\kappa_{\omega NN} = -0.12$. While for energies close to threshold (see $\sqrt{s} = 1.764$ GeV), this calculation hardly differs from C-p-γ+, a large difference can be seen for $\sqrt{s} = 1.9$ GeV at backward angles. For the energies above 1.8 GeV, one can also see an effect at forward angles, since the interference pattern between the t-channel ρ exchange and the nucleon contribution is altered. Note, that a value $g_{\omega NN} \approx 4$ is extracted in our calculations, even though the same nucleon cutoff $\Lambda_N \approx 1$ GeV (see Table 8.4 below) is used for all final states, which is in contrast to the results found in single-energy analysis (see, e.g., [179]).

t-Channel Formfactors

It is interesting to compare our value of $g_{\omega NN} \sim 4$ with, e.g., the value of 15.9 which has been extracted in the Bonn-model for nucleon-nucleon scattering [112]. In nucleon-nucleon scattering, the ω only contributes via t-channel exchange and thus its coupling is always modified by a formfactor. The actual shape of the formfactor and the kinematic region are thus of great importance for the applicability of the extracted coupling.

We have examined the influence of the formfactor shape by performing calculations with two different formfactors F_p (3.29) and F_t (3.30) for the t-channel exchanges. In [51] no significant differences in the resulting quality of the fits have been found, when either of the two formfactors has been used and consequently, in [53] only calculations using F_t have been performed. However, as Table 8.1 shows, this result is not valid any more for the extended channel space and kinematic region of the present model. The calculations C-t-$\pi\pm$, which use F_t instead of F_p as in C-p-$\pi\pm$, result in an overall description, which is worse by more than 10%, with the largest differences in the $\pi N \to \omega N$ reaction. This reaction differs from ηN, $K\Lambda$, and $K\Sigma$, which have comparable χ^2, in that respect, that in the t-channel the ρ-meson is exchanged. Since this exchange also contributes to πN elastic scattering, the combination of coupling and formfactor for the $NN\rho$ vertex is tested in two different reactions and thus in a wide kinematic region. As a result of the larger data base for πN elastic scattering, the value of $g_{\rho NN}$ is adjusted to this reaction and there is no freedom left for $\pi N \to \omega N$. Since the calculations using F_p can describe both reactions simultaneously, the formfactor shape F_p seems to be applicable to a wider kinematic region than F_t.

This finding is even fortified, when we look at the global fits. We have also tried to perform global fitting calculations using F_t in the t-channel exchange processes (C-t-$\gamma\pm$), but have not found any satisfactory parameter set for a global description in this case. Even when the fitting procedure has been reduced to the five most important final states — γN, πN, $2\pi N$, ηN, and ωN — we have found for $\gamma/\pi N \to \eta N$ χ^2s of only ≈ 5 and for $\gamma N \to \omega N$ ($\pi N \to \omega N$) of ≈ 30 (≈ 7), while pion production and Compton scattering have been only slightly worse as compared to C-p-$\gamma\pm$. The much worse description using F_t in the global fits can be explained by the fact, that for the photon-induced reactions,

Λ_N [GeV]	$\Lambda^h_{\frac{1}{2}}$ [GeV]	$\Lambda^\gamma_{\frac{1}{2}}$ [GeV]	$\Lambda^h_{\frac{3}{2}}$ [GeV]	$\Lambda^\gamma_{\frac{3}{2}}$ [GeV]	Λ^h_t [GeV]
0.96	4.00	1.69	0.97	4.30	0.70
0.96	4.30	1.59	0.96	4.30	0.70
1.16	3.64	—	1.04	—	0.70
1.17	4.30	—	1.02	—	1.80
1.11	3.80	—	1.00	—	0.70

Table 8.4: Cutoff values for the formfactors. First line: C-p-$\gamma+$, 2nd line: C-p-$\gamma-$, 3rd line: C-p-$\pi+$, 4th line: P-p-$\pi+$, 5th line: C-t-$\pi+$. The upper index h or γ denotes, whether the value is applied to a hadronic or electromagnetic vertex, while the lower one denotes the particle going off-shell, i.e. N: nucleon, $\frac{1}{2}$: spin-$\frac{1}{2}$ resonance, $\frac{3}{2}$: spin-$\frac{3}{2}$ resonance, t: t-channel meson.

the $NN\omega$ coupling now not only appears as a final state coupling, but also contributes in the production of πN and ηN. Vice versa, the πNN coupling constant is now also of great importance in ω photoproduction. Thereby, the validity of the formfactors is tested in a wide kinematical region, since in our model, many of the t-channel meson couplings contribute to several reactions and also as final state couplings (cf. Table 3.1 in Section 3.8). We conclude, that F_p is preferable over F_t for the wide kinematic region accessed in the calculations. To find satisfactory results with the formfactor F_t in the present model, it would be necessary to lift the restriction of using only one cutoff value Λ_t for all t-channel diagrams.

t-Channel Couplings

Having performed calculations with two different t-channel formfactor shapes allows us to compare those couplings, which only contribute to t-channel processes. As can be seen from Table 8.3, large differences in these couplings are found comparing the calculations with the conventional spin-$\frac{3}{2}$ couplings, with the Pascalutsa couplings, and with the use of F_t instead of F_p in the t-channel, while in the two global fits C-p-$\gamma\pm$, differing only by the sign of $g_{\omega\rho\pi}$, the couplings are almost identical. The reduction of the t-channel couplings when F_t is used is not surprising, since the formfactor shape (3.30) leads to less damping than F_p (3.29). In the case of the Pascalutsa calculations, the need for background contributions also in lower partial waves is enhanced, thereby leading to larger cutoff values Λ_t, see Table 8.4. At the same time, the corresponding couplings have to be reduced to prevent an overshooting at forward angles and higher energies as in $\pi N \rightarrow K\Sigma$, see Section 8.1.6 above. Comparing the last three lines in Table 8.4, where basically three different background models have been used, one still finds that the off-shell behavior of the nucleon and resonance contributions are similarly damped, thus leading to similar resonant structures in the three calculations C-p-$\pi+$, P-p-$\pi+$, and C-t-$\pi+$.

Thus our analysis shows, coupling constants extracted from t-channel processes strongly depend on the chosen cutoff function and cutoff value. As in the $\pi N \rightarrow \omega N$ reaction, this can in particular lead to the effect that a calculation with a smaller t-channel coupling (P-p-$\pi+$) results in larger t-channel contributions than a calculation with a smaller coupling (C-p-$\pi+$), see Fig. 8.17 above. Only when those couplings are also tested close to the on-shell point or a wide kinematic range, the applicability of the couplings and formfactors is subjected to more stringent test and the extracted values and formfactor shapes become meaningful. In the present model, this holds true for $NN\rho$ and $NN\sigma$ in πN elastic scattering, and the $NN\omega$, $NN\pi$, and $NN\eta$ couplings, where the latter three appear simultaneously in s-, u-, and t-channel processes.

Hence couplings as $g_{\omega NN}$ from, e.g., the Bonn-model [112], can only be interpreted in combination with the cutoff used **and** in the kinematic region where it has been applied to. This point has also been examined by Pearce and Jennings [139]. These authors have shown that the use of formfactors as ours as compared to the one in the Bonn potential leads to large differences in the off-shell behavior of the effective couplings.

A similar consideration as for the πNN coupling has also to be applied to the ρNN coupling. Due to the fitting of the complete energy region from threshold up to 2 GeV, the resulting ρNN coupling represents an averaged coupling which can deviate from values extracted in a restricted kinematic regime. Furthermore, the ρNN coupling is also influenced by π and η photoproduction and also pion-induced ω production. Thus, it is a priori not clear, how well the resulting coupling reproduces the KSRF relation. As pointed out in Section 3.3.2, the KSRF relation, which relates the ρ t-channel exchange to the Weinberg-Tomazawa contact term, requires a coupling of $g_{\rho NN} = 2.84$. At first sight, it seems from Table 8.3 that only in the calculations when the Pascalutsa spin-$\frac{3}{2}$ couplings is used, this relation is fulfilled. However, the only meaningful quantity entering the calculations is the product of formfactor and coupling constant. Evaluating F_p for $\Lambda_t = 1.804$ (0.705) as in calculation P-p-$\pi+$ (C-p-$\pi+$) for $q^2 = 0$ shows that $g^{eff}_{\rho NN} = g_{\rho NN} \cdot F_p(q^2 = 0) = 2.62$ (2.31) at threshold; thus both calculation result in a similar effective coupling close to the KSRF-value. Although the ρ tensor coupling $\kappa_\rho \approx 1.6$ turns out to be small compared to the empirical VMD value of 3.71, it points in the direction of the value recently extracted in a model based on a gauge formalism including ρ mesons, baryons, and pionic loop contributions [87].

It is interesting to note that the ρNN coupling constant is decreased in the global fits as compared to the purely hadronic fits, thus deviating from the KSRF relation. The reason for this behavior is related to the cutoff value Λ_N of the nucleon formfactor. It is well known that the ρ and nucleon contributions interfere in low-energy πN elastic scattering. Since the pion photoproduction multipoles $E^{p/n}_{0+}$, see Fig. 8.23 below, demand a reduced nucleon contribution at higher energies, Λ_N is decreased from 1.15 GeV for the hadronic fits to 0.95 GeV for the global fits, thereby damping this contribution. At the same time, this also affects the interference between ρ and nucleon at lower energies, leading to the necessity of simultaneously reducing the ρNN coupling. Nevertheless, the same interference as in the hadronic fits cannot be achieved and the low-energy tails of the S_{11} and P_{11} are not as well described, see Fig. 8.3 above.

As we have pointed out above, chosing the chirally symmetric $\sigma\pi\pi$ coupling leads to consistently better results in πN elastic scattering, even in the intermediate energy region.

Our final results always require a positive $g_{\sigma NN} g_{\sigma\pi\pi}$ value as in Pearce and Jennings [139][5)], which means that the σ contribution is attractive in the S waves and repulsive in the P waves. The actual value of the σ coupling strongly depends on the choice of the spin-$\frac{3}{2}$ couplings. When the Pascalutsa couplings are used, we always find a larger value for this coupling, thereby indicating the need for stronger background contributions in πN elastic scattering, see Section 8.1.1 above.

The other t-channel couplings (a_0, K^*, K_0^*, and K_1), in particular those of the scalar mesons a_0 and K_0^*, turn out to be large in almost all calculations. However, since the value of t is rather negative and thus the t-channel meson far off-shell, the effective contribution is strongly damped by the formfactor in the corresponding processes. For $K\Lambda$ and $K\Sigma$ production, we have included two t-channel processes in the pion- (K^* and K_0^*) and two in the photon-induced (K^* and K_1) reactions. In the purely hadronic fits, the differentiation between the K_0^* and K^* meson is difficult; in the global fits, however, the freedom of the relative importance of the mesons is reduced, since the K^* contributes to both the hadro- and the photoproduction reactions. Note, that the only t-channel meson which exclusively contributes to photoproduction reactions in the present model, is the K_1 meson. Although the K_1 couplings are almost identical in both calculations, we find that it only plays a minor role in $K\Lambda$ and $K\Sigma$ photoproduction; far more important are the contributions from K^* exchange (see also Sections 8.4.4 and 8.4.5).

In the case of using the Pascalutsa spin-$\frac{3}{2}$ couplings, the t-channel couplings differ significantly from the values of the other calculations. This is because the missing spin-$\frac{1}{2}$ off-shell contributions of the spin-$\frac{3}{2}$ resonances have to be compensated by other background, i.e. t-channel, contributions and thus the extracted cutoff value for the t-channel processes Λ_t becomes much larger. This also means that the t-channel contributions are not only important in the extreme forward region (low $|t|$), but rather for the complete $\cos\vartheta$ range. Consequently, very large t-channel couplings for a_0, K^*, and K_0^* would not be in line with the angle-differential observables and thus the couplings are reduced; see also the discussion about $K\Sigma$ production in Section 8.1.6.

8.2.2 Scattering Lengths

The scattering lengths and effective ranges extracted from the present analysis are in general agreement with the values obtained by other groups, see Table 8.5. For the vectormeson state ωN we follow the notation of Lutz et al. [109] for the extraction of the scattering length:

$$\bar{a}^{\frac{1}{2}} = \tfrac{1}{3}\bar{a}^{\frac{1}{2}}(J=\tfrac{1}{2}) + \tfrac{2}{3}\bar{a}^{\frac{1}{2}}(J=\tfrac{3}{2}) \tag{8.2}$$

and similarly for $\bar{r}^{\frac{1}{2}}$. The upper index denotes the isospin. The ωN helicity state combinations contributing at threshold are [109]:

$$\begin{aligned} |\omega N; J=\tfrac{1}{2}\rangle &= |\omega N, \tfrac{1}{2}; J=\tfrac{1}{2}\rangle + \tfrac{1}{\sqrt{2}}|\omega N, +0; J=\tfrac{1}{2}\rangle \\ |\omega N; J=\tfrac{3}{2}\rangle &= |\omega N, \tfrac{3}{2}; J=\tfrac{3}{2}\rangle + \tfrac{1}{\sqrt{3}}|\omega N, \tfrac{1}{2}; J=\tfrac{3}{2}\rangle + \sqrt{\tfrac{2}{3}}|\omega N, +0; J=\tfrac{1}{2}\rangle\,. \end{aligned} \tag{8.3}$$

[5)] Note, that Pearce and Jennings [139] found a very large σ coupling of $g_{\sigma NN} g_{\sigma\pi\pi} \approx 1800$.

		present	Lutz et al. [109]	Others
πN	$a^{\frac{1}{2}}$	0.197		0.246^a
	$r^{\frac{1}{2}}$	0.660		
	$a^{\frac{3}{2}}$	-0.117		-0.130^a
	$r^{\frac{3}{2}}$	18.33		
ηN	$a^{\frac{1}{2}}$	$0.991 + \mathrm{i}0.347$	$0.43 + \mathrm{i}0.21$	$0.710(30) + \mathrm{i}0.263(23)^b$
	$r^{\frac{1}{2}}$	$-2.081 - \mathrm{i}0.812$		
$K\Lambda$	$a^{\frac{1}{2}}$	$-0.154 + \mathrm{i}0.084$	$0.26 + \mathrm{i}0.10$	
	$r^{\frac{1}{2}}$	$-3.021 + \mathrm{i}0.187$		
$K\Sigma$	$a^{\frac{1}{2}}$	$-0.270 + \mathrm{i}0.172$	$-0.15 + \mathrm{i}0.09$	
	$r^{\frac{1}{2}}$	$-4.032 + \mathrm{i}2.064$		
	$a^{\frac{3}{2}}$	$-0.011 + \mathrm{i}0.005$	$-0.13 + \mathrm{i}0.04$	
	$r^{\frac{3}{2}}$	$34.79 - \mathrm{i}3.561$		
ωN	$\bar{a}^{\frac{1}{2}}(J = \frac{1}{2})$	$-1.093 + \mathrm{i}0.958$	$-0.45 + \mathrm{i}0.31$	
	$\bar{r}^{\frac{1}{2}}(J = \frac{1}{2})$	$-0.001 + \mathrm{i}7.765$		
	$\bar{a}^{\frac{1}{2}}(J = \frac{3}{2})$	$-0.228 + \mathrm{i}0.621$	$-0.43 + \mathrm{i}0.15$	
	$\bar{r}^{\frac{1}{2}}(J = \frac{1}{2})$	$13.31 - \mathrm{i}17.11$		
	$\bar{a}^{\frac{1}{2}}$	$-0.516 + \mathrm{i}0.733$	$-0.44 + \mathrm{i}0.20$	$1.6 + \mathrm{i}0.30^c$
	$\bar{r}^{\frac{1}{2}}$	$8.873 - \mathrm{i}8.820$		

Table 8.5: Scattering length (in fm) from the present analysis in comparison with other calculations. The upper index denotes the isospin. ^{a}: [277]. ^{b}: [10]. ^{c}: [98].

The extracted scattering lengths, however, have to be taken with care, since the present analysis does not concentrate on the threshold regions of the reactions, but aims on a description of a large energy range. This can result in significant differences to well known values, as, e.g., in the πN elastic scattering, see the discussion in Sections 8.1.2 and 8.4.2. Furthermore, in particular in the ωN case, more polarization measurements are needed for a reliable determination of the exact decomposition of the production mechanism close to threshold, see Sections 8.1.7 and 8.4.6.

8.2.3 Resonance Masses and Widths

In the extension of the energy range and final state space, the inclusion of more resonances as compared to Feuster and Mosel [51, 53] has become necessary. We find striking evidence for three more resonances, which are of vital importance for a satisfactory description of all experimental data below 2 GeV: a $P_{31}(1750)$, a $P_{13}(1900)$, and a $P_{33}(1920)$, which are only rated by the PDG [67] by one star, two and three stars, respectively. Omitting one of these resonances, the calculations result in a considerably worse total χ^2 by more than 15%. We can furthermore corroborate the findings of Feuster and Mosel [51, 53], that there is a strong need for a D_{13} resonance in the energy range between 1.9 and 2 GeV.

In the global calculations, the properties of almost all considered resonances can be very

$L_{2I,2S}$	mass	Γ_{tot}	$R_{\pi N}$	$R_{2\pi N}$	$R_{K\Sigma}$
$S_{31}(1620)$	1611	196	34.3	65.7(−)	0.14^a
	1614	209	34.4	65.6(−)	0.16^a
	1612	175	36.0	64.0(−)	0.94^a
	1630	177	43.4	56.6(+)	0.48^a
$S_{31}(1900)^P$	1984	237	30.4	69.5(−)	0.1(−)
$P_{31}(1750)$	1712	660	0.8	99.1(+)	0.1(+)
	1712	626	1.0	98.9(+)	0.1(+)
	1752	632	2.3	97.2(+)	0.6(+)
	1975	676	19.5	79.4(+)	1.1(−)
$P_{33}(1232)$	1228	106	100.0	0.021(−)^b	—
	1228	107	100.0	0.040(−)^b	—
	1231	101	100.0	0.002(+)^b	—
	1230	94	100.0	0.000(+)^b	—
$P_{33}(1600)$	1667	407	13.3	86.7(+)	0.03^a
	1667	388	13.1	86.9(+)	0.05^a
	1652	273	13.7	86.3(+)	0.22^a
	1656	350	13.2	86.8(+)	0.28^a
$P_{33}(1920)$	2057	494	15.9	81.6(−)	2.4(−)
	2058	557	15.0	83.2(−)	1.8(−)
	2057	527	15.5	79.5(−)	5.0(−)
	2056	435	9.1	86.8(−)	4.1(−)
$D_{33}(1700)$	1678	591	13.9	86.1(+)	0.75^a
	1679	621	14.1	85.9(+)	0.97^a
	1680	591	13.6	86.4(+)	2.09^a
	1674	678	14.6	85.4(+)	3.68^a

Table 8.6: Properties of $I = \frac{3}{2}$ resonances considered in the present calculation. Mass and total width Γ_{tot} are given in MeV, the decay ratios R in percent of the total width. In brackets, the sign of the coupling is given (all πN couplings are chosen to be positiv). ^{P}: Only found in calculation P-p-π+. ^{a}: The coupling is given since the resonance is below threshold. ^{b}: Decay ratio in 0.1‰. 1st line: C-p-γ+, 2nd line: C-p-γ−, 3rd line: C-p-π+, 4th line: P-p-π+.

well fixed (see Tables 8.6 − 8.9), even the couplings of the sub-threshold resonances are practically identical for C-p-γ+ and C-p-γ−. The only exceptions are the $P_{11}(1710)$, $P_{13}(1900)$, and the exact decomposition of the ωN strength into the ωN helicities. Note, that the properties of the $P_{11}(1710)$ also differ largely when comparing the references given in the PDG review [67]. Moreover, Arndt et al. [6] had similar problems with fixing the $P_{11}(1710)$ properties. However, in contrast to [6], in the present calculation the properties of the $S_{11}(1535)$ can be well fixed due to the simultaneous inclusion of ηN production data.

In the K-matrix formulation the resonance properties are identified with the implemented

$L_{2I,2S}$	mass	Γ_{tot}	$R_{\pi N}$	$R_{2\pi N}$	$R_{\eta N}$	$R_{K\Lambda}$	$R_{K\Sigma}$	$R_{\omega N}$
$S_{11}(1535)$	1524	121	36.6	9.8(+)	53.6(+)	-1.28^a	0.83^a	—
	1528	137	35.6	11.2(+)	53.3(+)	-1.62^a	1.00^a	—
	1542	148	37.7	11.5(+)	50.8(+)	0.02^a	0.27^a	—
	1545	117	36.6	0.9(−)	62.6(+)	-4.46^a	0.26^a	—
$S_{11}(1650)$	1664	131	67.6	28.3(+)	1.6(−)	2.4(−)	-0.59^a	—
	1667	155	61.8	34.7(+)	0.4(−)	3.1(−)	-0.72^a	—
	1671	158	65.1	22.7(+)	5.1(−)	7.1(−)	-0.54^a	—
	1699	276	68.2	14.7(−)	3.8(+)	13.3(−)	-0.50^a	—
$P_{11}(1440)$	1512	628	57.2	42.8(+)	1.69^a	-2.70^a	0.53^a	—
	1522	709	57.1	42.9(+)	1.79^a	-6.65^a	6.78^a	—
	1490	463	61.5	38.5(+)	3.27^a	3.43^a	-1.01^a	—
	1515	639	60.6	39.4(+)	4.17^a	1.97^a	3.64^a	—
$P_{11}(1710)$	1749	445	7.4	38.5(−)	24.9(+)	3.4(+)	12.6(−)	13.4
	1755	327	21.7	12.1(−)	47.0(+)	7.4(+)	0.0(−)	11.7
	1770	430	2.0	42.7(+)	31.6(−)	0.9(+)	6.3(−)	16.4
	1701	348	8.5	25.7(−)	38.3(+)	26.3(−)	1.3(−)	—
$P_{13}(1720)$	1696	165	19.1	69.0(+)	0.1(+)	11.8(−)	0.0(−)	—
	1715	310	14.8	79.1(+)	0.4(−)	5.6(−)	0.1(−)	—
	1724	295	15.4	65.2(+)	1.2(+)	9.9(−)	7.5(−)	0.7
	1700	148	14.2	83.1(+)	0.0(+)	1.7(+)	1.0(+)	—
$P_{13}(1900)$	2003	581	14.6	42.7(−)	9.4(−)	0.1(−)	2.0(−)	31.2
	1898	664	17.9	14.7(+)	19.2(−)	0.0(+)	0.0(−)	48.1
	1962	683	19.1	58.2(−)	11.9(+)	1.9(−)	0.8(+)	8.1
	1963	694	15.7	58.2(−)	3.0(+)	0.1(+)	0.0(+)	22.9
$D_{13}(1520)$	1509	99	55.8	44.2(−)	2.0^b(+)	-0.09^a	1.13^a	—
	1510	102	55.5	44.5(−)	2.7^b(+)	-0.35^a	0.84^a	—
	1512	95	58.7	41.3(−)	3.1^b(+)	0.44^a	1.20^a	—
	1509	91	60.1	39.9(−)	2.2^b(+)	0.86^a	-3.23^a	—
$D_{13}(1700)^P$	1745	55	1.6	43.4(+)	1.7(+)	6.7(−)	1.2(−)	45.3
$D_{13}(1950)$	1946	865	12.9	67.2(+)	5.4(+)	0.0(−)	0.3(+)	14.1
	1946	852	10.7	51.3(+)	8.6(+)	0.4(−)	1.1(−)	27.9
	1946	885	16.2	49.1(+)	2.2(−)	1.2(+)	1.9(+)	29.4
	1943	573	13.3	50.8(+)	0.0(−)	2.2(−)	0.7(+)	32.9

Table 8.7: Properties of $I = \frac{1}{2}$ resonances considered in the calculation. Notation as in Table 8.6.

parameters [183], thus the given decay widths and branching ratios are calculated at the resonance mass ($\sqrt{s} = m_R$) with the help of Eqs. (E.25), (E.26), and (E.37). Since the widths are energy dependent and the $RN\phi$ vertices are modified by formfactors, the total decay widths do *not* necessarily respresent the full width at half maximum (FWHM), which can, e.g., be observed in the πN elastic partial waves.

Just as the extracted resonance masses and couplings, the spin-$\frac{3}{2}$ off-shell parameters a,

$L_{2I,2S}$	mass	Γ_{tot}	$R_{\omega N}$	$R^0_{\omega N}$	$R^{\frac{1}{2}}_{\omega N}$	$R^{\frac{3}{2}}_{\omega N}$
$S_{11}(1535)$	1524	121	—	3.64^{a1}	6.10^{a2}	—
	1528	137	—	1.77^{a1}	5.66^{a2}	—
	1542	148	—	-4.51^{a1}	-2.61^{a2}	—
	1545	117	—	2.50^{a1}	4.99^{a2}	—
$S_{11}(1650)$	1664	131	—	4.75^{a1}	-1.78^{a2}	—
	1667	155	—	3.24^{a1}	3.42^{a2}	—
	1671	158	—	-0.15^{a1}	0.00^{a2}	—
	1699	276	—	1.84^{a1}	5.35^{a2}	—
$P_{11}(1440)$	1512	628	—	-18.73^{a1}	10.14^{a2}	—
	1522	709	—	15.56^{a1}	10.82^{a2}	—
	1490	463	—	-1.55^{a1}	2.09^{a2}	—
	1515	639	—	-6.30^{a1}	3.95^{a2}	—
$P_{11}(1710)$	1749	445	13.4	0.0(−)	13.3(−)	—
	1755	327	11.7	0.0(−)	11.7(−)	—
	1770	430	16.4	10.1(−)	6.3(+)	—
	1701	348	—	5.2^{a1}	-5.3^{a2}	—
$P_{13}(1720)$	1696	165	—	-14.0^{a1}	-21.3^{a2}	5.3^{a3}
	1715	310	—	-9.4^{a1}	-15.9^{a2}	-7.5^{a3}
	1724	295	0.7	$1.5(+)^{b}$	$7.8(+)^{b}$	$62.1(+)^{b}$
	1700	148	0.0	8.8^{a1}	-2.8^{a2}	-2.8^{a3}
$P_{13}(1900)$	2003	581	31.2	0.0(−)	7.8(+)	23.4(+)
	1898	664	48.1	16.7(−)	19.3(+)	12.1(+)
	1962	683	8.1	0.9(+)	0.0(−)	7.2(+)
	1963	694	22.9	5.3(+)	0.0(+)	17.6(+)
$D_{13}(1520)$	1509	99	—	-21.33^{a1}	-7.12^{a2}	-7.71^{a3}
	1510	102	—	-11.68^{a1}	14.67^{a2}	16.32^{a3}
	1512	95	—	-13.07^{a1}	21.37^{a2}	-3.91^{a3}
	1509	91	—	-3.98^{a1}	-5.36^{a2}	7.04^{a3}
$D_{13}(1700)^{P}$	1745	55	45.3	14.2(−)	7.5(−)	23.6(−)
$D_{13}(1950)$	1946	865	14.1	13.0(+)	1.1(−)	0.0(+)
	1946	852	27.9	7.0(+)	14.7(+)	6.2(+)
	1946	885	29.4	9.8(+)	2.1(+)	17.5(+)
	1943	573	32.9	12.1(+)	0.1(+)	20.7(+)

Table 8.8: ωN helicity decay ratios of $I = \frac{1}{2}$ resonances. The total widths are given in MeV, all ratios in percent. ^{a1} (^{a2}, ^{a3}) : The coupling g_1 (g_2, g_3) is given. ^{b}: The ratio is given in 0.1‰. ^{P}: Only found in calculation P-p-π+. 1st line: C-p-γ+, 2nd line: C-p-γ−, 3rd line: C-p-π+, 4th line: P-p-π+.

given in Table 8.9, are also very similar in the two global calculations with the exception of the ωN values. Large differences only occur, when the coupling of the resonance to the final state is also largely changed, thus keeping the product $g \cdot a$ in the same range.

$L_{2I,2S}$	$a_{\pi N}$	$a_{\zeta N}$	$a_{\eta N}$	$a_{K\Lambda}$	$a_{K\Sigma}$	$a_{\omega N1}$	$a_{\omega N2}$	$a_{\omega N3}$
$P_{13}(1720)$	−0.658	0.832	−4.000	0.573	−0.473	0.679	−3.072	3.495
	−0.005	0.768	−3.999	0.018	−3.998	1.758	−4.000	2.648
	0.183	0.587	1.943	−0.625	−2.728	1.108	−3.499	−1.858
	0.258	0.726	−1.953	−0.053	—	—	—	—
$P_{13}(1900)$	−1.249	−0.457	−0.003	0.852	−3.999	2.920	0.897	−3.874
	2.123	−0.362	−1.628	−3.828	−4.000	−0.945	−3.647	−0.180
	0.205	0.437	−0.739	3.410	−3.687	2.195	0.092	1.454
	NC	—	—	—	—	—	—	—
$D_{13}(1520)$	0.872	−0.249	0.366	0.794	0.501	−2.442	−4.000	−4.000
	0.871	−0.407	0.744	1.164	0.318	0.774	−3.998	2.562
	0.861	−0.351	1.796	0.856	2.692	0.344	−0.445	−1.050
	0.819	−0.158	1.146		—	—	—	—
$D_{13}(1950)$	0.789	0.588	0.353	1.661	2.091	−0.685	−0.247	−2.000
	0.663	0.365	1.025	0.503	0.215	−0.153	−3.986	0.284
	0.966	0.668	0.211	1.019	0.663	−0.016	−0.976	−1.152
	0.924	1.387	1.016	1.116	—	—	—	—
$P_{33}(1232)$	0.222	−1.156	—	—	—	—	—	—
	0.211	−1.006	—	—	—	—	—	—
	0.233	4.000	—	—	—	—	—	—
	0.148		—	—	—	—	—	—
$P_{33}(1600)$	1.798	0.363	—	—	−3.047	—	—	—
	1.937	0.363	—	—	−4.000	—	—	—
	1.266	0.291	—	—	−0.783	—	—	—
	0.400	−0.253	—	—	—	—	—	—
$P_{33}(1920)$	−2.827	1.244	—	—	−1.762	—	—	—
	−2.492	1.111	—	—	−1.683	—	—	—
	−3.137	1.264	—	—	−1.145	—	—	—
	NC	—	—	—	—	—	—	—
$D_{33}(1700)$	−0.282	0.414	—	—	−0.156	—	—	—
	−0.288	0.413	—	—	0.001	—	—	—
	−0.220	0.425	—	—	0.473	—	—	—
	−0.181	0.867	—	—	—	—	—	—

Table 8.9: Off-shell parameters a of the spin-$\frac{3}{2}$ resonances. 1st line: C-p-$\gamma+$, 2nd line: C-p-$\gamma-$, 3rd line: C-p-$\pi+$, 4th line: SM95-pt-3 of [53]. “NC”: not considered (energy range ended at 1.9 GeV).

Note, that our values are also very close to the preferred global fit SM95-pt-3 of [53] and that the observed discrepancies can be explained by the additional resonances considered in the present calculation.

In Tables 8.10 and 8.11 we give a direct comparison of the extracted resonance properties of the best global fit C-p-$\gamma+$ with the values given by the PDG [67], extracted by Feuster

$L_{2I,2S}$	mass	Γ_{tot}	$R_{\pi N}$	$R_{2\pi N}$	$R_{K\Sigma}$
$S_{31}(1620)$	1611	196	34	66	
	1620	150	25(5)	75(5)	
	1579	153	21	79	
	1617(15)	143(42)	45(5)		
$S_{31}(1900)^P$	1984	237	30	70	0.1
	1900	200	20(10)		
	NC				
	1802(87)	48(45)	33(10)		
$P_{31}(1750)$	1712	660	1	99	0.1
	1750	300	8		
	NF				
	1721(61)	70(50)	6(9)		
$P_{31}(1910)^P$	1975	676	19	79	1.1
	1910	250	23(7)		
	NC				
	1995(12)	713(465)	29(21)		
$P_{33}(1232)$	1228	106	100	0.02^a	
	1232	120	> 99	0	
	1228	110	100		
	1234(5)	112(18)	100(1)		
$P_{33}(1600)$	1667	407	13	87	
	1600	350	18(7)	82(8)	
	1721	485	15	85	
	1687(44)	493(75)	28(5)		
$P_{33}(1920)$	2057	494	16	82	2.4
	1920	200	13(7)		
	NC				
	1889(100)	123(53)	5(4)		
$D_{33}(1700)$	1678	591	14	86	
	1700	300	15(5)	85(5)	
	1677	387	14	86	
	1732(23)	119(70)	5(1)		

Table 8.10: Properties of $I = \frac{3}{2}$ resonances for the calculation C-p-γ+ (1st line) in comparison with the values from [67] (2nd line), [53] (3rd line), and [183] (4th line). In brackets, the estimated errors are given. The mass and total width are given in MeV, the decay ratios in percent. "NC": not considered (energy range ended at 1.9 GeV). ^{a}: The decay ratio is given in 0.1‰. ^{P}: Calculation P-p-π+, see text and Tables 8.6, 8.7 above.

and Mosel [53], and extracted by the $\pi N \to \pi N/2\pi N$ analysis of Vrana et al. [183]. Note, that in some cases (e.g. $P_{11}(1710)$ mass and width, $D_{13}(1950)$ and $P_{33}(1920)$ mass, etc.) noticeable differences to the estimated values of the particle data group [67] are found.

$L_{2I,2S}$	mass	Γ_{tot}	$R_{\pi N}$	$R_{2\pi N}$	$R_{\eta N}$	$R_{K\Lambda}$	$R_{K\Sigma}$	$R_{\omega N}$
$S_{11}(1535)$	1524	121	36	10	54			
	1535	150	45(10)	6(5)	43(12)			
	1549	215	31	6	63			
	1542(3)	112(19)	35(8)					
$S_{11}(1650)$	1664	131	68	28	1.6	2.4		
	1650	150	72(17)	15(5)	6(3)	7(4)		
	1684	194	73	22	1	5		
	1689(12)	202(40)	74(2)					
$P_{11}(1440)$	1512	628	57	43				
	1440	350	65(5)	35(5)				
	1479	513	62	38				
	1479(80)	490(120)	72(5)					
$P_{11}(1710)$	1749	445	7	39	25	3.4	13	13
	1710	100	15(5)	65(25)		15(10)		
	1709	284	0	51	32	17		
	1699(65)	143(100)	27(13)					
$P_{13}(1720)$	1696	165	19	69	0.1	12	0.0	
	1720	150	15(5)	> 70		8(7)		
	1801	637	21	75	4	1		
	1716(112)	121(39)	5(5)					
$P_{13}(1900)$	2003	581	15	43	9	0.1	2.0	31
	1900	500	26	45				
	NC							
	NF							
$D_{13}(1520)$	1509	99	56	44	2.0^a			
	1520	120	55(5)	45(5)				
	1512	93	56	44	4.3^a			
	1518(3)	124(4)	63(2)					
$D_{13}(1700)^P$	1745	55	2	43	1.7	7	1.2	45
	1700	100	10(5)	90(5)		< 3		
	NF							
	1736(33)	175(133)	4(2)					
$D_{13}(1950)$	1946	865	13	67	5	0	0.3	14
	2080							
	1940	412	10	75	14	0		
	2003(18)	1070(858)	4(2)					

Table 8.11: Comparison of $I = \frac{1}{2}$ resonance properties. Notation as in Table 8.10.

In the following, the extracted resonance properties are discussed in detail for each partial wave. We refer in particular to Figs. 8.3 − 8.6 in the discussion.

Isospin-$\frac{1}{2}$ Resonances

$\mathbf{S_{11}}$:

For the two four-star resonances in this partial wave ($S_{11}(1535)$ and $S_{11}(1650)$), the parameters can be well fixed in the present model; the differences between the global and purely hadronic fit parameters are not very large. The exact properties of $S_{11}(1535)$ can, however, only be extracted in the simultaneous analysis of pion- and photon-induced data, which has already been pointed out by Feuster and Mosel [52, 53]. The second S_{11} resonance has an almost negligible ηN width, but nevertheless interferes desctructively in the $\pi N \to \eta N$ reaction with the $S_{11}(1535)$, see Section 8.1.4. In the purely hadronic fits the extracted properties of the $S_{11}(1535)$ and $S_{11}(1650)$ are very similar to the values of Vrana et al. [183] and Batinić et al. [10], who found the masses 1.542 (1.543) and 1.689 (1.668) GeV and the widths 112 (155) and 202 (209) MeV. The inclusion of the photoproduction data, however, requires the lowering of the $S_{11}(1535)$ mass and total width, in particular for a description of the E^p_{0+} multipole, cf. Fig. 8.20 below. Note, that the decay ratios of the $S_{11}(1535)$ are almost identical in the global and hadronic calculations. Furthermore, it is worth mentioning, that the $K\Lambda$ decay ratio of the $S_{11}(1650)$ is considerably lowered as compared to Feuster and Mosel [53]. This is a consequence of the fact, that in the best global calculation C-p-γ+, the $K\Lambda$ production is now explained by a dominating P_{13} mechanism, while the $S_{11}(1650)$ is only important very close to threshold, see Section 8.1.5 above.

Since in the resonance analyses of Vrana et al. [183], Batinić et al. [10], and Manley and Saleski [113] a third S_{11} has been found below 2 GeV (i.e. at 1.82, 1.705, and 1.93 GeV, resp.), we have also checked whether the inclusion of a third S_{11} below 2 GeV would improve the results. However, the fit has always decreased all partial decay widths of such a resonance to zero. Hence, we do not find any hint for a third S_{11} resonance below 2 GeV in our analysis.

$\mathbf{P_{11}}$:

The mass and width of the Roper $P_{11}(1440)$ resonance turn out to be rather large in the global fits in comparison with other analyses (note, however, the range of the width given by Vrana et al. [183]: 490±120 MeV, and that Cutcosky and Wang [33] found in analyzing the $\pi N \to \pi N$ and $\pi N \to 2\pi N$ data for the P_{11} partial wave values for the width of 661 and 545 MeV, depending on the $\pi N \to \pi N$ single energy partial wave analysis used). The reason for these large values is, that the $P_{11}(1440)$ parameters are extremely sensitive to background contributions, i.e. to the interference pattern between nucleon and ρ. Since in the global fit, the nucleon cutoff has been reduced for a better description of the $E^{p/n}_{0+}$ photoproduction multipoles (see Section 8.4.2 below), the description of the P_{11} wave (and also S_{11}) at low energies has become worth. The fit has tried to compensate this effect by increasing the $P_{11}(1440)$ mass and width. This problem might also be related to the fact, that there are hints, that the $P_{11}(1440)$ resonance is a quasi-bound σN state [102], which cannot be generated in the present K-matrix approach. The decay ratios into πN and $2\pi N$, however, turn out to be reliably determined in all calculations.

Once the photoproduction data are included, the mass of the largely inelastic $P_{11}(1710)$ resonance is fixed at around 1.75 GeV due to its important contributions to ηN and ωN; a mass, which is 40 MeV above the PDG [67] estimate. In all calculations, it turns out to have a decay ratio of more than 10% to ωN and more than 25% to ηN. The latter result has also been found by Batinić et al. [10]. The $K\Sigma$ decay ratio seems not to be well determined, since the large value of 12.6% of C-p-$\gamma+$ is not confirmed in the calculation C-p-$\gamma-$. However, also in C-p-$\gamma-$ a large P_{11} contribution to $K\Sigma$ is found, which can be seen by the increase of the $K\Sigma$ coupling constant of the $P_{11}(1440)$. Since the switch of the sign of $g_{\omega\rho\pi}$ leads to a change of sign of $\kappa_{\omega NN}$ (see Table 8.3) due to interference effects in ωN production, also the behavior of the P_{11} $K\Sigma$ wave, which reacts sensitiv on ωN rescattering, has to be altered. However, since the simultaneous description of photon- and pion-induced data is much better in the calculation C-p-$\gamma+$ (see Table 8.1), the large $P_{11}(1710)$ $K\Sigma$ decay ratio seems to be favored by the experimental data. In contrast to Feuster and Mosel [53] and the PDG [67], we find a reduced $K\Lambda$ decay ratio of the $P_{11}(1710)$, which is due to the shift of this strength to the P_{13} sector. Note that the increasing πN inelasticity of the P_{11} wave above 1.6 GeV (see Fig. 8.6) is caused by the ηN channel.

Manley and Saleski [113] have found a third P_{11} around 1.88 GeV, while Vrana et al. [183] have identified such a resonance only around 2.08 GeV, but with a huge width of more than 1 GeV, thus also having a large influence on this partial wave below 2 GeV. Therefore, we have checked the contribution of an additional P_{11} around 1.9 GeV, but just as in the S_{11} wave, its contribution is always decreased to zero in the fit, and we do not find any indication for a missing P_{11} contribution below 2 GeV.

$\mathbf{P_{13}}$:

In all calculations, the mass of the first P_{13} is well fixed between 1.695 and 1.725 GeV. We find important contributions of this resonance to $K\Lambda$ and also ωN; in the latter case although the resonance position is below threshold. In comparison to Feuster and Mosel [53] the $P_{13}(1720)$ plays a less important role in ηN (which is mainly due to the inclusion of a second P_{13}, see below), but turns out to be much more important in $K\Lambda$ production. Guided by the observation of Feuster and Mosel, that there are contributions missing in this partial wave for higher energies ($\sqrt{s} > 1.8$ GeV), we have included apart from the well established $P_{13}(1720)$ the PDG two-star $P_{13}(1900)$ resonance in the calculation. Although the mass of the second resonance cannot be well fixed in the present calculation ($1.9 \leq m_R \leq 2$ GeV), it turns out that this second resonance gives very important contributions in all pion-induced reactions – in particular the ηN, $K\Lambda$, and ωN production –, and to some minor degree also in the photoproduction reactions. The inclusion of this second P_{13} also strongly influences the properties of the $P_{13}(1720)$. As compared to [53], the $P_{13}(1720)$ ηN decay ratio and the mass are reduced. Note that the $P_{13}(1720)$ mass now turns out to be in the PDG region, in contrast to the value found in [53]. In the higher energy region ($\sqrt{s} > 1.8$ GeV), a reasonable fit to the various reactions is virtually impossible without including a second P_{13} resonance. Especially in the ωN production, the resulting χ^2 turns out to be at least 2 times worse when such a resonance is excluded. It is interesting to note, that Manley and Saleski [113] have also found a second P_{13} resonance at 1.88 GeV with a large width of about 500 MeV, a third of which has been attributed to the (effective) ωN channel.

As discussed in Section 8.1.3, we also find indications for missing flux in this partial wave, i.e. contributions of a final state which is not included in the present model (e.g. a $3\pi N$ state).

$\mathbf{D_{13}}$:
In this partial wave, we find discrepancies in the description of the lower tail of the $D_{13}(1520)$ resonance. The asymmetric behavior around the $D_{13}(1520)$ partial wave cannot be described within our model, neither in elastic πN scattering, see Fig. 8.3, nor in $\pi N \to 2\pi N$, see Fig. 8.5 (nor in the E_{2-} and M_{2-} proton and neutron multipoles, see Figs. 8.20 and 8.21 below). Even after allowing different cutoff values in the πN and the $2\pi N$ channel or using a different cutoff shape, i.e. a cutoff $F_t(q^2)$ (3.30), for this resonance, the slope of the partial wave below the $D_{13}(1520)$ resonance position cannot be reproduced, in neither channel. From the inelasticity and the $2\pi N$ production (see Figs. 8.5 and 8.6 above) one deduces, that this might be due to the description of the $2\pi N$ channel by an effective ζ meson with a fixed mass. Both the inelastic and the $2\pi N$ production cross sections rise steeper than in the present calculation. A more physical $2\pi N$ description by including $\pi\Delta$ and ρN might change this behavior because of the spectral functions of the Δ and the ρ. Furthermore, in the $J^P = \frac{3}{2}^-$ wave, the ρN and $\pi\Delta$ states can be produced in an S wave, leading to a stronger rise of the $2\pi N$ production cross section, while our ζ meson can only be produced in a P wave for $J^P = \frac{3}{2}^-$.
This is confirmed by the analyses of Manley and Saleski [113] and Vrana et al. [183], since both groups extracted a dominant $2\pi N$ S wave decay of the $D_{13}(1520)$ into ρN and $\pi\Delta$. It is also interesting to note, that the rise of the $2\pi N$ partial wave cross section in the P_{33} partial wave (see Fig. 8.5), where ρN and $\pi\Delta$ cannot be produced in an S wave, is well described in the present model. Since we have not yet included these effects in the calculation, an increase of the errors of the D_{13} $2\pi N$ partial wave cross section by 1 mb up to 1.46 GeV is introduced to prevent the calculation from putting too much weight into this shortcoming of the present model. Upcoming investigations will reveal whether the inclusion of more realistic two-pion nucleon final states, which allow for the correct partial-wave behavior and account for the spectral functions of the two-body states will resolve this problem.
Furthermore, we confirm the finding of Refs. [4, 51, 53] that there is no strong evidence – if at all – for a resonance in this partial wave between 1.7 and 1.9 GeV, see below. Moreover, we corroborate the importance of a D_{13} resonance between 1.9 and 2 GeV as in [51, 53], especially in ηN and ωN production at higher energies; although the ηN decay ratio is found to be small as compared to [53]. Due to rescattering, this resonance also gives large background contributions at higher energies in the πN elastic amplitude. It is also interesting to note, that when only the pion-induced data are considered, the importance of this resonance is even stronger in the ωN channel and becomes also visible in $K\Sigma$ production. We have checked this finding by also performing fits without this resonance, but always ended up with much higher χ^2, no matter which spin-$\frac{3}{2}$ couplings and $g_{\rho\omega\pi}$ coupling sign have been initialized. The final structure of this resonance is always very broad, having a width of more than 600 MeV. Note, that also other resonance analyses identified a very broad D_{13} resonance in this energy region: For example, Batinić et al. [10] (analyzing $\pi N \to \pi N$ for $I = \frac{1}{2}$ and $\pi N \to \eta N$) and Vrana et al. [183] (analyzing $\pi N \to \pi N$, $\pi N \to 2\pi N$, and using the results from [10]) both have found a D_{13} resonance at 2 GeV with a large width of about 1 GeV.
When we allow for another D_{13} resonance in the energy region between 1.7 and 1.9 GeV for the calculation using the conventional spin-$\frac{3}{2}$ couplings, the fit systematically decreases the resonance's width until it is only be visible via its off-shell contributions in the spin-$\frac{1}{2}$

waves. The outcome is a very narrow ($\Gamma_{tot} \leq 30$ MeV) resonance, and the best χ^2 in this situation is still worse than in the calculation when such a resonance is neglected. However, the situation is slightly different in the case when using the Pascalutsa couplings. Adding a $D_{13}(1700)$ in this case improves the overall χ^2 by about $5-10$ percent. The resulting total width is 50-55 MeV, half of which are due to $2\pi N$ and the other half due to ωN. The πN decay ratio is only about 2%, hence the resulting resonance is similarly inelastic as in the analysis of Vrana et al. [183] and Batinić et al. [10]. Since we only find small χ^2 improvements due to this resonance in the Pascalutsa calculations, the indication for a $D_{13}(1700)$ in the experimental data seems to be only weak and not of resonant nature, and can thus also be described by non-resonant contributions generated by spin-$\frac{3}{2}$ off-shell (or additional other background) contributions. It is interesting to note that the slight hump around 1.76 GeV in the imaginary part of the $\pi N \to \pi N$ partial wave is close to the ωN and $K\Sigma$ thresholds and could therefore be due to kinematic effects of these two channels.

Isospin-$\frac{3}{2}$ Resonances

In the isospin-$\frac{3}{2}$ sector, a very good agreement among the resonance parameters extracted from the different calculations can be observed, cf. Table 8.6 above. Even the inclusion of the photoproduction data basically only changes the $K\Sigma$ couplings and decay ratios.

$\mathbf{S_{31}}$:
In all our calculations, the first S_{31} resonance is found around 1.62 GeV with a width of about 175 MeV. Depending on the spin-$\frac{3}{2}$ prescription, the value for its mass is either 1.61 or 1.63 GeV, for the conventional and the Pascalutsa, resp., couplings. The former value is corroborated upon taking into account the pion-photoproduction multipoles. The $E_{0+}^{\frac{3}{2}}$ multipole helps to pin down the exact resonance properties, in particular the mass, see Fig. 8.22 below. In the global fits, the mass is fixed at 1.611 GeV, in agreement with the value of the pion-photoproduction analysis of Arndt et al. [6], but smaller than the PDG [67] value.
The particle data group [67] lists a second S_{31} resonance around 1.9 GeV with a two-star status, which has been found by Manley and Saleski [113] and Vrana et al. [183]. However, in the latter analysis, this resonance turns out to be very narrow with large uncertainties in the width: $\Gamma_{tot} = 48 \pm 45$ MeV. We have also checked the importance of such a resonance in the present model, and only found very weak indications for its existence. Upon inclusion of a second S_{31} above 1.85 GeV, the χ^2 is greatly enhanced in the πN elastic and $\pi N \to 2\pi N$ channels for the case of the conventional spin-$\frac{3}{2}$ couplings. Using the Pascalutsa spin-$\frac{3}{2}$ couplings, additional strength is needed in the S_{31} partial wave above 1.9 GeV, and thus a second S_{31} resonance improves the χ^2 slightly. The mass is found in P-p-π+ and P-p-$\pi-$ between 1.9 and 1.99 GeV, while the width is 180 to 240 MeV, about 30% of which are due to πN and the other 70% due to $2\pi N$. This shows, similarly to the $D_{13}(1700)$ case, that the indications for a second S_{31} resonance are only weak and rather of non-resonant nature. Hence the needed S_{31} strength above 1.85 GeV can also be explained easily by background contributions. Note, that Arndt et al. [4] have not found a $S_{31}(1900)$ either.

$\mathbf{P_{31}}$:

In this partial wave, the particle data group [67] lists two resonances below 2 GeV, a one-star at 1.75 GeV and a four-star at 1.91 GeV. Therefore, we have checked the importance of these two resonances, which have not been considered by Feuster and Mosel [51, 53]. As in the S_{31} partial wave, we do not find a resonance in the energy region above 1.85 GeV when using the conventional spin-$\frac{3}{2}$ couplings. Again, the inclusion of such a resonance deteriorates the χ^2 tremendously in the πN elastic and $\pi N \to 2\pi N$ channel. However, there is a strong need for a very inelastic $P_{31}(1750)$ resonance below 1.8 GeV to be able to correctly reproduce the change of slope in the real part of the πN elastic partial wave. This is in stark contrast to the four-star rating of the $P_{31}(1910)$ and the one-star rating of the $P_{31}(1750)$ PDG [67]. Only in the calculation with the Pascalutsa couplings, the P_{31} resonance moves to approximately 1.98 GeV with a broad inelastic width of around 700 MeV. But as is obvious from Fig. 8.4, this resonance can rather be seen as a compensation of missing background in the high energy region, since the high-energy tail of the P_{31} partial wave starts deviating from the data in this calculation. In the conventional coupling calculation, this additional strength is generated by spin-$\frac{3}{2}$ off-shell contributions. Thus also the indication for a $P_{31}(1910)$ is very weak in the experimental data and seems to be only of non-resonant nature. This finding is confirmed upon inclusion of the photoproduction data, which allows to additionally nail down the $P_{31}(1750)$ properties. The change of slope of the imaginary part of the $M_{1+}^{\frac{3}{2}}$ multipole (see Fig. 8.22) leads to a reduction of the P_{31} mass by about 40 MeV, while its total width and inelasticity stay about the same.

$\mathbf{P_{33}}$:

In all calculations, the extracted properties of the $P_{33}(1232)$ are almost identical. A striking difference, however, is seen in the total width extracted in the Pascalutsa calculation, which is rather low with 94 MeV. However, this value is not surprising. As a result of the additional factor s/m_Δ^2 in the amplitude (see Section 3.4.1), the effective width of the resonance is increased above the resonance position. To prevent large discrepancies with the πN partial-wave data, the width at the resonance position has to be reduced. This effect is only visible for this resonance, since the higher the resonance mass, the smaller is the variation of s/m_R^2 around the corresponding resonance position.

Besides the well fixed $P_{33}(1232)$ resonance, we can also confirm the need for a $P_{33}(1600)$ as in [51, 53], [113], and [183]. While the width and decay ratios are similar to the values of the PDG [67] and of Feuster and Mosel [53], the mass is fixed due to the $2\pi N$ production at 1.665 GeV, which is considerably higher than the PDG value, but lower than the value of Feuster and Mosel.

Furthermore, in the present calculation, there is a need for additional (πN) strength in this partial wave at higher energies, which is not generated by the implemented background. This gives rise to the necessity of the inclusion of a third P_{33}. Although its mass is fixed above 2 GeV (see Table 8.6), its resonant structure already shows up below 2 GeV, see Fig. 8.4. However, as a result of the high mass, the extracted properties of this third P_{33} resonance can only be of qualitative nature, i.e. that the resonance has a large inelastic decay fraction, and also gives important contribution in $K\Sigma$ production. The inclusion of the third P_{33} also affects the properties of the $P_{33}(1600)$. In particular, the $P_{33}(1600)$ mass is lowered in all calculations to about 1.66 GeV, as compared to the results of Feuster and Mosel, who have found in their global fit a mass of 1.72 GeV. Similarly as in the P_{13} wave, we find indications for a missing inelastic contribution of about 1 mb in the P_{33} partial wave above 1.7 GeV (cf. Fig. 8.5) in the present model, i.e. the contribution of a $3\pi N$ state as $\rho\Delta$. While the $2\pi N$ partial-wave cross section decreases to about 2 mb, the inelastic partial-wave cross section stays almost constant at 3 mb. The missing inelasticity can only be compensated in our model above 1.91, since there are no $2\pi N$ data points any more and thus inelastic strength can be shifted to the $2\pi N$ channel.

$\mathbf{D_{33}}$:
In the D_{33} partial wave, we only need one resonance below 2 GeV for a satisfying description of the experimental data. In all calculations, the resulting properties are very similar. The width is found to be about 600 MeV, 86% of which coming from the $2\pi N$ decay. Due to the $\pi N \to 2\pi N$ partial-wave cross section data, already in the hadronic fits the mass of the $D_{33}(1700)$ is well fixed between 1.675 and 1.68 GeV. This mass is confirmed in the global fit, where the resulting value of 1.678 is also in accordance with the value of 1.668 GeV of Arndt et al. [6]. Moreover, the inelasticity is in good agreement with [6] and also with Manley and Saleski [113], while Vrana et al. [183] found a much narrower ($\Gamma = 120$ MeV) and even more inelastic (95%) resonance at 1.73 GeV. Although the resonance position is just below the $K\Sigma$ threshold, it gives important contributions to pion- and photon-induced $K\Sigma$ production, see Sections 8.1.6 and 8.4.5.
As in the D_{13} case, the resulting $2\pi N$ production cross section does not rise steeply enough from 1.3 GeV up to the $D_{33}(1700)$ resonance position. For the same reasons as discussed for the $D_{13}(1520)$, this is probably due to the deficiency of the effective treatment of the $2\pi N$ final state in the present model.

8.3 Summary of Pion-Induced Results

A very good description of all pion-induced data on πN, $2\pi N$, ηN, $K\Lambda$, $K\Sigma$, and ωN with one parameter set is possible within our unitary model. This shows, that all important contributions up to 2 GeV are included and also, that the experimental data of all channels are consistent with each other. The extension of the energy range and model space has required the inclusion of additional resonances ($P_{13}(1900)$, $P_{31}(1750)$, $P_{33}(1920)$) as compared to the previous analysis of Feuster and Mosel [53], where the former two are particularly important in the production mechanisms of the higher-lying final states $K\Lambda$, $K\Sigma$, and ωN. These extensions lead to differences in the descriptions of some final states, as, e.g., the $K\Lambda$ production, which is now dominated by a $IJ^P = \frac{1}{2}\frac{3}{2}^+$ (P_{13}) in contrast to the $IJ^P = \frac{1}{2}\frac{1}{2}^+$ (P_{11}) dominance of earlier analyses [53, 113]. Since a good desciption of all channels is possible although no spin-$\frac{5}{2}$ resonances are considered in our model, this indicates, that higher-spin ($\geq \frac{5}{2}$) resonances are only of minor importance in the production of ηN, $K\Lambda$, $K\Sigma$, and ωN. This point is investigated further at present [162].

Due to the inclusion of all important final states below 2 GeV, all threshold effects are included correctly. As compared to the calculation of Feuster and Mosel [51, 53], this leads especially to an improvement of the description of the $K\Lambda$ channel, which is influenced by both, the $K\Sigma$ and the ωN thresholds. Thus, in contrast to the speculation of [51, 53], the inclusion of u-channel contributions from hyperon resonances is far less important for a good description of the associated strangeness channels $\pi N \to K\Lambda/K\Sigma$ than the correct treatment of all unitarity effects.

The effects of chiral symmetry have been checked by allowing for a chirally symmetric or a chiral symmetry breaking $\sigma\pi\pi$ coupling vertex. The chiral symmetric one has proven superior not only for the low, but also for the intermediate energy region in πN elastic scattering.

The description of the pion-induced data is also still possible, when we further reduce the freedom of our background contributions by using Pascalutsa spin-$\frac{3}{2}$ vertices instead of the conventional ones. These couplings remove the off-shell spin-$\frac{1}{2}$ contributions of the spin-$\frac{3}{2}$ resonance processes, thus reducing the background contributions in the spin-$\frac{1}{2}$ sector. This reduction automatically leads to an increase of the importance of the t-channel diagrams, resulting in a much harder cutoff value Λ_t. Thereby, the contributions of the t-channel diagrams become more important in the lower partial waves and agreement with the experimental data is achieved. However, the increase of the total χ^2 from the conventional to the Pascalutsa prescription ($2.66 \to 3.53$) shows, that indeed additional background terms are necessary for a better description of the experimental data.

As a result of the additional inclusion of the photoproduction data on all channels, the description of the pion-induced reactions becomes worse. This is not unexpected, since due to the more recent photoproduction data of high quality, the reaction process is much more constrained and thus allows for less freedom. However, the pion-induced data are still well described in a global calculation including all pion- and photon-induced data. The largest changes are observed in the $I, J = \frac{1}{2}$ (S_{11} and P_{11}) waves, where the properties of the $S_{11}(1535)$, $S_{11}(1650)$, and $P_{11}(1710)$ can be better controlled once the photoproduction data — in particular on ηN, $K\Lambda$, and ωN — are included. Differences are also found in the background ρNN coupling, which turns out to be close to the KSRF value in the hadronic calculations. The differences in the global fits can be traced back to the necessity of changing the nucleon formfactor cutoff Λ_N for the description of the pion-photoproduction multipoles, see also Section 8.4.2 below. The Born couplings extracted from the global fits are close to SU(3) values.

There are also some indications for room for improvement of the Giessen model. Assuming that the $2\pi N$ data [278] are correct, these are evidences for important additional $3\pi N$ final state contributions, which are not considered up to now, in the $J^P = \frac{3}{2}^+$ partial waves. We also find evidences for the necessity of a more correct treatment of the $2\pi N$ state in the low-energy tails of the $D_{13}(1520)$ and $D_{33}(1700)$ resonance.

The influence of the sign of $g_{\omega\rho\pi}$ can be best summarized when comparing the results of the two global calculations C-p-$\gamma+$ and C-p-$\gamma-$. Switching the sign of $g_{\omega\rho\pi}$ leads to basically the same extracted couplings and resonance parameters. The main difference is a switch of signs of some ωN couplings, i.e. $\kappa_{NN\omega}$, g_{ω_1} of the $P_{11}(1440)$, and g_{ω_2} and g_{ω_3} of the $D_{13}(1520)$, while almost all other ωN contributions are similar. This indicates that the same interference pattern between these specific contributions and the t-channel contribution is preferred in the pion-induced ωN production, while the remaining contributions are rather unaffected. Comparing the quality of the fits, there is a tendency of preferring the positive $g_{\omega\rho\pi}$ sign in line with SU(3) flavor symmetry. This becomes most obvious in the χ^2 of the ωN production channels, while all other channels remain basically unchanged. Especially the pion-induced ωN production can be much better described with the positive sign, when the photoproduction data are included.

8.4 Results on Photon-Induced Reactions

Similar to Feuster and Mosel [53] our first attempt for the inclusion of the photoproduction data in the calculation has been to keep all hadronic parameters fixed to their values obtained in the fit to the pion-induced reactions. In contrast to the findings of [53], no satisfactory description of the photoproduction reactions has been achieved with these hadronic parameters. As a consequence of the smaller data base used in [53] at most three photoproduction reactions ($\gamma N \to \gamma N$, $\gamma N \to \pi N$, $\gamma N \to \eta N$) had to be fitted simultaneously. Above 1.6 GeV, no data were available on η photoproduction.

The extended model space and data base now constrains all production mechanisms more strongly, especially for energies above 1.7 GeV, where precise photoproduction data on all reactions (besides Compton scattering) are used. Due to the lack of precise data in the high energy region for pion-induced ηN and ωN production, these production mechanisms have not been correctly decomposed in the purely hadronic calculations, thus leading to contradictions in the photoproduction reactions when the hadronic parameters are kept fixed. Moreover, as pointed out in Section 8.2.1, the Born couplings in the associated strangeness production only play a minor role in pion-induced reactions while, as a result of the gauging procedure, these contributions are enhanced in the photoproduction thus allowing for a more reliable determination of the corresponding couplings. Consequently, also the $K\Lambda/\Sigma$ photoproduction turns out to be hardly describable when the hadronic parameters are kept fixed. Only when also these parameters are allowed to vary a simultaneous description of all pion- and photon-induced reactions is possible. The results of the photoproductoin reactions are discussed in detail in the following for the two global calculations C-p-γ+ and C-p-γ−.

8.4.1 Compton Scattering

A simultaneous description of Compton scattering together with the inelastic channels is essential because this process is dominated by the electromagnetic coupling and may thus impose more stringent requirements on those. As a consequence of the new data from [203, 207, 208, 211] we have doubled the Compton scattering data base from 266 to 538 data points as compared to [53]. This means that the description of Compton scattering becomes more difficult, resulting in larger χ^2 values than in [53]. However, as Fig. 8.18 shows, our calculations are able to describe the differential cross section in the considered energy region up to $\sqrt{s} = 1.6$ GeV. Only in the intermediate energy region between 1.3 and 1.5 GeV there are indications for contributions missing in the present model. These missing contributions are due to the lack of $2\pi N$ rescattering contributions, since in the present model only resonant $2\pi N$ photoproduction mechanisms are included,

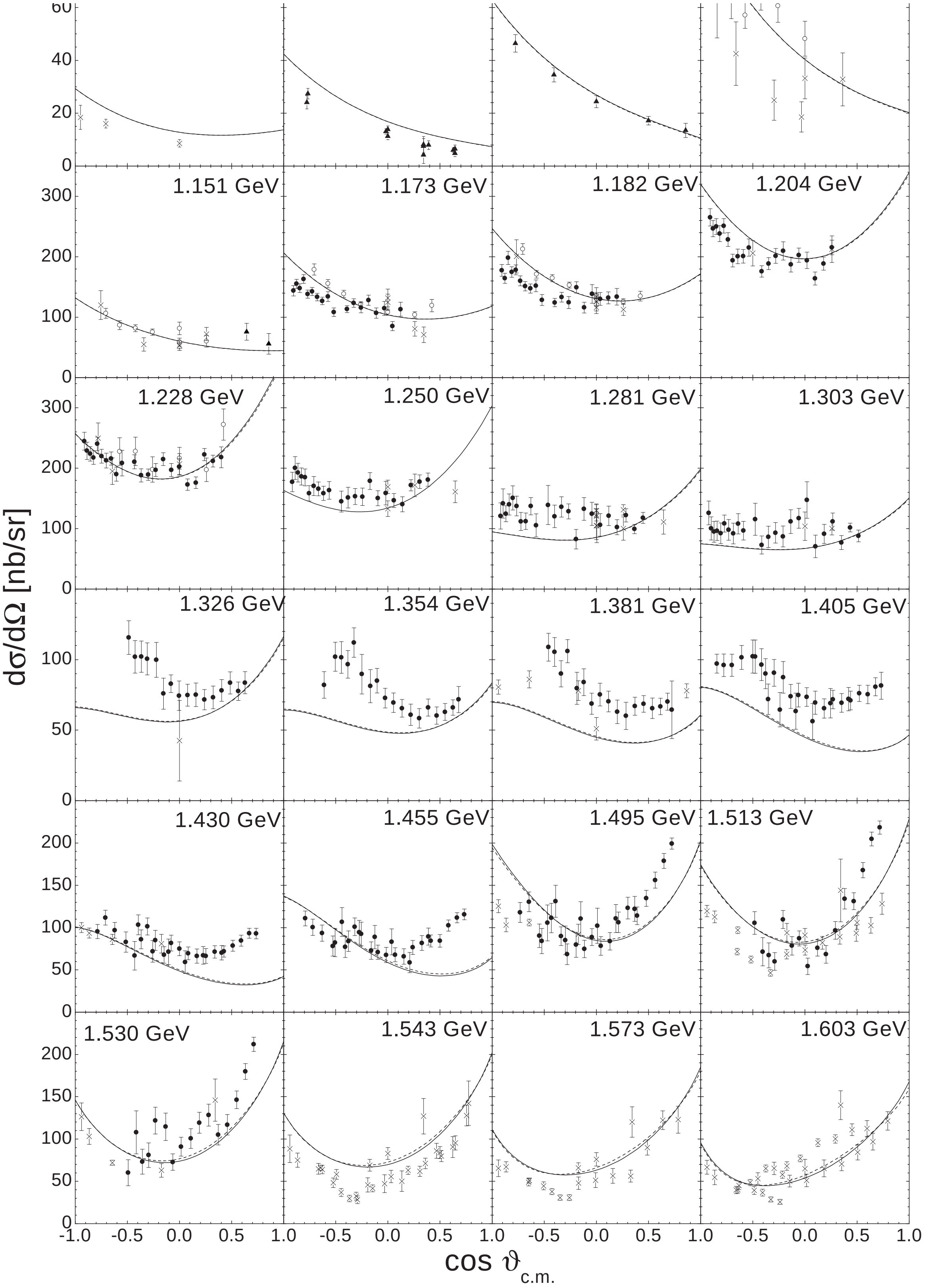

Figure 8.18: $\gamma p \to \gamma p$ differential cross section for different $\sqrt{s}$ as indicated in the figure. Calculation C-p$\gamma+$: solid line, C-p$\gamma-$: dashed line. Data are from ▲ [210], ○ [207], ● [208], × older data, see Section 7.2.1.

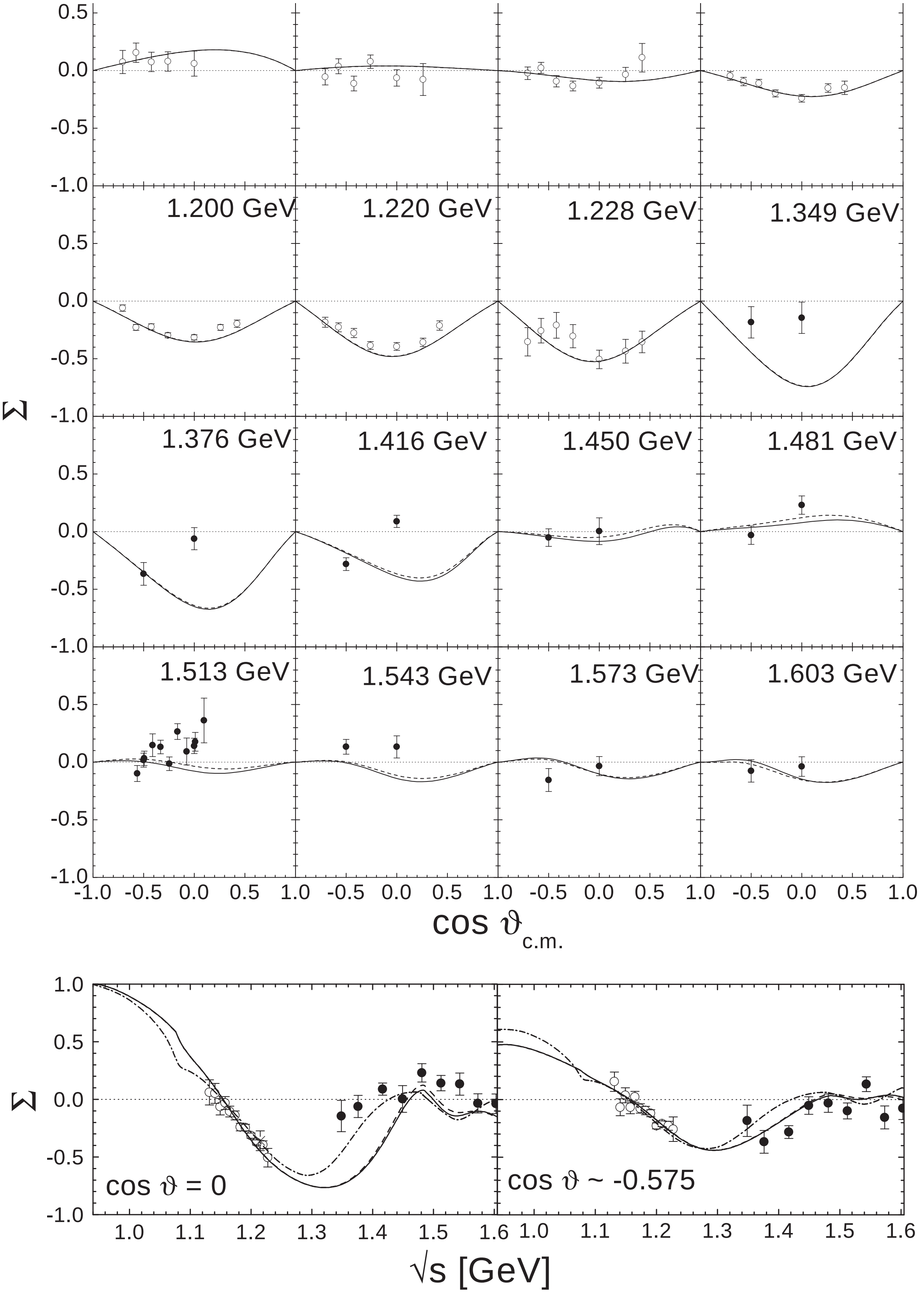

Figure 8.19: $\gamma p \rightarrow \gamma p$ differential beam polarization. Line code as in Fig. 8.18. In addition, the results of the analysis of L'vov et al. [110] are given by the dash-dotted line. Data are from ○ [207], ● [203], × [206].

see Section 7.1.2. This leads to the lack of background contributions in the low energy two-pion photoproduction, see also the discussion in Section 8.4.7 below.

The same discrepancy in this energy region can also be observed in the 90 degree region of the beam polarization, see Fig. 8.19, which is for energies below 1.3 and above 1.45 GeV and also other angles well described. For comparison, we also display the results on the beam polarization of the dispersion theoretical analysis of L'vov et al. [110]. In the model of [110], analyticity constraints are taken into account by saturating s-channel dispersion relations with use of the VPI pion-photoproduction multipole analysis and resonance photocouplings. In addition, also two-pion photoproduction background contributions have been taken into account. These authors' description of the beam asymmetry is rather close to our description, with the exception of the above mentioned energy region and the πN threshold region. This asserts the findings of Pearce and Jennings [139] (see Section 3.2), that due to the extracted soft formfactor the off-shell rescattering contributions of the intermediate two-particle propagator, which are neglected in the K-matrix approximation, have to be damped by a very soft formfactor in πN elastic scattering. Thus the effects of the off-shell rescattering part only become visible very close to the πN threshold, in line with the above comparison of the present model with the dispersion theoretical analysis of L'vov et al. [110]. The cusp in the beam polarization at the πN threshold is due to the $\mathcal{T}^{EE}_{1-}$ multipole amplitude (cf. Eq. (6.10)), which has also been found by Kondratyuk and Scholten [100].

As expected, the two global fits C-p-$\gamma\pm$ lead to practically identical results since Compton scattering is only considered up to 1.6 GeV, which is still far below ωN threshold. The slight differences between the two calculations also below 1.6 GeV can be explained by the necessity of changing resonance contributions above the ωN threshold, which also have an influence on lower energies due to their widths. The dominant contributions to Compton scattering stem from the nucleon, the $P_{33}(1232)$, and the $D_{13}(1520)$, while the $P_{11}(1440)$ and $S_{11}(1535)$ only give small contributions.

8.4.2 Pion Photoproduction

Pion photoproduction is most precisely measured of all the channels considered in the present work. This has also lead to the development of a large amount of models on this reaction (see references in [53]), most of them concentrating on the low-energy ($\Delta(1232)$) region. The Mainz MAID isobar model of Drechsel et al. [174] covers a similar energy region as the present analysis. In MAID, the Born and vector meson background contributions are K-matrix unitarized with the help of the VPI $\pi N \to \pi N$ partial waves [277]. Instead of using a formfactor for the πNN vertex, a PV-PS mixture scheme is introduced to regularize the nucleon contributions at higher energies. Since the resonance contributions are generated by unitarized Breit-Wigners, the resonances do not create additional background by u-channel diagrams. The advantage of this procedure is that the inclusion of spin-$\frac{5}{2}$ resonances is straightforward and consequently, the $F_{15}(1680)$ is also taken into account. The free parameters (e.g. the vector meson couplings) are adjusted to the VPI multipoles [221] and a very good description is achieved. As a consequence of the Breit-Wigner description and the restriction on pion photoproduction, the extracted electromagnetic helicity amplitudes of the resonances are very close to the PDG values [67], while in our analysis, all resonance contributions are also constrained by Compton scattering, η, $K\Lambda/\Sigma$, and ω photoproduction data.

As a consequence of the precise experimental data, the pion-photoproduction channel is of great importance in our data base and contains about 40% of all data points, many of which with very small error bars. Thus this channels strongly influences the photon and pion couplings and also the masses of the resonances. For example, the masses of the $S_{11}(1535)$, $S_{31}(1620)$, $P_{31}(1750)$, and $D_{33}(1700)$ are influenced by the pion-photoproduction multipoles, see Tables 8.6, 8.7 and Figs. 8.20, 8.21, 8.22. Although the resulting χ^2 seems to be rather high (~ 10), Figs. 8.20 $-$ 8.22 reveal, that the properties of almost all multipoles up to $J = \frac{3}{2}$ are well described in the present model.

The largest contributions to the total χ^2 stem from the real parts of the E^p_{1+}, E^p_{2-}, $M^{\frac{3}{2}}_{1+}$, and $E^{\frac{3}{2}}_{2-}$ multipoles. In the latter three cases, this is a consequence of the fact, that around the resonances $D_{13}(1520)$, $P_{33}(1232)$, and $D_{33}(1700)$ the multipoles are known with very high accuracy, and thus even very small deviations in the calculation lead to a large χ^2. For the $D_{13}(1520)$ multipoles $E^{p/n}_{2-}$ and M^p_{2-}, but also for the $D_{33}(1700)$ multipole $E^{\frac{3}{2}}_{2-}$, we observe in the imaginary parts the same problem of the increasing behavior below the resonance position as in the corresponding πN partial waves (see Sections 8.1.2 and 8.1.3), which is probably due to deficiencies in the present model concerning the $2\pi N$ final state description. In the case of the E^p_{1+} multipole the deviation is due to the lack of some background contribution, which might be related to the problem in the description of the πN P_{13} partial wave described above in Sections 8.1.2 and 8.1.3 due to a missing ($3\pi N$) inelastic channel. It is interesting to note that the discrepancy between the calculation and the VPI data points in the E^p_{1+} multipole starts around 1.6 GeV, which is the same energy, where the problems in the P_{13} $\pi N \to \pi N$ wave arise and also where a sudden increase in the total cross section of $\gamma p \to p\pi^+\pi^-\pi^0/n\pi^+\pi^+\pi^-$ is observed in experiments [271, 276]. For the neutron $J^P = \frac{3}{2}^+$ multipoles, there are only data of the energy-dependent solution available at energies above 1.8 GeV. Since these data are model dependent, they only enter with enlarged error bars in the present calculation, and the high-energy tails of the neutron multipoles are not well fixed. This explains the pronounced resonant structure in the imaginary part of the E^n_{1+} and M^n_{1+} multipoles, not observed in the VPI multipole data [221].

As can be seen in Figs. 8.20 $-$ 8.22, the differences between the two global calculations C-p-γ+ and C-p-$\gamma-$ can be mainly found in the $J^P = \frac{3}{2}^+$ multipoles above the ωN threshold. This is a consequence of the fact, that these multipoles give important contributions to the ωN production mechanism (see Sections 8.1.7 above and 8.4.6 below) and are thus very sensitive to the change of sign of the t-channel background contribution in $\pi N \to \omega N$.

Apart from the E^p_{1+} multipole discussed above, we find indications for missing background only in the M^n_{2-} and $M^{\frac{3}{2}}_{2-}$ multipoles, while in all other multipoles the background contributions seem to be in line with the VPI [221] analysis. Since the background is mainly generated by the Born terms, the multipoles strongly influence the nucleon cutoff value Λ_N. In Fig. 8.23 we show the sensitivity of the E^n_{0+}, M^n_{1+}, and $M^{\frac{3}{2}}_{1-}$ multipoles on the cutoff value Λ_N, which is used in the πNN formfactor. As pointed out in Section 8.1.2, the

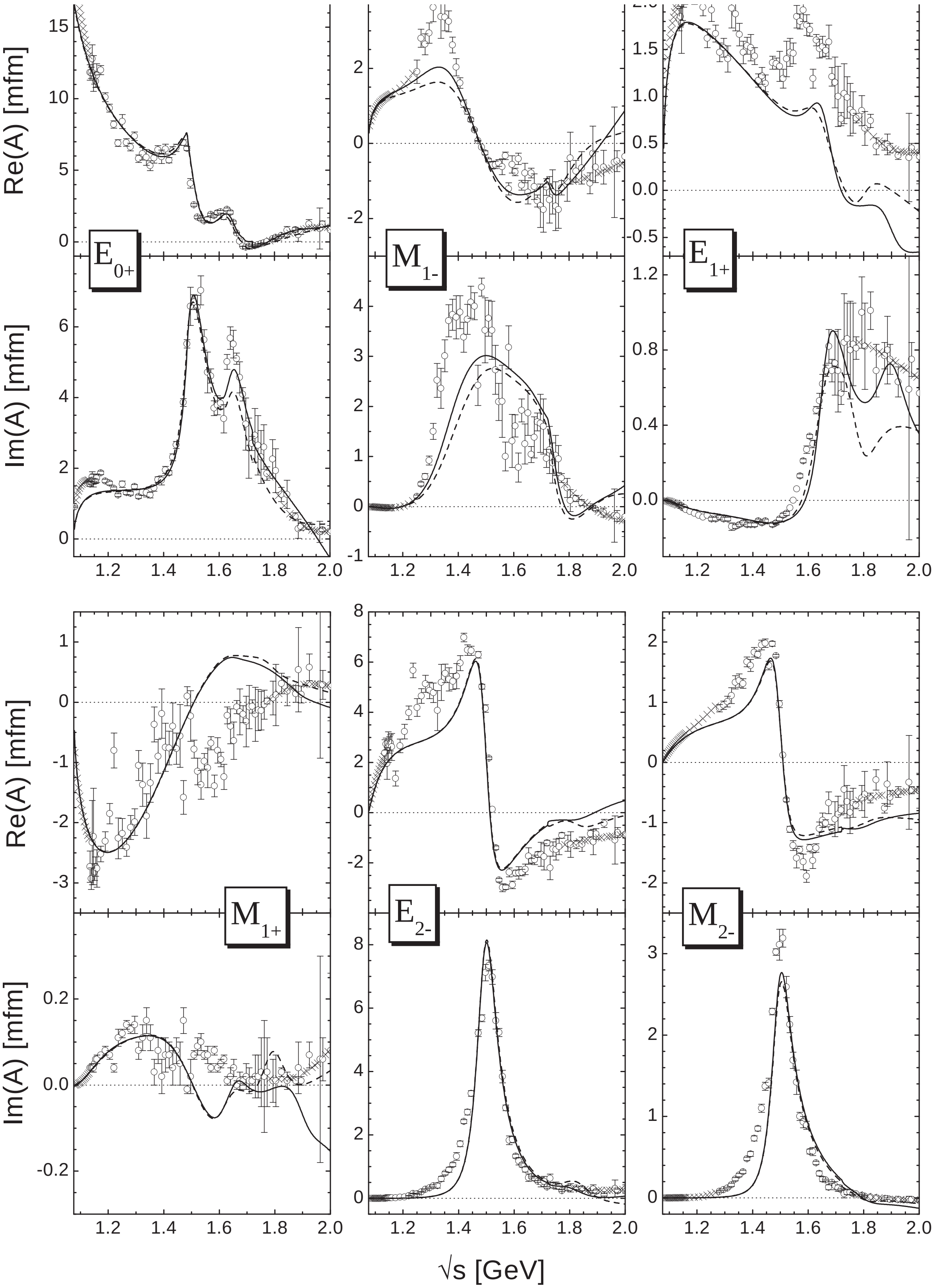

Figure 8.20: $\gamma N \rightarrow \pi N$ proton multipoles. Line code as in Fig. 8.18. Data are from the VPI [221] single-energy (○) and energy-dependent (×) solution.

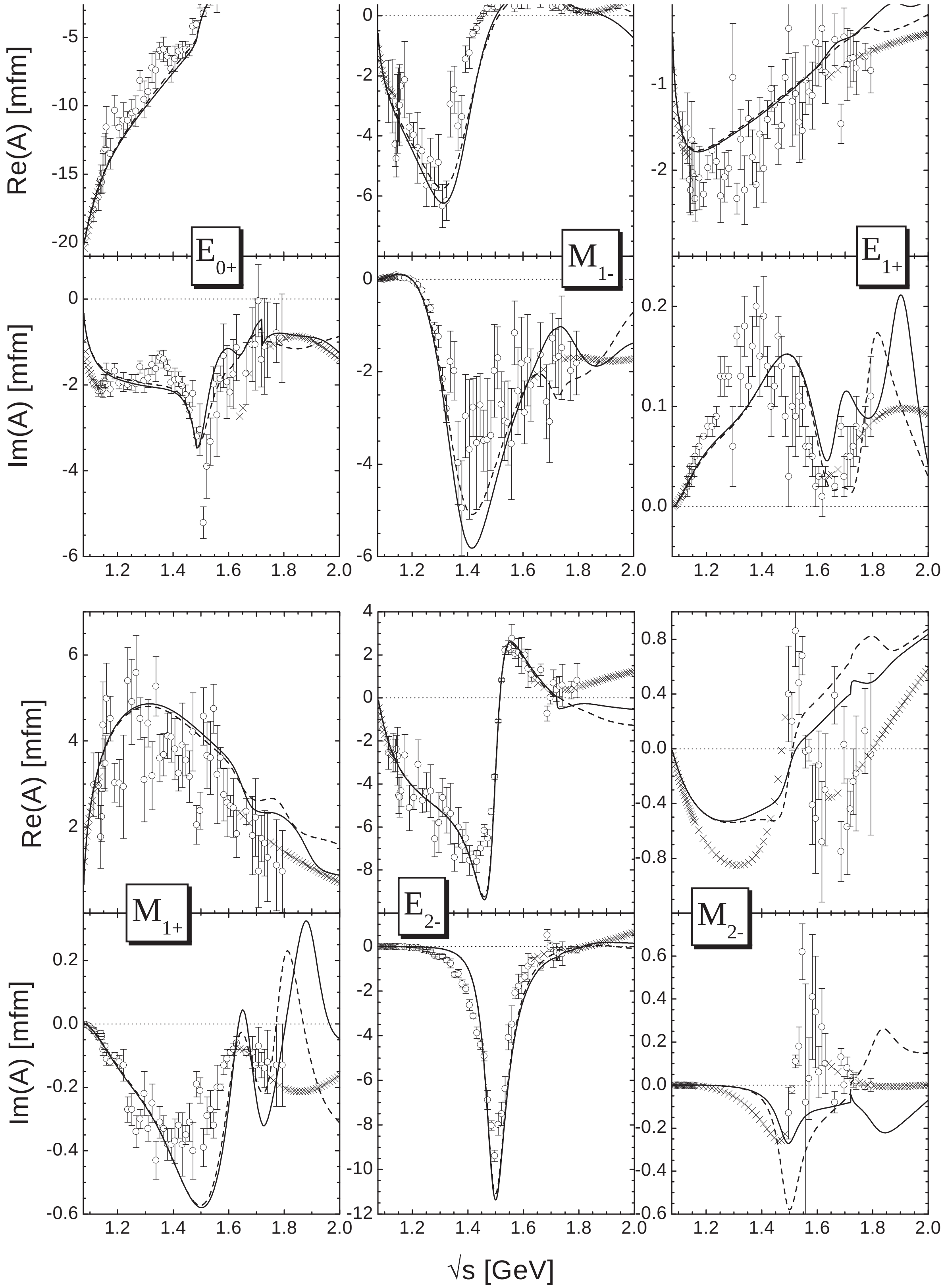

Figure 8.21: $\gamma N \to \pi N$ neutron multipoles. Line code as in Fig. 8.18, data as in Fig. 8.20.

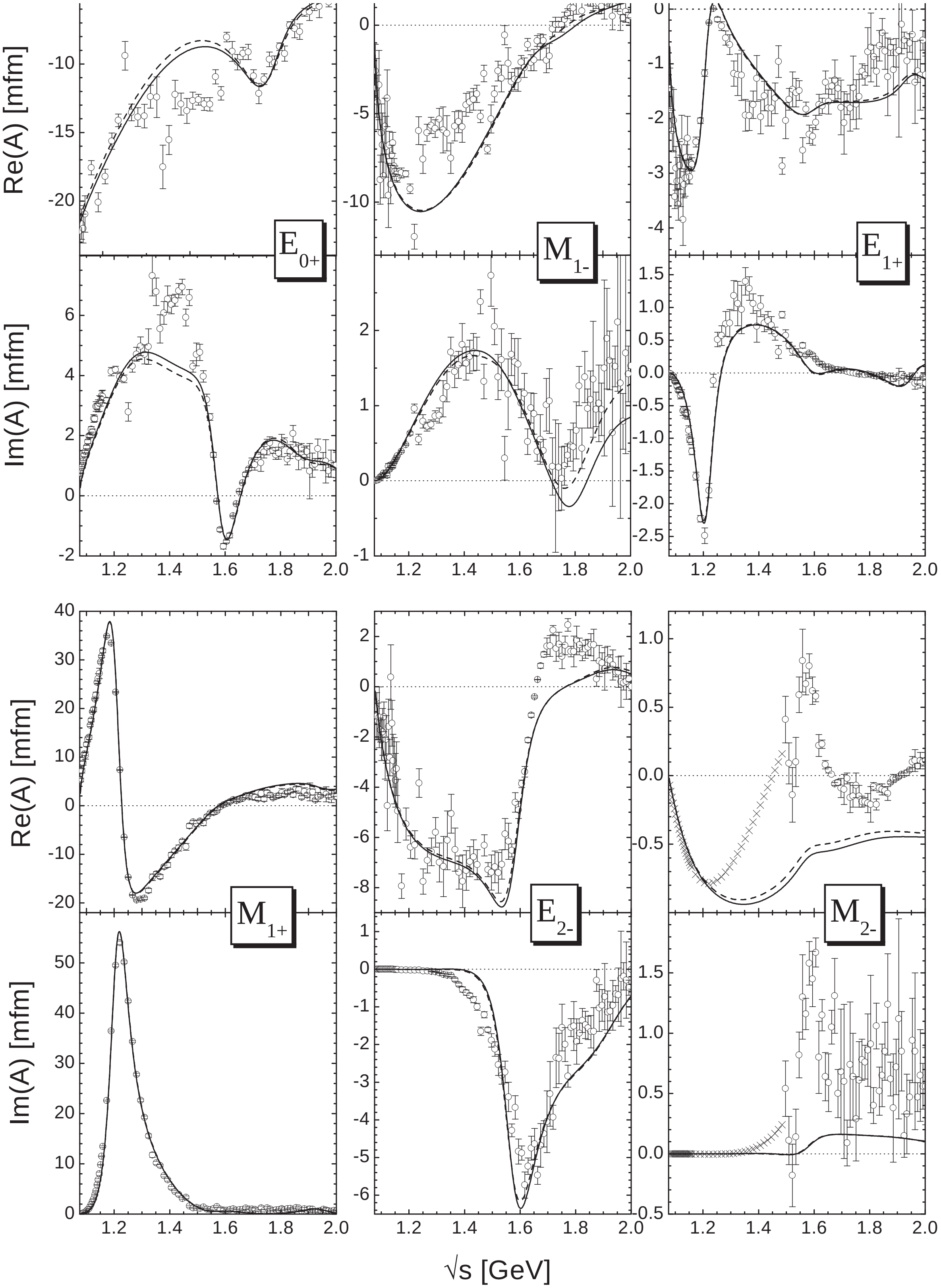

Figure 8.22: $\gamma N \to \pi N$ $I = \frac{3}{2}$ multipoles. Line code as in Fig. 8.18, data as in Fig. 8.20.

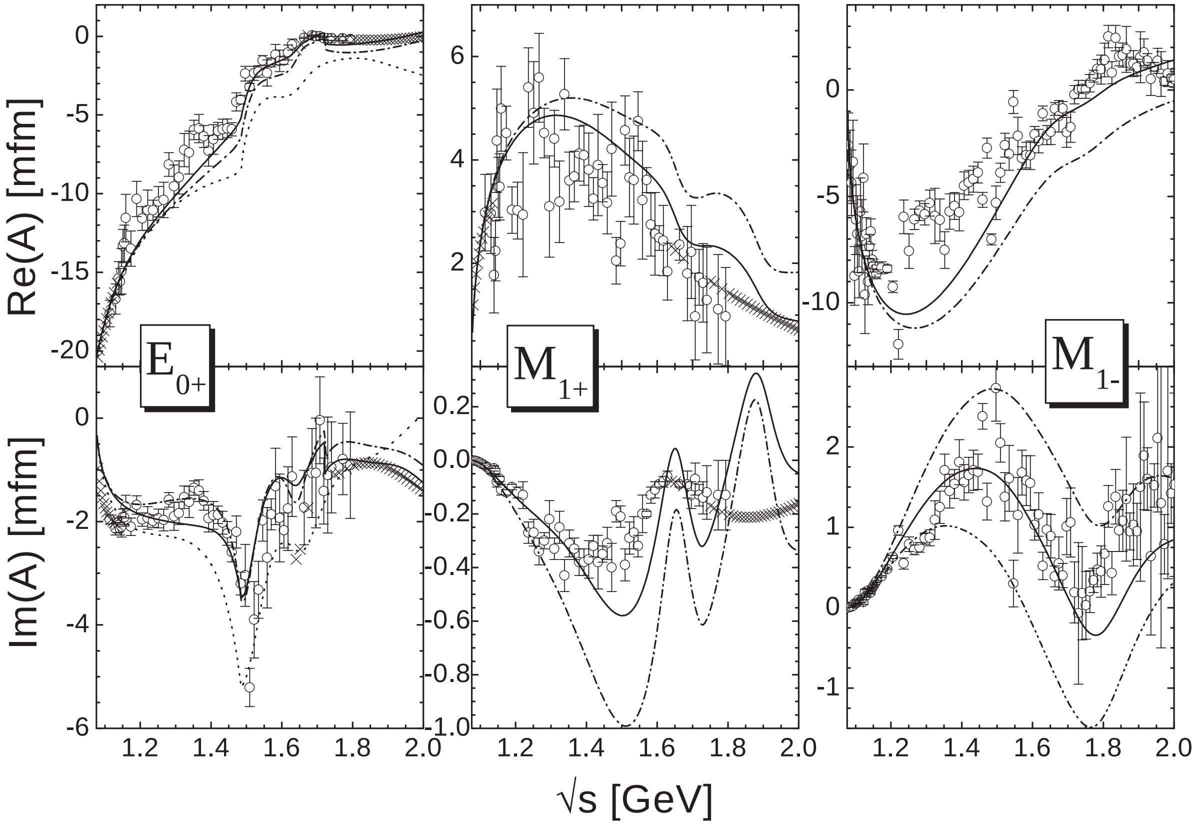

Figure 8.23: Examples for the influence of the nucleon cutoff value Λ_N on the pion-photoproduction multipoles: neutron E^n_{0+} (*left*), neutron M^n_{1+} (*middle*), $I = \frac{3}{2}$ $M^{\frac{3}{2}}_{1-}$ (*right*). C-p-γ+ with $\Lambda_N = 0.96$ GeV: solid line, C-p-γ+ with $\Lambda_N = 1.16$ GeV: dash-dotted line. For E^n_{0+}, also the calculation of [52, 53] is displayed (dotted line). For the imaginary part of $M^{\frac{3}{2}}_{1-}$, also calculation C-p-γ+ using the Haberzettl gauging procedure is shown (dash-double-dotted line).

S_{11} and P_{11} $\pi N \to \pi N$ partial waves are worsely described once the pion-photoproduction data is included. This effect can be traced back to the necessity of reducing the value of $\Lambda_N = 1.16$ GeV of the hadronic calculation to $\Lambda_N = 0.96$ GeV in the global calculation. Using the latter value, the background contributions in the multipoles are in line with the VPI analysis [221], while with the former value the incorrect background description leads to largely increased χ^2 values. The price one has to pay for the improvement in the mentioned multipoles is the deterioration in the S_{11} and P_{11} πN elastic partial waves. Since the Born terms are very sensitive to the gauging procedure, the resulting good description of most of the background features also indicates, that the Davidson-Workman gauging procedure (3.33) is supported by the pion-photoproduction data. As an example, we show the effect of switching to the Haberzettl gauging procedure (3.32) in the imaginary part of the $M_{1-}^{\frac{3}{2}}$ multipole in Fig. 8.23. Similar observations are also made in other multipoles. This is also related to the large χ^2 improvement of the present calculation as compared to [53], where the Haberzettl gauging procedure has been used. The largest differences as compared to Feuster and Mosel [53] can be observed in the real part of the $I = \frac{1}{2}$ E_{0+} multipoles, see e.g. E_{0+}^n in Fig. 8.23. Note, that it has already been speculated in [53], that modifying the gauging procedure might improve the description in these multipoles.

In the $M_{2-}^{\frac{3}{2}}$ multipole, in addition to the missing background mentioned above, also a too small resonance contribution is extracted in the present model. However, this contribution is also strongly constrained by the spin-$\frac{1}{2}$ off-shell contributions of the $D_{33}(1700)$ to the $E_{0+}^{\frac{3}{2}}$ and $M_{1-}^{\frac{3}{2}}$ multipoles. Since these multipoles are more precisely known than the $M_{2-}^{\frac{3}{2}}$, the fitting procedure is dominated by the background contributions of the $D_{33}(1700)$ in the spin-$\frac{1}{2}$ multipoles, resulting in photon couplings which deteriorate the $M_{2-}^{\frac{3}{2}}$ description.

8.4.3 η Photoproduction

Several investigations [14, 53, 157] have shown, that the ηN photoproduction is dominated by a $J^P = \frac{1}{2}^-$ production mechanism, in particular at threshold. While we find in the pion-induced reaction still important $\frac{1}{2}^+$ and $\frac{3}{2}^+$ cross-section contributions, only a small contribution of the $P_{11}(1710)$ is visible in the photon-induced reaction, and the $\frac{1}{2}^-$ contribution is by far dominant up to 2 GeV, see Fig. 8.24. Here, we have also displayed the so-called reduced cross section, which takes out effects caused by phase space and is given by $\sigma_{red} = \sqrt{\sigma_{tot}\,\mathrm{k}/(4\pi\,\mathrm{k}')}$ (cf. Appendix G), and allows for more conclusive investigations close to threshold. As can be clearly seen in Fig. 8.24, the production mechanism is well under control in the present model down to the very threshold. Thus, the energy dependence of the ηN total cross section is correctly described, although the inclusion of the pion photoproduction E_{0+}^p multipole data requires a reduction of the $S_{11}(1535)$ mass from ≈ 1.544 GeV to ≈ 1.526 GeV, see Table 8.7. Note, that our calculations do not follow the increase of the GRAAL total cross section [240] around 1.7 GeV, which is not observed in the estimated total cross section from the CLAS collaboration [230] either.

In the first coupled channel model on photon- and pion-induced ηN production up to $\sqrt{s} = 1.75$ GeV by Sauermann et al. [157], it has been found, that an important production mechanism is due to the vector meson (ρ and ω) exchanges. In line with these

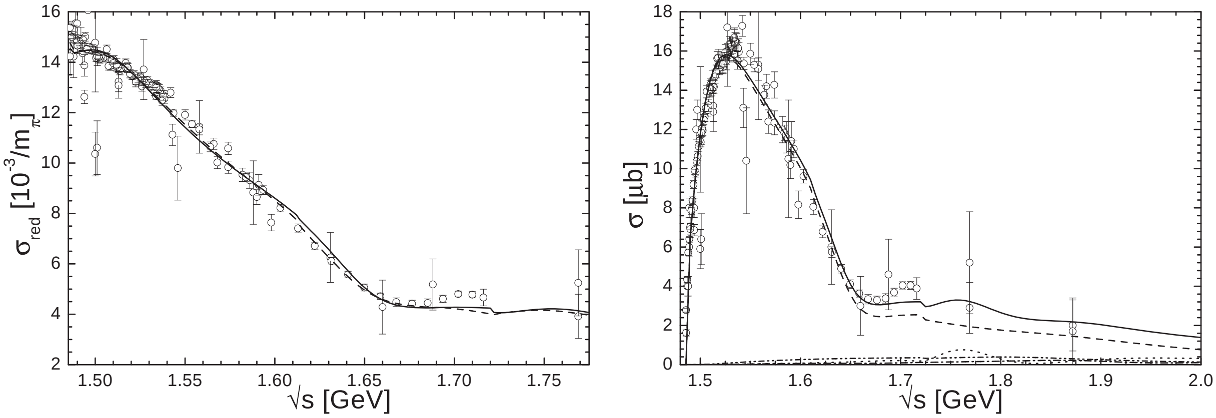

Figure 8.24: $\gamma p \rightarrow \eta p$. Data as given in Section 7.2.2. *Left:* Reduced cross section. Line code as in Fig. 8.18. *Right:* Partial-wave decomposition of the total cross section, $J^P = \frac{1}{2}^-$: dashed, $\frac{1}{2}^+$: dotted, $\frac{3}{2}^+$: dash-dotted, $\frac{3}{2}^-$: dash-double-dotted.

author's findings, it also turns out in the present model, that these exchanges give important contributions in all partial waves and the neglect would lead to total cross sections below the experimental data already at 1.55 GeV. Note, that in the present calculation the forward peaking behavior of the differential cross section at higher energies is less pronounced as compared to [53] (see Fig. 8.25), which is in line with the preliminary CLAS [230] and the older experimental data.

The resulting decomposition of the ηN photoproduction describes the differential cross sections and polarization measurements very well in the complete considered energy region, see Figs. 8.25 and 8.26. As pointed out in Section 7.2.2 prior to the differential cross section measurements of the CLAS collaboration [230], there have hardly been any measurements taken above 1.7 GeV. Consequently, the preliminary CLAS data give strong constraints on the reaction mechanism in the upper energy region, which would otherwise be mainly determined by the pion-induced ηN data being of poor quality at higher energies, cf. Section 8.1.4.

It is interesting to note, that we find a considerably smaller $D_{13}(1520)$ ηN widths than, e.g., Batinić et al. [10]. However, since the $D_{13}(1520)$ basically gives the only contribution to the low energy behavior of the beam polarization Σ [53], our value of around 20 KeV (as compared to 140 KeV) is strongly corroborated by the measurements of the GRAAL collaboration [223], since these data are very well described in the complete measured region, see Fig. 8.26. Note also, that Tiator et al. [175] have deduced from the GRAAL beam asymmetry data a $D_{13}(1520)$ ηN branching ratio of 0.8 ± 0.1‰, which is about half of our value. This is related to the fact, that in these authors' analysis, the PDG [67] electromagnetic helicity amplitudes have been used, which are larger than the ones deduced from our analysis, see Table 8.14 below. In [175] it has also been shown, that the forward-backward asymmetry of the beam polarization Σ between 1.65 and 1.7 GeV (see Fig. 8.26) can only be explained by contributions with spin $J \geq \frac{5}{2}$. Since in the present model no $J \geq \frac{5}{2}$ resonances are included, the asymmetric behavior is generated by the vector meson exchanges. Since the GRAAL data cannot be completely described

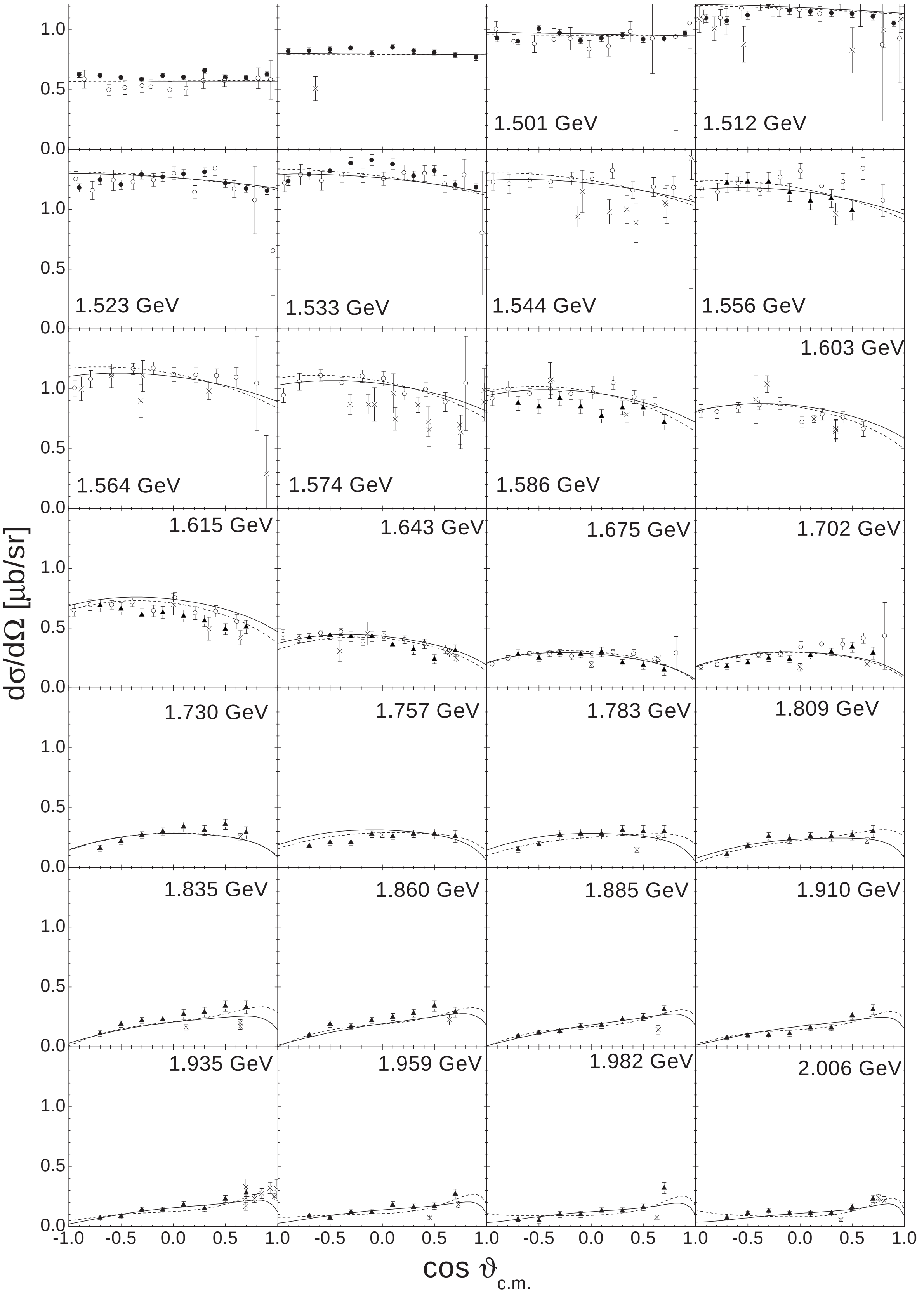

Figure 8.25: $\gamma p \to \eta p$ differential cross section. Line code as in Fig. 8.18. Data are from ● [237], ○ [240], ▲ [230], × other data (see Section 7.2.2).

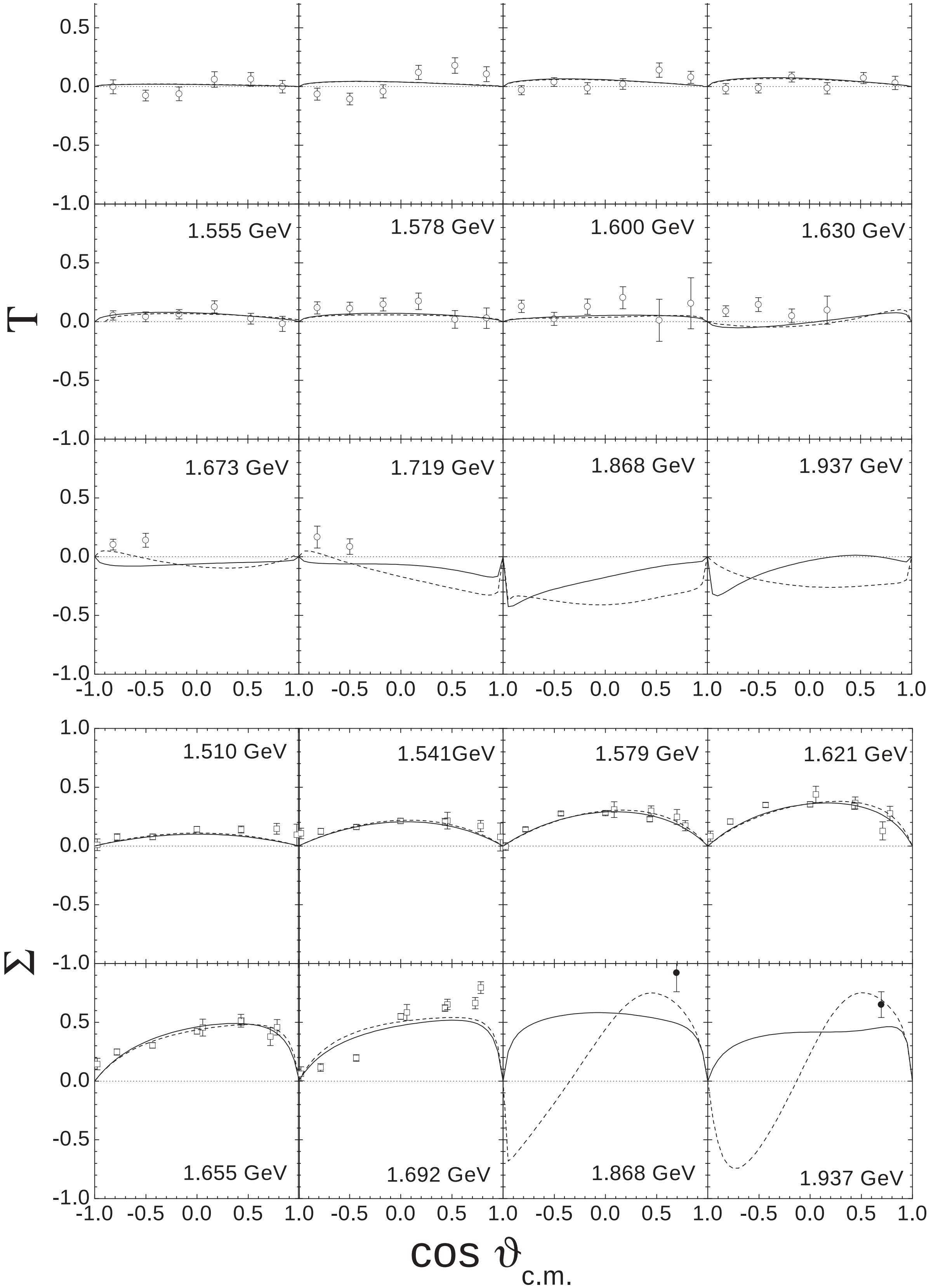

Figure 8.26: $\gamma p \to \eta p$ target- (*upper panel*) and beam- (*lower panel*) polarization measurements. Line code as in Fig. 8.18. Data are from ○ [226], □ [223], ● [241].

at 1.69 GeV, this might be an indication that spin-$\frac{5}{2}$ resonances indeed play a role in η photoproduction. At higher energies ($\sqrt{s} > 1.8$ GeV), an opposite behavior of the beam asymmetry for our two calculations at backward angles is observed. Since there are no data points, only the behavior at forward angles is fixed. The difference in the two calculations can be explained by the opposite photon helicity amplitudes of the $D_{13}(1950)$ (see Table 8.14 in Section 8.4.8 below) and the different ηN strength (see Table 8.7 in Section 8.2.3 above). Thus beam-asymmetry measurements at energies above 1.7 GeV for ηN photoproduction would be a great tool to study the properties of this "missing" resonance and also the necessity for the inclusion of a spin-$\frac{5}{2}$ resonance in more detail.

For the target polarization, we find small values in the complete energy region, see Fig. 8.26. Only in the lowest energy bins, the experimental data seem to indicate a nodal structure. Tiator et al. [175] have shown, that this behavior can only be explained by a strong energy dependence of the relative phase between the $S_{11}(1535)$ and $D_{13}(1520)$ contributions, which is not found in the present calculation. For the region above 1.6 GeV, our calculations change from positive to negative values, which seems not to be supported by the Mainz data [226] at backward angles. It turns out, that the target polarization is dominated in our calculation by the $P_{11}(1710)$ resonance properties and hence, more experimental data on the target polarization at higher energies would also help to clarify whether this resonance plays such an important role in ηN photoproduction as found in the present analysis.

8.4.4 $K\Lambda$ Photoproduction

The decomposition of the $K\Lambda$ photoproduction channel turns out to be very similar to the pion-induced reaction. In contrast to Feuster and Mosel [53], where the $S_{11}(1650)$ and the $P_{11}(1710)$ dominated this reaction, in the present calculation the former one turns out to be important only very close to threshold, while the latter one hardly gives any sizeable contribution at all, see Fig. 8.27. At low energies, the $P_{13}(1720)$ ($J^P = \frac{3}{2}^+$) resonance is dominating causing a resonant structure around 1.7 GeV. At higher energies, the $P_{13}(1900)$ gives important contributions due to rescattering in spite of its small $K\Lambda$ width. The strong $\frac{1}{2}^-$ contribution very close to threshold, which is caused by the $S_{11}(1650)$, is strongly influenced by the ωN threshold leading to a sudden increase in the total cross section. Note, that the finite width of the ω meson of 8 MeV, which is not taken into account in the present model, smears out this threshold effect. A similar observation of the feeding of $K\Lambda$ (and also $K\Sigma$, see Section 8.4.5 below) photoproduction through threshold effects has also been made in the coupled-channel model of Lutz et al. [109]. As a consequence of the inclusion of the K^* and K_1 meson exchanges, we also find important contributions to the total cross section by partial waves with $J \geq \frac{5}{2}$, cf. Fig. 8.27.

A striking difference to the pion-induced $K\Lambda$ production mechanism is observed in the $\frac{1}{2}^+$ wave, which exhibits a structure resonating around 1.9 GeV, where also a second peak is visible in the SAPHIR total cross section data [257]. However, there is no P_{11} resonance included in the present model around this energy. It turns out, that the $\frac{1}{2}^+$ behavior is caused by the interference of the nucleon and K^* contributions. Switching these two

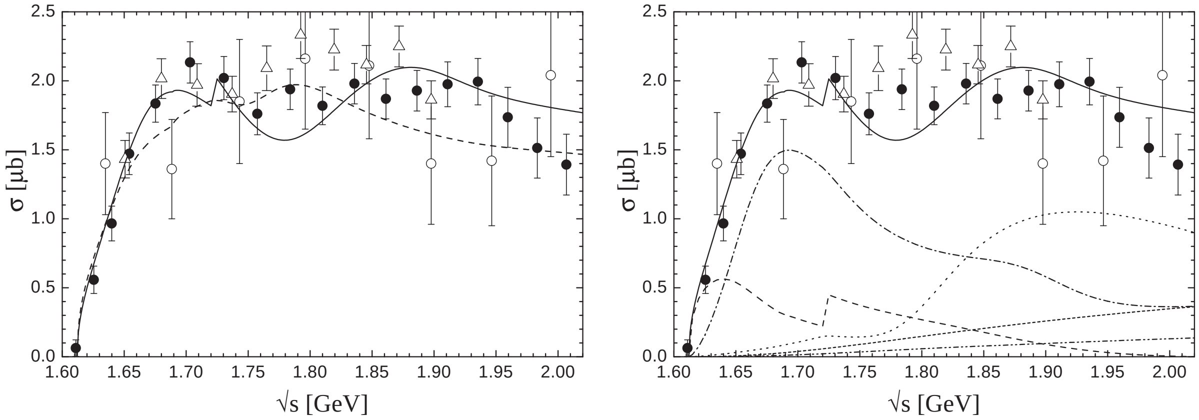

Figure 8.27: $\gamma p \to K^+\Lambda$ total cross section. Data are from ● [257], △ [244], ○ [248]. *Left:* Line code as in Fig. 8.18. *Right:* Partial-wave decomposition. Notation as in Fig. 8.24. In addition, the contribution of higher partial waves ($J \geq \frac{5}{2}$) is indicated by the short-dashed line.

contributions off leads to a $\frac{1}{2}^+$ wave, which is practically zero for energies higher than the $P_{11}(1710)$ peak. This is in contrast to the findings of the single-channel model of Mart and Bennhold [114], where the peaking behavior in the SAPHIR total cross section [257] has been explained by the same $D_{13}(1950)$ resonance, which was found by Feuster and Mosel [51, 53] around 1.9 GeV. This example emphasizes the importance of coupled-channel analyses for the correct identification of missing resonances. Although the $D_{13}(1950)$ is included in the present calculation, in the simultaneous analysis of all channels it turns out to be of negligible importance for $K\Lambda$ photoproduction. Similar results have already been found by Janssen et al. [85]. Using a field-theoretic model, these authors have deduced that the present $K\Lambda$-photoproduction data alone is insufficient to identify the exact properties of a missing resonance in a single-channel analysis on $K\Lambda$ photoproduction. Moreover, these properties also depend on the background contributions. Since in the present model, the background is uniformly generated for the various reaction channels, and pion- and photon-induced data are analyzed simultaneously, the extracted background and resonance contributions are more strongly constrained than in [114] and more reliable conclusions can be drawn.

The recoil polarization (see Fig. 8.28) is equally well described in the two global calculations C-p-γ+ and C-p-$\gamma-$, although the difference in the $g_{\omega\rho\pi}$ sign leads to changes in the P-wave resonance couplings. However, since the differential cross section displayed in Fig. 8.28 is P wave dominated, slight changes in the forward peaking and backward decrease can be seen in this observable. This different behavior is the reason for the better χ^2 value of C-p-$\gamma-$ as compared to C-p-γ+, and again shows, that $K\Lambda$ production reacts very sensitive on rescattering effects due to ωN.

As a consequence of the inclusion of the photoproduction data, the $NK\Lambda$ coupling is only reduced from -18.8 to -12.2 from the best hadronic (C-p-π+) to the best global (C-p-γ+) fit, see Table 8.3 in Section 8.2.1. Thus, in contrast to other models on $K\Lambda$ photoproduction, the resulting agreement of the present calculation with experimental data is neither achieved with a very low $NK\Lambda$ coupling far off SU(3) predictions, nor

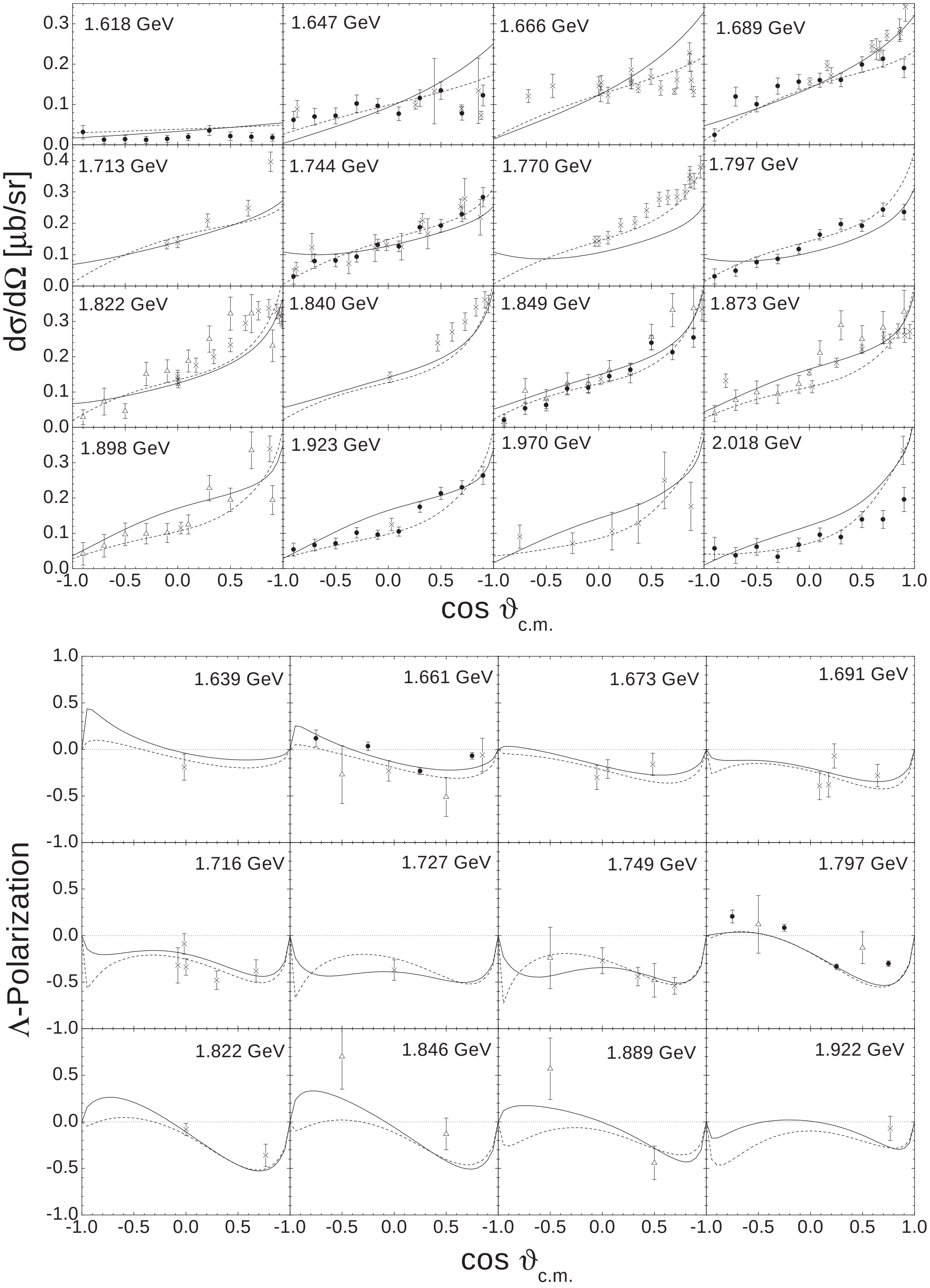

Figure 8.28: $\gamma p \to K^+\Lambda$ differential cross section (*upper panel*) and Λ-recoil polarization (*lower panel*). Line code as in Fig. 8.18. Data are from ● [257], △ [244], × other data (see Section 7.2.3).

Fit	Total $\chi^2_{\gamma\Sigma}$	$\chi^2(\gamma p \to K^+\Sigma^0)$	$\chi^2(\gamma p \to K^0\Sigma^+)$
C-p-γ+	2.74	2.81	2.38
C-p-γ−	2.27	2.28	2.17

Table 8.12: Resulting χ^2 of the two global fits for the two different charge reactions in $\gamma p \to K\Sigma$.

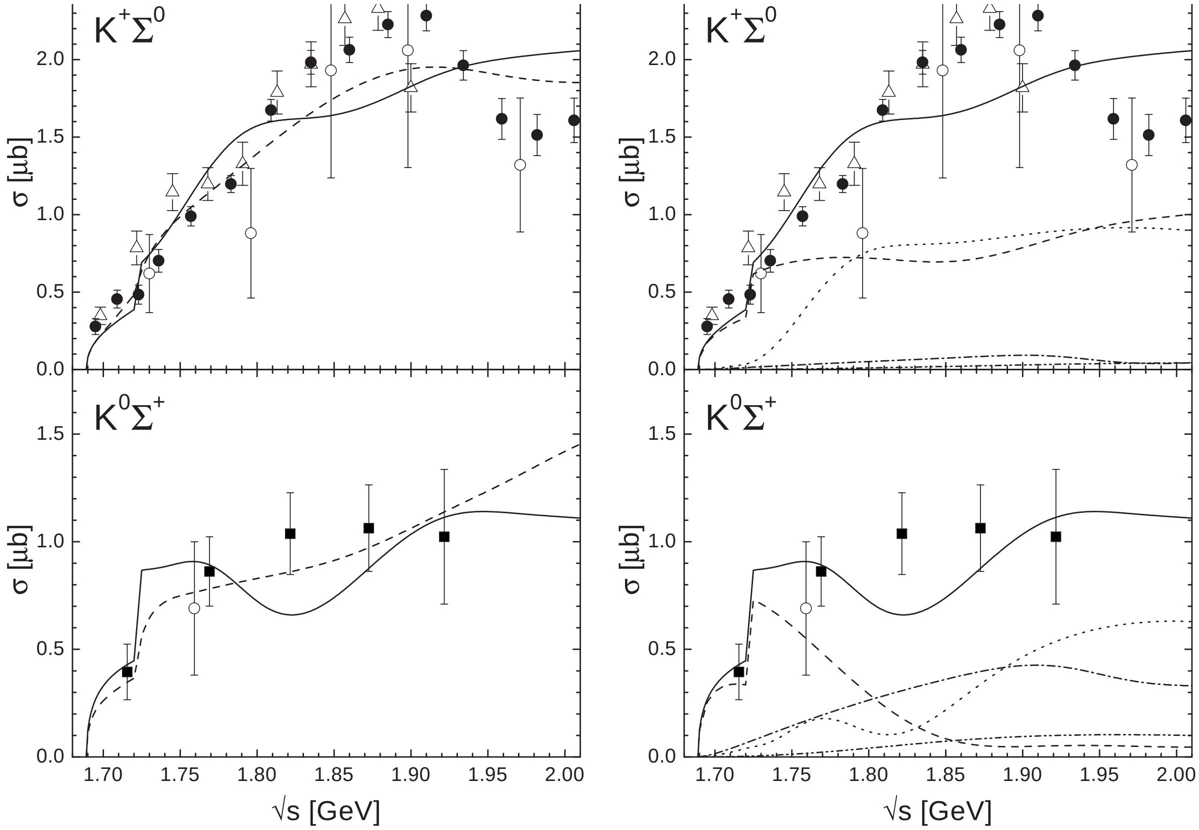

Figure 8.29: $\gamma p \to K\Sigma$ total cross sections. Data are from ● [267], ○ [261], △ [259], and ■ [264]. *Left:* Line code as in Fig. 8.18. *Right:* Partial-wave decomposition. Line code as in Fig. 8.24.

with a very soft nucleon formfactor, see Table 8.4 in Section 8.2.1. Note, that the same cutoff value $\Lambda_N = 0.96$ GeV is used in all nucleon s- and u-channel diagrams.

8.4.5 $K\Sigma$ Photoproduction

As it turns out in the present model, it is also possible to simultaneously describe both measured $\gamma p \to K\Sigma$ charge reactions (see Table 8.12 and Fig. 8.29), while still being in line with all three pion-induced $K\Sigma$ charge channels (see Table 8.2 and Section 8.1.6). Similarly to $K\Lambda$ photoproduction, the $K\Sigma$ mechanism also proves to be very sensitive to rescattering effects via ωN. The $IJ^P = \frac{1}{2}\frac{1}{2}^-$ $K\Sigma$ wave is fed by the ωN channel leading to the sudden increase in the $K^+\Sigma^0$ and $K^0\Sigma^+$ total cross sections. As pointed out in Section 8.4.4, such an effect has also been observed in the coupled-channel model of Lutz et al. [109]. Note, that the finite width of the ω meson of 8 MeV, which is not taken into account in the present model, smears out this threshold effect.

The total cross section of $\gamma p \to K^+\Sigma^0$ is dominantly composed of $J^P = \frac{1}{2}^-$ and $\frac{1}{2}^+$ contributions, where the latter one is generated by the $P_{31}(1750)$ and also K^* exchange contributions. The higher partial waves, especially those with $J \geq \frac{5}{2}$, hardly play any role. In the $\gamma p \to K^0\Sigma^+$ reaction, the situation is changed in such a way, that the contribution of the $P_{11}(1710)$ becomes more pronounced, and the the $J^P = \frac{3}{2}^+$ contribution due to the $P_{33}(1920)$ and in particular the $P_{13}(1900)$ is emphasized. The $J^P = \frac{3}{2}^-$ and higher partial-wave contributions remain negligible. A similar decomposition of the $K\Sigma$-photoproduction mechanism has been found by Janssen et al. [86]. By applying a tree-level isobar model, these authors have been able to exclude any relevance of the D_{13} wave and to identify important contributions from the $P_{11}(1710)$ and $S_{11}(1650)$ as in our model. Also P_{13}, S_{31}, and P_{31} contributions have been identified, however, those have been attributed to the $P_{13}(1720)$, $S_{31}(1900)$, and $P_{31}(1910)$ resonances, instead of $P_{13}(1900)$, $S_{31}(1620)$, and $P_{31}(1750)$ in the present model. Note, that we have checked for the importance of $S_{31}(1900)$ and $P_{31}(1910)$ contributions within the present model, but have not found any sizeable contributions.

The differential cross section behavior of $\gamma p \to K^+\Sigma^0$, shown in Fig. 8.30, is very similar for the two global calculations C-p-$\gamma\pm$ with different coupling signs of $g_{\omega\rho\pi}$. Both describe the angular structure of the cross sections very well and show a tendency to decrease at forward angles for higher energies, which is caused by the K^* exchange. In the Σ^0 recoil polarization of $\gamma p \to K^+\Sigma^0$, the two calculations C-p-$\gamma+$ and C-p-$\gamma-$ show a behavior opposite in sign for energies above 1.9 GeV. This difference can be traced back to the different $P_{11}(1440)$, $P_{11}(1710)$, and $D_{13}(1950)$ contributions in the two calculations. Thus, more precise experimental data in the higher energy region on the Σ^0 polarization would certainly help to clarify the exact decomposition.

We also observe a very similar behavior of the two calculations for the $\gamma p \to K^0\Sigma^+$ (see Fig. 8.31) differential cross section and Σ^+ polarization. Unfortunately, the few SAPHIR data points [264] are not precise enough to judge the quality of the description.

We also display a comparison of the two angle-differential data points for $\gamma n \to K^+\Sigma^-$ of Anderson et al. [258] (see Fig. 8.32), which are not considered in the fitting procedure. One can see, that although both global calculations are in line with the data points, more data on this reaction would certainly allow for an even better disentanglement of the $K\Sigma$-photoproduction reaction process.

As a result of the inclusion of the photoproduction data, the $NK\Sigma$ coupling is reduced from 15.4 to 2.5 from the best hadronic (C-p-$\pi+$) to the best global (C-p-$\gamma+$) fit. As pointed out in Section 8.2.1, the pion-induced reactions are only slightly influenced by the exact $NK\Sigma$ coupling value and are thus still be well described in the global calculation. The final value for the $NK\Sigma$ coupling is close to SU(3) expectations, see Section 8.2.1.

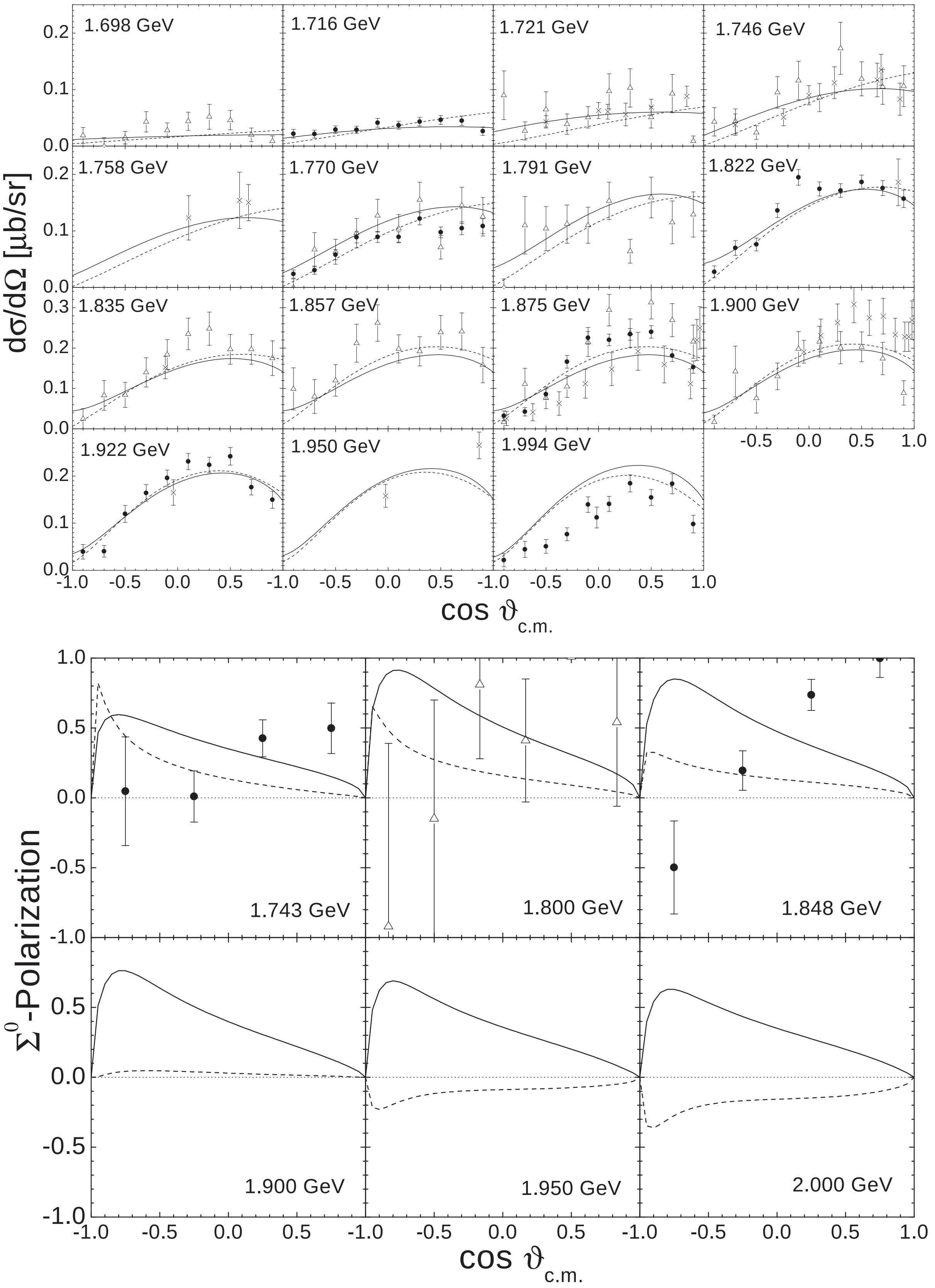

Figure 8.30: $\gamma p \to K^+\Sigma^0$. *Upper panel:* differential cross section, *lower panel:* Σ^0-recoil polarization. Line code as in Fig. 8.18. Data are from ● [267], △ [259], and × other data (see Section 7.2.4).

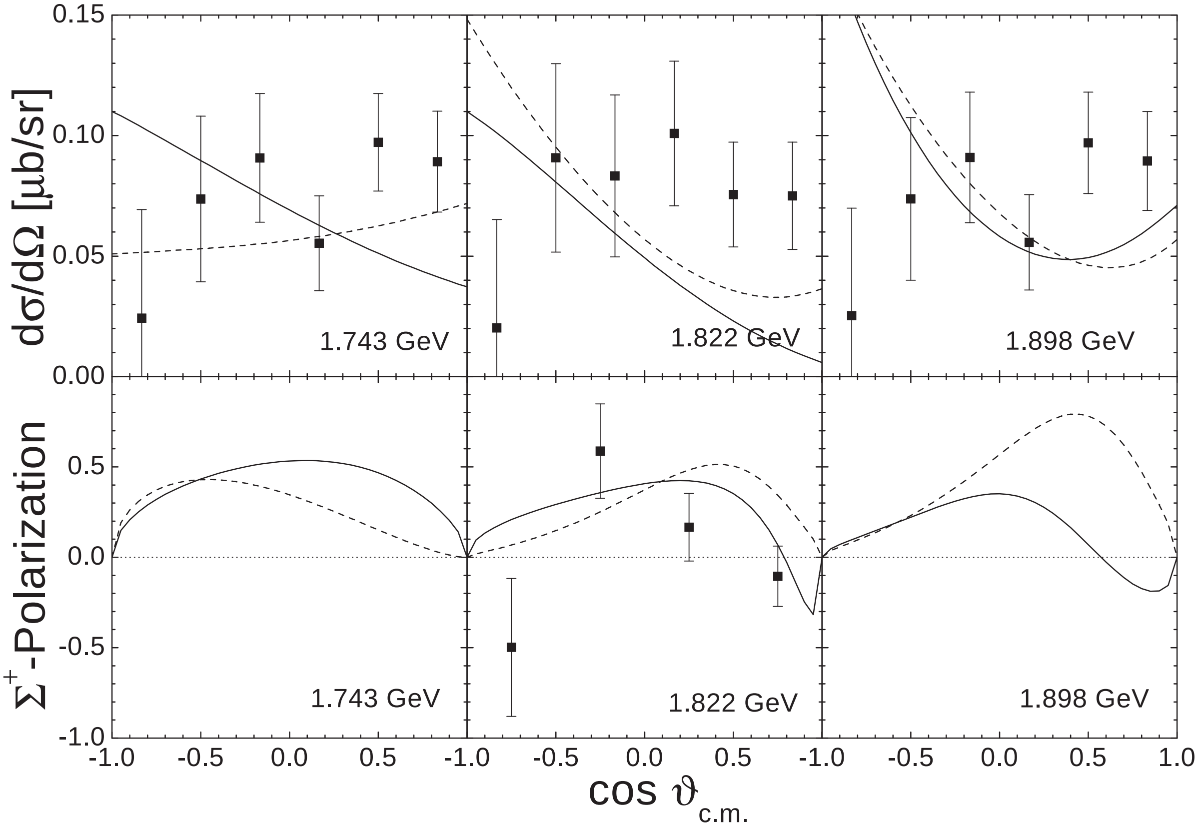

Figure 8.31: $\gamma p \to K^0\Sigma^+$ differential cross section and Σ^+-recoil polarization. Line code as in Fig. 8.18. Data are from [264].

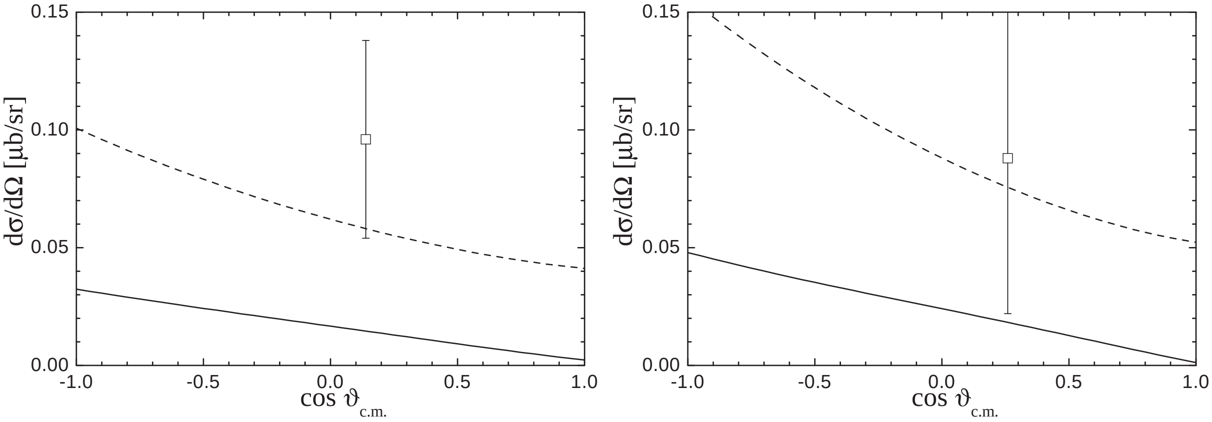

Figure 8.32: $\gamma n \to K^+\Sigma^-$ differential cross section for *left:* $\sqrt{s} = 1.728$ GeV and *right:* $\sqrt{s} = 1.741$ GeV. Data are from [258]. Line code as in Fig. 8.18.

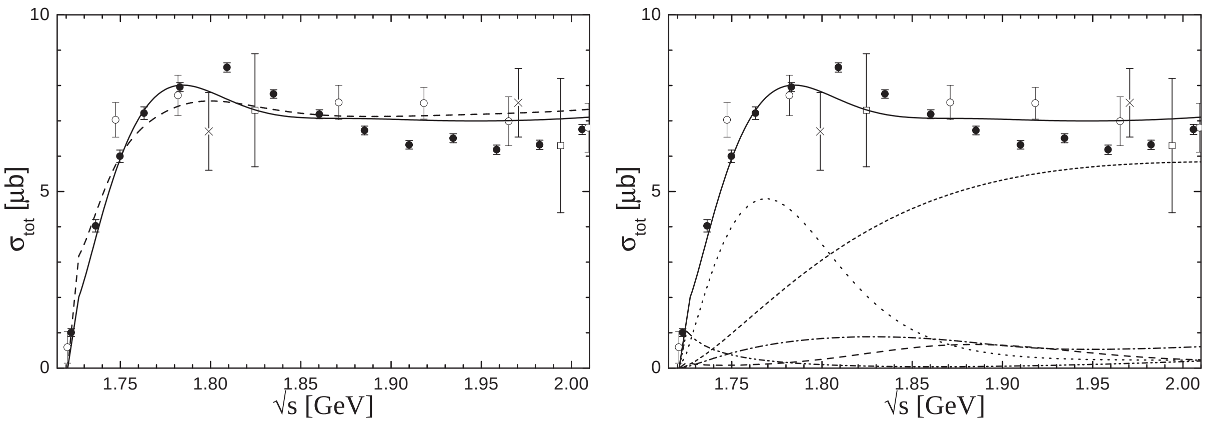

Figure 8.33: $\gamma p \to \omega p$ total cross section. Data are from ● [269], ○ [273], × [271], □ [270]. *Left:* Line code as in Fig. 8.18. *Right:* Partial-wave decomposition. Notation as in Fig. 8.27.

8.4.6 ω Photoproduction

The literature on ω photoproduction does not offer a clear picture on the importance of individual resonance mechanisms in this channel, which is due to the fact, that basically all models are only single-channel analyses. Hence rescattering effects and the impact of the drawn conclusions on other channels are neglected. While Titov and Lee [180] have recently found important contributions of the sub-threshold $D_{13}(1520)$ and $F_{15}(1680)$ resonances, Oh et al. [132] extracted dominant contributions from a $P_{13}(1910)$ and a $D_{13}(1960)$ resonance. Furthermore, in the model of Zhao [199] the $P_{13}(1720)$ and $F_{15}(1680)$ give dominant contributions, but also the low lying $S_{11}(1535)$ and $D_{13}(1520)$ are important. All models agree, however, on the importance of the π^0 exchange, which has already been considered in one of the first models on ω photoproduction by Friman and Soyeur [54]. The higher partial-wave contributions of the π^0 mechanism also dominate the cross section behavior above $\sqrt{s} \approx 1.82$ GeV in the present model, see Fig. 8.33. The clear dominating threshold contribution stems from the $P_{11}(1710)$, just as in the pion-induced case (see Section 8.1.7). The importance of the other resonances, however, is reduced and only the $J^P = \frac{3}{2}^+$ contributions of the $P_{13}(1720)$ and $P_{13}(1900)$ remain non-negligible.

The dominance of the π^0 exchange mechanism becomes even more obvious in the differential cross section, see Fig. 8.34. However, in particular in the middle- and backward-angle region the resonance contributions destructively interfering with the pion exchange are mandatory to describe the precise preliminary SAPHIR data [269], which cover the complete angular range. When these resonance contributions are neglected, the total cross section behavior is strongly altered and the calculation largely overestimates the total cross section, see Fig. 8.35.

The upper limit of the partial-wave decomposition J_{max} turns out to be essential for the ω photoproduction channel because of the importance of the pseudoscalar π^0 exchange. Performing the decomposition only up to $J_{max} = \frac{11}{2}$ as in [51, 53], the full upward bending behavior at forward angles is not reproduced. This is displayed in Fig. 8.35. We have

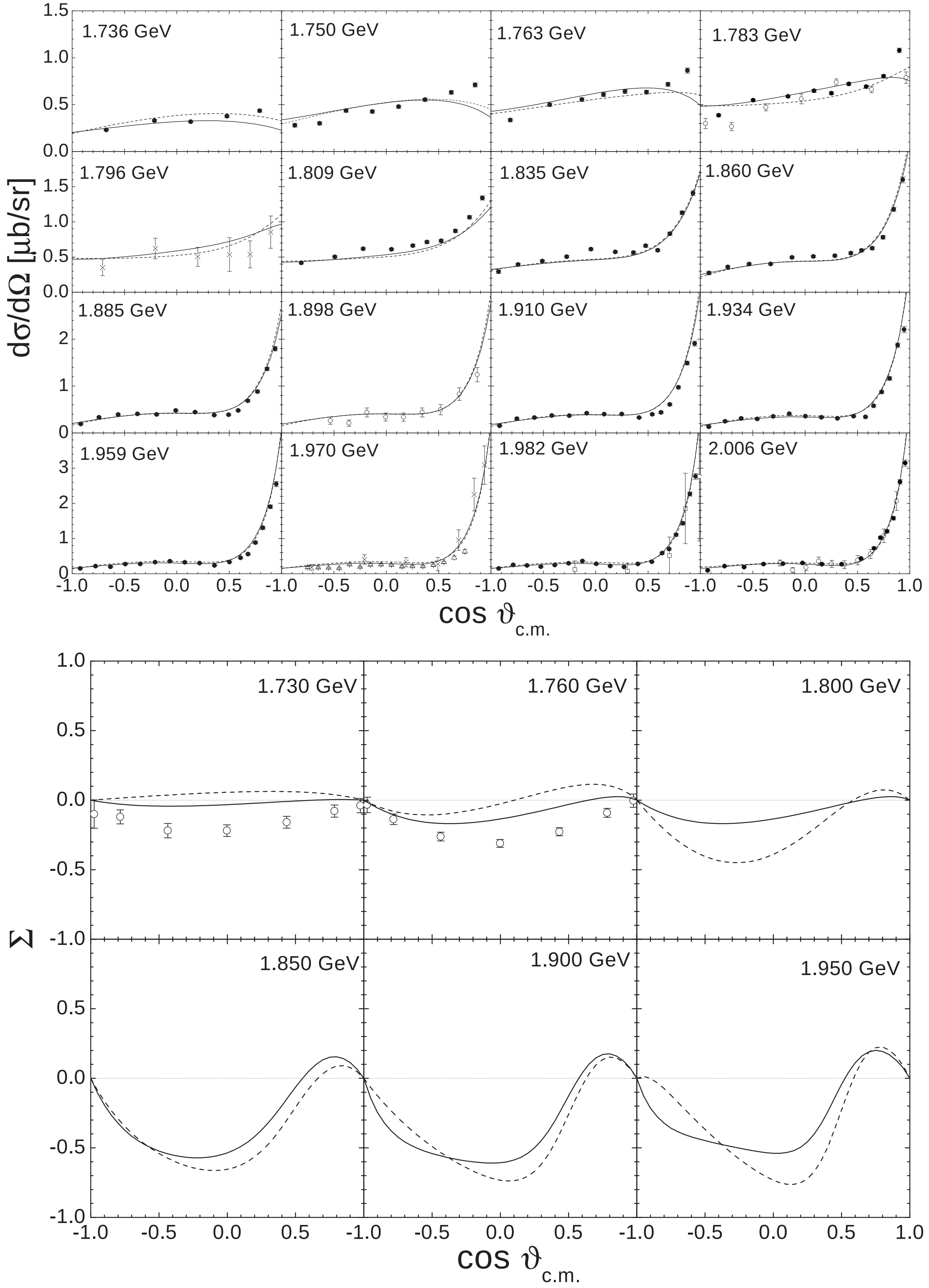

Figure 8.34: $\gamma p \to \omega p$. Line code as in Fig. 8.18. *Upper panel:* differential cross section. Data are from ● [269], ○ [273], × [271], □ [270], △ [275]. *Lower panel:* Beam asymmetry Σ. Preliminary data are from [268].

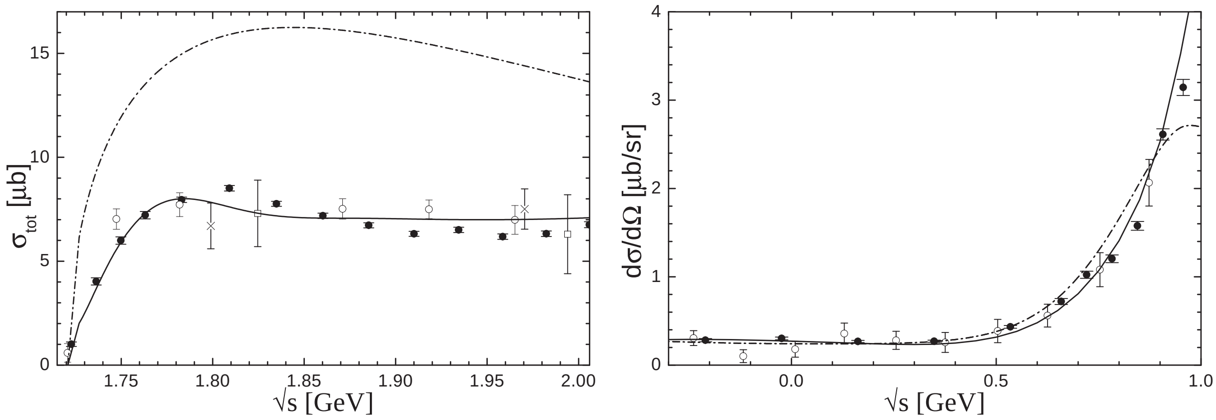

Figure 8.35: $\gamma p \to \omega p$. Data as in Fig. 8.33. *Left:* total cross section. Solid line: full calculation C-p-γ+. Dash-dotted line: C-p-γ+ with resonance contributions switched off. *Right:* Solid line: full calculation C-p-γ+. Dash-dotted line: C-p-γ+ with $J_{max} = \frac{11}{2}$, see text.

checked for J_{max} providing good convergence in the angular structure and found a satisfying behavior for $J_{max} \approx \frac{27}{2}$, which is consequently used in the partial-wave decomposition for the present calculation. The necessity of the consideration of higher partial waves when pseudoscalar exchange mechanisms are included has also been pointed out recently by Davidson and Workman [36]. These authors demonstrated striking differences in the forward peaking behavior for a pion-photoproduction calculation at 1.66 GeV using SAID multipoles only up to $\ell_\pi = 5$ ($\Leftrightarrow J_{max} = \frac{11}{2}$) or additionally taking into account the full angular structure of the Born terms, in particular the pion-Bremsstrahlung contribution.

Although the inclusion of the precise SAPHIR photoproduction data [269] allows for a better disentanglement of the importance of different resonances, the various resonance (helicity) couplings to ωN cannot be fixed with certainty, see Table 8.8. To clarify the situation, there is an urgent need for data on polarization observables of ωN photoproduction, as, e.g., currently extracted at GRAAL. For comparison, we give our results on the beam asymmetry Σ in Fig. 8.34. Note, that the preliminary GRAAL data [268] have not yet been included in the fit.

8.4.7 Photoabsorption on the Nucleon

In the present model, we have included all important inelastic πN channels below $\sqrt{s} = 2$ GeV, and hence, we can also compare the resulting total photoabsorption cross section $\sigma^T_{abs} = \frac{1}{2}(\sigma^{\frac{1}{2}}_{abs} + \sigma^{\frac{3}{2}}_{abs})$ on the proton with experimental data [201, 202]. As can be seen from Fig. 8.36 our model is in line with experiment all through the $\Delta(1232)$ region, but we cannot describe the total photoabsorption cross section σ^T_{abs} above the $2\pi N$ threshold. This is not unexpected: the photoproduction of $2\pi N$ cannot be described within our model as well as the pion-induced $2\pi N$ production, since in the photon-induced reaction, e.g., also ρN or $\pi\Delta$ contact (Kroll-Rudermann like) interactions are known to be important [78, 120, 121].

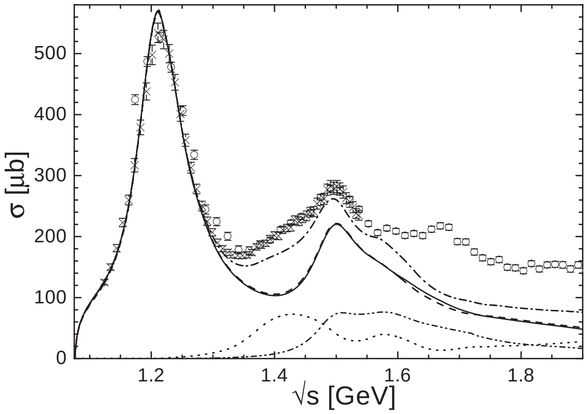

Figure 8.36: Total photoabsorption cross section on the proton $\gamma p \rightarrow X$. Calculation C-p-γ+: solid line, C-p-γ−: dashed line, cross section $\Delta\sigma$ of [110] (see text): dotted line, sum of calculation C-p-γ+ and $\Delta\sigma$: dash-dotted line; $\gamma p \rightarrow 2\pi N$ of C-p-γ+: dash-double-dotted line (see text). Data are from × [202] and ∘ [201].

In the dispersion theoretical analysis of Compton scattering by L'vov et al. [110], exactly this part of the total photoabsorption cross section has been determined. By subtracting from the experimental total photoabsorption cross section $\sigma^T_{abs} = \frac{1}{2}(\sigma^{\frac{1}{2}}_{abs} + \sigma^{\frac{3}{2}}_{abs})$ on the proton [201, 202] the single-pion photoproduction cross section, determined via the VPI multipoles, and their $2\pi N$ cross section simulated via nucleon resonances, they extracted a remaining cross section $\Delta\sigma$ supposed to be due to the aforementionned background interactions. Ignoring interference effects (see [110]), one can just add $\Delta\sigma$ to our total photoabsorption cross section. The resulting sum is remarkably close to the experimental photoabsorption cross section [201, 202] up to about 1.6 GeV, see Fig. 8.36, above which important contributions of spin-$\frac{5}{2}$ resonances can be expected. Thus it seems, that the resonance contributions to the $2\pi N$ photoproduction, displayed in Fig. 8.36 by the dash-double-dotted line, are rather well described within the present model. This provides an additional cross check that at least up to 1.6 GeV all important channels are correctly described in our model. The last point can be extended to higher energies as soon as the inclusion of spin-$\frac{5}{2}$ resonances in the present model is completed [162]. Above 1.6 GeV the data of the ABBHHM collaboration on $3\pi N$ photoproduction [271] indicate, that also this channel contributes $\approx 30 - 40$ μb to σ^T_{abs}, less than 10 μb of which are due to ωN.

Realizing the limitations of the present model, we can nevertheless give estimates on the contributions of the various final states to the Gerasimov-Drell-Hearn (GDH) sum rule [60] (see also [41] and references therein)

$$I_{GDH} = \int\limits_{E_\gamma^{thr}}^{\infty} \left(\sigma^{\frac{1}{2}}_{abs} - \sigma^{\frac{3}{2}}_{abs}\right) \frac{\mathrm{d}E_\gamma^{lab}}{E_\gamma^{lab}} = -\frac{2\pi^2\alpha\kappa_N}{m_N^2} \,, \qquad (8.4)$$

which allows to relate the static property of the anomalous magnetic moment of the nucleon to the photoabsorption reaction via dispersion relations. In Eq. (8.4), E_γ^{thr} gives the threshold photon laboratory energy for pion photoproduction. The contributions of the individual reactions on the proton target up to $\sqrt{s} = 2$ GeV are given in Table 8.13. As is clear from the above discussion, our estimates for πN and $2\pi N$ deviate from the rather well known values for reasons well understood. For all other final states (ηN, $K\Lambda$, $K\Sigma$, and ωN) our model is compared to all available experimental observables and thus allows for reasonable estimates of the contributions to the GDH sum rule. It is interesting to note (see Table 8.13) that our values for the contributions from ηN, $K\Lambda$, $K\Sigma$, and in particular ωN deviate from the values of Refs. [177, 166, 200], all of which have been extracted in single-channel analyses.

πN	$2\pi N$	ηN	$K\Lambda$	$K\Sigma$	ωN
-157.5	-21.2	$+9.2$	$+1.1$	$+1.6$	$+0.8$
-162.7	-20.7	$+8.6$	$+0.9$	$+1.8$	$+0.1$
-171^a	-45^a	$+15^a$	$+1.7^b$	$+2.4^b$	-2.0^c

Table 8.13: Contributions (in μb) of the individual final states to the GDH sum rule up to $\sqrt{s} = 2$ GeV on the proton target. 1st line: Calculation C-p-$\gamma+$, 2nd line: C-p-$\gamma-$. 3rd line: Values are from ^{a}: [177], ^{b}: [166], ^{c}: [200]. .

8.4.8 Resonance Electromagnetic Helicity Amplitudes

In Tables 8.14, 8.15, and 8.16 the extracted electromagnetic properties of the resonances are summarized in comparison with the values of the PDG [67], Feuster and Mosel [53], and the pion photoproduction analysis of Arndt et al. [6]. In the following, these values are discussed in detail.

Isospin-$\frac{1}{2}$ Resonances

$\mathbf{S_{11}}$:
In contrast to Arndt et al. [6] the properties and in particular the helicity amplitudes of the $S_{11}(1535)$ can be well fixed in the present calculation, which is a result of the inclusion of the η-photoproduction data. The extracted lower value for $A^p_{\frac{1}{2}}$ as compared to Feuster and Mosel [53] is caused by the different gauging procedure and the fact, that a lower mass is extracted in the present calculation. The differences in the neutron value, however, can be explained by the improved data base underlying the pion-photoproduction neutron multipoles, see Fig. 8.21.
The helicity coupling of the $S_{11}(1650)$ is also influenced by $K\Lambda$ photoproduction in our analysis, but the extracted value agrees well with the PDG [67] value. However, the most recent VPI photoproduction single-energy analysis presented in [6] indicates, that the structure of this resonance is enlarged as compared to the analysis [221] used in the present calculation, which leads to the larger values found by Arndt et al..

$\mathbf{P_{11}}$:
The $P_{11}(1440)$ values are extremely sensitive to the damping of the nucleon contributions

$L_{2I,2S}$	$A^p_{\frac{1}{2}}$	$A^n_{\frac{1}{2}}$	$A^p_{\frac{3}{2}}$	$A^n_{\frac{3}{2}}$
$S_{11}(1535)$	90/93	$-24/-34$		—
	90(30)	$-46(29)$		—
	106	-63		—
	NG			—
$S_{11}(1650)$	49/47	$-11/-13$		—
	53(16)	$-15(21)$		—
	45	-26		—
	74(1)	$-28(4)$		—
$P_{11}(1440)$	$-87/-81$	121/112		—
	$-64(4)$	40(10)		—
	-84	47		—
	$-67(2)$	47(5)		—
$P_{11}(1710)$	44/28	$-24/41$		—
	9(22)	$-2(14)$		—
	19	-19		—
	NG			—
$P_{13}(1720)$	$-53/-65$	$-4/3$	27/34	3/2
	18(30)	1(15)	$-19(20)$	$-29(61)$
	23	2	75	-17
	NG			
$P_{13}(1900)$	$-17/-18$	$-16/-21$	31/8	$-2/-28$
	NC			
$D_{13}(1520)$	$-3/1$	$-84/-74$	151/153	$-159/-161$
	$-24(9)$	$-59(9)$	166(5)	$-139(11)$
	3	-47	136	-98
	$-24(2)$	$-67(4)$	135(2)	$-112(3)$
$D_{13}(1950)$	$12/-1$	$23/-15$	$-10/-22$	$-9/22$
	5	47	41	-55

Table 8.14: Electromagnetic helicity amplitudes (in 10^{-3} GeV$^{-\frac{1}{2}}$) of $I = \frac{1}{2}$ resonances considered in the calculation. 1st line: C-p-$\gamma+$/C-p-$\gamma-$, 2nd line PDG [67], 3rd line Feuster and Mosel [53], 4th line: Arndt et al. [6]. In brackets, the estimated errors are given. "NF": not found. "NG": not given. "NC": not considered (energy range ended at 1.9 GeV).

and consequently the gauging procedure. This leads to large differences in the neutron amplitude as compared to Feuster and Mosel, the PDG, and Arndt et al.. However, the error bars in the neutron multipole allow for a large range of resonance contributions (see

$L_{2I,2S}$	$A_{\frac{1}{2}}$	$A_{\frac{3}{2}}$	$L_{2I,2S}$	$A_{\frac{1}{2}}$	$A_{\frac{3}{2}}$
$S_{31}(1620)$	$-50/-53$	—	$P_{33}(1232)$	$-128/-129$	$-247/-248$
	$27(11)$	—		$-135(6)$	$-255(8)$
	-4	—		-126	-233
	$-13(3)$	—		$-129(1)$	$-243(1)$
$P_{31}(1750)$	$53/30$	—	$P_{33}(1600)$	$0/0$	$-24/-24$
				$-23(20)$	$-9(21)$
	NC	—		-26	-52
$D_{33}(1700)$	$96/96$	$154/153$	$P_{33}(1920)$	$-7/-9$	$-1/-2$
	$104(15)$	$85(22)$		$40(14)$	$23(17)$
	75	98		NC	
	$89(10)$	$92(7)$			

Table 8.15: Electromagnetic helicity amplitudes of $I = \frac{3}{2}$ resonances. Notation as in Table 8.14.

Fig. 8.21).
Similarly to Arndt et al., the electromagnetic properties of the second P_{11} cannot be completely fixed in the present calculation. While in the proton case, the $P_{11}(1710)$ photon coupling is roughly identical for both global calculations, the lack of precise neutron target pion-photoproduction data especially above 1.8 GeV (see Fig. 8.21) does not allow to pin down the $P_{11}(1710)$ neutron coupling.

$\mathbf{P_{13}}$:
Since both P_{13} resonances considered in the present calculation not only give important contributions to pion photoproduction, but also to $K\Lambda$ and ω photoproduction, the resulting proton couplings are rather well determined, although the structure in the E^p_{1+} pion photoproduction multipole cannot be completely described (see Section 8.4.2). This is in contrast to Arndt et al. [6], where the values of the $P_{13}(1720)$ are not given. Note, that our coupling signs for the $P_{13}(1720)$ are opposite to the PDG values, but in line with the ones of the Arndt, Strakovsky, and Workman [5]: $A^p_{\frac{1}{2}} = -15(15)$, $A^p_{\frac{3}{2}} = 7(10)$ (in brackets, the estimated errors are given). The newly included $P_{13}(1900)$ also influences the $P_{13}(1720)$ properties, thus explaining the differences in the couplings of the latter one to Feuster and Mosel [53]. As pointed out in Section 8.4.2, the lack of neutron data for the pion-photoproduction multipoles above 1.8 GeV leaves the $P_{13}(1900)$ neutron photon couplings essentially undetermined.

$\mathbf{D_{13}}$:
As shown in [53], the $D_{13}(1520)$ photon couplings are extremely sensitive to Compton scattering. Therefore and due to the enlarged Compton data base, the differences to the values of Arndt et al. [6] and Feuster and Mosel [53] can be understood. Furthermore, as pointed out in Section 8.4.2, the $D_{13}(1520)$ neutron photon couplings are also influenced by the lack of precise M^n_{2-} multipole data, thus fixing the $D_{13}(1520)$ neutron photon couplings partially by its influences on the $J = \frac{1}{2}$ multipoles. The $D_{13}(1950)$ photon

couplings always result in small values, since neither in pion photoproduction nor in the other photoproduction channels such a resonant structure is found. However, more polarization measurements on the non-pion photoproduction data would allow for a more closer determination of the electromagnetic properties of this resonance.

$\mathbf{S_{31}}$:
Similarly to the $IJ = \frac{1}{2}\frac{1}{2}$ channels, also the $E_{0+}^{\frac{3}{2}}$ multipole is very sensitive to background contributions. Thus, although in our calculation and in the analysis of Arndt et al. [6] the resonance peak of the S_{31} is nicely described, the extracted helicity amplitude differs by a factor of 4. Feuster and Mosel [53] have also found a smaller helicity value, which, however, can be explained by the fact, that in the older multipole analysis used in [53], this resonance's peak was less pronounced.

$\mathbf{P_{31}}$:
As a consequence of the large error bars in the $M_{1-}^{\frac{3}{2}}$ multipole, the photon coupling of the $P_{31}(1750)$ differs in the two global calculations. However, the extracted values describe the tendency in the data correctly and are also in line with the influence of the $P_{31}(1750)$ on $K\Sigma$ photoproduction.

$\mathbf{P_{33}}$:
Although Compton scattering is simultaneously analysed in the present model, our helicity coupling nicely agree with the recent analysis of Arndt et al., corroborating the compatibility of the Compton and pion-photoproduction experimental data. The ratio of electric and magnetic transition strength for the Δ ($P_{33}(1232)$) resonance is of special interest, because it vanishes for a zero quadrupol deformation of this excited nucleon state. Combining Eqs. (6.6) and (E.41) and using the normalization entering Eq. (6.8), we find:

$$R^{\Delta}_{E/M} = \frac{A^{\Delta}_{\frac{1}{2}} - A^{\Delta}_{\frac{3}{2}}/\sqrt{3}}{A^{\Delta}_{\frac{1}{2}} + \sqrt{3}A^{\Delta}_{\frac{3}{2}}} = -\frac{g^{\Delta}_1 - g^{\Delta}_2 \frac{m_\Delta}{2m_N}}{g^{\Delta}_1 \frac{3m_\Delta + m_N}{m_\Delta - m_N} - g^{\Delta}_2 \frac{m_\Delta}{2m_N}} \; . \tag{8.5}$$

Our value of -2.6% (-2.5%) of calculation C-p-$\gamma+$ (C-p-$\gamma-$) is also identical with the PDG [67] value of $-2.5 \pm 0.5\%$ and the one of Tiator et al. [176] -2.5 ± 0.1, even though the $E_{1+}^{\frac{3}{2}}$ multipole is very sensitive to rescattering [53].
For the two higher lying P_{33} resonances, we find small electromagnetic contributions resulting in hardly any visible structure in the $M_{1+}^{\frac{3}{2}}$ and $E_{1+}^{\frac{3}{2}}$ pion multipoles. However, since these resonances also influence $K\Sigma$ photoproduction, both global calculations result in basically identical values.

$\mathbf{D_{33}}$:
As pointed out in Section 8.4.2, we observe problems in the description of the $M_{2-}^{\frac{3}{2}}$ multipole due to the lack of a background contribution in this multipole. This leads to the differences of our $A_{\frac{3}{2}}$ values as compared to the other references. Note, that also in [53] similar observations have been made and the extracted $A_{\frac{3}{2}}$ strength has ranged from $98 - 172$.

Electromagnetic off-shell parameters:
The electromagnetic off-shell parameters a_γ, see Sections 3.4.1 and 3.4.2, turn out to

$L_{2I,2S}$	a_{γ_1}	a_{γ_2}	$L_{2I,2S}$	a_{γ_1}	a_{γ_2}
$P_{13}(1720)$	-1.324	0.266	$P_{33}(1232)$	0.471	0.932
	0.148	0.429		0.538	0.809
	-0.352	1.586		0.233	-0.158
$P_{13}(1900)$	-3.599	0.488	$P_{33}(1600)$	-2.006	2.650
	2.893	0.149		-3.281	3.000
	NC			3.282	-3.979
$D_{13}(1520)$	0.075	-0.571	$P_{33}(1920)$	4.000	-0.579
	0.002	-0.873		4.000	-2.123
	0.235	0.025		NC	
$D_{13}(1950)$	0.035	1.101	$D_{33}(1700)$	-3.999	-1.580
	-2.114	-3.944		-3.993	-1.666
	-0.671	-1.822		0.962	-0.362

Table 8.16: Electromagnetic off-shell parameters a_γ of spin-$\frac{3}{2}$ resonances. 1st line: C-p-$\gamma+$, 2nd line: C-p-$\gamma-$, 3rd line: SM95-pt-3 of [53]. “NC”: not considered (energy range ended at 1.9 GeV).

be mostly well fixed in the two global calculations, see Table 8.16. Exceptions are the a_{γ_1} values of the P_{13} resonances, which can, however, be explained by the fact that the corresponding couplings g_{γ_1} are very small and thus the off-shell parameters very sensitive to any changes. In the $D_{13}(1950)$ case, the differences between the two calculations are related to the fact, that also the helicity amplitudes cannot be well fixed, see Table 8.14. Since the off-shell parameters determine the background contributions in the $J = \frac{1}{2}$ waves, it is also quite clear, that these parameters are very sensitive to the gauging procedure, which has already been found by Feuster and Mosel [53]. This explains, why even in the case of the $P_{33}(1232)$ resonance, our values differ from those extracted in [53], where the Haberzettl gauging procedure (3.32) was used instead of the Davidson-Workman procedure (3.33) (note, that the values of [53] for the hadronic off-shell parameters are mostly similar to ours, see Table 8.9).

8.5 Summary of Photoproduction Results

Within the present model, also almost all features of the photoproduction of γN, πN, ηN, $K\Lambda$, $K\Sigma$, and ωN can be described. No global fit has been possible, when the formfactor F_t (3.30) is used for the t-channel exchange diagrams. Even when using F_p a readjustment of the parameters obtained from purely hadronic reactions is necessary, since especially in the ηN and ωN channels, the resonance contributions cannot be well fixed using the pion-induced data alone. In addition, in the associated strangeness channels the Born couplings have to be readjusted, since in photoproduction, the corresponding contributions are largely enhanced as a consequence of the gauging procedure. The resulting Born couplings of the best global parameter set are still close to SU(3) predictions. The background in pion photoproduction proves to be very sensitive to the nucleon contributions, and therefore on the gauging procedure. Although this background is fixed by only a few parameters, it is well in accordance with most multipoles, thus giving confidence in the applied Davidson-Workman gauging procedure (3.33). However, we find indications for a problem of the simultaneous description of the low-energy behavior of the $IJ = \frac{1}{2}\frac{1}{2}$ πN partial waves and photoproduction multipoles.

Although we have largely extended our data base on pion photoproduction and Compton scattering, both channels (and ηN photoproduction) are still well described in the energy region below $\sqrt{s} = 1.6$ GeV. The extracted electromagnetic properties of the $P_{33}(1232)$ resonance perfectly agree with other analyses. In general, the agreement with the previous analysis of Feuster and Mosel [53] is quite good. The main differences are found for resonances in those partial waves, where additional higher-lying states have been added, and in the electromagnetic off-shell parameters a of the spin-$\frac{3}{2}$ resonances, which is a consequence of the different applied gauging procedures.

In the $K\Lambda$, $K^0\Sigma^+$, and ωN channels we find a strong need for contributions of a $P_{13}(1900)$ resonance between 1.9 and 2 GeV, similar to the pion-induced reactions. The inclusion of this resonane also leads to changes in the properties of the $P_{13}(1720)$ as compared to previous analyses. In particular, we find that the role of the $P_{13}(1720)$ is largely enhanced in $K\Lambda$ photoproduction. However, for a clear disentanglement of the resonant contributions in the energy region above 1.7 GeV more polarization measurements in particular on ωN and ηN are needed to completely determine the $P_{13}(1900)$ and also the $D_{13}(1950)$ resonance properties.

The associated strangeness photoproduction channels prove to be very sensitive to the ωN threshold and also on interference effects between different contributions. This leads to the explanation of a resonance-like structure in the $K\Lambda$ total cross section by an interference of K^* and nucleon contributions, instead of a resonance. The ωN production is mostly dominated by the π^0 exchange mechanism, but large interference effects due to the implemented resonances are necessary to find a satisfactory description of the preliminary SAPHIR cross section data [269]. The pseudoscalar nature of the π^0 exchange mechanism requires the inclusion of partial waves up to $J_{max} = \frac{27}{2}$ in the PWD. The threshold behavior of ω photoproduction is mostly explained by a large $P_{11}(1710)$ contribution, in contrast to all other models on ωN photoproduction. For a clear disentanglement of the resonant contributions in the energy region above 1.7 GeV more polarization measurements in particular on ωN and ηN are needed, especially with respect on the roles played by the $P_{13}(1900)$ and $D_{13}(1950)$ resonances.

The good description of all photoproduction channels enables us to evaluate the GDH sum rule contributions of the various final states. We find small values for the contributions from ηN, $K\Lambda$, $K\Sigma$, and ωN, which are remarkably different from those extracted in single-channel analyses.

Deficiencies of the present model concerning the $2\pi N$ photoproduction are visible in Compton scattering, where a background contribution in the energy region between the $P_{33}(1232)$ and $D_{13}(1520)$ resonance is missing. We have nevertheless shown, that the resonance contributions to $2\pi N$ photoproduction are well under control in the present model. Moreover, similar to πN elastic scattering, there are also evidences for the influence of a $3\pi N$ final state in the $J^P = \frac{3}{2}^+$ multipole E^p_{1+}.

Chapter 9

Summary and Outlook

The presented Giessen model, originally introduced by Feuster and Mosel [51, 53] for center-of-mass energies below 1.9 GeV, provides a unique tool for the analysis of nucleon resonances up to energies of $\sqrt{s} = 2$ GeV. It comprises a unified description of meson- and photon-induced reactions on the nucleon, where unitarity is guaranteed by solving the Bethe-Salpeter scattering equation via the K-matrix approximation. The extension of the energy range requires the additional incorporation of the $K\Sigma$ and in particular the ωN final states. Hence, unitarity effects are correctly taken into account, because now, all important final states, i.e. πN, $2\pi N$, ηN, $K\Lambda$, $K\Sigma$, and ωN, are included. Since the driving potential is built up by the use of effective Lagrangians for Born-, t-channel, spin-$\frac{1}{2}$, and spin-$\frac{3}{2}$ resonance contributions, also the background contributions are generated consistently for all partial waves and the number of parameters is greatly reduced. The inclusion of the vector meson nucleon final state ωN within the model has required the generalization of the partial-wave formalism. The presented formalism allows to decompose any meson-(photon-) baryon reaction on an equal footing.

Within this model, the effects of chiral symmetry have been checked by allowing for a chirally symmetric and a chiral symmetry breaking $\sigma\pi\pi$ coupling vertex. The chiral symmetric one has proven superior not only for the low-, but also for the intermediate-energy region in πN elastic scattering. The dependence on different descriptions for the spin-$\frac{3}{2}$ resonance vertices has been investigated for the pion-induced reactions and similar results have been found. However, when the spin-$\frac{1}{2}$ off-shell contributions of the spin-$\frac{3}{2}$ resonances are turned off, the t-channel background contributions are enhanced and the overall description becomes worse, thus indicating that indeed additional background contributions are required in this case.

The simultaneous consideration of the γN final state guarantees access to a much larger and more precise data base than the pion-induced data alone. This allows for strong tests on all resonance contributions. It has turned out that a readjustment of the hadronic parameters is necessary, in particular in the ηN and ωN channels, once the photon data are taken into account. Therefore, the inclusion of photoproduction data is inevitable to extract the resonance masses and widths reliably. Allowing for such a readjustment, the simultaneous description of all pion- and photon- induced reactions on the above final states is possible with one parameter set, which, however, turns out to require a specific formfactor shape in the t-channel exchanges. The determined properties of the well-settled resonances are in agreement with other analyses and the extracted Born couplings are close to SU(3) values. A side effect of the consideration of all the above final states within our model is that the consistency of the experimental data for the various reactions can be checked, and basically no discrepancies are found. We only experience difficulties in the simultaneous description of the background in the $J = \frac{1}{2}$ waves in the $\pi N \to \pi N$ and $\gamma N \to \pi N$ reactions.

In the analysis of the higher-lying final states $K\Lambda$, $K\Sigma$, and ωN, we find strong evidences for excitations in the $IJ^P = \frac{1}{2}\frac{3}{2}^+$ (P_{13}) wave between 1.9 and 2 GeV, in the $IJ^P = \frac{1}{2}\frac{3}{2}^-$ (D_{13}) around 1.945 GeV, in the $IJ^P = \frac{3}{2}\frac{1}{2}^+$ (P_{31}) around 1.71 GeV, and in the $IJ^P = \frac{3}{2}\frac{3}{2}^+$ (P_{33}) at the border of our energy range (2 GeV), which do not correspond to well-settled nucleon resonance states. In particular the $P_{13}(1900)$ plays an important role in the production mechanisms of these final states. Vice versa, these higher lying final states prove to be sensitive on contributions of the aforementioned resonances, thereby allowing for fixing the properties of these resonances.

It is shown, that especially for a conclusive examination of those resonances, which are not yet clearly identified, the consideration of rescattering effects is inevitable. For example, although the $P_{13}(1900)$ is important for $K\Lambda$ production, a hump in the total photoproduction cross section around 1.9 GeV is explained by a background interference effect in contrast to single-channel analyses. On the other side, the inclusion of the $P_{13}(1900)$ also leads to changes in the properties of the $P_{13}(1720)$ resonance as compared to previous analyses. In particular, we find that the role of the $P_{13}(1720)$ is largely enhanced in $K\Lambda$ production, now dominating both the pion- and the photon-induced reaction. Consequently, the discrepancy between the P_{11} πN inelastic and $2\pi N$ partial-wave cross sections above 1.6 GeV is not explained by $K\Lambda$ anymore but by a strong $P_{11}(1710)$ ηN decay. However, more polarization data above 1.7 GeV, especially on ηN and ωN, are needed to completely determine the properties of the $P_{13}(1900)$, $D_{13}(1950)$, $P_{31}(1750)$, and $P_{33}(1920)$ resonances.

We find that $K\Sigma$ production is dominated by $J^P = \frac{1}{2}^+$ waves, caused by the contributions of the $P_{11}(1710)$ and $P_{31}(1750)$ resonances. The $P_{11}(1710)$ also plays a large role in ωN production close to threshold, while for higher energies the $P_{13}(1900)$ is important in the latter channel. This is at variance with all other (single-channel) analyses on the ωN final state. It turns out, that the consideration of this state can largely influence the asscociated strangeness channels $K\Lambda$ and $K\Sigma$.

Since in the present model, all important final states up to $\sqrt{s} = 2$ GeV are now included, we can give estimates for the contributions from the individual final states to the GDH sum rule. The contributions from the final states $K\Lambda$, $K\Sigma$, and ωN are small, but significantly different from the values extracted in single-channel analyses.

There are indications for room for improvement of the Giessen model. Assuming that the implemented $\pi N \to 2\pi N$ data are correct, these are evidences for important additional $3\pi N$ final state contributions, which are not considered up to now, in the $J^P = \frac{3}{2}^+$ partial waves. We also find evidences for the necessity of a more correct treatment of the $2\pi N$ state in the low-energy tails of the $D_{13}(1520)$ and $D_{33}(1700)$ resonance and in missing background contributions, generated by $2\pi N$ rescattering, in Compton scattering. Moreover, as a consequence of the lack of spin-$\frac{5}{2}$ resonances, the analysis of Compton scattering is restricted to energies below $\sqrt{s} = 1.6$ GeV so far. Since all data on ηN, $K\Lambda$, $K\Sigma$, and ωN are well described up to 2 GeV without such resonances, they seem to be of minor importance in these reactions. This point is investigated further at present [162].

Using the generalization of the partial-wave decomposition a more realistic description of the $2\pi N$ final state in terms of ρN and $\pi\Delta$ is now straightforward. The inclusion of these final states allows to mimic the $2\pi N$ three particle phase space while still dealing with two-body unitarity. This extension will probably improve the description of the D_{I3} waves below the first resonances and also generate the needed additional background in Compton scattering.

While for larger energies threshold effects due to unitarity are of main importance, at lower energies considerable effects are known to be caused by analyticity. This has been demonstrated by comparison of the present analysis with models also taking analyticity into account. Therefore, also work along analytic extensions of the K-matrix ansatz, e.g., in the direction proposed by Kondratyuk and Scholten [100], should be pursued.

Appendix A

Notation and Normalization

A.1 Metric and Momentum States

We work in the metric of Bjorken and Drell [18], i.e. $g_{\mu\nu} = \mathrm{diag}(1,-1,-1,-1)$. Four-momenta are denoted by italic letters (p, k, q, etc.), three-momenta by bold letters ($\boldsymbol{p}$, $\boldsymbol{k}$, $\boldsymbol{q}$, etc.)[1], their absolute values by upright letters (p, k, q, etc.), and their unit vectors by $\hat{\boldsymbol{p}}$, $\hat{\boldsymbol{k}}$, $\hat{\boldsymbol{q}}$, etc.

In general, incoming, outgoing, and intermediate meson (baryon) momenta are denoted by k, k', and k_q (p, p', and p_q), respectively. Hence one has, e.g., $p^\mu = (E_B = \sqrt{m_B^2 + \mathrm{p}^2}, \boldsymbol{p})$.

The Mandelstam variables are defined as:

$$\begin{aligned} s &= (p+k)^2 = (p'+k')^2 \\ u &= (p-k')^2 = (p'-k)^2 \\ t &= (p-p')^2 = (k'-k)^2 \\ s+t+u &= m_B^2 + m_M^2 + m_{B'}^2 + m_{M'}^2 \;. \end{aligned}$$

If not specified otherwise, we work in the center-of-mass (c.m.) system ($\boldsymbol{p} = -\boldsymbol{k}$), where the total four-momentum is denoted by $P^\mu \equiv (p+k)^\mu = (p'+k')^\mu = (\sqrt{s}, \boldsymbol{0})$. The incoming (outgoing) meson momentum is taken to be $k^\mu = (E_M, 0, 0, \mathrm{k})$ ($k'^\mu = (E_{M'}, \mathrm{k}'\sin\vartheta, 0, \mathrm{k}'\cos\vartheta)$), i.e. the z-axis is chosen along the three-momentum of the incoming meson. Here, the absolute value of the incoming meson momentum is given by

$$\mathrm{k} = \frac{1}{2\sqrt{s}}\sqrt{\left(s-(m_B+m_M)^2\right)\left(s-(m_B-m_M)^2\right)} \tag{A.1}$$

and similarly for the outgoing meson.

Single-particle momentum states $|\boldsymbol{p}, \lambda\rangle$ with three-momentum $\boldsymbol{p}$ and helicity λ are normalized as in [18]:

$$\begin{aligned} \langle \boldsymbol{p}', \lambda' | \boldsymbol{p}, \lambda \rangle &= \delta^3(\boldsymbol{p}' - \boldsymbol{p})\delta_{\lambda'\lambda} \\ &= \frac{1}{\mathrm{p}^2}\delta(\mathrm{p}' - \mathrm{p})\delta(\Omega' - \Omega)\delta_{\lambda'\lambda} \;, \end{aligned} \tag{A.2}$$

---

[1] Note, that three-vectors are denoted in general by bold letters.

where we have used

$$\delta(f(x)) = \left(\left| \frac{\partial f}{\partial x} \right|_{x_0} \right)^{-1} \delta(x - x_0) \; . \tag{A.3}$$

The particle helicity λ is the projection of its spin s on its direction of motion. Thus, in the c.m. system $\lambda = s_z$ for incoming mesons and $\lambda = -s_z$ for incoming baryons (and in the same way for the outgoing particles). From Eq. A.2 we can deduce the normalization of a two-particle momentum state, rewritten in terms of a total four-momentum conserving expression:

$$\begin{aligned} \langle \boldsymbol{p}'\boldsymbol{k}', \lambda' | \boldsymbol{p}\,\boldsymbol{k}\,, \lambda \rangle &= \delta^3(\boldsymbol{p}' - \boldsymbol{p})\delta^3(\boldsymbol{k}' - \boldsymbol{k})\delta_{\lambda'\lambda} \\ &= \delta^3(\boldsymbol{P}' - \boldsymbol{P})\delta^3(\boldsymbol{k}' - \boldsymbol{k})\delta_{\lambda'\lambda} \\ &= \delta^3(\boldsymbol{P}' - \boldsymbol{P})\frac{1}{\mathrm{k}^2}\delta(\mathrm{k}' - \mathrm{k})\delta(\Omega'_k - \Omega_k)\delta_{\lambda'\lambda} \\ &= \delta^4(P' - P)\frac{\sqrt{s}}{\mathrm{k}E_B E_M}\delta(\Omega'_k - \Omega_k)\delta_{\lambda'\lambda} \\ &= \delta^4(P' - P)\frac{\sqrt{s}}{\mathrm{k}E_B E_M}\langle \vartheta'\varphi', \lambda' | \vartheta\varphi, \lambda \rangle \\ &= \frac{\sqrt{s}}{\mathrm{k}E_B E_M}\langle P'; \vartheta'\varphi', \lambda' | P; \vartheta\varphi, \lambda \rangle \end{aligned} \tag{A.4}$$

and thus

$$|\boldsymbol{p}\,\boldsymbol{k}\,, \lambda\rangle = \sqrt{\frac{\sqrt{s}}{\mathrm{k}E_B E_M}} |P; \vartheta\varphi, \lambda\rangle \; . \tag{A.5}$$

Here, the final-state helicities λ are related to the particle helicities by $\lambda \equiv \lambda_k - \lambda_p$, $\lambda' \equiv \lambda_{k'} - \lambda_{p'}$ since $\boldsymbol{p} = -\boldsymbol{k}$. The fourth equality in (A.4) follows from the total energy $\sqrt{s}$ in the CMS:

$$\frac{\mathrm{d}\sqrt{s}}{\mathrm{d}\,\mathrm{k}} = \frac{\mathrm{d}\,(E_B + E_M)}{\mathrm{d}\,\mathrm{k}} = \frac{\mathrm{d}\left(\sqrt{m_B^2 + \mathrm{k}^2} + \sqrt{m_M^2 + \mathrm{k}^2}\right)}{\mathrm{d}\,\mathrm{k}} = \frac{\mathrm{k}\sqrt{s}}{E_B E_M} \; . \tag{A.6}$$

Asymptotic two-particle momentum states are also abbreviated as

$$\langle \boldsymbol{p}'\boldsymbol{k}', \lambda' | \equiv \langle f | \qquad \text{and} \qquad |\boldsymbol{p}\,\boldsymbol{k}\,, \lambda\rangle \equiv |i\rangle \; . \tag{A.7}$$

A.2 Dirac Matrices, Spinors, and all the Rest

The three-dimensional antisymmetric tensor is given by

$$\varepsilon_{ijk} = \begin{cases} +1 & \text{if } \{i,j,k\} \text{ is a cyclic permutation of } \{1,2,3\} \\ -1 & \text{if it is an odd permutation} \\ \;\;0 & \text{otherwise} \end{cases} \; . \tag{A.8}$$

The totally antisymmetric four-dimensional Levi-Civita tensor is defined as

$$\varepsilon^{\mu\nu\rho\sigma} = -\varepsilon_{\mu\nu\rho\sigma} = \begin{cases} +1 & \text{if } \{\mu,\nu,\rho,\sigma\} \text{ is an even permutation of } \{0,1,2,3\} \\ -1 & \text{if it is an odd permutation} \\ \ \ 0 & \text{otherwise} \end{cases} \tag{A.9}$$

and fulfills the following useful identities:

$$\begin{aligned} \varepsilon^{\mu\nu\rho\sigma}\varepsilon^{\mu'\nu'\rho'\sigma'} &= -\det(g^{\alpha\alpha'}) \qquad \alpha=\mu,\nu,\rho,\sigma \quad \alpha'=\mu',\nu',\rho',\sigma' \\ \varepsilon^{\mu\nu\rho\sigma}\varepsilon_{\mu}{}^{\nu'\rho'\sigma'} &= -\det(g^{\alpha\alpha'}) \qquad \alpha=\nu,\rho,\sigma \quad \alpha'=\nu',\rho',\sigma' \\ \varepsilon^{\mu\nu\rho\sigma}\varepsilon_{\mu\nu}{}^{\rho'\sigma'} &= -2(g^{\rho\rho'}g^{\sigma\sigma'} - g^{\rho\sigma'}g^{\rho'\sigma}) \\ \varepsilon^{\mu\nu\rho\sigma}\varepsilon_{\mu\nu\rho}{}^{\sigma'} &= -6g^{\sigma\sigma'} \\ \varepsilon^{\mu\nu\rho\sigma}\varepsilon_{\mu\nu\rho\sigma} &= -24\ . \end{aligned}$$

The γ matrices satisfy

$$\{\gamma^\mu,\gamma^\nu\} \equiv \gamma^\mu\gamma^\nu + \gamma^\nu\gamma^\mu = 2g^{\mu\nu} \tag{A.10}$$

with γ_0 hermitian and γ_i $(i=1,2,3)$ antihermitian, which can also be expressed as

$$\gamma^{\mu\dagger} = \gamma_0\gamma^\mu\gamma_0\ . \tag{A.11}$$

Some useful combinations are

$$\begin{aligned} \gamma_5 &\equiv \mathrm{i}\gamma^0\gamma^1\gamma^2\gamma^3 = -\mathrm{i}\gamma_0\gamma_1\gamma_2\gamma_3 = \gamma^5 = \gamma_5^\dagger = -\gamma^0\gamma_5\gamma^0 \\ \sigma^{\mu\nu} &\equiv \frac{\mathrm{i}}{2}\left[\gamma^\mu,\gamma^\nu\right] \equiv \frac{\mathrm{i}}{2}\left(\gamma^\mu\gamma^\nu - \gamma^\nu\gamma^\mu\right)\ . \end{aligned}$$

The contraction of the γ matrix four-vector γ^μ with a four-vector a^μ is abbreviated by $\not{a} \equiv \gamma_\mu a^\mu$. From the properties of γ_5

$$\begin{aligned} \gamma_5^2 &= \mathbb{1}_4 \\ \{\gamma_5,\gamma^\mu\} &= 0 \\ \gamma_5 &= -\mathrm{i}\tfrac{1}{4!}\varepsilon_{\mu\nu\rho\sigma}\gamma^\mu\gamma^\nu\gamma^\rho\gamma^\sigma \end{aligned} \tag{A.12}$$

one deduces the following relations to the Levi-Civita tensor being of great use for rewriting matrix elements (cf. Appendix I):

$$\begin{aligned} \gamma^\mu &= \mathrm{i}\tfrac{1}{4!}\varepsilon^{\alpha\nu\rho\sigma}\gamma_5\gamma^\mu\gamma_\alpha\gamma_\nu\gamma_\rho\gamma_\sigma \\ &= \mathrm{i}\tfrac{1}{6}\varepsilon^{\mu\nu\rho\sigma}\gamma_5\gamma_\nu\gamma_\rho\gamma_\sigma \end{aligned} \tag{A.13}$$

and leading to

$$\begin{aligned} \gamma_5\sigma^{\mu\nu} &= \mathrm{i}\tfrac{1}{2}\varepsilon^{\mu\nu\rho\sigma}\sigma_{\rho\sigma} \\ \varepsilon^{\mu\nu\rho\sigma}\gamma_\mu &= \mathrm{i}\gamma_5\left(\gamma^\nu\gamma^\rho\gamma^\sigma - g^{\nu\rho}\gamma^\sigma - g^{\rho\sigma}\gamma^\nu + g^{\nu\sigma}\gamma^\rho\right)\ . \end{aligned} \tag{A.14}$$

The specific representation of the γ matrices chosen here is the Dirac representation:

$$\gamma_0 = \gamma^0 = \begin{pmatrix} \mathbb{1}_2 & 0 \\ 0 & -\mathbb{1}_2 \end{pmatrix}, \qquad \gamma^i = \boldsymbol{\gamma} = \begin{pmatrix} 0 & \boldsymbol{\sigma} \\ -\boldsymbol{\sigma} & 0 \end{pmatrix}, \qquad \gamma_5 = \begin{pmatrix} 0 & \mathbb{1}_2 \\ \mathbb{1}_2 & 0 \end{pmatrix}, \tag{A.15}$$

where we have introduced the Pauli matrices

$$\sigma_1 = \begin{pmatrix} 0 & 1 \\ 1 & 0 \end{pmatrix} , \quad \sigma_2 = \begin{pmatrix} 0 & -\mathrm{i} \\ \mathrm{i} & 0 \end{pmatrix} , \quad \sigma_3 = \begin{pmatrix} 1 & 0 \\ 0 & -1 \end{pmatrix} . \tag{A.16}$$

They fulfill the relations

$$\begin{aligned} \boldsymbol{\sigma} \cdot \boldsymbol{a} \boldsymbol{\sigma} \cdot \boldsymbol{b} &= \boldsymbol{a} \cdot \boldsymbol{b} + \mathrm{i} \boldsymbol{\sigma} \cdot (\boldsymbol{a} \times \boldsymbol{b}) \\ [\sigma_i, \sigma_j] &= 2(\sigma_i \sigma_j - \delta_{ij}) = 2(\delta_{ij} - \sigma_j \sigma_i) , \end{aligned} \tag{A.17}$$

which can be proven by using their (anti-) commutation relations

$$[\sigma_i, \sigma_j] = 2\mathrm{i}\varepsilon_{ijk}\sigma_k , \qquad \{\sigma_i, \sigma_j\} = 2\delta_{ij} . \tag{A.18}$$

A.2.1 Dirac (Spin-$\frac{1}{2}$) Spinors

The Dirac spinors $u(p,s)$ and the adjungated spinors $\bar{u}(p,s) \equiv u(p,s)^\dagger \gamma_0$ fulfill the free Dirac equation

$$\begin{aligned} (\not{p} - m_B) u(p,s) &= 0 \\ \bar{u}(p,s)(\not{p} - m_B) &= 0 \end{aligned} \tag{A.19}$$

and are normalized such that

$$\bar{u}(p,s')u(p,s) = \delta_{s,s'} . \tag{A.20}$$

Hence the Dirac spinors are explicitly given by:

$$u(p,s) = \sqrt{\frac{E_B + m_B}{2m_B}} \begin{pmatrix} \mathbb{1}_2 \\ \dfrac{\boldsymbol{\sigma} \cdot \boldsymbol{p}}{E_B + m_B} \end{pmatrix} \cdot \chi_s . \tag{A.21}$$

The spin states are given in the c.m. system by

$$\chi^i_{+\frac{1}{2}} = \begin{pmatrix} 1 \\ 0 \end{pmatrix} , \quad \chi^i_{-\frac{1}{2}} = \begin{pmatrix} 0 \\ 1 \end{pmatrix} \tag{A.22}$$

for incoming spin-$\frac{1}{2}$ particles and by ($\varphi = 0$)

$$\begin{aligned} \chi^f_{s'} &= d^{\frac{1}{2}}_{+\frac{1}{2}s'}(\vartheta)\chi^i_{+\frac{1}{2}} + d^{\frac{1}{2}}_{-\frac{1}{2}s'}(\vartheta)\chi^i_{-\frac{1}{2}} = \begin{pmatrix} d^{\frac{1}{2}}_{+\frac{1}{2}s'}(\vartheta) \\ d^{\frac{1}{2}}_{-\frac{1}{2}s'}(\vartheta) \end{pmatrix} , \\ \Longrightarrow \quad \chi^f_{+\frac{1}{2}} &= \begin{pmatrix} \cos\frac{\vartheta}{2} \\ \sin\frac{\vartheta}{2} \end{pmatrix} , \quad \chi^f_{-\frac{1}{2}} = \begin{pmatrix} -\sin\frac{\vartheta}{2} \\ \cos\frac{\vartheta}{2} \end{pmatrix} . \end{aligned} \tag{A.23}$$

for outgoing spin-$\frac{1}{2}$ particles. The d-functions are given in Appendix B.2. Using the spin-$\frac{1}{2}$ operator $\boldsymbol{\sigma}/2$ enjoying the properties (s. Eqs. (A.16) and (A.18))

$$\left(\frac{\boldsymbol{\sigma}}{2}\right)^2 = \frac{1}{2}\left(\frac{1}{2} + 1\right) = \frac{3}{4} , \qquad \left[\frac{\sigma_i}{2}, \frac{\sigma_j}{2}\right] = \mathrm{i}\varepsilon_{ijk}\frac{\sigma_k}{2} \tag{A.24}$$

one finds

$$\begin{aligned}\tfrac{1}{2}\boldsymbol{\sigma}\cdot\hat{\boldsymbol{k}}\,\chi^{i}_{\pm\frac{1}{2}} &= \pm\tfrac{1}{2}\chi^{i}_{\pm\frac{1}{2}}\\ \tfrac{1}{2}\boldsymbol{\sigma}\cdot\hat{\boldsymbol{k}}'\,\chi^{f}_{\pm\frac{1}{2}} &= \pm\tfrac{1}{2}\chi^{f}_{\pm\frac{1}{2}}\ . \end{aligned} \tag{A.25}$$

Note that in the c.m. frame spin up (down) corresponds to negative (positive) nucleon helicity ($\boldsymbol{p}=-\boldsymbol{k}$).

It is interesting to note that the behavior of the adjungated spinor $\bar{u}(p,s)$ upon the action of the parity operator $\mathrm{i}\gamma_5$ in the c.m. system ($\boldsymbol{p}'=-\boldsymbol{k}'$) is (cf. Section 5.2):

$$\begin{aligned}\bar{u}(p',s')(\mathrm{i}\gamma_5)=u(p',s')^{\dagger}(\mathrm{i}\gamma_0\gamma_5) &= \mathrm{i}\sqrt{\frac{E_{B'}+m_{B'}}{2m_{B'}}}\chi^{\dagger}_{s'}\left(\mathbb{1}_2,\frac{\boldsymbol{\sigma}\cdot\boldsymbol{p}'}{E_{B'}+m_{B'}}\right)\begin{pmatrix}0 & \mathbb{1}_2\\ -\mathbb{1}_2 & 0\end{pmatrix}\\ &= \mathrm{i}\sqrt{\frac{E_{B'}+m_{B'}}{2m_{B'}}}\chi^{\dagger}_{s'}\left(\frac{\boldsymbol{\sigma}\cdot\boldsymbol{k}'}{E_{B'}+m_{B'}},\mathbb{1}_2\right)\\ &= \sqrt{\frac{E_{B'}+m_{B'}}{2m_{B'}}}\chi^{\dagger}_{s'}\left((E_{B'}-m_{B'})\,\mathbb{1}_2,\boldsymbol{\sigma}\cdot\boldsymbol{k}'\right)\frac{\mathrm{i}\boldsymbol{\sigma}\cdot\boldsymbol{k}'}{\mathrm{k}'^2}\\ &= \bar{u}(p',s',E_{B'}+m_{B'}\to E_{B'}-m_{B'})(\mathrm{i}\boldsymbol{\sigma}\cdot\hat{\boldsymbol{k}}') \qquad (A.26)\\ &\overset{(A.25)}{=} \pm\mathrm{i}\bar{u}(p',s',E_{B'}+m_{B'}\to E_{B'}-m_{B'}) \qquad (A.27)\end{aligned}$$

for $s'=\pm\frac{1}{2}$.

The spin-$\frac{1}{2}$ projection operator on states with mass m_B result by summing over the spins:

$$\Lambda(p)=2m_B\sum_s u(p,s)\bar{u}(p,s)=\not{p}+m_B\ . \tag{A.28}$$

An important identity closely related to the anomalous magnetic moment of a spin-$\frac{1}{2}$ particle [18, 82, 153] is the Gordon decomposition of the current:

$$\bar{u}(p')\gamma^{\mu}u(p)=\bar{u}(p')\left[\frac{(p+p')^{\mu}}{2m_B}+\frac{\mathrm{i}\sigma^{\mu\nu}(p'-p)_{\nu}}{2m_B}\right]u(p)\ . \tag{A.29}$$

A.2.2 Spin-1 Polarization Vectors

Spin-1 particle fields fulfill the free Proca equation:

$$\partial_{\mu}V^{\mu\nu}+m_V^2V^{\nu}=0 \tag{A.30}$$

with

$$V_{\mu\nu}=\partial_{\mu}V_{\nu}-\partial_{\nu}V_{\mu}\ ,$$

which immediately leads to

$$m_V^2\partial_{\mu}V^{\mu}=0\,. \tag{A.31}$$

For massive ($m_V^2 \neq 0$) spin-1 particles (e.g. ρ, ω), V_μ is divergenceless and Eq. (A.30) reduces to

$$\left(\Box + m_V^2\right) V^\nu = 0 \; , \qquad \qquad \partial_\mu V^\mu = 0 \; . \tag{A.32}$$

Hence massive spin-1 particles are described by polarization vectors ε_μ (cf. Eq. (3.2)) that are four-transversal with respect to the particle momentum[2)]. The explicit cartesian forms in space of the three possible polarization settings for the z-component ($\lambda_V = \pm 1$, $\lambda_V = 0$) are determined by the properties of the three-dimensional polarization vectors: Two are transversal and one is longitudinal with respect to the three-momentum of the particle:

$$\boldsymbol{\varepsilon}_{\pm 1} = \frac{\mp 1}{\sqrt{2}} \begin{pmatrix} 1 \\ \pm \mathrm{i} \\ 0 \end{pmatrix} \; , \quad \boldsymbol{\varepsilon}_0 = \begin{pmatrix} 0 \\ 0 \\ 1 \end{pmatrix} \; , \tag{A.33}$$

valid for incoming particles in the c.m. system. This choice is in line with the Condon-Shortley convention [30]. For outgoing particles the three-vectors have to be rotated by the d-functions (cf. Appendix B.2):

$$\begin{aligned}
\boldsymbol{\varepsilon}'_\lambda(\vartheta) &= d^1_{+1\lambda}(\vartheta)\boldsymbol{\varepsilon}_{+1} + d^1_{0\lambda}(\vartheta)\boldsymbol{\varepsilon}_0 + d^1_{-1\lambda}(\vartheta)\boldsymbol{\varepsilon}_{-1} \\
\Longrightarrow \quad \boldsymbol{\varepsilon}'_{+1}(\vartheta) &= \frac{1}{2}(1+\cos\vartheta)\boldsymbol{\varepsilon}_{+1} + \frac{1}{\sqrt{2}}\sin\vartheta\boldsymbol{\varepsilon}_0 + \frac{1}{2}(1-\cos\vartheta)\boldsymbol{\varepsilon}_{-1} = \frac{1}{\sqrt{2}}\begin{pmatrix} -\cos\vartheta \\ -\mathrm{i} \\ \sin\vartheta \end{pmatrix} \\
\boldsymbol{\varepsilon}'_{-1}(\vartheta) &= \frac{1}{2}(1-\cos\vartheta)\boldsymbol{\varepsilon}_{+1} - \frac{1}{\sqrt{2}}\sin\vartheta\boldsymbol{\varepsilon}_0 + \frac{1}{2}(1+\cos\vartheta)\boldsymbol{\varepsilon}_{-1} = \frac{1}{\sqrt{2}}\begin{pmatrix} \cos\vartheta \\ -\mathrm{i} \\ -\sin\vartheta \end{pmatrix} \\
\boldsymbol{\varepsilon}'_0(\vartheta) &= -\frac{1}{\sqrt{2}}\sin\vartheta\boldsymbol{\varepsilon}_{+1} + \cos\vartheta\boldsymbol{\varepsilon}_0 + \frac{1}{\sqrt{2}}\sin\vartheta\boldsymbol{\varepsilon}_{-1} = \begin{pmatrix} \sin\vartheta \\ 0 \\ \cos\vartheta \end{pmatrix} \; .
\end{aligned}$$

The four-dimensional form ε^μ_λ of the polarization vectors follows by giving to the polarization vectors $\varepsilon^\mu_\lambda \equiv (0, \boldsymbol{\varepsilon}_\lambda)$ their momentum $\boldsymbol{k}$ via a Lorentz boost

$$L^{\mu\nu}(\boldsymbol{k}) = \frac{1}{m_V} \begin{pmatrix} E_V & k_x \quad k_y \quad k_z \\ k_x & \\ k_y & m_V \delta_{i,j} + \dfrac{k_i k_j}{E_V + m_V} \\ k_z & \end{pmatrix} \; .$$

The resulting polarization vectors ($L^{\mu\nu}\varepsilon_\nu$) are four-transversal (cf. (A.31)) and are normalized to $\varepsilon^\dagger_\mu \varepsilon^\mu = -1$:

$$\varepsilon^\mu_{\pm 1}(k) = (0, \boldsymbol{\varepsilon}_\pm) \; , \quad \varepsilon^\mu_0(k) = \frac{1}{m_V}(\mathrm{k}, E_V \boldsymbol{\varepsilon}_0) \tag{A.34}$$

for incoming c.m. particles with $k^\mu = (E_V, \boldsymbol{k})$. For outgoing c.m. particles with $k'^\mu = (E_{V'}, \boldsymbol{k}')$ one has to take the adjungated $(\varepsilon'^\mu_\lambda(k')^\dagger)$ of

$$\varepsilon'^\mu_{\pm 1}(k') = (0, \boldsymbol{\varepsilon}'_\pm) \; , \quad \varepsilon'^\mu_0(k') = \frac{1}{m_{V'}}(\mathrm{k}', E_{V'} \boldsymbol{\varepsilon}'_0) \; . \tag{A.35}$$

[2)] In Coulomb-/Feynman-gauge $\boldsymbol{\nabla} \cdot \boldsymbol{A} = 0$, which is used here, the same holds true for the real photon field $A_\mu = (0, \boldsymbol{A})$.

A.2.3 Rarita-Schwinger (Spin-$\frac{3}{2}$) Spinors

Rarita-Schwinger (spin-$\frac{3}{2}$) spinors u^μ result from the coupling of a spin-1 polarization vector with a spin-$\frac{1}{2}$ spinor:

$$u^\mu(p,s) \;\equiv\; \sum_{r,m} (\tfrac{3}{2}, s|1, r; \tfrac{1}{2}, m) u(p,m) \varepsilon^\mu_r(p)$$

and explicitly evaluating the Clebsch-Gordan coefficients for the $1 \oplus \frac{1}{2} = \frac{3}{2}$ coupling:

$$\begin{aligned} u^\mu(p, \pm\tfrac{3}{2}) &= u(p, \pm\tfrac{1}{2}) \varepsilon^\mu_{\pm 1}(p) \\ u^\mu(p, \pm\tfrac{1}{2}) &= \tfrac{1}{\sqrt{3}} u(p, \mp\tfrac{1}{2}) \varepsilon^\mu_{\pm 1}(p) + \sqrt{\tfrac{2}{3}} u(p, \pm\tfrac{1}{2}) \varepsilon^\mu_0(p) \; . \end{aligned} \tag{A.36}$$

For incoming spin-$\frac{3}{2}$ spinors in the c.m. system with $p^\mu = (E, 0, 0, \pm \mathrm{p})$ this can also be written as

$$u^\mu(p,s) = \sqrt{\frac{E+m}{2m}} \begin{pmatrix} \mathbb{1}_2 \\ \frac{\boldsymbol{\sigma} \cdot \boldsymbol{p}}{E+m} \end{pmatrix} S^\mu \chi_s \; , \tag{A.37}$$

where the spin states are

$$\chi_{+\frac{3}{2}} = \begin{pmatrix} 1 \\ 0 \\ 0 \\ 0 \end{pmatrix} \; , \quad \chi_{+\frac{1}{2}} = \begin{pmatrix} 0 \\ 1 \\ 0 \\ 0 \end{pmatrix} \; , \quad \chi_{-\frac{1}{2}} = \begin{pmatrix} 0 \\ 0 \\ 1 \\ 0 \end{pmatrix} \; , \quad \chi_{-\frac{3}{2}} = \begin{pmatrix} 0 \\ 0 \\ 0 \\ 1 \end{pmatrix} \tag{A.38}$$

and the spin-coupling matrix S^μ

$$\begin{aligned} S_0 &= \frac{p}{m} \begin{pmatrix} 0 & \sqrt{\frac{2}{3}} & 0 & 0 \\ 0 & 0 & \sqrt{\frac{2}{3}} & 0 \end{pmatrix} \; , \\ S_x &= \begin{pmatrix} -\frac{1}{\sqrt{2}} & 0 & \frac{1}{\sqrt{6}} & 0 \\ 0 & -\frac{1}{\sqrt{6}} & 0 & \frac{1}{\sqrt{2}} \end{pmatrix} \; , \quad S_y = -\mathrm{i} \begin{pmatrix} \frac{1}{\sqrt{2}} & 0 & \frac{1}{\sqrt{6}} & 0 \\ 0 & \frac{1}{\sqrt{6}} & 0 & \frac{1}{\sqrt{2}} \end{pmatrix} \; , \quad S_z = \frac{\pm E}{\mathrm{p}} S_0 \; . \end{aligned}$$

The adjungated spinor is given in the same way as for spin-$\frac{1}{2}$ particles: $\bar{u}(p,s)^\mu \equiv u(p,s)^{\mu\dagger} \gamma_0$.

The spinors $u(p,s)^\mu$ fulfill the Rarita-Schwinger equations [149]

$$\begin{aligned} (\not{p} - m) u^\mu(p,s) &= 0 \\ p_\mu u^\mu(p,s) &= 0 \\ \gamma_\mu u^\mu(p,s) &= 0 \end{aligned} \tag{A.39}$$

and are normalized in the following way:

$$\bar{u}^\mu(p,s) u_\mu(p,s') \;=\; -\delta_{s,s'} \; .$$

The Eqs. (A.39) reduce the 16 degrees of freedom of the spinor u^μ to the desired number of 8. These equations and the normalization can be easily proven by using Eq. (A.36) and the spin-$\frac{1}{2}$ spinors and spin-1 polarization vectors from the previous sections.

The spin-$\frac{3}{2}$ projection operator on states with mass m results by summing over the spins:

$$\begin{aligned} \Lambda^{\mu\nu}_{\frac{3}{2}}(p) &= 2m \sum_s u^\mu(p,s)\bar{u}^\nu(p,s) \\ &= -(\not{p}+m)\left(g^{\mu\nu} - \frac{1}{3}\gamma^\mu\gamma^\nu - \frac{2}{3m^2}p^\mu p^\nu + \frac{1}{3m}(p^\mu\gamma^\nu - p^\nu\gamma^\mu)\right) , \end{aligned} \tag{A.40}$$

which is related to the Rarita-Schwinger propagator $G^{\mu\nu}_{\frac{3}{2}}(p)$ by:

$$G^{\mu\nu}_{\frac{3}{2}}(p) = \frac{\Lambda^{\mu\nu}_{\frac{3}{2}}(p)}{p^2 - m^2} . \tag{A.41}$$

Since $(\not{p} + \sqrt{p^2})\not{p} = \sqrt{p^2}(\not{p} + \sqrt{p^2})$ the projection operator can on-shell ($\sqrt{p^2} = m$) also be written as:

$$\Lambda^{\mu\nu}_{\frac{3}{2}}(p) = -(\not{p}+m)\left(g^{\mu\nu} - \frac{1}{3}\gamma^\mu\gamma^\nu - \frac{1}{3p^2}(\not{p}\gamma^\mu p^\nu + p^\mu\gamma^\nu\not{p})\right) . \tag{A.42}$$

Appendix B

Legendre Polynomials and Wigner Simplified Rotation Matrices

B.1 Legendre Polynomials

The Legendre polynomials are defined in the usual way [47, 88]:

$$P_l(x) = \frac{1}{2^l l!}\frac{\mathrm{d}^l}{\mathrm{x}^l}(x^2-1)^l \qquad \text{with } x = \cos\vartheta \tag{B.1}$$

and enjoy the following important properties:

$$\begin{aligned} \int_{-1}^{+1} \mathrm{d}P_l(x)P_{l'}(x) &= \frac{2}{2l+1}\delta_{ll'} \\ xP_l'(x) &= P_{l+1}'(x) - (l+1)P_l(x) = P_{l-1}'(x) + lP_l(x)\ , \end{aligned} \tag{B.2}$$

from which all derivatives $P_l'(x) \equiv \mathrm{d}P_l(x)/\mathrm{d}x$ can be extracted.

B.2 Wigner Simplified Rotation Matrices (*d*-functions)

The Wigner functions [61, 83, 88, 152]:

$$\mathcal{D}^J_{MM'}(\alpha,\beta,\alpha) = e^{-\mathrm{i}\alpha M} d^J_{MM'}(\beta) e^{-\mathrm{i}\alpha M'} \tag{B.3}$$

are the matrix elements of a rotation which transforms the $|J, M\rangle$ component of the unit vector $\boldsymbol{e}_z$ into the $|J, M'\rangle$ component of the unit vector $(\cos\alpha\sin\beta, \sin\alpha\sin\beta, \cos\beta)$. The non-trivial part of the Wigner functions is contained in the Wigner Simplified Rotation Matrices (d-functions) describing the middle rotation about the y-axis, which mixes different M-values. They are in general given by [88, 152]:

$$d^J_{\lambda\lambda'}(\vartheta) \;=\; \sum_k (-1)^{k+\lambda-\lambda'} \frac{\sqrt{(J+\lambda)!(J-\lambda)!(J+\lambda')!(J-\lambda')!}}{(J-\lambda-k)!(J+\lambda'-k)!(k+\lambda-\lambda')!k!}$$

$$\times \left(\cos\frac{\vartheta}{2}\right)^{2J-2k+\lambda'-\lambda}\left(\sin\frac{\vartheta}{2}\right)^{2k+\lambda-\lambda'} .$$

Some important symmetry properties of the d-functions are:

$$\begin{aligned}
d^J_{\lambda\lambda'}(\vartheta) &= d^J_{-\lambda'-\lambda}(\vartheta) \\
d^J_{\lambda\lambda'}(\vartheta) &= (-1)^{\lambda-\lambda'} d^J_{\lambda'\lambda}(\vartheta) && \text{(B.4)} \\
\Longrightarrow d^J_{\lambda\lambda'}(\vartheta) &= (-1)^{\lambda-\lambda'} d^J_{-\lambda-\lambda'}(\vartheta) && \text{(B.5)} \\
d^J_{\lambda\lambda'}(\vartheta) &= d^J_{\lambda\lambda'}(-\vartheta) \\
d^J_{\lambda\lambda'}(\vartheta) &= (-1)^{J+\lambda} d^J_{\lambda-\lambda'}(\pi-\vartheta) \\
d^J_{\lambda\lambda'}(\pi) &= (-1)^{J-\lambda'}\delta_{\lambda,-\lambda'} \\
\Longrightarrow d^J_{\lambda\lambda'}(0) &= (-1)^{J+\lambda} d^J_{\lambda,-\lambda'}(\pi) = (-1)^{J+\lambda-J-\lambda'}\delta_{\lambda\lambda'} = \delta_{\lambda\lambda'} . && \text{(B.6)}
\end{aligned}$$

Since in meson nucleon scattering we only deal with half-integer total spin J, we give explicit formulae for $J = l + \frac{1}{2}$, l positive integer ($x = \cos\vartheta$) [61, 83, 88]:

$$\begin{aligned}
d^J_{+\frac{1}{2}+\frac{1}{2}}(\vartheta) &= \frac{1}{l+1}\cos\frac{\vartheta}{2}\left[P'_{l+1}(x) - P'_l(x)\right] \\
d^J_{-\frac{1}{2}+\frac{1}{2}}(\vartheta) &= \frac{1}{l+1}\sin\frac{\vartheta}{2}\left[P'_{l+1}(x) + P'_l(x)\right] \\
d^J_{+\frac{1}{2}+\frac{3}{2}}(\vartheta) &= \frac{1}{l+1}\sin\frac{\vartheta}{2}\left[\sqrt{\frac{l}{l+2}}P'_{l+1}(x) + \sqrt{\frac{l+2}{l}}P'_l(x)\right] \\
d^J_{-\frac{1}{2}+\frac{3}{2}}(\vartheta) &= \frac{1}{l+1}\cos\frac{\vartheta}{2}\left[-\sqrt{\frac{l}{l+2}}P'_{l+1}(x) + \sqrt{\frac{l+2}{l}}P'_l(x)\right] . && \text{(B.7)}
\end{aligned}$$

Since we also deal with vector meson (photon) nucleon final states, there is a need for a closed formula for $d^J_{\pm\frac{3}{2}\pm\frac{3}{2}}$. With the help of the following general recursion formula [61, 83, 88]

$$\begin{aligned}
2\sqrt{(J+\lambda')(J+\lambda'-1)}\,d^J_{\lambda\lambda'}(\vartheta) &= \sqrt{(J+\lambda)(J+\lambda-1)}(1+\cos\vartheta)d^{J-1}_{\lambda-1,\lambda'-1}(\vartheta) + \\
&\quad 2\sqrt{(J+\lambda)(J-\lambda)}\sin\vartheta\, d^{J-1}_{\lambda,\lambda'-1}(\vartheta) + \\
&\quad \sqrt{(J-\lambda)(J-\lambda-1)}(1-\cos\vartheta)d^{J-1}_{\lambda+1,\lambda'-1}(\vartheta)
\end{aligned}$$

one finds, setting $\lambda = \lambda' = -\frac{1}{2}$,

$$\begin{aligned}
d^{J-1}_{+\frac{3}{2}+\frac{3}{2}}(\vartheta) &= \frac{-1}{(1+\cos\vartheta)}\times \\
&\left[2d^J_{+\frac{1}{2}+\frac{1}{2}}(\vartheta) + \sqrt{\frac{J+\frac{1}{2}}{J-\frac{3}{2}}}\left(2\sin\vartheta\, d^{J-1}_{+\frac{1}{2}+\frac{3}{2}}(\vartheta) - (1-\cos\vartheta)d^{J-1}_{-\frac{1}{2}+\frac{3}{2}}(\vartheta)\right)\right]
\end{aligned}$$

and, setting $\lambda = -\lambda' = +\frac{1}{2}$,

$$\begin{aligned}
d^{J-1}_{+\frac{3}{2}-\frac{3}{2}}(\vartheta) &= \frac{1}{(1-\cos\vartheta)}\times \\
&\left[2d^J_{-\frac{1}{2}+\frac{1}{2}}(\vartheta) + \sqrt{\frac{J+\frac{1}{2}}{J-\frac{3}{2}}}\left(2\sin\vartheta\, d^{J-1}_{-\frac{1}{2}+\frac{3}{2}}(\vartheta) - (1+\cos\vartheta)d^{J-1}_{+\frac{1}{2}+\frac{3}{2}}(\vartheta)\right)\right] .
\end{aligned}$$

Note, that these two formulae do not appear explicitly in the literature. All other necessary $J\lambda\lambda'$ combinations can be deduced from Eqs. (B.4) and (B.5).

The only case where we also need integer J d-functions is for the rotation of the spin-1 polarization vector from incoming to outgoing final state. The needed functions are (l integer):

$$\begin{aligned} d^l_{00}(\vartheta) &= P_l(x) \\ d^l_{10}(\vartheta) &= \frac{-1}{\sqrt{l(l+1)}} \sin\vartheta P'_l(x) \\ d^l_{m1}(\vartheta) &= \frac{1}{\sqrt{l(l+1)}} \left[-m \frac{1+\cos\vartheta}{\sin\vartheta} \sin\vartheta d^l_{m0}(\vartheta) - \sqrt{(l-m)(l+m+1)} d^l_{m+1,0}(\vartheta) \right] . \end{aligned}$$

Finally, we note that the d-functions are normalized such that

$$\int_{-1}^{+1} \mathrm{d}(\cos\vartheta) d^J_{\lambda\lambda'}(\vartheta) d^{J'}_{\lambda\lambda'}(\vartheta) = \frac{2}{2J+1} \delta_{JJ'} \; . \tag{B.8}$$

Appendix C

Formal Scattering Theory

C.1 Fundamental Matrices

The relation between the scattering matrix S and the transition matrix T is defined as:

$$S \equiv 1 + 2\mathrm{i}T \; . \tag{C.1}$$

With the two-particle states given in Appendix A, the matrix M is then introduced as in [18]

$$\langle f|S|i\rangle = \delta_{fi} - \mathrm{i}(2\pi)^4\delta^4(P_f - P_i)\left(\prod_{j=1}^{4} N_j\right)\langle f|M|i\rangle \tag{C.2}$$

with the normalization factors

$$N_B = \sqrt{\frac{2m_B}{(2\pi)^3 2E_B}} \quad \text{for baryons and} \quad N_M = \sqrt{\frac{1}{(2\pi)^3 2E_B}} \quad \text{for mesons} \tag{C.3}$$

and hence

$$\langle f|T|i\rangle = -\frac{1}{2}(2\pi)^4\delta^4(P_f - P_i)\left(\prod_{j=1}^{4} N_j\right)\langle f|M|i\rangle \; . \tag{C.4}$$

C.2 Optical Theorem

From the unitarity of the scattering matrix $SS^\dagger = S^\dagger S = 1$ follows the *optical theorem*:

$$\mathrm{i}(T - T^\dagger) = -2\mathrm{Im}T = -2TT^\dagger \; . \tag{C.5}$$

Now we take the matrix element of this equation between asymptotic two-particle momentum states $\langle f|$ and $|i\rangle$. To evaluate the right-hand side we insert a complete normalized set of intermediate two-particle momentum states $\sum_{n,\lambda_q}\int \mathrm{d}^3p_q \int \mathrm{d}^3k_q |\boldsymbol{p}_q\boldsymbol{k}_q,\lambda_q\rangle\langle\boldsymbol{p}_q\boldsymbol{k}_q,\lambda_q|$, where the sum over n denotes the various, energetically allowed final states:

$$\langle f|T^+ - T|i\rangle = 2\mathrm{i}\sum_{n,\lambda_q}\int \mathrm{d}^3p_q \int \mathrm{d}^3k_q \langle f|T|\boldsymbol{p}_q\boldsymbol{k}_q,\lambda_q\rangle\langle\boldsymbol{p}_q\boldsymbol{k}_q,\lambda_q|T^+|i\rangle\ . \tag{C.6}$$

Plugging in (C.4) we arrive at the optical theorem under the assumption of two-particle unitarity:

$$\begin{aligned}\langle f|M - M^\dagger|i\rangle &= -\mathrm{i}\sum_{n,\lambda_q}\int \mathrm{d}^3p_q \int \mathrm{d}^3k_q (2\pi)^4\delta^4(P - p_q - k_q)\frac{m_{B_q}}{(2\pi)^6 2E_{M_q}E_{B_q}}\times\\ &\qquad\langle f|M|\boldsymbol{p}_q\boldsymbol{k}_q,\lambda_q\rangle\langle\boldsymbol{p}_q\boldsymbol{k}_q,\lambda_q|M^\dagger|i\rangle\\ &= -\mathrm{i}\sum_{n,\lambda_q}\int \mathrm{d}^3k_q\delta(\sqrt{s} - p_q^0 - k_q^0)\frac{m_{B_q}}{(2\pi)^2 2E_{M_q}E_{B_q}}\times\\ &\qquad\langle f|M|\boldsymbol{p}_q\boldsymbol{k}_q,\lambda_q\rangle\langle\boldsymbol{p}_q\boldsymbol{k}_q,\lambda_q|M^\dagger|i\rangle\\ &= -\mathrm{i}\sum_{n,\lambda_q}\int \mathrm{d}^4q\delta(\sqrt{s}/2 - E_{B_q} - q_0)\delta(\sqrt{s}/2 - E_{M_q} + q_0)\frac{2m_{B_q}}{(4\pi)^2 E_{B_q}E_{M_q}}\times\\ &\qquad\langle f|M|\boldsymbol{p}_q\boldsymbol{k}_q,\lambda_q\rangle\langle\boldsymbol{p}_q\boldsymbol{k}_q,\lambda_q|M^\dagger|i\rangle\end{aligned} \tag{C.7}$$

times an overall δ-function. Here, we have routed the intermediate momenta symmetrically with respect to P:

$$k_q = P/2 + q \qquad \text{and} \qquad p_q = P/2 - q\ . \tag{C.8}$$

C.3 Matrix Relations and Notations

Since T is four-momentum conserving we find from the normalization of the two-particle momentum states (A.4), (A.5) using (C.4) and (C.3) ($\mathrm{p} = \mathrm{k}$ in the c.m. system):

$$\begin{aligned}\langle f|T|i\rangle &= \delta^4(P' - P)\frac{\sqrt{s}}{\sqrt{\mathrm{p}\,\mathrm{p}' E_B E_{B'} E_M E_{M'}}}\langle\vartheta'\varphi',\lambda'|T(\sqrt{s})|\vartheta\varphi,\lambda\rangle\\ &\overset{!}{=} -\frac{1}{2}(2\pi)^4\delta^4(P' - P)\sqrt{\frac{m_{B'}m_B}{(2\pi)^{12}4E_{B'}E_{M'}E_B E_M}}\langle f|M|i\rangle\end{aligned} \tag{C.9}$$

and hence we define

$$\mathcal{T}^{fi}_{\lambda'\lambda} \equiv \langle\vartheta'\varphi',\lambda'|T(\sqrt{s})|\vartheta\varphi,\lambda\rangle = -\frac{\sqrt{\mathrm{p}\,\mathrm{p}' m_{B'}m_B}}{(4\pi)^2\sqrt{s}}\langle f|M|i\rangle\ . \tag{C.10}$$

In the same way the $\mathcal{K}$-matrix is defined:

$$\mathcal{K}^{fi}_{\lambda'\lambda} \equiv \langle\vartheta'\varphi',\lambda'|K(\sqrt{s})|\vartheta\varphi,\lambda\rangle = -\frac{\sqrt{\mathrm{p}\,\mathrm{p}' m_{B'}m_B}}{(4\pi)^2\sqrt{s}}\langle f|\tilde{K}|i\rangle\ , \tag{C.11}$$

where $\tilde{K} = V$ in the K-matrix Born approximation (see Chapter 2). Note that $\mathcal{T}$ and $\mathcal{K}$ are defined differently as $\mathcal{M}$ and $\mathcal{V}$ in Chapter 2: $\mathcal{M}^{fi} \equiv \langle f|M|i\rangle$, $\mathcal{V}^{fi} \equiv \langle f|V|i\rangle$ with the asymptotic states as defined in (A.7). Since we work in the c.m. frame, we usually write

$$\begin{aligned} \mathcal{T}^{fi}_{\lambda'\lambda}(\vartheta) &\equiv \langle \vartheta, \varphi = 0, \lambda'|T(\sqrt{s})|00, \lambda\rangle \\ \mathcal{K}^{fi}_{\lambda'\lambda}(\vartheta) &\equiv \langle \vartheta, \varphi = 0, \lambda'|K(\sqrt{s})|00, \lambda\rangle \ . \end{aligned}$$

For total isospin $I = \frac{1}{2}$ all of the above matrices (S, M, T, K, $\tilde{K}$, and V) have to be understood as $12 \otimes 12$ matrices built up by all final states, e.g.:

$$S \equiv \begin{pmatrix} S_{\gamma^0_{\frac{1}{2}}\gamma^0_{\frac{1}{2}}} & S_{\gamma^0_{\frac{1}{2}}\gamma^0_{\frac{3}{2}}} & S_{\gamma^0_{\frac{1}{2}}\gamma^1_{\frac{1}{2}}} & S_{\gamma^0_{\frac{1}{2}}\gamma^1_{\frac{3}{2}}} & S_{\gamma^0_{\frac{1}{2}}\pi} & S_{\gamma^0_{\frac{1}{2}}\zeta} & S_{\gamma^0_{\frac{1}{2}}\eta} & S_{\gamma^0_{\frac{1}{2}}\Lambda} & S_{\gamma^0_{\frac{1}{2}}\Sigma} & S_{\gamma^0_{\frac{1}{2}}\omega_0} & S_{\gamma^0_{\frac{1}{2}}\omega_{\frac{1}{2}}} & S_{\gamma^0_{\frac{1}{2}}\omega_{\frac{3}{2}}} \\ S_{\gamma^0_{\frac{3}{2}}\gamma^0_{\frac{1}{2}}} & S_{\gamma^0_{\frac{3}{2}}\gamma^0_{\frac{3}{2}}} & S_{\gamma^0_{\frac{3}{2}}\gamma^1_{\frac{1}{2}}} & S_{\gamma^0_{\frac{3}{2}}\gamma^1_{\frac{3}{2}}} & S_{\gamma^0_{\frac{3}{2}}\pi} & S_{\gamma^0_{\frac{3}{2}}\zeta} & S_{\gamma^0_{\frac{3}{2}}\eta} & S_{\gamma^0_{\frac{3}{2}}\Lambda} & S_{\gamma^0_{\frac{3}{2}}\Sigma} & S_{\gamma^0_{\frac{3}{2}}\omega_0} & S_{\gamma^0_{\frac{3}{2}}\omega_{\frac{1}{2}}} & S_{\gamma^0_{\frac{3}{2}}\omega_{\frac{3}{2}}} \\ S_{\gamma^1_{\frac{1}{2}}\gamma^0_{\frac{1}{2}}} & S_{\gamma^1_{\frac{1}{2}}\gamma^0_{\frac{3}{2}}} & S_{\gamma^1_{\frac{1}{2}}\gamma^1_{\frac{1}{2}}} & S_{\gamma^1_{\frac{1}{2}}\gamma^1_{\frac{3}{2}}} & S_{\gamma^1_{\frac{1}{2}}\pi} & S_{\gamma^1_{\frac{1}{2}}\zeta} & S_{\gamma^1_{\frac{1}{2}}\eta} & S_{\gamma^1_{\frac{1}{2}}\Lambda} & S_{\gamma^1_{\frac{1}{2}}\Sigma} & S_{\gamma^1_{\frac{1}{2}}\omega_0} & S_{\gamma^1_{\frac{1}{2}}\omega_{\frac{1}{2}}} & S_{\gamma^1_{\frac{1}{2}}\omega_{\frac{3}{2}}} \\ S_{\gamma^1_{\frac{3}{2}}\gamma^0_{\frac{1}{2}}} & S_{\gamma^1_{\frac{3}{2}}\gamma^0_{\frac{3}{2}}} & S_{\gamma^1_{\frac{3}{2}}\gamma^1_{\frac{1}{2}}} & S_{\gamma^1_{\frac{3}{2}}\gamma^1_{\frac{3}{2}}} & S_{\gamma^1_{\frac{3}{2}}\pi} & S_{\gamma^1_{\frac{3}{2}}\zeta} & S_{\gamma^1_{\frac{3}{2}}\eta} & S_{\gamma^1_{\frac{3}{2}}\Lambda} & S_{\gamma^1_{\frac{3}{2}}\Sigma} & S_{\gamma^1_{\frac{3}{2}}\omega_0} & S_{\gamma^1_{\frac{3}{2}}\omega_{\frac{1}{2}}} & S_{\gamma^1_{\frac{3}{2}}\omega_{\frac{3}{2}}} \\ S_{\pi\gamma^0_{\frac{1}{2}}} & S_{\pi\gamma^0_{\frac{3}{2}}} & S_{\pi\gamma^1_{\frac{1}{2}}} & S_{\pi\gamma^1_{\frac{3}{2}}} & S_{\pi\pi} & S_{\pi\zeta} & S_{\pi\eta} & S_{\pi\Lambda} & S_{\pi\Sigma} & S_{\pi\omega_0} & S_{\pi\omega_{\frac{1}{2}}} & S_{\pi\omega_{\frac{3}{2}}} \\ & & & & & \cdots & & & & & & \end{pmatrix}, \tag{C.12}$$

where the upper γ index corresponds to the isospin of the photon (see appendix F.1.2). The lower γ and ω indices define the helicity state, see Section 5.2. For total isospin $I = \frac{3}{2}$, the matrix is reduced to $5 \otimes 5$:

$$S := \begin{pmatrix} S_{\gamma^1_{\frac{1}{2}}\gamma^1_{\frac{1}{2}}} & S_{\gamma^1_{\frac{1}{2}}\gamma^1_{\frac{3}{2}}} & S_{\gamma^1_{\frac{1}{2}}\pi} & S_{\gamma^1_{\frac{1}{2}}\zeta} & S_{\gamma^1_{\frac{1}{2}}\Sigma} \\ S_{\gamma^1_{\frac{3}{2}}\gamma^1_{\frac{1}{2}}} & S_{\gamma^1_{\frac{3}{2}}\gamma^1_{\frac{3}{2}}} & S_{\gamma^1_{\frac{3}{2}}\pi} & S_{\gamma^1_{\frac{3}{2}}\zeta} & S_{\gamma^1_{\frac{3}{2}}\Sigma} \\ S_{\pi\gamma^1_{\frac{1}{2}}} & S_{\pi\gamma^1_{\frac{3}{2}}} & S_{\pi\pi} & S_{\pi\zeta} & S_{\pi\Sigma} \\ S_{\zeta\gamma^1_{\frac{1}{2}}} & S_{\zeta\gamma^1_{\frac{3}{2}}} & S_{\zeta\pi} & S_{\zeta\zeta} & S_{\zeta\Sigma} \\ S_{\Sigma\gamma^1_{\frac{1}{2}}} & S_{\Sigma\gamma^1_{\frac{3}{2}}} & S_{\Sigma\pi} & S_{\Sigma\zeta} & S_{\Sigma\Sigma} \end{pmatrix} . \tag{C.13}$$

Appendix D

Properties of the Bethe-Salpeter Equation

D.1 Connection to the Optical Theorem

In this appendix, from the BS equation a condition for the imaginary part of the Bethe-Salpeter propagator is derived, whose relation to the optical theorem (C.7) is established in Section 2.2.

From the hermiticity of the potential

$$\langle f|\tilde{V}(p',p;\sqrt{s})|i\rangle^\dagger = \langle i|\tilde{V}^\dagger(p',p;\sqrt{s})|f\rangle = \langle i|\tilde{V}(p,p';\sqrt{s})|f\rangle \tag{D.1}$$

we find that the complex conjugate of the BS equation (2.6) takes the following form:

$$\begin{aligned}\langle i|M^\dagger(p',p;\sqrt{s})|f\rangle &= \langle i|\tilde{V}(p,p';\sqrt{s})|f\rangle + \\ &\int \frac{d^4q}{(2\pi)^4}\langle i|\tilde{V}(p,q;\sqrt{s})G^\dagger_{BS}(q;\sqrt{s})M^\dagger(p',q;\sqrt{s})|f\rangle\ .\end{aligned} \tag{D.2}$$

Hence, omitting the dependence of all quantities on the c.m. energy $\sqrt{s}$,

$$\begin{aligned}&\langle f|M(p',p) - M^\dagger(p,p')|i\rangle \\ =\ &\int \frac{d^4q}{(2\pi)^4}\langle f|M(p',q)G_{BS}(q)\tilde{V}(q,p) - \tilde{V}(p',q)G^\dagger_{BS}(q)M^\dagger(p,q)|i\rangle \\ =\ &\int \frac{d^4q}{(2\pi)^4}\langle f|M(p',q)G_{BS}(q)\left(M^\dagger(p,q) - \int\frac{d^4\tilde{q}}{(2\pi)^4}\tilde{V}(q,\tilde{q})G^\dagger_{BS}(\tilde{q})M^\dagger(p,\tilde{q})\right) - \\ &\qquad \tilde{V}(p',q)G^\dagger_{BS}(q)M^\dagger(p,q)|i\rangle \\ =\ &\int \frac{d^4q}{(2\pi)^4}\langle f|M(p',q)G_{BS}(q)M^\dagger(p,q)|i\rangle - \\ &\int \frac{d^4q}{(2\pi)^4}\int\frac{d^4\tilde{q}}{(2\pi)^4}\langle f|M(p',q)G_{BS}(q)\tilde{V}(q,\tilde{q})G^\dagger_{BS}(\tilde{q})M^\dagger(p,\tilde{q})|i\rangle - \\ &\int \frac{d^4q}{(2\pi)^4}\langle f|\tilde{V}(p',q)G^\dagger_{BS}(q)M^\dagger(p,q)|i\rangle\end{aligned}$$

$$\begin{aligned}
&= \int \frac{d^4q}{(2\pi)^4}\langle f|M(p',q)G_{BS}(q)M^\dagger(p,q)|i\rangle - \\
&\quad \int \frac{d^4q}{(2\pi)^4}\langle f|\left(\int \frac{d^4\tilde{q}}{(2\pi)^4}M(p',\tilde{q})G_{BS}(\tilde{q})\tilde{V}(\tilde{q},q) + \tilde{V}(p',q)\right) G^\dagger_{BS}(q)M^\dagger(p,q)|i\rangle \\
&= \int \frac{d^4q}{(2\pi)^4}\langle f|M(p',q)G_{BS}(q)M^\dagger(p,q) - M(p',q)G^\dagger_{BS}(q)M^\dagger(p,q)|i\rangle \\
&= \int \frac{d^4q}{(2\pi)^4}\langle f|M(p',q)2\mathrm{i}\mathrm{Im}\left(G_{BS}(q)\right)M^\dagger(p,q)|i\rangle \ .
\end{aligned} \qquad \text{(D.3)}$$

D.2 Imaginary Part of the Bethe-Salpeter Propagator

In this section the action of the imaginary part of the BS propagator G_{BS} under the $\int \mathrm{d}q_0 \mathrm{d}\,\mathrm{q}$ part of the four-dimensional integral in the BS equation is investigated. For the subsequent discussion we write the denominator of G_{BS} as

$$\begin{aligned}
G_{BS}(q;\sqrt{s}) &= \mathrm{i}\frac{2m_{B_q}\sum_{\lambda_{B_q}} u(p_q,\lambda_{B_q})\bar{u}(p_q,\lambda_{B_q})}{(\frac{1}{2}\sqrt{s}-q^0)^2-\boldsymbol{q}^2-m^2_{B_q}+\mathrm{i}\varepsilon}\frac{1}{(\frac{1}{2}\sqrt{s}+q^0)^2-\boldsymbol{q}^2-m^2_{M_q}+\mathrm{i}\varepsilon'} \\
&\equiv \mathrm{i}\frac{\Lambda(p_q)}{(p^0_q-E_{B_q}+\mathrm{i}\delta)(p^0_q+E_{B_q}-\mathrm{i}\delta)}\frac{1}{(k^0_q-E_{M_q}+\mathrm{i}\delta')(k^0_q+E_{M_q}-\mathrm{i}\delta')} \ ,
\end{aligned}$$

where we have defined $k_q = P/2+q$, $p_q = P/2-q$ with the intermediate four-momentum q, the total four momentum $P = (\sqrt{s},\boldsymbol{0})$, $E_{B_q} = \sqrt{m^2_{B_q}+\boldsymbol{p}^2_q}$, $E_{M_q} = \sqrt{m^2_{M_q}+\boldsymbol{k}^2_q}$, $\delta = \varepsilon/(2E_{B_q})$, $\delta' = \varepsilon'/(2E_{M_q})$, and the projection operator $\Lambda(p_q)$ as defined in Eq. (A.28). Rewriting the q_0-integration by k^0_q, G_{BS} has four poles in the complex k^0_q plane:

$$\begin{aligned}
p^0_q = \sqrt{s}-k^0_q = \pm(E_{B_q}-\mathrm{i}\delta) \Longrightarrow k^0_q &= \sqrt{s}\mp(E_{B_q}-\mathrm{i}\delta) \equiv B_\pm \\
k^0_q &= \pm(E_{M_q}-\mathrm{i}\delta') \equiv M_\pm \ ,
\end{aligned}$$

where the first two ($B_\pm$) correspond to positive/negative baryon energy poles and the last two ($M_\pm$) to positive/negative meson energy poles. The k^0_q-integration can be performed by closing the integration in the complex plane in the lower half plane (or similarly in the upper half plane), thus picking up contributions from a positive-energy meson (particle) pole and a negative-energy baryon (antiparticle) pole, see Fig. D.1. The arche is parametrized via $k^0_q = Re^{\mathrm{i}\varphi}$, $\varphi\epsilon[\pi \leftarrow 2\pi]$ with the Jacobian $|\mathrm{d}k^0_q/\mathrm{d}\varphi| = R$. Letting $R\to\infty$ one finds

$$\left|\int_{C_A}\mathrm{d}k^0_q G_{BS}\right| \sim \int_{C_A}\mathrm{d}\varphi\frac{R^2}{R^4} \overset{R\to\infty}{\longrightarrow} 0 \ . \qquad \text{(D.4)}$$

Hence

$$\int\limits_{-\infty}^{+\infty}\mathrm{d}k^0_q G_{BS} = \oint_{C_A}\mathrm{d}k^0_q G_{BS}$$

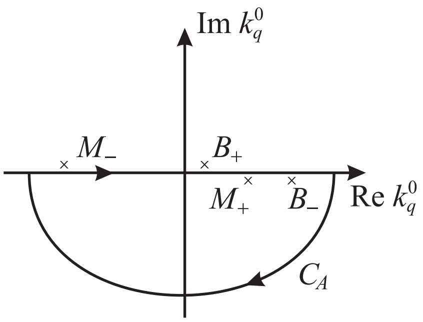

Figure D.1: C_A contour in the complex k_q^0 plane.

$$\begin{aligned}
&= -2\pi\mathrm{i}\sum \mathrm{Res}(k_q^0 \to M_+, k_q^0 \to B_-) \\
&= -2\pi\mathrm{i}^2\left[\frac{1}{2E_{M_q}}\frac{\Lambda(p_q)}{(\sqrt{s}-E_{M_q})^2-E_{B_q}^2+\mathrm{i}\varepsilon}+\frac{1}{2E_{B_q}}\frac{\Lambda(p_q)}{(\sqrt{s}+E_{B_q})^2-E_{M_q}^2+\mathrm{i}\varepsilon'}\right] \\
&= \int\limits_{-\infty}^{+\infty}\mathrm{d}k_q^0\pi\left[\frac{1}{E_{M_q}}\frac{\Lambda(p_q)\delta(k_q^0-E_{M_q})}{(\sqrt{s}-E_{M_q})^2-E_{B_q}^2+\mathrm{i}\varepsilon}+\frac{1}{E_{B_q}}\frac{\Lambda(p_q)\delta(k_q^0-\sqrt{s}-E_{B_q})}{(\sqrt{s}+E_{B_q})^2-E_{M_q}^2+\mathrm{i}\varepsilon'}\right] .
\end{aligned} \tag{D.5}$$

To evaluate the q-integration we use

$$\int \mathrm{d}x\frac{1}{x-a\pm\mathrm{i}\eta} = \mathrm{P}\int\mathrm{d}x\frac{1}{x-a}\mp\mathrm{i}\pi\int\mathrm{d}x\delta(x-a) \tag{D.6}$$

and $m_{B_q} > m_{M_q}$, so that we only pick up an imaginary contribution from G_{BS} in the q-integration from the first term under the integral in (D.5). Evaluating this integration leads to

$$\begin{aligned}
&\int\limits_0^\infty \mathrm{q}^2\mathrm{d}\,\mathrm{q}\frac{\pi}{E_{M_q}}\frac{1}{(\sqrt{s}-E_{M_q})^2-{E_{B_q}}^2+\mathrm{i}\varepsilon} \\
&= \pi\int\limits_0^\infty \mathrm{q}\mathrm{d}E_{M_q}\frac{1}{(\sqrt{s}-E_{M_q})-E_{B_q}+\mathrm{i}\delta}\frac{1}{(\sqrt{s}-E_{M_q})+E_{B_q}-\mathrm{i}\delta} \\
&= \pi\left[P\int\limits_0^\infty \mathrm{q}\mathrm{d}E_{M_q}\frac{1}{(\sqrt{s}-E_{M_q})^2-{E_{B_q}}^2}-\mathrm{i}\pi\int\limits_0^\infty \mathrm{q}\mathrm{d}E_{M_q}\frac{\delta(\sqrt{s}-E_{B_q}-E_{M_q})}{2E_{B_q}(\hat{\mathrm{q}})}\right] ,
\end{aligned}$$

where we have used $\mathrm{q}\mathrm{d}\,\mathrm{q} = E_{M_q}\mathrm{d}E_{M_q}$. The only pole contribution comes from the first denominator in the second line for $\sqrt{s} = E_{M_q}+E_{B_q}$ and thus $\mathrm{q} = \hat{\mathrm{q}}$, where $\hat{\mathrm{q}}$ is the c.m. three-momentum of the intermediate state when both particles are on their mass shell. Now we use Eq. (A.3) to find

$$\delta(\sqrt{s}-E_{B_q}-E_{M_q}) \;=\; \left(\left|\frac{\partial(\sqrt{s}-E_{B_q}-E_{M_q})}{\partial\,\mathrm{q}}\right|_{\mathrm{q}=\hat{\mathrm{q}}}\right)^{-1}\delta(\mathrm{q}-\hat{\mathrm{q}})$$

$$
\begin{aligned}
&= \left(\frac{\hat{\mathrm{q}}}{E_{B_q}} + \frac{\hat{\mathrm{q}}}{E_{M_q}}\right)^{-1} \delta(\,\mathrm{q} - \hat{\mathrm{q}}) \\
&= \frac{E_{B_q} E_{M_q}}{\hat{\mathrm{q}}\sqrt{s}} \delta(\,\mathrm{q} - \hat{\mathrm{q}}) \; .
\end{aligned}
$$

Taking everything together we conclude that the imaginary part of G_{BS} acts under the integral as

$$
\begin{aligned}
& \int \mathrm{d}^4 q \mathrm{i} \mathrm{Im}(G_{BS}) \\
= & \int \mathrm{d}^4 q \left[-\mathrm{i}\pi^2 \frac{m_{B_q} \sum_{\lambda_{B_q}} u(p_q, \lambda_{B_q}) \bar{u}(p_q, \lambda_{B_q})}{\mathrm{q}\sqrt{s}} \delta(q^0 + \sqrt{s}/2 - E_{M_q}) \delta(\,\mathrm{q} - \hat{\mathrm{q}}) \right] \\
= & \int \mathrm{d}^4 q \left[-\mathrm{i}\pi^2 \frac{m_{B_q} \sum_{\lambda_{B_q}} u(p_q, \lambda_{B_q}) \bar{u}(p_q, \lambda_{B_q})}{E_{B_q} E_{M_q}} \delta(k_q^0 - E_{M_q}) \delta(p_q^0 - E_{B_q}) \right] \\
= & \int \mathrm{d}^4 q \left[-\mathrm{i}(2\pi)^2 m_{B_q} \sum_{\lambda_{B_q}} u(p_q, \lambda_{B_q}) \bar{u}(p_q, \lambda_{B_q}) \delta(k_q^2 - m_{M_q}^2) \delta(p_q^2 - m_{B_q}^2) \Theta(k_q^0) \Theta(p_q^0) \right] \; ,
\end{aligned}
$$

i.e. sets the intermediate particles on their mass shell.

Appendix E

Lagrangians, Widths, and Couplings

All interaction Lagrangians given below also contain an isospin part, which is discussed in Appendix F.2.

E.1 Born and t-channel Interactions

The electromagnetic vertex of the asymptotic baryons (N, Λ, Σ) is given by

$$\mathcal{L} = -e\bar{u}_{B'}(p')\left(\hat{e}\gamma_\mu A^\mu + \frac{\kappa}{2m_N}\sigma_{\mu\nu}F^{\mu\nu}\right)u_B(p) \tag{E.1}$$

with

$$F^{\mu\nu} = \partial^\mu A^\nu - \partial^\nu A^\mu \ . \tag{E.2}$$

The charge operator $\hat{e}$, of course, vanishes for the neutron, Λ, Σ^0, and the transition $\Sigma^0 \to \Lambda\gamma$. However, care, has to be applied to the extraction of the anomalous magnetic moments of the hyperons Λ and Σ. The values of the *magnetic moments* are given in [67] by multiples of the nuclear magneton μ_N:

$$\mu_\Lambda = -0.613\mu_N \ , \quad \mu_{\Sigma^0\to\Lambda\gamma} = 1.61\mu_N \ , \quad \mu_{\Sigma^+} = 2.458\mu_N \ , \quad \mu_{\Sigma^-} = -1.160\mu_N$$

with

$$\mu_N = \frac{e}{2m_N} \ ,$$

where m_N is the nucleon mass. For the sign of the magnetic transition moment $\mu_{\Sigma^0\to\Lambda\gamma}$, which is experimentally not accessible, we use the de Swart [169] convention. For a spin-$\frac{1}{2}$ particle (e.g. the final state baryons) the *anomalous magnetic moments* $\tilde{\kappa}$ are related to the magnetic moments μ by (see also the Gordon decomposition Eq. (A.29))

$$\mu = \frac{e_B}{2m_B}(1+\tilde{\kappa}) \ , \tag{E.3}$$

where m_B (e_B) is the mass (charge) of the corresponding baryon. For the neutral baryons, e_B is set to $|e|$. This leads to the anomalous magnetic moments of the nucleon: $\kappa_p = \tilde{\kappa}_p =$

1.793 and $\kappa_n = \tilde{\kappa}_n = -1.913$. For the extraction of the hyperon anomalous magnetic moments from the PDG values for the magnetic moments, however, the latter ones have to be rescaled by m_Y/m_N, where m_Y is the hyperon mass, leading to

$$\tilde{\kappa}_\Lambda = -0.729 \; , \quad \tilde{\kappa}_{\Sigma^+} = 2.125 \; , \quad \tilde{\kappa}_{\Sigma^-} = 0.475 \; . \tag{E.4}$$

In the Lagrangian (E.1) the coupling to the anomalous magnetic moments is normalized by a factor of $(2m_N)^{-1}$, so that one finally has for the values that enter the calculation:

$$\kappa_\Lambda = -0.613 \; , \quad \kappa_{\Sigma^0 \to \Lambda\gamma} = 1.61 \; , \quad \kappa_{\Sigma^+} = 1.671 \; , \quad \kappa_{\Sigma^-} = -0.374 \; . \tag{E.5}$$

Note, that only the anomalous magnetic moments of the neutral cases are identical to a naive extraction neglecting the differences in the mass of the nucleon and the hyperons. This has not been carefully considered in, e.g, [86], who have extracted an anomalous magnetic moment for the Σ^+ of $\kappa_{\Sigma^+} = 1.458$.

The electromagnetic charge coupling of the pseudoscalar final state mesons π and K follows from minimal coupling (cf. Section 3.3.1) in the free Klein-Gordon Lagrangian $\mathcal{L}_{KG} = (\partial_\mu \varphi)^* \partial_\mu \varphi - m_\varphi^2 \varphi^* \varphi$ and is given by (cf. [18, 118]):

$$\mathcal{L} = -\mathrm{i}\hat{e}e\varphi^* \left(\partial_\mu^\varphi - \partial_\mu^{(\varphi^*)} \right) \varphi A^\mu \; . \tag{E.6}$$

Since we have chosen the pseudovector coupling scheme for the interaction between the nucleon and the charged asymptotic mesons $\varphi = \pi^\pm, K^+$ (cf. Section 3.3.2 and Eq. (E.12) below), minimal coupling (cf. Section 3.3.1) also generates a four-point (Kroll-Rudermann) term:

$$\mathcal{L} = -e \frac{g_\varphi}{m_B + m_{B'}} \bar{u}_{B'}(p') \gamma_5 \gamma_\mu u_B(p) A^\mu \; . \tag{E.7}$$

The vector meson baryon couplings are chosen in the same way as the electromagnetic baryon couplings:

$$\mathcal{L} = -g_V \bar{u}_{B'}(p') \left(\gamma_\mu V^\mu + \frac{\kappa_V}{2m_N} \sigma_{\mu\nu} V^{\mu\nu} \right) u_B(p) \tag{E.8}$$

with

$$V^{\mu\nu} = \partial^\mu V^\nu - \partial^\nu V^\mu \; . \tag{E.9}$$

For the coupling of the axialvector meson K_1 to $N\Lambda/\Sigma$ an additional parity operator $\mathrm{i}\gamma_5$ is needed:

$$\mathcal{L} = -\mathrm{i} g_{K_1} \bar{u}_{B'}(p') \left(\gamma_\mu K_1^\mu + \frac{\kappa_{K_1}}{2m_N} \sigma_{\mu\nu} K_1^{\mu\nu} \right) \gamma_5 u_B(p) \tag{E.10}$$

with

$$K_1^{\mu\nu} = \partial^\mu K_1^\nu - \partial^\nu K_1^\mu \; . \tag{E.11}$$

The interaction between the final state baryons and the (pseudo-)scalar mesons is given by:

$$\mathcal{L} \;\; = \;\; -\bar{u}_{B'}(p') \left[\frac{g_\varphi}{m_B + m_{B'}} \gamma_5 \gamma_\mu (\partial^\mu \varphi) + g_\eta \mathrm{i} \gamma_5 \eta + g_S S \right] u_B(p) \; , \tag{E.12}$$

where S denotes a scalar meson (σ, a_0, K_0^*) and φ the pseudoscalar mesons π and K.

The couplings between the intermediate mesons and the final state pseudoscalar mesons are given by:

$$\mathcal{L} = -\frac{g_S}{2m_\pi}(\partial_\mu \varphi')(\partial^\mu \varphi)S - g_V \varphi'(\partial_\mu \varphi)V^\mu \ . \tag{E.13}$$

Note, that for comparison, also a nonderivative $S\varphi\varphi$ coupling $\mathcal{L} = -g'_S m_S \varphi' \varphi S$ is used in one calculation. Here, g'_S is related to g_S via $g'_S = -g_S(m_S^2 - m_\varphi^2 - m_{\varphi'}^2)/(4m_S m_\pi)$.

The interaction between two 1^- vector particles (V, V') and a 0^- pseudoscalar particle (φ), as, e.g., in $\omega \to \gamma\pi$, $\pi/\eta \to \gamma\gamma$, $\omega \to \rho\pi$, is given by:

$$\mathcal{L} = -\frac{g}{4m_\varphi}\varepsilon_{\mu\nu\rho\sigma}V^{\mu\nu}V'^{\rho\sigma}\varphi \ . \tag{E.14}$$

The radiative decay of the K_1 axialvector meson (1^+) into $K\gamma$ is described by:

$$\mathcal{L}_{K_1 K\gamma} = e\frac{g_{K_1 K\gamma}}{2m_K}K F_{\mu\nu}K_1^{\mu\nu} \ . \tag{E.15}$$

With the Lagrangians (E.13), (E.14), and (E.15) the meson decay widths can be calculated:

For the hadronic vector meson decays one finds:

$$\Gamma_{V\to\varphi\varphi'} = f_{fs}\frac{g^2}{24\pi}\frac{\mathrm{k}_\varphi^3}{m_V^2} \ , \tag{E.16}$$

where the final state factor f_{fs} is $f_{fs} = 4$ for $\rho \to \pi\pi$ (since due to the isospin operator structure, the Lagrangian results in, e.g., $\mathcal{L} \sim (\pi^+\partial^\mu\pi^- - \pi^-\partial^\mu\pi^+)\rho_\mu^0 = 2\pi^+\partial^\mu\pi^-\rho_\mu^0$) and $f_{fs} = 3$ for $K^*(892) \to K\pi$ due to isospin. For the scalar meson decays the result is

$$\Gamma_{S\to\varphi\varphi'} = f_{fs}\frac{g_S^2}{8\pi}\mathrm{k}_\varphi\left(\frac{m_S^2 - m_\varphi^2 - m_{\varphi'}^2}{4m_S m_\pi}\right)^2 \tag{E.17}$$

with $f_{fs} = 1$ for $a_0 \to \eta\pi$ and $f_{fs} = 3$ for $K_0^*(1270) \to K\pi$.

The radiative decay width ($V \to \varphi\gamma$) is given for all (pseudo-) vector mesons by:

$$\Gamma_{V\to\varphi\gamma} = \frac{e^2 g^2}{96\pi m_\varphi^2}\left(\frac{m_V^2 - m_\varphi^2}{m_V}\right)^3 \tag{E.18}$$

and for the two-photon decays of π^0 and η

$$\Gamma_{\varphi\to\gamma\gamma} = \frac{e^4 g^2}{64\pi}m_\varphi \ , \tag{E.19}$$

where a factor of $\frac{1}{2}$ is included to account for the phase space of two identical particles.

Using the values for the decay widths from [67] and [3] ($\Gamma(K_1^0(1270) \to K^0\gamma) = 73$ keV), the following couplings are extracted:

$$\begin{array}{lrlrlr}
g_{\rho\pi\pi} & = 6.020\,, & g_{\omega\rho\pi} & = 2.060\,, & g_{K^*K\pi} & = -6.500\,, \\
g_{K_0^*K\pi} & = -0.900\,, & g_{a_0\eta\pi} & = -2.100\,, & & \\
g_{\rho\pi\gamma} & = 0.105\,, & g_{\rho\eta\gamma} & = -0.805\,, & & \\
g_{\omega\pi\gamma} & = 0.313\,, & g_{\omega\eta\gamma} & = -0.291\,, & & \\
g_{K^{*+}K^+\gamma} & = -0.414\,, & g_{K^{*0}K^0\gamma} & = 0.631\,, & & \\
g_{K_1^+K^+\gamma} & = 0.217\,, & g_{K_1^0K^0\gamma} & = 0.217\,, & & \\
g_{\pi\gamma\gamma} & = 0.037\,, & g_{\eta\gamma\gamma} & = 0.142\,. & &
\end{array} \tag{E.20}$$

Note, that the relative sign and magnitude of $g_{\rho\pi\pi}$ and $g_{K^*K\pi}$ is in accordance with the SU(3) values [119]$^{1)}$. For the use of the $g_{\rho\pi\gamma}$ coupling in the various isospin cases, see Appendix F.2.1. The ratio between the radiative decay of the charged and the neutral $K_1(1270)$ meson has not yet been measured. Lee et al. [108] have thus tried to determine the ratio by fitting the experimental data for $\gamma p \to K^+\Sigma^0$ and $\gamma p \to K^0\Sigma^+$, but due to the limited amount of data for the latter reaction, they have not succeeded in a reliable extraction; however, the value for the charged decay has been found to be at least two times larger. For simplicity, we use $g_{K_1^+K^+\gamma} = g_{K_1^0K^0\gamma}$$^{2)}$. For the relative sign between the charged and the neutral K^* coupling, we follow the quark model prediction of Singer and Miller [164].

The $\omega\rho\pi$ coupling constant is determined from the $\omega \to \rho\pi \to \pi^+\pi^-\pi^0$ decay width of ≈ 7.4 MeV by

$$\Gamma_{\omega\to 3\pi} = \int\limits_{2m_\pi}^{m_\omega - m_\pi} \Gamma_{\omega\to\rho\pi}(\mu)\frac{2}{\pi}\frac{\mu m_\rho \Gamma_{\rho\to\pi\pi}(\mu)}{(\mu^2 - m_\rho^2)^2 + m_\rho^2\Gamma_{\rho\to\pi\pi}^2}\mathrm{d}\mu \tag{E.21}$$

with

$$\begin{aligned}
\Gamma_{\omega\to\rho\pi}(\mu) &= \frac{3g^2}{4\pi}\frac{\mathrm{k}_\rho(\mu)^3}{m_\pi^2}\,, \\
\Gamma_{\rho\to\pi\pi}(\mu) &= \Gamma^0_{\rho\to\pi\pi}\frac{m_\rho}{\mu}\left(\frac{\mu^2 - 4m_\pi^2}{m_\rho^2 - 4m_\pi^2}\right)^{\frac{3}{2}}\theta(\mu^2 - 4m_\pi^2)\,,
\end{aligned}$$

where the ρ-spectral function is taken into account. The resulting value $g_{\omega\rho\pi} = 2.06$ is in accordance with the effective Lagrangian study of vector meson properties by Klingl et al. [96], who have extracted a value of 1.8 by considering an additional direct decay for $\omega \to 3\pi$, and with predictions of many other models [95].

Finally, a remark on the ρ and ω radiative decays into $\eta\gamma$ is in order. Unfortunately, the decay widths are known only with large uncertainties; the values above represent the

---

1) Instead of (E.13) in the code $\mathcal{L} = -2g_{K^*}K(\partial_\mu\pi)K^{*\mu}$ is used for the K^* vector meson leading to the implemented coupling of $\tilde{g}_{K^*K\pi} = \frac{1}{2}g_{K^*K\pi} = -3.25$.

2) Note, that the value $g_{K_1^+K^+\gamma} = 0.217$ is close to 0.33, which has been estimated through VMD considerations by Cheoun et al. [26].

estimated mean given in [67]. Taking into account the given errors, the ranges for the couplings are:

$$|g_{\rho\eta\gamma}| \in [0.636, 0.930] \ , \qquad |g_{\omega\eta\gamma}| \in [0.268, 0.313] \ . \tag{E.22}$$

Due to the uncertainties, these couplings are allowed to vary within the given ranges during the fitting procedure. However, in all calculations, larger values for both couplings are preferred and consequently, these couplings are set to $g_{\rho\eta\gamma} = -0.930$ and $g_{\omega\eta\gamma} = -0.313$. Note, that all other meson decay constants are also kept fixed to the values given in (E.20).

E.2 Baryon Resonance Interactions

E.2.1 Spin-$\frac{1}{2}$ Resonances

(Pseudo-)Scalar Meson Decay

For negative-parity spin-$\frac{1}{2}$ resonances, PS coupling is used:

$$\mathcal{L}^{PS}_{\frac{1}{2}B\varphi} = -g_{RB\varphi}\bar{u}_R \begin{pmatrix} 1 \\ -\mathrm{i}\gamma_5 \end{pmatrix} u_B \varphi \ . \tag{E.23}$$

For positive-parity spin-$\frac{1}{2}$ resonances, PV coupling is used:

$$\mathcal{L}^{PV}_{\frac{1}{2}B\varphi} = -\frac{g_{RB\varphi}}{m_R \pm m_B}\bar{u}_R \begin{pmatrix} \gamma_5 \\ \mathrm{i} \end{pmatrix} \gamma_\mu u_B \partial^\mu \varphi \ . \tag{E.24}$$

In both cases, the upper (lower) sign and operator hold for pseudoscalar (scalar) mesons φ.

For negative-parity resonances (PS coupling), this leads to the decay width:

$$\Gamma^{PS}_{\pm} = f_I \frac{g^2_{RB\varphi}}{4\pi} \mathrm{k}_\varphi \frac{E_B \mp m_B}{\sqrt{s}} \tag{E.25}$$

and for positive-parity resonances (PV coupling) to:

$$\begin{aligned} \Gamma^{PV}_{\pm} &= f_I \frac{g^2_{RB\varphi}}{4\pi} \mathrm{k}_\varphi \frac{E_B \mp m_B}{\sqrt{s}} \left(\frac{\sqrt{s} \pm m_B}{m_R \pm m_B} \right)^2 \\ &\overset{\sqrt{s}=m_R}{=} f_I \frac{g^2_{RB\varphi}}{4\pi} \mathrm{k}_\varphi \frac{E_B \mp m_B}{\sqrt{s}} \\ &= \Gamma^{PS}_{\pm} \ , \end{aligned} \tag{E.26}$$

where the absolute value of the meson three-momentum k_φ is given in Eq. (A.1). The upper (lower) sign always corresponds to a parity-flip (parity-non-flip) transition, e.g. $P_{11}(1440) \to \pi N$ ($S_{11}(1535) \to \pi N$). The isospin factor f_I is equal to 1 for isospin-$\frac{3}{2}$ resonances, equal to 3 for the decay of isospin-$\frac{1}{2}$ resonances into an $I = 1 \oplus \frac{1}{2}$ final state, and equal to 1 for the decay of isospin-$\frac{1}{2}$ resonances into $I = 0 \oplus \frac{1}{2}$. See also Appendix F.2.

Vector Meson Decay

For the ωN decay we apply the Lagrangian:

$$\mathcal{L}_{\frac{1}{2}N\omega} = -\bar{u}_R \begin{pmatrix} 1 \\ -\mathrm{i}\gamma_5 \end{pmatrix} \left(g_1 \gamma_\mu - \frac{g_2}{2m_N} \sigma_{\mu\nu} \partial^\nu_\omega \right) u_N \omega^\mu \; . \tag{E.27}$$

The upper (lower) operator corresponds to a positive- (negative-) parity resonance.

From these couplings the helicity decay amplitudes describing the transition for a specific resonance helicity state into a specific ωN helicity state can be deduced:

$$\begin{aligned} A^{\omega N}_{\frac{1}{2}} &= \mp \frac{\sqrt{E_N \mp m_N}}{\sqrt{m_N}} \left(g_1 + g_2 \frac{m_N \pm m_R}{2m_N} \right) \; , & \text{(E.28)} \\ A^{\omega N}_{0} &= \mp \frac{\sqrt{E_N \mp m_N}}{m_\omega \sqrt{2m_N}} \left(g_1 (m_N \pm m_R) + g_2 \frac{m_\omega^2}{2m_N} \right) \; . & \text{(E.29)} \end{aligned}$$

The lower indices correspond to the ωN helicities and are determined by the ω and nucleon helicities: $\frac{1}{2}$: $\lambda_\omega - \lambda_N = 1 - \frac{1}{2} = \frac{1}{2}$ and 0: $0 + \frac{1}{2} = \frac{1}{2}$. The resonance ωN decay widths are then given by

$$\Gamma^{\omega N} = \frac{2}{2J+1} \sum_{\lambda=0}^{\lambda=+J} \Gamma^{\omega N}_\lambda \; , \quad \Gamma^{\omega N}_\lambda = \frac{\mathrm{k}_\omega m_N}{2\pi m_R} \left| A^{\omega N}_\lambda \right|^2 \; . \tag{E.30}$$

Electromagnetic Decay

The radiative decay of the spin-$\frac{1}{2}$ resonances is described by:

$$\mathcal{L}_{\frac{1}{2}N\gamma} = -e \frac{g_1}{4m_N} \bar{u}_R \begin{pmatrix} 1 \\ -\mathrm{i}\gamma_5 \end{pmatrix} \sigma_{\mu\nu} u_N F^{\mu\nu} \; . \tag{E.31}$$

The upper (lower) operator 1 ($-\mathrm{i}\gamma_5$) corresponds to positive- (negative-) parity resonances.

Since the ωN vertices are analogous to the electromagnetic vertices one can use the ωN helicity amplitudes (E.29) to calculate the electromagnetic helicity amplitudes, which are normalized by an additional factor $(2E_\gamma)^{-\frac{1}{2}}$ [186]:

$$\begin{aligned} A^{\gamma N}_{\frac{1}{2}} &= \frac{\xi_R}{\sqrt{2E_\gamma}} \langle u_R, \lambda_R = \tfrac{1}{2} | \Gamma_\mu | u, \lambda = \tfrac{1}{2} \rangle A^\mu \\ &= \mp e g \frac{\xi_R}{\sqrt{2E_\gamma}} \frac{\sqrt{E_N \mp m_N}}{\sqrt{m_N}} \frac{m_N \pm m_R}{2m_N} \\ &= -e g \frac{\xi_R}{2m_N} \frac{\sqrt{m_R^2 - m_N^2}}{\sqrt{2m_N}} \; . \end{aligned} \tag{E.32}$$

Here, ξ_R denotes the phase at the $RN\pi$ vertex. Furthermore, the relation between vertex and Lagrangian $\bar{u}_R \Gamma_\mu u A^\mu = \mathrm{i}\mathcal{L}_{int}$, and Eq. (A.1) with $m_\gamma = 0$ have been used.

E.2.2 Spin-$\frac{3}{2}$ Resonances

For all the conventional spin-$\frac{3}{2}$ couplings given below, the corresponding Pascalutsa couplings can be extracted by the replacement:

$$\Gamma_\mu u_R^\mu \rightarrow \Gamma_\mu \gamma_5 \gamma_\nu \tilde{U}_R^{\nu\mu} \; , \tag{E.33}$$

where the dual of the resonance field tensor is given by: $\tilde{U}_R^{\mu\nu} = \frac{1}{2}\varepsilon^{\mu\nu\alpha\beta} U_{R\alpha\beta} = \frac{1}{2}\varepsilon^{\mu\nu\alpha\beta}(\partial_\alpha u_{R\beta} - \partial_\beta u_{R\alpha})$. As discussed in detail in Section 3.4.1, the use of the Pascalutsa couplings (E.33) leads to the same Feynman amplitude as when the conventional spin-$\frac{3}{2}$ couplings are used, with the only differences that the Rarita-Schwinger propagator $G^{\mu\nu}_{\frac{3}{2}}(q)$ of Eq. (A.41) is replaced by its pure spin-$\frac{3}{2}$ part $\Lambda^{\mu\nu}_{\frac{3}{2}}(q)/(q^2 - m_R^2)$ with $\Lambda^{\mu\nu}_{\frac{3}{2}}(q)$ of Eq. (A.42) and an additional overall factor of q^2/m_R^2. At the same time, the off-shell projectors $\Theta_{\mu\nu}(a)$ (cf. Eq. (E.36)) are dropped.

(Pseudo-)Scalar Meson Decay

The interaction with (pseudo-)scalar mesons for positive-parity spin-$\frac{3}{2}$ resonances is

$$\mathcal{L}_{\frac{3}{2}B\varphi} = \frac{g_{RB\varphi}}{m_\pi} \bar{u}_R^\mu \Theta_{\mu\nu}(a_{RB\varphi}) \begin{pmatrix} 1 \\ -\mathrm{i}\gamma_5 \end{pmatrix} u_B \partial^\nu \varphi \tag{E.34}$$

and for negative-parity resonances

$$\mathcal{L}_{\frac{3}{2}B\varphi} = -\frac{g_{RB\varphi}}{m_\pi} \bar{u}_R^\mu \Theta_{\mu\nu}(a_{RB\varphi}) \begin{pmatrix} \mathrm{i}\gamma_5 \\ 1 \end{pmatrix} u_B \partial^\nu \varphi \; . \tag{E.35}$$

As in the spin-$\frac{1}{2}$ case, the upper (lower) operator holds for pseudoscalar (scalar) mesons φ. $\Theta_{\mu\nu}$ is the off-shell projector:

$$\Theta_{\mu\nu}(a) = g_{\mu\nu} - a\gamma_\mu\gamma_\nu \; , \tag{E.36}$$

where a is related to the commonly used off-shell parameter z by $a = (z + \frac{1}{2})$.

These couplings lead to the decay width:

$$\Gamma^{\frac{3}{2}}_{\pm} = f_I \frac{g^2_{RB\varphi}}{12\pi m_\pi^2} \mathrm{k}_\varphi^3 \frac{E_B \pm m_B}{\sqrt{s}} \; . \tag{E.37}$$

The upper (lower) sign corresponds to the decay of a resonance into a meson with opposite (identical) parity, e.g. $P_{33}(1232) \rightarrow \pi N$ ($D_{13}(1520) \rightarrow \pi N$). The isospin factor f_I is the same as in Eqs. (E.25) and (E.26).

Vector Meson Decay

For the ωN decay we use

$$\mathcal{L}_{\frac{3}{2}N\omega} \;=\; -\bar{u}_R^\mu \begin{pmatrix} \mathrm{i}\gamma_5 \\ 1 \end{pmatrix} \left(\frac{g_1}{2m_N}\gamma^\alpha + \mathrm{i}\frac{g_2}{4m_N^2}\partial_N^\alpha + \mathrm{i}\frac{g_3}{4m_N^2}\partial_\omega^\alpha \right) \left(\partial_\alpha^\omega g_{\mu\nu} - \partial_\mu^\omega g_{\alpha\nu} \right) u_N \omega^\nu \, . \tag{E.38}$$

The upper (lower) operator corresponds to a positive- (negative-) parity resonance. Note, that for clarity, the off-shell projectors $\Theta_{\mu\nu}(a)$ (cf. Eq. (E.36)), which are contracted with each coupling operator, are not displayed.

From the above couplings the helicity decay amplitudes of the resonances to ωN can be deduced:

$$\begin{aligned}
A^{\omega N}_{\frac{3}{2}} &= -\frac{\sqrt{E_N \mp m_N}}{\sqrt{2m_N}}\frac{1}{2m_N}\left(g_3\frac{m_\omega^2}{2m_N} - g_1(m_N \pm m_R) + g_2\frac{m_R^2 - m_N^2 - m_\omega^2}{4m_N}\right) , \\
A^{\omega N}_{\frac{1}{2}} &= \pm\frac{\sqrt{E_N \mp m_N}}{\sqrt{6m_N}}\frac{1}{2m_N}\left(g_3\frac{m_\omega^2}{2m_N} \pm g_1\frac{m_N(m_N \pm m_R) - m_\omega^2}{m_R} + g_2\frac{m_R^2 - m_N^2 - m_\omega^2}{4m_N}\right) , \\
A^{\omega N}_{0} &= \pm m_\omega\frac{\sqrt{E_N \mp m_N}}{\sqrt{3m_N}}\frac{1}{2m_N}\left(g_1 \mp g_2\frac{m_R^2 + m_N^2 - m_\omega^2}{4m_R m_N} \mp g_3\frac{m_R^2 - m_N^2 + m_\omega^2}{4m_R m_N}\right) . \qquad \text{(E.39)}
\end{aligned}$$

The helicity notation is the same as in the spin-$\frac{1}{2}$ case; in addition, there is the helicity state $\frac{3}{2}$: $1 + \frac{1}{2} = \frac{3}{2}$. The resonance ωN decay widths is given by Eq. (E.30).

Electromagnetic Decay

The radiative decay of the spin-$\frac{3}{2}$ resonances is described by:

$$\mathcal{L}_{\frac{3}{2}N\gamma} = \bar{u}_R^\mu e \begin{pmatrix} \mathrm{i}\gamma_5 \\ 1 \end{pmatrix} \left(\frac{g_1}{2m_N}\gamma^\nu + \mathrm{i}\frac{g_2}{4m_N^2}\partial_N^\nu\right) u_N F_{\mu\nu} . \qquad \text{(E.40)}$$

The upper (lower) factor corresponds to positive- (negative-) parity resonances. Note, that for clarity, the off-shell projectors $\Theta_{\mu\nu}(a)$ (cf. Eq. (E.36)), which are contracted with each coupling operator, are not displayed.

In the same way as for the spin-$\frac{1}{2}$ resonances (see Eq. (E.32)) the electromagnetic helicity amplitudes can be calculated by taking the additional factor $(2E_\gamma)^{-\frac{1}{2}}$ into account:

$$\begin{aligned}
A^{\gamma N}_{\frac{1}{2}} &= +\frac{e\xi_R}{4m_N}\frac{\sqrt{m_R^2 - m_N^2}}{\sqrt{3m_N}}\left(\pm g_1\frac{m_N}{m_R} - g_2\frac{m_N \mp m_R}{4m_N}\right) \\
A^{\gamma N}_{\frac{3}{2}} &= \pm\frac{e\xi_R}{4m_N}\frac{\sqrt{m_R^2 - m_N^2}}{\sqrt{m_N}}\left(g_1 + g_2\frac{m_N \mp m_R}{4m_N}\right) , \qquad \text{(E.41)}
\end{aligned}$$

where ξ_R denotes the phase at the $RN\pi$ vertex. Note the differences to the formulae given in [52, 53], which are due to the different sign choice for the g_1 coupling in Eq. (E.40) for negative-parity resonances.

Appendix F

Isospin

The idea of introducing isospin as a symmetry for hadronic reactions originated from the experimental observation, that the nuclear force between any two nucleons is independent of charge. Formally this can be expressed by describing the two charge states of the nucleon as an isospin doublet ($|I, I_z\rangle = |\frac{1}{2}, \pm\frac{1}{2}\rangle$):

$$|p\rangle \equiv \chi_p = |\tfrac{1}{2}, +\tfrac{1}{2}\rangle = \begin{pmatrix} 1 \\ 0 \end{pmatrix} \,, \qquad |n\rangle \equiv \chi_n = |\tfrac{1}{2}, -\tfrac{1}{2}\rangle = \begin{pmatrix} 0 \\ 1 \end{pmatrix} \,. \tag{F.1}$$

The corresponding isospin-$\frac{1}{2}$ operators $\boldsymbol{\tau}/2$ are given by the Pauli matrices of Eq. (A.16). They have the properties:

$$\begin{gathered} \left(\frac{\boldsymbol{\tau}}{2}\right)^2 = \frac{1}{2}\left(\frac{1}{2}+1\right) = \frac{3}{4} \\ \frac{\tau_3}{2}\chi_p = +\frac{1}{2}\chi_p \,, \qquad \frac{\tau_3}{2}\chi_n = -\frac{1}{2}\chi_n \,. \end{gathered}$$

The inclusion of pions in this formalism is due to Watson [187][1]. He extended the nucleon charge symmetry to a general symmetry principal governing hadronic reactions. This symmetry in charge space is equivalent to rotational invariance in usual three-dimensional space and thus the isospin operators are representations of the rotation group (rotation in charge space) fulfilling the commutation algebra

$$[I_i, I_j] = \mathrm{i}\varepsilon_{ijk} I_k \,. \tag{F.2}$$

Using Eq. (A.18) this is obviously fulfilled for the isospin-$\frac{1}{2}$ operator $\boldsymbol{\tau}/2$. Watson thus introduced the pion field in such a way that the three pion states form an isospin triplet ($I = 1$) and transform under a charge rotation as the components of a three-dimensional vector, just as a usual three-dimensional vector in space (cf. Eq. (A.33)). Hence the pion field is given in a cartesian basis as:

$$\boldsymbol{\pi} \equiv \boldsymbol{\varphi} = \begin{pmatrix} \varphi_1 \\ \varphi_2 \\ \varphi_3 \end{pmatrix} \,. \tag{F.3}$$

---

[1] The transformation properties of pions in “charge space“ were first observed by Kemmer [94]. The consequences of the charge indepependence hypothesis for meson scattering have first been developed by Heitler [77], see Eqs. (F.11) and (F.12).

The physically realized charged states are related to the above ones by

$$|\pi^\pm\rangle = |\varphi^\pm\rangle = \frac{\mp 1}{\sqrt{2}}|\varphi_1 \pm \mathrm{i}\varphi_2\rangle = \frac{\mp 1}{\sqrt{2}}\begin{pmatrix} 1 \\ \pm\mathrm{i} \\ 0 \end{pmatrix} , \qquad |\pi^0\rangle = |\varphi^0\rangle = |\varphi_3\rangle = \begin{pmatrix} 0 \\ 0 \\ 1 \end{pmatrix} , \tag{F.4}$$

corresponding to incoming (initial state) pions $|\boldsymbol{\pi}\rangle = \boldsymbol{\pi}^\dagger|0\rangle$; see also Eqs. (F.9) and (F.10) below. Outgoing (final state) pions follow from the above ones (F.4) by taking the hermitian conjugate: $\langle\pi^\pm| = |\pi^\pm\rangle^\dagger$, $\langle\pi^0| = |\pi^0\rangle^\dagger$. Note the behavior of the pion field under charge conjugation: $C|\pi^\pm\rangle = -|\pi^\mp\rangle$, $C|\pi^0\rangle = |\pi^0\rangle$.

The isospin operators for isospin-1 particles fulfilling Eq. (F.2) are given by

$$[t_i]_{jk} = -\mathrm{i}\varepsilon_{ijk} \quad \text{and explicitly} \tag{F.5}$$

$$t_1 = \mathrm{i}\begin{pmatrix} 0 & 0 & 0 \\ 0 & 0 & -1 \\ 0 & 1 & 0 \end{pmatrix} , \quad t_2 = \mathrm{i}\begin{pmatrix} 0 & 0 & 1 \\ 0 & 0 & 0 \\ -1 & 0 & 0 \end{pmatrix} , \quad t_3 = \mathrm{i}\begin{pmatrix} 0 & -1 & 0 \\ 1 & 0 & 0 \\ 0 & 0 & 0 \end{pmatrix}$$

having the properties

$$\begin{gathered} \boldsymbol{t}^2 = 1(1+1) = 2 \\ t_3|\pi^+\rangle = +|\pi^+\rangle , \quad t_3|\pi^-\rangle = -|\pi^-\rangle , \quad t_3|\pi^0\rangle = 0|\pi^0\rangle . \end{gathered}$$

The choice of the pion field (F.4) guarantees that the amplitudes for $\pi N \to \pi N$ have the correct behavior under charge conjugation, see Eq. (F.10). It is in line with the Condon-Shortley convention [30], which is also used for the extraction of Clebsch-Gordan coefficients (see [67]). Note that in the literature, this pion field definition is only rarely applied ([42], [56], [61], [129], [184]). Mostly (e.g. [18], [28], [47], [82], [168]) a different definition of the π^+ field $|\pi^+\rangle \to |\pi^+\rangle = \frac{1}{\sqrt{2}}(+1, +\mathrm{i}, 0)$ is used, which leads to a different amplitude behavior under charge conjugation, see Eq. (F.13).

In our model there are more isospin $1 \oplus \frac{1}{2}$ final states included than just πN. The 2π meson ζ has the same isospin as the pion. In the reactions involving strangeness the same formalism can also be applied, but the isospin properties of the baryon and the meson are interchanged: The kaon appears as the isospin doublet (K^+, K^0) and the Sigma as the isospin triplet $(\Sigma^\pm, \Sigma^0)$. The treatment of photons in the isospin context is discussed in Section F.1.2.

F.1 Isospin Decomposed Amplitudes

F.1.1 Hadronic reactions

Since the rotation in charge space corresponds to a symmetry of reactions purely governed by the hadronic interaction, the total isospin is a conserved quantity. Therefore, the partial-wave decomposition of Section 4.2 has to be extended to isospin space.

Scattering of $(I = 1 \oplus \frac{1}{2})$ Asymptotic States into $(I = 1 \oplus \frac{1}{2})$

Final states involving an isospin-$\frac{1}{2}$ and an isospin-1 particle can couple to either total isospin $1 \oplus \frac{1}{2} = \frac{1}{2}$ or $1 \oplus \frac{1}{2} = \frac{3}{2}$. Therefore, the amplitudes have to be decomposed into an isospin-$\frac{1}{2}$ part $T_{fi}^{1/2}$ and an isospin-$\frac{3}{2}$ part $T_{fi}^{3/2}$. The projection operators to these total isospins are extracted from the operator of the total isospin:

$$\boldsymbol{I} \;=\; \frac{\boldsymbol{\tau}}{2} + \boldsymbol{t} \;. \tag{F.6}$$

From Eq. (F.6) one extracts by computing $\boldsymbol{I}^2$

$$\boldsymbol{t} \cdot \boldsymbol{\tau} \;=\; I(I+1) - 2 - \tfrac{3}{4} \;,$$

leading to the projection operators

$$\begin{aligned} \hat{P}_{\frac{1}{2}} &= \frac{1}{3}(1 - \boldsymbol{t} \cdot \boldsymbol{\tau}) \\ \hat{P}_{\frac{3}{2}} &= \frac{1}{3}(2 + \boldsymbol{t} \cdot \boldsymbol{\tau}) = 1 - \hat{P}_{\frac{1}{2}} \;. \end{aligned}$$

Using

$$\langle \varphi_k | \boldsymbol{t} \cdot \boldsymbol{\tau} | \varphi_j \rangle \overset{(F.5)}{=} -\mathrm{i}\varepsilon_{ijk}\tau_i \overset{(F.2)}{=} \tfrac{1}{2}\left[\tau_j, \tau_k\right] \overset{(A.17)}{=} \delta_{kj} - \tau_k\tau_j \;,$$

where $|\varphi_j\rangle$ and $\langle\varphi_k|$ refer to the incoming and outgoing asymptotic isospin-1 particles in the cartesian basis, the above projection operators can be rewritten as

$$\begin{aligned} \left[\hat{P}_{\frac{1}{2}}\right]_{kj} &\equiv \langle \varphi_k | \hat{P}_{\frac{1}{2}} | \varphi_j \rangle = \frac{1}{3}\tau_k\tau_j \\ \left[\hat{P}_{\frac{3}{2}}\right]_{kj} &\equiv \langle \varphi_k | \hat{P}_{\frac{3}{2}} | \varphi_j \rangle = \delta_{kj} - \frac{1}{3}\tau_k\tau_j \;. \end{aligned} \tag{F.7}$$

Now the possible charge amplitudes can be decomposed into isospin amplitudes

$$\begin{aligned} \langle \varphi_k; I = \tfrac{1}{2} |\, T_{fi} \,| \varphi_j; I = \tfrac{1}{2} \rangle &= \langle \varphi_k; I = \tfrac{1}{2} |\, \hat{P}_{\frac{1}{2}} T_{fi}^{\frac{1}{2}} + \hat{P}_{\frac{3}{2}} T_{fi}^{\frac{3}{2}} \,| \varphi_j; I = \tfrac{1}{2} \rangle \\ &= \langle I = \tfrac{1}{2} |\, \tfrac{1}{3}\tau_k\tau_j T_{fi}^{\frac{1}{2}} + (\delta_{kj} - \tfrac{1}{3}\tau_k\tau_j) T_{fi}^{\frac{3}{2}} \,| I = \tfrac{1}{2} \rangle \;, \end{aligned} \tag{F.8}$$

where $|I = \frac{1}{2}\rangle$ and $\langle I = \frac{1}{2}|$ have to be replaced by the isospinors $\chi_\pm = |\frac{1}{2}, \pm\frac{1}{2}\rangle$ and $\chi_\pm^\dagger = \langle \frac{1}{2}, \pm\frac{1}{2}|$ of Eq. (F.1). The τ_k, τ_j have to be replaced according to (cf. Eq. (F.4))

$$\boldsymbol{\tau} \cdot |\boldsymbol{\varphi}^{\pm}\rangle = \mp\sqrt{2}\tau_\pm \;, \qquad\qquad \boldsymbol{\tau} \cdot |\boldsymbol{\varphi}^{0}\rangle = \tau^0 \;, \tag{F.9}$$

where we have defined

$$\tau_\pm = \tfrac{1}{2}(\tau_1 \pm \mathrm{i}\tau_2)$$

with the properties

$$\tau_\pm \chi_\mp = \chi_\pm \;, \qquad\qquad \tau_\pm \chi_\pm = 0 \;.$$

Thus Eq. (F.8) leads explicitly to

$$\begin{aligned}
\langle 1,+1;\ \tfrac{1}{2},+\tfrac{1}{2}|\ T_{fi}\ |1,+1;\ \tfrac{1}{2},+\tfrac{1}{2}\rangle &= T_{fi}^{\frac{3}{2}} \\
\langle 1,-1;\ \tfrac{1}{2},-\tfrac{1}{2}|\ T_{fi}\ |1,-1;\ \tfrac{1}{2},-\tfrac{1}{2}\rangle &= T_{fi}^{\frac{3}{2}} \\
\langle 1,-1;\ \tfrac{1}{2},+\tfrac{1}{2}|\ T_{fi}\ |1,-1;\ \tfrac{1}{2},+\tfrac{1}{2}\rangle &= \frac{1}{3}(T_{fi}^{\frac{3}{2}}+2T_{fi}^{\frac{1}{2}}) \\
\langle 1,+1;\ \tfrac{1}{2},-\tfrac{1}{2}|\ T_{fi}\ |1,+1;\ \tfrac{1}{2},-\tfrac{1}{2}\rangle &= \frac{1}{3}(T_{fi}^{\frac{3}{2}}+2T_{fi}^{\frac{1}{2}}) \\
\langle 1,\ \ 0;\ \tfrac{1}{2},-\tfrac{1}{2}|\ T_{fi}\ |1,-1;\ \tfrac{1}{2},+\tfrac{1}{2}\rangle &= \frac{\sqrt{2}}{3}(T_{fi}^{\frac{3}{2}}-T_{fi}^{\frac{1}{2}}) \qquad \text{(F.10)} \\
\langle 1,\ \ 0;\ \tfrac{1}{2},+\tfrac{1}{2}|\ T_{fi}\ |1,+1;\ \tfrac{1}{2},-\tfrac{1}{2}\rangle &= \frac{\sqrt{2}}{3}(T_{fi}^{\frac{3}{2}}-T_{fi}^{\frac{1}{2}}) \\
\langle 1,\ \ 0;\ \tfrac{1}{2},+\tfrac{1}{2}|\ T_{fi}\ |1,\ \ 0;\ \tfrac{1}{2},+\tfrac{1}{2}\rangle &= \frac{1}{3}(2T_{fi}^{\frac{3}{2}}+T_{fi}^{\frac{1}{2}}) \\
\langle 1,\ \ 0;\ \tfrac{1}{2},-\tfrac{1}{2}|\ T_{fi}\ |1,\ \ 0;\ \tfrac{1}{2},-\tfrac{1}{2}\rangle &= \frac{1}{3}(2T_{fi}^{\frac{3}{2}}+T_{fi}^{\frac{1}{2}})\ .
\end{aligned}$$

This isospin decomposition applied to πN elastic scattering is also in line with the relations first developed by Heitler [77]:

$$\begin{aligned}
\mathcal{M}(\pi^+ n \to \pi^0 p) &= \mathcal{M}(\pi^0 p \to \pi^+ n) = \mathcal{M}(\pi^- p \to \pi^0 n) = \mathcal{M}(\pi^0 n \to \pi^- p) \\
\mathcal{M}(\pi^+ p \to \pi^+ p) &= \mathcal{M}(\pi^- n \to \pi^- n) \\
\mathcal{M}(\pi^+ n \to \pi^+ n) &= \mathcal{M}(\pi^- p \to \pi^- p) \\
\mathcal{M}(\pi^0 n \to \pi^0 n) &= \mathcal{M}(\pi^0 p \to \pi^0 p) \qquad \text{(F.11)}
\end{aligned}$$

and

$$\begin{aligned}
\mathcal{M}(\pi^0 p \to \pi^0 p) &= \frac{1}{2}\left(\mathcal{M}(\pi^+ p \to \pi^+ p) + \mathcal{M}(\pi^- p \to \pi^- p)\right) \\
\mathcal{M}(\pi^- p \to \pi^0 n) &= \frac{1}{\sqrt{2}}\left(\mathcal{M}(\pi^+ p \to \pi^+ p) - \mathcal{M}(\pi^- p \to \pi^- p)\right)\ . \qquad \text{(F.12)}
\end{aligned}$$

The choice of $|\pi^+\rangle \to |\pi^+\rangle = \frac{1}{\sqrt{2}}(+1,+\mathrm{i},0)$ would have lead to the amplitude behavior

$$\langle 1,\ \ 0;\ \tfrac{1}{2},-\tfrac{1}{2}|\ T_{fi}\ |1,-1;\ \tfrac{1}{2},+\tfrac{1}{2}\rangle = -\langle 1,\ \ 0;\ \tfrac{1}{2},+\tfrac{1}{2}|\ T_{fi}\ |1,+1;\ \tfrac{1}{2},-\tfrac{1}{2}\rangle\ , \qquad \text{(F.13)}$$

which is not compatible with the usual Clebsch-Gordan coefficients.

Scattering of ($I = 1 \oplus \frac{1}{2}$) Asymptotic States into ($I = 0 \oplus \frac{1}{2} = \frac{1}{2}$) or Vice Versa

In this case one of the final states is a pure isospin $0 \oplus \frac{1}{2} = \frac{1}{2}$ state (e.g., $\pi N \to \eta N$), and thus the total isospin can only be $I = \frac{1}{2}$. The $I = \frac{1}{2}$ projection operator now only acts on the $|I = 1; I = \frac{1}{2}\rangle$ state and is chosen in accordance with the Condon-Shortley convention and hence correctly normalized[2]:

$$\left[\hat{P}_{\frac{1}{2}}\right]_j = \frac{-1}{\sqrt{3}}\tau_j\ .$$

---

[2] Note that this does not hold true for the usual choice in this case: $[\hat{P}_{\frac{1}{2}}]_j = \tau_j$. The incorrect normalization leads to additional factors that have to be implemented in the rescattering equation, cf. Eqs. (D.17) and (D.28-31) in Ref. [156].

Note the relation to $\hat{P}_{\frac{1}{2}}$ of Eq. (F.7). This leads to

$$\langle I=0;\ I=\tfrac{1}{2}|\ T_{fi}\ |I=1;\ I=\tfrac{1}{2}\rangle = \langle I=\tfrac{1}{2}|\ -\tfrac{1}{\sqrt{3}}\tau_j T_{fi}^{\frac{1}{2}}\ |I=\tfrac{1}{2}\rangle \tag{F.14}$$

and explicitly

$$\begin{aligned}
\langle 0,0;\ \tfrac{1}{2},-\tfrac{1}{2}|\ T_{fi}\ |1,-1;\ \tfrac{1}{2},+\tfrac{1}{2}\rangle &= -\frac{\sqrt{2}}{\sqrt{3}}T_{fi}^{\frac{1}{2}} \\
\langle 0,0;\ \tfrac{1}{2},+\tfrac{1}{2}|\ T_{fi}\ |1,+1;\ \tfrac{1}{2},-\tfrac{1}{2}\rangle &= \frac{\sqrt{2}}{\sqrt{3}}T_{fi}^{\frac{1}{2}} \\
\langle 0,0;\ \tfrac{1}{2},+\tfrac{1}{2}|\ T_{fi}\ |1,\ \ 0;\ \tfrac{1}{2},+\tfrac{1}{2}\rangle &= \frac{-1}{\sqrt{3}}T_{fi}^{\frac{1}{2}} \\
\langle 0,0;\ \tfrac{1}{2},-\tfrac{1}{2}|\ T_{fi}\ |1,\ \ 0;\ \tfrac{1}{2},-\tfrac{1}{2}\rangle &= \frac{1}{\sqrt{3}}T_{fi}^{\frac{1}{2}}\ .
\end{aligned} \tag{F.15}$$

F.1.2 Reactions Involving Photons

In this section, methods are presented that allow to extend the isospin formalism of the purely hadronic reactions to those including photons, thus allowing for a unified isospin description of all reaction channels entering the potential of the model.

Photoproduction of $(I = 1 \oplus \frac{1}{2})$ Final States

Assuming for the moment that only the meson current influences the charge symmetry properties of pion photoproduction, i.e. the photon behaves as an isoscalar particle, one obtains cross section relations as in, e.g., $\pi N \to \eta N$:

$$\begin{aligned}
\sigma(\gamma p \to \pi^+ n) &= \sigma(\gamma n \to \pi^- p) \\
\sigma(\gamma p \to \pi^0 p) &= \sigma(\gamma n \to \pi^0 n)\ .
\end{aligned}$$

These are obviously not satisfied by experimental observations and therefore, the photon must be of a more complicated isospin nature. It is due to the fact that electromagnetic couplings are dependent on the different charge states of a particle and thus break the isospin symmetry. From a field theoretical point of view, this problem can formally be solved by the introduction of the electromagnetic interaction by "minimal coupling" in the Lagrangians of the theory containing nucleons and pions:

$$\partial_\mu \to \partial_\mu - \mathrm{i}\hat{Q}A_\mu\ . \tag{F.16}$$

Here, A_μ is the photon vector potential and $\hat{Q}$ is the charge operator, which acts in the particle isospin space. For the nucleon field, $\hat{Q} = e(1+\tau_3)/2$ and for the pion field $\hat{Q} = et_3$. Therefore, as first pointed out by Watson [187], the photon is composed of an isoscalar $|I, I_z\rangle = |0,0\rangle$ and the third component of an isovector $|I, I_z\rangle = |1,0\rangle$ particle. The isospin formalism of the previous sections can now be extended easily to reactions involving photons; the only difference to the purely hadronic reactions is that experimentally only the $I_z = 0$ component is observed. Watson hence deduced a decomposition of the observable charge reactions into isovector (A_V and B_V) and isoscalar (S_0) contributions of the photon (cf. Eq. (F.20) below):

$$\begin{aligned} \mathcal{M}(\gamma p \to \pi^0 p) &= A_V + S_0 \\ \mathcal{M}(\gamma n \to \pi^0 n) &= A_V - S_0 \\ \mathcal{M}(\gamma p \to \pi^+ n) &= B_V - \sqrt{2} S_0 \\ \mathcal{M}(\gamma n \to \pi^- p) &= B_V + \sqrt{2} S_0 \end{aligned} \tag{F.17}$$

with the isovector contributions

$$A_V \equiv \frac{1}{\sqrt{3}} \left(2T_2 - \frac{1}{2} T_1 \right) , \qquad B_V \equiv \frac{1}{\sqrt{3}} \left(\sqrt{2} T_2 + \frac{1}{\sqrt{2}} T_1 \right) . \tag{F.18}$$

The amplitudes T_1 and T_2 will be identified below. Note that the isovector part behaves under charge conjugation just as a pion, hence $\mathcal{M}(\gamma_V p \to \pi^+ n) = \mathcal{M}(\gamma_V n \to \pi^- p)$. This is, again, not fulfilled for the often used choice of $\pi^+ = \frac{1}{\sqrt{2}}(1, +\mathrm{i}, 0)$!

This isospin ambivalence of the photon can be introduced into the isospin decomposition for the photoproduction amplitude of $I = 1 \oplus \frac{1}{2}$ hadronic final states (πN, ζN, $K\Sigma$) by combining Eqs. (F.8) and (F.14):

$$\langle \varphi_k ;\ I = \tfrac{1}{2} |\ T_{f\gamma}\ | \gamma ;\ I = \tfrac{1}{2} \rangle = \langle I = \tfrac{1}{2} |\ \tfrac{1}{3} \tau_k \tau_3 T^{\frac{1}{2}}_{f\gamma} + (\delta_{k3} - \tfrac{1}{3} \tau_k \tau_3) T^{\frac{3}{2}}_{f\gamma} - \tfrac{1}{\sqrt{3}} \tau_k T^0_{f\gamma}\ | I = \tfrac{1}{2} \rangle , \tag{F.19}$$

where $\langle \varphi_k |$ refers to the outgoing asymptotic isospin-1 particle. The meaning of the upper indices is similar to the helicity notation:

- 0: isoscalar photon coupling with the nucleon (total isospin $I = \frac{1}{2}$),
- $\frac{1}{2}$: isovector photon coupling with the nucleon to total $I = \frac{1}{2}$,
- $\frac{3}{2}$: isovector photon coupling with the nucleon to total $I = \frac{3}{2}$.

This leads explicitly to the following amplitudes:

$$\begin{aligned} \langle 1, \ \ 0;\ \tfrac{1}{2}, +\tfrac{1}{2} |\ T_{f\gamma}\ | \gamma ;\ \tfrac{1}{2}, +\tfrac{1}{2} \rangle &= \frac{1}{3} (2 T^{\frac{3}{2}}_{f\gamma} + T^{\frac{1}{2}}_{f\gamma}) - \frac{1}{\sqrt{3}} T^0_{f\gamma} \\ \langle 1, \ \ 0;\ \tfrac{1}{2}, -\tfrac{1}{2} |\ T_{f\gamma}\ | \gamma ;\ \tfrac{1}{2}, -\tfrac{1}{2} \rangle &= \frac{1}{3} (2 T^{\frac{3}{2}}_{f\gamma} + T^{\frac{1}{2}}_{f\gamma}) + \frac{1}{\sqrt{3}} T^0_{f\gamma} \\ \langle 1, +1;\ \tfrac{1}{2}, -\tfrac{1}{2} |\ T_{f\gamma}\ | \gamma ;\ \tfrac{1}{2}, +\tfrac{1}{2} \rangle &= \frac{\sqrt{2}}{3} (T^{\frac{3}{2}}_{f\gamma} - T^{\frac{1}{2}}_{f\gamma}) + \frac{\sqrt{2}}{\sqrt{3}} T^0_{f\gamma} \\ \langle 1, -1;\ \tfrac{1}{2}, +\tfrac{1}{2} |\ T_{f\gamma}\ | \gamma ;\ \tfrac{1}{2}, -\tfrac{1}{2} \rangle &= \frac{\sqrt{2}}{3} (T^{\frac{3}{2}}_{f\gamma} - T^{\frac{1}{2}}_{f\gamma}) - \frac{\sqrt{2}}{\sqrt{3}} T^0_{f\gamma} . \end{aligned} \tag{F.20}$$

Note the identity with Eq. (F.17) by identifying $T^{\frac{3}{2}}_{f\gamma} = \sqrt{3} T_2$, $T^{\frac{1}{2}}_{f\gamma} = -\frac{\sqrt{3}}{2} T_1$, and $T^0_{f\gamma} = -\sqrt{3} S_0$.

In one of the first partial-wave analyses of pion-photoproduction data [117] so-called proton ($T^p_{\pi\gamma}$) and neutron ($T^n_{\pi\gamma}$) isospin amplitudes were introduced. They are commonly used amplitude combinations with total isospin $I = \frac{1}{2}$ and related to the above ones in the following way:

$$\begin{aligned} T^p_{\pi\gamma} &\equiv \tfrac{1}{3}(-\sqrt{2}\langle\pi^+ n|T|\gamma p\rangle + \langle\pi^0 p|T|\gamma p\rangle) = +\tfrac{1}{3}T^{\frac{1}{2}}_{\pi\gamma} - \tfrac{1}{\sqrt{3}}T^0_{\pi\gamma} \\ T^n_{\pi\gamma} &\equiv \tfrac{1}{3}(+\sqrt{2}\langle\pi^- p|T|\gamma n\rangle - \langle\pi^0 n|T|\gamma n\rangle) = -\tfrac{1}{3}T^{\frac{1}{2}}_{\pi\gamma} - \tfrac{1}{\sqrt{3}}T^0_{\pi\gamma} \; . \end{aligned}$$

The different isospin notations usually used would lead to $T^0_{\pi\gamma}$ instead of $-\frac{1}{\sqrt{3}}T^0_{\pi\gamma}$ and the commonly applied redefinition $-\langle\pi^+ n|T|\gamma p\rangle \rightarrow +\langle\pi^+ n|T|\gamma p\rangle$.

Photoproduction of $(I = 0 \oplus \frac{1}{2} = \frac{1}{2})$ Final States

For photoproduction of $I = 0 \oplus \frac{1}{2} = \frac{1}{2}$ hadronic final states (ηN, $K\Lambda$, ωN) only a total isospin of $I = \frac{1}{2}$ is allowed and Eq. (F.14) has to be modified in the following way:

$$\langle I=0;\; I=\tfrac{1}{2}|\; T_{f\gamma}\; |\gamma;\; I=\tfrac{1}{2}\rangle = \langle I=\tfrac{1}{2}|\; T^0_{f\gamma} - \tfrac{1}{\sqrt{3}}\tau_3 T^{\frac{1}{2}}_{f\gamma}\; |I=\tfrac{1}{2}\rangle \; .$$

The resulting proton ($T^p_{f\gamma}$) and neutron ($T^n_{f\gamma}$) isospin amplitudes are:

$$\begin{aligned} T^p_{f\gamma} &\equiv \langle 0,0;\; \tfrac{1}{2},+\tfrac{1}{2}|\; T_{f\gamma}\; |\gamma;\; \tfrac{1}{2},+\tfrac{1}{2}\rangle = -\tfrac{1}{\sqrt{3}}T^{\frac{1}{2}}_{f\gamma} + T^0_{f\gamma} \\ T^n_{f\gamma} &\equiv \langle 0,0;\; \tfrac{1}{2},-\tfrac{1}{2}|\; T_{f\gamma}\; |\gamma;\; \tfrac{1}{2},-\tfrac{1}{2}\rangle = +\tfrac{1}{\sqrt{3}}T^{\frac{1}{2}}_{f\gamma} + T^0_{f\gamma} \; . \end{aligned}$$

Compton Scattering

For Compton scattering, the incoming and outgoing photon are decomposed into their isoscalar and isovector contributions. Thus the isospin decomposition now reads

$$\langle\gamma; I=\tfrac{1}{2}|\; T_{\gamma\gamma}\; |\gamma; I=\tfrac{1}{2}\rangle = \langle I=\tfrac{1}{2}|\; T^{00}_{\gamma\gamma} - \tfrac{1}{\sqrt{3}}\tau_3(T^{01}_{\gamma\gamma} + T^{10}_{\gamma\gamma}) + \tfrac{1}{3}T^{11,\frac{1}{2}}_{\gamma\gamma} + \tfrac{2}{3}T^{11,\frac{3}{2}}_{\gamma\gamma}|I=\tfrac{1}{2}\rangle \quad \text{(F.21)}$$

because of $\tau_3^2 = 1\!\!1_2$. The upper indices denote the isospin of the outgoing and incoming photons. For the case that both photons are isovector (^{11}), also the total isospin of the γN system is given.

Experimentally, only two amplitudes ($\gamma p \rightarrow \gamma p$ and $\gamma n \rightarrow \gamma n$) are accessible. For these cases (F.21) results in

$$\begin{aligned} \langle\gamma; p|\; T_{\gamma\gamma}\; |\gamma; p\rangle &= T^{00}_{\gamma\gamma} - \tfrac{1}{\sqrt{3}}(T^{01}_{\gamma\gamma} + T^{10}_{\gamma\gamma}) + \tfrac{1}{3}T^{11,\frac{1}{2}}_{\gamma\gamma} + \tfrac{2}{3}T^{11,\frac{3}{2}}_{\gamma\gamma} \\ \langle\gamma; n|\; T_{\gamma\gamma}\; |\gamma; n\rangle &= T^{00}_{\gamma\gamma} + \tfrac{1}{\sqrt{3}}(T^{01}_{\gamma\gamma} + T^{10}_{\gamma\gamma}) + \tfrac{1}{3}T^{11,\frac{1}{2}}_{\gamma\gamma} + \tfrac{2}{3}T^{11,\frac{3}{2}}_{\gamma\gamma} \; . \end{aligned} \quad \text{(F.22)}$$

I_1	I_2	I_3	operator
0	$\frac{1}{2}$	$\frac{1}{2}$	$\chi_3^\dagger \chi_2$
0	1	1	$\boldsymbol{\varphi}_3^\dagger \boldsymbol{\varphi}_2$
1	$\frac{1}{2}$	$\frac{1}{2}$	$\chi_3^\dagger \boldsymbol{\tau} \cdot \boldsymbol{\varphi}_1 \chi_2$
1	1	1	$\mathrm{i}\boldsymbol{\varphi}_3^\dagger \cdot (\boldsymbol{\varphi}_1 \times \boldsymbol{\varphi}_2)$
1	$\frac{1}{2}$	$\frac{3}{2}$	$\boldsymbol{T}_3^\dagger \cdot \boldsymbol{\varphi}_1 \chi_2$

Table F.1: Isospin operators in the interaction Lagrangians for $1 + 2 \to 3$. For the notation, see text. The missing normalization factor of $\frac{1}{2}$ for $1 \oplus \frac{1}{2} \to \frac{1}{2}$ is absorbed in the coupling constant. Note that in the last case, the coefficient resulting from the transition operator is just the Clebsch-Gordan coefficient $(\frac{3}{2}, I_{3z}|1, I_{1z}; \frac{1}{2}, I_{2z})$.

F.2 Isospin Operators in the Interaction Lagrangians

For the specification of the isospin operators appearing in the interaction Lagrangian, also the isospin description of particles appearing in four different charge states (Δ resonances) has to be defined. Those particles form an isospin quartet ($I = \frac{3}{2}$) and the corresponding isospin vector $\boldsymbol{T}$ is given by the coupling of an isospin 1 to an isospin $\frac{1}{2}$ particle:

$$\boldsymbol{T}(M)^\dagger = \sum_{r,m} (\tfrac{3}{2}, M|1, r; \tfrac{1}{2}, m) \boldsymbol{\varphi}_r^\dagger \chi_m^\dagger \ ,$$

where $(\frac{3}{2}, M|1, r; \frac{1}{2}, m)$ are the usual Clebsch-Gordan coefficients (see, e.g., [67]).

The isospin operators in the hadronic interaction Lagrangians for $1 + 2 \to 3$ are given in Table F.1. The convention used for transitions of $(I = 1) \oplus (I = 1) \to (I = 1)$ concerning the ordering of isovectors is that the intermediate particle is identified with $\boldsymbol{\varphi}_1$, e.g. for the meson vertex of the ρ^0 t-channel diagram contributing to $\pi^+ p \to \pi^+ p$:

$$\mathrm{i}\boldsymbol{\varphi}_3^\dagger \cdot (\boldsymbol{\varphi}_1 \times \boldsymbol{\varphi}_2) \equiv \mathrm{i}\boldsymbol{\pi}^{+\dagger} \cdot (\boldsymbol{\rho}^0 \times \boldsymbol{\pi}^+) = 1 \ .$$

Thus one deduces the isospin factors for the reaction $1 + 2 \to 3 + 4$ as given in Table F.2. They have to be multiplied to the corresponding Feynman diagram (I_q is the isospin of the intermediate particle propagating in the s-, u-, or t-channel). Combining these coefficients with Eqs. (F.10) and (F.15) one gets the isospin factors that have to be multiplied with the Feynman diagrams to find out their contributions to the $I = \frac{1}{2}$ and $I = \frac{3}{2}$ amplitudes.

F.2.1 Isospin Decomposed Photon Couplings

The isospin decomposition of photon amplitudes as presented in Section F.1.2 means, that if one assigns right from the start different couplings to the two photon isospin states (g_{i0} for the isoscalar and g_{i1} for the isovector photon) in line with the isospin operators given in Table F.1, the isospin decomposition is completely identical to the procedure described above for the hadronic reactions. The resulting relations are given in Table F.3.

$\langle I_1, I_{1z};\ I_2, I_{2z} \mid I_3, I_{3z};\ I_4, I_{4z}\rangle$	I_q	diagram type	factor
$\langle 1, +1;\ \frac{1}{2}, +\frac{1}{2} \mid 1, +1;\ \frac{1}{2}, +\frac{1}{2}\rangle$	0	s	0
	0	u	1
	0	t	1
	1	s	0
	1	u	1
	1	t	1
	$\frac{1}{2}$	s	0
	$\frac{1}{2}$	u	2
	$\frac{1}{2}$	t	2
	$\frac{3}{2}$	s	1
	$\frac{3}{2}$	u	$\frac{1}{3}$
$\langle 1, 0;\ \frac{1}{2}, -\frac{1}{2} \mid 1, -1;\ \frac{1}{2}, +\frac{1}{2}\rangle$	0	s	0
	0	u	0
	0	t	0
	1	s	0
	1	u	$\sqrt{2}$
	1	t	$\sqrt{2}$
	$\frac{1}{2}$	s	$-\sqrt{2}$
	$\frac{1}{2}$	u	$\sqrt{2}$
	$\frac{1}{2}$	t	$\sqrt{2}$
	$\frac{3}{2}$	s	$\frac{\sqrt{2}}{3}$
	$\frac{3}{2}$	u	$-\frac{\sqrt{2}}{3}$
$\langle 0, 0; \frac{1}{2}, -\frac{1}{2} \mid\ 1, -1;\ \frac{1}{2}, +\frac{1}{2}\rangle$	0	s	0
	0	u	0
	0	t	0
	1	s	0
	1	u	$\sqrt{2}$
	1	t	$\sqrt{2}$
	$\frac{1}{2}$	s	$\sqrt{2}$
	$\frac{1}{2}$	u	$\sqrt{2}$
	$\frac{1}{2}$	t	$\sqrt{2}$
	$\frac{3}{2}$	s	0
	$\frac{3}{2}$	u	0

Table F.2: Isospin factors of Feynman diagrams. Note that the u- and t-channel coefficients are identical.

$\|I_1, I_{1z}\rangle$	$\langle I_2, I_{2z}\|$	example	$g_{\gamma+1\to 2}$
$\|1, \pm 1\rangle$	$\langle 1, \pm 1\|$	$\gamma\pi^\pm \to \pi^\pm$	$g_{i0} \mp g_{i1}$
$\|1, \quad 0\rangle$	$\langle 1, \quad 0\|$	$\gamma\rho^0 \to \pi^0$	g_{i0}
$\|1, \quad 0\rangle$	$\langle 0, \quad 0\|$	$\gamma\rho^0 \to \eta$	g_{i1}
$\|0, \quad 0\rangle$	$\langle 1, \quad 0\|$	$\gamma\omega \to \pi^0$	g_{i1}
$\|0, \quad 0\rangle$	$\langle 0, \quad 0\|$	$\gamma\omega \to \eta$	g_{i0}
$\|\frac{1}{2}, +\frac{1}{2}\rangle$	$\langle\frac{1}{2}, +\frac{1}{2}\|$	$\gamma p \to p$	$g_{i0} + g_{i1}$
$\|\frac{1}{2}, -\frac{1}{2}\rangle$	$\langle\frac{1}{2}, -\frac{1}{2}\|$	$\gamma K^0 \to K^0$	$g_{i0} - g_{i1}$

Table F.3: Isospin decomposition of the photon couplings for $\gamma + 1 \to 2$. g_{i0} corresponds to the coupling to an isoscalar, g_{i1} to the coupling to an isovector photon. Note that the combination for $|\gamma; 1, \pm 1\rangle \to |1, \pm 1\rangle$ is just counterintuitive, which is due to the definition of the isospin operator in Table F.1.

Since the isospin-$\frac{3}{2}$ (Δ) resonances can only decay via isovector photons and the isospin coefficients resulting from the isospin transition operators are correctly normalized, the photon coupling is directly given as the isovector coupling g_{i1}. A similar argument holds true for the electromagnetic transition of an isoscalar into an isoscalar particle: This is only possible via an isoscalar photon and hence the photon coupling is directly given as the isoscalar coupling g_{i0}.

Two remarks are in order at this point:

- In the photoproduction of pions there is also a t-channel contribution via ρ exchange. From the decay widths of $\rho \to \pi\gamma$ [67] one deduces the following couplings: $g(\rho^\pm \to \pi^\pm\gamma) = 0.103$ and $g(\rho^0 \to \pi^0\gamma) = 0.122$. Since the charged couplings are identical, a glance at Table F.3 shows, that only an isoscalar photon transition is allowed. But this would also mean that $g^\pm = g^0$, which seems not to be fulfilled. However, taking into account the uncertainties in these couplings [67], it follows that $g^\pm$ and g^0 are indeed compatible with the assumption of pure isoscalar coupling. The minimal χ^2 value for g_{i0} results in $g_{i0} = 0.105$.
- In Compton scattering, there are also contributions from intermediate pseudoscalar mesons, $\pi^0 \to \gamma\gamma$ and $\eta \to \gamma\gamma$. In the first case, one has to note that the decay is only possible into an isoscalar and an isovector photon, since the pion is an isovector particle. Thus, the resulting isospin decomposed coupling is $g_{i0,i1} = \frac{1}{2}g(\pi^0 \to \gamma\gamma)$ (cf. Eq. (F.21)). In the second case, there could be two decay modes: either into two isoscalar or two isovector photons. However, since the rescattering effects in Compton scattering are calculated only perturbatively (see Compton scattering in the following section and (F.21)), there is no difference in extracting the physical proton and neutron amplitudes between the two coupling modes.[3]

---

[3] Even if one would not calculate the Compton amplitude perturbatively, the difference between the two coupling modes would be negligible since the $\eta \to \gamma\gamma$ coupling is very small. In addition, the full rescattering differs only slightly from the perturbative one due to the smallness of the fine structure constant α.

F.2.2 Isospin Decomposed Photons and Gauge Invariance

Having decomposed the photon into two isospin particles, the question arises, whether the resulting isospin amplitudes are gauge invariant individually. This point is important since the isospin-$\frac{1}{2}$ and isospin-$\frac{3}{2}$ amplitudes enter in independent scattering equations due to isospin decomposition. The consequence is, that they are weighed with different rescattering parts. A situation similar to the problem of gauge invariance after the introduction of hadronic formfactors for the Born diagrams (cf. Section 3.7) could arise, and therefore, the independent gauge invariance of the different isospin amplitudes has to be checked. This will be discussed in the following.

Meson Photoproduction

As shown in Section 3.3.1 all electromagnetic transition couplings for the baryon resonances and intermediate mesons are constructed in such a way that they separately fulfill the gauge invariance requirement $k_\mu \Gamma^\mu = 0$, which obviously still holds true for isospin decomposed photons. On the other side, the Born contributions, i.e. the charge couplings of the asymptotic particles, only fulfill gauge invariance when all contributions are summed up and charge is conserved in the reaction. Since the charge couplings are differently decomposed into isovector and isoscalar contributions for the various asymptotic particles, cf. Table F.3, we have to check whether gauge invariance independently holds for the $I = \frac{1}{2}$ and $I = \frac{3}{2}$ amplitudes.

As an example, we discuss the photoproduction of pions in details. As demonstrated in Section F.2.1, the photon isospin charge couplings to the pion result in $g^\pi_{i0} = 0$, $g^\pi_{i1} = -1$ and to the nucleon in $g^N_{i0} = g^N_{i1} = \frac{1}{2}$. Recall, that the index $_{i0}$ denotes the isoscalar and $_{i1}$ the isovector coupling.

Since $g^\pi_{i0} = 0$, there are only contributions from s- and u-channel diagrams to the isoscalar photon amplitude $T^0_{\pi\gamma}$. The sum of the these two contributions to the isospin-$\frac{1}{2}$ amplitude for $A_\mu \to k_\mu$ results in (cf. Section 3.3.1)

$$\tilde{\mathcal{M}}^0_s + \tilde{\mathcal{M}}^0_u = (g^N_{i0}(-\sqrt{3}) - g^N_{i0}(-\sqrt{3}))\frac{g_{NN\pi}}{2m_N}\bar{u}(p')\gamma_5 \not{k}' u(p) = 0\,.$$

The isospin factor $-\sqrt{3}$ arises from the πNN coupling and can be deduced from Table F.2 and Eq. (F.15).

For the isovector photons, there are now two isospin amplitudes to be considered separately: $T^{\frac{3}{2}}_{\pi\gamma}$ and $T^{\frac{1}{2}}_{\pi\gamma}$. The necessary overall isospin factors for the contributions of the four diagrams to the two isospin amplitudes can be inferred from Table F.2 and Eq. (F.10): For the isospin-$\frac{3}{2}$ amplitude one finds $f^I_s = 0$, $f^I_u = 2$, and $f^I_t = f^I_4 = 1$; for the isospin-$\frac{1}{2}$ amplitude $f^I_s = 3$, $f^I_u = -1$, and $f^I_t = f^I_4 = -2$. The total contribution of the four diagrams to the $I = \frac{3}{2}$ amplitude thus is for $A_\mu \to k_\mu$:

$$\begin{aligned}
\tilde{\mathcal{M}}^{\frac{3}{2}}_s + \tilde{\mathcal{M}}^{\frac{3}{2}}_u + \tilde{\mathcal{M}}^{\frac{3}{2}}_t + \tilde{\mathcal{M}}^{\frac{3}{2}}_4 &= (-2g^N_{i1} - g^\pi_{i1})\frac{g_{NN\pi}}{2m_N}\bar{u}(p')\gamma_5 \not{k}' u(p) \\
&= (-2 \cdot \tfrac{1}{2} - (-1))\frac{g_{NN\pi}}{2m_N}\bar{u}(p')\gamma_5 \not{k}' u(p) \\
&= 0
\end{aligned}$$

and to the $I=\frac{1}{2}$ amplitude:

$$\begin{aligned}\tilde{\mathcal{M}}_s^{\frac{1}{2}}+\tilde{\mathcal{M}}_u^{\frac{1}{2}}+\tilde{\mathcal{M}}_t^{\frac{1}{2}}+\tilde{\mathcal{M}}_4^{\frac{1}{2}} &= (g_{i1}^N(3-(-1))-g_{i1}^\pi(-2))\frac{g_{NN\pi}}{2m_N}\bar{u}(p')\gamma_5\not{k}'u(p) \\ &= (\tfrac{1}{2}\cdot 4-(-1)(-2))\frac{g_{NN\pi}}{2m_N}\bar{u}(p')\gamma_5\not{k}'u(p) \\ &= 0\ .\end{aligned}$$

Hence, all three isospin amplitudes $T^0_{\pi\gamma}$, $T^{\frac{1}{2}}_{\pi\gamma}$, and $T^{\frac{3}{2}}_{\pi\gamma}$ are independently gauge invariant.

For the photoproduction of isoscalar mesons (η, ω), only the $I=\frac{1}{2}$ amplitudes $T^0_{\pi\gamma}$ and $T^{\frac{1}{2}}_{\pi\gamma}$ contribute. For isoscalar photons, there can only be s- and u-channel diagram contributions just as in the isovector meson case4) and the same result is obtained as above with the only change that the isospin factor $-\sqrt{3}$ has to be replaced by 1. For isovector photons, there can now also only be s- and u-channel diagram contributions, and the isospin factors result in $f_s^I=f_u^I=-\sqrt{3}$. Hence, we have for the $T^{\frac{1}{2}}_{\eta\gamma}$ amplitude for $A_\mu\to k_\mu$:

$$\tilde{\mathcal{M}}_s^{\frac{1}{2}}+\tilde{\mathcal{M}}_u^{\frac{1}{2}}=(g_{i1}^N-g_{i1}^N)(-\sqrt{3})\frac{g_{NN\eta}}{2m_N}\bar{u}(p')\gamma_5\not{k}'u(p)=0\ .$$

Therefore, in meson photoproduction gauge invariance is fulfilled independently for the three isospin amplitudes $T^0_{\pi\gamma}$, $T^{\frac{1}{2}}_{\pi\gamma}$, and $T^{\frac{3}{2}}_{\pi\gamma}$.

Compton Scattering

Proceeding in the same way as for meson photoproduction, one finds the following expression when checking for gauge invariance of the Born contributions (nucleon s- and u-channel) on the incoming photon side (cf. Eq. (3.10) in Chapter 3 for $\gamma N\to\rho N$):

$$\tilde{\mathcal{M}}_s+\tilde{\mathcal{M}}_u \;=\; e^2(f_s^I-f_u^I)g_i^N\bar{u}(p')\left(g_i^{N'}-\frac{\kappa_i'}{2m_N}\not{k}'\right)\not{\epsilon}'u(p)\ .$$

Here, we have already dropped the tensor coupling to the incoming photon since it fulfills gauge invariance directly. The isospin coupling g_i^N of the incoming nucleon and $g_i^{N'}$, κ_i' of the outgoing nucleon refer to the considered isospin amplitude ($T^{00}_{\gamma\gamma}$, $T^{01}_{\gamma\gamma}$, $T^{10}_{\gamma\gamma}$, $T^{11,\frac{1}{2}}_{\gamma\gamma}$, or $T^{11,\frac{3}{2}}_{\gamma\gamma}$; see Appendix F.1.2). The isospin factors f_s^I and f_u^I can be deduced in exactly the same way as in meson photoproduction above:

For isoscalar incoming photons as in $T^{00}_{\gamma\gamma}$ and $T^{10}_{\gamma\gamma}$, the isospin factors f_s^I and f_u^I are always identical (either $f_s^I=f_u^I=1$ or $f_s^I=f_u^I=-\sqrt{3}$, see above), and for isovector incoming photons and isoscalar outgoing photons ($T^{01}_{\gamma\gamma}$) as well: $f_s^I=f_u^I=-\sqrt{3}$. Therefore, in these isospin amplitudes gauge invariance is fulfilled.

---

4) For $K\Lambda$ photoproduction, there are only s- and t-channel Born contributions and in the subsequent discussion u and t have to be exchanged.

However, the situation is different for the isovector-isovector amplitudes $T^{11}_{\gamma\gamma}$. For the amplitude with total isospin $\frac{1}{2}$ $\left(T^{11,\frac{1}{2}}_{\gamma\gamma}\right)$, the isospin factors result in $f^I_s = 3$, $f^I_u = -1$, and for $T^{11,\frac{3}{2}}_{\gamma\gamma}$ with total isospin $\frac{3}{2}$ in $f^I_s = 0$, $f^I_u = 2$. Evidently, gauge invariance is violated in both cases.

In principle, gauge invariance could be restored, by artificially adding a four-point Compton diagram with a structure as

$$\sim (f^I_s - f^I_u)\bar{u}(p') \left\{ \frac{g^{N\,2}_{i1}}{p\cdot k} \left[\gamma_\mu p'_\nu + \gamma_\nu p_\mu - \frac{\not{k}}{2} \left(g_{\mu\nu} + \frac{p_\mu p'_\nu}{p'\cdot k'} + \frac{p'_\mu p_\nu}{p\cdot k'} \right) \right] - g^N_{i1} \frac{\kappa_{i1}\sigma_{\mu\nu}}{4m_N} \right\} u(p)\varepsilon^\mu \varepsilon'^\nu . \tag{F.23}$$

However, this is not satisfying from a field-theoretical point of view. There is a different, more elegant solution by taking into account the smallness of the electromagnetic coupling and demanding that only the proton and neutron amplitudes (F.22) are physical quantities which should satisfy gauge invariance. This also explains, why rescattering effects in Compton scattering are usually calculated in a basis using physical ($\pi^0 p$, $\pi^+ n$, $\pi^- p$, $\pi^0 n$), not isospin states [13].

The above problem can be circumvented by including the electromagnetic interaction only perturbatively[5)] thus assuming that the implemented electromagnetic couplings are already the renormalized ones (in particular below the πN threshold). Looking at the BS equation (cf. Eq. (4.19))

$$\mathcal{T}^{IJ\pm}_{\lambda',\lambda} = \mathcal{K}^{IJ\pm}_{\lambda',\lambda} + \mathrm{i} \sum_a \sum_{\lambda_a > 0} \mathcal{T}^{IJ\pm}_{\lambda',\lambda_a} \mathcal{K}^{IJ\pm}_{\lambda_a,\lambda} \, , \tag{F.24}$$

the perturbative inclusion is equivalent to neglecting all intermediate electromagnetic states a in the rescattering part. Due to the smallness of the fine structure constant α, this approximation is reasonable. The consequence is that the calculation of the hadronic scattering decouples from the electromagnetic one and can be extracted independently. Hence, the full K-matrix equation (cf. Eq. (2.12))

$$\mathcal{T}^{IJ\pm}_{fi} = \left[\frac{\mathcal{K}^{IJ\pm}}{1 - \mathrm{i}\mathcal{K}^{IJ\pm}} \right]_{fi} .$$

is only solved for the hadronic states. In the second step, the meson-photoproduction amplitudes can be extracted via

$$\mathcal{T}^{IJ\pm}_{f\gamma} = \mathcal{K}^{IJ\pm}_{f\gamma} + \mathrm{i} \sum_a \mathcal{T}^{IJ\pm}_{fa} \mathcal{K}^{IJ\pm}_{a\gamma} \, , \tag{F.25}$$

where the helicity indices are omitted. The sum over a runs only over hadronic states. Finally, the Compton amplitudes result from

$$\mathcal{T}^{IJ\pm}_{\gamma\gamma} = \mathcal{K}^{IJ\pm}_{\gamma\gamma} + \mathrm{i} \sum_a \mathcal{T}^{IJ\pm}_{\gamma a} \mathcal{K}^{IJ\pm}_{a\gamma} \tag{F.26}$$

[5)] The difference between the full rescattering calculation (where gauge invariance is violated in Compton scattering) and the perturbative calculation have been checked and found to be less than 1 per mille.

with a running again only over hadronic states. Since the Compton isospin amplitudes of the potential only enter in the direct contribution $\mathcal{K}_{\gamma\gamma}^{IJ\pm}$ and for the purpose of comparison with experiment, only the proton and neutron Compton amplitudes of Eq. (F.22) are of interest, for gauge invariance only these two amplitudes have to be checked. Since $T_{\gamma\gamma}^{00}$, $T_{\gamma\gamma}^{01}$, and $T_{\gamma\gamma}^{10}$ have already been proven to be gauge invariant, it remains to be shown that the combination

$$T_{\gamma\gamma}^{11,\frac{1}{2}} + 2T_{\gamma\gamma}^{11,\frac{3}{2}} \tag{F.27}$$

also fulfills the gauge constraint. Adding up the isospin factors, we find:

$$f_s^{\frac{1}{2}} - f_u^{\frac{1}{2}} + 2(f_s^{\frac{3}{2}} - f_u^{\frac{3}{2}}) = 3 - (-1) + 2(0 - 2) = 0 \; . \tag{F.28}$$

Thus, gauge invariance is also fulfilled for Compton scattering on the nucleon as long as the photon is introduced perturbatively in the K-matrix formalism.

Appendix G

Observables and Partial Waves

In an experiment, only (polarization) dependent count rates can be extracted, which have to be related to the partial waves presented in Chapter 6. We restrict ourselves to those observables used in the calculation.

G.1 Cross Sections

The advantage of our partial-wave formalism becomes also obvious in the deduction of (total) cross sections from the partial-wave amplitudes (cf., e.g., the formulae in Appendix G of [52]). From the general two-body differential cross section formula [153] a uniform expression for all reactions can be derived:

$$\begin{aligned} \frac{d\sigma}{d\Omega} &= \frac{4m_B m'_B}{4(4\pi)^2 s}\frac{\mathrm{k}'}{\mathrm{k}}\frac{1}{s_i}\sum_{\lambda,\lambda'}\left|\mathcal{M}_{\lambda'\lambda}(\vartheta)\right|^2 \\ &= \frac{(4\pi)^2}{\mathrm{k}^2}\frac{1}{s_i}\sum_{\lambda,\lambda'}\left|\mathcal{T}_{\lambda'\lambda}(\vartheta)\right|^2 \ , \end{aligned}$$

where Eq. (C.10) has been used and the sum extends over all values of λ and λ'. s_i is the usual spin averaging factor for the initial state (equal to the number of spin states). The amplitude $\mathcal{T}_{\lambda'\lambda}(\vartheta)$ can be extracted from Eq. (4.7), e.g. for $\lambda, \lambda' > 0$:

$$\begin{aligned} \mathcal{T}_{\lambda'\lambda}(\vartheta) &= \frac{1}{2\pi}\sum_J (J+\tfrac{1}{2}) d^J_{\lambda\lambda'}(\vartheta)\mathcal{T}^J_{\lambda'\lambda} \\ &= \frac{1}{4\pi}\sum_J (J+\tfrac{1}{2}) d^J_{\lambda\lambda'}(\vartheta)\left(\mathcal{T}^{J+}_{\lambda'\lambda}+\mathcal{T}^{J-}_{\lambda'\lambda}\right) \ . \qquad \text{(G.1)} \end{aligned}$$

The amplitudes $\mathcal{T}^{JP}_{\lambda'\lambda}$ are constructed in isospin space as described in Appendix F.1.

Due to the orthogonality of the d-functions, the formula for the total cross section becomes even simpler:

$$\sigma = \frac{4\pi}{\mathrm{k}^2}\frac{1}{s_i}\sum_{J,P}\sum_{\lambda,\lambda'}(J+\tfrac{1}{2})\left|\mathcal{T}^{JP}_{\lambda'\lambda}\right|^2 \ .$$

Note that because of the definition of the helicity partial-wave amplitudes (Eq. (4.13)) the second sum extends only over positive λ and λ'.

Since there is no interference between the contributions from different partial waves, the total cross section can also be divided into partial-wave cross sections, allowing a direct access to the importance of the individual partial waves:

$$\sigma^{IJP} = \frac{4\pi}{\mathrm{k}^2} \sum_{\lambda,\lambda'} (J + \tfrac{1}{2}) \left| \mathcal{T}^{IJP}_{\lambda'\lambda} \right|^2 \; .$$

Closely related to this is another meaningful quantity, the inelastic partial-wave cross section (cf. Eq. (C.5)):

$$\sigma^{IJP}_{in} = \frac{4\pi}{\mathrm{k}^2} \sum_{\lambda,\lambda'} (J + \tfrac{1}{2}) \left(\mathrm{Im}\mathcal{T}^{IJP}_{\lambda'\lambda} - \left| \mathcal{T}^{IJP}_{\lambda'\lambda} \right|^2 \right) \; .$$

It allows, in particularly for $\pi N \to \pi N$, to extract information about the importance of other pion-induced channels in each partial wave, i.e. how much of the partial-wave flux goes away from πN.

In the case of photoproduction of η mesons there is also the so-called reduced cross section defined, which is more directly related to the amplitude since the phase space is divided out:

$$\sigma_{red} = \sqrt{\frac{\sigma}{4\pi} \frac{\mathrm{k}}{\mathrm{k}'}} = \sqrt{\frac{1}{\mathrm{k}\,\mathrm{k}'} \frac{1}{s_i} \sum_{J,P} \sum_{\lambda,\lambda'} (J + \tfrac{1}{2}) \left| \mathcal{T}^{JP}_{\lambda'\lambda} \right|^2} \; .$$

G.2 Polarization Observables

Depending on the intrinsic spins of the incoming and outgoing particles there are additional spin-dependent count rates that can be measured. The baryon single polarization observables (asymmetries) are defined in the following way:

$$\Omega = \frac{d\sigma_\uparrow - d\sigma_\downarrow}{d\sigma_\uparrow + d\sigma_\downarrow} \; . \tag{G.2}$$

The arrows ↑ and ↓ stand for the corresponding adjustment of the target ($\mathcal{T}$) or recoil ($\mathcal{P}$) baryon spin, usually in the y-direction given by $\boldsymbol{k} \times \boldsymbol{k}'$.

The photon beam polarization is usually measured in terms of the photon asymmetry (Σ)

$$\Sigma = \frac{d\sigma_\perp - d\sigma_\parallel}{d\sigma_\perp + d\sigma_\parallel} \; , \tag{G.3}$$

where the linear polarization vectors in plane ($\|$) and out of plane ($\perp$) of the photon are related to the circular polarization vectors of Appendix A.2.2 by

$$\begin{aligned} \boldsymbol{\varepsilon}_{\parallel} &\equiv \boldsymbol{e}_x = \frac{-1}{\sqrt{2}} (\boldsymbol{\varepsilon}_{+1} - \boldsymbol{\varepsilon}_{-1}) \\ \boldsymbol{\varepsilon}_{\perp} &\equiv \boldsymbol{e}_y = \frac{\mathrm{i}}{\sqrt{2}} (\boldsymbol{\varepsilon}_{+1} + \boldsymbol{\varepsilon}_{-1}) \; . \end{aligned} \tag{G.4}$$

In the following, we use the cross section intensity

$$\mathcal{I}(\vartheta) \equiv \frac{1}{2} \sum_{\lambda,\lambda'} |\mathcal{T}_{\lambda'\lambda}(\vartheta)|^2 \ , \tag{G.5}$$

where the sum extends over all possible values for λ and λ'.

G.2.1 Pion-Induced (Pseudo-) Scalar Meson Production

The recoil asymmetry results in

$$\mathcal{I}(\vartheta)\mathcal{P} \;=\; 2\mathrm{Im}\mathcal{T}_{\frac{1}{2}\frac{1}{2}}\mathcal{T}^*_{-\frac{1}{2}\frac{1}{2}} \tag{G.6}$$

with the amplitude $\mathcal{T}_{\lambda'\lambda}(\vartheta)$ as given in Eq. (G.1) and the cross section intensity $\mathcal{I}(\vartheta)$ as in (G.5).

Furthermore, a so-called spin-rotation angle is defined. This angle was introduced by [93, 289] to remove an ambiguity of partial-wave decompositions of 0^-N scattering solely based on differential cross sections and measurements of the polarization (G.6). Both are invariant under the transformation

$$(f \pm \mathrm{i}g\sin\vartheta) \to e^{\pm\mathrm{i}\epsilon(\vartheta)}(f \pm \mathrm{i}g\sin\vartheta) \ ,$$

where the functions f and g defined in (5.9) were introduced and ϵ is an arbitrary real function of ϑ. The phase ambiguity mixes high and low partial waves, and a unique partial-wave decomposition is impossible without additional assumptions, such as the truncation of the partial-wave expansion or a specific ansatz for the higher partial waves. By measuring the spin-rotation angle

$$\beta \;\equiv\; \arg\left(\frac{f - \mathrm{i}g\sin\vartheta}{f + \mathrm{i}g\sin\vartheta}\right) = \tan^{-1}\left(\frac{-2\sin\vartheta\mathrm{Re}f^*g}{|f|^2 - \sin^2\vartheta|g|^2}\right) \tag{G.7}$$

this ambiguity is removed and a direct approach to a partial-wave decomposition is possible.

G.2.2 Photoproduction of (Pseudo-) Scalar Mesons

The single polarization observables are given by (see also [184] for a detailed discussion)

$$\begin{array}{rcll}
\mathcal{I}(\vartheta)\Sigma & = & 2\mathrm{Re}\left(\mathcal{T}_{\frac{1}{2}\frac{3}{2}}\mathcal{T}^*_{\frac{1}{2}-\frac{1}{2}} + \mathcal{T}_{\frac{1}{2}\frac{1}{2}}\mathcal{T}^*_{\frac{1}{2}-\frac{3}{2}}\right) & \qquad \text{photon asymmetry} \\
\mathcal{I}(\vartheta)\mathcal{P} & = & 2\mathrm{Im}\left(\mathcal{T}_{\frac{1}{2}\frac{3}{2}}\mathcal{T}^*_{\frac{1}{2}-\frac{3}{2}} - \mathcal{T}_{\frac{1}{2}\frac{1}{2}}\mathcal{T}^*_{\frac{1}{2}-\frac{1}{2}}\right) & \qquad \text{recoil asymmetry} \\
\mathcal{I}(\vartheta)\mathcal{T} & = & 2\mathrm{Im}\left(\mathcal{T}_{\frac{1}{2}\frac{3}{2}}\mathcal{T}^*_{\frac{1}{2}\frac{1}{2}} - \mathcal{T}_{\frac{1}{2}-\frac{3}{2}}\mathcal{T}^*_{\frac{1}{2}-\frac{1}{2}}\right) & \qquad \text{target asymmetry}
\end{array}$$

with the amplitudes $\mathcal{T}_{\lambda'\lambda}(\vartheta)$ as given in Eq. (G.1) and the cross section intensity $\mathcal{I}(\vartheta)$ as in (G.5).

G.2.3 Compton Scattering

The single polarization observables are given by

$$\begin{aligned}
\mathcal{I}(\vartheta)\Sigma &= 2\mathrm{Re}\left(\left(\mathcal{T}_{\frac{3}{2}\frac{3}{2}}+\mathcal{T}_{\frac{1}{2}\frac{1}{2}}\right)^{*}\mathcal{T}_{\frac{1}{2}-\frac{3}{2}}+\left(\mathcal{T}_{\frac{3}{2}-\frac{3}{2}}-\mathcal{T}_{\frac{1}{2}-\frac{1}{2}}\right)^{*}\mathcal{T}_{\frac{3}{2}\frac{1}{2}}\right)\\
\mathcal{I}(\vartheta)\mathcal{T} &= 2\mathrm{Im}\left(\left(\mathcal{T}_{\frac{3}{2}\frac{3}{2}}+\mathcal{T}_{\frac{1}{2}\frac{1}{2}}\right)^{*}\mathcal{T}_{\frac{3}{2}\frac{1}{2}}-\left(\mathcal{T}_{\frac{3}{2}-\frac{3}{2}}-\mathcal{T}_{\frac{1}{2}-\frac{1}{2}}\right)^{*}\mathcal{T}_{\frac{1}{2}-\frac{3}{2}}\right)=\mathcal{I}(\vartheta)\mathcal{P}
\end{aligned}$$

for the photon and target/recoil asymmetry, respectively. The amplitudes $\mathcal{T}_{\lambda'\lambda}(\vartheta)$ are as given in Eq. (G.1) and the cross section intensity $\mathcal{I}(\vartheta)$ as in (G.5).

G.2.4 Photoproduction of Vector Mesons

The single polarization observables are given by (see also [178] for further details)

$$\begin{aligned}
\mathcal{I}(\vartheta)\Sigma &= 2\mathrm{Re}\left(+\mathcal{T}^{*}_{\frac{3}{2}\frac{3}{2}}\mathcal{T}_{\frac{3}{2}-\frac{1}{2}}+\mathcal{T}^{*}_{\frac{1}{2}\frac{1}{2}}\mathcal{T}_{\frac{1}{2}-\frac{3}{2}}+\mathcal{T}^{*}_{\frac{3}{2}-\frac{3}{2}}\mathcal{T}_{\frac{3}{2}\frac{1}{2}}+\mathcal{T}^{*}_{\frac{1}{2}-\frac{1}{2}}\mathcal{T}_{\frac{1}{2}\frac{3}{2}}+\mathcal{T}^{*}_{0\frac{3}{2}}\mathcal{T}_{0-\frac{1}{2}}+\mathcal{T}^{*}_{0-\frac{3}{2}}\mathcal{T}_{0\frac{1}{2}}\right)\\
\mathcal{I}(\vartheta)\mathcal{T} &= 2\mathrm{Im}\left(+\mathcal{T}^{*}_{\frac{3}{2}\frac{3}{2}}\mathcal{T}_{\frac{3}{2}\frac{1}{2}}-\mathcal{T}^{*}_{\frac{1}{2}\frac{1}{2}}\mathcal{T}_{\frac{1}{2}\frac{3}{2}}-\mathcal{T}^{*}_{\frac{3}{2}-\frac{3}{2}}\mathcal{T}_{\frac{3}{2}-\frac{1}{2}}+\mathcal{T}^{*}_{\frac{1}{2}-\frac{1}{2}}\mathcal{T}_{\frac{1}{2}-\frac{3}{2}}+\mathcal{T}^{*}_{0\frac{3}{2}}\mathcal{T}_{0\frac{1}{2}}-\mathcal{T}^{*}_{0-\frac{3}{2}}\mathcal{T}_{0-\frac{1}{2}}\right)\\
\mathcal{I}(\vartheta)\mathcal{P} &= 2\mathrm{Im}\left(-\mathcal{T}^{*}_{\frac{3}{2}\frac{3}{2}}\mathcal{T}_{\frac{1}{2}\frac{3}{2}}+\mathcal{T}^{*}_{\frac{1}{2}\frac{1}{2}}\mathcal{T}_{\frac{3}{2}\frac{1}{2}}-\mathcal{T}^{*}_{\frac{3}{2}-\frac{3}{2}}\mathcal{T}_{\frac{1}{2}-\frac{3}{2}}+\mathcal{T}^{*}_{\frac{1}{2}-\frac{1}{2}}\mathcal{T}_{\frac{3}{2}-\frac{1}{2}}-\mathcal{T}^{*}_{0\frac{3}{2}}\mathcal{T}_{0-\frac{3}{2}}+\mathcal{T}^{*}_{0\frac{1}{2}}\mathcal{T}_{0-\frac{1}{2}}\right)
\end{aligned}$$

for the photon and target/recoil asymmetry, respectively. The amplitudes $\mathcal{T}_{\lambda'\lambda}(\vartheta)$ are as given in Eq. (G.1) and the cross section intensity $\mathcal{I}(\vartheta)$ as in (G.5). The notation for the VN helicity states follows Section 5.2. The vector meson and some double polarization observables can be found in Appendix B of Ref. [178].

Schilling et al. [159] have also introduced density matrix elements $\rho^{i}_{\lambda_V\lambda'_V}$, which can be directly related to the decay angular distribution of the vector meson. These density matrix elements are directly given by the helicity amplitudes:

$$\begin{aligned}
\rho^{0}_{\lambda_V\lambda'_V} &= \frac{1}{2\mathcal{I}}\sum_{\lambda_\gamma,\lambda_{N'},\lambda_N}\mathcal{T}_{\lambda_V\lambda_{N'},\lambda_\gamma\lambda_N}\mathcal{T}^{*}_{\lambda'_V\lambda_{N'},\lambda_\gamma\lambda_N}\\
\rho^{1}_{\lambda_V\lambda'_V} &= \frac{1}{2\mathcal{I}}\sum_{\lambda_\gamma,\lambda_{N'},\lambda_N}\mathcal{T}_{\lambda_V\lambda_{N'},-\lambda_\gamma\lambda_N}\mathcal{T}^{*}_{\lambda'_V\lambda_{N'},\lambda_\gamma\lambda_N}\\
\rho^{2}_{\lambda_V\lambda'_V} &= \frac{\mathrm{i}}{2\mathcal{I}}\sum_{\lambda_\gamma,\lambda_{N'},\lambda_N}\lambda_\gamma\mathcal{T}_{\lambda_V\lambda_{N'},-\lambda_\gamma\lambda_N}\mathcal{T}^{*}_{\lambda'_V\lambda_{N'},\lambda_\gamma\lambda_N}\\
\rho^{3}_{\lambda_V\lambda'_V} &= \frac{1}{2\mathcal{I}}\sum_{\lambda_\gamma,\lambda_{N'},\lambda_N}\lambda_\gamma\mathcal{T}_{\lambda_V\lambda_{N'},\lambda_\gamma\lambda_N}\mathcal{T}^{*}_{\lambda'_V\lambda_{N'},\lambda_\gamma\lambda_N}\ . \qquad \text{(G.8)}
\end{aligned}$$

Appendix H

Parameters of Further Calculations

In Tables H.1 − H.8 the parameters of those calculations, which are not displayed and whose parameters are not given in Chapter 8, are summarized.

g	value	g	value	g	value	g	value
$g_{NN\pi}$	12.80	$g_{NN\sigma} \cdot g_{\sigma\pi\pi}$	31.58	$g_{NN\rho}$	5.74	$\kappa_{NN\rho}$	1.37
	13.01		13.66		2.21		1.30
	12.84		15.22		2.03		1.42
	13.00		3.33		5.45		1.58
	12.79		36.82		2.77		1.08
$g_{NN\eta}$	1.90	g_{NNa_0}	32.34	$g_{NN\omega}$	3.91	$\kappa_{NN\omega}$	−0.86
	0.29		8.60		3.94		−0.90
	0.90		3.90		5.65		−1.74
	0.17		−19.47		4.50		−0.70
	0.96		−2.56		3.91		−1.43
$g_{N\Lambda K}$	−16.87	$g_{N\Lambda K_0^*}$	−58.40	$g_{N\Lambda K^*}$	−34.70	$\kappa_{N\Lambda K^*}$	−0.39
	−11.53		−11.58		−5.86		−0.39
	−14.91		7.54		−5.75		−0.55
	−15.13		54.96		−24.66		−0.34
	−16.18		18.36		−6.79		−0.62
$g_{N\Sigma K}$	14.60	$g_{N\Sigma K_0^*}$	62.22	$g_{N\Sigma K^*}$	2.56	$\kappa_{N\Sigma K^*}$	0.18
	2.50		11.06		0.71		−0.11
	13.54		11.20		1.11		−0.14
	15.24		54.62		2.66		0.57
	14.33		−3.72		−4.26		−0.32

Table H.1: Nucleon and *t*-channel couplings. First line: C-p-$\pi-$, 2nd line: C-t-$\pi+$, 3rd line: C-t-$\pi-$, 4th line: C-p-$\pi\not\chi+$, 5th line: P-p-$\pi-$.

Λ_N [GeV]	$\Lambda^h_{\frac{1}{2}}$ [GeV]	$\Lambda^h_{\frac{3}{2}}$ [GeV]	Λ^h_t [GeV]
1.16	4.26	1.05	0.70
1.11	3.80	1.00	0.70
1.10	4.30	1.01	0.73
1.15	2.81	1.05	0.70
1.17	3.87	1.03	1.89

Table H.2: Cutoff values for the formfactors. The upper index h shows, that the value is applied to a hadronic vertex, while the lower one denotes the particle going off-shell, i.e. N: nucleon, $\frac{1}{2}$: spin-$\frac{1}{2}$ resonance, $\frac{3}{2}$: spin-$\frac{3}{2}$ resonance, t: t-channel meson. Line ordering as in Table H.1.

$L_{2I,2S}$	mass	Γ_{tot}	$R_{\pi N}$	$R_{2\pi N}$	$R_{\eta N}$	$R_{K\Lambda}$	$R_{K\Sigma}$	$R_{\omega N}$
$S_{11}(1535)$	1537	166	39.0	10.1(+)	50.9(+)	0.25^a	-0.21^a	—
	1538	117	35.2	8.4(−)	56.5(+)	0.90^a	-0.84^a	—
	1541	110	39.4	8.3(−)	52.3(+)	0.61^a	-0.36^a	—
	1534	118	34.6	7.6(+)	57.8(−)	0.00^c	0.00^c	—
	1533	103	35.1	1.0(−)	63.9(+)	-0.94^a	3.97^a	—
$S_{11}(1650)$	1676	169	74.1	22.2(+)	0.3(+)	3.4(−)	-0.33^a	—
	1682	176	68.8	23.9(+)	1.4(−)	5.9(−)	0.92^a	—
	1692	240	74.8	20.0(+)	0.0(+)	5.2(−)	-0.76^a	—
	1678	177	70.1	22.9(+)	0.8(+)	6.1(−)	0.69^a	—
	1694	188	75.2	19.5(−)	0.7(−)	4.6(−)	-1.08^a	—
$P_{11}(1440)$	1498	500	60.5	39.5(+)	1.88^a	1.44^a	6.00^a	—
	1500	546	59.0	41.0(+)	4.76^a	0.89^a	3.24^a	—
	1500	550	59.1	40.9(+)	5.02^a	1.44^a	1.37^a	—
	1482	443	62.1	37.9(+)	-1.88^a	0.00^c	0.00^c	—
	1520	656	62.1	37.9(+)	3.96^a	-3.33^a	-0.97^a	—
$P_{11}(1710)$	1695	281	5.6	52.7(+)	41.6(+)	0.0(+)	0.1(−)	0.0
	1787	541	4.4	47.7(+)	25.6(−)	0.0(+)	17.1(+)	5.2
	1716	197	0.0	51.4(−)	45.7(+)	2.8(−)	0.0(+)	0.0
	1786	689	5.4	38.8(−)	23.2(−)	1.1(−)	10.4(+)	21.0
	1756	547	0.0	47.3(+)	27.6(−)	1.9(−)	20.8(+)	2.5

Table H.3: Properties of $I = \frac{1}{2}$, $J = \frac{1}{2}$ resonances considered in the calculation. The mass and the total width Γ_{tot} are given in MeV, the partial decay width ratios R in percent of the total width. All πN couplings are chosen positiv. "NF": not found in the corresponding calculation. "NFA": not found below 2 GeV in any calculation. ^{a}: The coupling is given. ^{b}: The decay ratio is given in 0.1‰. ^{c}: Not varied in the fit. Line ordering as in Table H.1.

$L_{2I,2S}$	mass	Γ_{tot}	$R_{\pi N}$	$R_{2\pi N}$	$R_{\eta N}$	$R_{K\Lambda}$	$R_{K\Sigma}$	$R_{\omega N}$
$P_{13}(1720)$	1725	205	16.7	51.9(+)	9.3(+)	10.7(−)	11.3(−)	0.1
	1703	117	17.7	70.4(+)	1.4(−)	8.1(−)	2.4(−)	5.2
	1699	68	16.3	79.6(+)	0.4(−)	3.4(−)	0.3(+)	0.0
	1722	251	17.1	69.8(+)	1.9(−)	6.1(−)	4.7(−)	0.2
	1737	79	19.6	67.8(+)	4.2(+)	7.9(−)	0.0(−)	0.4
$P_{13}(1900)$	1894	562	16.8	28.9(+)	22.8(−)	2.7(−)	0.2(+)	28.7
	1936	707	18.1	35.3(−)	14.5(+)	6.3(−)	1.2(−)	24.6
	1939	705	12.3	49.3(−)	20.1(+)	1.7(−)	1.2(−)	15.3
	1951	603	19.4	42.0(−)	10.5(−)	4.5(−)	0.2(−)	23.4
	1824	823	14.9	50.5(+)	7.4(−)	9.5(−)	0.0(+)	17.8
$D_{13}(1520)$	1510	92	58.6	41.4(−)	1.2^{b}(+)	0.44^{a}	0.54^{a}	—
	1511	102	57.2	42.8(−)	3.2^{b}(+)	1.91^{a}	1.45^{a}	—
	1510	93	56.7	43.3(−)	6.5^{b}(+)	0.90^{a}	-3.60^{a}	—
	1510	92	57.8	42.1(−)	2.5^{b}(−)	0.00^{c}	0.00^{c}	—
	1509	95	59.7	40.3(−)	2.0^{b}(+)	-0.67^{a}	-3.95^{a}	—
$D_{13}(1700)$	NF							
	NF							
	NF							
	NF							
	1748	50	1.6	49.0(−)	2.0(+)	0.7(−)	9.3(+)	37.3
$D_{13}(2080)$	1944	848	16.1	50.9(+)	14.6(+)	0.8(+)	0.2(−)	17.4
	1946	603	12.7	63.1(−)	2.8(−)	1.3(+)	4.2(+)	16.0
	1982	668	9.7	64.2(+)	5.1(−)	0.0(+)	6.7(+)	14.3
	1946	1.075	16.0	47.3(+)	1.4(+)	1.1(+)	1.5(+)	32.5
	1942	765	15.5	54.4(+)	2.4(+)	0.1(−)	2.5(+)	25.1

Table H.4: Properties of $I = \frac{1}{2}$, $J = \frac{3}{2}$ resonances considered in the calculation. Notation and line ordering as in Table H.1.

$L_{2I,2S}$	mass	Γ_{tot}	$R_{\pi N}$	$R_{2\pi N}$	$R_{K\Sigma}$
$S_{31}(1620)$	1617	187	37.5	62.5(−)	0.80^a
	1614	211	33.7	66.3(−)	0.25^a
	1613	202	34.6	65.4(−)	0.61^a
	1607	158	33.5	66.5(−)	0.06^a
	1627	162	43.9	56.1(+)	0.50^a
$S_{31}(1900)$	NF				
	NF				
	NF				
	NF				
	1908	173	34.7	65.3(−)	0.0(+)
$P_{31}(1750)$	1742	614	2.0	97.6(+)	0.4(+)
	1753	622	2.6	97.3(+)	0.1(+)
	1737	622	1.6	98.1(+)	0.3(+)
	1834	615	9.1	89.9(+)	1.0(−)
	1982	651	21.3	77.7(+)	1.1(−)
$P_{33}(1232)$	1231	101	100.0	$0.002(+)^b$	—
	1230	104	100.0	$0.012(+)^b$	—
	1230	103	100.0	$0.008(-)^b$	—
	1230	102	100.0	$0.001(+)^b$	—
	1230	92	100.0	$0.003(-)^b$	—
$P_{33}(1600)$	1655	296	13.6	86.4(+)	0.19^a
	1662	303	13.6	86.4(+)	0.41^a
	1657	288	13.5	86.5(+)	0.32^a
	1653	270	14.2	85.8(+)	0.71^a
	1670	410	13.6	86.4(+)	0.14^a
$P_{33}(1920)$	2056	465	14.9	81.1(−)	4.0(−)
	2055	531	16.4	76.9(−)	6.7(−)
	2056	589	15.8	78.3(−)	5.9(−)
	2036	379	13.5	80.0(+)	6.5(+)
	2056	346	6.7	88.8(−)	4.5(−)
$D_{33}(1700)$	1680	594	13.6	86.4(+)	2.56^a
	1678	638	13.7	86.3(+)	2.38^a
	1681	643	13.6	86.4(+)	2.11^a
	1680	598	13.6	86.4(+)	0.92^a
	1677	665	14.5	85.5(+)	3.94^a

Table H.5: Properties of $I = \frac{3}{2}$ resonances considered in the calculation. Notation and line ordering as in Table H.1.

$L_{2I,2S}$	mass	Γ_{tot}	$R_{\omega N}$	$R^{0}_{\omega N}$	$R^{\frac{1}{2}}_{\omega N}$	$R^{\frac{3}{2}}_{\omega N}$
$S_{11}(1535)$	1537	166	—	-5.40^{a1}	-0.52^{a2}	—
	1538	117	—	-0.46^{a1}	1.98^{a2}	—
	1541	110	—	-2.52^{a1}	-4.55^{a2}	—
	1534	118	—	0.00^{c}	0.00^{c}	—
	1533	103	—	0.79^{a1}	-1.58^{a2}	—
$S_{11}(1650)$	1676	169	—	1.22^{a1}	0.00^{c}	—
	1682	176	—	-0.17^{a1}	0.00^{c}	—
	1692	240	—	1.15^{a1}	0.00^{c}	—
	1678	177	—	-0.22^{a1}	0.00^{c}	—
	1694	188	—	-1.52^{a1}	-4.35^{a2}	—
$P_{11}(1440)$	1498	500	—	-4.92^{a1}	7.99^{a2}	—
	1500	546	—	4.16^{a1}	0.19^{a2}	—
	1500	550	—	-6.00^{a1}	-0.19^{a2}	—
	1482	443	—	0.00^{c}	0.00^{c}	—
	1520	656	—	4.55^{a1}	-5.70^{a2}	—
$P_{11}(1710)$	1695	281	—	-4.99^{a1}	-1.71^{a2}	—
	1755	327	11.7	0.0(−)	11.7(−)	—
	1787	541	5.2	2.8(+)	2.4(+)	—
	1716	197	—	-5.60^{a1}	-0.31^{a2}	—
	1786	689	21.0	11.0(+)	10.0(−)	—
	1756	547	2.4	2.1(−)	0.4(+)	—

Table H.6: ωN decay ratios of $I = \frac{1}{2}$, $J = \frac{1}{2}$ resonances. The total widths are given in MeV, all ratios in percent. ^{a1} (^{a2}, ^{a3}): The coupling g_1 (g_2, g_3) is given. ^{b}: The ratio is given in 0.1‰. ^{c}: Not varied in the fit. Line ordering as in Table H.1.

$L_{2I,2S}$	mass	Γ_{tot}	$R_{\omega N}$	$R^{0}_{\omega N}$	$R^{\frac{1}{2}}_{\omega N}$	$R^{\frac{3}{2}}_{\omega N}$
$P_{13}(1720)$	1725	205	0.05	0.00(+)	0.00(+)	0.05(+)
	1703	117	—	10.60^{a1}	-2.44^{a2}	-1.75^{a3}
	1699	68	—	3.88^{a1}	-6.23^{a2}	-6.60^{a3}
	1722	251	0.2	0.01(+)	0.02(+)	0.25(+)
	1737	79	0.4	0.00(−)	0.05(−)	0.32(−)
$P_{13}(1900)$	1894	562	28.6	1.1(+)	6.2(+)	21.3(+)
	1936	707	24.6	2.0(+)	8.7(+)	13.9(+)
	1939	705	15.3	0.0(−)	1.1(−)	14.2(−)
	1951	603	23.4	2.4(+)	0.0(−)	20.9(+)
	1824	823	17.8	0.1(−)	2.4(−)	15.3(−)
$D_{13}(1520)$	1510	92	—	0.74^{a1}	7.20^{a2}	-4.09^{a3}
	1511	102	—	7.76^{a1}	-11.49^{a2}	-5.12^{a3}
	1510	93	—	9.20^{a1}	-5.02^{a2}	-4.49^{a3}
	1510	92	—	0.00^{c}	0.00^{c}	0.00^{c}
	1509	95	—	8.97^{a1}	8.41^{a2}	1.81^{a3}
$D_{13}(1700)$	NF					
	NF					
	NF					
	NF					
	1748	50	37.6	12.3(−)	6.6(−)	19.2(−)
$D_{13}(2080)$	1944	848	17.4	1.6(+)	1.9(−)	13.9(+)
	1946	603	16.0	5.5(−)	10.4(−)	0.1(+)
	1982	668	14.3	0.9(+)	2.5(+)	10.9(−)
	1946	1.075	32.5	12.3(+)	0.3(+)	19.9(+)
	1942	765	25.1	6.3(−)	0.0(−)	16.8(−)

Table H.7: ωN decay ratios of $I = \frac{1}{2}$, $J = \frac{3}{2}$ resonances. Notation as in Table H.6, line ordering as in Table H.1.

$L_{2I,2S}$	$a_{\pi N}$	$a_{\zeta N}$	$a_{\eta N}$	$a_{K\Lambda}$	$a_{K\Sigma}$	$a_{\omega N1}$	$a_{\omega N2}$	$a_{\omega N3}$
$P_{13}(1720)$	-1.342	0.451	1.178	0.089	1.511	1.386	-4.000	-3.999
	2.335	0.280	-3.674	0.752	-0.016	-2.372	-3.397	-3.998
	3.047	0.460	3.999	3.997	-3.999	-4.000	-4.000	3.996
	-0.669	0.424	-5.997	2.031	-2.703	0.974	-5.994	0.000^c
$P_{13}(1900)$	1.425	0.918	-0.306	-3.164	3.499	-0.389	-0.012	3.963
	-3.094	0.897	0.837	-0.086	-1.307	1.601	2.885	2.983
	1.336	0.283	0.294	3.997	2.892	-3.599	3.998	-3.992
	-1.332	0.667	-0.698	4.316	-0.305	4.672	5.994	0.000^c
$D_{13}(1520)$	0.917	-0.482	1.335	2.448	1.380	-2.809	-1.731	3.693
	0.828	0.449	1.857	0.464	-3.982	-4.000	3.995	-3.822
	0.887	0.105	1.182	-0.452	0.773	3.711	3.902	-3.874
	0.892	0.106	1.659	0.000^c	0.000^c	0.000^c	0.000^c	0.000^c
$D_{13}(2080)$	0.415	-1.000	-0.799	-1.426	-3.993	0.768	3.735	1.174
	2.672	-0.956	-2.159	0.830	-2.281	2.155	3.841	-0.058
	1.417	0.824	0.170	-3.970	0.512	1.711	3.997	0.026
	1.026	0.840	0.493	1.589	1.012	1.659	2.704	0.000^c
$P_{33}(1232)$	0.254	3.520	—	—	0.000^c	—	—	—
	0.217	4.000	—	—	0.000^c	—	—	—
	0.199	3.916	—	—	0.000^c	—	—	—
	0.129	5.146	—	—	0.000^c	—	—	—
$P_{33}(1600)$	1.275	0.293	—	—	-0.794	—	—	—
	1.755	0.335	—	—	-0.673	—	—	—
	1.696	0.350	—	—	-0.171	—	—	—
	1.148	0.172	—	—	-1.749	—	—	—
$P_{33}(1920)$	-3.108	1.234	—	—	-1.502	—	—	—
	-2.592	1.151	—	—	-0.511	—	—	—
	-2.679	1.147	—	—	-0.758	—	—	—
	-4.341	1.440	—	—	0.293	—	—	—
$D_{33}(1700)$	-0.222	0.419	—	—	0.413	—	—	—
	-0.263	0.417	—	—	0.279	—	—	—
	-0.248	0.397	—	—	0.321	—	—	—
	-0.226	0.452	—	—	0.843	—	—	—

Table H.8: Off-shell parameters a of the spin-$\frac{3}{2}$ resonances. ^{c}: Not varied in the fit. First line: C-p-$\pi-$, 2nd line: C-t-$\pi+$, 3rd line: C-t-$\pi-$, 4th line: C-p-$\pi\not\chi+$.

Appendix I

Numerical Methods and Extraction of Partial Waves

In this final appendix, the general strategy for the calculation of the results and the numerical procedures, which help to optimize the numerical manipulation of all Feynman diagrams for the various reactions, are presented. The necessary integrations for the extraction of the partial waves and matrix inversions for the determination of the scattering matrix $\mathcal{T}$ (see Eqs. (4.8) and (4.20)) are realized by standard Simpson and LU-decomposition methods [130].

I.1 Extraction of Feynman Diagram Contributions and Calculation of Observables

The Feynman amplitude $-\mathrm{i}\mathcal{M}^{(1)}_{fi} = -\mathrm{i}\langle f|V|i\rangle = \bar{u}(p')\ldots u(p)$ for each diagram, resulting from the usual Feynman rules with the help of the Lagrangians summarized in Appendix E, is rewritten by means of the algebraic manipulator REDUCE[1] in the following way:

- Using four-momentum conservation, the intermediate and final momenta are reexpressed by the baryon momenta p and p' and the incoming meson (photon) momentum k (in the case of spin-0 baryon scattering, instead of k the average of the meson momenta $\bar{k} = (k+k')/2$ is used, cf. Section 5.1.1) and the Mandelstam variables s and u.

- All Levi-Civita tensors $\varepsilon_{\mu\nu\rho\sigma}$ appearing in $1^-1^-0^-$-vertices (as in, e.g., $\pi \to \gamma\gamma$, $\omega \to \rho\pi$) are recasted in terms of γ matrices using Eqs. (A.12), (A.13), and (A.14).

- All γ_5 matrices are moved to the left next to $\bar{u}(p')$ by applying the anticommutation relation (A.12). Depending on the spin and parity properties of the initial and final state, one is either left with $\bar{u}(p')\gamma_5^2 = \bar{u}(p')\mathbb{1}_4$ or $\bar{u}(p')\gamma_5$.

---

[1] In principle, for reasons of unification and future advancements, exporting all REDUCE routines to MATHEMATICA would be desirable.

- With the help of the anticommutation property of the γ matrices (A.10), all four-momenta contractions $\not{p}'$ are moved to the left next to $\bar{u}(p')$ and the contractions $\not{p}$ to the right next to $u(p)$. The Dirac Equation (A.19) then transforms the contractions $\bar{u}(p')\not{p}'$ and $\not{p}u(p)$ into $m_{B'}\bar{u}(p')\mathbb{1}_4$ and $m_B\mathbb{1}_4\bar{u}(p)$, respectively.

The resulting expression then is of the form (5.4), (5.15), or (5.21), depending on the participating final states. Thus the contribution of the diagram to the spin-dependent amplitude can be extracted as described in Chapter 5.

As an example, the above procedure is applied to the contribution of the u-channel Born diagram to πN elastic scattering. From the Feynman rules one finds:

$$-\,\mathrm{i}\mathcal{M}_u^{(1)} = \mathrm{i}\frac{g_{\pi NN}^2}{4m_N^2}\bar{u}(p',s')\gamma_5\not{k}\frac{\not{q}+m_N}{q^2-m_N^2}\gamma_5\not{k}'u(p,s)\ .$$

Applying the above transformation rules ($q = p - k'$), this is rewritten as

$$-\,\mathrm{i}\mathcal{M}_u^{(1)} = \mathrm{i}\frac{g_{\pi NN}^2}{4m_N^2}\bar{u}(p',s')\frac{-\bar{\not{k}}(q^2+3m_N^2)-2m_N(q^2-m_N^2)}{q^2-m_N^2}u(p,s)$$

with $q^2 = u$ and hence A and B of Eq. (5.4) are identified by ($\mathcal{V} = \mathcal{M}^{(1)}$)

$$\begin{aligned} A_u &= +2m_N g_{\pi NN}^2 \\ B_u &= +g_{\pi NN}^2\frac{q^2+3m_N^2}{q^2-m_N^2}\ . \end{aligned}$$

The procedure works completely analogously for all other diagrams and all other reaction channels.

Looking at Eqs. (C.11) and (2.1) one deduces that the actual $\mathcal{K}$-matrix elements entering the calculation are related to the amplitudes extracted from the Feynman rules by

$$\mathcal{K}_{\lambda'\lambda} = -\frac{\sqrt{\mathrm{p}\mathrm{p}'m_B'm_B}}{(4\pi)^2\sqrt{s}}\langle f|V|i\rangle = \frac{\sqrt{\mathrm{p}\mathrm{p}'m_B'm_B}}{(4\pi)^2\sqrt{s}}(-\mathcal{M}_{\lambda'\lambda}^{(1)})\ . \tag{I.1}$$

These $\mathcal{K}$-matrix elements are then decomposed into amplitudes of total isospin $I = \frac{1}{2}$ and $I = \frac{3}{2}$ as described in Appendix F. In the next step, the spin-dependent isospin amplitudes $\mathcal{K}_{\lambda'\lambda}^{I}$ are further decomposed into helicity partial waves $\mathcal{K}_{\lambda'\lambda}^{IJ\pm}$ of good total spin J and parity P as described in Chapter 4 (cf. Eqs. (4.8) and (4.13)). All the hadronic $\mathcal{K}_{\lambda'\lambda}^{IJ\pm}$ amplitudes enter Eq. (4.20) for the extraction of the hadronic $\mathcal{T}_{\lambda'\lambda}^{IJ\pm}$ amplitudes. The photoproduction and Compton scattering $\mathcal{T}_{\lambda'\lambda}^{IJ\pm}$ amplitudes are then extracted as described in Appendix F.2.2 (cf. Eqs. (F.25) and (F.26)). Finally, from the $\mathcal{T}_{\lambda'\lambda}^{IJ\pm}$ the experimental observables given in Appendix G can be calculated.

The relations for the contributions of the Feynman diagrams to the spin-dependent amplitudes $\mathcal{M}_{\lambda'\lambda}^{(1)} = \mathcal{V}_{\lambda'\lambda}$ given in Eqs. (5.10), (5.13), (5.19), (5.20), and (5.24) in Chapter 5 have been checked with the help of the algebraic manipulator MATHEMATICA [116]; in addition, the formulae in Eq. (5.24) have been tested numerically against the calculation method developed in [158]. We have refrained from implementing the constraints

reaction	factor
$\pi N \rightarrow \pi N$	$+1$
$\pi N \rightarrow \zeta N$	$-\mathrm{i}$
$\zeta N \rightarrow \pi N$	$+\mathrm{i}$
$\zeta N \rightarrow \zeta\pi N$	$+1$
$VN \rightarrow \pi N$	$(-\mathrm{i}) \cdot (+1)$
$VN \rightarrow \zeta N$	$(-\mathrm{i}) \cdot (-\mathrm{i})$
$\pi N \rightarrow VN$	$(+1) \cdot (+\mathrm{i})$
$\zeta N \rightarrow VN$	$(+\mathrm{i}) \cdot (+\mathrm{i})$
$VN \rightarrow VN$	$+1$

Table I.1: Additional factors for the conversion of the Feynman amplitudes $\mathcal{M}^{(1)}$ into purely real $\mathcal{K}$-matrix elements.

following from gauge invariance (see Eqs. (5.27), (5.33), and (5.34) in Section 5.4) in the rewriting procedure of the Feynman diagrams. However, gauge invariance has been checked numerically by proving Eqs. (5.27), (5.33), and (5.34) for the sum of all Feynman diagram contributions.

Similarly as for the spin-dependent amplitudes, the relations for the resonance decay widths (E.25) , (E.26), (E.37), and helicity decay amplitudes (E.29), (E.39) in Appendix E have been verified. These methods can be easily combined to evaluate relations analogous to the ones given in (5.24) for reactions involving the $\pi\Delta$ final state.

For further simpification of the numerical manipulation, we have chosen specific relations between the interaction Lagrangians for positive- and negative-parity resonances. The field theoretical primer for the choice of all Lagrangians is that the interaction should satisfy the same symmetries as the underlying fundamental theory. However, since all baryon resonance interactions are introduced explicitly by hand, there is still some freedom concerning the relative sign between the interaction Lagrangian of positive- and negative-parity resonances. The idea for the choice in Section 3.4 is, that in the resulting full expression for the Feynman diagrams the negative-parity resonance contribution can easily be deduced from the positive-parity expression by simply reversing the sign of the resonance mass: $\mathcal{M}^{(1)}_{(P=-)}(m_R) = \mathcal{M}^{(1)}_{(P=+)}(m_R \rightarrow -m_R)$. Thus, the Feynman diagram manipulation presented above in Section I.1 needs to be applied only to the diagram of the positive-parity resonance.

I.2 Performance Optimization

Looking at the Lagrangian of the linear σ model for πN scattering (cf. Section 3.3.2) $\bar{u}_N(\sigma + \mathrm{i}\boldsymbol{\pi} \cdot \boldsymbol{\tau}\gamma_5)u_N$, one deduces, that the coupling of the nucleon to a pseuodscalar and to a scalar meson differ by a factor of $\mathrm{i}\gamma_5$. Extracting now for example a $\pi N \rightarrow N \rightarrow \pi N$ and a $\pi N \rightarrow N \rightarrow \sigma N$ $\mathcal{K}$-matrix element contribution as described in Section I.1 above (note, that the latter one is not included in the present model, see Section 3.3.2), the result is purely real for $\pi N \to \pi N$, while due to the coupling difference of $\mathrm{i}\gamma_5$ it is purely imaginary for $\pi N \to \sigma N$. This directly translates into completely real contributions from all diagrams to $\pi N \to \pi N$, and into completely imaginary contributions from all diagrams to $\pi N \to \zeta N$.

However, since real number crunching is less (computational) time consuming than complex number crunching, it is favorable to deal with a purely real, symmetric $\mathcal{K}$ matrix instead of a hermitian, but complex one. Thus the $\mathcal{K}$-matrix elements extracted by the above procedure are additionally multiplied by the factors given in Table I.1; the resulting $\mathcal{K}$ matrix is purely real. It can be easily shown that upon applying these factors, all rescattering contributions still enter in $\mathcal{T}$ (cf. Eq. (4.20)) with the correct sign.

A critical point in the numerical calculation is the maximum number of partial waves J_{max}. The number of angular integration steps, which have to be calculated (see above), increases linearly with the maximum number of partial waves. Since computation time is of great importance in the fitting procedure, it is essential to find a minimal value for J_{max}, which still gives results with sufficient accuracy. In [51, 52, 53] the partial-wave decomposition has been performed up to $J_{max} = \frac{11}{2}$. However, for the purposes of the present model, an increase of this number is of vital importance. In the ωN photoproduction, the π^0 exchange proves to be a very important mechanism at forward angles. Taking into account only partial waves up to $J_{\mathrm{max}} = \frac{11}{2}$, one neglects large contributions of the higher partial waves; this is also discussed in Section 8.4.6. Consequently, an increase of J_{max} is mandatory. We have tested the calculation for an optimal value and have found reasonable convergence at a value of $J_{max} = \frac{27}{2}$.

Bibliography

[**1**] R.A. Adelseck and B. Saghai, *Phys. Rev.* **C42**, 108 (1990).

[**2**] S.L. Adler, *Phys. Rev.* **139**, B1638 (1965).

[**3**] A. Alavi-Harati et al., `hep-ex/0110016`, submitted to *Phys. Rev. Lett.*.

[**4**] R.A. Arndt, I.I. Strakovsky, R.L. Workman, and M.M. Pavan, *Phys. Rev.* **C52**, 2120 (1995).

[**5**] R.A. Arndt, I.I. Strakovsky, and R.L. Workman, *Phys. Rev.* **C53**, 430 (1996).

[**6**] R.A. Arndt, W.J. Briscoe, I.I. Strakovsky, and R.L. Workman, `nucl-th/0205067`; see also Ref. [221].

[**7**] I.G. Aznaurian and K.A. Oganesian, *Sov. J. Nucl. Phys.* **47**, 1097 (1988).

[**8**] H. Babacan, T. Babacan, A. Gokalp, and O. Yilmaz, *Eur. Phys. J.* **A13**, 355 (2002).

[**9**] W.A. Bardeen and Wu-Ki Tung, *Phys. Rev.* **173**, 1423 (1968).

[**10**] M. Batinić, I. Šlaus, A. Švarc, and B.M.K. Nefkens, *Phys. Rev.* **C51**, 2310 (1995), *Erratum ibid*, **C57**, 1004 (1998); see also M. Batinić, I. Dadić, I. Šlaus, A. Švarc, B.M.K. Nefkens, and T.-S.H. Lee, `nucl-th/9703023`. For the discussion of the $\pi N \to \eta N$ database, see Ref. [29].

[**11**] C. Bennhold and H. Tanabe, *Nucl. Phys.* **A530**, 625 (1991).

[**12**] M. Benmerrouche, R.M. Davidson, and N.C. Mukhopadhyay, *Phys. Rev.* **C39**, 2339 (1989); R.M. Davidson, N.C. Mukhopadhyay, and R. Wittman, *Phys. Rev. Lett.* **56**, 804 (1986).

[**13**] M. Benmerrouche and N.C. Mukhopadhyay, *Phys. Rev.* **46**, 101 (1992).

[**14**] M. Benmerrouche, N.C. Mukhopadhyay, and J.F. Zhang, *Phys. Rev.* **51**, 3237 (1995).

[**15**] The original paper dates back to H.A. Bethe and E.E. Salpeter, *Phys. Rev.* **84**, 1232 (1951). A survey article was published e.g. by N. Nakanishi, *Supplement of the Progress of Theoretical Physics* 43, 1 (1969). The BS equation is also derived in Refs. [82, 144].

[16] M. Betz and T.-S.H. Lee, *Phys. Rev.* **C23**, 375 (398)1981.

[17] R. Bijker, F. Iachello, and A. Leviatan, *Ann. Phys. (N.Y.)* **284**, 89 (2000); A. Leviatan and R. Bijker, *πN-Newsletter* **13**, 209 (1997); R. Bijker, F. Iachello, and A. Leviatan, *Phys. Rev.* **55**, 2862 (1997); A. Leviatan and R. Bijker, *πN-Newsletter* **11**, 142 (1995); R. Bijker, F. Iachello, and A. Leviatan, *Ann. Phys. (N.Y.)* **236**, 69 (1994).

[18] J.D. Bjorken and S.D. Drell, *Relativistic Quantum Mechanics*, McGraw-Hill, New York, 1964.

[19] D. Bofinger and W.S. Woolcock, *Nuov. Cim.* **A104**, 1489 (1991).

[20] J.W. Bos, S. Scherer, and J.H. Koch, *Nucl. Phys.* **A547**, 488 (1992).

[21] S.J. Brodsky and G.R. Farrar, *Phys. Rev.* **11**, 1309 (1975).

[22] D.J. Candlin et al., *Nucl. Phys.* **B238**, 477 (1984).

[23] S. Capstick, *Quark Models of Baryon Masses and Decays*, invited talk at COSY Workshop on Baryon Excitations, Julich, Germany, 2-3 May 2000, `nucl-th/0011082`.

[24] S. Capstick and W. Roberts, *Phys. Rev.* **58**, 074011 (1998); S. Capstick and W. Roberts, *Phys. Rev.* **49**, 4570 (1994); *ibid*, **D47**, 1994 (1993); S. Capstick, *Phys. Rev.* **46**, 2864 (1992); S. Capstick and N. Isgur, *Phys. Rev.* **34**, 2809 (1986).

[25] G. Agakichiev et al. (CERES Collaboration), *Phys. Lett.* **B422**, 405 (1998); G. Agakichiev et al. (CERES/NA45 Collaboration), *Nucl. Phys.* **A610**, 317 (1996); A. Drees et al. (CERES Collaboration), *Nucl. Phys.* **A610**, 536 (1996); G. Agakichiev et al. (CERES Collaboration), *Phys. Rev. Lett.* **75**, 1272 (1995); G. Agakichiev et al. (CERES Collaboration), *Nucl. Phys.* **A590**, 103 (1995).

[26] M.K. Cheoun, B.S. Han, B.G. Yu, and I.-T. Cheon, *Phys. Rev.* **C54**, 1811 (1996) and Ref. [72].

[27] G.F. Chew, M.L. Goldberger, F.E. Low, and Y. Nambu, *Phys. Rev.* **106**, 1337 (1957).

[28] G.F. Chew, M.L. Goldberger, F.E. Low, and Y. Nambu, *Phys. Rev.* **106**, 1345 (1957).

[29] M. Clajus and B.M.K. Nefkens, *πN-Newsletter* **7**, 76 (1992).

[30] E.U. Condon and G.H. Shortley, *Theory of Atomic Spectra*, Macmillan Company, New York, 1935; E.P. Wigner, *Group Theory*, Academic Press, New York, 1959; M.R. Rose, *Elementary Theory of Angular Momentum*, Wiley, New York, 1957.

[31] A.P. Contogouris, *Nuov. Cim.* **25**, 104 (1962).

[32] R.E. Cutkosky, C.P. Forsyth, R.E. Hendrick, and R.L. Kelly, *Phys. Rev.* **20**, 2839 (1979).

[33] R.E. Cutkosky and S. Wang, *Phys. Rev.* **42**, 235 (1990).

[34] R.M. Davidson, Nimai C. Mukhopadhyay, and. R.S. Wittman, *Phys. Rev.* **43**, 71 (1991).

[35] R.M. Davidson and R. Workman, *Phys. Rev.* **C63**, 025210 (2001).

[36] R.M. Davidson and R. Workman, *Phys. Rev.* **C63**, 058201 (2001).

[37] S.R. Deans, R.W. Mitchell, D.L. Montgomery, G.C. Wood, and J.E. Rush, *Nucl. Phys.* **B96**, 90 (1975).

[38] P. Dennery, *Phys. Rev.* **124**, 2000 (1961).

[39] J. Denschlag, L. Tiator, and D. Drechsel, *Eur. Phys. J.* **A3**, 171 (1998).

[40] H.-C. Dönges, M. Schäfer, and U. Mosel, *Phys. Rev.* **C51**, 950 (1995).

[41] D. Drechsel, S.S. Kamalov, and L. Tiator, *Phys. Rev.* **63**, 2001 (114010); D. Drechsel, *Prog. Part. Nucl. Phys.* **34**, 181 (1995).

[42] O. Dumbrajs, R. Koch, H. Pilkuhn, G.C. Oades, H. Behrens, J.J. de Swart, and P. Kroll, *Nucl. Phys.* **B216**, 277 (1983).

[43] J.W. Durso, A.D. Jackson, and B.J. Verwest, *Nucl. Phys.* **A345**, 471 (1980); C. Schütz, K. Holinde, J. Speth, B.C. Pearce, and J.W. Durso, *Phys. Rev.* **C51**, 1374 (1995).

[44] S.A. Dytman, T.P. Vrana, and T.-S.H. Lee, *πN-Newsletter* **14**, 17 (1998).

[45] P.J. Ellis and H.-B. Tang, *Phys. Rev.* **C57**, 3356 (1998).

[46] Y. Elmessiri and M.G. Fuda, *Phys. Rev.* **C60**, 044001 (1999); *ibid*, **C57**, 2149 (1998).

[47] T. Ericson and W. Weise, *Pions and Nuclei*, Calderon Press, Oxford, 1988.

[48] H.W. Fearing and S. Scherer, *Phys. Rev.* **C62**, 034003 (2000), *Nucl. Phys.* **A684**, 499 (2001).

[49] T. Feuster, Diploma thesis, Universität Gießen 1993; T. Feuster, H.C. Dönges, M. Schäfer, and U. Mosel, *Em. Form Factors for Pion and Eta Photoproduction*, Proceedings of the *XXXII. International Winter Meeting on Nuclear Physics*, Bormio (Italy), 24.-28.01.1994, p. 457.

[50] T. Feuster and U. Mosel, *Nucl. Phys.* **A612**, 375 (1997).

[51] T. Feuster and U. Mosel, *Phys. Rev.* **C58**, 457 (1998).

[52] T. Feuster, Ph.D. dissertation, Universität Gießen 1998.

[53] T. Feuster and U. Mosel, *Phys. Rev.* **C59**, 460 (1999).

[**54**] B. Friman and M. Soyeur, *Nucl. Phys.* **A600**, 477 (1996).

[**55**] M. Gari and W. Krümpelmann, *Z. Phys.* **A322**, 689 (1985).

[**56**] S. Gasiorowicz, *Elementary Particle Physics*, John Wiley and Sons, New York, 1966.

[**57**] S. Gasiorowicz and D.A. Geffen, *Rev. Mod. Phys.* **41**, 531 (1969).

[**58**] G. v.Gehlen, *Nucl. Phys.* **B9**, 17 (1969).

[**59**] M. Gell-Mann and M. Lvy, *Nuov. Cim.* **16**, 705 (1960).

[**60**] S.B. Gerasimov, *Yad. Fiz.* **2**, 598 (1965) [*Sov. J. Nucl. Phys.* **2**, 430 (1966)]; S.D. Drell and A.C. Hearn, *Phys. Rev. Lett.* **16**, 908 (1966).

[**61**] M.L. Goldberger and K.M. Watson, *Collision Theory*, Wiley, New York, 1964.

[**62**] P.F.A. Goudsmit, H.J. Leisi, and E. Matsinos, *Phys. Lett.* **B299**, 6 (1993).

[**63**] P.F.A. Goudsmit, H.J. Leisi, E. Matsinos, B.L. Birbrair, and A.B. Gridnev, *Nucl. Phys.* **A575**, 673 (1994).

[**64**] M. Gourdin and J. Dufour, *Nuov. Cim.* **27**, 1410 (1963).

[**65**] A.M. Green and S. Wycech, *Phys. Rev.* **C60**, 035208 (1999); *ibid*, **C55**, 2167 (1998).

[**66**] A.B. Gridnev and N.G. Kozlenko, *Eur. Phys. J.* **A4**, 187 (1999).

[**67**] D.E. Groom et al., *Eur. Phys. J.* **C15**, 1 (2000).

[**68**] F. Gross and Y. Surya, *Phys. Rev.* **C47**, 703 (1993); Y. Surya and F. Gross, *Phys. Rev.* **C53**, 2422 (1996).

[**69**] H. Haberzettl, *Phys. Rev.* **C56**, 2041 (1997); H. Haberzettl, C. Bennhold, T. Mart, and T. Feuster, *Phys. Rev.* **C58**, R40 (1998).

[**70**] F. Hachenberg and H.J. Pirner, *Ann. Phys. (N.Y.)* **112**, 401 (1978).

[**71**] F. Halzen and A.D. Martin, *Quarks and Leptons*, John Wiley and Sons, New York, 1984.

[**72**] B.S. Han, M.K. Cheoun, K.S. Kim, and I.-T. Cheon, *Nucl. Phys.* **A691**, 713 (2001).

[**73**] C. Hanhart and A. Kudryavtsev, *Eur. Phys. J.* **A6**, 325 (1999).

[**74**] We thank C. Hanhart for pointing out this second possibility to us.

[**75**] C. Hanhart, A. Sibirtsev, and J. Speth, `nucl-th/0107245`.

[**76**] A.C. Hearn and E. Leader, *Phys. Rev.* **126**, 789 (1962).

[**77**] W. Heitler, *Proc. Roy. Irish Acad.* **51**, 33, (1946).

[**78**] M. Hirata, K. Ochi, and T. Takaki, *Prog. Theor. Phys.* **100**, 681 (1998); M. Hirata, K. Ochi, and T. Takaki, `nucl-th/9711031`; K. Ochi, M. Hirata, and T. Takaki, *Phys. Rev.* **C56**, 1472 (1997).

[**79**] C.-T. Hung, S.N. Yang, and T.-S.H. Lee, *Phys. Rev.* **C64**, 034309 (2001); C.-T. Hung, S.N. Yang, and T.-S.H. Lee, *J. Phys.* **G20**, 1531 (1994).

[**80**] *IMSL Subroutine Library Documentation*, IBM, Houston, 1984.

[**81**] T. Inoue, E. Oset, and M.J.V. Vacas, *Phys. Rev.* **C65**, 035204 (2002).

[**82**] C. Itzykson and J.-B. Zuber, *Quantum Field Theory*, McGraw-Hill, Singapore, 1980.

[**83**] M. Jacob and G.C. Wick, *Ann. Phys. (N.Y.)* **7**, 404 (1959).

[**84**] L. Jäde, *Phys. Rev.* **C58**, 96 (1998).

[**85**] S. Janssen, J. Ryckebusch, D. Debruyne, and T. Van Cauteren, *Phys. Rev.* **C65**, 2002 (015201).

[**86**] S. Janssen, J. Ryckebusch, D. Debruyne, and T. Van Cauteren, `nucl-th/0202074`, submitted to *Phys. Rev.* **C**.

[**87**] D. Jido, E. Oset, and J.E. Palomar, `nucl-th/0202070`.

[**88**] C.J. Joachain, *Quantum Collision Theory*, North-Holland Publ. Comp., Amsterdam, 1975.

[**89**] K. Johnson and E.C.G Sudarshan, *Ann. Phys. (N.Y.)* **13**, 126 (1961); G. Velo and D. Zwanziger, *Phys. Rev.* **186**, 267 (1969); *ibid*, **186**, 1337 (169); *ibid*, **188**, 2218 (1969).

[**90**] F.E. de Jong, Ph.D. dissertation, Rijksuniversiteit Groningen, 1992.

[**91**] K. Kawarabayashi and M. Suzuki, *Phys. Rev. Lett.* **16**, 255 (1966); Riazuddin and Fayyazuddin, *Phys. Rev.* **147**, 1071 (1966); F.J. Gilman and H.J. Schnitzer, *ibid*, **150**, 1362 (1966); J.J. Sakurai, *Phys. Rev. Lett.* **17**, 552 (1966); M. Ademollo, *Nuov. Cim.* **46**, 156 (1966).

[**92**] M.T. Keil, G. Penner, and U. Mosel, *Phys. Rev.* **C63**, 045202 (2001).

[**93**] R.L. Kelly, J.C. Sandusky, and R.E. Cutkosky, *Phys. Rev.* **10**, 2309 (1974).

[**94**] N. Kemmer, *Proc. Cambridge Phil. Soc.*, **34**, 354 (19389.

[**95**] F. Kleefeld, E. van Beveren, and G. Rupp, *Nucl. Phys.* **A694**, 470 (2001); P. Jain, R. Johnson, U.G. Meissner, N.W. Park, and J. Schechter, *Phys. Rev.* **37**, 3252 (1988); T. Fujiwara, T. Kugo, H. Terao, S. Uehara, and K. Yamawaki, *Prog. Theor. Phys.* **73**, 926 (1985); Ö. Kaymakcalan, S. Rajeev, and J. Schechter, *Phys. Rev.* **30**, 594 (1984); V.L. Eletsky, B.L. Ioffe, Y.I. Kogan, *Phys. Lett.* **B122**, 423 (1983).

[**96**] F. Klingl, N. Kaiser, and W. Weise, *Z. Phys.* **A356**, 193 (1996).

[97] F. Klingl, Ph.D. dissertation, University of Munich 1998 (Hieronymus, Munich, 1998).

[98] F. Klingl, T. Waas, and W. Weise, *Nucl. Phys.* **A650**, 299 (1999).

[99] V. Koch, *Introduction to Chiral Symmetry*, Contribution to TAPS Workshop, Bosen, Germany, Sep. 1995, `nucl-th/9512029`.

[100] S. Kondratyuk and O. Scholten, *Phys. Rev.* **C64**, 024005 (2001); S. Kondratyuk and O. Scholten, *Nucl. Phys.* **A677**, 396 (2000); S. Kondratyuk and O. Scholten, *Phys. Rev.* **C62**, 025203 (2000).

[101] A.Y. Korchin, O. Scholten, and R.G.E. Timmermans, *Phys. Lett.* **B438**, 1 (1998).

[102] O. Krehl, C. Hanhart, S. Krewald, and J. Speth, *Phys. Rev.* **C62**, 025207 (2000); C. Schütz, J. Haidenbauer, J. Speth, and J.W. Durso, *Phys. Rev.* **C57**, 1464 (1998).

[103] B. Krusche, N.C. Mukhopadhyay, J.F. Zhang, and M. Benmerrouche, *Phys. Lett.* **B397**, 171 (1997).

[104] A.D. Lahiff and I.R. Afnan, *Phys. Rev.* **C60**, 024608 (1999).

[105] Landolt-Börnstein, *Total Cross-Sections for Reactions of High-Energy Particles*, edited by H. Schopper, New Series, Group I, Vol. 12a, Pt. I, Springer, Berlin, 1988.

[106] W. Langbein and F. Wagner, *Nucl. Phys.* **B53**, 251 (1973).

[107] F.X. Lee and D.B. Leinweber, *Nucl. Phys. Proc. Suppl.* **73**, 258 (1999); F.X. Lee and D.B. Leinweber, *Phys. Rev.* **59**, 074504 (1999).

[108] F.X. Lee, T. Mart, C. Bennhold, H. Haberzettl, and L.E. Wright, *Nucl. Phys.* **A695**, 237 (2001).

[109] M.F.M. Lutz, G. Wolf, and B. Friman, *Nucl. Phys.* **A706**, 431 (2002); in *Proceedings of the International Workshop XXVIII on Gross Properties of Nuclei and Nuclear Excitations*, Hirschegg, Austria, 2000, edited by M. Buballa, B.-J. Schaefer, W. Nörenberg, J. Wambach (Gesellschaft für Schwerionenphysik (GSI), Darmstadt, 2000), `nucl-th/0003012`; M. Lutz, G. Wolf, and B. Friman, *Nucl. Phys.* **A661**, 526 (1999); B. Friman, *Acta Phys. Polon.* **B29**, 3195 (1998); B. Friman, talk given at the *APCTP Workshop on Astro-Hadron Physics*, Seoul, Korea, 25-31 October 1997, `nucl-th/9801053`.

[110] A.I. L'vov, V.A. Petrun'kin, and M. Schumacher, *Phys. Rev.* **C55**, 359 (1997).

[111] D.H. Lyth, *Exclusive Electroproduction Processes*, in A. Donnachie and G. Shaw, *Electromagnetic Interactions of Hadrons*, Plenum-Press, New York and London, 1978.

[112] R. Machleidt, K. Holinde, and C. Elster, *Phys. Rept.* **149**, 1 (1987).

[113] D.M. Manley and E.M. Saleski, *Phys. Rev.* **45**, 4002 (1992).

[114] T. Mart and C. Bennhold, *Phys. Rev.* **C61**, 012201(R) (1999).

[115] T. Mart, *Phys. Rev.* **C62**, 038201 (2000).

[116] S. Wolfram, *Mathematica*, Addison-Wesley Pub., Reading/MA, 1991.

[117] R.G. Moorhouse, H. Oberlack, and A.H. Rosenfeld, *Phys. Rev.* **9**, 1 (1974).

[118] U. Mosel, *Fields, Symmetries, and Quarks*, Springer-Verlag, Berlin and Heidelberg, 1999.

[119] A. Müller-Groeling, K. Holinde, and J. Speth, *Nucl. Phys.* **A513**, 557 (1990).

[120] L.Y. Murphy and J.-M. Laget, DAPNIA-SPhN 96-10 (1996); L.Y. Murphy and J.-M. Laget, DAPNIA-SPhN 95-42 (1995).

[121] J.C. Nacher and E. Oset, *Nucl. Phys.* **A697**, 372 (2002); J.C. Nacher, E. Oset, M.J. Vicente, and L. Roca, *Nucl. Phys.* **A695**, 295 (2001);J.A. Gómez Tejedor, F. Cano, and E. Oset, *Phys. Lett.* **B379**, 39 (1996); J.A. Gómez Tejedor, and E. Oset, *Nucl. Phys.* **A600**, 413 (1996); J.A. Gómez Tejedor and E. Oset, *Nucl. Phys.* **A571**, 667 (1994).

[122] S.I. Nagorny and A.E.L. Dieperink, *Eur. Phys. J.* **A5**, 417 (1999); S.I. Nagorny, Y.A. Kasatkin, I.K. Kirichenko, and E.V. Inopin, *Sov. J. Nucl. Phys.* **53**, 228 (1991); *ibid*, **49**, 465 (1989).

[123] H.W.L. Naus and J.H. Koch, *Phys. Rev.* **C36**, 2459 (1987).

[124] H.W.L. Naus and J.H. Koch, *Phys. Rev.* **C39**, 1907 (1989).

[125] L.M. Nath, B. Etemadi, and J.D. Kimel, *Phys. Rev.* **3**, 2153 (1971).

[126] L.M. Nath and B.K. Bhattacharyya, *Z. Phys.* **C5**, 9 (1980).

[127] P. van Nieuwenhuizen, *Phys. Rev.* **68**, 189 (1981).

[128] J. Nieves and E.R. Arriola, *Phys. Rev.* **64**, 116008 (2001).

[129] S. Nozawa, B. Blankleider, and T.-S.H. Lee, *Nucl. Phys.* **A513**, 1990 (459).

[130] *Numerical Recipes in Fortran 77: The Art of Scientific Computing*, Cambridge University Press, New York, 1997.

[131] Y. Oh and T.-S.H. Lee, `nucl-th/0204035`; Y. Oh and T.-S.H. Lee, talk given at the *International Symposium on Electromagnetic Interactions in Nuclear and Hadron Physics (EMI 2001)*, Osaka, Ibaraki, Japan, 4-7 Dec 2001, `nucl-th/0201016`; Y. Oh, A.I. Titov, and T.-S.H. Lee, in *Proceedings of the Workshop on The Physics of Excited Nucleons, NStar 2001*, edited by D. Drechsel and L. Tiator (World Scientific, Singapore, 2001), `nucl-th/0104046`; Y. Oh, A.I. Titov, and T.-S.H. Lee, Ref. [132]; Y. Oh, A.I. Titov, and T.-S.H. Lee, talk given at *14th International Spin Physics Symposium (SPIN 2000)*, Osaka, Japan, 16-21 Oct 2000, published in Osaka 2000, Spin physics, `nucl-th/0012012`; Y. Oh, A.I. Titov, and T.-S.H. Lee, talk given at

NStar 2000: The Physics of Excited Nucleons, Newport News, Virginia, 16-19 Feb 2000, `nucl-th/0004055`.

[132] Y. Oh, A.I. Titov, and T.-S.H. Lee, *Phys. Rev.* **C63**, 025201 (2001).

[133] K. Ohta, *Phys. Rev.* **C40**, 1335 (1989); *ibid*, **C41**, 1213 (1990).

[134] M.G. Olsson and E.T. Osypowski, *Nucl. Phys.* **B101**, 136 (1975).

[135] V. Pascalutsa, *Phys. Rev.* **58**, 096002 (1998).

[136] V. Pascalutsa and R. Timmermans, *Phys. Rev.* **C60**, 042201(R) (1999).

[137] V. Pascalutsa and J.A. Tjon, *Phys. Rev.* **C61**, 054003 (2000).

[138] V. Pascalutsa, *Phys. Lett.* **B503**, 85 (2001).

[139] B.C. Pearce and B.K. Jennings, *Nucl. Phys.* **A528**, 655 (1991).

[140] R.D. Peccei, *Phys. Rev.* **176**, 1812 (1968).

[141] R.D. Peccei, *Phys. Rev.* **181**, 778 (1969).

[142] G. Penner, Diploma thesis, Universität Gießen 1997.

[143] W. Pfeil, H. Rollnik, and S. Stankowski, *Nucl. Phys.* **B73**, 166 (1974).

[144] H.M. Pilkuhn, *Relativistic Particle Physics*, Springer-Verlag, New York, 1979.

[145] M. Post and U. Mosel, *Nucl. Phys.* **A688**, 808 (2001).

[146] M. Post, S. Leupold, and U. Mosel, *Nucl. Phys.* **A689**, 753 (2001).

[147] R.E. Prange, *Phys. Rev.* **110**, 240 (1958).

[148] J.C. Ramon, N. Kaiser, S. Wetzel, and W. Weise, *Nucl. Phys.* **A672**, 249 (2000); N. Kaiser, *Prog. Part. Nucl. Phys.* **44**, 391 (2000); N. Kaiser, T. Waas, and W. Weise, *Nucl. Phys.* **A612**, 297 (1997).

[149] W. Rarita and J. Schwinger, *Phys. Rev.* **60**, 61 (1941).

[150] A.C. Hearn, *Reduce User's Manual*, RAND Publication, Santa Monica/CA, 1995.

[151] D.O. Riska and G.E. Brown, *Nucl. Phys.* **A679**, 577 (2001).

[152] J.J. Sakurai, *Modern Quantum Mechanics*, Addison-Wesley, New York, 1994.

[153] J.J. Sakurai, *Advanced Quantum Mechanics*, Addison-Wesley, New York, 1967.

[154] S. Sasaki, T. Blum, and S. Ohta, *Phys. Rev.* **65**, 074503 (2002).

[155] T. Sato and T.-S.H. Lee, *Phys. Rev.* **C54**, 2660 (1996).

[156] C. Sauermann, Ph.D. dissertation, Technische Hochschule Darmstadt 1996.

[157] C. Sauermann, B.L. Friman, and W. Nörenberg, *Phys. Lett.* **B341**, 261 (1995); C. Deutsch-Sauermann, B. Friman, and W. Nörenberg, *ibid*, **B409**, 51 (1997).

[158] M. Schäfer, Ph.D. dissertation, Universität Gießen 1994.

[159] K. Schilling, P. Seyboth, and G. Wolf, *Nucl. Phys.* **B15**, 397 (1970), *Erratum ibid*, **B18**, 332 (1970); see also R.L. Thews, *Phys. Rev.* **175**, 1749 (1968).

[160] O. Scholten, A.Y. Korchin, V. Pascalutsa, and D. Van Neck, *Phys. Lett.* **B384**, 13 (1996).

[161] J. Schwinger, *Ann. Phys. (N.Y.)* **2**, 407 (1957).

[162] V. Shklyar, G. Penner, and U. Mosel, in preparation.

[163] A. Sibirtsev and A. Cassing, *Eur. Phys. J.* **A7**, 407 (2000).

[164] P. Singer and G.A. Miller, *Phys. Rev.* **33**, 141 (1986).

[165] M. Sotona and J. Žofka, *Prog. Theor. Phys.* **81**, 160 (1989).

[166] S. Sumowidagdo and T. Mart, *Phys. Rev.* **C60**, 028201 (1999).

[167] Y.S. Surovtsev, D. Krupa, and M. Nagy, *Phys. Rev.* **63**, 054024 (2001).

[168] R.A. Arndt, R.L. Workman, Z. Li, and L.D. Roper, *Phys. Rev.* **C42**, 1853 (1990).

[169] J.J. de Swart, *Rev. Mod. Phys.* **35**, 916 (1963), *Erratum ibid*, **37**, 326 (1965).

[170] H.-B. Tang and P.J. Ellis, *Phys. Lett.* **B387**, 9 (1996).

[171] L. Theußl and R.F. Wagenbrunn, *Phys. Rev.* **C64**, 068201 (2001); L. Theußl, R.F. Wagenbrunn, B. Desplanques, and W. Plessas, *Eur. Phys. J.* **A12**, 91 (2001), *Nucl. Phys.* **A689**, 394 (2001).

[172] H. Thom, *Phys. Rev.* **151**, 1322 (1966).

[173] L. Tiator, C. Bennhold, and S.S. Kamalov, *Nucl. Phys.* **A580**, 455 (1994).

[174] D. Drechsel, O. Hanstein, S.S. Kamalov, and L. Tiator, *Nucl. Phys.* **A645**, 145 (1999); S.S. Kamalov, D. Drechsel, O. Hanstein, L. Tiator, and S.N. Yang, *Nucl. Phys.* **A684**, 321 (2001).

[175] L. Tiator, D. Drechsel, G. Knöchlein, and C. Bennhold, *Phys. Rev.* **C60**, 035210 (1999).

[176] L. Tiator, D. Drechsel, O. Hanstein, S.S. Kamalov, and S.N. Yang, *Nucl. Phys.* **A689**, 205 (2001).

[177] L. Tiator, *Helicity amplitudes and sum rules for real and virtual photons*, talk given at *Symposium on the Gerasimov-Drell-Hearn Sum Rule and the Nucleon Spin Structure in the Resonance Region (GDH 2000)*, Mainz, Germany, 14-17 Jun 2000, `nucl-th/0012045`.

[178] A.I. Titov, Y. Oh, S.N. Yang, and T. Morii, *Phys. Rev.* **C58**, 2429 (1998).

[179] A.I. Titov, B. Kämpfer, and B.L. Reznik, `nucl-th/0102032`.

[180] A.I. Titov and T.-S.H. Lee, `nucl-th/0205052`.

[181] Y. Tomazawa, *Nuov. Cim.* **46A**, 707 (1966).

[182] N.A. Törnqvist and A.D. Polosa, *Nucl. Phys.* **A692**, 259 (2001); N.A. Törnqvist, *Eur. Phys. J.* **C11**, 359 (1999), *Erratum ibid*, **C13**, 711 (2000); see also N.A. Törnqvist, Invited talk at the Conference *Possible Existence of the Light Sigma Resonance and its Implications to Hadron Physics*, Yukawa Institute forTheoretical Physics, Kyoto, Japan, June 11-14 2000, `hep-ph/0008135`.

[183] T.P. Vrana, S.A. Dytman, and T.-S.H. Lee, *Phys. Rept.* **328**, 181 (2000).

[184] R.L. Walker, *Phys. Rev.* **182**, 1729 (1969).

[185] C. Ward, *Phys. Rev.* **78**, 182 (1950), Y. Takahashi, *Nuov. Cim.* **6**, 371 (1957).

[186] M. Warns, H. Schröder, W. Pfeil, and H. Rollnik, *Z. Phys.* **C45**, 627 (1990).

[187] K.M. Watson, *Phys. Rev.* **85**, 852 (1952); K.A. Brückner and K.M. Watson, *Phys. Rev.* **83**, 1 (1951); see also [188].

[188] K.M. Watson, *Phys. Rev.* **95**, 228 (1954).

[189] S. Weinberg, *Phys. Rev. Lett.* **17**, 616 (1966).

[190] S. Weinberg, *Phys. Rev. Lett.* **18**, 188 (1967).

[191] S. Weinberg, *Phys. Rev.* **166**, 1568 (1968).

[192] H.T. Williams, *Phys. Rev.* **C29**, 2222 (1984); *ibid*, **C31**, 2297 (1985); R.A. Adelseck, C. Bennhold, and L.E. Wright, *ibid*, **C32**, 1681 (1985).

[193] K.G. Wilson, *Phys. Rev.* **10**, 2445 (1974).

[194] R.L. Workman, H.W.L. Naus, and S.J. Pollock, *Phys. Rev.* **C45**, 2511 (1992).

[195] R.J. Yaes, *Phys. Rev.* **3**, 3086 (1971).

[196] J.M. Zanotti, S. Bilson-Thompson, F.D.R. Bonnet, P.D. Coddington, D.B. Leinweber, A.G. Williams, J.B. Zhang, W. Melnitchouk, and F.X. Lee (CSSM Lattice Collaboration), *Phys. Rev.* **65**, 074507 (2002).

[197] Q. Zhao, Z. Li, and C. Bennhold, *Phys. Rev.* **C58**, 2393 (1998).

[198] Q. Zhao, talk given at *International Symposium on Electromagnetic Interactions in Nuclear and Hadron Physics (EMI 2001)*, Osaka, Ibaraki, Japan, 4-7 Dec 2001, `nucl-th/0202023`; Q. Zhao, in *Proceedings of the Workshop on The Physics of Excited Nucleons, NStar 2001*, edited by D. Drechsel and L. Tiator (World Scientific, Singapore, 2001), `nucl-th/0106030`; Q. Zhao, Ref. [199]; Q. Zhao, *Nucl. Phys.*

A675, 217 (2000); Q. Zhao, Z. Li, and C. Bennhold, *πN-Newsletter* **14**, 185 (1998); Ref. [197]; `nucl-th/9803021`; *Phys. Lett.* **B436**, 42 (1998); `nucl-th/9711061`.

[**199**] Q. Zhao, *Phys. Rev.* **C63**, 025203 (2001).

[**200**] Q. Zhao, J.S. Al-Khalili, and C. Bennhold, *Phys. Rev.* **C65**, 2002 (032201).

References on experimental data:

$\gamma\mathbf{N} \rightarrow \mathbf{X}$:

[**201**] T.A. Armstrong et al., *Phys. Rev.* **5**, 1640 (1972).

[**202**] M. MacCormick et al., *Phys. Rev.* **C53**, 41 (1996).

$\gamma\mathbf{N} \rightarrow \gamma\mathbf{N}$:

[**203**] F. Adamian et al., *J. Phys.* **G19**, L139 (1993).

[**204**] P.S. Baranov, V.A. Kuznetsova, L.I. Slovokhotov, G.A. Sokol, and L.N. Shtarkov *Yad. Fiz.* **3**, 1083 (1966) [*Sov. J. Nucl. Phys.* **3**, 791 (196)].

[**205**] P.S. Baranov, G.M. Buinov, V.G. Godin, V.A. Kuznetsova, V.A. Petrunkin, L.S. Tatarinskaya, V.S. Shirchenko, L.N. Shtarkov, V.V Yurchenko, and Y.P. Yanulis, *Yad. Fiz.* **21**, 689 (1975) [*Sov. J. Nucl. Phys.* **21**, 355 (1975)].

[**206**] G. Barbiellini, G. Capon, G. De Zorzi, and G.P. Murtas, *Phys. Rev.* **174**, 1665 (1968).

[**207**] G. Blanpied et al. (LEGS Collaboration), *Phys. Rev.* **C64**, 025203 (2001); G. Blanpied et al., *Phys. Rev. Lett.* **76**, 1023 (1996).

[**208**] G. Galler et al. (LARA Collaboration), *Phys. Lett.* **B503**, 245 (2001); S. Wolf et al., *Eur. Phys. J.* **A12**, 231 (2001).

[**209**] B. E. MacGibbon, G. Garino, M. A. Lucas, A. M. Nathan, G. Feldman, and B. Dolbilkin, *Phys. Rev.* **C52**, 2097 (1995).

[**210**] E.L. Hallin et al., *Phys. Rev.* **C48**, 1497 (1993).

[**211**] A. Hünger et al., *Nucl. Phys.* **A620**, 385 (1997); J. Peise et al., *Phys. Lett.* **B384**, 37 (1996); C. Molinari et al., *Phys. Lett.* **B371**, 181 (1996).

[**212**] T. Ishii et al., *Nucl. Phys.* **B165**, 189 (1980).

[**213**] T. Ishii et al., *Nucl. Phys.* **B254**, 458 (1985).

[**214**] M. Jung, J. Kattein, H. Kuck, P. Leu, K.D. de Marne, R. Wedemeyer, and N. Wermes, *Z. Phys.* **C10**, 197 (1981).

[**215**] S. Kabe, T. Fujii, T. Kamei, R. Yamada, T. Yamagata, S. Kato, I. Kita, and T. Kiyoshima, *Nucl. Phys.* **B50**, 17 (1972).

[216] K. Toshioka et al., *Nucl. Phys.* **B141**, 364 (1978).

[217] Y. Wada et al., *Nuov. Cim.* **A63**, 57 (1981).

[218] Y. Wada, K. Egawa, A. Imanishi, T. Ishii, S. Kato, K. Ukai, F. Naito, H. Nara, T. Noguchi, and K. Takahashi, *Nucl. Phys.* **B247**, 313 (1984).

[219] F. Wissmann et al., *Nucl. Phys.* **A660**, 232 (1999).

[220] A. Zieger, R. Van de Vyver, D. Christmann, A. De Graeve, C. Van den Abeele, and B. Ziegler, *Phys. Lett.* **B278**, 34 (1992).

$\gamma\mathbf{N} \to \pi\mathbf{N}$:

[221] R.A. Arndt, R.L. Workman, Z. Li, and L.D. Roper, *Phys. Rev.* **C42**, 1853 (1990); Z. Li, R.A. Arndt, L.D. Roper, and R.L. Workman, *Phys. Rev.* **C47**, 2759 (1993); R.A. Arndt, I.I. Strakovsky, and R.L. Workman, *Phys. Rev.* **C53**, 430 (1996); updates available on the web: http://gwdac.phys.gwu.edu/.

$\gamma\mathbf{N} \to \eta\mathbf{N}$:

[222] L.O. Abramian et al., *J. Exp. Theo. Phys. Lett.* **25**, 560 (1977) (*Pisma Zh. Eksp. Teor. Fiz.* **25** 5970 (1977)).

[223] J. Ajaka et al. (GRAAL Collaboration), *Phys. Rev. Lett.* **81**, 1797 (1998).

[224] C. Bacci, R. Baldini-Celio, C. Mencuccini, A. Reale, M. Spinetti, and A. Zallo, *Phys. Rev. Lett.* **20**, 571 (1968); C. Bacci, G. Penso, G. Salvini, C. Mencuccini, and V. Silverstrini, *Nuov. Cim.* **45A**, 983 (1966).

[225] E.D. Bloom, C.A. Heusch, C.Y. Prescott, and L.S. Rochester, *Phys. Rev. Lett.* **21**, 1100 (1968).

[226] A. Bock et al., *Phys. Rev. Lett.* **81**, 534 (1998).

[227] P.S.L. Booth, L.J. Carroll, J.R. Holt, J.N. Jackson, W.H. Range, K. Sprakes, and J.R. Wormald, *Nucl. Phys.* **B71**, 211 (1974); P.S.L. Booth, J.S. Barton, L.J. Carroll, J.R. Holt, J.N. Jackson, W.H. Range, K.A. Sprakes, and J.R. Wormald, *Nucl. Phys.* **B25**, 510 (1971).

[228] A. Christ et al., *Lett. Nuov. Cim.* **8**, 1039 (1973).

[229] B. Delcourt, J. Lefrançois, J.P. Perez-Y-Jorba, G. Sauvage, and G. Mennessier, *Phys. Lett.* **B29**, 75 (1969).

[230] M. Dugger, Ph.D. dissertation, Arizona State University, 2001; M. Dugger et al. (CLAS Collaboration), submitted to *Phys. Rev. Lett.*; V.D. Burkert, `hep-ph/0207149`.

[231] S.A. Dytman et al., *Phys. Rev.* **C51**, 2710 (1995).

[**232**] C.A. Heusch, C.Y. Prescott, E.D. Bloom, and L.S. Rochester, *Phys. Rev. Lett.* **17**, 573 (1966).

[**233**] C.A. Heusch, C.Y. Prescott, L.S. Rochester, and B.D. Winstein, *Phys. Rev. Lett.* **25**, 1381 (1970).

[**234**] P. Hoffmann-Rothe et al., *Phys. Rev. Lett.* **78**, 4697 (1997).

[**235**] S. Homma, M. Kanazawa, K. Maruyama, Y. Murata, H. Okuno, A. Sasaki, and T. Taniguchi, *J. Phys. Soc. Jap.* **57** 828 (1988).

[**236**] M. Hongoh et al., *Lett. Nuov. Cim.* **2**, 317 (1971).

[**237**] B. Krusche et al., *Phys. Rev. Lett.* **74**, 3736 (1995); *ibid*, **75**, 3023 (1995); *Phys. Lett.* **B358**, 40 (1995).

[**238**] R. Prepost, D. Lundquist, and D. Quinn, *Phys. Rev. Lett.* **18**, 82 (1967).

[**239**] J.W. Price et al., *Phys. Rev.* **C51**, R2283 (1995).

[**240**] F. Renard et al. (GRAAL Collaboration), *Phys. Lett.* **B528**, 215 (2002).

[**241**] G.A. Vartapetian, and S.E. Piliposian, *Yad. Fiz.* **32**, 1553 (1980) [*Sov. J. Nucl. Phys.* **32**, 804 (1980)].

$\gamma\mathbf{N} \rightarrow \mathbf{K}\boldsymbol{\Lambda}$:

[**242**] R.L. Anderson, E. Gabathuler, D. Jones, B.D. McDaniel, and A.J. Sadoff, *Phys. Rev. Lett.* **9**, 131 (1962).

[**243**] A. Bleckmann, S. Herda, U. Opara, W. Schulz, W.J. Schwille, and H. Urbahn, *Z. Phys.* **239**, 1 (1970).

[**244**] M. Bockhorst et al., *Z. Phys.* **C63**, 37 (1994).

[**245**] H.M. Brody, A.M. Wetherell, and R.L. Walker, *Phys. Rev.* **119**, 1710 (1960).

[**246**] D. Dcamp, B. Dudelzak, P. Eschtruth, Th. Fourneron, Preprint LAL 1236, Orsay, 1970.

[**247**] P.L. Donoho and R.L. Walker, *Phys. Rev.* **112**, 981 (1958).

[**248**] R. Erbe et al. (ABBHHM Collaboration), *Phys. Rev.* **188**, 2060 (1969).

[**249**] P. Feller, D. Menze, U. Opara, W. Schulz, and W.J. Schwille, *Nucl. Phys.* **B39**, 413 (1972).

[**250**] T. Fujii et al., *Phys. Rev.* **2**, 439 (1970).

[**251**] H. Göing, W. Schorsch, J. Tietge, and W. Weilnböck, *Nucl. Phys.* **B26**, 121 (1971).

[**252**] M. Grilli, L. Mezzetti, M. Nigro, and E. Schiavuta, *Nuov. Cim.* **38**, 1467 (1965); B. Borgia, M. Grilli, P. Joos, L. Mezzetti, M. Nigro, E. Schiavuta, and F. Villa, *Nuov. Cim.* **32**, 218 (1964).

[**253**] D.E. Groom and J.H. Marshall, *Phys. Rev.* **159**, 1213 (1967).

[**254**] R. Haas, T. Miczaika, U. Opara, K. Quabach, W.J. Schwille, *Nucl. Phys.* **B137**, 261 (1978).

[**255**] C.W. Peck, *Phys. Rev.* **135**, B830 (1964).

[**256**] H. Thom, E. Gabathuler, D. Jones, B.D. McDaniel, and W.M. Woodward, *Phys. Rev. Lett.* **11**, 433 (1963).

[**257**] M.Q. Tran et al. (SAPHIR Collaboration), *Phys. Lett.* **B445**, 20 (1998).

$\gamma\mathbf{N} \rightarrow \mathbf{K\Sigma}$:

[**258**] R.L. Anderson, F. Turkot, and W.M. Woodward, *Phys. Rev.* **123**, 1003 (1961); R.L. Anderson, E. Gabathuler, D. Jones, B.D. McDaniel, and A.J. Sadoff, Ref. [242].

[**259**] M. Bockhorst et al., Ref. [244].

[**260**] H.M. Brody, A.M. Wetherell, and R.L. Walker, Ref. [245].

[**261**] R. Erbe et al. (ABBHHM Collaboration), Ref. [248].

[**262**] T. Fujii et al., Ref. [250].

[**263**] P. Feller, D. Menze, U. Opara, W. Schulz, and W.J. Schwille, Ref. [249].

[**264**] S. Goers et al. (SAPHIR Collaboration), *Phys. Lett.* **B464**, 331 (1999).

[**265**] H. Göing, W. Schorsch, J. Tietge, and W. Weilnböck, Ref. [251].

[**266**] B.D. McDaniel, A. Silverman, R.R. Wilson, and G. Cortellessa, *Phys. Rev.* **115**, 1039 (1959).

[**267**] M.Q. Tran et al. (SAPHIR Collaboration), Ref. [257].

$\gamma\mathbf{N} \rightarrow \omega\mathbf{N}$:

[**268**] J. Ajaka et al. (GRAAL Collaboration), Proceedings of the *14th International Spin Physics Symposium (SPIN 2000)*, AIP Conference Proceedings, edited by K. Hatanaka et al., Vol. 570, Issue 1, p. 198, Melville NY, 2001.

[**269**] J. Barth, Ph.D. dissertation, *Photoproduction of the Vector Mesons* $\omega(782)$ *and* $\phi(1020)$ *on the Proton from Threshold up to a Photon Energy of 2.6 GeV* (in German), SAPHIR Collaboration, BONN-IR-2002-06, May 2002, to be published.

[**270**] H.R. Crouch et al., *Phys. Rev.* **155**, 1476 (1967).

[**271**] R. Erbe et al. (ABBHHM Collaboration), *Phys. Rev.* **175**, 1669 (1968).

[**272**] J. Hannappel, Ph.D. dissertation, Universität Bonn 1996, BONN-IR-97-15.

[**273**] F.J. Klein et al. (SAPHIR Collaboration), *πN-Newsletter* **14**, 141 (1998).

[**274**] F.J. Klein, Ph.D. dissertation, Universität Bonn 1996, BONN-IR-96-08.

[**275**] J.J. Manak et al. (CLAS Collaboration), *Nucl. Phys.* **A663**, 671 (2000).

[**276**] J. Wißkirchen, Ph.D. dissertation, Universität Bonn 1999, BONN-IR-99-21.

$\pi \mathbf{N} \rightarrow \pi \mathbf{N}$:

[**277**] M.M. Pavan, R.A. Arndt, I.I. Strakovsky, and R.L. Workman, *Phys. Scr.* **T87**, 62 (2000), *πN-Newsletter* **15**, 171 (1999), `nucl-th/9807087`; R.A. Arndt, I.I. Strakovsky, R.L. Workman, and M.M. Pavan, Ref. [4]; updates available via: http://gwdac.phys.gwu.edu/.

$\pi \mathbf{N} \rightarrow \mathbf{2}\pi \mathbf{N}$:

[**278**] D.M. Manley, R.A. Arndt, Y. Goradia, and V.L. Teplitz, *Phys. Rev.* **30**, 904 (1984).

$\pi \mathbf{N} \rightarrow \eta \mathbf{N}$:

[**279**] R.D. Baker et al., *Nucl. Phys.* **B156**, 93 (1979).

[**280**] R.M. Brown et al., *Nucl. Phys.* **B153**, 89 (1979).

[**281**] F. Bulos et al., *Phys. Rev.* **187**, 1827 (1969).

[**282**] J.S. Danburg, M.A. Abolins, O.I. Dahl, D.W. Davies, P.L. Hoch, J. Kirz, D.H. Miller, and R.K. Rader, *Phys. Rev.* **2**, 2564 (1970).

[**283**] N.C. Debenham et al., *Phys. Rev.* **12**, 2545 (1975).

[**284**] W. Deinet, H. Müller, D. Schmitt, H.M. Staudenmaier, S. Buniatov, and E. Zavattini, *Nucl. Phys.* **B11**, 495 (1969).

[**285**] J. Feltesse, R. Ayed, P. Bareyre, P. Borgeaud, M. David, J. Ernwein, Y. Lemoigne, and G. Villet, *Nucl. Phys.* **B93**, 242 (1975).

[**286**] T.W. Morrison, Ph.D. dissertation, The George Washington University, 2000.

[**287**] W.B. Richards et al., *Phys. Rev.* **1**, 10 (1970).

$\pi \mathbf{N} \rightarrow \mathbf{K}\mathbf{\Lambda}$:

[**288**] R.D. Baker et al., *Nucl. Phys.* **B141**, 29 (1978).

[**289**] K.W. Bell et al., *Nucl. Phys.* **B222**, 389 (1983).

[**290**] L. Bertanza, P.L. Connolly, B.B. Culwick, F.R. Eisler, T. Morris, R. Palmer, A. Prodell, and N.P. Samios, *Phys. Rev. Lett.* **8**, 332 (1962).

[**291**] T.O. Binford, M.L. Good, V.G. Lind, D. Stern, R. Krauss, and E. Dettman, *Phys. Rev.* **183**, 1134 (1969).

[**292**] O.I. Dahl, L.M. Hardy, R.I. Hess, J. Kirz, D.H. Miller, and J.A. Schwartz, *Phys. Rev.* **163**, 1430 (1967), *Erratum: ibid,* **183**, 1520 (1969).

[**293**] O. Goussu, M. Sen, B. Ghidini, S. Mongelli, A. Romano, P. Waloschek, and V. Alles-Borelli, *Nuov. Cim.* **A42**, 607 (1966).

[**294**] T.M. Knasel et al., *Phys. Rev.* **11**, 1 (1975).

[**295**] D.H. Saxon et al., *Nucl. Phys.* **B162**, 522 (1980).

[**296**] L.L. Yoder, C.T. Coffin, D.I. Meyer, and K.M. Terwilliger, *Phys. Rev.* **132**, 1778 (1963).

$\pi\mathbf{N} \rightarrow \mathbf{K\Sigma}$:

[**297**] R.D. Baker, J.A. Blissett, I.J. Bloodworth, T.A. Broome, J.C. Hart, V.K. Magon, R. Maybury, A.G. Parham, B.T. Payne, D.H. Saxon, and T.G. Walker, *Nucl. Phys.* **B145**, 402 (1978).

[**298**] C. Baltay, H. Courant, W.J. Fickinger, E.C. Fowler, H.L. Kraybill, J. Sandweiss, J.R. Sanford, D.L. Stonehill, and H.D. Taft, *Rev. Mod. Phys.* **33**, 374 (1961).

[**299**] E.H. Bellamy et al., *Phys. Lett.* **39B**, 299 (1972).

[**300**] T.O. Binford, M.L. Good, V.G. Lind, D. Stern, R. Krauss, and E. Dettman, Ref. [291].

[**301**] D.J. Candlin et al., *Nucl. Phys.* **B226**, 1 (1983).

[**302**] F.S. Crawford, Jr., F. Grard, and G.A. Smith, *Phys. Rev.* **128**, 368 (1962); F.S. Crawford, Jr., R.L. Douglass, M.L. Good, G.R. Kalbfleisch, M.L. Stevenson, and H.K. Ticho, *Phys. Rev. Lett.* **3**, 394 (1959).

[**303**] O.I. Dahl, L.M. Hardy, R.I. Hess, J. Kirz, D.H. Miller, and J.A. Schwartz, Ref. [292].

[**304**] J.C. Doyle, F.S. Crawford, and J.A. Anderson, *Phys. Rev.* **165**, 1483 (1968).

[**305**] M.L. Good and R.R. Kofleret al., *Phys. Rev.* **183**, 1142 (1969).

[**306**] O. Goussu, M. Sen, B. Ghidini, S. Mongelli, A. Romano, P. Waloschek, and V. Alles-Borelli, Ref. [293].

[**307**] J. Haba, T. Homma, H. Kawai, M. Kobayashi, K. Miyake, T.S. Nakamura, N. Sasao, and Y. Sugimoto, *Nucl. Phys.* **B299**, 627 (1988), *Erratum: ibid,* **B308**, 948 (1988).

[**308**] J.C. Hart et al., *Nucl. Phys.* **B166**, 73 (1980).

[**309**] M. Winnik, S. Toaff, D. Revel, J. Goldberg, and L. Berny, *Nucl. Phys.* **B128**, 66 (1977).

[**310**] L.L. Yoder, C.T. Coffin, D.I. Meyer, and K.M. Terwilliger, [296].

$\pi\mathbf{N} \rightarrow \omega\mathbf{N}$:

[**311**] D.M. Binnie et al., *Phys. Rev.* **8**, 2789 (1973).

[**312**] J.S. Danburg, M.A. Abolins, O.I. Dahl, D.W. Davies, P.L. Hoch, J. Kirz, D.H. Miller, and R.K. Rader, Ref. [282].

[**313**] H. Karami, J. Carr, N.C. Debenham, D.A. Garbutt, W.G. Jones, D.M. Binnie, J. Keyne, P. Moissidis, H.N. Sarma, and I. Siotis, *Nucl. Phys.* **B154**, 503 (1979).

[**314**] J. Keyne, D.M. Binnie, J. Carr, N.C. Debenham, A. Duane, D.A. Garbutt, W.G. Jones, I. Siotis, and J.G. McEwen, *Phys. Rev.* **14**, 28 (1976).

Deutsche Zusammenfassung

Eines der großen Ziele der modernen theoretischen Physik ist es, sämtliche in der Natur beobachteten Phänomene mithilfe quantenfeldtheoretischer Methoden zu beschreiben. Ein Meilenstein in Richtung dieses Ziels war die Vereinheitlichung der elektromagnetischen und der schwachen Kraft in der elektroschwachen Theorie in den 1960ern und 70ern durch Salam und Weinberg. In diesen Rahmen fügte sich auch bald darauf die Quantenchromodynamik (QCD), die allgemein akzeptierte Theorie zur Beschreibung der starken Kraft und somit auch des Aufbaus der Nukleonen. Lediglich die Gravitation hat sich bislang einer vereinheitlichten quantenfeldtheoretischen Beschreibung entzogen.

Der Erfolg der feldtheoretischen Beschreibungen der subatomaren Welt ist auf die beeindruckende Vorhersagekraft der elektroschwachen Theorie zurückzuführen, und im Besonderen der Quantenelektrodynamik (QED). Die Kleinheit der elektromagnetischen Feinstrukturkonstante α_{em} erlaubt eine Entwicklung der Theorie nach Ordnungen in α_{em} (Störungstheorie). Durch die Anwendung dieser mächtigen Methode hat die elektromagnetische Feldtheorie sämtliche experimentellen Tests mit Bravour bestanden.

Bei ausreichend hohen Energien ist auch die Kopplungskonstante der QCD α_S so klein, dass die QCD störungstheoretischen Methoden zugänglich ist. Bei diesen Energien verhalten sich die Quarks wie unter einer freien Theorie, was zur Anwendbarkeit der Konstituentenquarkmodelle führt. Für niedrige Energien jedoch wird α_S so groß, dass die Quarks in den bekannten Hadronen gebunden werden, was aber auch bedeutet, dass störungstheoretische Methoden zusammenbrechen. Wilson gelang es 1974 zu zeigen, wie die QCD auf einem vierdimensionalen euklidischen Gitter so diskretisiert werden kann, dass sie gleichzeitig numerisch handhabbar für große Kopplungen α_S bleibt. Dies war die Geburtsstunde der Gitter-QCD. Solange keine analytischen Lösungen der QCD vorliegen, stellt die Gitter-QCD die vielversprechendste Methode dar, Eigenschaften hadronischer Grund- und auch angeregter Zustände (Resonanzen) theoretisch vorherzusagen. Allerdings sind dafür enorme numerische Anstrengungen notwendig, so dass gerade erst damit begonnen wird, die Massen und Zerfallsbreiten von Resonanzen zu beschreiben. Diese Probleme führten zur Entwicklung einer Vielzahl von Quarkmodellen, die versuchen, die Komplexität des stark selbstwechselwirkenden Multi-Quark-Gluon-Systems auf ein effektives Zwei- oder Drei-Quark-System zu reduzieren.

Auch auf experimenteller Seite ist das Niederenergieverhalten der QCD nicht direkt zugänglich. Der einzig mögliche, kontollierbare Zugang zur inneren Struktur der Baryonen ist die Anregung des Nukleons mithilfe mesonischer oder elektromagnetischer Sonden. Bedingt durch die extrem kurzen Lebensdauern der angeregten Baryonzustände können lediglich deren Zerfallsprodukte nachgewiesen werden. Dementsprechend haben sich die experimentellen Anstrengungen, Informationen über Baryonresonanzen zu gewinnen, auf die Produktion von Mesonen am Nukleon konzentriert.

Da die Gitter-QCD noch weit davon entfernt ist, Nieder- und Mittelenergiestreuprozesse berechnen zu können, müssen effektive Methoden zur Untersuchung der dynamischen Struktur solcher Prozesse herangezogen werden. Dabei wird die innere Struktur der Baryonen insofern berücksichtigt, dass explizite Resonanzzustände eingeführt werden, deren Eigenschaften durch Vergleich mit den experimentellen Observablen bestimmt werden. Ziel ist, die extrahierten Eigenschaften letztendlich mit den Vorhersagen der Gitter-QCD bzw. der Quark-Modelle zu vergleichen.

Der Großteil der Informationen über die bislang experimentell identifzierten Nukleonresonanzzustände stammt aus Partialwellenanalysen der Reaktionen $\gamma N \to \pi N$ und $\pi N \to \pi N$ (und zum Teil auch $\pi N \to 2\pi N$). Dies ist auch der Grund dafür, dass diese Resonanzen nach dem relativen πN-Bahndrehimpuls L, dem total Isospin I und dem totalen Drehimpuls J klassifiziert werden. Für einige der identifizierten Resonanzen — wie beispielsweise die $L_{(2I)(2J)} = P_{33}(1232)$- ($\Delta$-) Resonanz, die die elastische πN-Streuung im unteren Energiebereich dominiert — finden die verschiedenen Analysen übereinstimmende Massen und Breiten, während es für andere wie die $S_{11}(1535)$-Resonanz große Unterschiede gibt. Im speziellen Fall der $S_{11}(1535)$ liegen die Unterschiede in der Nähe zur ηN-Produktionsschwelle begründet, was bereits zeigt, dass in vielen Fällen die simultane Berücksichtigung möglichst vieler Endzustände mithilfe so genannter Coupled-Channel-Analysen notwendig ist. Auf der anderen Seite sagen die Quark-Modelle ein wesentlich umfangreicheres Resonanzspektrum voraus als bislang in der Pionenproduktion gefunden wurde. Dies führte zu Spekulationen, dass viele der Resonanzen nur in anderen Produktionskanälen identifiziert werden könnten, was zur Grundlage einer Vielzahl von Analysen wurde, die sich auf die Suche dieser fehlenden Resonanzen konzentrierten. Leider haben fast alle dieser Analysen den Nachteil, dass sie sich lediglich auf einen Produktionskanal beschränken und dadurch vernachlässigen, wie sich die extrahierten Resonanzeigenschaften über Rückstreuung auf andere Reaktionskanäle auswirken. Aus diesem Grund besteht auf dem Gebiet der Nukleonresonanzanalyse ein großes Interesse an Modellen, die gleichzeitig alle wichtigen Reaktionskanäle berücksichtigen und analysieren. Andererseits bedeutet dies allerdings auch die Bestimmung einer Vielzahl a priori unbekannter Resonanzmassen und -kopplungen. Die Prämisse solch eines Modells sollte daher nicht nur die simultane Analyse sämtlicher Kanäle in einem möglichst großen Energiebereich sein, sondern auch *konsistent* den gleichen Lagrangian für die pion- und die photoninduzierten Reaktionen zu benutzen. Dabei werden alle nichtresonanten Beiträge dynamisch durch Born-, u- und t-Kanalbeiträge gleichzeitig für sämtliche Partialwellen erzeugt und die Anzahl der freien Parameter enorm reduziert. Da die QCD als die der starken Wechselwirkung zu Grunde liegende Theorie allgemein akzeptiert ist, sollte eine effektive Lagrangetheorie idealerweise aus der QCD abgeleitet sein und dadurch so gut wie möglich die Eigenschaften der QCD widerspiegeln. Demnach sollte die effektive Theorie die selben Symmetrien erfüllen, während die enthaltenen Freiheitsgrade durch Mesonen und Baryonen anstelle von Quarks und Gluonen beschrieben werden. Für die πN-Streuung erfordert dies die Konformität mit der chiralen Symmetrie, die eine wichtige Rolle im Niederenergiebereich der Pion-Nukleon-Physik spielt.

Ein Weg in Richtung der simultanen Analyse aller wichtigen Reaktionskanäle unter gleichzeitiger Berücksichtigung der genannten Bedingungen ist durch das Modell von Feuster und Mosel [51, 52, 53] geebnet worden. In dieser Nukleonresonanzanalyse im Schwerpunktsenergiebereich bis zu 1,9 GeV ist die Produktion der Endzustände γN, πN, $2\pi N$, ηN und $K\Lambda$ im Rahmen einer unitären, effektiven Lagrangetheorie berücksichtigt worden, wobei die Komplexität des $2\pi N$-Systems durch Einführung eines effektiven ζN-Endzustands approximiert worden ist. Eine wichtige Schlußfolgerung ist gewesen, dass die zusätzliche Berücksichtigung der experimentellen Photoproduktionsdaten von elementarer Bedeutung für die verlässliche Extraktion der Resonanzeigenschaften ist. Allerdings sind durch die Vernachlässigung des wichtigen Vektormesonenendzustands ωN Unzulänglichkeiten bei der gleichzeitigen Beschreibung der beinhalteten Kanäle bei höheren Energien zu Tage getreten.

Demzufolge wird in der hier vorgestellten Arbeit das Modell von Feuster und Mosel erweitert, um auch den ωN-Endzustand einzubeziehen und somit die verlässliche Extraktion der Eigenschaften von energetisch höher liegenden Resonanzen zu ermöglichen. Dieser Endzustand ist bislang noch nicht konsistent und in seiner vollen Komplexität in einem Coupled-Channel-Modell berücksichtigt worden. Die zuvor entwickelten Modelle betrachteten diesen Endzustand meist isoliert, wodurch der Produktionsmechanismus nur wenigen Einschränkungen unterlag. Dies ändert sich vollständig in einer Coupled-Channel-Rechnung, da sich jede Änderung der ωN-Beschreibung durch Unitarität und Rückstreuung sofort auf alle anderen Kanäle und insbesondere die πN-Produktion auswirkt.

Vektormesonenproduktion am Nukleon ist aber auch an sich bereits von großem Interesse. Da Vektormesonen elektromagnetisch in Leptonenpaare zerfallen, stellen sie eine ideale Sonde dar, um die Eigenschaften von heißer und dichter Materie, die bei Schwerionenstößen entsteht, zu untersuchen. Da Leptonen lediglich über die elektroschwache Kraft wechselwirken, erlaubt ihr Nachweis einen direkten Zugang zur Untersuchung des Einflusses des umgebenden Mediums auf die Eigenschaften der Vektormesonen. In der Tat wird die Überhöhung der in ultrarelativistischen Schwerionenkollisionen beobachteten Dileptonenerzeugungsrate bei kleinen invarianten Dileptonenmassen derzeit als Veränderung der Masse und Breite des ρ-Vektormesons in Kernmaterie interpretiert. Zur zuverlässigen und schlüssigen Untersuchung solcher QCD-Phänomene ist das Verständnis des zu Grunde liegenden fundamentalen Prozesses der Vektormesonenproduktion im Vakuum essentiell. Auf experimenteller Seite werden hierzu in naher Zukunft Untersuchungen durch die Analyse der Dileptonenproduktion mit dem Spektrometer HADES an der GSI in Darmstadt durchgeführt.

Wie erwähnt erfordert die theoretische Analyse von energetisch höher liegenden Resonanzen und der Vektormesonenproduktion die Minimierung von Freiheiten mit Hilfe der Berücksichtigung von Unitaritätseffekten und aller wichtigen Endzustände. In der vorliegenden Arbeit wird das erweiterte Coupled-Channel effektive Lagrangemodell präsentiert, vollständig diskutiert und die Ergebnisse vorgestellt. Es stellt sich heraus, dass sich neben dem ωN-Endzustand auch der $K\Sigma$-Endzustand auf die Beschreibung der übrigen Reaktionskanäle merklich auswirken kann. Insbesondere die $K\Lambda$-Produktion erweist sich als darauf sensitiv. Durch die nun erreichte simultane Berücksichtigung der Endzustände γN, πN, $2\pi N$, ηN, $K\Lambda$, $K\Sigma$ und ωN spielt dieses Modell eine herausragende Rolle für die Analyse von Nukleonresonanzen im Energiebereich bis 2 GeV.

Das Wechselwirkungspotential, welches die Reaktionen zwischen allen erwähnten Endzuständen beschreibt, wird in der Arbeit diskutiert, insbesondere im Hinblick auf die berücksichtigten Symmetrien und im Vergleich mit anderen Modellen. In dem vorgestellten Modell wird die Unitarität durch die sogenannte K-Matrix-Bornnäherung gewahrt, welche es erlaubt, die vierdimensionale Integralgleichung (Bethe-Salpeter-Gleichung), die die Streuprozesse beschreibt, in eine algebraische Gleichung umzuformen, die durch einfache Matrixinvertierung gelöst wird. Dafür ist allerdings noch eine zusätzliche Partialwellenzerlegung sämtlicher Reaktionsamplituden in die Quantenzahlen Isospin I, totaler Drehimpuls J und Parität P notwendig. Aufgrund seiner Quantenzahlen wird für die Partialwellenzerlegung des ωN-Endzustands nach J und P eine Erweiterung des in der Literatur üblichen Formalismus notwendig. Die hier vorgestellte Methode erlaubt es, sämtliche berücksichtigten Reaktionen einheitlich zu handhaben und lässt sich insbesondere auf beliebige Meson- und Photon-Baryon-Reaktionen anwenden. Es wird auch gezeigt, wie sich die dadurch extrahierten Helizitätspartialwellen leicht in der in der Literatur üblichen Partialwellenform darstellen lassen. Die letztlich noch notwendige Berechnung der spinabhängigen Amplituden wird in einer vereinheitlichten Beschreibung für sämtliche Reaktionskanäle präsentiert.

Ein Problem bei der simultanen Beschreibung einer Vielzahl von Reaktionskanälen stellt die Behandlung der experimentellen Datenbasis dar. Für die verschiedenen pion- und photoninduzierten Reaktionen variieren die experimentellen Daten sowohl in Quantität als auch in Qualität. Während beispielsweise sehr detaillierte Daten zur Pionenproduktion im gesamten betrachteten Energiebereich zur Verfügung stehen, ist die Datenlage zur ω-Produktion sehr eingeschränkt. Daher ist es notwendig, einen Ausgleich in der experimentellen Datenbasis zu schaffen und die experimentellen Fehler sinnvoll zu modifzieren.

Die Extraktion der Resonanz- und Hintergrundeigenschaften durch Vergleich des Modells mit der so modifizierten Datenbasis erlaubt eine Vielzahl von Untersuchungen. Der erste Schritt in der Analyse ist die alleinige Berücksichtigung der pioninduzierten Reaktionen (hadronischer Fit), da der dadurch reduzierte Parameterraum sich numerisch leichter behandeln lässt. Darauf aufbauend lassen sich dann Rechnungen durchführen, in denen die gesamte pion- und photoninduzierte Datenbasis berücksichtigt wird (globaler Fit). Die gleichzeitige Einbeziehung des γN-Endzustands gestattet die Verwendung einer wesentlich größeren und genaueren Datenbasis und somit strengerer Tests, was die Resonanzbeiträge betrifft.

Für die pioninduzierten Reaktionen lassen sich die Auswirkungen verschiedener Spin-$\frac{3}{2}$-Resonanzkopplungen, die zu unterschiedlichen Hintergrundbeiträgen (Offshellbeiträgen) in den Spin-$\frac{1}{2}$-Partialwellen führen, untersuchen. Die Ergebnisse für die beiden hier implementierten Kopplungen sind sehr ähnlich, doch es stellt sich heraus, dass durch die zusätzlichen Offshellbeiträge in den Spin-$\frac{1}{2}$-Partialwellen eine bessere Beschreibung der experimentellen Daten möglich ist. Die Notwendigkeit von zusätzlichem Hintergrund im Spin-$\frac{1}{2}$-Sektor wird auch dadurch deutlich, dass die Beiträge der t-Kanaldiagramme bei ausgeschalteten Offshellbeiträgen wichtiger werden. Die Untersuchung des Einflusses der chiralen Symmetrie durch Benutzung verschiedener $\sigma\pi\pi$-Kopplungen innerhalb des Modells zeigt, dass in der Tat eine Wechselwirkung, die im Einklang mit der chiralen Symmetrie steht, nicht nur im Nieder-, sondern auch im Mittelenergiebereich die experimentellen πN-Daten besser beschreibt.

In den globalen Fits stellt sich heraus, dass eine Readjustierung der Parameter, die im hadronischen Fit bestimmt wurden, zur Beschreibung der experimentellen Photoproduktionsdaten notwendig ist. Dies gilt insbesondere für den ηN-und den ωN-Endzustand, aber auch für die assoziierten Strangenessproduktionskanäle $K\Lambda$ und $K\Sigma$. Während dies in den ersten beiden Fällen vor allem an den unzureichenden pioninduzierten Daten liegt, ist in den letzteren beiden Fällen die aufgrund der elektromagnetischen Eichinvarianz verstärkte Bedeutung der Borndiagramme für die Probleme in der Beschreibung der Photoproduktionsdaten verantwortlich. Dies zeigt, dass die Berücksichtigung der Photoproduktionsdaten zur verlässlichen Extraktion von Nukleonresonanzeigenschaften unbedingt notwendig ist. Werden jedoch auch die hadronischen Parameter neu bestimmt, so ist eine gleichzeitige Beschreibung aller pion- und photoninduzierten Reaktionen oben genannter Endzustände mit einem Parametersatz möglich. Im Vergleich zweier verschiedener Formfaktoren für die t-Kanalprozesse zeigt sich allerdings, dass die globale Beschreibung die Benutzung eines bestimmten Formfaktors erfordert. Die im globalen Fit gefundenen Eigenschaften der gut bekannten Resonanzen stimmen mit anderen Analysen überein, und die extrahierten Bornkopplungen sind nicht weit von den aus SU(3)-Betrachtungen erwarteten Werten entfernt. Nebenbei ist es mit dem vorgestellten Modell auch möglich, die Konsistenz der experimentellen Daten untereinander zu überprüfen, wobei aber keine Diskrepanzen feststellbar sind. Einzig in der simultanen Beschreibung des Hintergrunds der Spin-$\frac{1}{2}$-Partialwellen in $\pi N \to \pi N$ und $\gamma N \to \pi N$ ergeben sich Schwierigkeiten innerhalb des Modells.

In der Analyse der energetisch höher liegenden Endzustände $K\Lambda$, $K\Sigma$ und ωN finden sich deutliche Hinweise auf Resonanzen in den Partialwellen $IJ^P = \frac{1}{2}\frac{3}{2}^+$ (P_{13}) zwischen 1,9 und 2 GeV, $IJ^P = \frac{1}{2}\frac{3}{2}^-$ (D_{13}) um 1,95 GeV, $IJ^P = \frac{3}{2}\frac{1}{2}^+$ (P_{31}) um 1,71 GeV und $IJ^P = \frac{3}{2}\frac{3}{2}^+$ (P_{33}) am oberen Ende des betrachteten Energiebereichs (2 GeV). Insbesondere die identifizierte $P_{13}(1900)$-Resonanz spielt eine wichtige Rolle in den Produktionsmechanismen dieser Endzustände. Umgekehrt erweisen sich diese höher liegenden Endzustände als sehr sensitiv auf die Beiträge dieser Resonanzen und erlauben es somit, deren Eigenschaften genauer festzulegen.

Gerade zur zuverlässigen Bestimmung der Eigenschaften solcher Resonanzen, die bislang noch nicht eindeutig identifiziert worden sind, ist die Berücksichtigung von Rückstreuungseffekten unvermeidlich. Beispielsweise stellt sich heraus, dass, obwohl die $P_{13}(1900)$ wichtig für den $K\Lambda$-Produktionsmechanismus ist, die beobachtete Überhöhung des totalen Photoproduktionswirkungsquerschnitts um 1,9 GeV nicht auf diese Resonanz, sondern auf einen Interferenzeffekt verschiedener Hintergrundbeiträge zurückzuführen ist. Andererseits beeinflusst die $P_{13}(1900)$ auch die Eigenschaften der $P_{13}(1720)$ im Vergleich zu vorherigen Analysen. Insbesondere wird die Bedeutung der $P_{13}(1720)$ für die $K\Lambda$-Produktion verstärkt, so dass sie sowohl die pion- als auch die photoninduzierte Reaktion dominiert. Dies führt weiterhin dazu, dass die Diskrepanz zwischen der P_{11}-πN-Inelastizität und dem $2\pi N$-Partialwellenwirkungsquerschnitt oberhalb von 1,6 GeV nun nicht mehr durch die $K\Lambda$-Produktion, sondern durch eine große $P_{11}(1710)$-ηN-Zerfallsbreite erklärt wird. Nichtsdestotrotz werden weitere Polarisationsdaten oberhalb von 1,7 GeV besonders für ηN und ωN benötigt, um die Rolle oben genannter Resonanzen endgültig klären zu können.

Der $K\Sigma$-Produktionsmechanismus wird durch $J^P = \frac{1}{2}^+$-Wellen dominiert, die durch die

Beiträge der $P_{11}(1710)$- und der $P_{31}(1750)$-Resonanzen erzeugt werden. Die $P_{11}(1710)$ bestimmt auch die ωN-Produktion in der Nähe der Schwelle, während in diesem Kanal für höhere Energien die $P_{13}(1900)$ überwiegt. Dieses Ergebnis steht im Gegensatz zu sämtlichen anderen (Einkanal-) Analysen zur ωN-Produktion. Ebenso stellt sich heraus, dass der ωN-Kanal großen Einfluss auf die assozierte Strangenessproduktion ($K\Lambda$ und $K\Sigma$) hat.

Da im vorgestellten Modell alle wichtigen Endzustände bis zu Energien von 2 GeV implementiert sind, ist es ebenfalls möglich, Abschätzungen für die Beiträge der verschiedenen Endzustände zur GDH-Summenregel zu machen. Die gefundenen Beiträge von $K\Lambda$, $K\Sigma$ und ωN sind klein, unterscheiden sich aber deutlich von Werten, die in Einkanalanalysen extrahiert worden sind.

Es existieren allerdings auch Anzeichen dafür, dass es notwendig ist, das in dieser Arbeit vorgestellte Modell noch zu erweitern. Unter der Annahme, dass die hier verwendeten $2\pi N$-Daten richtig sind, finden sich in den $J^P = \frac{3}{2}^+$-Wellen Hinweise für wichtige zusätzliche $3\pi N$-Endzustandsbeiträge, die bislang nicht berücksichtigt sind. Es zeigt sich auch, dass eine physikalisch korrekte Behandlung des $2\pi N$-Systems notwendig ist, um das Niederenergieverhalten der $J^P = \frac{3}{2}^-$-Partialwellen unterhalb der $D_{13}(1520)$- und $D_{33}(1700)$-Resonanzen vollständig erklären zu können. Ein weiterer Hinweis zur Notwendigkeit der Erweiterung des Modells in diese Richtung ist in fehlenden Hintergrundbeiträgen in der Comptonstreuung zu finden, die durch $2\pi N$-Rückstreuung erzeugt werden könnten. Da aus vielen Analysen bekannt ist, dass Spin-$\frac{5}{2}$-Resonanzen wichtige Beiträge zur Comptonstreuung oberhalb von 1,6 GeV liefern, solche jedoch im vorgestellten Modell bislang nicht enthalten sind, ist die Analyse dieses Kanals auf den Energiebereich unterhalb von 1,6 GeV beschränkt. Da jedoch ohne solche Resonanzen sämtliche Daten zur ηN-, $K\Lambda$-, $K\Sigma$- und ωN-Produktion hier dennoch gut beschrieben werden können, scheinen sie keine große Rolle in diesen Reaktionen zu spielen. Dies wird zur Zeit in weiterführenden Rechnungen untersucht [162].

Die für die Berücksichtigung des ωN-Endzustands notwendig gewordene Vereinheitlichung der Partialwellenzerlegung erlaubt es nun, auf unkomplizierte Weise eine realistischere Beschreibung des $2\pi N$-Endzustands durch Aufspaltung in ρN und $\pi\Delta$ zu implementieren. Mithilfe dieser Endzustände ist es möglich, den $2\pi N$-Dreiteilchenphasenraum zu imitieren und sich gleichzeitig auf Zweiteilchenunitarität zu beschränken. Die zusätzliche Mitnahme der Spektralfunktionen des ρ-Mesons und des Δ-Baryons würde es schließlich erlauben, den $2\pi N$-Endzustand vollständig innerhalb des vorgestellten Modells zu beschreiben. Diese Erweiterung wird voraussichtlich die Beschreibung der D_{I3}-Partialwellen unterhalb der ersten Resonanzen verbessern und den benötigten zusätzlichen Hintergrund in der Comptonstreuung erzeugen.

Während für höhere Energien die korrekte Berücksichtigung sämtlicher durch Unitarität verursachter Schwelleneffekte von hauptsächlicher Bedeutung ist, werden für niedrigere Energien ebenso bedeutsame Effekte durch die Analytizität erwartet. Da durch die implementierte K-Matrix-Bornnäherung die analytischen Eigenschaften der Bethe-Salpeter-Gleichung verloren gehen, wäre es auch erstrebenswert, das vorgestellte Model über diese Näherung hinaus zu erweitern, und somit, ähnlich wie Kondratyuk und Scholten [100], auch Auswirkungen der Analytizität auf die Streuprozesse untersuchen zu können.

Danksagung

Zu guter Letzt darf natürlich ein Dankeswort an all diejenigen nicht fehlen, die auf direkte oder indirekte Weise zum Gelingen dieser Arbeit beigetragen haben.

An erster Stelle möchte ich Prof. Dr. Ulrich Mosel für die Aufnahme an seinem Institut sowie die interessante Themenstellung und seinem Interesse am Fortgang dieser Arbeit danken. Weiterhin hat er mir die Teilnahme an vielen Konferenzen und mehrere Auslandsaufenthalte ermöglicht.

Meinem (finalen) Zimmerkollegen Marcus Post kommt auch großer Dank zuteil, da er sich (fast) nie genervt von meinen zahlreichen Diskussionsanregungen zeigte und stets ein offenes Ohr und offene Kritik parat hatte. Nicht zu vergessen, dass er sich durch die ersten Entwürfe dieser Arbeit quälte.

Dem gesamten Institut sei gedankt für die gute und produktive Stimmung, im Besonderen Sascha Juchem, Gunnar Martens, Dr. Stephan (Öll) Leupold, PD Dr. Carsten Greiner, Thomas Falter und Jürgen Lehr. Zu vergessen ist natürlich auch nicht mein Mittags- und Langzeitstudiengenosse Dr. Martin Kotulla, dem ich für all die vielen Diskussionen danke.

Ein Dank geht auch an die Ehemaligen, die mich am Anfang dieser Promotion noch begleitet und mir den Arbeitsalltag wesentlich erleichtert hatten, insbesondere Dr. Thomas Feuster, Dr. Wolfram Peters, Dr. Frank Hofmann, Dr. Alexander (Hombi) Hombach, Tino Mehlmann, Mathias Th. (Matze) Keil, ...

I thank Barry Ritchie for providing the preliminary CLAS data on η photoproduction and Walter Schwille for providing the preliminary SAPHIR data on ω photoproduction. Special thanks also go to the George Washington University, Washington D.C./USA and in particular to Cornelius Bennhold for the invitations and the hospitality.

Elke Jung und Christiane Pausch standen mir beim immerwährenden Kampf mit Formularen, Leihscheinen, Fristen und allen übrigen bürokratischen Hemmnissen stets hilfreich zur Seite.

Auch danke ich meinen Eltern, die immer wieder ein aufmunterndes Wort in allen Lagen für mich parat hatten. Und zu guter Letzt möchte ich noch Katja und unseren kleinen Sonnenschein Jan erwähnen, ohne deren kleine und große Ablenkungen mein Alltag doch um einiges grauer wäre.